

REPORT DOCUMENTATION PAGE

Form Approved
OMB-No. 0704-0188

Public reporting burden for this collection of information is estimated to average 1 hour per response, including the time for reviewing instructions, searching existing data sources, gathering and maintaining the data needed, and completing and reviewing the collection of information. Send comments regarding this burden estimate or any other aspect of this collection of information, including suggestions for reducing this burden, to Washington Headquarters Services, Directorate for Information Operations and Reports, 1215 Jefferson Davis Highway, Suite 1204, Arlington, VA 22202-4302, and to the Office of Management and Budget, Paperwork Reduction Project (0704-0188), Washington, DC 20503.

1. AGENCY USE ONLY (Leave blank)		2. REPORT DATE	3. REPORT TYPE AND DATES COVERED FINAL 01 May 96 To 31 Oct 96	
4. TITLE AND SUBTITLE TENTH INTERNATIONAL SYMPOSIUM ON MOLTEN SALTS			5. FUNDING NUMBERS F49620-96-1-0157 2303/BS 61102F	
6. AUTHOR(S) Dr Richard T. Carlin				
7. PERFORMING ORGANIZATION NAME(S) AND ADDRESS(ES) The Electrochemical Society, Inc. 10 South Main Street Pennington NJ 08534-1902			AFOSR-TR-96 0579	
9. SPONSORING/MONITORING AGENCY NAME(S) AND ADDRESS(ES) AFOSR/NL 110 Duncan Ave Room B115 Bolling AFB DC 20332-8080 Capt. Hugh C. De Long			10. SPONSORING/MONITORING AGENCY REPORT NUMBER	
11. SUPPLEMENTARY NOTES				

12a. DISTRIBUTION/AVAILABILITY STATEMENT

12b. DISTRIBUTION CODE

Approved for public release:
distribution unlimited.

13. ABSTRACT (Maximum 200 words)

The symposium was attended by internationally recognized speakers from sixteen countries. Sixty-six papers were presented at the symposium of which fifty-four are contained in this proceedings volume. Much of the symposium centered around technological opportunities in molten salts and related materials. In keeping with this theme, Prof. Niels J. Bjerrum in his 1996 Max Bredig Award address emphasized that molten salt electrochemistry has a rich past with a bright future in numerous technologically important areas, including alloy electrodeposition, production of amorphous metals, electrosynthesis of superhard materials, electrocatalysis, and corrosion. Of course, the basis for these technological advances is derived from the fundamental understanding of molten salts provided by numerous researchers, and excellent papers were presented that provided further insight into the complexity of molten salt thermodynamics, transport properties, structure, and spectroscopy.

14. SUBJECT TERMS			15. NUMBER OF PAGES	
			16. PRICE CODE	
17. SECURITY CLASSIFICATION OF REPORT (U)	18. SECURITY CLASSIFICATION OF THIS PAGE (U)	19. SECURITY CLASSIFICATION OF ABSTRACT (U)	20. LIMITATION OF ABSTRACT (U)	

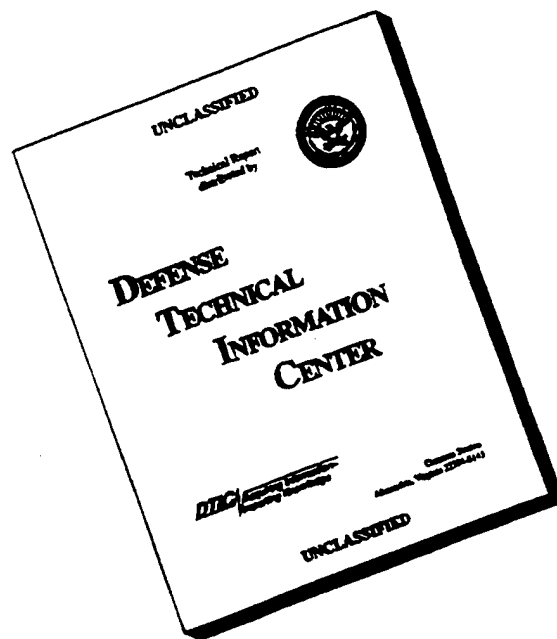
Approved to release,
distributed unlimited

AIR FORCE OF SCIENTIFIC RESEARCH (AFSC)
NOTICE OF TECHNICAL TALK

This technical report is classified and is
approved for release under AFM 190-12
distributed.

Joan Boyd,
STINFO Program Manager

DISCLAIMER NOTICE



**THIS DOCUMENT IS BEST
QUALITY AVAILABLE. THE
COPY FURNISHED TO DTIC
CONTAINED A SIGNIFICANT
NUMBER OF PAGES WHICH DO
NOT REPRODUCE LEGIBLY.**

PROCEEDINGS OF THE TENTH
INTERNATIONAL SYMPOSIUM ON

MOLTEN SALTS

Editors

Richard T. Carlin
Covalent Associates, Inc.
Woburn, Massachusetts

Shigehito Deki
Kobe University
Kobe, Japan

Morio Matsunaga
Kyushu Institute of Technology
Kitakyushu, Japan

David S. Newman
Bowling Green State University
Bowling Green, Ohio

J. Robert Selman
Illinois Institute of Technology
Chicago, Illinois

Gery R. Stafford
National Institute of Standards
and Technology
Gaithersburg, Maryland

19961205 046

PHYSICAL ELECTROCHEMISTRY AND
HIGH TEMPERATURE MATERIALS DIVISIONS

Proceedings Volume 96-7

DTC QUALITY INSPECTED 4



THE ELECTROCHEMICAL SOCIETY, INC.,
10 South Main St., Pennington, NJ 08534-2896

Copyright 1996 by The Electrochemical Society, Inc.
All rights reserved.

This book has been registered with Copyright Clearance Center, Inc.
For further information, please contact the Copyright Clearance Center,
Salem, Massachusetts.

Published by:

The Electrochemical Society, Inc.
10 South Main Street
Pennington, New Jersey 08534-2896
Telephone (609) 737-1902
Fax (609) 737-2743

ISBN 1-56677-159-5

Printed in the United States of America

PREFACE

The Tenth International Symposium on Molten Salts was held during the 189th Meeting of the Electrochemical Society in Los Angeles, California, May 6-10, 1996. Financial support for this symposium came from several generous sources, including the Physical Electrochemistry and High Temperature Materials Divisions of the Society, the Molten Salt Committee of the Electrochemical Society of Japan, and the Air Force Office of Scientific Research. In addition to these contributors, acknowledgement is made to the Donors of The Petroleum Research Fund, administered by the American Chemical Society, for partial support of this symposium. The co-organizers of this symposium were Richard T. Carlin, Covalent Associates, Shigehito Deki, Kobe University, Morio Matsunaga, Kyushu Institute of Technology, David S. Newman, Bowling Green State University, J. Robert Selman, Illinois Institute of Technology, David A. Shores, University of Minnesota, and Gery R. Stafford, National Institute of Standards and Technology.

The symposium was attended by internationally recognized speakers from sixteen countries. Sixty-six papers were presented at the symposium of which fifty-four are contained in this proceedings volume. Much of the symposium centered around technological opportunities in molten salts and related materials. In keeping with this theme, Prof. Niels J. Bjerrum in his 1996 Max Bredig Award address emphasized that molten salt electrochemistry has a rich past with a bright future in numerous technologically important areas, including alloy electrodeposition, production of amorphous metals, electrosynthesis of superhard materials, electrocatalysis, and corrosion. Of course, the basis for these technological advances is derived from the fundamental understanding of molten salts provided by numerous researchers, and excellent papers were presented that provided further insight into the complexity of molten salt thermodynamics, transport properties, structure, and spectroscopy.

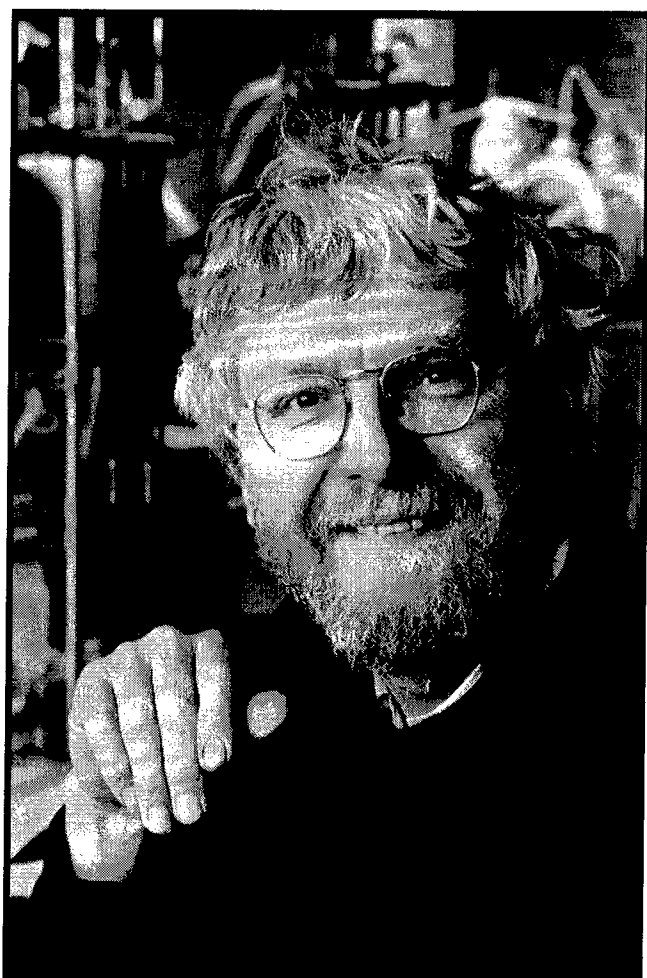
During the past two years, we have lost two exceptional colleagues -- Profs. Gleb Mamantov and Tormod Førlund. The opening session of this symposium was dedicated to Prof. Mamantov, whose dynamic career and life were eloquently celebrated in the proceedings of the Ninth International Symposium on Molten Salts as the recipient of the 1994 Max Bredig Award. Prof. Førlund's outstanding contributions to molten salts and to the world are memorialized in this proceedings volume.

The senior editor wishes to express his appreciation to the Staff of The Electrochemistry Society, especially, Mr. John Stanley and Mr. Brian Rounsavill, for their support and cooperation. Also, special thanks are due to Dr. Joan Fuller for her untiring help during both the symposium and the proceedings preparation and to Ms. Johanna Fox at Covalent Associates for her assistance throughout this process.

Richard T. Carlin,
Covalent Associates, Inc., June, 1996

Niels J. Bjerrum

Recipient of the 1996 Max Bredig Award



NIELS J. BJERRUM
1996 Recipient of the Max Bredig Award

Niels J. Bjerrum received his university education at the University of Copenhagen (1958-1964). After graduating he received a post-doctoral fellowship from the Oak Ridge National Laboratory (1964-1966) where he worked on molten salt systems, investigating the lower oxidation states of bismuth in chloroaluminate melts and tellurium. It was at this time that he became acquainted with several prominent scientists, including Max Bredig.

In 1966 Dr. Bjerrum left Oak Ridge and took a position at the Technical University of Denmark as an Assistant Professor. At the university he continued the work he had begun at Oak Ridge, first working with the lower oxidation states of tellurium then continuing with those of selenium and sulfur. In 1971 Dr. Bjerrum was promoted to Associate Professor, and in 1976 he was awarded an honorary Danish prize of the Ole Rømer Foundation. The cycle came full circle in 1979 when he was the recipient of the Ellen and Niels Bjerrum Prize in Chemistry, an award named after his grandfather Niels Bjerrum (1879-1958).

In 1982 Dr. Bjerrum received the degree Doctor of Science for his work on sulfur, selenium, and tellurium in chloroaluminate melts. That same year he and a small group of like minded scientists established a new scientific academy in Denmark, The Danish Academy of Natural Sciences. Dr. Bjerrum was named Secretary for this new academy, a position he still holds. Since this time the work at the academy has taken on a more electrochemical nature, including work on the development of molten salt batteries inspired by work done in the United States at Argonne National Laboratory.

In 1989 Dr. Bjerrum was promoted to a Full Professorship at the Technical University of Denmark, and in 1992 he became a Foreign Member of the Ukrainian Academy of Sciences. Since then he has been honored with the Højgaard & Schultz Jubilee Prize, a prestigious Danish Award (1994) and has been named as a Foreign Member of the Norwegian Academy of Technological Sciences (1995).

Tormod (Tommy) Førland
June 6, 1920 - November 10, 1995



Tormod Førland, Emeritus Professor of Physical Chemistry at the Norwegian University of Science and Technology (NTNU) died suddenly on November 10, 1995. He was a brilliant pioneer in molten salt chemistry and was at home with both theory and experiment. With Haakon Flood and Kai Grjotheim giant strides were made in understanding a complex problem in reciprocal salt systems in which some components can have large negative deviations from ideal behavior while others can have large positive deviations from ideality. His clarity and depth of understanding simplified the complex and provided the major elements of the modern theory of these systems that accurately predicts their thermodynamic properties. His theoretical and experimental work on mixing "asymmetric" binary systems with two cations of different charge was a *tour de force* and, among other advances, it illustrated the importance of representing the excess free energies of mixing (logarithm of the activity coefficients) in terms of equivalent fractions. This concept has greatly simplified the mathematical representations of these systems and made computer predictions of thermodynamic properties simpler and more robust. His contribution to molten silicate chemistry are incorporated into most theories of these complex melts. These and many other ideas have left an indelible mark on many aspects of molten salt chemistry.

Around 1965, he became interested in irreversible thermodynamics and focused on rewriting the formal equations used at that time for irreversible processes in ionic systems in order to represent them in terms of components and not ions. The old formalisms often led to incorrect solutions of the equations. His work, with the collaboration of his wife, Katrine Seip Førland, and his successor and former student, Signe Kjelstrup, led to a new formalism that avoided the pitfalls and errors made with the old ways. Their book, "Irreversible Thermodynamics, Theory and Applications" (John Wiley and Sons, Chichester, 1988) is already considered by many to be a classic. Applications of these theories by the authors and coworkers were made to a variety of subjects including biology (e.g., muscle contraction, ionic transport in mitochondria) and engineering (e.g., and explanation of frost heave). Some of his most recent papers are electrochemical, *i.e.*, on transference numbers in molten salts, an alternative approach to electrochemistry and a theory of a solid state electrode. His breadth of understanding is further reflected in many of his other papers on a variety of subjects.

Tommy and his wife, Katrine (Tine), had a deep interest in the world about them. They spent a number of years in Kenya and Tanzania with the support of the Norwegian Agency for International Development (1967-69, 1973-74, 1980-81, 1990-91, 1992-93). In 1970 they recommended the establishment of chemical engineering studies to meet the

needs of a growing chemical industry in Africa. After many years of discussions a chemical engineering unit was established in 1976 which evolved to become the Department of Chemical and Process Engineering in the Faculty of Engineering of the University of Dar Es Salaam in Tanzania. The Førland's continued to be associated with the University.

Tommy received many honors from different organizations including The Norwegian Chemical Society, the University of Dar Es Salaam, the Gunneras Medal of the Norwegian Society of Sciences and Letters and won a prize from Nyfotek A/S for the application of a novel reference electrode concept to technological problems.

Tommy was gentle and soft spoken, his scientific accomplishments were many and important and his contribution to the world was selfless and generous. We will miss him.

Milton Blander
QUEST Research
June, 1996

TABLE OF CONTENTS

Max Bredig Award

Molten Salt Electrochemistry: Present and Future Priorities N. J. Bjerrum	1
--	---

Opening Session: A Dedication to Gleb Mamantov

Minimizing Fouling and Corrosion by Ionic Liquids Formed in the Combustion of Biomass M. Blander.....	3
Vibrational Modes and Structure of Rare Earth Fluorides and Bromides in Binary Melts: $\text{LnX}_3\text{-KX}$ ($\text{X}=\text{F}, \text{Br}$; $\text{Ln}=\text{Y}, \text{La}, \text{Ce}, \text{Nd}, \text{Sm}, \text{Gd}, \text{Dy}, \text{Yb}$) B. Borresen, V. Dracopoulos, G. Photiadis, B. Gilbert, and G. N. Papatheodorou	11
Effects of Hydrophobic Interaction in <i>n</i> -Alkanecarboxylate Hydrate Melt S. Deki, H. Nakahara, J. Kondo, and A. Kanjinami.....	28
Electrodeposition of Cobalt-Aluminum Alloys from the Aluminum Chloride-1-Methyl-3-Ethylimidazolium Chloride Room-Temperature Molten Salt C. L. Hussey, J. A. Mitchell, W. R. Pitner, and G. R. Stafford.....	36
Near Infrared Spectroscopy of Anionic Conducting Polymer Membranes D. S. Newman, G. Bi, D. L. Snavely, J. Dubsky, F. Zamborini, and T. S. Cina	53
Electrochemical Reactions of Nitrogen in Molten Chloride System Y. Ito, M. Tada, and T. Goto.....	62

Catalysis and Acid-Base Chemistry

Nonaqueous Room-Temperature Ionic Liquids: A New Class of Solvents for Catalytic Organic Reactions H. Olivier and Y. Chauvin	70
Physico-Chemical and Structural Properties of DeNO_x and SO_2 Oxidation Catalysts S. G. Masters, C. Oehlers, K. Nielsen, K. M. Eriksen, R. Fehrmann, A. Chrissanthopoulos, and S. Boghosian	74

Acidity of HCl in Neutral Buffered Chloroaluminate Molten Salts D. King and R. A. Osteryoung	80
Molten Salt and Related Acids K. E. Johnson, W. D. Chandler, and B. D. Fahlman.....	92
Gutmann Acceptor Properties of LiCl, NaCl, and KCl Buffered Ambient-Temperature Chloroaluminate Liquids R. A. Mantz, P. C. Trulove, R. T. Carlin, and R. A. Osteryoung	104
Electrochemical Studies of Acyl Halide Reduction in a Room-Temperature Molten Salt G. T. Cheek	116
A Study of Binary Molten Pyridinium Salts A. M. Elias, M. E. Elias, and A. J. S. Carmo	125
Measuring the Rates of Solid State Reactions Between AlCl ₃ and C ₅ H ₆ NCI Using Differential Scanning Calorimetry D. S. Newman, J. Rosinski, and K. S. Leis	135
Effect of Alkali Metal Fluoride on Anodic Reaction in a Molten NH ₄ F-HF System A. Tasaka, T. Kawagoe, and T. Osada	144
Spectroscopic Investigation of Effect of Lewis Basicity on the Valent-State of an Uranium (V) Chloride Complex in Ambient Temperature Melts S. Dai, L. M. Toth, G. D. Del Cul, G. R. Hayes, and J. R. Peterson.....	152

Metals and Alloys

Electrodeposition of Magnesium from Halide Melts B. Børresen, G. M. Haarberg, R. Tunold, A. Kiszka, and J. Kazmierczak.....	157
Effect of Additives on Ti Electrorefining in Molten Chloride T. Takenaka, A. Sugimoto, Y. Mitani, and M. Kawakami	171
Cathodic Behavior of the Deposition of Nb and Al in NaCl-AlCl ₃ Melt Y. Sato, K. Iwabuchi, N. Kawaguchi, H. Zhu, M. Endo, T. Yamamura, and S. Saito	179
Electrochemical Properties of Nb ₃ Cl ₈ in the MgCl ₂ -NaCl Eutectic at 471°C M. Mohamedi, N. Kawaguchi, Y. Sato, and T. Yamamura.....	189

Demonstration Experiment of Uranium Metal Production System T. Suzuki, T. Sakata, H. Tsuchiya, K. Ota, Y. Takasawa, N. Teramae, S. Yamagami, and K. Endo	204
A Study of Production Process of Uranium Metal by Molten Salt Electrolysis Using Zinc Cathode - A Study of Uranium Chloride Production Step H. Tsuchiya, T. Sakata, T. Suzuki, J. Takahashi, T. Fukamachi, Y. Kijima, and K. Toyabe	213
Corrosion Behavior of Materials Used in Uranium Metal Production Y. Hoshino, K. Ota, S. Yamagami, K. Endo, H. Tsuchiya, T. Sakata, and T. Suzuki.....	222
Development of Transuranium Elements Recovery from High-Level Radioactive Liquid Waste Y. Akai and R. Fujita	230
Characteristics of Cathodic Reactions in $\text{BaCl}_2\text{-NaCl}$ Melts Containing AlF_3 Components M. Ueda, S. Konda, T. Sasaki, and T. Ishikawa	236
Electrochemical Behavior of Glassy Carbon and Some Metals in a $\text{ZnCl}_2\text{-NaCl}$ Melt Y. Okano and A. Katagiri	244
A New Experimental Approach to Measure Electrical Conductivity of Molten Fluoride Electrolytes X. Wang and R. D. Peterson	254
Titration of Refractory Metal Compounds in Molten Salts by Square Wave Voltammetry P. Chamelot, B. Lafage, and P. Taxil.....	269
EQCM Studies of Aluminum and Aluminum Alloys in Room Temperature Molten Salts H. C. De Long and P. C. Trulove.....	276
EQCM Measurements of Cobalt-Aluminum Alloys H. C. De Long and R. T. Carlin	284
Electrodeposition and Nucleation of Lead from Chloride Melts T. Støre, G. M. Haarberg, T. E. Jentoftsen, and R. Tunold.....	290
High Temperature Electrochemical Synthesis of Zirconium Diboride from Chloro-Fluoride Melts V. P. Lugovoi, S. V. Deviatkin, G. Kaptay, and S. A. Kuznetsov	303

High Temperature Interaction of Boron Oxide with Aluminum Fluoride S. V. Deviatkin, K. I Arsenin, and G. Kaptay	312
Formation of LaNi_5 Film on Nickel Substrate by Electrolysis in Molten Chloride and Its Hydrogen Absorption Property M. Okido, R. Ichino, and R. Tamura	320
Elimination of Primary Silicon Phase in Hyper-Eutectic Al-Si Alloy by Molten Salt Process T. Inoue, H. Kanematsu, Y. Kunieda, S. Hayashi, and T. Oki.....	334

Batteries

Modification of LiCl-LiBr-KBr Electrolyte for LiAl/FeS_2 Batteries T. D. Kaun, A. N. Jansen, G. L. Henriksen, and D. R. Vissers	342
Polarization Phenomena at β "-Alumina/Molten Salt Interface M. Matsunaga, K. Minamoto, and M. Morimitsu	355
Rechargeable Alkali Metal and Li-Al Alloy Anodes in Ionic Liquid Electrolytes R. T. Carlin and J. Fuller	362
Morphology of Lithium and Sodium Electrodeposits in Room-Temperature Molten Salts J. Fuller and R. T. Carlin	372
Electrochemistry of Vanadium Oxides in Room Temperature Molten Salt Electrolytes D. M. Ryan and T. L. Riechel	381

Fuel Cells

The Role of Melt Chemistry in Molten Carbonate Fuel Cell (MCFC) Technology J. R. Selman and M. S. Yazici	388
Mass Transfer and Steady State Concentration Distributions of Binary Electrolytes and Additives in MCFCs Th. Brenscheidt, O. Böhme, and H. Wendt.....	396
High Temperature Corrosion of Tantalum with the Presence of Molten Carbonate K. Ota, K. Toda, T. Kojima, N. Motohira, and No. Kamiya.....	406

High Temperature Corrosion of Separator Material in Li_2CO_3 - Na_2CO_3 and Electrolyte Consumption for MCFC M. Yanagida, K. Tanimoto, T. Kojima, Y. Tamiya, T. Asai, and Y. Miyazaki.....	417
Electrochemical Response of Stainless Steel 310, 316L and Nickel-Rich Alloy in Molten Carbonate M. S. Yazici and J. R. Selman	422
Thermodynamics, Transport Properties, Structure, and Spectroscopy	
Thermochemistry, Physico-Chemical Properties and Modeling of the Liquid MX-LnX_3 Mixtures (M = alkali, Ln = rare-earth, X = halide) M. Gaune-Escard.....	439
Electron Mobilities in Solutions of Alkali Metals in Molten Alkali Halides G. M. Haarberg and J. J. Egan	468
Application of Thermodynamic Databases to Calculation for Surface Tension of Molten Salt Mixtures T. Tanaka and S. Hara	484
Copper Deposition from Cu(I) Ions in CuCl-BPC Molten Salts - Microstructural Analysis of the Melts N. Koura, N. Tanabe, S. Seiki, S. Takahashi, M.-L. Saboungi, L. A. Curtiss, and K. Suzuya.....	492
Ionic Dissociation Model for (Li, K)X Binary Melts (X=F, Cl, Br or I) P. Hebant and G. S. Picard.....	500
Anomalous Behavior of Ag(I) and Tl(I) Ions in Mobilities of Molten Nitrates I. Okada and P. Chou.....	511
New Development of Fiberoptic Raman Spectroscopic Probes for High Temperature Molten Salts S. Dai, H. M. Xiao, Y. H. Lee, and J. P. Young	524
Raman Spectroscopic and Electrochemical Studies of Tungsten Species in Alkali Chloride Melts G. Carountzos, C. Hasiotis, and C. G. Kontoyannis.....	530

Local Structure of K_2O - SiO_2 Glasses and Melts N. Umesaki, K. Handa, N. Ohtori, and N. Kamiyo	541
Author Index	561
Subject Index	563

FACTS ABOUT THE ELECTROCHEMICAL SOCIETY, INC.

The Electrochemical Society, Inc., is an international, nonprofit, scientific, educational organization founded for the advancement of the theory and practice of electrochemistry, electrothermics, electronics, and allied subjects. The Society was founded in Philadelphia in 1902 and incorporated in 1930. There are currently over 6000 scientists and engineers from more than 60 countries who hold individual membership; the Society is also supported by more than 100 corporations through Patron and Sustaining Memberships.

The Technical activities of the Society are carried on by Divisions and Groups. Local Sections of the Society have been organized in a number of cities and regions.

Major international meetings of the Society are held in the Spring and Fall of each year. At these meetings, the Divisions and Groups hold general sessions and sponsor symposia on specialized subjects.

The Society has an active publications program which includes the following:

Journal of The Electrochemical Society - The Journal is a monthly publication containing technical papers covering basic research and technology of interest in the areas of concern to the Society. Papers submitted for publication are subjected to careful evaluation and review by authorities in the field before acceptance, and high standards are maintained for the technical content of the JOURNAL.

Interface - Interface is a quarterly publication containing news, reviews, advertisements, and articles on technical matters of interest to Society Members in a lively, casual format. Also featured in each issue are special pages dedicated to serving the interests of the Society and allowing better communication between Divisions, Groups, and Local Sections.

Meeting Abstracts (*formerly Extended Abstracts*) - Meeting Abstracts of the technical papers presented at the Spring and Fall Meetings of the Society are published in serialized softbound volumes.

Proceedings Series - Papers presented in symposia at Society and Topical Meetings are published from time to time as serialized Proceedings Volumes. These provide up-to-date views of specialized topics and frequently offer comprehensive treatment of rapidly developing areas.

Monograph Volumes - The Society has, for a number of years, sponsored the publication of hardbound Monograph Volumes, which provide authoritative accounts of specific topics in electrochemistry, solid state science, and related disciplines.

For more information on these and other Society activities, visit the ECS Home Page at the following address on the World Wide Web:

<http://www.electrochem.org>.

MOLTEN SALT ELECTROCHEMISTRY: PRESENT AND FUTURE PRIORITIES

Niels J. Bjerrum

Materials Science Group, Chemistry Department A, Technical University of Denmark,
DK-2800 Lyngby, Denmark

Molten salt electrochemistry is by no means a new research area. Some of the initial experiments go back two hundred years in history (e.g., electroreduction of alkali metals) and such an important metal as aluminum has been produced for more than hundred years by an electrolysis of a molten salt electrolyte (the Hall-Héroult process).

However, molten salt electrochemistry is a very dynamic scientific and industrial area of electrochemistry looking not into the past but into the future.

There are numerous important technical areas in molten salt electrochemistry. In some of these areas enough knowledge have been accumulated to develop qualitative improvement and often parameter optimization:

(i) *Electrochemical production of metals* is one of the most mature areas. In connection with aluminum production the main aim of developments is to obtain a higher efficiency of the process and to solve serious ecological problems.

(ii) *Electroplating of protective layers on metal surfaces.* The recent developments are mostly concerned with the electrodeposition of refractory metals from molten salt electrolytes. The most important problem in this technology is control of the composition of the molten electrolytes. Another problem with refractory metal electroplating can be illustrated with the help of the example of tantalum deposition. Two different crystal forms of tantalum can be obtained electrochemically: α - and β -tantalum. The deposit with the α -form has better mechanical properties than that consisting of the β -form. Therefore, the problem of the optimization of the electrolysis parameters has to be solved with allowance for this special factor.

However, the most interesting scientific results and applications are expected in the new areas of molten salt electrochemistry:

(iii) *Metal alloy production* is an area with a considerable potential. This technique gives a possibility to obtain, for example, the alloys of aluminum with lithium (metals with high and low melting points), or in general alloys which are difficult to make by a direct combination.

(iv) *Electrodeposition of amorphous metal layers* is a technique which can be realized in molten salt electrolytes and may be the background for progressive technologies for the production of highly corrosion resistant materials.

(v) *Electrosynthesis of superhard materials*. Many such materials can be obtained electrochemically from boron-, carbon- or nitrogen-containing melts. This could be a relatively cheap technology giving a useful modification of metal surfaces. To the same area we can add the high temperature electrochemical technologies for the improvement of surface properties of superhard materials with electroplated metal layers.

(vi) *High-temperature electrocatalysis* is a process in which material is consumed or produced in an electrochemical reaction on a catalyst that is an electronic conductor. Obviously, the currently most interesting and important cases in this area are the molten carbonate fuel cells. The main problem here is to obtain non-soluble and catalytically active electrode materials.

(vii) *Electrochemical promotion of catalysts* deals with the change of activity or selectivity of molten salt catalysts using inert electrodes. It can provide an effective management concerning quality and composition of the products of the catalytic reactions.

(viii) *Hot corrosion* has the possibility of becoming a very important area of molten salt electrochemistry taking into account the perspective of combustion of new types of fuels or traditional but low quality fuels. It has been proven that the most severe hot corrosion problems are caused by a thin molten salt layer on the surface of the exposed metal and therefore have an electrochemical nature. Another example where hot corrosion is important is provided by high-temperature batteries and molten carbonate fuel cells. Electrochemical techniques can be powerful tools in searching for new ways of corrosion protection.

(ix) *High-temperature electrochemical protection from corrosion*. Cathodic and anodic protection are well known and widely used at ambient temperatures but have not to any extent been used in connection with hot (or molten salt) corrosion. For example, in connection with fire tube corrosion in boilers at power stations electrochemical protection can be one of several possible ways of prolonging the lifetime of power-station hardware.

MINIMIZING FOULING AND CORROSION BY IONIC LIQUIDS FORMED IN THE COMBUSTION OF BIOMASS

Milton Blander
QUEST Research
1004 East 167th Place
South Holland, IL 60473-3114
U.S.A.

ABSTRACT

The combustion of biomass produces ionic liquids which are the probable cause of fouling and corrosion in combustion systems. Calculations of the combustion products of aspen wood at ten atmospheres indicate that a molten potassium sulfate rich liquid forms at high temperatures and is completely crystallized before 1015.3°C. A second liquid rich in calcium and potassium carbonates forms at 909.7°C and crystallizes completely by 802.5°C. This undesirable molten carbonate presents a problem for the combustor and any equipment downstream. Addition of sulfur (or SO₂) to the combustor eliminates the carbonate rich phase and raises the temperature below which no liquid is present to 912.3°C by the formation of a calcium-potassium sulfate rich liquid. The combustion of wheat straw produces a liquid silica-potassium rich silicate containing small quantities of chlorides, sulfates and carbonates at high temperatures which persists to temperatures below 500°C. Mixing the wheat straw with alumina rich mixed paper waste and silica raises the temperature below which no liquid is present to 837°C. Solution theories for the prediction of the properties of multicomponent molten salts and silicates are a key factor in defining the probable cause of fouling and corrosion and in deducing possible solutions to these problems.

INTRODUCTION

Biomass is a possible alternative to fossil fuels which does not lead to a net increase of CO₂ in the atmosphere and produces a non-polluting ash which may be returned to the soil as a fertilizer. However, the combustion of biomass produces molten salts and/or silicates which are the probable root cause of fouling and corrosion in combustion systems. In order to minimize the problems of fouling and corrosion we need to determine the chemistry of these liquids and deduce a means for ameliorating the problems which arise because of them. To do this, we utilize the Conformal Ionic Solution Theory for molten reciprocal salt systems (1) and the Modified Quasichemical Theory (2) for molten silicates which permits one to predict the properties of

multicomponent molten salts and silicates from the subsidiary binaries and, for silicates, also ternaries. These theories are combined with a large database for binary molten salt solutions, binary and ternary molten silicate solutions, solid solutions and over 6000 solid, liquid and gaseous species. All this information is contained in the FACT computer system (3) which also uses the CHEMSAGE algorithm for minimizing the total free energy of a chemical system (4) to calculate the equilibrium chemistry. In this paper, we discuss calculations for two typical kinds of biomass. The first is aspen wood with a composition given in Table I which contains no silica and produces molten carbonate-sulfate salts as combustion products. The second is wheat straw with a composition given in Table II which is high in silica and potassium which produces very low melting silicates as combustion products.

Table I. Composition of aspen wood (wt %)

C	51.57	P	0.0085	S	0.025040
H	6.27	K	0.0810	B	0.000360
N	0.47	Ca	0.1524	Mn	0.001008
O	39.52	Mg	0.0256	Fe	0.001872
		Al	0.001008		

Zn (0.00245 wt %) and Cu (0.000216 wt %) were not included as they form a small amount of benign oxides and Na (0.000432 wt %) was left out because it was overshadowed by potassium which is present in much greater abundance. 188 gm O and 619 gm N were added to 100 gm of aspen wood.

COMBUSTION OF ASPEN WOOD (5)

Because aspen wood has been considered for use in driving a turbine, we will discuss calculations for the combustion of aspen wood in an excess of oxygen at 10 atmospheres. (5) It has been shown that, at this pressure, the calculation of the inorganic chemistry of combustion indicates that a molten potassium sulfate rich liquid is formed at high temperatures, begins to crystallize at 1024.9°C and is completely crystallized at 1015.0°C to form a slightly contaminated (mole fraction 0.998) K_2SO_4 solid. A second liquid rich in calcium and potassium carbonates forms at 909.7°C and crystallizes completely by 802.5°C to a potassium sulfate-carbonate solid solution and $CaCO_3$.

In this paper we will examine the addition of sulfur (or SO_2) to aspen wood. The problem is the carbonate rich liquid. It is formed because the moles of potassium is larger than twice the moles of sulfur in aspen wood (Table I). As a consequence, after the potassium, sulfur and oxygen react to form a sulfate rich liquid, there is a significant amount of basic KOH vapor molecules left in the gas phase as well as solid CaO to react with the weakly acidic CO_2 molecules at low temperatures. The result is a carbonate rich

liquid which is likely to be deleterious to the combustor and to pose a definitive threat to the operation of a downstream turbine. Since $\text{SO}_2 + 1/2\text{O}_2$ is a stronger acid than CO_2 , addition of sulfur (or SO_2) will help to eliminate the molten carbonate phase by forming relatively high melting sulfates at higher temperatures. It is hoped that the separation of the consequent solids can be accomplished by a cyclone and/or filter system to effectively remove these solids well enough to operate a turbine using the combustion effluents with no significant corrosive or erosive effects.

Table II. Elemental composition of 100 moles of wheat straw and 80 moles of waste paper.

Element	Wheat Straw	Waste Paper
C	27.2655	24.59998
H	49.0240	40.49816
N	0.4747	0.06157
O	22.1420	14.17705
S	0.0425	0.02432
Si	0.6528	0.23988
Al	0.0228	0.52877
Ti	0.0008	0.02752
Fe	0.0078	0.00517
Ca	0.0298	0.06853
Mg	0.0387	0.03005
Na	0.0406	0.00874
K	0.1923	0.00173
Cl	0.0542	-----

Calculations were performed at 10 atmospheres at 25° intervals between 1200°C and 600°C for 100 g of the composition of aspen wood given in Table I with 0.115 g of S added. In Table III, one can see that a sulfate rich liquid is already present at 1200°C and, at equilibrium, disappears at 912.3°C to form the solid stoichiometric compounds CaSO_4 and $\text{K}_2\text{Ca}_2(\text{SO}_4)_3$ by a peritectic reaction. The second solid, $\text{K}_2\text{Ca}_2(\text{SO}_4)_3$, decomposes to a K_2SO_4 rich (0.998 K_2SO_4 at 800°C) solid solution and CaSO_4 . If a large fraction of the solid CaO , which is present at very high temperatures, precipitates in the high temperature region of the combustor, the liquid sulfate would be much higher in potassium, would have a higher liquidus temperature and thus would crystallize earlier at a higher temperature. Careful design for this separation might be possible and could improve the efficiency of the combustor. In Table IV, the mole fractions of the important gas species in the 30.769 moles of gas are given. The most important results are the low values for KOH and SO_2 mole fractions at 600°C which are both $<10^{-9}$. Thus we have managed to reduce the KOH content in the gas by the addition of sulfur and prevented the formation of a deleterious molten carbonate without having a significant amount of SO_2 as an environmental pollutant. Other acidic additives might further broaden the range of temperatures in which no ionic liquid is present. In addition to the above gaseous and

solution phases there are a number of stoichiometric solids formed which are exhibited in Table V and a spinel solid solution formed exhibited in Table VI.

Table III. Mole fractions of components and number of moles of molten and solid salt solutions produced in the combustion of 100 gm of aspen wood with 0.115 gm of S added at 10 atmospheres.

T(°C)	1200	1100	912.3	800	600
CaSO ₄ (liq)	0.771	0.730	0.536	-----	-----
K ₂ SO ₄ (liq)	0.215	0.258	0.462	-----	-----
CaCO ₃ (liq)	1.04 E-2	8.98 E-3	1.08 E-3	-----	-----
K ₂ CO ₃ (liq)	2.91 E-3	3.17 E-3	9.36 E-4	-----	-----
moles	3.41 E-3	3.64 E-3	0	0	0
K ₂ SO ₄ (ss)	-----	-----	----- ¹	0.998	1.000
CaSO ₄ (ss)	-----	-----	-----	1.92 E-3	3.91 E-4
K ₂ CO ₃ (ss)	-----	-----	-----	4.18 E-5	7.41 E-5
CaCO ₃ (ss)	-----	-----	-----	8.04 E-8	2.90 E-8
moles	0	0	0	1.04 E-3	1.04 E-3

liq refers to the liquid solution and ss refers to the solid solution

¹ Note that there is no solid solution at 912.3°C because the stable solids are CaSO₄ and K₂Ca₂(SO₄)₃.

Table IV. Mole fractions of gaseous species formed during the combustion of 100 gm of aspen wood with 0.115 gm S added, at 10 atmospheres.

T(°C)	1100	1000	900	800	700	600
NO	2.84 E-4	1.53 E-4	7.37 E-5	3.11 E-5	1.10 E-5	3.05 E-6
OH	9.02 E-6	2.95 E-6	7.99 E-7	1.69 E-7	2.62 E-8	2.64 E-8
KOH	4.25 E-6	6.50 E-7	1.19 E-7	2.51 E-8	2.81 E-9	-----
SO ₂	4.40 E-6	1.13 E-6	5.99 E-8	-----	-----	-----
NO ₂	3.11 E-6	2.49 E-6	1.93 E-6	1.42 E-6	9.80 E-7	6.24 E-7
KBO ₂	7.49 E-7	9.57 E-8	6.31 E-9	-----	-----	-----
K ₂ SO ₄	3.45 E-7	1.04 E-7	1.81 E-8	1.64 E-9	-----	-----
SO ₃	2.14 E-7	1.07 E-7	1.24 E-8	-----	-----	-----
HBO ₂	1.26 E-7	4.47 E-8	5.88 E-9	-----	-----	-----
O	3.91 E-8	6.83 E-9	-----	-----	-----	-----
H ₃ BO ₃	2.07 E-7	2.65 E-7	1.58 E-7	8.49 E-8	3.95 E-8	1.51 E-8
N ₂ O	4.83 E-8	2.69 E-8	1.36 E-8	6.12 E-9	2.34 E-9	-----
Ca(OH) ₂	4.02 E-9	-----	-----	-----	-----	-----
Mg(OH) ₂	2.45 E-9	-----	-----	-----	-----	-----

The fractional partial pressures and total number of moles of the major species are essentially constant at all temperatures at N₂ = 0.7186, CO₂ = 0.1395, H₂O = 0.1011, O₂ = 0.0406 and 30.769 moles.

----- denotes <10⁻⁹ mole fraction in the gas phase.

Table V. Moles of solid compounds produced in the combustion of 100 gm of aspen wood with 0.115 gm of S added at 10 atmospheres.

T(°C)	1200	1100	1000	900	700	600
MgO	1.05 E-3	1.05 E-3	1.01 E-3	1.00 E-3	9.86 E-4	9.70 E-4
CaO	5.85 E-4	-----	-----	-----	-----	-----
CaSO ₄	-----	6.23 E-4	1.58 E-3	1.26 E-3	3.33 E-3	3.33 E-3
Ca ₅ HO ₁₃ P ₃	9.15 E-5	9.15 E-5	9.15 E-5	9.15 E-5	9.15 E-5	9.15 E-5
Ca ₃ Al ₂ O ₆	1.87 E-5	-----	-----	-----	-----	-----
Ca ₂ Fe ₂ O ₅	1.67 E-5	1.67 E-5	1.44 E-5	-----	-----	-----
Mn ₃ O ₄	6.12 E-6	1.27 E-6	1.75 E-6	-----	-----	-----
Mg ₃ B ₂ O ₆	-----	-----	1.04 E-5	1.40 E-5	1.60 E-5	1.64 E-5
K ₂ Ca ₂ (SO ₄)	-----	-----	-----	1.03 E-3	-----	-----
CaFe ₂ O ₄	-----	-----	2.36 E-6	1.31 E-5	1.26 E-5	-----
Mn ₂ O ₃	-----	-----	-----	3.70 E-6	7.09 E-6	8.35 E-6
MgFe ₂ O ₄	-----	-----	-----	3.65 E-6	4.16 E-6	1.67 E-5
CaCO ₃	-----	-----	-----	-----	-----	1.27 E-5

Table VI. Spinel solid solutions formed during combustion of aspen wood with added sulfur at 10 atm.

T°C	1100	1000	900	800	700	600
MnAl ₂ O ₄	0.778	0.701	0.586	0.409	0.223	0.088
MgAl ₂ O ₄	0.222	0.299	0.414	0.591	0.777	0.912
FeAl ₂ O ₄	4.7 E-5	1.3 E-5	7.9 E-5	2.2 E-5	4.3 E-6	4.8 E-7

Moles of spinel are constant at all temperatures at 1.87 E-5.

COMBUSTION OF WHEAT STRAW

Wheat straw is a common waste which is a potential source of energy that does not contribute to the greenhouse effect. However, combustion of wheat straw leads to problems with fouling and corrosion of combustors and power systems (6). This has led to the derating of experimental combustors in several European countries (6). In order to understand this problem, we have performed calculations of the inorganic chemistry of 100 moles of wheat straw using the composition given in Table II. The most striking result is given in Table VII which gives the compositions (mol%) and moles of a silicate melt which is present at 1200°C and persists to temperatures below 500°C. The melt is largely composed of silica and potassium oxide (88-94 mole%) with lesser amounts of the oxides of Ca, Na, Mg, and Al. The Cl, SO₄, and CO₃ designate the sums of the concentrations of the anions in salts of these ions with K, Ca, Na, and Mg. These were combined to simplify the Table with an insignificant loss of information.

Table VII. Composition of molten condensates in wheat straw combustion effluents (mol %)

T°C	1200	1000	800	600	500
SiO ₂	80.91	82.65	80.49	77.82	76.28
K ₂ O	9.66	11.23	11.15	11.79	11.71
CaO	2.92	0.49	0.64	0.82	0.85
Na ₂ O	2.57	2.81	4.24	4.89	5.66
MgO	2.46	1.11	0.37	0.06	0.02
Al ₂ O ₃	1.47	1.61	2.67	3.78	4.51
Cl	0.61 E-3	4.46 E-3	65.59 E-3	0.50	0.50
SO ₄	0.51 E-3	89.93 E-3	0.39	0.35	0.33
CO ₃	0.38 E-5	0.33 E-5	1.75 E-5	23.08 E-5	0.47
Moles	0.7736	0.7083	0.4269	0.3014	0.2526

Obviously, wheat straw produces deleterious molten silicates in a combustor and this is the root cause of the problems which led to derating of combustors by lowering the operating temperature. Any methods for converting these liquids to solids might help to make the efficient combustion of wheat straw for power production feasible.

One possible additive is alumina which tends to form some relatively high melting aluminosilicates. Rather than use alumina directly, we chose to use an alumina rich mixed waste paper with a composition given in Table II. Aluminum is the most abundant element in this waste after H, C and O. Calculations were made for 100 elemental moles of wheat straw, 80 elemental moles of mixed waste paper, 148.5 moles of O, 558.6 moles of N and 0.5 moles of SiO₂. The silica was added because of a flaw in the computer program for silicates with high alumina content. The silica addition helped to circumvent this flaw which didn't allow the calculation to converge and which we

Table VIII. Molten silicate compositions (mol%) produced in the combustion of 100 moles of wheat straw mixed with 80 moles of mixed waste paper and 0.5 moles of SiO₂.

T(°C)	1150	1050	950	850	837
SiO ₂	72.80	78.88	82.06	81.62	81.29
Al ₂ O ₃	13.60	10.75	9.00	8.73	8.80
K ₂ O	5.60	5.68	5.04	4.84	4.85
Na ₂ O	1.45	2.04	2.37	3.45	3.68
CaO	3.81	1.85	1.30	1.22	1.22
MgO	2.72	0.80	0.23	0.12	0.12
Cl	8.32 E-5	8.54 E-5	1.06 E-4	3.90 E-4	5.13 E-4
SO ₄	9.53 E-6	3.75 E-5	3.03 E-4	2.17 E-2	4.39 E-2
CO ₃	1.00 E-8	-----	-----	-----	-----
Moles	1.693	1.052	0.946	0.769	0.000

hope to correct in the near future. Equilibrium compositions were calculated at 25° intervals between 550°C and 1150°C. Some of the results for the molten silicate are exhibited in Table VIII. The liquid contains considerably more alumina than do the liquids produced by wheat straw alone. The liquid crystallizes completely at 837°C, thus significantly raising the temperature below which there is no liquid present. The 392.8 moles of residual gases are not displayed and tend to be acidic. Tables IX and X exhibit the stoichiometric solids and the ideal solid plagioclase solution. Clearly, the use of additives shows promise for improving the performance of biomass as a source of energy. When the flaw in the current program is corrected, we can aggressively examine the ability of a number of additives to optimize the performance of wheat straw.

Table IX. Moles of stoichiometric solids formed in the combustion of wheat straw mixed with waste paper and 0.5 mole SiO₂.

T(°C)	1050	950	850	750	650	550
KAlSi ₂ O ₆	0.0420	0.0672	0.1060	0.0833	0.0765	-----
Mg ₂ Al ₄ Si ₅ O ₁₈	0.0297	0.0333	0.0342	0.0344	0.0344	0.0344
Fe ₂ O ₃	0.0065	0.0065	0.0065	0.0065	0.0065	0.0065
Al ₆ Si ₂ O ₁₃	0.0109	-----	-----	-----	-----	-----
Al ₂ SiO ₅	-----	0.0366	0.0394	0.0372	0.1024	0.1040
SiO ₂	-----	-----	0.2920	0.3415	0.3994	0.3241
CaSO ₄	-----	-----	-----	-----	0.0651	0.0668

Table X. Mole % and number of moles of hypothetical ideal plagioclase solid solution formed in combustion of 100 moles of wheat straw mixed with 80 moles of waste paper and 0.5 moles SiO₂.

T(°C)	1150	1050	950	850	750	650	550
CaAlSi ₃ O ₈	89.69	79.81	70.62	49.44	38.06	16.60	11.47
KAlSi ₃ O ₈	9.84	18.90	25.79	33.54	42.85	58.75	70.59
NaAlSi ₃ O ₈	0.47	1.30	3.59	17.02	19.09	24.64	17.94
Moles	0.038	0.096	0.122	0.193	0.258	0.200	0.275

CONCLUSIONS

Calculations of the inorganic chemistry of the combustion of aspen wood and wheat straw have defined the root causes of fouling and corrosion. Calculations of the influence of additives have demonstrated potential improvements in performance of the combustion products. Further calculations will be needed to find additives which might provide optimal performance beyond these promising results. These calculations were made possible by theories of molten salts and silicates which permit one to make reliable

calculations of the thermodynamic properties of multicomponent solutions from properties of the lower order binary and (for silicates only) ternary systems.

ACKNOWLEDGEMENTS

This work was supported by the National Renewable Energy Laboratory (NREL) under subcontract no. TCD-5-15623-01. The author is indebted to Tom Milne of NREL for many valuable suggestions and discussions.

REFERENCES

1. M. Blander and S. J. Yosim, *J. Chem. Phys.*, **39** 2610 (1963)
2. M. Blander and A. D. Pelton, *Geochim. Cosmochim. Acta*, **51** 85-95 (1987)
3. C. W. Bale, A. D. Pelton and W. T. Thompson, Facility for the Analysis of Chemical Thermodynamics, CRCT, Ecole Polytechnique de Montreal, P. O. Box 6079, Station "Downtown", Montreal, Quebec H3C3A7, Canada
4. G. Eriksson and K. Hack, *Metall. Trans.*, **21B** 1013 (1990)
5. M. Blander, K. W. Ragland, R. L. Cole, J. A. Libera and A. D. Pelton, *Biomass and Bioenergy*, **8** 29-38 (1995)
6. T. R. Miles, T. R. Miles Jr., L. L. Baxter, R. W. Bryers, B. M. Jenkins and L. L. Oden, Alkali Deposits Found in Biomass Power Plants: A Preliminary Investigation of Their Extent and Nature, Summary Report, NREL/TP-433-8142, National Renewable Energy Laboratory, Golden, CO, U. S. A.

**VIBRATIONAL MODES AND STRUCTURE OF RARE EARTH
FLUORIDES AND BROMIDES IN BINARY MELTS: $\text{LnX}_3\text{-KX}$**
(X= F, Br; Ln= Y, La, Ce, Nd, Sm, Gd, Dy, Yb)

B. Borresen^(a), V. Dracopoulos^(a), G. Photiadis^(a),
B. Gilbert^(b) and G.N. Papatheodorou^(a)

^(a)Institute of Chemical Engineering and High Temperature Chemical Processes
ICE/HT-FORTH, P.O.Box 1414 and Department of Chemical Engineering
University of Patras, GR-26500 Patras, GREECE

^(b)Laboratoire de Chimie Analytique B6, Université de Liege, Sart Tilman
B-4000 Liege, BELGIUM

ABSTRACT

Raman spectra of the following binary molten salt systems have been measured. Fluorides: $\text{YF}_3\text{-KF}$, $\text{LaF}_3\text{-KF}$, $\text{CeF}_3\text{-KF}$, $\text{NdF}_3\text{-KF}$, $\text{SmF}_3\text{-KF}$, $\text{DyF}_3\text{-KF}$, $\text{YbF}_3\text{-KF}$; Bromides: $\text{YBr}_3\text{-KBr}$, $\text{LaBr}_3\text{-KBr}$, $\text{NdBr}_3\text{-KBr}$ and $\text{GdBr}_3\text{-KBr}$. The spectral changes occurring upon melting the K_3YF_6 , $\text{Cs}_2\text{NaLnBr}_6$ and LnBr_3 solids were also measured. The data indicate that in mixtures rich in alkali halide (fluoride or bromide) the LnX_6^{3-} are the predominant species. In fluoride mixtures rich in LnF_3 strong anisotropic scattering overcomes the low frequency region. The origin of this band is rather physical (induced polarizability fluctuations) than chemical (formation of species). In molten mixtures rich in LnBr_3 a new strong polarized band appears in the spectra which shifts to higher energies with increasing LnBr_3 content. This behavior as well as the spectral changes observed on melting pure LnBr_3 suggest that the melt structure consists of edge sharing octahedra and is independent of the coordination geometry that the Ln ion has in the LnBr_3 crystals.

INTRODUCTION

Rare earth halide melts and their mixtures with alkali halides are important for industrial electrolytic processes where they have been used for either the production of the corresponding rare earth metals [e.g. Nd (1)] or as additives to improve the electrolytic production of light metals [e.g. Al (2)].

The structural and thermodynamic properties of certain rare earth chloride-alkali chloride melts have been studied rather extensively. This includes the well studied, by Raman spectroscopy (3), calorimetry (4) and neutron diffraction (5) binaries of $\text{YCl}_3\text{-ACl}$ ($A = \text{Li} \dots \text{Cs}$) as well as Raman spectroscopic studies of the LaCl_3 and NdCl_3 binaries with alkali chlorides (6). A large number of calorimetric enthalpies of mixing for the $\text{LnCl}_3\text{-ACl}$ ($\text{Ln} = \text{La}, \text{Ce}, \text{Nd}, \text{Pr}, \text{Dy} \dots$) systems have been also reported (7). No studies have been reported so far for neither the fluoride nor the bromide rare earths with alkali halides.

The purpose of the present work is to investigate the systematic structural properties of the $\text{LnX}_3\text{-KX}$ binary mixtures where X is fluoride or bromide. Raman spectroscopy has been used for determining the vibrational frequencies of certain of these binary melts and solid compounds. The measured spectra are correlated to the structural properties of the melt mixtures and of the pure component LnX_3 melts.

EXPERIMENTAL

Two different experimental set-ups were used to measure the Raman spectra. For the fluoride melts the windowless graphite cell technique and a modified Cary 81 spectrometer was used in the Liege (B) laboratory (8). For the bromide melts fused silica cells and a Spex 0.85 m double monochromator was used in the Patras (GR) laboratory (9). Details of the experimental set-ups have been described in the references cited.

The LaF_3 , CeF_3 , NdF_3 , DyF_3 , YF_3 (Aldrich Co.) and the SmF_3 , YbF_3 (Alfa Co) were 99.9% in purity and were dried overnight under dynamic vacuum at 350°C . The KF (Merck Chem. Co) was purified by slow crystallizations from the melt. Vitreous carbon crucibles and an inert atmosphere furnace were used for the crystallization procedure. The anhydrous rare earth bromides LaBr_3 , NdBr_3 , GdBr_3 and YBr_3 were obtained by reacting the corresponding oxides (99.9% from Cerac Co.) with HBr aqueous solutions. The so-obtained hexahydrate was dried under dynamic vacuum by slowly raising the temperature ($t < 200^\circ\text{C}$) during a period of several days. The anhydrous bromides were subsequently sublimed under high vacuum ($\sim 10^{-7}$ mbar). The alkali bromides (CsBr , NaBr and KBr purchased from Merck) were dried under vacuum and then melted in an inert atmosphere furnace.

All operations for handling the purified salts and filling the appropriate Raman cells were carried out in fused silica containers and/or a controlled Ar atmosphere glove box.

RESULTS AND DISCUSSION

Table I and II list the temperature and composition of all the liquid binary systems

for which Raman spectra were measured. The **main** frequencies observed are also listed. All the solid compounds investigated, the measured frequencies and frequency changes occurring upon melting are presented in Table III. The spectral behavior of all fluoride systems was rather similar but different than that of the bromide systems which also show similarities within their group. The two sets of systems will be thus presented and discussed separately as follows.

I. Fluoride Systems

The high melting points of all LnF_3 salts and the vapor pressure over the binary fluoride mixtures have limited our spectral measurements up to 1000°C . At this temperature the liquidus line in the LnF_3 -KF binaries have a maximum at compositions of LnF_3 between 40-50 mole%.

Ia. Structural changes upon melting K_3YF_6

There are several allotropic forms of the K_3YF_6 crystals (10). At temperatures below melting the crystal transforms to its cubic O_h^5 structure which is known to have the Y in a nearly octahedral YF_6^{3-} site symmetry. Factor group analysis predicts four Raman active modes; three internal modes $\nu_1(\text{A}_{1g})$, $\nu_2(\text{E}_g)$ and $\nu_5(\text{F}_{2g})$ due to the YF_6^{3-} octahedra and a translational $\nu_{11}(\text{F}_{2g})$ lattice mode. Fast cooling of the K_3YF_6 solid to room temperature quenched the O_h^5 structure as seen from the spectra in Fig. 1. The four bands observed are assigned to the O_h^5 crystal as follows: $\nu_1(\text{A}_{1g}) = 466 \text{ cm}^{-1}$, $\nu_2(\text{E}_g) \approx 380 \text{ cm}^{-1}$, $\nu_5(\text{F}_{2g}) = 218 \text{ cm}^{-1}$, $\nu_{11}(\text{F}_{2g}) \approx 120 \text{ cm}^{-1}$. The assignment of the ν_1 , ν_2 and ν_5 modes to the YF_6^{3-} octahedral is further supported from the relation $\nu_1^2 \approx \nu_2^2 + \frac{3}{2}\nu_5^2$ (3). With increasing temperature the ν_1 band shifts to lower frequencies while the ν_2 band is not seen at temperatures above room temperature.

The melt spectra of K_3YF_6 (Fig. 1) possess a strong polarized band at $\sim 442 \text{ cm}^{-1}$ and a depolarized band at $\sim 208 \text{ cm}^{-1}$. Thus, it seems that upon melting the vibrational modes of the YF_6^{3-} , which exist in the solid, are transferred into the liquid. The situation is similar to that occurring upon melting the $\text{Cs}_2\text{NaLnX}_6$ [$\text{X} = \text{Cl}$ (3,6) or $\text{X} = \text{Br}$ (see section IIa)] crystals and indicates that the predominant species in the K_3YF_6 melt are the YF_6^{3-} octahedra.

Ib. The LnF_6^{3-} octahedron in KF-rich melts

The spectra of all LnF_3 -KF mixtures at compositions 10 and 25 mole % in LnF_3 are rather similar (Fig. 2) showing a polarized and a depolarized band at frequencies

expected for the LnF_6^{3-} octahedral species. Thus the spectra in Fig. 2 in conjunction with the evidence given in Fig. 1 and section Ia, are interpreted to indicate that the predominant species in all KF-rich binary mixtures are the LnF_6^{3-} octahedra. The ν_1 stretching frequency of the octahedra is in the range between ~ 400 to $\sim 450 \text{ cm}^{-1}$ and its value increases with the ionic strength ($1/r$) of the Ln cation. This is shown in Fig. 3 where an approximately linear relation appears to exist.

The depolarized ν_5 bands are broad with frequencies as expected in the range 180 - 210 cm^{-1} . However, for the 25 mole % composition the depolarization ratio of the low frequency (ν_5) bands was found to increase with increasing the size of the central cation. This effect is more pronounced in LnF_3 rich mixtures and will be discussed in the following section.

Ic. Composition effects in LnF_3 -rich melts

The binary melts involving LaF_3 , CeF_3 and YF_3 were investigated at composition up to 40 mole % for LaF_3 and CeF_3 and up to 50 mole % for YF_3 (Table I). Representative isotropic and anisotropic spectra in the reduced Raman representation (11) are given in Fig. 4 for the two "end" (in ionic radii) binaries of YF_3 -KF and LaF_3 -KF.

The isotropic spectra show (Fig. 4) a strong main band with frequency close to the ν_1 band of the KF-rich melts. For the YF_3 -KF system a "blue" shift of $\sim 15 \text{ cm}^{-1}$ occurs on going from the 10 to the 50 mole % mixture, while for the LaF_3 -KF and CeF_3 -KF system the position of the isotropic band does not change up to the 40 mole % mixtures. It seems that the Ln-F (ν_1) band of the LnF_6^{3-} octahedra is preserved in these melt mixtures at compositions up to 40 or 50 mole % which were the concentration/temperature limits of our measurements.

The anisotropic spectra of the KF-rich compositions show the expected depolarized ν_5 (F_{2g}) band. As the LnF_3 mole fraction is increased a new anisotropic band appears at higher energies. For the YF_3 -KF system the new band is at $\sim 365 \text{ cm}^{-1}$ and its intensity increases with increasing YF_3 content (Fig. 4). For the LaF_3 -KF system the overall intensity of the anisotropic spectra increases drastically; the new band is at $\sim 300 \text{ cm}^{-1}$ and its intensity competes to that of the isotropic spectra. The appearance of such strong anisotropic light scattering has been observed before in alkali halide melts where enhanced DID interaction between the ions were involved (12).

The presence of the two bands (ν_1 and ν_5) associated with the LnF_6^{3-} octahedra at compositions above 25 mole % LnF_3 suggests that the vibrational modes in the overall range of compositions are overcome by the octahedral "species". Presumably at $X_{\text{LnF}_3} > 0.25$ the probability of having two Ln atoms as a second nearest neighbors increases gradually; in other words the LnF_6^{3-} start sharing common fluorides in a manner

analogous to that found for the rare earth chlorides (3,6) and bromide (see following section) melts.

The relative ionic radii of F^- (1.33 Å) and of the rare earth cations (0.86 - 1.032 Å) do not allow anion contact in the LnF_6^{3-} octahedra. The distances between the fluorides surrounding the Ln are large relative to the distances in the corresponding chlorides and/or bromide species. Furthermore, the F-F distance in the LnF_6^{3-} octahedra is shorter for $Ln=Y$ than for $Ln=La$. This implies a better shielding of the central cation in the YF_6^{3-} anions versus the LaF_6^{3-} anions. When the LnF_3 content increases the LnF_6^{3-} start sharing fluorides, as said above, and the cation - cation interaction should also increase. Due to these interactions and to bridging the shielding is likely to decrease but we can reasonably assume that the shielding differences between Y and La containing anions remains. In such case, the polarizability fluctuations induced by the cation-cation interactions are enhanced in the La relative to the Y melts. This implies that interactions giving rise to anisotropic light scattering [mainly DID (12,13)] will be more pronounced in the LaF_3 systems. In other words, we attribute the strong anisotropic spectra of Fig. 4 to polarizability fluctuations induced by the La-La interactions.

II. Bromide Systems

The phase diagrams of the rare earth tribromides with alkali bromides show the formation of liquid mixtures at relatively low temperatures and thus Raman spectroscopic measurements were possible in the overall composition range of the binary including the pure $LnBr_3$ melts. In many respects the structural and thermodynamics properties of the $LnBr_3$ salts and of their binary solid compounds with alkali bromides are very similar to those of the corresponding chloride salts. This is expected from the closeness of the ionic radii of the chloride (1.81 Å) and bromide (1.96 Å) anions. Thus the choice of the melt mixtures and solids studied was based on our previous investigations on the $LnCl_3$ -ACl [$Ln=La, Nd, Y$ (3,6)] systems.

IIa. Structural changes upon melting $Cs_2NaLnBr_6$ ($Ln=La, Nd, Gd, Y$)

A large number of crystals of the type Cs_2NaLnX_6 ($Ln = \text{rare earth, actinide; } X=Cl, Br$) have been found to be isostructural (elapsolites) having a cubic $Fm\bar{3}m$ (O_h^5) symmetry. The Ln atom in these crystals is six-fold coordinated having an almost ideal octahedral (O_h) site symmetry. Factor group analysis (3) shows that there are three intramolecular Raman active vibrations of the LnX_6^{3-} octahedra [$A_{1g} + E_g + F_{2g}$] plus a lattice Raman active translatory mode [F_{2g}].

Four compounds with $X=Br$ and $Ln=La, Nd, Gd$ and Y were prepared and their Raman spectra were measured from room temperature up to melting. All spectra were

similar as seen for the "end" cases of La and Y in Fig. 5. As with the chloride salts (3,6) all four expected Raman bands are present in the room temperature spectra. The $\nu_1(A_{1g})$ band shifts to lower energies with increasing temperature while the $\nu_5(F_{2g})$ band is insensitive to temperature. Upon melting the lattice mode disappears but the strong intramolecular modes $\nu_1(A_{1g})$ and $\nu_5(F_{2g})$ are preserved indicating the presence of the LnBr_6^{3-} octahedral species in the melt.

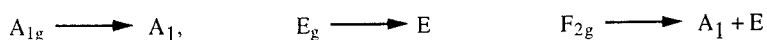
IIb. Composition effects in the LnBr_3 -KBr (Ln=La,Nd,Gd,Y) liquid mixtures

The Raman spectra of all four representative binary systems studied were rather similar. Figure 6 shows the reduced isotropic and anisotropic spectra at selective composition of the two "end" systems (La and Y). For all four systems studied the following main common observations are noteworthy.

(i) For all mixtures with $X_{\text{LnBr}_3} \leq 0.25$ two main bands are present; one polarized around $150\text{-}160\text{ cm}^{-1}$ and one depolarized at lower frequencies (around 70 cm^{-1}). The intensities of these band increase almost linearly with increasing LnBr_3 composition while their position remains unchanged. In agreement with the previous section (IIa) and previous studies of the chloride salts (3,6) it is evident that the main species in all LnBr_3 -KBr melts, rich in KBr are the LnBr_6^{3-} octahedra. The polarized and depolarized bands are thus assigned to the octahedral $\nu_1(A_{1g})$ and $\nu_5(F_{2g})$ modes respectively.

(ii) At compositions $X_{\text{LnBr}_3} > 0.25$ the isotropic spectra show that the ν_1 frequency remains practically unchanged while a new polarized band (P_2) appears whose position shifts "continuously" to higher energies with increasing LnBr_3 composition. This effect is more pronounced for the YBr_3 binaries and decreases gradually as we change Y with Gd, Nd and La.

(iii) The anisotropic spectra also show the appearance of a new depolarized band which rises with increasing LnBr_3 composition. It seems that all spectra at high LnBr_3 content are characterized by four main bands; two polarized P_1 and P_2 and two depolarized D_1 and D_2 . The frequencies of P_1 and D_1 are close to the octahedra ν_1 and ν_5 bands respectively and are composition independent while the P_2 and D_2 bands shift in energy with composition changes. The situation is very similar to that of the chloride mixtures discussed in refs 3 and 6. The continuous shift of the P_2 band indicates (3) a gradual distortion of the LnBr_6^{3-} octahedra. Within this scheme on going from O_h symmetry to a D_3 octahedral distortion the vibrational modes are correlated as:



which accounts for the number and polarization characteristics of the observed bands.

In contrast to the fluoride melts, the polarized $\nu_1(A_{1g})$ mode of the bromide octahedra does not vary with the ionic size along the rare earth series. Figure 3 shows the $\nu_1(A_{1g})$ dependence on the ionic strength (r^{-1}) for the fluorides, bromides as well as for the chlorides; obviously the slope increases systematically in the sequence Br, Cl and F. From the relative ionic radii of the three anions and all the Ln cations involved it can be rendered that in the LnX_6^{3-} octahedra the central Ln cation is better shielded in the cases of the bromide and chloride than in the case of the fluoride. As already mentioned above the shielding also decreases with increasing size of the central cation. Thus, the less the shielding of the central cation the easier it is for the counter alkali cation to approach the halide voids around the octahedra. This in turn weakens the Ln-X bonding especially in the case of fluorides and accounts for the systematic variations seen in Fig. 3.

IIc. Structural changes upon melting rare earth tribromides

The crystal structures of the rare earth tribromides (and trichlorides) change along the series depending on the size of metal atom. Thus, YBr_3 and all the lanthanide tribromides from Lu to Gd are rhombohedral having the Ln in six fold coordination, the Eu to Nd tribromides are orthorhombic with an eight-fold coordination for Ln while the Pr, Ce and La tribromides are hexagonal having the Ln in nine-fold coordination. For these three different crystal structures we present in Fig. 7 the simplified general skeletons indicating the coordination of the Ln and the bridging through the bromines. Structures A or B have all coordinated bromines (6 or 8 respectively) bridged between neighboring Ln atoms while structure C has 6 bridged and 3 terminal bromines.

The Raman spectra of the three different types of solids are shown in Fig. 8 for the bromides of Y and Gd (type A) Nd (type B) and La (type C). Measurements from room temperature up to melting have shown that the bands of the solid shift gradually and become broader. At temperature before melting the spectra of the three different solid structures (A, B, C) are different while the spectra of the solids of the same crystal structure are similar [i.e. the YBr_3 and $GdBr_3$ in Fig. 8]. However, upon melting all three structures yield a rather uniform spectrum which is characterized, as mentioned in the previous section, by two strong polarized P_1 and P_2 bands and two depolarized band D_1 and D_2 . The pattern of behavior of all liquid spectra in Fig. 8 is analogous to that of the YCl_3 melt for which a network structure of bridged distorted octahedra (structure L) was proposed (3). Such a liquid structure is closely related to the rhombohedral A solid and has been further confirmed by neutron diffraction studies of molten YCl_3 (5). Thus it seems that the melting of the three different types of $LnBr_3$ solid structures (A, B, C) lead to a common melt structure (L). The six fold coordination is preserved for structure

A while structures B and C change the Ln coordination from eight or nine in the solid to six in the melt.

Finally, due to the edge bridging of the octahedra in the liquid structure (L) the central cation is in an effectively low symmetric field, consisting of three sets of two bromides bridged to the neighboring cations. Thus, the Raman spectra of the liquid could be considered as arising from the vibrations of a pyramidal like $\text{Ln}[(\text{Br}_b)_2]_3$ unit, where the Br_b denotes the bridging character of the bromides. Such units give rise to four dominant Raman active "internal" modes of the liquid with polarization and energy characteristics similar to those observed in Fig. 7.

CONCLUSIONS

Raman spectroscopic measurements of the $\text{LnX}_3\text{-KX}$ ($\text{Ln} = \text{La, Ce, Nd, Sm, Gd, Dy, Y, Yb}$; $\text{X} = \text{F, Br}$) binary mixtures in the liquid (molten) and solid phases have shown that:

- (i) the octahedral LnF_6^{3-} is the predominant species in fluoride melts mixtures rich in KF.
- (ii) the six-fold coordination is preserved in fluoride melt mixtures at LnF_3 compositions up to 40-50 mole%.
- (iii) strong anisotropic light scattering arises from LnF_3 -rich molten mixture which is attributed to polarizability fluctuations induced by Ln-Ln interactions.
- (iv) the octahedral LnBr_6^{3-} is the predominant species in bromide melt mixtures rich in KBr.
- (v) a new polarized band appears in the $\text{LnBr}_3\text{-KBr}$ melts which shifts continuously to higher energies with increasing LnBr_3 composition. This band is attributed to distortions of LnBr_6^{3-} octahedra which are bridged to each other through bromides.
- (vi) the melting of the LnBr_3 solids with different crystal structures having the Ln in 6, 8 or 9 fold coordination, results to a common liquid structure where the Ln is predominantly six-fold coordinated forming a network-like liquid with "octahedra" sharing edges.

ACKNOWLEDGEMENTS

This work has been supported by the "Human Capital and Mobility" Network Program of the E.U. through which the participation of the young scientists B.Borresen and V.Dracopoulos in our laboratories in Patras and Liege was possible.

REFERENCES

1. R.A. Sharma and R.A. Roge, *J. Am. Ceram. Soc.* **75** (9), 2484 (1992).
2. E.W. Dewing, G.M. Haarberg, S. Rolseth, L. Ronne, J. Thonstad, and N. Aalberg, *Metal. and Mat. Trans. B* **26B**, 81-86 (1995).
3. G.N. Papatheodorou *J. Chem. Phys.*, **66**, 2893 (1977).
4. G.N. Papatheodorou, O. Waernes and T. Ostvold, *Acta Chem. Scand. A* **33**, 1799 (1979).
5. M.L. Saboungi, D.L. Price, C. Scanehorn and M.P. Tosi, *Europhys. Lett.* **15**, 283 (1991).
6. G.N. Photiadis, G.A. Voyiatzis and G.N. Papatheodorou, *Molten Salt Forum* **1-2**, 183 (1993/94) and references therein.
7. R. Takagi, L. Rycerz and M. Gaune-Escard, "Proc. 9th Inter. Symp. Molten Salts" C.L. Hussey, D.S. Newman, G.Mamantov and Y. Ito Eds. **Vol. 94-13** p. 284 (The Electrochem. Soc. Inc. 1994) and references therein.
8. B. Gilbert and T. Materne, *Appl. Spectr.* **44**, 299 (1990) and references therein.
9. S. Boghosian and G.N. Papatheodorou, *J. Phys. Chem.* **93**, 415 (1989) and references therein.
10. L.P. Reshetuskova, I.B. Shaimuradov, V.A. Efremov and A.V. Novoselova, "Dokl. Akad. Nauk. SSSR" **213**, 98 (1973).
11. M.H. Brooker and G.N. Papatheodorou, in "Advances in Molten Salt Chemistry" G. Mamantov and C.B. Mamantov Eds., **Vol. 5** p. 25 Elsevier (1983).
12. S.G. Kalogrianitis, T.G. Mihopoulos, E.A. Pavlatou and G.N. Papatheodorou, "Proc. 9th Int. Symp. Molten Salts", C.L. Hussey, D.S. Newman, G.Mamantov and Y. Ito Eds., **Vol. 94-13**, p. 284 (The Electrochem. Soc. Inc. 1994).
13. P.A. Madden, K.F. O'Sullivan, J.A.B. Board and P.W. Fowler, *J. Chem. Phys.*, **94**, 918 (1991).

Table I: Main Raman frequencies observed in the $\text{LnF}_3\text{-KF}$ mixtures at different compositions and temperatures.

System mole% LnF_3	T ($^{\circ}\text{C}$)	Main frequencies (cm^{-1})	
$\text{LaF}_3\text{-KF}$			
10%	850	400	(180) ^a
	1000	400	(180)
20%	1000	400	(180)
25%	1000	400	(180)
30%	1000	400	(280)
40%	1000	400	(280)
$\text{CeF}_3\text{-KF}$			
10%	850	406	(190)
	1000	406	(190)
20%	700	406	(190)
	800	406	(189)
	900	406	
	1000	406	
25%	1000	406	(189)
30%	1000	406	(298)
40%	1000	406	(298)
$\text{NdF}_3\text{-KF}$			
10%	850	415	(195)
25%	850	415	(195)
$\text{SmF}_3\text{-KF}$			
10%	850	427	(197)
	1000	427	(197)
25%	1000	427	(197)
$\text{DyF}_3\text{-KF}$			
10%	850	440	(203)
	1000	440	(203)
25%	1000	440	(203)
$\text{YF}_3\text{-KF}$			
10%	850	442	(208)
	1000	442	(208)
13%	800	442	(208)
	900	442	(208)
	1000	442	(208)
20%	1000	442	(208)
25%	1000	442	(208)
30%	1000	444	(210)
40%	1000	446	(360)
43%	850	446	(360)
	900	446	(360)
	1000	446	
50%	1000	449	(361)
$\text{YbF}_3\text{-KF}$			
10%	850	452	214
	1000	452	(214)

^aNumbers in parentheses indicate shoulder bands and the estimated frequencies with an error of 10cm^{-1} .

Table II: Binary bromide systems studied and the major frequencies observed.

System mole% LnBr ₃	Temperature °C		Main frequencies (cm ⁻¹)	
LaBr ₃ -KBr				
10%	750	147	62	
20%	750	147	62	
25%	750	147	61	
33%	750	146		[178] ^a
45%	750	144		[179]
60%	750	140		[184]
80%	750	138		[198]
100%	810	135		[218]
NdBr ₃ -KBr				
8%	710	150	64	
15%	710	152	65	
25%	710	152	63	
33%	725	152	63	[172]
50%	710	151		[180]
66%	740	148		[185]
80%	740	147		[191]
100%	740	144		[220]
GdBr ₃ -KBr				
8%	750	154	68	
16%	750	155	68	
25%	750	155	66	
33%	750	159	61	
50%	750	158		
66%	750	154		[186]
84%	780	155		[195]
100%	800	154		[217]
YBr ₃ -KBr				
5%	800	153	74	
10%	800	155	72	[280]
20%	800	154	72	[283]
25%	800	154	69	[203]
33%	800	154	59	[201]
50%	800	155		[218]
60%	800	153		[221]
80%	850	152		[231]
100%	920	151		[250]

a) Values in brackets were obtained from reduced Raman spectra.

Table III: Compounds studied and main frequencies observed in solid and liquid phases.

Compound	T (°C)	Main frequencies (cm ⁻¹)						
K ₃ YF ₆	25 1000	466 422		380		218 208		120
Cs ₂ NaYBr ₆	25 785	179 155		139		81 65		41
Cs ₂ NaGdBr ₆	25 750	178 155		140		77 62		39
Cs ₂ NaNdBr ₆	25 750	174 147		137		74 53		38
Cs ₂ NaLaBr ₆	25 745	170 145		134		71 51		30
YBr ₃	25 920	210 250	161 151	128	104	62		44
GdBr ₃	25 800	178 217	158 154	139	127	89	58	41
NdBr ₃	25 740	165 220	153 144	135	115	108	90	53
LaBr ₃	25 810		134 135		118	111		77

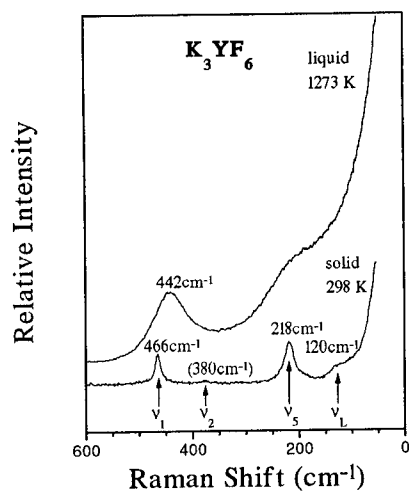


Fig. 1: Raman spectra of polycrystalline and molten K_3YF_6

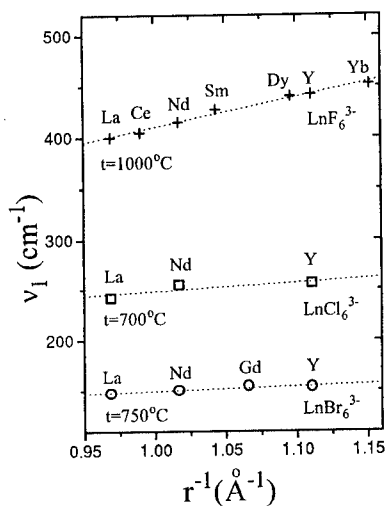


Fig. 3: The ν_1 frequency of the LnX_6^{3-} v.s. the ionic strength of the Ln^{3+} ion.

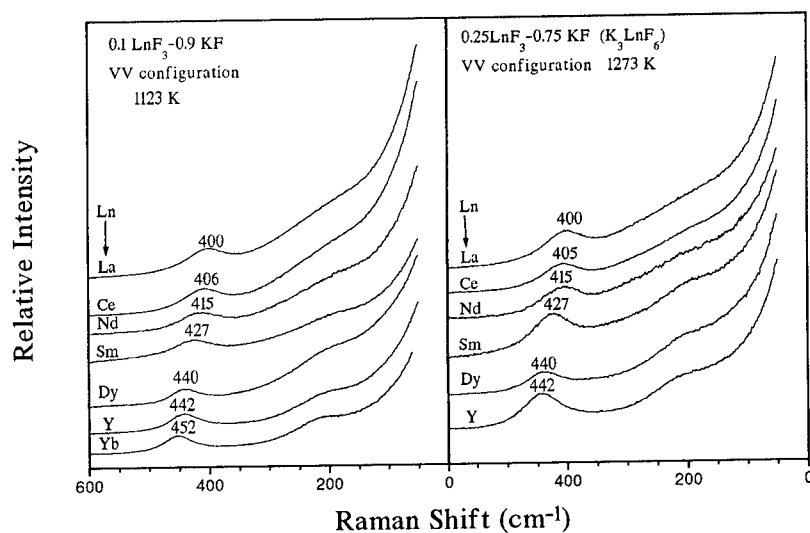


Fig. 2: Raman VV spectra of 0.9 KF-0.1 LnF_3 and K_3LnF_6 melts.

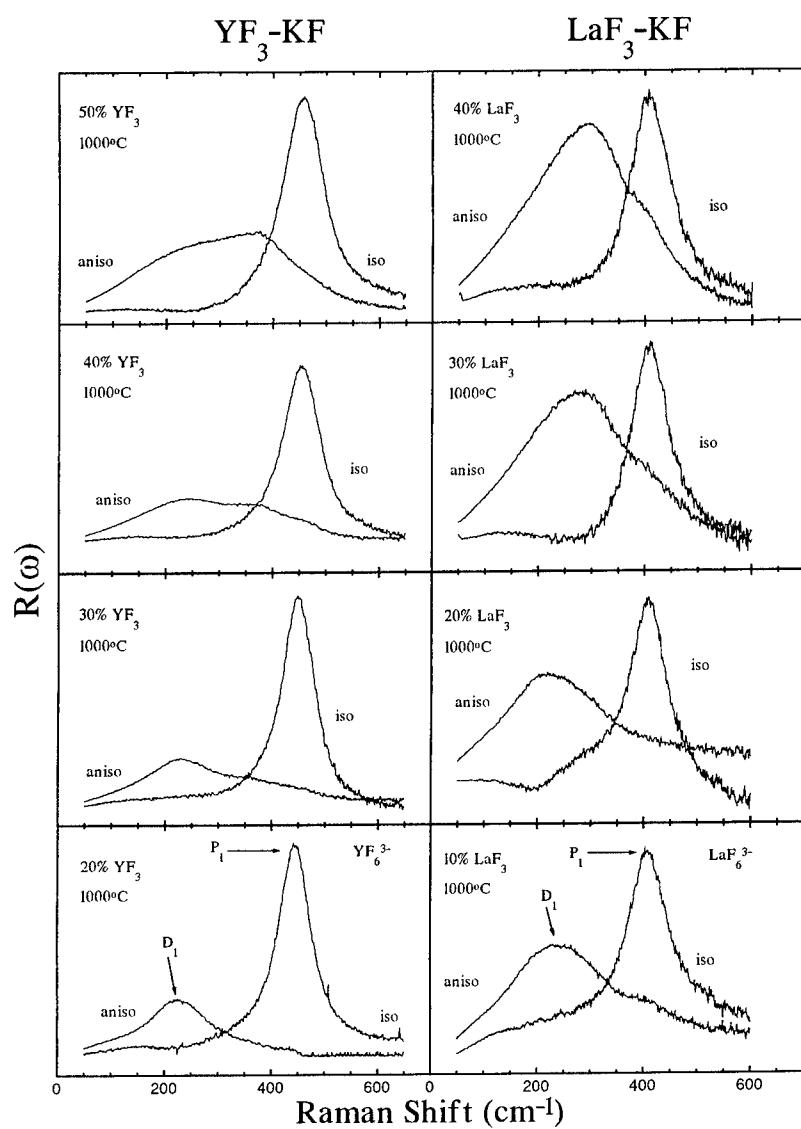


Fig. 4: Reduced isotropic and anisotropic spectra of the KF-LnF_3 (Ln: La, Y) liquid mixtures.

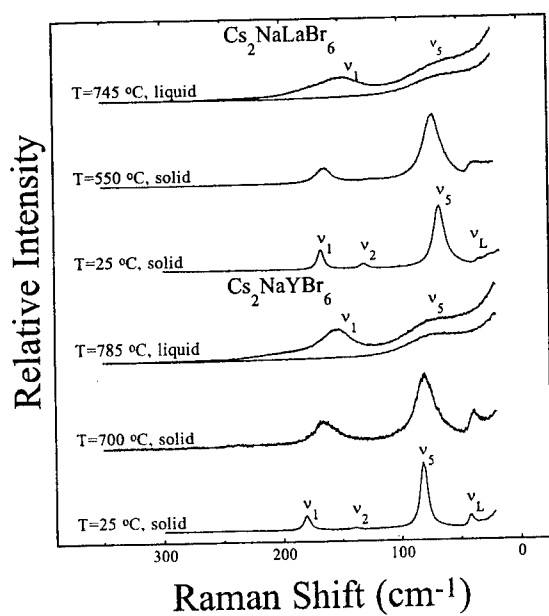


Fig. 5: Raman spectra of polycrystalline and molten $\text{Cs}_2\text{NaLaBr}_6$ and $\text{Cs}_2\text{NaYBr}_6$.

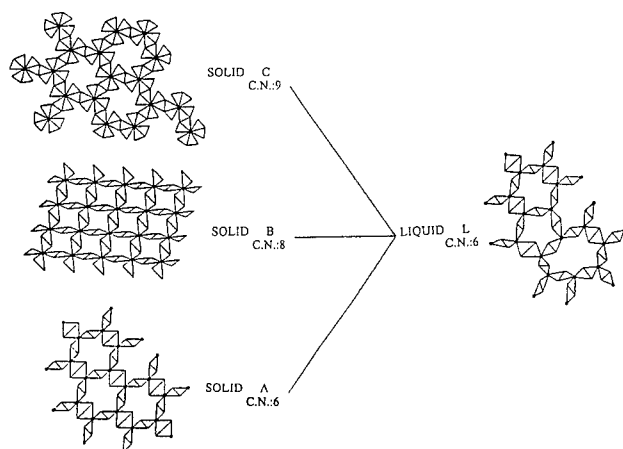


Fig. 7: Structural changes occurring upon melting rare earth trihalides.

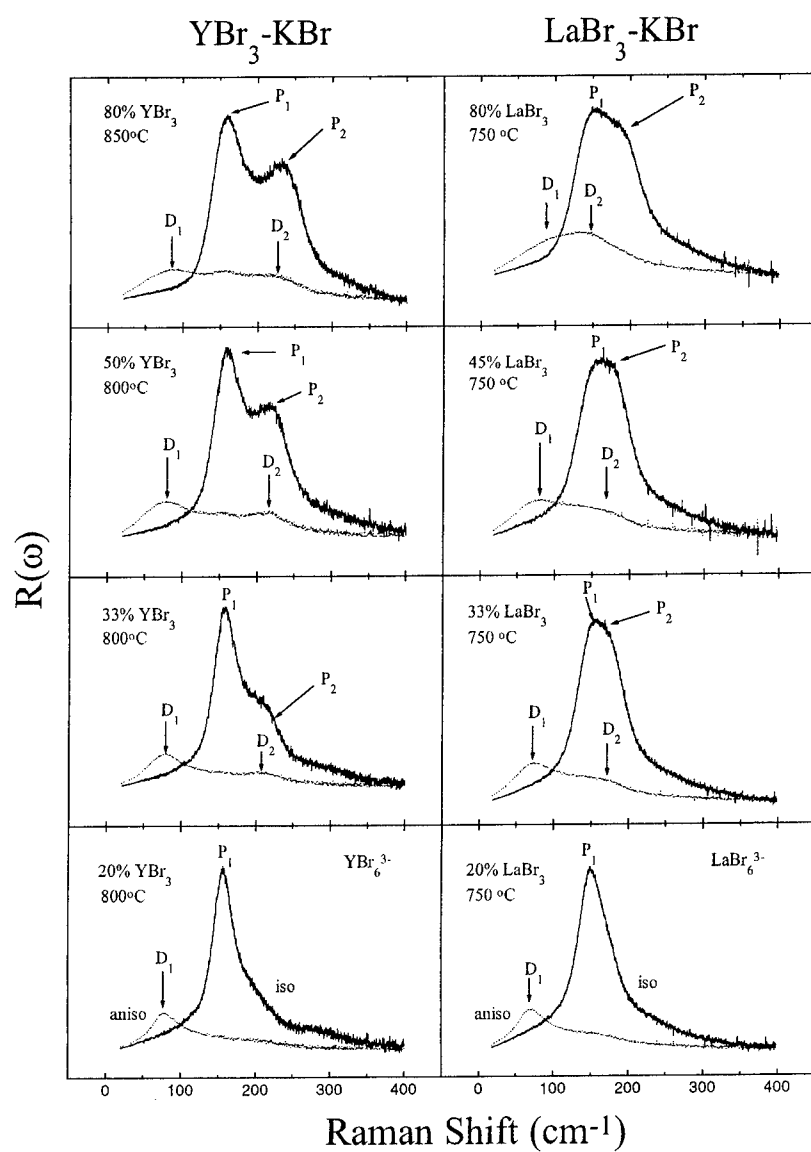


Fig. 6: Reduced isotropic and anisotropic Raman spectra of $\text{YBr}_3\text{-KBr}$ and $\text{LaBr}_3\text{-KBr}$.

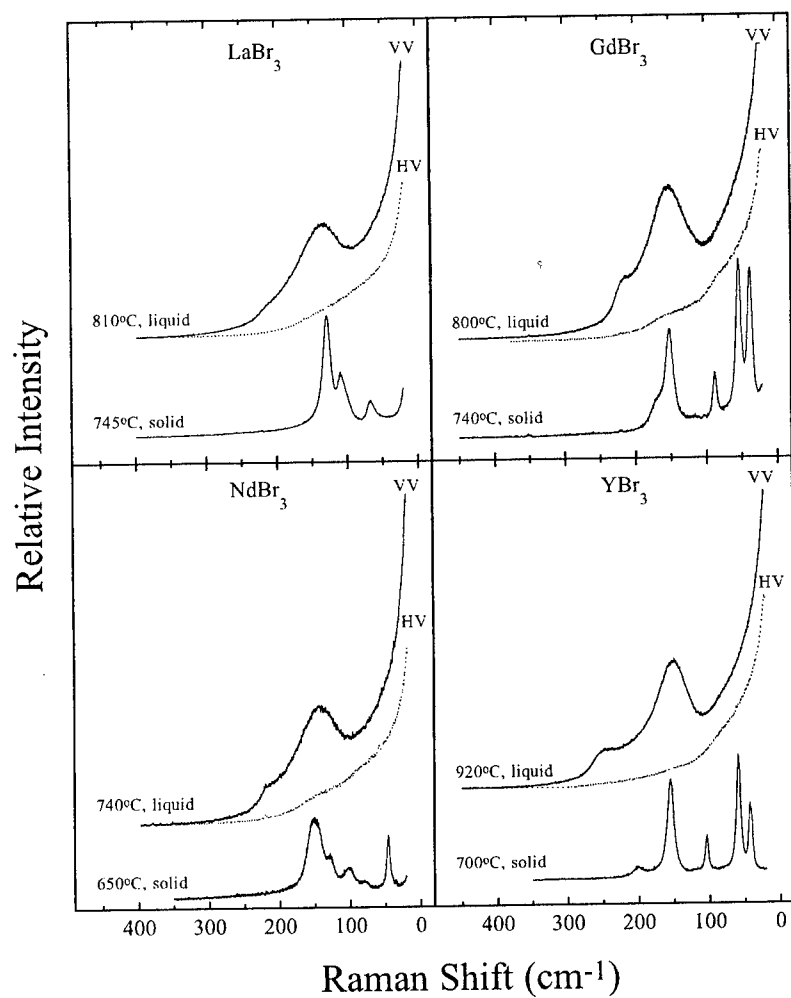


Fig. 8: Raman spectra of solid and liquid LnBr₃ (Ln=La, Nd, Gd, Y).

**EFFECTS OF HYDROPHOBIC INTERACTION
IN
n-ALKANECARBOXYLATE HYDRATE MELT**

Shigehito DEKI, Hiroshi NAKAHARA, Junji KONDO, and Akihiko KAJINAMI

*Department of Chemical Science & Engineering,
Faculty of Engineering, Kobe University
Rokkodai-cho, Nada-ku, Kobe 657, Japan*

Ultrasonic velocity, u , and adiabatic compressibility, β , were measured for sodium n -alkanecarboxylate hydrate, $C_nH_{2n+1}COONa$, melts ($n=0-4$). The maximal value of u and minimal value of β were observed in a systems except that of sodium formate hydrate at the composition range of $R=[H_2O]/[salt] = 4-20$. The linear relationships were obtained between these values and the alkyl chain length, n . Because these maximal or minimal values were not observed for the systems containing the salts without hydrophobic groups, this composition dependence seems to be related to the hydrophobic hydration in hydrate melts. The several systems containing alkali metal n -alkanecarboxylate hydrate melts were measured. However, the differences of values of u and β caused by the difference of cation species were smaller than those by anion. Consequently, the hydrophobic effect caused by n -alkyl chain was dominant for the interactions among the dissolved species in these systems.

INTRODUCTION

A large amount of research has been done on hydrophobic interaction among nonpolar molecules or nonelectrolyte molecules with comparatively simple structure (1). Those hydrophobic effects in monohydric-alcohol solutions lead to a large negative excess entropy of mixing, a positive heat capacity of solution, and a negative excess partial molar volume of alcohol. These results suggested that hydrophobic groups form the voluminous cage structure with hydrogen bonding effect, which causes the anomalous properties of water at higher temperature range. Organic molten salts show most distinctive physicochemical properties, in case that the ratio of ionic charge to the total number of atoms in the ion is fairly high. In this case, strong primary electrostatic forces among the ionic species are not highly shielded by the organic part in the ion. Ionic interactions in these systems have some influence on the hydration. However, few kinds of electrolyte solution have been investigated sufficiently.

Aqueous alkali metal *n*-alkanecarboxylate systems can cover wide composition range from aqueous solution to hydrate melt. The system keeps a stable liquid state in the relatively low water content range such as hydrate melt and even at the temperature below the melting point as a supercooled liquid. Therefore, these systems are suitable for the investigation of properties in the boundary region between the molten salt and the aqueous solution. Additionally, the *n*-alkanecarboxylate anion which is one of the components in these systems is different from inorganic anions in the nature, because both a hydrophilic carboxyl and a hydrophobic alkyl groups are included in their molecular structures.

We have been focusing on alkali metal *n*-alkanecarboxylate /water systems, which can cover widely composition range in aqueous solution and hydrate melt. Various physical properties (2) and structural analysis by X-ray diffraction (3) have been reported for the system containing alkali metal acetate and water in a wide concentration range between dilute aqueous solution and hydrate melt. Formate, acetate, propionate, butyrate, and valerate ions were chosen as anions in order to discuss hydrophobic interactions in the highly concentrated solution and the hydrate melt. Changing the alkyl chain length in *n*-alkanecarboxylate anions gives some information regarding the effect of the hydrophobic interaction in the system.

For these systems, the ultrasonic velocity were measured and the adiabatic compressibility was calculated in the wide composition range. The effect of the anionic hydration condition is discussed for several kinds of *n*-alkanecarboxylate ions.

EXPERIMENTAL

Preparation of Samples

Several kinds of sodium *n*-alkanecarboxylate hydrate melt were prepared. Component table of cation and anion is shown in Table 1. Double distilled water was used for dissolving and diluting. As a reference, aqueous sodium chloride solution was prepared. These samples were filtered with a sintered glass filter through a hot funnel in order to eliminate precipitations and solid impurities. The concentration was determined by the gravimetry. Concentration of each solution was represented by the molar ratio; $R=[H_2O]/[salt]$. Though the concentration ranges depend on the solubilities, it was concentrated enough to discuss in this study. The values of *R* ranged from ca. 2 to 50 for most of the system containing hydrate.

Ultrasonic Measurement

A send-receive type ultrasonic cell equipped with an x-cut quartz crystal as a transducer was used for the measurement of ultrasonic velocity in the sample liquid. The schematic drawings of block diagram are shown in Fig.1. Model UAC-77-S ultrasonic attenuation comparator (Teitsu Denshi Kenkyusho Co. Ltd.), model UAC-77-012 synchronous divider (Teitsu Denshi Kenkyusho Co. Ltd.), and DL2120 digital oscilloscope (Yokogawa Denki Co. Ltd.) were assembled for the measurement of the ultrasonic velocity. The path-length of the ultrasonic wave was adjusted with a micrometer. In order to prevent contamination caused by cell components, most of parts contacted with liquid were made of glass and polytetrafluoroethylene. Ultrasonic velocity was directly obtained from the delay time

required for the propagation of the pulsed ultrasonic wave with the variation of the path-length. All measurements were carried out at a frequency of 10 MHz and in the temperature range between 30 and 65°C. The temperature of the sample was controlled within $\pm 0.1^\circ\text{C}$ of each designated temperature by immersion of the ultrasonic cell in a water bath.

Calculation of Adiabatic Compressibility

Adiabatic compressibility, β , is given by the Eq. [1].

$$\beta = 1/dv^2 \quad [1]$$

where, d is the density of the hydrate. In order to calculate β , the density of the hydrate melt should have been measured. The density was measured by the Archimedean method weighing a ceramic sinker with an electronic balance.

RESULTS AND DISCUSSION

Ultrasonic Velocity

Composition dependence of the ultrasonic velocity was observed for the ultrasonic velocity in sodium *n*-alkanecarboxylate hydrate as shown in Fig.2. For the system containing sodium formate only, the ultrasonic velocity increased as the water content decreased simply, as well as the dependence for the system of aqueous NaCl solution. For the other systems; $\text{CH}_3\text{COONa}\cdot\text{H}_2\text{O}$, $\text{C}_2\text{H}_5\text{COONa}\cdot\text{H}_2\text{O}$, $n\text{-C}_3\text{H}_7\text{COONa}\cdot\text{H}_2\text{O}$ and $n\text{-C}_4\text{H}_9\text{COONa}\cdot\text{H}_2\text{O}$, which have hydrophobic parts in themselves, each composition dependence of ultrasonic velocity showed a maximal value. In the composition range of $R > 25$, those four systems having a hydrophobic parts showed nearly similar values at the same water content. In the range of $R < 25$, the longer the *n*-alkyl chain length was, the more gently the curve rose toward the maximal. Ultrasonic velocities for the systems having hydrophobic parts were larger than that of the system without hydrophobic group in the composition range at $R > 25$, where water molecules are considered to exist enough to form the hydration structure.

Adiabatic Compressibility

Calculated adiabatic compressibility, β , are shown in Fig.2. As well as the results of the ultrasonic velocity, these composition dependences were classified in two groups based on the structural difference of ions. The compressibility decreased simply as the water content decreased for the system containing sodium formate. Based on the hydrate structure of formate acid, formate anion forms hydration structure with six water molecules (4). In dilute concentration range of sodium formate solution, this bulky cluster may lead to larger adiabatic compressibility in $\text{HCOONa}\cdot\text{H}_2\text{O}$ than that in the other sodium *n*-alkanecarboxylates. For the system containing the anion having hydrophobic groups, the minimal values of the compressibility were observed and increased as the alkyl chain length increased.

We also measured the temperature dependence of the adiabatic compressibility. In the higher concentration range of R (dilute range), the value of β has a minimal point around 40°C . However the linear relationship between the compressibility and temperature was observed at a range lower than R at which the compressibility has the minimal value. This

results also suggested that the hydration structure changed at this concentration range.

The values of β were ranged at $2 - 4 \times 10^{10} \text{ Pa}^{-1}$. These values were smaller than that of the adiabatic compressibility in aqueous media forming a hydrogen bonding network such as water ($4.2 \times 10^{10} \text{ Pa}^{-1}$ at 60°C) and acetic acid ($7.0 \times 10^{10} \text{ Pa}^{-1}$ at 60°C). This result indicates that the hydrophobic group influences the water-water interaction and forms the hydrophobic hydration.

The adiabatic compressibility decreased gradually as n -alkyl chain length increased from $\text{CH}_3\text{COONa-H}_2\text{O}$ to $\text{C}_4\text{H}_9\text{COONa-H}_2\text{O}$ in composition range of $R > 30$. Also, the values of adiabatic compressibility for these four systems were clearly smaller than those of $\text{NaCl-H}_2\text{O}$ and $\text{HCOONa-H}_2\text{O}$ systems which do not include the hydrophobic group. It is considered that an increase of the region of hydrophobic hydration lead to expansion with the alkyl chain length. An adiabatic compressibility showed the minimum value for each system containing the ion having hydrophobic part, such as $\text{C}_n\text{H}_{2n+1}\text{COONa}$ ($n=1-4$). The composition range in which minimal values appeared increased as the alkyl chain length, as well as the variation for the ultrasonic velocity. In the following section, the effect of hydrophobic part of alkyl chain in the alkanecarboxylate ions are discussed.

Hydrophobic Effect

In the composition range of $R < 25$, different composition dependences appeared as shown in Fig.2 and 3. It is considered that the number of water molecule is not enough to make hydration structure and ion-water interactions and cation-anion interactions become dominant. In this composition range, at first, the number of water molecules which correlated to anion-water interactions decreases as water content decreased toward the minimal point of the adiabatic compressibility. A contribution of water-water interaction to ultrasonic velocity will be quite small due to a lack of water molecules in the solution. Considering the above results, the n -alkyl chain length may significantly influence the interactions among the dissolved species in a hydrate melt structure.

The minimal point of the adiabatic compressibility for each system appeared at higher water content with an increase of n -alkyl chain length in an anion as shown in Fig.4. These plots show a linear relationship of which gradient, $R/\text{C-atom}$, is ca. 4.7. This clear dependence suggests that this value is related to anion-water interaction, especially, between one-methylene group and water. The minimal points may appear at the composition at which the hydrophobic hydration of individual n -alkyl group-water interaction cannot be kept. The larger the n -alkyl chain length in the anion is, the more dominant the hydrophobic interactions may be in the melt, because the maximal ultrasonic velocity decreased in the increase of n -alkyl chain length. It is considered that an increase of the number of C-atoms caused that water molecules enter to the compressible part in the hydrate melt at the minimal point of adiabatic compressibility. Those water molecules in hydrate melt may form voluminous structure which have low energy of configurations such as the structure of ice (5). Consequently, it is concluded that the hydrophobic groups occupy large part of the hydrate melt and interactions in hydrate melt are related to the hydrophobic hydration of the alkyl groups.

In this composition range, in which hydrate melt exists, the ultrasonic velocity rapidly decreased as water content decreased. The size and chemical nature of the surfactant

hydrophobic *n*-alkyl chain have an important bearing on the magnitude of the critical micelle concentration, CMC. The values of CMC for this aqueous sodium *n*-alkanecarboxylate media represent that the hydrophobic and hydrophilic parts assemble the micelle structure. The values of CMC in the reference corresponded to the values of *R* in which the maximal values of the ultrasonic velocity was obtained in this study (6). It is suggested that the micelle structure was formed and the phase separation between hydrophilic and hydrophobic parts occurred in these liquid media and related to the ultrasonic phenomena.

Effect of Hydration of Cationic Species

As mentioned above, the hydrophobic hydration effect of anion was dominant for the aqueous *n*-alkanecarboxylate. In order to support this result, we discuss the cation effect on the hydration phenomena in the viewpoint of ultrasonic properties. The variations of the ultrasonic velocities and the adiabatic compressibility with the composition ratio, *R*, are shown in Fig.5. Though values for the three kinds of hydrate melt are different at the same value of *R*, the minimal points of compressibility were close values among these systems. For the other systems containing the *n*-alkanecarboxylate, the same tendencies were observed. As described in previous section, the relationship between the values of *R* at the minimal point of adiabatic compressibility and the number of C-atoms in the *n*-alkyl chain of carboxylate anion is shown in Fig.6. Linear relationships are observed for each kind of carboxylate. However, the difference among the cationic species are quite smaller than those of anions. Therefore, cationic species have a smaller effect in these systems than the anionic hydrophobic hydration in the alkali metal *n*-alkanecarboxylate hydrate.

CONCLUSIONS

The ultrasonic velocity and adiabatic compressibility were measured for the various kind of alkali metal *n*-alkanecarboxylate hydrates. The maximal value of the velocity and the minimal value of the compressibility were obtained for the system containing the anion having a hydrophobic part in itself. These results suggested that the phase separation related to molecular hydrophilicity occurred in the hydrate. The effect of hydrophobic hydration was larger than that of the cationic hydration in the alkali metal *n*-alkanecarboxylate hydrate melt.

REFERENCES

- 1) F. Franks and D. J. Ives, *Rev. Chem. Soc.*, **20**, 1 (1966).
- 2) S. Deki, T. Inuzuka, H. Nakahara, A. Kajinami, and Y. Kanaji, Proceedings of the Fourth Japan-China Bilateral Conference on Molten Salt Chemistry and Technology, p. 154, Kyoto, (1992)
- 3) A. Kajinami, T. Otsuka, S. Deki, and Y. Kanaji, *ibid*, p. 142, Kyoto (1992).
- 4) R. P. Varma and A. Kumer, *Tenside Surf. Det.*, **29**[5], 359 (1992).
- 5) A. Shi, J. V. Ford, S. Sei, and A. W. Castleman, Jr, *J. Chem. Phys.*, **99**, 8009 (1993).
- 6) I. J. Lin, *Soc. Mining Eng., AIME*, **250**, 225(1971).

Table I. Component table of cation and anion of prepared samples. G.R.: anhydrous guaranteed reagent purchased. NTRL :neutralized from corresponding acid and hydroxide. All of reagents were guaranteed reagent.

cation \ anion	formic HCOO^-	acetic CH_3COO^-	propionic $n\text{-C}_2\text{H}_5\text{COO}^-$	<i>n</i> -butyric $n\text{-C}_3\text{H}_7\text{COO}^-$	<i>n</i> -valeric $n\text{-C}_4\text{H}_9\text{COO}^-$
Li^+	—	G.R.	NTRL	NTRL	—
Na^+	G.R.	G.R.	G.R.	NTRL	NTRL
K^+	—	G.R.	NTRL	NTRL	—

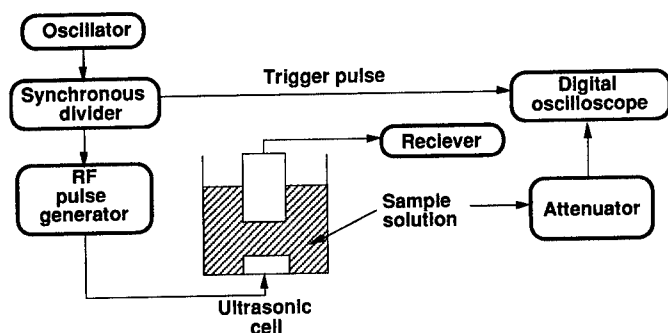


Fig. 1. Block diagram of the pulse method for measurement of ultrasonic velocity.

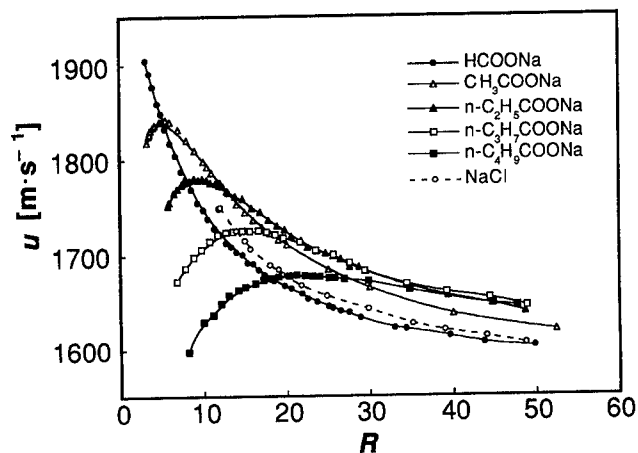


Fig.2. Composition dependence of the ultrasonic velocity for sodium *n*-alkanecarboxylate hydrate and sodium chloride systems at 60°C.

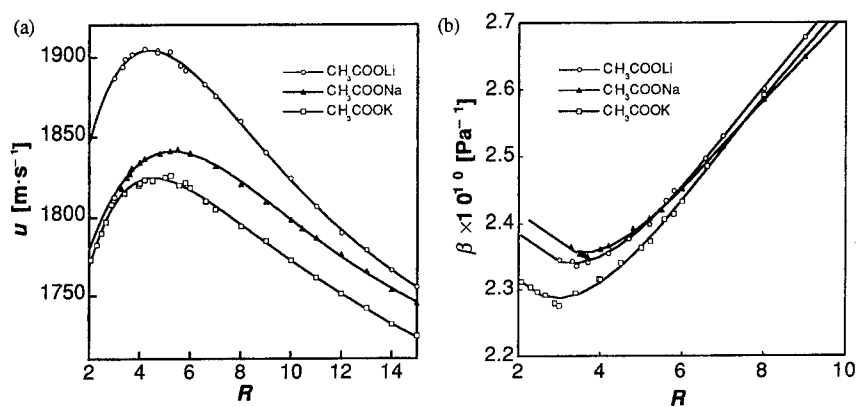


Fig.5. Variations of (a) the ultrasonic velocities and (b) the adiabatic compressibilities with the compositions for the alkali metal acetate hydrate melt at 60°C.

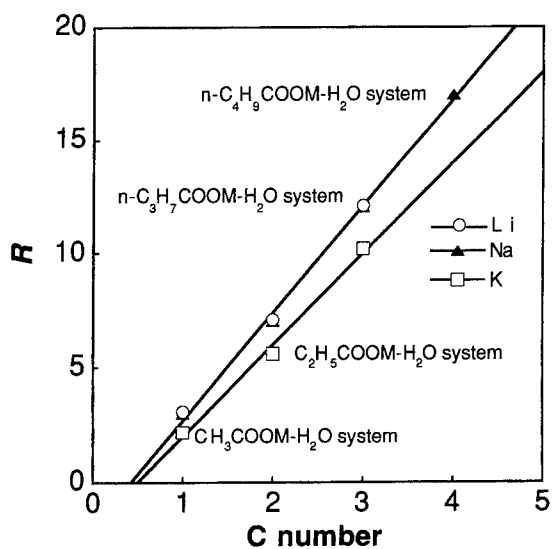


Fig.6. Relationships of R at the minimal points of the adiabatic compressibilities with the number of C atoms in the alkyl chain of the carboxylate anion for the alkali metal n -alkanecarboxylate hydrate melt.

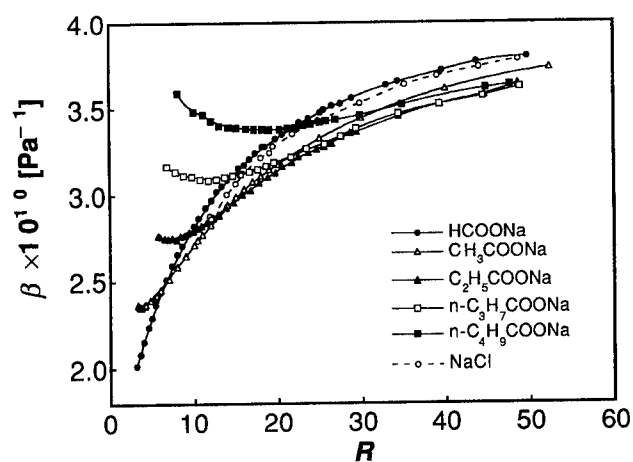


Fig.3. Composition dependence of the adiabatic compressibility for sodium *n*-alkanecarboxylate hydrate and sodium chloride systems at 60°C.

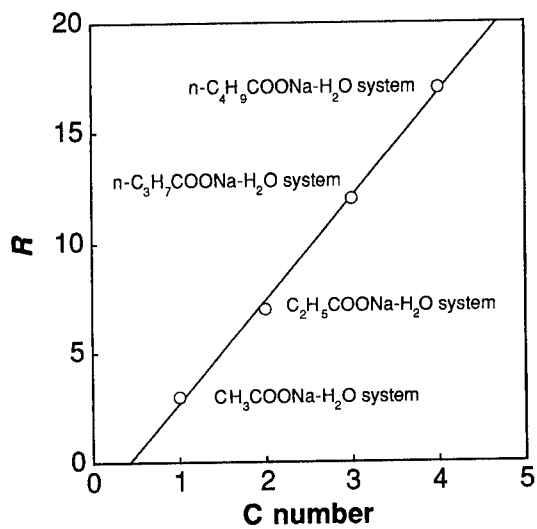


Fig.4. Relationship of *R* at the minimal points of the adiabatic compressibility with the number of C-atoms in the *n*-alkyl group of carboxylate anion for $C_nH_{2n+1}COONa-H_2O$ ($n=1-4$).

ELECTRODEPOSITION OF COBALT-ALUMINUM ALLOYS FROM THE
ALUMINUM CHLORIDE-1-METHYL-3-ETHYLIMIDAZOLIUM
CHLORIDE ROOM-TEMPERATURE MOLTEN SALT

John A. Mitchell, William R. Pitner, and Charles L. Hussey
Department of Chemistry
University of Mississippi
University, MS 38677

Gery R. Stafford
Materials Science and Engineering Laboratory
National Institute of Standards and Technology
Gaithersburg, MD 20899

The electrodeposition of magnetic cobalt-aluminum alloys was investigated in the Lewis acidic aluminum chloride-1-methyl-3-ethylimidazolium chloride (60.0-40.0 mole %) molten salt containing electrogenerated Co(II) at 25 °C. Alloy deposits containing up to 62 atomic % aluminum were produced at potentials positive of that for the bulk deposition of aluminum. The onset of the underpotential driven aluminum co-deposition process occurred at around 0.40 V versus the Al/Al(III) couple. The Co-Al alloy composition displayed an inverse dependence on the Co(II) concentration, but tended to become independent of concentration as the potential was decreased. A RRDE voltammetry technique was developed to analyze the composition and structure of the Co-Al alloy deposits. SEM-EDS analysis of bulk electrodeposits revealed that the deposit morphology depends strongly upon the aluminum content/deposition potential; deposits produced at 0.40 V consisted of 10-20 μm diameter multifaceted nodules of pure hcp cobalt whereas those obtained at 0.20 V were dense and fine grained, containing about 4 atomic % Al. Deposits produced at 0 V had the visual appearance of a loosely adherent black powder. XRD diffraction measurements revealed a lattice expansion and a decrease in grain size as the hcp cobalt was alloyed with increasing amounts of aluminum.

INTRODUCTION

Transition metal-aluminum alloys are of great interest because of their structural properties, corrosion resistance, and, in some cases, unusual magnetic properties. These materials are often difficult to prepare using conventional metallurgical processes; however, electrodeposition offers a convenient route to some of these materials. Lewis acidic (AlCl_3 -rich) chloroaluminate molten salts are useful electrolytes for the electrodeposition of transition

metal-aluminum alloys. The attractiveness of these molten salts stems in part from the fact that they constitute a concentrated reservoir of reducible aluminum-containing species such as Al_2Cl_7^- . Of the extant chloroaluminate melts, the AlCl_3 -NaCl system has received the most attention, and the electrodeposition of several nonequilibrium binary alloys, e.g., Cr-Al,¹ Mn-Al,^{2,3} Ni-Al,⁴ and Ti-Al,⁵ has been achieved in this melt.

Low melting salts are obtained when the alkali chloride component(s) of traditional chloroaluminate melts are replaced with certain unsymmetrical quaternary ammonium chloride salts such as 1-(1-butyl)pyridinium chloride (BupyCl) or 1-methyl-3-ethylimidazolium chloride (MeEtimCl). The physical and electrochemical properties of these organic salt-based molten salt systems have been reviewed.^{6,7} The AlCl_3 -BupyCl and AlCl_3 -MeEtimCl molten salts are less conductive and more viscous than the AlCl_3 -NaCl and related inorganic systems, but in actuality they present fewer experimental challenges. For example, they can be employed at room temperature, and they exhibit no vapor pressure due to the escape of AlCl_3 and/or Al_2Cl_6 , which is a debilitating characteristic of the Lewis acidic inorganic chloroaluminates.

In a previous article, we described the electrodeposition of magnetic Ni-Al alloys from solutions of nickel(II) in the acidic AlCl_3 -MeEtimCl melt at 40 °C.⁸ Ni-Al alloys containing up to 40 atomic % aluminum were obtained. The mechanism leading to the formation of Ni-Al involves the underpotential deposition (UPD) of aluminum during the mass-transport-limited electrodeposition of nickel. It was recently reported^{9,10} that magnetic Co-Al alloys containing up to 62 atomic % aluminum can be electrodeposited from solutions of cobalt(II) in the AlCl_3 -MeEtimCl melt and that the co-deposition of aluminum is driven by a UPD mechanism similar to that found for the Ni-Al system. However, few experimental details are given in these reports, and the influence of the cobalt(II) concentration and deposition potential on the composition, surface morphology, and crystal structure of the electrodeposited alloys is unknown. In this article, we describe the results of an investigation of the electrodeposition of Co-Al alloys from the acidic AlCl_3 -MeEtimCl molten salt. Thin layer Co-Al electrodeposits were studied under the idealized mass transport conditions afforded by rotating electrode voltammetry, and bulk deposits were prepared on copper wire electrodes and characterized by SEM-EDS and XRD techniques.

EXPERIMENTAL

The glove box system and the methods used to prepare and purify the AlCl_3 -MeEtimCl melt were identical to those employed previously.⁸ Rotating-disk electrode (RDE) voltammetry and controlled-potential coulometry experiments were performed with an EG&G Princeton Applied Research Corp.^a (EG&G PARC) Model 173 potentiostat/galvanostat,

^aCertain commercial materials and instruments are identified in this report to adequately specify the experimental procedure. In no instance does such identification imply recommen-

Model 179 digital coulometer plug-in module, and Model 175 universal programmer. Rotating-ring-disk electrode (RRDE) voltammetry experiments were carried out by using a Pine Instrument Co. Model RDE 3 bipotentiostat combined with an EG&G PARC Model 379 digital coulometer. Controlled electrode rotation was provided by a Pine Model AFMSRX electrode rotator. RRDE data were recorded with two Linseis Model 1600 X-Y/Y-t recorders. The electrodes used for RDE and RRDE voltammetry were Pine Instrument Co. Teflon-sheathed platinum disk (geometrical area = 0.196 cm²) and platinum ring-disk ($r_1 = 2.29$ mm, $r_2 = 2.46$ mm, and $r_3 = 2.69$ mm) electrodes, respectively. Before use, these electrodes were polished to a mirror finish with an aqueous slurry of 0.05 μm alumina by using a Buehler Metaserve grinder/polisher, rinsed with distilled water, and dried under vacuum in the glove box antechamber. They were conditioned before each experiment by holding them at the positive limit of the melt (~ 2.2 V) for about 30 s. The electrode rotation rate employed for all RDE and RRDE experiments was 104.7 rad s⁻¹. The counter electrode was a spiral of 1-mm diameter cobalt wire (Alfa/AESAR, Puratronic) immersed directly in the bulk melt. All potentials were referenced to the Al/Al(III) couple in the 60.0-40.0 mole % (m/o) melt. The reference electrode was identical in design to that described in a previous article,⁸ i.e., an aluminum wire (Alfa/AESAR, Puratronic) spiral was placed in a melt-filled tube terminated by an ACE porosity E glass frit. This tube was submerged in the bulk melt in the cell so that the liquid levels inside and outside the tube were equal. Cobalt(II) was introduced into the melt by anodization of a cobalt wire working electrode identical to the counter electrode. However, in this case the counter electrode was similar to the reference electrode described above. The solubility of cobalt(II) in the melt was not determined, but 0.10 mol L⁻¹ solutions of cobalt(II) were routinely prepared by using this procedure. All experiments were conducted in the 60.0-40.0 m/o melt at 25 \pm 1 $^{\circ}\text{C}$.

Protonic impurities were removed from the melt prior to its use in order to avoid the co-deposition of hydrogen. Therefore, the AlCl₃-MeEtimCl molten salt was electrolyzed between aluminum electrodes in the glove box for several days as previously described.⁸ After filtering the melt through a medium porosity glass frit to remove aluminum particles that had detached from the aluminum cathode during electrolysis, the melt was evacuated to 1.3 $\times 10^{-3}$ Pa for 24 h.

The composition and structure of bulk alloy electrodeposits were probed with scanning electron microscopy (SEM), energy dispersive x-ray spectroscopy (EDS), and x-ray diffraction (XRD) techniques (Cu-K α radiation) using the facilities at the National Institute of Standards and Technology. SEM and EDS were carried out on polished cross sections of alloy electrodeposited on 1-mm diameter copper wire. Samples were overplated with copper using a copper cyanide strike followed by bright copper from a copper sulfate electrolyte.¹¹

ation or endorsement by the National Institute of Standards and Technology, nor does it imply that the material identified is necessarily the best available for this purpose.

For quantitative analysis, the EDS results were referenced to pure aluminum and cobalt standards. The reported values are the averages of at least six measurements.

RESULTS AND DISCUSSION

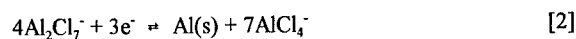
Voltammetric Results

Solutions of cobalt(II) in the 60.0-40.0 m/o melt were prepared by the controlled-potential coulometric anodization of a cobalt wire electrode at a potential of 1.30 V. Calculations based on the charge passed and the weight loss of the electrode resulting from anodization confirmed that cobalt(II) was the oxidation product. Figure 1 shows RDE voltammograms recorded point-by-point in 5.00, 10.0, 25.0, and 50.0 mmol L⁻¹ solutions of cobalt(II) at a Pt-RDE. Each data point in these voltammograms is the average of no less than two independent experiments. The procedure used to record these voltammograms involved pulsing the potential of the Pt-RDE from 1.20 V, where no reduction current was observed, to the desired final potential and then holding the electrode at this potential until a steady-state current was obtained. Such a current was usually attained in less than 30 s, and in no case was a continuous rise in the current observed that suggested the growth of a dendritic deposit with dimensions exceeding those of the electrode diffusion layer. After the current for the data point of interest was recorded, the electrode was held at a potential of 2.20 V for 30-45 s to strip the electrodeposit and then the process was repeated at a new potential. The resulting voltammograms were found to be more reproducible than those constructed from potentiostatic current-time transients acquired at a stationary electrode in the traditional way. Also shown in Fig. 1 is a voltammogram recorded in pure melt by using the same technique; no significant reduction current was obtained at the Pt-RDE, indicating that the concentration of reducible protonic impurities was very low in the melt used in this investigation.

Each of the voltammograms in Fig. 1 displays a well-defined limiting current; this limiting current corresponds to the following mass-transport-limited reaction



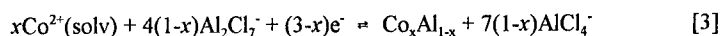
where $\text{Co}^{2+}(\text{solv})$ represents cobalt(II) solvated by the molten salt. The average diffusion coefficient for cobalt(II), calculated from the limiting currents of the four voltammograms shown in Fig. 1, is $(3.4 \pm 0.1) \times 10^{-7} \text{ cm}^2 \text{ s}^{-1}$. In pure melt, i.e., melt without dissolved cobalt(II), the bulk deposition of aluminum



was not observed unless the Pt-RDE was held at potentials slightly negative of 0 V. Thus, to avoid interference from this process, all experiments were conducted at or above this potential.

At lower potentials, each of the voltammograms in Fig. 1 exhibits an increase in current due to the co-deposition of aluminum with cobalt. The exact potential at which the onset of this current increase takes place can not be stated due to the imprecision of the voltammograms shown in Fig. 1, but it does seem to depend on the cobalt(II) concentration, commencing between 0.40 and 0.35 V in the 5.00 mmol L⁻¹ solution and between 0.35 and 0.30 V in the 50.0 mmol L⁻¹ solution. A similar rise in current due to the co-deposition of aluminum with nickel is seen at about 0.40 V during the reduction of nickel(II) on glassy carbon in acidic AlCl₃-MeEtimCl. However, the onset of aluminum co-deposition and the potential at which the nickel(II) reduction reaction becomes limited by mass-transport coincide (*cf.* Fig. 2, ref. 8). Thus, in that case, the voltammograms do not exhibit a well-defined limiting current.

For convenience, the co-deposition of aluminum with cobalt can be represented by the following reaction



where x and $1-x$ represent the mole fractions of Co and Al in the Co-Al alloy, i.e., $\text{Co}_x\text{Al}_{1-x}$. The value of $1-x$ was estimated from each of the Pt-RDE voltammograms in Fig. 1 with the following expression

$$1-x = 1/[1 + 1.5i_l/(i_t - i_l)] \quad [4]$$

where i_l is the limiting current for the reaction in Eq. 1, and i_t is the total current at potentials where the reaction in Eq. 3 is observed. Plots of $1-x$ versus potential that resulted from these calculations are presented in Fig. 2. These graphs show that $1-x$ is dependent upon both the cobalt(II) concentration and the applied potential. However, the alloy composition becomes nearly independent of both variables as the potential is decreased with $1-x$ approaching ~ 0.62 (62 atomic % Al) at 0 V. This behavior indicates that the aluminum co-deposition process is kinetically limited, i.e., the co-deposition of aluminum can not keep pace with the mass-transport-controlled deposition of cobalt, except at very negative potentials.

Thin-layer Deposition-Stripping Experiments

The composition and structure of Co-Al alloy electrodeposits were examined further by carrying out anodic linear sweep voltammetry (ALSV) deposition-stripping experiments at a Pt-RRDE. These experiments were similar in principle to those described by Andricacos and coworkers¹²⁻¹⁴ in which a thin-layer alloy film is electrodeposited on a RRDE under controlled-potential conditions in a plating solution and then anodically dissolved from the disk electrode in a suitable stripping solution with slow scan ALSV. During the anodic dissolution step, the ring electrode potential, E_r , is held at a value that results in the oxidation of the metal ions of one of the alloy components produced at the disk. For example, during the anodic dissolution of Ni-Fe alloys, both iron(II) and nickel(II) are produced at the disk

electrode, and E_r is set to a value where iron(II) is oxidized to iron(III). Because nickel(II) can not be oxidized within the potential window of the solvent, the oxidation waves that correspond to the dissolution of iron from the alloy deposit can be identified by observing the ring current as a function of the disk potential.¹² The alloy composition can be calculated from the ring and disk charges, Q_r and Q_d , respectively, and knowledge of the experimental collection efficiency, N_{exp} , of the RRDE electrode.

In the present case, neither aluminum(III) or cobalt(II), the Co-Al alloy dissolution products, can be oxidized within the potential window of the melt. However, as discussed above, it is possible to carry out the mass-transport-limited reduction of cobalt(II) without electrodepositing either Co-Al alloy or bulk aluminum. Thus, by setting E_r to 0.500 V, it should be possible to reduce any cobalt(II) produced during anodic dissolution of the Co-Al alloy at the ring, permitting identification of those alloy stripping waves that have a current component arising from the oxidation of cobalt. Before the proposed method can be employed, N_{exp} must be known, and its value must be in reasonable accord with theoretical predictions. Therefore, collection experiments were carried out by electrodepositing cobalt metal on the disk electrode at a deposition potential of 0.500 V in a solution of cobalt(II) with the ring electrode inactive. The cobalt was then anodically dissolved from the disk in pure melt with slow scan (0.002 V s⁻¹) ALSV while the ring was held at 0.50 V. These experiments yielded a value of $N_{exp} = 0.221$; this result is in excellent agreement with the theoretical collection efficiency of 0.220 for this electrode, which was calculated from r_1 , r_2 , and r_3 .¹⁵

In view of these very favorable results, a series of ALSV experiments were carried out at the Pt-RRDE over the range of deposition potentials where the formation of Co-Al alloy is expected, i.e., from 0.400 to 0 V. In these experiments, 425 mC cm⁻² electrodeposits were produced on the disk electrode in a 5.00 mmol L⁻¹ solution of cobalt(II). During a previous study of Ni-Al alloys, the deposit composition was found to depend on the charge density.⁸ This phenomenon is believed to arise from the thermodynamic instability of aluminum in the alloy in solutions of nickel(II). The Co-Al alloy was found to display similar instability in cobalt(II) solutions, and a minimum charge density of ca. 325 mC cm⁻² was needed to obtain Co-Al deposits of constant composition. The electrode was then transferred to pure melt, and the Co-Al electrodeposit was slowly oxidized from the disk electrode as described above for the collection experiments.

Typical voltammograms illustrating the disk and corrected ring currents that resulted from several of these experiments are shown in Figs. 3 and 4. For deposits produced at 0.400 V, the major feature of the disk voltammogram was a wave with an anodic peak potential, E_p^a , of 0.93 V. The large ring current that was observed as the disk potential was scanned through this stripping wave indicates that a major component of the current arises from the oxidation of cobalt in the deposit. However, the charge corresponding to this wave was slightly larger than the corrected ring charge, Q_r/N_{exp} , indicating that some of the current must be due to the oxidation of aluminum. For the deposit prepared at 0.300 V, the disk voltam-

mogram (Fig. 3) revealed oxidation waves with $E_p^a = 0.83$ and 0.55 V, respectively. A ring current was associated with the former but not the latter, indicating that the wave at 0.55 V must arise from the selective dealloying of aluminum. The disk voltammograms corresponding to the 0.200 , 0.100 , and 0 V deposits (Fig. 4) were similar in appearance to that of the 0.300 V deposit, except that the aluminum wave was shifted to $E_p^a = 0.67$ V in the case of the 0.200 V deposit and appeared at $E_p^a = 0.63$ and 0.56 V in the voltammograms of the 0.100 and 0 V deposits, respectively. A small amount of aluminum was also oxidized from each of these deposits at potentials proximate to the oxidation of cobalt.

These shifts in the position of the aluminum stripping wave indicate that the activity of aluminum in the alloy is changing with the aluminum content of the alloy. However, it is unclear why aluminum dissolution occurs at two different potentials. If one assumes that the deposit is two phase and that the second dissolution is due to aluminum contained in a cobalt-rich phase, then the two phases cannot be in equilibrium because the aluminum activity must be different in each phase. Alternatively, the aluminum associated with the second dissolution process may simply be inaccessible to oxidation until some dissolution of cobalt occurs. The negative shift in the cobalt stripping wave associated with alloyed deposits may then be due to the more favorable dissolution kinetics of a porous cobalt layer over that of a pure, compact deposit.¹⁶

The characteristics of anodic linear sweep voltammograms for the dissolution of an alloy deposit are very sensitive to the composition and structure of the deposit. Theoretical and experimental studies have attempted to correlate peak shape and location with the type of alloy that is electrodeposited.^{16,17} However, a detailed analysis of the voltammograms in Figs. 3 and 4 beyond that given here would be purely speculative without reliable information about the phase distribution in Co-Al alloys containing up to 62 atomic % aluminum.

The alloy composition ($1-x$) as a function of deposition potential was calculated from N_{exp} and the values of Q_r and Q_d that resulted from numerous experiments similar to those described above by using the following expression

$$1-x = 1/\{1 + 1.5[Q_r/(N_{exp}Q_d - Q_r)]\} \quad [5]$$

The resulting values of $1-x$ are plotted as a function of potential in Fig. 2, and they are in very good agreement with the values of $1-x$ derived from the Pt-RDE voltammetric currents observed in a 5.00 mmol L^{-1} cobalt(II) solution.

Preparation and Characterization of Bulk Alloy Electrodeposits

Bulk electrodeposits were prepared on 1-mm copper wire electrodes at potentials ranging from 0.400 to 0 V in a 50.0 mmol L^{-1} solution of cobalt(II) at 40°C . During deposition, the solution in the cell was agitated with a small Teflon-coated stir bar. At the conclusion of each experiment, the copper electrode was rinsed with dry benzene to remove

residual melt. A charge density of 60 C cm^{-2} was used to prepare each deposit. This should result in a deposit thickness of $20 \mu\text{m}$, assuming 100 % current efficiency for cobalt. The surface morphology of these electrodeposits is shown in Fig. 5. The as-deposited surface morphology showed significant variations as a function of deposition potential. For example, deposits prepared at 0.400 V (Fig. 5a) were fairly rough, consisting of nodules on the order of $10\text{-}20 \mu\text{m}$ in diameter. At higher magnification, these nodules seemed to be multifaceted, revealing their crystallographic nature. EDS analysis of these deposits indicated that they were pure cobalt and free of chloride. In contrast, smooth, spherical nodules were also occasionally observed. These nodules have an appreciable chloride content and were the likely remnants of electrolyte trapped within the nodular structure. Figure 5b shows that deposits produced at 0.200 V were very dense and fine-grained. Interestingly, nucleation appeared to follow a longitudinal pattern associated with surface defects on the drawn copper wire. For deposits prepared at 0.100 V (Fig. 5c), a nucleation pattern similar to that seen in the 0.200 V deposit was observed; however, the features are much larger and each nodule has a round, smooth appearance. This nodule morphology was quite similar to that observed in amorphous Mn-Al electrodeposits.¹⁸ The darker regions between the rows of nodules have a high chloride content and were extensively cracked. Again this is likely to be due to the inter-nodular entrapment of electrolyte. Electrodeposits prepared at 0 V had the visual appearance of a loosely adherent, fine black powder, which is clearly seen in Fig. 5d.

Polished cross-sections of these deposits were prepared and compositions were determined by EDS. All of the deposits, except that prepared at 0 V, yielded cross-sections of sufficient quality that the compositions could be determined quantitatively; i.e., the deposits were free of contaminants such as chloride, and the volume examined was sufficiently large so that the copper substrate and overplate did not interfere with the analysis. The composition results are shown in Fig. 6. Electrodeposits prepared at 0.400 and 0.300 V consisted of pure cobalt. The total x-rays detected from the EDS analysis was 97.5% of that obtained from the pure cobalt standard, indicating that the deposit density was close to that of the metallurgical standard. In contrast to the thin-layer voltammetric results presented above, aluminum was first detected in bulk electrodeposits prepared at 0.200 V. It is presently unclear whether the reduced nodule size of this sample (compare Figs. 5a and 5b) resulted from the addition of aluminum or was a natural consequence of the lower deposition potential. The value of $1-x$ increased to about 0.16 for deposits produced at 0.100 V. In addition, the deposit density, based on the total x-rays detected, dropped to about 85 % of theoretical relative to the pure cobalt and aluminum standards, indicating either a decrease in the density or an increase in the deposit porosity at the lower deposition potentials. In cross-section, the deposit formed at 0 V appeared as clusters of $0.5\text{-}1.0 \mu\text{m}$ size "islands" of Co-Al in a copper matrix (overplate). Quantitative analysis could not be performed on these samples due to the small volume of Co-Al alloy as compared to the EDS excitation volume. Consequently, a copper-free analysis could not be made; however, a comparison of only the cobalt and aluminum signals suggested that $1-x$ is on the order of 0.20-0.25 for this deposit. This is likely to be a low estimate of the aluminum content.

The x-ray diffraction patterns for electrodeposits formed at potentials ranging from 0 to 0.400 V are shown in Fig. 7. Several structural changes were observed as the deposition potential was decreased. At 0.400 V, the deposit was clearly hexagonal close-packed (hcp) cobalt. The absence of the (200) reflection, which should appear at 51.5° , suggested that there was no face-centered cubic (fcc) cobalt present in the deposit. At lower deposition potentials, the reflections for hcp cobalt shifted to lower values of 2θ and became somewhat broader. At 0 V, the electrodeposit was entirely amorphous. In addition, reflections due to the copper substrate ((111) at 43.3° , (200) at 50.4° , etc.) began to appear in the deposit prepared at 0.300 V and increased in intensity as the deposition potential was lowered. This implies that the deposits became thinner or that the average atomic weight became reduced as the potential was decreased. Both of these changes would be expected to occur as more aluminum is incorporated into deposits of equal charge density. However, the fact that the copper substrate was seen in the 0.300 V deposit that contained no appreciable aluminum suggests that the appearance of the substrate reflections was not due to chemical changes in the film, but to nonuniform morphology and thickness between samples.

Figure 8 shows the lattice parameters obtained from the diffraction patterns in Fig. 7. The Nelson-Riley technique was used to determine the lattice parameters in order to eliminate systematic errors such as sample displacement.¹⁹ These results indicate that both hcp lattice parameters were near their equilibrium values at a deposition potential of 0.400 V and increased as the deposition potential was reduced, suggesting that the alloying of hcp cobalt was taking place. An overall lattice volume expansion of 0.71 % was observed over the range of deposition potentials examined.

The x-ray diffraction patterns in Fig. 7 show that the hcp cobalt reflections became broader as the deposition potential was reduced. The Scherrer equation²⁰ can be used to estimate the grain size for electrodeposited cobalt from the full-width at half-maximum (FWHM). This grain size must be viewed as a lower limit because the treatment fails to consider microstrain, which can be appreciable in electrodeposits. Figure 9 is a plot of the grain size, calculated from three fundamental reflections, as a function of deposition potential. The data in this figure show that the average grain size drops significantly with decreasing deposition potential. Because the crystallographic grain size is expected to be inversely proportional to nucleation density, the observed decrease in grain size was consistent with electrocrystallization theory that predicts a higher nucleation density with increased overpotential. The grain refinement observed in the x-ray diffraction patterns may also result from the addition of aluminum to the cobalt.

The equilibrium, room-temperature structure of cobalt is hcp. At temperatures between 422 and 1495 °C, the fcc high-temperature variant is stable.²¹ The free energy difference of these two structures is quite small; consequently, the fcc structure can be retained at room temperature by rapid solidification.²² Electrodeposition from aqueous electrolytes has also been used to form both structures at room temperature.²³⁻²⁸ The microstructure of electrodeposits produced from low pH (~1.6) electrolytes consists of

highly-faulted fcc regions; at higher pH (~5.7), the hcp phase is formed and the fault density is greatly reduced.²⁶ It has been proposed that the formation of fcc cobalt, most likely in the form of a metastable hydride, is facilitated by the adsorption and subsequent incorporation of atomic hydrogen into the electrodeposit.²⁶ The absence of fcc cobalt in electrodeposits produced from $\text{AlCl}_3\text{-MeEtimCl}$ melts supports this notion of the hydride assisted deposition of the fcc phase. Though it is suspected that the proton content of these melts can significantly alter the deposit morphology, its effect on crystallographic structure has not been investigated. In any case, the level of reducible protonic impurities was very low in the melt used for this investigation.

The room temperature solubility of aluminum into hcp cobalt is quite small, significantly less than 0.5 atomic %.¹⁹ For aluminum compositions above this solubility limit and extending to 42 atomic % aluminum, a two phase field consisting of hcp cobalt and ordered bcc Co-Al (CsCl-type) exists. Aluminum has a much higher solubility in fcc cobalt, and an equilibrium solubility as high as 16 atomic % can be achieved at 1400 °C. Rapidly cooled alloys containing 5 to 16 atomic % aluminum often retain the fcc structure over the two phase hcp-bcc equilibrium structure.^{22,29} However, a martensitic transformation to an hcp structure has been reported in this composition range for alloys quenched from 1300 to -196 °C.³⁰ The hcp structure is formed by the periodic introduction of stacking faults in the close-packed {111} fcc layers. Four martensitic hcp phases, each having a different stacking fault periodicity have been identified.³⁰

The development of the x-ray diffraction patterns of the Al-Co electrodeposits with lower deposition potentials indicates that the addition of aluminum to the alloy causes a decrease in the deposit grain size and an increase in the hcp lattice volume. A further increase in the aluminum content results in amorphization of the deposit. Because the equilibrium phase diagram predicts a two phase terminal hcp-ordered bcc structure, the electrodeposit is clearly metastable over the entire composition range examined.

When considering non-equilibrium processing methods, one can often gain a better understanding of phase development by comparing the free energy of the possible metastable structures over the composition range of interest. The free energy-composition curves for the Co-Al system at 40 °C were calculated using the constitutive equations from Kaufman et al.^{31,32} (Fig. 10). The free energy for the amorphous phase was assumed to be that of the supercooled liquid. In addition, ordering and compound formation were not considered. As a consequence, the free energy of equilibrium Co-Al (ordered bcc) will be somewhat lower than that depicted by the disordered bcc curve. Clearly, the hcp-bcc common tangent minimizes the free energy over most of the composition range giving rise to a two-phase hcp-bcc region from essentially 0 to about 42 atomic % Al. One can see that the free energy of the hcp and fcc structures are quite close, with the fcc becoming more stable for alloy compositions greater than about 4 atomic % aluminum. This stabilization of the fcc structure with the addition of aluminum is seen experimentally in rapidly solidified alloys.^{22,29} Also apparent in the free energy diagram is the thermodynamic stability of the amorphous phase

with respect to the hcp and fcc structures for alloys containing greater than 25 atomic % aluminum. If nucleation of the equilibrium bcc phase were kinetically hindered, one might expect the formation of an amorphous phase over a disordered fcc or hcp structure, based on these calculations.

We have experimental evidence for the deposition of an hcp Co-Al solid solution and an amorphous phase, both of which can be rationalized thermodynamically. What is not clear is the extent of the supersaturation of aluminum in the hcp cobalt and the composition at which the amorphous phase first nucleates; i.e., does the amorphous phase co-exist with the supersaturated hcp cobalt or replace it at some critical aluminum concentration? We know that aluminum substitutes into the hcp lattice causing an increase in the lattice volume (Fig. 8). One would expect such an increase when a larger aluminum atom substitutes for cobalt in the lattice. The lattice volume for fcc cobalt is reported to increase by 0.17% per atomic % Al in the 0-16 atomic % Al composition range.²² Exactly how much aluminum is going into the hcp lattice in these electrodeposited alloys is unclear because lattice parameter-composition data for hcp Co-Al is not available in the literature. Further, the measured alloy compositions cannot be associated with the hcp phase alone unless it has been established that these deposits are single phase.

The electrodeposits containing appreciable aluminum may be a two phase mixture of supersaturated hcp cobalt and an amorphous phase of higher aluminum composition. Such phase development has been reported in Mn-Al alloys electrodeposited from chloroaluminate electrolytes at 150 °C.³³ At low manganese concentrations (less than 5 atomic %) the deposit is single phase, supersaturated fcc and one observes a linear decrease in lattice parameter with increasing manganese content. Above 5 atomic % manganese, a Mn-Al amorphous phase (nominally $Mn_{0.15}Al_{0.85}$) co-deposits with fcc Al, causing a dramatic relaxation in the fcc supersaturation and an increase in the fcc lattice parameter to that of a 1 atomic % manganese solid solution. One can clearly determine the potential (or alloy composition) where the deposit becomes two phase by the discontinuity in the fcc lattice parameter. In the 5 to 15 atomic % manganese composition range, a metastable two-phase equilibrium between the fcc phase and the amorphous phase is established. In this region, the fcc lattice parameter is invariant, indicating that only the phase distribution, not the composition of each phase, is changing with overall alloy composition. One would expect this type of behavior from common tangent construction in the two phase region. The 15 atomic % manganese electrodeposit is entirely amorphous. If a metastable two-phase equilibrium does exist in the electrodeposited Co-Al alloys, then one should be able to estimate the phase distribution from a common tangent construction of the hcp and amorphous free energy curves in Fig. 10. Such a construction would predict an hcp phase containing about 4 atomic % aluminum in metastable equilibrium with an amorphous phase containing about 46 atomic % aluminum. Applying this to the electrodeposits, the 4 atomic % aluminum deposit would be single phase hcp, whereas in the 16 atomic % deposit the amorphous phase would co-exist with the hcp phase. The composition of the hcp phase in each alloy would be identical. Unfortunately, our x-ray data does not support this scenario. Under the conditions of a two-phase equilibrium,

one would not expect to see an increase in the hcp lattice parameter between the 4 and 16 atomic % aluminum alloy, Fig. 8.

Alternatively, the phase development from the hcp to the amorphous structure may proceed by a partitionless or near-partitionless phase transition. Metastable processing methods with very high effective quenching rates are generally required so that the partitionless transformation is kinetically favored over a metastable two-phase equilibrium. Concentration profiles are essentially frozen in place forcing the phases to evolve locally without the aid of long range diffusion.^{34,35} Partitionless transformations have been observed in Zr-Al alloys produced by mechanical alloying.³⁶ This system is a particularly interesting example because zirconium, like cobalt, is hcp at room temperature and, at equilibrium, it accommodates little aluminum in solid solution. Alloys containing up to 17 atomic % aluminum were reported to be single phase hcp with the zirconium lattice parameters decreasing linearly with composition. Above 17 atomic % aluminum, the alloys were completely amorphous. It was concluded that the continuous decrease of the lattice parameters with composition up to the point at which full amorphization took place was an indication of the absence of a two-phase metastable equilibrium region. Free energy calculations not only indicated that the amorphous structure would be thermodynamically more stable than the alternative polymorphs, but the intersection of the hcp and amorphous free energy curves indicated that the partitionless transition would occur at 20 atomic % aluminum, quite close to the experimental value.

Qualitatively, very similar phase development is seen in the electrodeposited Co-Al alloys. The increase in the hcp lattice parameter up to 16 atomic % aluminum suggests that the supersaturation of aluminum into hcp cobalt extends up to amorphization and that a partitionless transformation takes place between 16 and 25 atomic % aluminum. This is reasonably consistent with the crossover of the calculated hcp and amorphous free energy curves, which occurs at about 25 atomic % aluminum (Fig. 10). Quantitatively, there may be problems applying a partitionless mechanism to the electrodeposited Co-Al data. The lattice volume for an ideal, Co-Al hcp solid solution would increase by about 8 % when the aluminum composition is increased from 0 to 16 atomic %. Over this composition range, the lattice volume of the electrodeposited alloys increases by only 0.71 %. Though ideal behavior is certainly not expected, a lattice expansion that is an order of magnitude less than the ideal case does suggest that not all of the aluminum is going into the hcp solid solution. It appears that a more thorough structural study will be required to resolve this issue.

ACKNOWLEDGEMENTS

Research performed at the University of Mississippi was supported by National Science Foundation Grant No. 9411165. WRP acknowledges support from the Chemistry Division of the NSF to participate in the NSF-NIST Cooperative Research Program. GRS acknowledges the technical contributions of Alexander Shapiro and Frank Gayle as well as the assistance of Sandra Claggett. The authors express their gratitude to John Wilkes, USAF

Academy, for the loan of a Pt-RRDE and to Thomas Moffat of NIST for many helpful suggestions.

REFERENCES

1. T. P. Moffat, *J. Electrochem. Soc.*, **141**, L115 (1994).
2. G. R. Stafford, *ibid.*, **136**, 635 (1989).
3. G. R. Stafford, B. Grushko, and R. D. McMichael, *J. Alloys and Compounds*, **200**, 107 (1993).
4. T. P. Moffat, *J. Electrochem. Soc.*, **141**, 3059 (1994).
5. G. R. Stafford, *ibid.*, **141**, 945, (1994).
6. R. A. Osteryoung, in *Molten Salt Chemistry: An Introduction and Selected Applications*, G. Mamantov and R. Marassi, Editors, pp. 329-364, Reidel, Dordrecht (1987).
7. C. L. Hussey, in *Chemistry of Nonaqueous Solutions: Current Progress*, G. Mamantov and A. I. Popov, Editors, pp. 227-275, VCH, New York (1994).
8. W. R. Pitner, C. L. Hussey, and G. R. Stafford, *J. Electrochem. Soc.*, **143**, 130 (1996).
9. R. T. Carlin, H. C. DeLong, and P. C. Trulove, Abstract 652, p. 981, *The Electrochemical Society Extended Abstracts*, Vol. 95-1, Reno, NV, Meeting, May 21-26, 1995.
10. H. C. DeLong and R. T. Carlin, Abstract 647, p. 974, *The Electrochemical Society Extended Abstracts*, Vol. 95-1, Reno, NV, Meeting, May 21-26, 1995.
11. L. J. Durney, *Electroplating Engineering Handbook*, 4th ed., pp. 185-188, Van Nostrand Reinhold, New York (1984).
12. P. C. Andricacos, J. Tabib, and L. T. Romankiw, *J. Electrochem. Soc.*, **135**, 1172 (1988).
13. K. H. Wong and P. C. Andricacos, *ibid.*, **137**, 1087 (1990).
14. J. Horkans, I-C. H. Chang, P. C. Andricacos, and E. J. Podlaha, *ibid.*, **138**, 411 (1991).
15. A. J. Bard and L. R. Faulkner, *Electrochemical Methods*, p. 302, John Wiley and Sons, New York (1980).
16. S. Swathirajan, *J. Electrochem. Soc.*, **133**, 671 (1986).
17. V. D. Jovic, R. M. Zejnilovic, A. R. Despic, and J. S. Stevanovic, *J. Appl. Electrochem.*, **18**, 511 (1988).
18. T. P. Moffat, G. R. Stafford, and D. E. Hall, *J. Electrochem. Soc.*, **140**, 2779 (1993).
19. B. D. Cullity, *Elements of X-Ray Diffraction*, 2nd ed., Addison-Wesley, Redding, MA (1978).
20. L. V. Azaroff, *Elements of X-Ray Crystallography*, McGraw-Hill, New York (1968).
21. *Binary Alloy Phase Diagrams*, T. B. Massalski, Ed., ASM (1986).
22. H.-L. Luo and P. Duwez, *Can. J. Phys.*, **41**, 758 (1963).
23. Yu. M. Polukarov, *Russ. J. Phys. Chem.*, **34**, 68 (1960).
24. J. Goddard and J. G. Wright, *Br. J. Appl. Phys.*, **15**, 807 (1964).
25. J. Scoyer and R. Winand, *Surf. Tech.*, **5**, 169 (1977).
26. S. Nakahara and S. Mahajan, *J. Electrochem. Soc.*, **127**, 283 (1980).
27. I. Croll, *IEEE Trans. on Mag.*, **23**, 59 (1987).

-
28. R. Sard, C. D. Schwartz, and R. Weil, *J. Electrochem. Soc.*, **113**, 424 (1966).
 29. A. J. Bradley and G. C. Seager, *J. Inst. of Metals, London*, **64**, 81 (1939).
 30. B.I. Nikolin and N.N. Shevchenko, *Fiz. Metal. Metalloved.*, **51**, 316 (1981).
 31. L. Kaufman and H. Nesor, *CALPHAD*, **2**, 325 (1978).
 32. L. Kaufman, *CALPHAD*, **1**, 1 (1977).
 33. B. Grushko and G.R. Stafford, *Met. Trans. A*, **20**, 1351 (1989).
 34. E. Ma, *J. Mater. Res.*, **9**, 592 (1994).
 35. W.L. Johnson, Y.T. Cheng, M. van Rossum, and M-A. Nicolet, *Nucl. Instrum. Methods in Phys. Res.*, **B 7/8**, 657 (1985).
 36. E. Ma and M. Atzmon, *Mod. Phys. Lett.*, **6B**, 127 (1992).

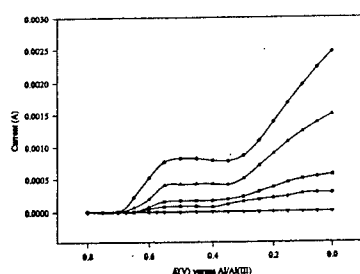


Figure 1. Voltammograms recorded point-by-point at a Pt-RDE for the reduction of Co(II) in the 60.0-40.0 m/o melt. The Co(II) concentrations were (●) 5.00, (■) 10.0, (▲) 25.0, and (◆) 50.0 mmol L⁻¹. Also shown is a voltammogram recorded in pure melt before the addition of Co(II) (▼). The angular velocity of the electrode was 104.7 rad s⁻¹.

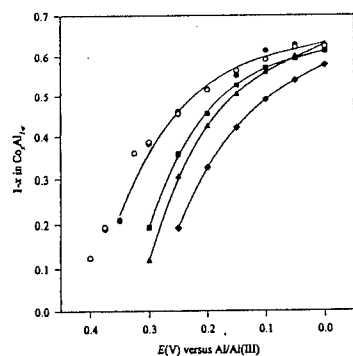


Figure 2. Alloy composition as a function of potential as derived from the RDE voltammetric currents in Fig. 1 by using Eq. 4. The Co(II) concentrations were (●) 5.00, (■) 10.0, (▲) 25.0, and (◆) 50.0 mmol L⁻¹. Also shown are the results of ALSV-RRDE experiments (○).

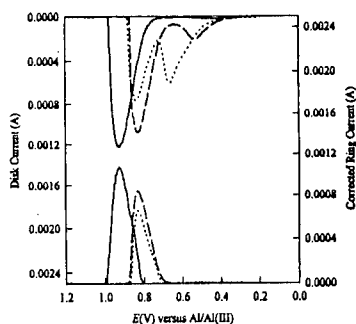


Figure 3. Disk and ring voltammograms recorded during the oxidation of thin-layer Co-Al electrodeposits from a Pt-RRDE in pure 60.0-40.0 melt. These deposits were produced with a charge density of 425 mC cm⁻² in melt containing 5.00 mmol L⁻¹ M Co(II) at the following deposition potentials: (—) 0.400, (---) 0.300, and (···) 0.200 V. During stripping, the disk electrode was scanned at 0.002 V s⁻¹, and E_r was held at 0.500 V. The angular velocity of the RRDE was 104.7 rad s⁻¹.

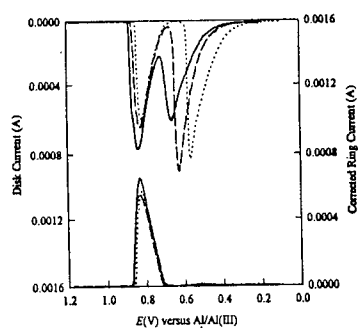


Figure 4. Disk and ring voltammograms recorded during the oxidation of thin-layer Co-Al electrodeposits from a Pt-RRDE in pure 60.0-40.0 melt. The deposits were prepared as described in Fig. 3 at the following deposition potentials: (—) 0.200, (---) 0.100, and (···) 0 V. The stripping conditions were the same as those used to produce Fig. 3.

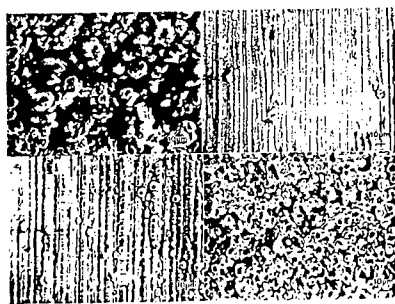


Figure 5. SEM micrographs of bulk Co and Co-Al alloy electrodeposits on a copper wire substrate. These deposits were produced in a 50.0 mmol L⁻¹ solution of Co(II) in 60.0-40.0 m/o melt at 40 °C. The deposition potentials were (a) 0.400, (b) 0.200, (c) 0.100, and (d) 0 V.

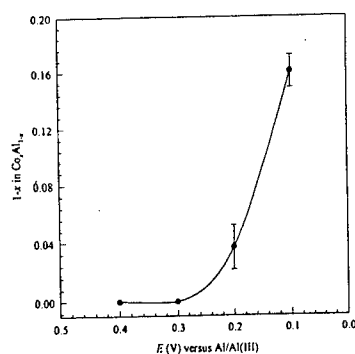


Figure 6. Co-Al alloy composition as a function of deposition potential for the electrodeposits described in Fig. 5.

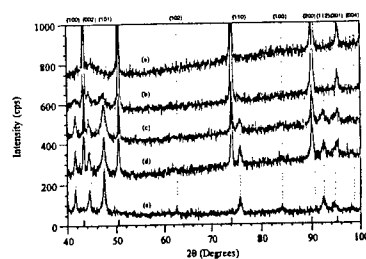


Figure 7. XRD patterns (Cu-Kα) of the electrodeposits described in Fig. 5. The deposition potentials were (a) 0, (b) 0.100, (c) 0.200, (d) 0.300, and (e) 0.400 V. The dashed vertical lines represent the reflections for pure hcp cobalt, JCPDS card# 5-0727. The reflections due to the copper wire substrate are denoted by the heavy tick marks on the 2θ axis.

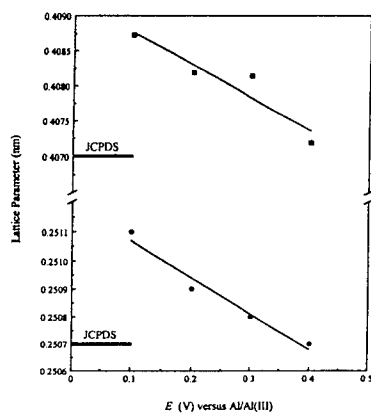


Figure 8. Lattice parameters of electrodeposited hcp cobalt as a function of deposition potential taken from the diffraction patterns shown in Fig. 7: (●) a_0 and (■) c_0 .

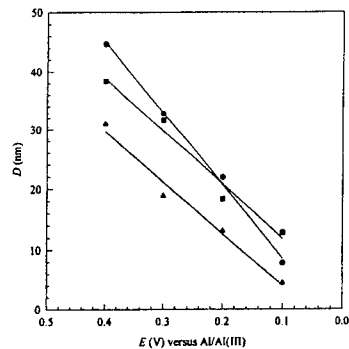


Figure 9. Estimated grain size of electrodeposited hcp cobalt as a function of deposition potential calculated from the diffraction patterns shown in Fig. 7. Grain size was estimated from the peak broadening of the (●) (100), (■) (002), and (▲) (101) reflections using the Scherrer equation.²⁰

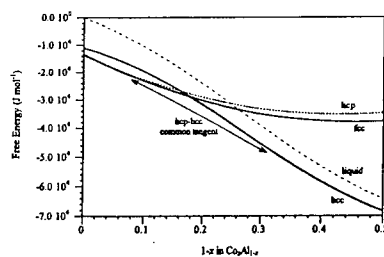


Figure 10. Calculated free energy of formation diagram for the Co-Al system at 40 °C using liquid cobalt as the reference state. The constitutive equations of Kaufman et al.^{31,32} were used in the calculations.

NEAR INFRARED SPECTROSCOPY OF ANIONIC CONDUCTING POLYMER MEMBRANES

David S. Newman, Guangping Bi, Deanne L. Snavely,
John Dubsy, Frank Zamborini and Thomas S. Cina

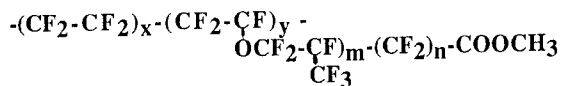
Department of Chemistry
Bowling Green State University
Bowling Green, OH 43403

ABSTRACT

Flemion is a perfluorocarboxylated polymer somewhat similar to Nafion and is widely used in the chlor-alkali industry as the separator between anolyte and catholyte compartments of the electrolysis cell. The structure of Flemion was altered by converting the methylester functional group to an acyl group and then acylating the benzene ring of either dibenzo-18-crown-6 ether or benzo-18-crown-6 ether under Friedel-Crafts conditions, thereby attaching the crown ether to the Flemion as a "pendent". The bonded crown ether was then complexed with alkali metal halides to produce a solid electrolyte with mobile anions. Fluorescence spectroscopy, near IR spectroscopy, mid IR spectroscopy, UV-Visible spectroscopy and chemical analysis were used to assay the various reactions. A combination of fluorescence spectroscopy and near IR spectroscopy allowed us to unambiguously decide whether crown ethers were bonded to the membrane, dissolved in the membrane, or both.

INTRODUCTION

Flemion [1] is a perfluorocarboxylated polymer membrane which is prepared by copolymerizing tetrafluoroethylene and carboxylated perfluorovinyl ether [2,3]. Flemion is manufactured by Asahi Glass Ltd. of Japan. The chemical formula for Flemion is:



where m is 0 or 1 and n has values between 1 and 5. The average molecular weight of a methylester containing unit of Flemion is approximately 700 amu. The methylester group on the Flemion is readily hydrolyzed to a carboxylic acid. The carboxylic acid form of Flemion is widely used in the chlor-alkali industry as the membrane separating the anodic and cathodic compartments of chlor-alkali cells because of its chemical inertness, its high cationic conductivity in aqueous media, and its ability to reject anions such as Cl^- and OH^- . The reason anions cannot readily pass through the membrane, but cations can, is that, in aqueous media, especially at high pH, the carboxylic acid is partially dissociated leaving a negatively charged pendant group which repels other negative charges while allowing positively charged species, such as Na^+ ions, to hop from site to site within the membrane. However, when completely or nearly completely dry, neither the carboxylic acid form of Flemion (FI-COOH) nor the sodium salt of the carboxylated Flemion (FI-COONa) exhibit high ionic conductivity.

There are many potential applications for a material with properties similar to FI-COOH, but which conducts anions such as Cl^- and OH^- and rejects cations. Among the more intriguing of these applications is as the separator in the Al/Cl_2 methylethylimidazolium chloride- AlCl_3 battery [4] and in the production of a Na_2SO_4 salt splitter using both the anionic and cationic conducting forms of Flemion [5,6]. Therefore, the principal objective of our Flemion research was to convert it to an anion conducting membrane, while still retaining its other desirable properties. This objective was achieved by hanging a positively charged pendant group on the Teflon backbone rather than a negatively charged species.

The approach taken for introducing a positively charged species was to attach a crown ether (CE) as the pendent group hanging from the polymer chain and then complexing the CE with an alkali metal halide, the assumption being that the alkali metal ion would lock in the crown and the halide would carry the current. This approach differs from that used in the fabrication of Neosepta in which a basic nitrogen group is the pendent and this group acquires a positive charge by bonding to a proton in acidic media. In an earlier study, we were able to bond dibenzo-18-cr-6-ether (DBCE) to Flemion, using a series of reactions, the last one of which was a Friedel-Crafts acylation of the benzene ring of DBCE using the ambient temperature molten salt, pyridinium heptachloroaluminate, as both the reaction medium and as a Friedel-Crafts catalyst. The bonded DBCE was then complexed it with LiCl [6]. We found that this material was a solid electrolyte, with an electrical conductivity, κ , equal to $1.3 \times 10^{-5} \text{ S/cm}$. This conductivity was only an order of magnitude lower than that of the lithium chloride salt of DBCE which was shown to be a fast ion conductor in the solid state with the mobile species being the Cl^- ion [7,8]. Although the transport numbers of the membrane were not measured, the assumption was that the Cl^- ions and not the Li^+ ions were mobile.

In the FI-DBCE study [6] and again in this study, indications were that an ether was bonded to only about 5% of the possible sites on the Flemion, although the evidence was inconclusive. A possible reason for this was that, in the molten salt, the Flemion formed channels which were blocked or clogged by the large DBCE and the $\text{C}_5\text{H}_6\text{NAl}_2\text{Cl}_7$. It is known that Nafion forms channels in aqueous media [9,10] and direct evidence for channel formation in Flemion using transmission electron microscopy has been found and will be reported on elsewhere. In the present study, we used BF_3 in ether as the F-C catalyst and both DBCE and benzo-18-cr-6-ether (BCE) as pendent groups. The assumption being that the FI-BCE - LiCl complex would have properties similar to those of the FI-DBCE- LiCl complex, but because of the smaller size of both the catalyst and BCE, we would be able to bond more CE's to the Flemion. However, ascertaining the extent to which the CE bonded to the Flemion remained troublesome so we set out to develop analytical techniques to assay the extent of the various reactions and changes in membrane morphology that resulted from these reactions. The techniques used were FTIR and near IR spectroscopy, Fluorescence spectroscopy, UV-Vis spectroscopy, mercuric nitrate titration, and weighing the polymer coupons before and after each reaction, but the technique that proved most interesting, and the technique we report on here, was near IR spectroscopy.

EXPERIMENTAL DETAILS

Flemion sheet, which was 0.145 mm thick, was supplied by Asahi Glass Ltd. Coupons of this material, usually between 3 and 8 cm² were used for most of the experiments. The Flemion was converted to FI-COOH by immersing the coupon first in 50 w% NaOH for 16 hrs at 90 °C and then soaking it in 1 M HCl for 24 hrs at room temperature. The FI-COOH was then converted to the acyl containing Flemion, FICl, by refluxing the coupon in SOCl₂ for 16 hrs. The coupons of FI-COCl were rinsed in diethyl ether to remove excess SOCl₂. One coupon of this material served as a "standard" It was immersed in a known quantity of de ionized water and allowed to shake in a continuous rotation tumbler for 24 hrs. The purpose of this step was to convert all acyl groups back to carboxylic acid and HCl. The HCl released, was titrated using a standard mercuric nitrate titration (CAWW method 325.3) [11]. The moles of HCl equaled the moles of acyl groups in the membrane. The FI-COCl coupons were next refluxed in 40 ml of BF₃/ether to which approximately 0.2 g of crown ether, CE, had been added, for 16 hrs. Upon completion of the reflux, the coupons were each immersed in a known quantity of deionized water to convert any unreacted acyl groups to -COOH and HCl. The HCl was then titrated as before. It was assumed that the difference between the number of acyl groups in the standard coupon and the number of unreacted acyl groups in the coupon that had undergone the BF₃/ ether Friedel-Crafts reaction, was equal to the number of CE s that had been bonded to the Flemion.

Briefly, the mercuric nitrate titration consists of an acidified Cl⁻ containing sample being titrated with Hg(NO₃)₂ in the presence of mixed diphenylcarbazone-bromphenol blue indicator. The end-point of the titration is the formation of a blue-violet mercury-diphenylcarbazone complex. This is a modern version of the older, and more difficult, Mohr titration.

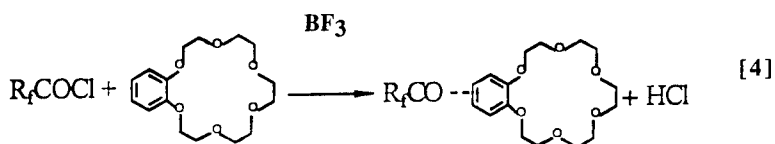
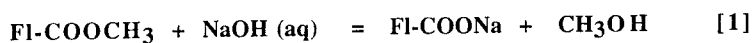
The FI-CO-DBCE and FI-CO-BCE coupons were complexed by soaking them in aqueous LiCl solutions of various concentrations ranging from saturated to 1 M for approximately 24 hrs.

All transfer and weighing operations were done in a controlled atmosphere Kewaunee glove box which used the boil-off from liquid nitrogen as the atmosphere and had a moisture content less than 10 ppm. Before and after each reaction, the coupons were dried and weighed on an analytical balance with 0.01 mg precision.

Spectra were taken of the membranes directly and no attempt was made to reduce the membrane's thickness or to dissolve the Flemion. Both the near IR and the mid IR spectra were obtained with a Mattson 6020 spectrophotometer. The fluorescence spectra were obtained with a Perkin-Elmer LS-5B luminescence spectrometer which automatically optimizes its sensitivity for each sample. The actual absorbance is observed by the operator at the time of analysis via a digital display. The carboxylic acid form of Flemion was used as the blank.

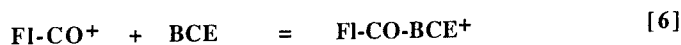
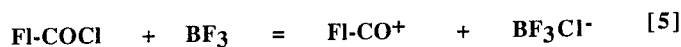
RESULTS AND DISCUSSION

The series of reactions used to convert the FI-COOCH₃ to FI-COBCE were:



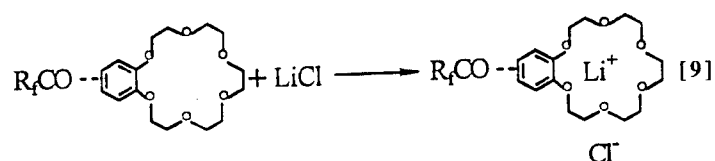
Thin layer chromatography indicated that only one product formed when acetyl chloride reacted with BCE in ethyl ether. This product was most likely the BCE acylated at the 3 or 4 position rather than at the 2 or 5 position, because the latter site is far more hindered. It was therefore assumed that in the more crowded Flemion, only one product formed and this was the BCE bonded to the carbonyl group at the 3 or 4 position of the CE's benzene ring.

The mechanism for Eq. [4] is probably



Gaseous HCl was isolated and identified in the reaction between BF₃ and coupons of FI-COCl. In addition to reactions [5] through [8], a side reaction occurs producing a complex of some sort which causes the membrane to turn purple. The exact structure of this complex is not yet known, but when purple acylated coupons of FI-CO-BCE were refluxed in 50 ml of approximately 1 M LiCl, much of the purple color disappeared and the LiCl solution was found to contain BCE and have a pH near 1. This indicated the colored complex was trapped in the membrane, but not bonded to it and that it probably dissociated in water into intact BCE and BF₃.

The complexing of the FI-CO-BCE with LiCl can be described by the equation:



The extent to which Eqs. [4] or [9] went to completion in the membrane varied considerably and was extremely difficult to assay. The usual FTIR spectra that are used to identify typical chemical bonds and other structural features of a species, were of only limited use in our experiments because of the thickness of the membrane. Most of the membranes absorbed too much light for the spectra to be anything more than a rough indication that a given reaction occurred. The same was true for the UV-Vis spectra. The membranes absorbed too strongly in the UV range. We therefore resorted to near IR spectroscopy because the overtones or second harmonics of quenched mid-IR absorptions appear in this region. [12,13]. Fig. 1 shows the near IR spectrum of bonded BCE and Fig. 2 shows the near IR spectrum of the same BCE that had diffused into the FI-COOH without any chemical reaction taking place. Fig. 3 shows the near IR spectrum of carboxylated Flemion with no CE present. It is obvious from these spectra that there is a qualitative difference between the spectrum of the dissolved CE and that of the bonded CE in the 4100-4450 cm^{-1} region of the spectrum. The bonded CE exhibits a distinct five sharp peak pattern which we think is an overtone of some harmonic motion of the carbonyl-benzene bond. The near IR spectrum of FI-DBCE was obtained and is shown in Fig. 4. An almost identical five peak pattern appears. In order to prove that this is due to a feature of the FI-CO-Benzene bond and not an overtone of the crown's motion, pyrene and benzene were bonded to the membrane under Friedel-Crafts conditions and the near IR spectra obtained. Both the benzene (FI-CO-Benzene) and the pyrene (FI-CO-Pyrene) gave a virtually identical pattern to that of the bonded BCE in the 4100-4450 cm^{-1} region indicating we had indeed discovered the "signature" of the carbonyl-benzene bond. The near IR spectrum of FI-CO-pyrene is shown in Fig.5.

The combination of techniques which seemed to give the most unambiguous qualitative results and which allowed us to readily distinguish between a CE molecule that was bonded to the Flemion and a CE molecule that had diffused into the Flemion without forming a chemical bond *when both were present*, turned out to be a combination of fluorescence spectroscopy and near-IR spectroscopy. A CE molecule that had diffused into the membrane without being bonded to it could readily be identified by its fluorescence spectrum whereas the fluorescence of both the bonded BCE in FI-CO-BCE and the bonded DBCE in FI-CO-DBCE was quenched under the conditions of our experiments. The reason why the fluorescence quenched is not known and is currently under investigation. Fig. 6 shows the fluorescence spectrum of BCE dissolved in FI-COOH and Fig. 7 shows the fluorescence spectrum of the same molecule dissolved in methanol. In order to prove that the CE is bonded and not dissolved, the following protocol is followed. The near IR spectrum and the fluorescence spectrum of the membrane are taken. If there is fluorescence and no CO-Benzene overtone in the 4360 to 4434 cm^{-1} range, the CE has diffused into the membrane without being bonded to it. If we do not get a fluorescence spectrum and we do get the characteristic overtone spectrum, the molecule is bonded and not dissolved. If we get both spectra, some CE is dissolved in the membrane and some is bonded to it.

CONCLUSION

We have successfully bonded BCE and DBCE to Flemion membranes and complexed these CE s with LiCl to form electrolytes with mobile anions. We have developed analytical techniques to assay the many reactions involved. We have produced solid electrolytes with mobile anions and cations and solid electrolytes with mobile anions only. We are currently in the process of measuring the transference numbers of the various membranes and well as using these membranes to develop a Na₂SO₄ salt splitter.

ACKNOWLEDGMENT

We wish to thank the NSF-REU program at Bowling Green State University for its continuing support.

LIST OF REFERENCES

1. Flemion is a registered trademark of the Asahi Glass Company, Ltd. Japan
2. H. Ukahashi, M. Yamabe, in *Perfluorinated Ionomer Membranes*; A. Eisenberg, H.L. Yeager, Editors, American Chemical Society: Washington, DC, 1982: ACS Symposium Series No. 180
3. E. Blatt, W.H.F. Sasse, A.W.H. Mau, *J. Phys Chem*, **92**, 4151 (1988)
4. F.M. Donahue, J.S. Wilkes, J.S. Reynolds, G. Fredric, in: *Proceedings of the Fifth International Symposium on Molten Salts*; M. Saboungi, D.S. Newman, K.E. Johnson, D. Inman, Editors, The Electrochemical Society Softbound Proceedings Series, pv-86-1, pp332-343, Pennington NJ 1986
5. J.D. Genders, D. Hartsough, J. Thompson, Novel Approaches To Salt Splitting, *Extended Abstracts* **94-1** 185th Electrochemical Society Meeting, May 22-27, 1994
Abstract # 704. Ch. Kot, M-M. Letord, Production of Sodium Hydroxide and Sulfuric Acid From Sodium Sulfate Solutions, *ibid*, Abstract # 705
6. D.S. Newman, S. Li, T. Howard, L. Hunt. in : *Proceedings of the Eight International Symposium on Molten Salts*, R.G. Gale, G. Blomgren, H Kojima, Editors, The Electrochemical Society Softbound Proceedings Series, PV-92-16, pp 250-261 Pennington, NJ, 1992
7. D.S. Newman, D. Hazlett, K.F. Mucker; *Solid State Ionics*, **3/4** 389 (1981)
8. M. Fujimoto, T. Nogami, H. Mikawa, *Chem. Let.* 547-550, 1982
9. M.W. Verbrugge, R.F. Hill, *J. Electrochem. Soc.* **137**, 893(1990)
10. S. W. Capeci, P.N. Pintauro, R.F. Hill, *ibid*, **136**, 2876(1989)

11. United States Environmental Monitoring and Support Laboratory, *Methods For Chemical Analysis of Water and Wastes*, Ohio, March 1983.
12. K.A.Bunding Lee, *Applied Spectroscopy Reviews*, **28(3)**, 231(1984)
13. W. F. McClure, *Analytical Chemistry*, **66**, 43 A (1994)

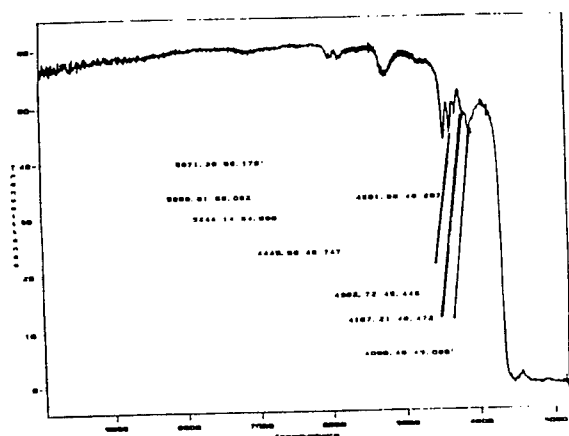


Fig.1. Near-IR Spectrum of Bonded BCE

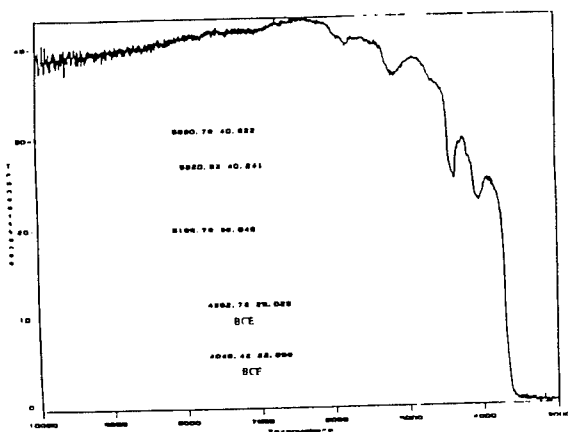


Fig.2. Near-IR Spectrum of BCE that has Diffused Into Fl-COOH

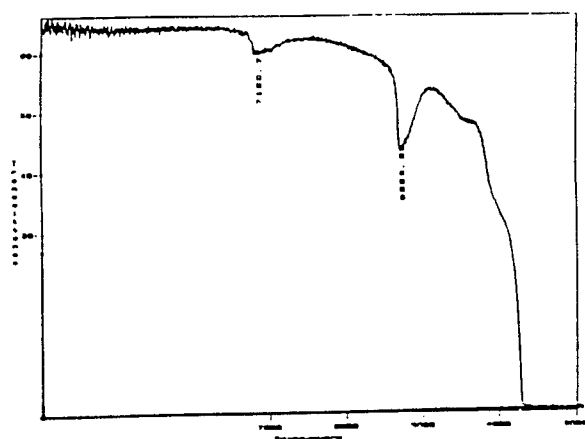


Fig.3.
Near-IR Spectrum of FI-COOH

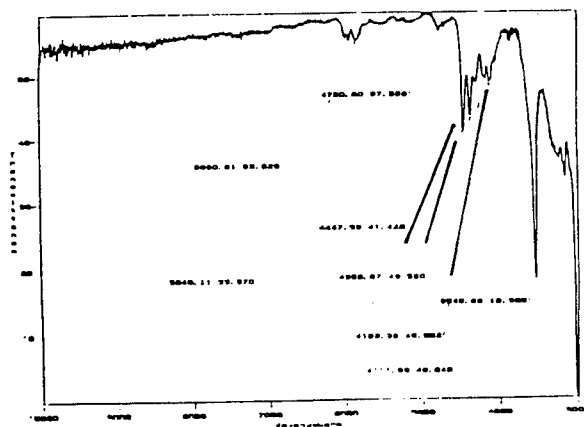


Fig.4. Near-IR Spectrum of Bonded DBCE

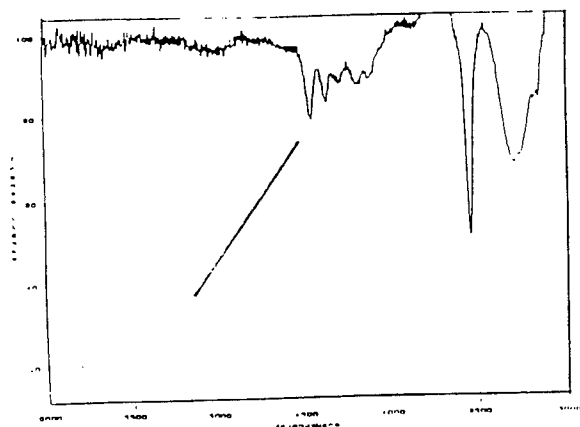


Fig.5. Near-IR Spectrum of FI-CO-pyrene

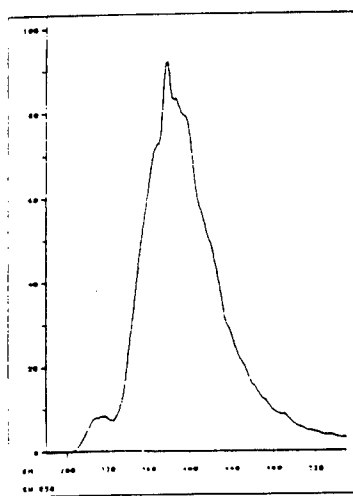


Fig.6. Fluorescence Spectrum of BCE Diffused into FI-COOH

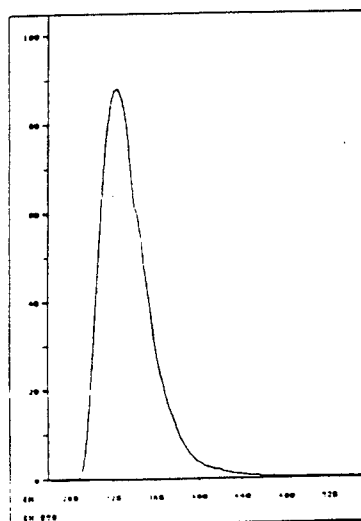


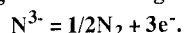
Fig.7. Fluorescence Spectrum of BCE Dissolved in Methanol

ELECTROCHEMICAL REACTIONS OF NITROGEN IN A MOLTEN CHLORIDE SYSTEM

Yasuhiko Ito, Masayuki Tada and Takuya Goto

Department of Fundamental Energy Science
Faculty of Energy Science
Kyoto University
Sakyo-ku, Kyoto 606, Japan

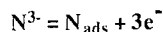
The electrochemical reactions of nitride ion and nitrogen gas in LiCl-KCl eutectic melt have been studied by cyclic voltammetry, chronopotentiometry, chronoamperometry and gas analysis. Nitride ion is anodically oxidized to form nitrogen gas almost quantitatively on nickel electrode according to the following reaction:

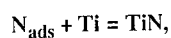


This is a reversible one-step three-electron reaction governed by a simple diffusion-controlled charge transfer process. The diffusion coefficient of nitride ion was estimated to be $\sim 1 \times 10^{-5} \text{ cm}^2\text{s}^{-1}$ at 470 °C. It has been found that nitrogen gas is cathodically reduced almost quantitatively to form nitride ion.

INTRODUCTION

The electrochemical behavior of nitrogen in molten chloride system is an interesting research subject from both scientific and industrial aspects. For example, a novel electrochemical process for the surface nitriding of titanium in molten chloride system has already been developed (1). The principle of the process is as follows; Let us use LiCl-KCl eutectic melt at 450 °C as a model solvent. When Li_3N is dissolved in the solvent and titanium electrode is anodically polarized in the melt, surface nitriding is achieved according to the following reaction steps:





where anodically produced adsorbed nitrogen atoms react with the outer most surface and diffuse towards the bulk of titanium electrode to form nitride layer. This principle has already been successfully confirmed by the experiment (1).

In this experiment, lithium nitride was used as a nitride ion source, which is rather expensive. Furthermore, if we consider a practical case, lithium ion will be accumulated in the melt by the continuous addition of lithium nitride, if the cathodic reaction is not available for its removal and recovery. These are not desirable in a practical or an industrial case, where the continuous operation is necessary. Thus, it would be very attractive if nitrogen gas could be electrochemically reduced at cathode to produce nitride ion without producing any other ionic species.

From such backgrounds, electrochemical behaviors of the nitride ion and nitrogen gas in LiCl-KCl-Li₃N system have been studied in detail. First, electron number and reversibility of reaction were studied by quantitative analysis of the generated gas, cyclic voltammetry and chronopotentiometry. Then diffusion coefficient of nitride ion was measured by cyclic voltammetry, chronopotentiometry and chronoamperometry. Furthermore, the possibility of cathodic reduction of nitrogen gas was examined with the use of fuel cell type nitrogen gas electrode.

EXPERIMENTAL

All experiments were carried out in a glove box of argon atmosphere with a continuous gas refining instrument [Nihon Pionics Co. Ltd. :MSGB].

The water contamination was always monitored and maintained at less than 1ppm.

The solvent was a binary eutectic mixture of LiCl-KCl prepared from vacuum dried reagent grade chemicals. Li₃N was added directly into the melt as a nitride ion source. Nickel plate electrode and nickel wire bundle type nitrogen gas electrode were used as working electrodes. Glassy carbon was used as a counter electrode and Li-Al alloy was used as a reference electrode (2). A dynamic reference electrode using electrochemically deposited lithium was used to correct the potential measured by Li⁺/Li-Al reference electrode and all potentials in this paper are referred to the dynamic reference electrode and shown as [V vs. Li⁺/Li] (3).

RESULTS AND DISCUSSION

Anodic reaction scheme

Figure 1 shows typical cyclic voltammograms for nickel electrode in the LiCl-KCl eutectic melt containing 0.04 mol % Li_3N at various sweep rates ranging from 0.05 Vs^{-1} to 0.5 Vs^{-1} . One anodic and a corresponding cathodic peak are observed, respectively. Both peak currents increase with the added amount of lithium nitride and the anodic peak varies linearly with the bulk concentration of nitride ion as shown in Fig. 2 (a). From these voltammetric data, the anodic current is considered to be due to the oxidation of nitride ion. Thus, it was suggested that nitride ion can be anodically oxidized to form nitrogen gas according to the following reaction:



In order to confirm this, quantitative analysis of the generated gas obtained after potentiostatic anodic oxidation of nitride ion at several potentials was conducted by a quadrupole mass analyzer. It was confirmed that the final product obtained after potentiostatic anodic oxidation of nitride ion is mainly pure nitrogen gas, see Table 1. Provided that all observed current was due to the reaction of eq. 1, the current efficiency was calculated to be around 90 % even without taking into account the loss of nitrogen gas due to experimental error. On the other hand, no nitrogen gas was detected before conducting potentiostatic electrolysis. That means that the amount of nitrogen gas coming from the thermal decomposition of lithium nitride is very small compared to the amount collected during the electrolysis.

Electrochemical behaviors

The anodic peak potentials scarcely change with sweep rate as shown in Fig. 1. And the ratio of anodic to cathodic peak current is estimated to be about 0.9, i.e. almost 1. According to Nicholson (4), this indicates that the anodic oxidation of nitride ion is very close to a reversible process. For such process with high reversibility, the following equation is available for the estimation of electron number (5) :

$$|E_{\text{PA}} - E_{\text{PA}1/2}| = 2.2RT/nF \quad [2],$$

where E_{PA} is the anodic peak potential, $E_{\text{PA}1/2}$ is the anodic half-peak potential, R

is the gas constant, T is the temperature, n is the electron number and F is Faraday constant. By means of eq. 2, the electron number is estimated to be 3.0 ± 0.2 , i.e. the number corresponds to the number of electrons for eq. 1. And the polarographic $E_{1/2}$ value is estimated to be 0.54 V. Figure. 2 (b) shows that anodic peak current varies linearly with square root of scan rate. Thus, the oxidation step is concluded to be a simple diffusion-controlled charge transfer process.

A further study of the electrochemical behavior of nitride ion was carried out by chronopotentiometry. Figure 3 represents a typical chronopotentiogram obtained at a nickel electrode for imposed anodic current density of 8.0 mAcm^{-2} . Transient time, τ , is defined as the interval time where the potential plateau is observed. It is directly proportional to the square of bulk concentration of nitride ion and to the reciprocal square of applied current density. This also supports the conclusions that the oxidation of nitride ion is a diffusion-controlled charge transfer process. As shown in Fig. 4, the electrode potential varies linearly with $\ln[(\tau^{0.5} \cdot t^{0.5}) / t^{0.5}]$. This means that following equation is valid :

$$E = E_{\tau/4} + (RT / nF) \ln [(\tau^{0.5} \cdot t^{0.5}) / t^{0.5}] \quad [3].$$

The slope of the straight line is RT/nF and the intercept on the potential axis is the quarter-wave point $E_{\tau/4}$. The slope of the line is close to the theoretical value for the three electron reversible process. The value of $E_{\tau/4}$ is estimated to be 0.54 V, which is almost equal to the value of $E_{1/2}$ obtained from cyclic voltammetry in Fig. 1.

Diffusion coefficient of nitride ion

The diffusion coefficient of nitride ion in LiCl-KCl eutectic melt was estimated from cyclic voltammetric and chronopotentiometric data according to the following relations:

$$j_{Ap} = 0.4463(nF)^{1.5} CD^{0.5} v^{0.5} (RT)^{-0.5} \quad [4]$$

$$j\tau^{0.5} / C = nFD^{0.5} \pi^{0.5} / 2 \quad [5],$$

where j_{Ap} is the anodic peak current density, C is the bulk concentration of nitride ion, D is the diffusion coefficient, v is the scan rate, j is the anodic current density and τ is the transition time. The results are summarized in Table 2.

The diffusion coefficient of nitride ion was also determined by means of

chronoamperometry. Figure 5 shows the Cottrell plot of chronoamperograms which represents the relation between the current and the reciprocal square of time. The currents varied linearly with the reciprocal square of time till about 2 s. Due to thermal convection, however, the linear relation observed in Fig. 5 was not kept beyond 2 s. The linear part of the curve shown in Fig. 5 obeys the Cottrell law as follows :

$$j(t) = nFD^{0.5}C(\pi t)^{-0.5} \quad [6].$$

Thus, the diffusion coefficient of nitride ion was calculated from the slope of the line and the result is summarized in Table 2.

Cathodic reduction of nitrogen gas

The possibility of cathodic reduction of nitrogen gas in LiCl-KCl-Li₃N system was examined with the use of fuel cell type nitrogen gas electrode.

Figure 6 shows the results of cathodic polarization curves of the nitrogen gas electrode. By supplying nitrogen gas to the electrode, cathodic current significantly increases as shown in Fig. 6. If the observed cathodic current is attributed to the formation of nitride ion, the cathodically produced nitride ion which is the most negative anion in the system will be oxidized to form nitrogen gas on the counter electrode.

In order to confirm this, after conducting a long-term electrolysis by the use of the cell schematically shown in Fig. 7, quantitative analysis of the generated gas from the counter electrode was conducted by a quadrupole mass analyzer. The resulting gas is mainly nitrogen gas. Provided that all observed current was due to the reactions shown in Fig. 7, the current efficiency was calculated to be around 93 %. Thus, it is indicated that nitrogen gas is cathodically reduced to form nitride ion according to the following reaction:



REFERENCES

- [1] T. Goto, M. Tada and Y. Ito *Electrochim. Acta*, 9, 1107 (1994)
- [2] R. A. Sharma and R. N. Seefurth, *J. Electrochem. Soc.* 123, 1763(1976)
- [3] T. Takenaka, Y. Ito and J. Oishi, *Denki Kagaku*, 53, 476 (1985)
- [4] R. S. Nicholson, *Anal. Chem.*, 36, 1351 (1965)
- [5] A. J. Bard and L. R. Faulkner, *Electrochemical Methods: Fundamentals and Applications*, John Wiley & Sons, New York (1980)

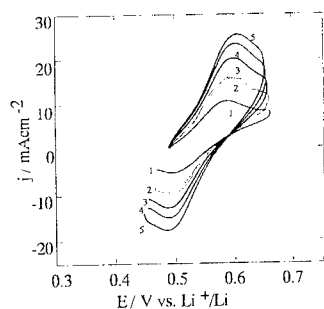


Fig. 1 Cyclic voltammograms for Ni electrode in LiCl-KCl containing 0.04 mol% Li₃N, scan rates: (1) 0.05, (2) 0.1, (3) 0.2, (4) 0.3 and (5) 0.5 V s⁻¹ at 470°C.

Table 1. Quantitative analysis of gas (constant potential electrolysis).

Applied potential V vs. Li ⁺ /Li	<i>Q</i> coul.	<i>Effic.</i>	Composition mol%	
		%	N ₂	Ar
0.55	1750	91	99	1
0.65	1632	89	99	1
0.85	1526	89	99	1

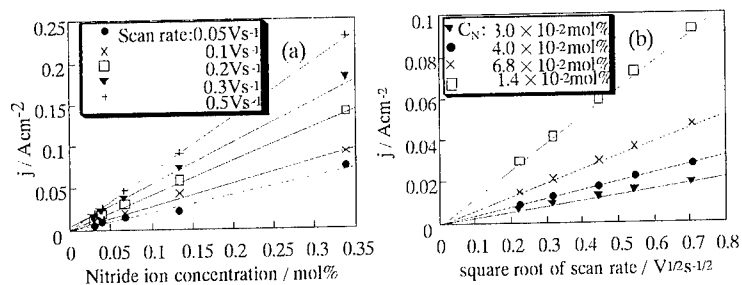


Fig. 2 (a) Variations of anodic peak current densities with nitride ion concentration and (b) with square root of potential scan rates.

Table 2 Nitride ion diffusion coefficients obtained by different techniques.

Technique	10 ⁵ D / cm ² s ⁻¹ (470°C)
Voltammetry ($p=f(v^{1/2})$)	1.8
Chronopotentiometry (<i>Sand's</i> eqn.)	1.2
Chronoamperometry (<i>Cottrell's</i> eqn.)	0.8

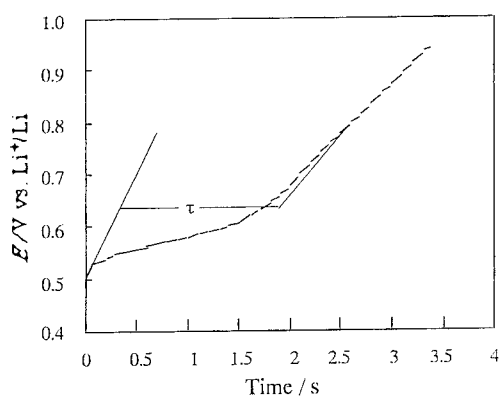


Fig. 3 Typical chronopotentiogram for nickel electrode in LiCl-KCl containing 0.04mol% Li_3N , applied anodic current density 8.0mAcm^{-2} .

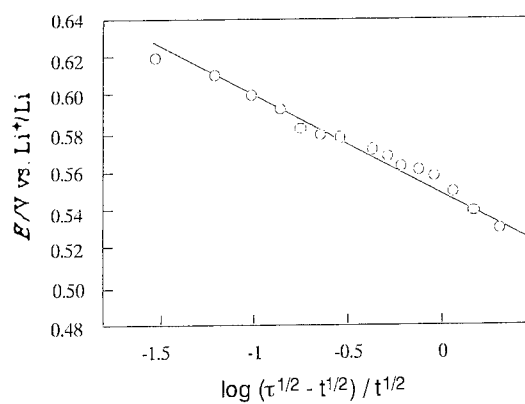


Fig. 4 Logarithmic analysis of chronopotentiogram for Ni electrode in LiCl-KCl- Li_3N (0.04mol%) at 470°C . Anodic current density 8.0mAcm^{-2} .

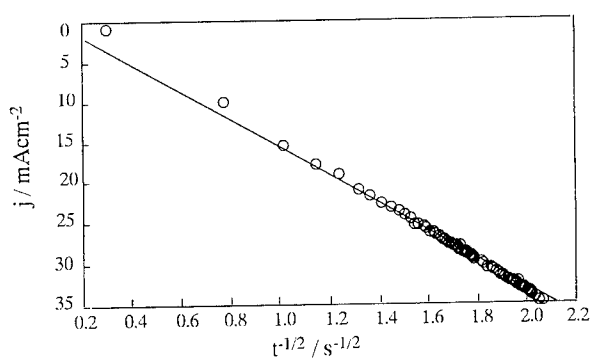


Fig. 5 Cottrell plot of chronoamperogram for nickel electrode in LiCl-KCl containing 0.04 mol% Li_3N at 470 °C. Applied potential 0.6 V.

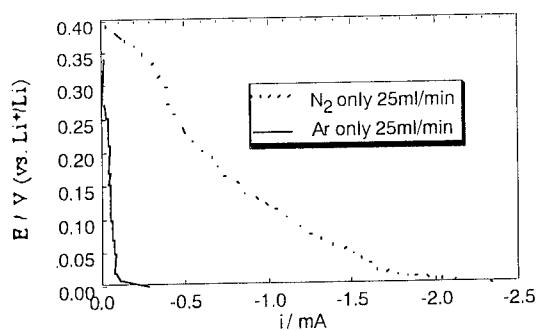


Fig. 6 Polarization curves in LiCl-KCl eutectic melt containing 0.05 mol% Li_3N at 430 °C.

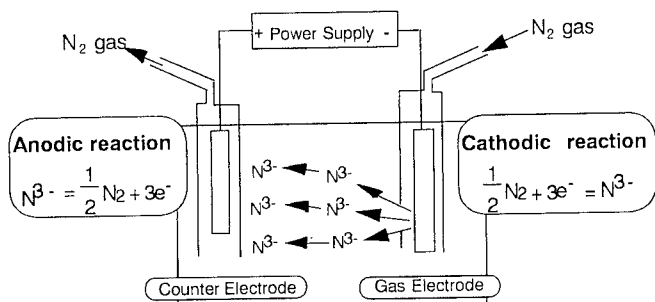


Fig. 7 Scheme of electrolytic cell for cathodic reduction and evolution of nitrogen gas.

NONAQUEOUS ROOM-TEMPERATURE IONIC LIQUIDS: A NEW CLASS OF SOLVENTS FOR CATALYTIC ORGANIC REACTIONS.

Hélène OLIVIER and Yves CHAUVIN

Institut Français du Pétrole,
BP 311, 92506 Rueil-Malmaison, France

Room-temperature organic-inorganic ionic liquids of the BMI^+A^- type (BMI^+ =1-butyl-3-methylimidazolium, A^- = Al_2Cl_7^- , AlCl_4^- , BF_4^- , PF_6^- and SbF_6^-) have been used as a new class of solvents for two-phase catalytic reactions. The chemical and physical properties of these media can be varied with the nature of the A^- anions and can be adjusted to the catalyst precursors and reactions involved. They are good solvents of various transition-metal catalysts and are poorly soluble with aliphatic hydrocarbons and aldehydes. Thus, the separation of the reaction products from the catalyst, one of the main drawback of homogeneous catalysis, can be easily achieved by simple decantation. Ionic liquids offer the opportunity to extend the field of two-phase catalysis to substrates, complexes and ligands which are poorly soluble or unstable in water.

The solvent in organic catalytic reactions can influence the course of a reaction by increasing reaction rates and allowing better reaction control of chemo-, regio-, stereo- and enantioselectivities. Despite the advantage of using a solvent, the major disadvantage is its separation from the catalyst and the products. An alternative approach is to use a solvent for the active species, which is a poor solvent for the reactant(s) and reaction product(s). All industrial applications of this two-phase catalysis technology have been restricted to aqueous-organic systems (1). However, water is a highly coordinating protic solvent and it is reactive toward many organometallic catalysts. For this reason, we have been investigating the use of room-temperature 1-butyl-3-methylimidazolium (BMI^+) ionic liquids as a new class of nonaqueous solvents for two-phase catalytic hydrocarbon transformations (2).

The organochloroaluminate ionic liquids, based on the mixture of aluminium trichloride and 1-butyl-3-methylimidazoliumchloride (BMICl), have the attractive property that their Lewis acidity can be controlled with the composition of the liquid. They favor the dissociation of ionic transition-metal complexes and may be regarded as Lewis acidic noncoordinating media. We have extended this class of liquids to aluminium compounds bearing an aluminium-carbon bond, such as EtAlCl_2 and its mixture with aluminium trichloride (3, 4). Nevertheless, acidic organochloroaluminate liquids are highly sensitive to moisture and may react with functionalized organic products and/or reactants. For this reason, we have extended the use of molten salts to the systems which make use of anions such as $[\text{BF}_4]^-$, $[\text{PF}_6]^-$, $[\text{SbF}_6]^-$, $[\text{CF}_3\text{SO}_3]^-$ (5), etc. Contrary to the $[\text{AlCl}_4]^-$ anion, such anions do not combine with their corresponding Lewis acids and thus do not form polynuclear anions. Hence these salts are neutral stoichiometric compounds and cannot have a potential acidity.

We have initiated a series of studies using these salts as solvents for catalytic reactions involving charged species (carbeniums and carbanions) or transition-metal

complexes. To this end, the solvation and coordination ability of ionic liquids is of the utmost importance. In this way ionic liquids can be classified according to the complexing ability of their anions (Table 1).

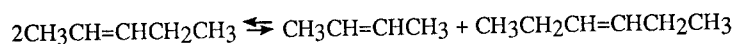
Olefin dimerization.

We first applied the two-phase catalysis concept to the dimerization of olefins catalyzed by nickel complexes. The active species involved in this reaction is a cationic nickel complex of the type $[\text{LNi-CH}_2\text{R}]^+ [\text{AlCl}_4]^-$ ($\text{L}=\text{PR}_3$) (6). Non coordinating acidic organochloroaluminate liquids proved to be superb solvents for stabilizing the active nickel catalyst. At 5°C and under atmospheric pressure, the propene dimerization reaction productivity was more than 250 kg of dimers per g of nickel, which is much greater than that obtained with organic solvents. The reaction products form a second upper phase which can easily be separated by simple decantation. The pale yellow-orange catalyst remains in the ionic phase and can be reused several times (7, 8).

The main advantage of performing the dimerization reaction in ionic liquids is a better use of nickel complexes, aluminium compounds and *costly* phosphine ligands which make possible the production of interesting propene dimerization isomers.

Olefin metathesis (9).

The reaction is usually described by the following equilibrated disproportionation of olefins and can be applied to most olefins:



We have obtained very good results in pen-2-ene metathesis by using $\text{W}(\text{OAr})_2\text{Cl}_4$ complexes ($\text{ArOH} = 2,6\text{-diphenylphenol}$ or $2,4,6\text{-triphenylphenol}$) dissolved in $\text{BMICl}:\text{AlCl}_3:\text{EtAlCl}_2$ (1:0.9:0.2) ionic liquids. The reaction equilibrium was reached in 4 hours. Active species are quite soluble, remain in the polar phase and can be reused several times after decantation of the hydrocarbon layer. Pent-1-ene is converted into ethylene and oct-4-ene, and the mixture of cyclopentene and pent-2-ene affords the expected telomers.

Hydrogenation of C=C bond.

As ionic liquids are known to dissolve charged species, we first applied them to the hydrogenation of pent-1-ene using the Osborn $[\text{Rh}(\text{NBD})(\text{PPh}_3)_2]^+ \text{PF}_6^-$ complex ($\text{NBD}=\text{norbornadiene}$) as the cationic catalyst precursor (10). Remarkable solvent effects are observed. When $\text{BMI}^+\text{SbF}_6^-$ salt is used, hydrogenation rates are nearly five times higher compared to the homogeneous reaction in acetone, in spite of the expected limited solubilities of reactants in the polar phase. When using ionic liquids prepared from BMI^+Cl^- and CuCl (1:1.5), only isomerization to pent-2-ene with 100% selectivity (98% of cis-pent-2-ene) is observed, in sharp contrast to the previous results. This demonstrates that the selectivity can be strongly influenced by the nature of the anion.

Conjugated diolefins such as cyclohexa-1,3-diene and 2-methylbuta-1,3-diene have also been hydrogenated. This is all the more interesting since diolefins are more soluble in ionic liquids than the corresponding monoalkenes (e.g. cyclohexa-1,3-diene is five times more soluble than cyclohexene in the $\text{MBI}^+\text{SbF}_6^-$ salt). This can potentially improve the selectivity of the hydrogenation.

In all these experiments, the ionic solutions containing the catalyst can be reused. Only a negligible loss of rhodium was observed (less than 0.02%; under the detection limit). Thus, as ionic liquids are known to stabilize preferably cationic species and do not solvate the Rh-complex, we assume that the prevailing active catalyst is a *cationic* not solvated Rh-dihydrido complex which has two free coordination sites. To our knowledge, this is the first example of two-phase hydrogenation reactions in which an active rhodium catalyst is "immobilized" in a polar phase without special ligand design.

Olefin hydroformylation.

Two-phase pent-1-ene hydroformylation can also be achieved, as hexanals are poorly soluble in ionic liquids. Experiments using the $\text{Rh}(\text{CO})_2(\text{acac})/\text{PPh}_3$ uncharged molecular system as catalyst precursor, show high catalytic activity in the $\text{BMI}^+\text{PF}_6^-$ salt ($\text{TOF} = 333 \text{ h}^{-1}$). After removal of the organic products, the ionic phase can also be reused and gives quite similar activity. However, a small part of the active Rh-catalyst is extracted into the organic phase. Thus, in contrast to the hydrogenation reactions, the uncharged $\text{Rh}(\text{CO})_2(\text{acac})$ catalyst precursor has to be immobilized in the salt by a polar ligand. For this purpose, the sodium salts of monosulfonated (TPPMS) and trisulfonated (TPPTS) triphenylphosphine ligands have been used. In this way, extraction of the Rh-catalyst could be completely avoided.

Butadiene dimerization.

" $\text{Fe}(\text{NO})_2$ " is a well known catalyst for the Diels-Alder dimerization of conjugate diolefins, such as butadiene, into 4-vinylcyclohexenes (11). This species is usually obtained by reduction of $\text{Fe}_2(\text{NO})_4\text{Cl}_2$. The slightly coordinating $[\text{MBI}]^+[\text{AF}_6]^-$ ($\text{A}=\text{P}$ or Sb) ionic liquids proved to be adequate solvents for stabilizing the active intermediate. The "ionic liquid solvent effect" is quite remarkable. Electrochemical reduction of the $\text{Fe}_2(\text{NO})_4\text{Cl}_2$ complex could be used with confidence in high-conductivity ionic liquids.

Organoaluminates as acidic catalysts (12).

The *alkylation reactions* of olefins with isobutane may proceed, in acidic chloroaluminates, in a way similar to that previously described with conventional liquid catalysts. However, one of the advantages of using organochloroaluminates is that their catalytic activity may be readily controlled through the $[\text{Al}_2\text{Cl}_7]^-$ anion concentration. Very acidic $\text{BMICl}:\text{AlCl}_3$ (1:2) mixtures promote the alkylation of ethene with isobutane (neither HF nor H_2SO_4 acids are effective for this reaction). The reaction provides 2,3-dimethylbutane as the main reaction product. The alkylation of but-2-ene with isobutane can be performed with the same acidic ionic liquids. However, due to the higher reactivity of butene, the acidity of the salt has to be carefully controlled to prevent side reactions. Some additives can improve the reaction. The catalyst productivity is eight times greater than that obtained with sulfuric acid catalyst, while the alkylate composition is maintained as described below. The imidazolium salt can be recovered by hydrolysis.

CONCLUSION

Ionic liquids show great promise as solvents for two-phase catalysis. It may be assumed that most of the known transition-metal catalyzed reactions could be carried out in organic-inorganic ionic liquids by fitting the liquid composition with the selected

catalyst precursors. This technique appears to be particularly valid in many cases: when transition metals and ligands are costly (e.g. in asymmetric catalysis); when the disposability of the catalyst systems raise difficulties. On other hand, advantage can be taken of the solubility of reactants and the poor solubility of products.

REFERENCES

1. ^aW.A. Herrmann and C.W. Kohlpaintner, *Angew. Chem. Int. Ed. Engl.* **32**, 1524 (1993); ^bB. Cornils and E. Wiebus *CHEMTECH* **34** (1995).
2. Y. Chauvin and H. Olivier *CHEMTECH*, **26** (1995).
3. Y. Chauvin, F. Di Marco-Van Tiggelen and H. Olivier, *J. Chem. Soc. Dalton Trans.* 1009 (1993).
4. B. Gilbert, Y. Chauvin, H. Olivier and F. Di Marco-Van Tiggelen, *J. Chem. Soc. Dalton Trans.* 3867 (1995).
5. J. Fuller, R.T. Carlin, H.C. De Long and D. Haworth, *J. Chem. Soc. Chem. Commun.* 299 (1994).
6. G. Wilke, B. Bogdanovic, P. Hardt, O. Heimbach, W. Kroner, W. Oberkirch, K. Tanaka, E. Steinrucke, D. Walter and H. Aimmerman, *Angew. Chem. Int. Ed. Engl.* **5**, 151 (1966).
7. Y. Chauvin, B. Gilbert and I. Guibard, *J. Chem. Soc. Chem. Commun.* 1715 (1990).
8. Y. Chauvin, S. Einloft and H. Olivier, *Ind. Eng. Chem. Res.* **34**, 1149 (1995).
9. H. Olivier, Y. Chauvin, F. Di Marco-Van Tiggelen and B. Gilbert, in *Molten Salts Ninth International Symposium*, C.L. Hussey, D.S. Newman, G. Mamantov, Y. Yto, Editors, p. 617, The Electrochemical Society Proceedings Series, Pennington, NJ (1994).
10. R.R. Schrock and J.A. Osborn, *J. Am. Chem. Soc.* **98**, 2134 (1976).
11. D. Huchette, B. Thery and F. Petit, *J. Mol. Catal.* **4**, 433 (1978).
12. Y. Chauvin, A. Hirschauer and H. Olivier, *J. Mol. Catal.* **92**, 155 (1994).

Table 1: Non aqueous room-temperature ionic liquids.

Cations	Anions	Coordination ability
	Cl ⁻	strong (basic)
NR ₄ ⁺ [a]	BF ₄ ⁻	weak (neutral)
PR ₄ ⁺	PF ₆ ⁻	
SR ₃ ⁺	SbF ₆ ⁻	
	CF ₃ SO ₃ ⁻	
	CuCl ₂ ⁻ , AlCl ₄ ⁻	
	Cu ₂ Cl ₃ ⁻ , Cu ₃ Cl ₄ ⁻	no (acidic)
	Al ₂ Cl ₇ ⁻ , Al ₃ Cl ₁₀ ⁻	

[a] *N*-alkylpyridinium, 1,3-dialkylimidazolium

PHYSICO-CHEMICAL AND STRUCTURAL PROPERTIES Of DeNO_x AND SO₂ OXIDATION CATALYSTS

*S.G. Masters¹, C. Oehlers¹, K. Nielsen¹,
K.M. Eriksen¹, R. Fehrmann¹
A.Chrissanthopoulos² and S. Boghosian²*

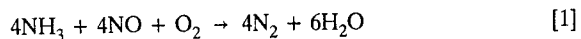
- ¹. Department of Chemistry, Building 207, Technical University of Denmark, DK-2800 Lyngby, Denmark.
- ². Institute of Chemical Engineering and High Temperature chemical Processes, P.O. Box 1414, University of Patras, GR-26500 Patras, Greece.

ABSTRACT

Commercial catalysts for NO_x removal and SO₂ oxidation and their systems have been investigated by spectroscopic, thermal, electrochemical and X-ray methods. Structural information on the vanadium complexes and compounds as well as physico-chemical properties for catalyst model systems have been obtained. The results are discussed in relation to proposed reaction mechanisms.

INTRODUCTION

Cleaning of flue gas and other industrial off-gases for sulfur- and nitrogen-oxides has increased the latest years due to increased concern for the environment, locally and globally. Recently a catalytical process has been developed - the so-called SNOX process - where SO_x and NO_x are removed simultaneously. Reduction of NO_x to N₂ and H₂O is performed by reaction with injected NH₃ and catalyzed by V₂O₅ (often promoted by WO₃ and MoO₃) on a TiO₂ (anatase) solid carrier at 350-400 °C. SO₂ is oxidized to SO₃ by V₂O₅ at around 420 °C, where the promoters (often Na, K and/or Cs sulfates) form pyrosulfates, which dissolve V₂O₅, leading to a Supported Liquid Phase (SLP) catalyst. The project is concerned with spectroscopic, thermal, electrochemical and X-ray characterization of the working catalysts and model systems in simulated flue gas from power plants, i.e. ~ 0.2% SO₂, 0.1% NO_x, 4% O₂, 7% H₂O, 14% CO₂, 75% N₂, and in traditional sulfuric acid synthesis gas, i.e. 10% SO₂, 11% O₂, 79% N₂. For the DeNO_x or SCR, (Selective Catalytic Reduction) catalyst a representative reaction scheme is



where NH_3 is injected into the flue gas in amounts equimolar to the NO content. In accordance with the proposed reaction mechanism a redox process involving V(V) and V(IV) should take place. Therefore in-situ EPR spectroscopy - as applied here - might be a convenient method to investigate the V(IV) species formed in the working DeNO_x catalyst. For the SO_2 oxidation the key process is



where SO_3 is absorbed in dilute sulfuric acid to yield commercial grade H_2SO_4 or oleum. Also for this catalyst several oxidation states of vanadium, i.e. V(III), V(IV) and V(V), are important both in the molten phase of the catalyst as well as in the solids that may precipitate and deactivate the catalyst and model systems. Information about the structures of these compounds and the phase diagrams of the catalyst model systems is considered important for the understanding of the reaction mechanism and for designing catalysts with high activity, also below $\sim 420^\circ\text{C}$.

EXPERIMENTAL

The composition of the industrial DeNO_x catalyst investigated here is 3.6 w/w% V_2O_5 and 7.8 w/w% WO_3 on TiO_2 (anatase) with $S_{\text{BET}} = 13 \text{ m}^2/\text{g}$.

In situ EPR measurements were made on a modified JEOL JES-ME-1X spectrometer equipped with a Bruker ER 4114 HT high temperature cavity. The catalyst sample was placed in a double tube reactor cell inside the cavity, allowing the inlet gas to be preheated before passing the catalyst bed.

The ^{39}K NMR spectra were measured on a Bruker MSL-400 spectrometer using a home made high temperature probe head. The natural isotope samples contained 93,26% ^{39}K . The spectra were measured at 18.67 MHz and the chemical shifts referred relatively to 0.1 M aqueous solution of KCl.

The flue gas was premixed in gas bottles using dry SO_2 , O_2 , CO_2 and N_2 to the desired composition. Wetting of gasses was done by bubbling the gas through water containing flasks heated to the appropriate temperature, e.g. 40°C for a water content of 7% (saturation). The SO_2 concentration was monitored by UV spectrophotometry using a gas cuvette with an optical path of 100 mm. The concentration of CO_2 , O_2 and N_2 was found by gas chromatography (Supelco Chromosorb 102 and Molecular Sieve 5 A). The H_2O concentration was measured

by a Jenway 5075 Humidity meter.

For the activity measurements and compound isolation the gas was led to a molten salt reactor cell of Pyrex, where the crushed catalyst or model melt is supported by the porous glass filter disk through which the gas bobbles. The reactor cell was placed in a double walled kanthal wire wound quartz furnace. The conversion of SO_2 was monitored spectrophotometrically (on line). This setup allowed direct visual inspection of the crystal formation and compound isolation at high temperature.

X-ray intensity data were collected on an Enraf-Nonius CAD-4F four-circle diffractometer using monochromated $\text{MoK}\alpha$ radiation and ω -scan technique. The data were corrected for Lorentz and polarization effects. Structural parameters were refined by full-matrix least-squares methods based on F^2 .

RESULTS AND DISCUSSION

DeNO_x Catalysts

The redox chemistry of the industrial DeNO_x catalyst has been investigated in N_2 , O_2 and 1% NH_3 (in N_2), i.e. in neutral, oxidizing and reducing atmosphere, by in situ EPR spectroscopy in the temperature range 20 - 400 °C. The spectra are shown in Figure 1. The main features include a temperature sensitive broad line (line width ~ 500 Gauss) and a smaller central line (line width < 100 Gauss), which only to a small degree is sensitive to gas composition and temperature. Both lines have earlier been attributed to V(IV) ions in different environments. We have recorded a series of spectra of the TiO_2 carrier alone at 20 - 450 °C, which surprisingly shows the broad temperature sensitive band, only. This is therefore attributed to the transition of paramagnetic species formed in the carrier. Since Ti^{4+} is diamagnetic the paramagnetic species are probably formed due to a non-stoichiometric composition of TiO_2 , which indeed is known to be the case for titanium oxides in general. The smaller central line (and the small peaks of badly resolved V^{+4} hyperfine structure) is attributed to a solid solution of V^{+4} in the TiO_2 lattice. This explains the small sensitivity of this band to the composition of the gas. Surprisingly no EPR signal seems to be obtained from the surface vanadium species, which are known to be reduced by NH_3 , based on FTIR measurements given in the literature. Probably EPR-silent tetrahedral coordinated V^{+4} species or V^{+3} species are formed. They may, however, be detected at liquid nitrogen or lower temperatures. Such measurements are in progress.

SO₂ oxidation catalysts

The oxidized form of the catalyst melt is well described by the $\text{M}_2\text{S}_2\text{O}_7 \cdot \text{V}_2\text{O}_5$

(M = Na, K and/or Cs) systems. The phase diagrams of these systems are constructed by electrical conductivity, thermal and NMR measurements. The line width of the ^{39}K NMR signal changes drastically by melting as shown in Figure 1 for some compositions of the $\text{K}_2\text{S}_2\text{O}_7 - \text{V}_2\text{O}_5$ system. In addition the electrical conductivity changes at the phase transition temperature. The combined results lead to the phase diagram shown in Figure 3.

Three compounds - possibly $\text{K}_3\text{VO}_2\text{SO}_4\text{S}_2\text{O}_7$, $\text{K}_4(\text{VO})_2\text{O}(\text{SO}_4)_4$ and KVO_2SO_4 - are known to be formed in good accordance with the diagram. A low melting eutectic is formed at $X_{\text{V}_2\text{O}_5} = 0.18$ - a possible candidate for a modified catalyst composition.

Interaction between the $\text{M}_2\text{S}_2\text{O}_7 - \text{V}_2\text{O}_5$ catalyst model system or industrial catalysts and SO_2 containing flue gases or sulfuric acid synthesis gases leads to catalyst deactivation below $\sim 420^\circ\text{C}$ and simultaneously precipitation of lower valence vanadium oxo sulfato compounds. As an example, part of the structure of the V(IV) compound $\text{Cs}_2(\text{VO})_2(\text{SO}_4)_3$ is shown in Figure 4. VO_6 octahedra are linked by SO_4 tetrahedra giving rise to large vacancies where the Cs-ions (not shown) are placed. During catalyst deactivation in flue gases $\text{VOSO}_4(\text{SO}_2, \text{SO}_3, \text{H}_2\text{O})_x$ type of V(IV) compounds are formed. Here SO_2 molecules (instead of SO_4^{2-}) link the VO_6 octahedra trans to the $\text{V}=\text{O}$ bond, and SO_3 and/or H_2O molecules fill out the vacancies in a disordered manner.

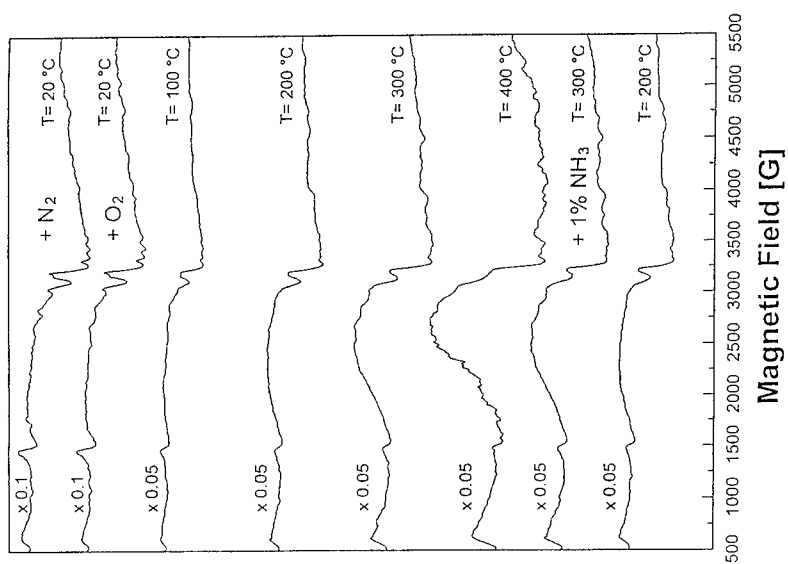
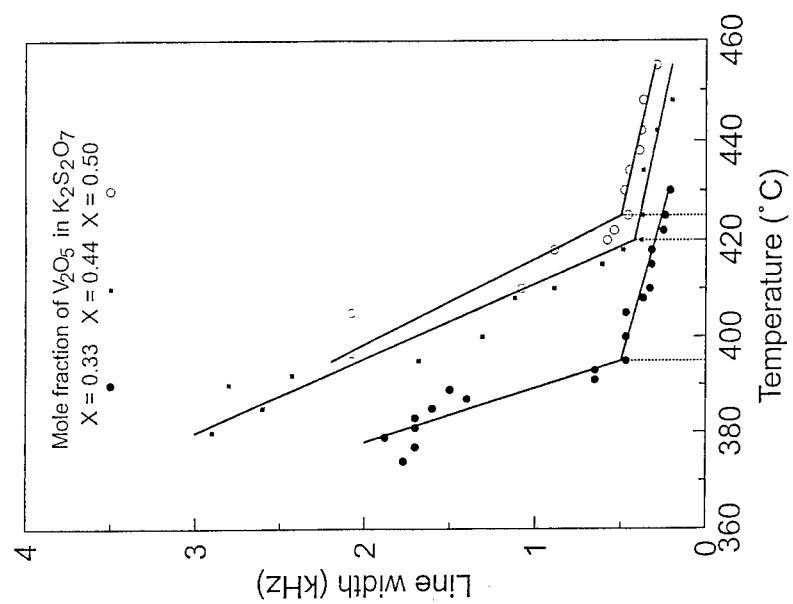
In a proposed mechanism for the SO_2 oxidation process this type of V(IV) compounds are probably those suggested to be formed by reduction of the oxidized catalyst by SO_2 . Further the SO_2 coordination to V(IV) may be a necessary step for a further reduction to V(III) compounds.

ACKNOWLEDGEMENTS

O. Lapina, V. Tersikh and B. Balzhinimaev from Boreskov Institute of Catalysis, Novosibirsk, Russia are thanked for experimental assistance. INTAS, contr. no. 93-3244, has supported this work.

REFERENCES

1. K.M. Eriksen, D.A. Karydis, S. Boghosian and R. Fehrmann, *J. Catal.*, **155**, 32 (1995).
2. N.-Y. Topsøe, *Science*, **265**, 1217 (1994).
3. K.M. Eriksen, K. Nielsen and R. Fehrmann, *Inorg. Chem.*, **35**, 480 (1996)



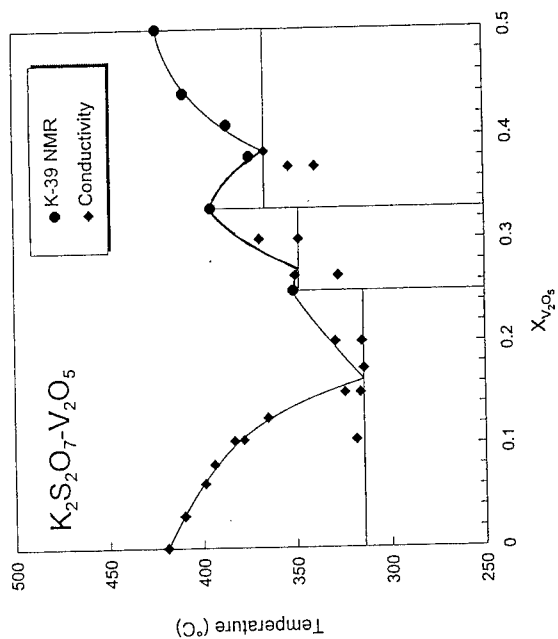


Figure 3. Phase diagram of the $K_2S_2O_7-V_2O_5$ system based on electrical conductivity and ^{39}K NMR measurements.

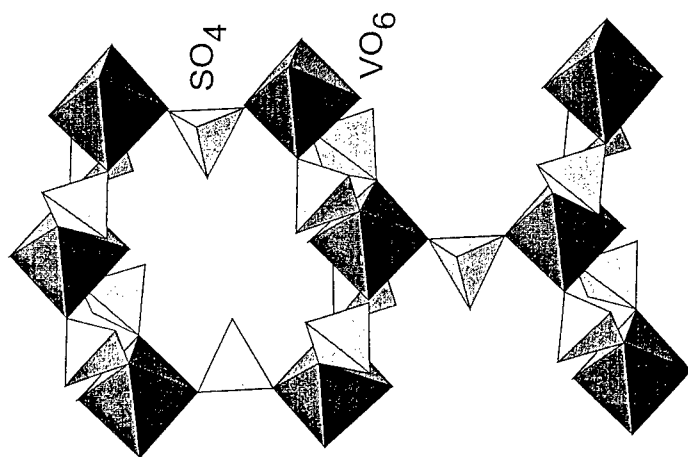


Figure 4. Part of the structure of $Cs_2(VO)_2(SO_4)_3$. Cs -ions are not shown.

ACIDITY OF HCL IN NEUTRAL BUFFERED CHLOROALUMINATE MOLTEN SALTS

Dawn King and Robert Osteryoung

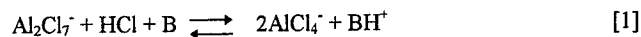
Department of Chemistry
North Carolina State University
Raleigh, NC 27695

ABSTRACT

The Brønsted acidity of HCl in neutral buffered AlCl_3 :1-ethyl-3-methyl imiazolium chloride melts has been compared to the Brønsted acidity of HCl in acidic (55mol% AlCl_3) melts. The acidities were compared using the spectrophotometric indicator method. Arenes were used as the weak indicator bases. The acidity of HCl in the neutral buffered melts is dependent on both the type of buffering agent (LiCl, NaCl) and on the concentration of the metal cation in the melt. An enhancement in Brønsted acidity of HCl is observed to a lesser degree than in the acidic melts.

INTRODUCTION

During the past decade investigations have revealed that HCl acts as a Brønsted superacid when dissolved in an acidic chloroaluminate molten salt (1,2). A Brønsted superacid is generally considered to be any acid more acidic than 100% sulfuric acid ($H_0 = -11.9$), (3) H_0 being the Hammett Acidity Function (4). A solution formed by combining a Brønsted acid with a strong Lewis acid can create a potential superacid. Acidic chloroaluminate melts contain the Al_2Cl_7^- anion which is a strong Lewis acid and provides the driving force in a melt to make a Brønsted acid behave as a superacid. The acidity of HCl in an acidic melt can be determined using the spectrophotometric indicator method. This method measures the ability of HCl to protonate a variety of weak bases.



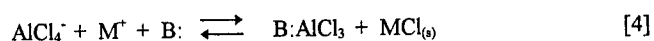
In our laboratory chloroaluminate ionic liquids, or molten salts, are prepared by combining aluminum chloride (AlCl_3) and an organic chloride, in this case 1-ethyl-3-methylimidazolium chloride (ImCl) (5). A melt is considered acidic, basic, or neutral dependent upon whether the mole ratio of AlCl_3 to ImCl is greater than, less than, or equal to unity. An acidic melt may be buffered to neutrality by addition of an alkali metal chloride, MCl , where the reaction:



takes place (6). The condition for neutrality is:

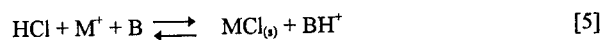
$$[\text{Im}^+] + [\text{M}^+] = [\text{AlCl}_4^-] \quad [3]$$

The alkali chloride is insoluble once the melt is neutralized, and thus provides a solid buffer. In previous work we showed that the neutral-buffered melts possess what we termed a latent acidity. A weak Lewis base, such as acetylferrocene, forms an AlCl_3 adduct in the neutral buffered melt, whereas it does not in a neutral unbuffered or basic melt (7). The additional driving force for this reaction apparently results from the precipitation of the solid MCl :



The extent of latent acidity is controlled by the concentration of M^+ ions present in the neutral-buffered melt, hence on the acid content of the melt from which it is prepared (8).

In this work experiments have been undertaken to determine if the reaction:



takes place in a neutral-buffered melt, i.e. if HCl in the neutral-buffered melt has an increased acidity relative to that in the neutral unbuffered or basic melts.

EXPERIMENTAL

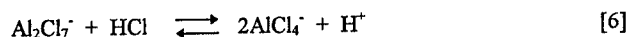
Aluminum chloride and 1-ethyl-3-methylimidazolium chloride were prepared as previously described (9). Melts were made by mixing weighed amounts of AlCl_3 and ImCl to produce a slightly basic melt (0.97:1.00). Proton and oxide impurities were then removed by treatment with high vacuum and phosgene. Acidic melts were prepared by first making a basic melt and removing impurities as described above. A weighed amount of AlCl_3 was then added to the basic melt to obtain the desired acidity. Neutral-buffered melts were prepared by adding excess LiCl or NaCl to an acidic melt. LiCl (Aldrich, 99.99+ %) and NaCl (Aldrich, 99.999%) were dried by heating to 399°C below 1×10^{-3} torr for 4 days. All melts preparation was done in a nitrogen-filled Vacuum Atmospheres drybox. Combined oxygen and water concentrations were maintained at a concentration of less than 5 ppm.

Solutions of arenes in the neutral-buffered melts were prepared by stirring a weighed amount of arene in a weighed amount of melt. The molar concentration of the arene was determined using the density of a unbuffered neutral melt. The concentration is varied depending on the arene of interest. The variation in concentration was necessary in order to keep the absorbance for the bands of interest between 0.1 and 1.0 absorbance units.

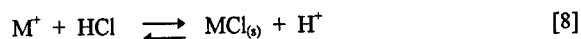
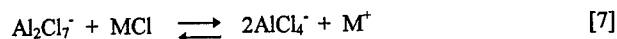
Protonation of the base: After the solution was prepared, approximately 3ml of melt was transferred by pipette to the side arm of the hydrochlorination cell (Figure 1). A quartz insert and its holder were then lowered into the cell and the vacuum stopcock closed to the outside atmosphere. The cell is then removed from the dry box and attached to a vacuum line designed for the determination of HCl pressure over the melt. The cell was slowly evacuated to avoid excessive bubbling of the melt. The cell was then isolated from the vacuum and HCl introduced. The melt was stirred in the side arm under the HCl pressure of interest. An instantaneous color change was observed in the melts upon the introduction of HCl . After the HCl pressure reaches equilibrium, the melt remains under pressure for 10 minutes of additional reaction time. The cell assembly was then removed from the line. The melt was poured into the cell and the spectra taken.

RESULTS AND DISCUSSION

An effort was made to compare the Brønsted acidity of HCl in neutral buffered melts to the Brønsted acidity of HCl in acidic (55mol% AlCl_3) melts. As previously mentioned, Smith and co-workers concluded that HCl (1atm) in acidic (55mol% AlCl_3) melts is a Brønsted superacid on the same order of acidity as 100% HF ($H_0 = -15.1$) (2). The strong Lewis acid, Al_2Cl_7^- present in acidic melts, acts as a Cl^- sink, providing the driving force for the enhanced acidity of the HCl .



In neutral buffered melts an enhancement in the Brønsted acidity of HCl is also observed, but to a lesser degree than in the acidic melts. The driving force for the enhanced acidity of HCl in the neutral buffered melts is provided by the precipitation of the alkali metal chloride from solution.



The spectrophotometric indicator method was used to compare the acidity of HCl in melts of various compositions. The melts exhibit a wide UV window (down to 240 nm) making it possible to observe both the protonated and unprotonated forms of the base. Arenes were used as weak indicator bases in order to directly compare these results to those of Smith and co-workers in the acidic melts.

Figure 2 represents a typical spectra taken for hexamethylbenzene at various pressures of HCl. As the pressure of HCl increases so too does the absorbance of the protonated form of the base observed at 285 nm and 396 nm. If the concentration of the protonated base is calculated at each pressure for the absorbance band at 396 nm and divided by the total initial concentration of base in the melt, the degree of protonation is obtained as seen in Figure 3. An increase in pressure results in an increase in the degree of protonation.

At a given pressure the relative acidity of HCl in the neutral buffered melts is dependent on the specific type of alkali metal cation, M^+ , in the melt and on the concentration of M^+ in solution. Acidic melts were buffered with LiCl and NaCl. Figure 4 shows the effect of the metal cation on the relative acidity of HCl in various neutral buffered melts. Using 9,10-dimethylantracene ($\text{pK}_B = 6.4$ in HF) as the indicator base, one can observe the change in the degree of protonation versus pressure for each buffering agent. Using the degree of protonation as an indicator for the acidity of HCl in the various melts, the effect of the cation on the acidity of HCl in the neutral buffered melts can be ranked: LiCl-buffered > NaCl-buffered. This work is in agreement with research previously conducted by Osteryoung and co-workers in which Guttmann acceptor numbers (AN) were used as a measure of the relative acidities of the various neutral buffered melt systems. Using triethylphosphine oxide as the probe molecule the same order of acidities was found (10).

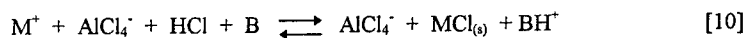
In addition to being dependent on the type of metal cation in the melt, the acidity of HCl is also dependent on the concentration of M^+ in solution. The metal cation concentration in a neutral buffered melt is equal to the initial $Al_2Cl_7^-$ concentration in the melt before buffering. The larger the M^+ concentration the larger the degree of protonation observed at that pressure, regardless of which buffering agent is employed. Figure 5 shows the effect of changing the initial $Al_2Cl_7^-$ concentration and buffering with the same alkali metal chloride. The degree of protonation is larger for the melts that were originally 60mol% $AlCl_3$ than for the melts that were originally 55mol% $AlCl_3$. The curvature in the line observed in the LiCl buffered melts is absent in the NaCl buffered melts. The linearity seen in the NaCl buffered can be attributed to fact that the concentration of the unprotonated base is so large in comparison to the protonated base, that we are essentially plotting the ionization ratio ($[BH^+]/[B]$) versus pressure of HCl as seen in equation [9].

$$\text{When } [B] \gg [BH^+], \quad \text{then } \frac{[BH^+]}{[B] + [BH^+]} \approx \frac{[BH^+]}{[B]} \quad [9]$$

[B] defined as the unprotonated base, and $[BH^+]$ as the protonated base.

Considering both the activity of the metal cation as well as the concentration of the metal cation, the relative acidity of HCl in neutral buffered melts can be compared to the acidity of HCl in the acidic (55mol% $AlCl_3$) melt based on the degree of protonation. (Table I) Basic melts exhibit no latent acidity and therefore show no degree of protonation for any base at any pressure. The order of the neutral buffered melts are as previously described -- LiCl buffered > NaCl buffered and within each buffered melt system, the greater the M^+ concentration the greater the relative acidity. The Brønsted acidity of HCl is the strongest in the acidic melts.

If a simple protonation reaction is written:



$$K' = \frac{[BH^+]}{[B][M^+]P_{HCl}} \quad [11]$$

plotting the ionization ratio ($[BH^+]/[B]$) versus the pressure of HCl (Figure 6), the slope of the line will be equal to $K'[M^+]$. Using the appropriate M^+ concentration, K' values were calculated for bases in the various melts, see Table II. The calculation for K' is based on the assumption that a linear variation of HCl solubility exists with pressure in the neutral buffered melts. This relationship has been shown to hold true in both acidic and slightly basic melts (11). As expected bases in the LiCl buffered melts have a higher equilibrium constant than the bases in the NaCl buffered melts. The difference in the equilibrium values between bases is due to the strength of the base. Thus 9,10-dimethylantracene ($pK_B = 6.4$ in HF) has larger equilibrium constants than hexamethylbenzene ($pK_B = 1.4$ in HF). The important point to note is that the order of magnitude between the LiCl and NaCl buffered melts remain constant.

Table II. Equilibrium Constants

	<u>Hexamethylbenzene</u>	<u>9,10 - Dimethylantracene</u>
LiCl buffered melts	$1.7 \text{ E } -03 \pm 2.3 \text{ E } -04$	$1.1 \text{ E } -01 \pm 3.2 \text{ E } -02$
NaCl buffered melts	$4.2 \text{ E } -05 \pm 3.8 \text{ E } -06$	$8.9 \text{ E } -03 \pm 1.3 \text{ E } -04$

In conclusion, it has been shown that the Brønsted acidity of HCl in chloroaluminate melts can be varied by changing numerous melt parameters. Adjustment of the pressure of HCl over the melt combined with altering the buffering agent and the metal cation concentration in solution allow the experimentalist to choose a specific HCl acidity. This tunable solvent system could provide unique opportunities in both complexation and reaction chemistry.

ACKNOWLEDGMENTS

This work was supported in part by the Air Force Office of Scientific Research.

REFERENCES

1. G.P. Smith, A.S. Dworkin, R.M. Pagni and S.P. Zingg, *J. Am. Chem. Soc.*, **111**, 5075 (1989).
2. G.P. Smith, A.S. Dworkin, R.M. Pagni and S.P. Zingg, *J. Am. Chem. Soc.*, **111**, 525 (1989).
3. T.A. O'Donnell, *Superacids and Acidic Melts as Inorganic Chemical Reaction Media*, p. 7, VCH Publishers, Inc., New York (1993).
4. L.P. Hammett and A.J. Deyrup, *J. Am. Chem. Soc.*, **54**, 2721 (1932).
5. J.S. Wilkes, J.A. Levisky, R.A. Wilson and C.L. Hussey, *Inorg. Chem.*, **21**, 1263 (1982).
6. T.J. Melton, J. Joyce, J.T. Maloy, J.A. Boon and J.S. Wilkes, *J. Electrochem. Soc.*, **137**, 3865 (1990).
7. I.C. Quarmby and R.A. Osteryoung, *J. Am. Chem. Soc.*, **116**, 2649 (1994).
8. R.A. Osteryoung, I.C. Quarmby, R.A. Mantz and L.M. Goldenberg, *Anal. Chem.*, **66**, 3558 (1994).
9. P.C. Trulove and R.A. Osteryoung, *Inorg. Chem.*, **31**, 3980 (1992).
10. R.A. Mantz, P.C. Trulove, R.T. Carlin and R.A. Osteryoung, in *Tenth International Symposium on Molten Salts/1996*, The Electrochemical Society Proceedings Series, Pennington, NJ (1996).
11. J.L.E. Campbell and K.E. Johnson, *J. Am. Chem. Soc.*, **117**, 7791 (1995).

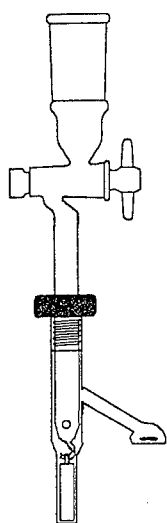


Figure 1. Protonation cell.

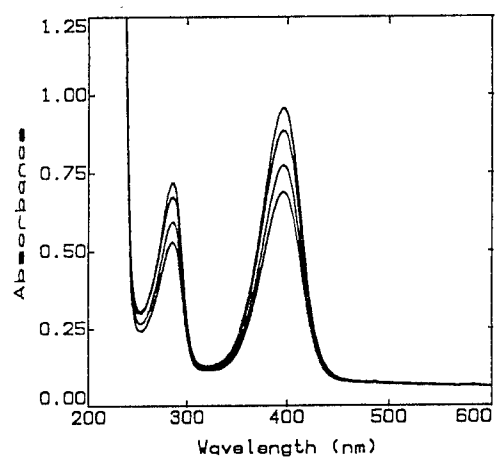


Figure 2. Absorption spectra of hexamethylbenzene. Protonated forms of the base at 285nm and 396nm can be seen increasing as the pressure of HCl is increased.

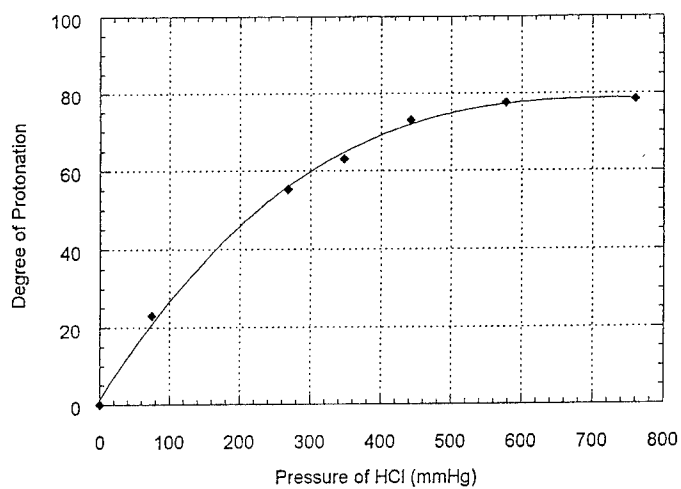


Figure 3. Degree of protonation of hexamethylbenzene versus pressure of HCl (mmHg) in a LiCl buffered melt, originally 60mol% AlCl_3 .

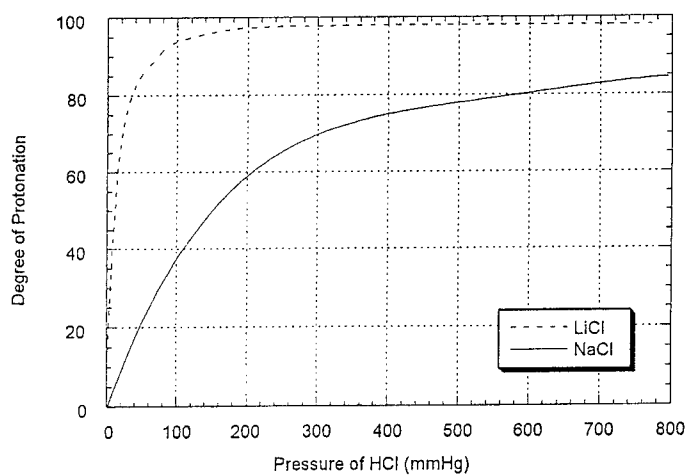


Figure 4. Degree of protonation of 9,10-dimethylantracene versus pressure of HCl (mmHg) for various neutral buffered melt systems, all originally 60mol% AlCl_3 .

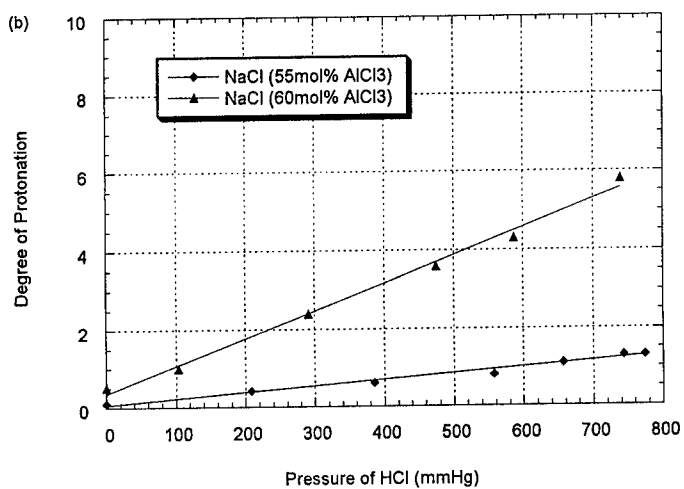
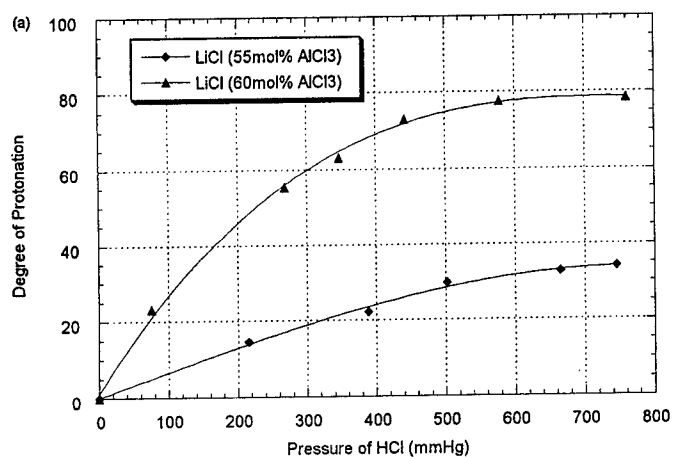


Figure 5. Degree of protonation of hexamethylbenzene versus pressure of HCl (mmHg) for various neutral buffered melt systems. (a) LiCl buffered melts (b) NaCl buffered melts

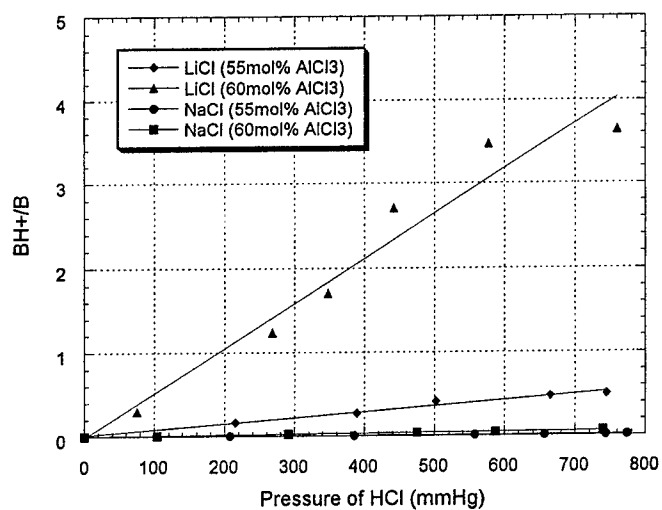


Figure 6. Ionization ratio versus pressure of HCl for various neutral buffered melts. Indicator base in all cases is hexamethylbenzene.

Table I. Degree of Protonation of Indicator Base ca 760 mmHg		
	9,10-dimethyl- anthracene (log K_B = 6.4)*	Hexamethyl- benzene (log K_B = 1.4)*
Basic melt	0	0
NaCl buffered (55mol% $AlCl_3$)	84	2
NaCl buffered (60mol% $AlCl_3$)	93	6
LiCl buffered (55mol% $AlCl_3$)	> 98	34
LiCl buffered (60mol% $AlCl_3$)	> 98	78
55mol% $AlCl_3$ Acidic melt**	100	98

*log K_B in HF, values taken from *Carbonium Ions*, Olah, G.A. and Schleyer, P. von R., Eds.; Wiley-Interscience: New York, 1970, Vol II.

** Values taken from *J. Am. Chem. Soc.* **1989**, *111*, 525-530.

MOLTEN SALT AND RELATED ACIDS

Keith E. Johnson
W. David Chandler
Brad D. Fahlman

Department of Chemistry, University of Regina
Regina, Saskatchewan, Canada S4S 0A2

Pressure-composition isotherms, ^1H NMR spectra and conductivity measurements indicate that $\text{SbCl}_5\text{:HCl}$ mixtures up to 24% mol HCl are non-electrolytes and contain one $\text{SbCl}_5\text{:HCl}$ adduct up to ~10% mol HCl and two adducts for the 10-24 mol% range. Since ^1H exchange between the two adducts was not seen, it is deduced that one, at least, contains a structurally sheltered proton. Calculations upon the $\text{BF}_3\text{:HF:MF}$ and $\text{BCl}_3\text{:HCl:MCl}$ systems gave data on the shapes and stabilities of the recently made B_2F_7^- ion and the likely species HBF_4 , HB_2F_7 , $\text{BF}_4(\text{HF})^-$, $\text{B}_2\text{F}_7(\text{HF})^-$ and $\text{BCl}_4(\text{HCl})^-$. ^1H NMR calculations which fit closely the experimental results for CH_4 , HCl and HCl_2^- , predicted the H_2Cl^+ resonance to occur at ~6 ppm.

INTRODUCTION

It has been known for many decades that hydrogen halides (HX) react with halide salts (MX) to produce compounds of the type MHX_2 , MH_2X_3 , etc. Some examples are KHF_2 , $(\text{pyH})\text{HCl}_2$ (1), ImH_2Cl_3 (2) ($\text{Im} \equiv$ 1-ethyl-3-methyl-1H-imidazolium) and $(\text{CH}_3)_3\text{SHBr}_2$ (3). Many of these compounds are liquid at modest temperature and are strong Bronsted acids. In the 1960's it was shown that the reaction of HF with the Lewis acid SbF_5 gave rise to superacidic liquids; the active species in these solutions have been taken to be the cations H_2F^+ and H_3F_2^+ (4,5).

When it was shown (6) that HCl, in combination with ImCl and AlCl_3 gave liquids which were strong acids where $n_{\text{ImCl}} > n_{\text{AlCl}_3}$ and superacids where $n_{\text{AlCl}_3} > n_{\text{ImCl}}$, the formation of H_2Cl^+ and H_3Cl_2^+ in the Lewis acidic liquids was advocated (7). However, precise HCl solubility measurements, supported by electrochemical and infrared spectroscopic data, indicated that rather than form cational species or neutral molecules such as HAlCl_4 , HCl reacts to form the hydrogen bonded anions ClHClAlCl_3^- and $\text{ClHClAl}_2\text{Cl}_6^-$, analogous to ClHCl^- , with $\text{ClHClAl}_2\text{Cl}_6^-$ apparently responsible for the superacidity (8).

To add further credence to these findings we began theoretical calculations of the energies, structures and vibrational frequencies of HF and HCl polymers and ions and $\text{AlCl}_3\text{-HCl}$ systems (9,10). Of particular significance these calculations suggested

distinctly different IR spectra for HCl_2^- and H_2Cl_3^- , the formation of stable compounds between HCl and chloroaluminate anions but not AlCl_3 , and the conversion of H_2Cl^+ into $\text{ClHClAl}_2\text{Cl}_6^-$ by AlCl_4^- and Al_2Cl_7^- .

EXPERIMENTAL

Solubility

The solubility of HCl in SbCl_5 was determined manometrically with essentially the apparatus described elsewhere (8). Antimony pentachloride (Aldrich 99.995+%) was transferred under argon to the sample cell by means of a Teflon cannula. After the cell was attached to the vacuum manifold, the SbCl_5 was degassed by three freeze-evacuation-thaw procedures (SbCl_5 melts at 4°C) and then the cell thermostated at $24.0 \pm 0.5^\circ\text{C}$. HCl gas (Matheson, Semiconductor grade, 99.995%) was added to the system as described previously; equilibration was complete after 15 minutes at each pressure.

NMR Spectroscopy

^1H (200 MHz) spectra were acquired with a Bruker AC200QNP spectrometer. Samples were transferred from the cell under argon to standard 5 mm tubes, each of which contained a coaxial capillary filled with DMSO-d_6 (Aldrich, 99.9% D) which served as the lock solvent. All spectra were referenced to TMS.

Conductivity

Conductivity measurements were obtained with a YS1 Model 31 Conductivity Bridge connected to a dip-type glass cell with platinum electrodes. 0.1 M aqueous KCl was used for cell calibration.

Theoretical Calculations

For the large antimony species the semi-empirical method PM3 was utilized, taken from the software package Spartan V4.0 operating on a Silicon Graphics INDY workstation (64 MB, 175 MHz). *Ab initio* calculations for boron species were performed using GAUSSIAN 92 (11) and GAUSSIAN 94 (12) commercial software packages running on a Silicon Graphics II processor server (512 MB, 150 MHz). Geometry optimizations and vibrational frequency calculations were carried out using the

3-21 + G(d,p) basis set at the density functional (BVWN) level. All *ab initio* energies were corrected for thermal energies, including zero-point vibrations, to yield internal energy values at 298 K. The final ΔG° values, it must be noted, refer to the gas phase and assume ideal gas behavior.

NMR shielding tensors were obtained using GIAO, CSGT, IGAIM and SGO methods at both Hartree-Fock (RHF) and BVWN levels of theory. Geometry optimization/magnetic susceptibility calculations were performed on smaller protic species using the above methods and the 6-311++G(3df,3pd) basis set.

RESULTS AND DISCUSSION

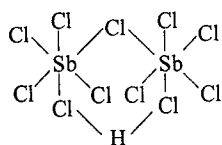
The Chloroantimononic Acid System

Figure 1 is a typical pressure-solubility isotherm for HCl in SbCl_5 . Plots are linear at low HCl concentrations with signs of saturation at higher concentrations in the form of the upward curvature. Figure 2 shows the ^1H NMR spectrum of the starting SbCl_5 : the peaks at 3.5 ppm and 2.5 ppm are from water and methyl protons, respectively, of the DMSO-d_6 lock solvent. The addition of HCl up to a concentration of 11 mol % gave rise to a peak at 2 ppm (Figure 3); further addition of HCl gave a second peak at -0.4 ppm which did not grow at the expense of the first (Figure 4). Spectra were not changed by raising the temperature at 363 K, indicating no proton exchange between the species responsible for the two resonances. Samples of less pure SbCl_5 - of poorer initial quality or not handled carefully enough - showed a broad resonance at 5 ppm. This broad 5 ppm peak from "wet" samples vanished upon HCl addition and the 2 ppm peak grew. Vacuum grease, a possible contaminant, merely generated a broad resonance at -1.0 ppm.

The electrical conductivity of both SbCl_5 and a 10 mol % HCl in SbCl_5 solution were negligible and the viscosity of the SbCl_5 appeared to be unaffected by HCl addition.

We deduce from these observations that the two protic species formed are NOT ionic, that one mole of the first (formed at ≤ 10 mol % HCl) arises per mole of HCl, that as the liquid begins to saturate with the first species, the second forms and that one of the proton environments is sufficiently sheltered structurally that proton exchange between the two is not seen in the ^1H NMR.

Feasible compositions for the two protic species are $\text{HSb}_2\text{Cl}_{11}$ and HSbCl_6 . The former could be formed at the lower HCl concentrations and, if it had a hydrogen-bonded structure such as I, might not readily exchange its proton with the latter on the NMR time scale.



I

The 2 ppm ^1H signal would correspond to this structure with the -0.4 ppm signal corresponding to HSbCl_6 , probably with the H bonded to one Cl.

Comparison of the $\text{SbCl}_5\text{--HCl}$ system with the $\text{SbF}_5\text{--HF}$ one is hampered by the fact that the more definitive measurements on the latter were made on HF-rich mixtures. These were electrically conducting and the ^{19}F NMR was interpretable in terms of the formation of SbF_6^- , $\text{Sb}_2\text{F}_{11}^-$ and $\text{Sb}_3\text{F}_{16}^-$ upon breakdown of polymeric SbF_5 (the viscosity of SbF_5 is 10 times that of SbCl_5) (4,13). Protons in these mixtures were first assumed to be in the sole cation H_2F^+ , but H_3F_2^+ was taken to be the lone cationic species up to 20% HF after IR studies (5) (this work hinged on the existence of a linear --F--H--F-- portion of H_3F_2^+ with F--H bond distances identical to those in HF_2^- : a situation confirmed by recent calculations (9).) One ^1H NMR signal was observed at -1 to 4 ppm relative to HF (4). Within mixtures of high SbF_5 content, no electrical conductivity was found (4) (analogous to the $\text{SbCl}_5\text{--HCl}$ results above) and speciation was less defined.

Calculations for the $\text{BCl}_3\text{:HCl:MCl}$ and $\text{BF}_3\text{:HF:MF}$ Systems

Figures 5 and 6 display the calculated structures for species of interest in the two boron halide systems. As expected, both halide dimers were unstable while the B_2F_7^- ion, in agreement with experiment (14), was stable, unlike B_2Cl_7^- . The greater electronegativity of fluorine means less n-p donation from F^- to B than from Cl^- so that BF_4^- will accept electrons from BF_3 whereas back-bonding more effectively stabilizes BCl_4^- .

The tetrahalide ion-HX and trihalide-HX adducts also show differences. The $\text{BCl}_4(\text{HCl})^-$ "link" is 2.30 Å while the $\text{BF}_4(\text{HF})^-$ link is much shorter at 1.58 Å. Further, the $\text{BF}_3\text{--FH}$ link is 2.63 Å compared to 4.9 Å in $\text{BCl}_3\text{--ClH}$. The binding energy of $\text{BF}_3\text{--FH}$ was calculated as 15.8 kJ mol $^{-1}$ compared to the value of 16.3 kJ mol $^{-1}$ of Phillips *et al.* (15), who calculated the long B--F distance as 2.50 Å and the H--F--B angle as 107.1° and measured these quantities as 2.544 Å and 104° by pulsed-nozzle FT microwave spectroscopy. The difference between our calculated values and those of Phillips *et al.* is due to the limited size of the basis set we employed.

The calculations are consistent with observed acidity trends in these systems. There is experimental evidence for the enhancement of HX acidity by BX_3 and the calculations support the stability of HBF_4 ; at a higher level of refinement they should determine whether or not HBCl_4 is stable.

Equilibria

Table 1 displays various equilibria for the boron, antimony and aluminum halide systems. The calculations for the antimony systems could only be made by the semi-empirical method, PM3, so may not be reliable. Notable species predicted to be stable are HBF_4 , HB_2F_7 , HBF_5^- , HB_2F_8^- and HBCl_5^- . Work is underway to find suitable cations for the isolation of the latter ions. For all the systems we notice that H_2X^+ formation is highly endothermic.

Table I
Gibb's Free Energies (ΔG°) of Various Equilibria
(Note: $\text{BX}_3:\text{HX}:\text{MX}$ and chloroaluminates using
BVWN/3-21+G**; $\text{SbX}_5:\text{H}^+:\text{MX}$ using PM3)

[All numbers given in kJ/mol]

A)	$\text{B}_2\text{Cl}_6 \rightarrow 2\text{BCl}_3$	
	$\text{B}_2\text{F}_6 \rightarrow 2\text{BF}_3$	
	$\text{Sb}_2\text{Cl}_{10} \rightleftharpoons 2\text{SbCl}_5$	= 232.0
	$\text{Sb}_2\text{F}_{10} \rightleftharpoons 2\text{SbF}_5$	= -138.0
	$\text{Al}_2\text{Cl}_6 \rightleftharpoons 2\text{AlCl}_3$	= 39.1
B)	$\text{B}_2\text{Cl}_7^- \rightarrow \text{BCl}_3 + \text{BCl}_4^-$	
	$\text{B}_2\text{F}_7^- \rightleftharpoons \text{BF}_3 + \text{BF}_4^-$	= 51.2
	$\text{Sb}_2\text{Cl}_{11}^- \rightleftharpoons \text{SbCl}_5 + \text{SbCl}_6^-$	= 438.4
	$\text{Sb}_2\text{F}_{11}^- \rightleftharpoons \text{SbF}_5 + \text{SbF}_6^-$	= 158.8
	$\text{Al}_2\text{Cl}_7^- \rightleftharpoons \text{AlCl}_3 + \text{AlCl}_4^-$	= 69.8
C)	$\text{HBCl}_4 \rightarrow \text{HCl} + \text{BCl}_3$	
	$\text{HBF}_4 \rightleftharpoons \text{HF} + \text{BF}_3$	= -20.0
	$\text{HSbCl}_6 \rightleftharpoons \text{HCl} + \text{SbCl}_5$	= -659.8
	$\text{HSbF}_6 \rightleftharpoons \text{HF} + \text{SbF}_5$	= 9.13
	$\text{HAlCl}_4 \rightleftharpoons \text{HCl} + \text{AlCl}_3$	= -15.8

Table I (Cont'd)

D)	$\text{BCl}_4^- + \text{HCl} \rightleftharpoons \text{BCl}_4(\text{HCl})^-$	= 1.45
	$\text{BF}_4^- + \text{HF} \rightleftharpoons \text{BF}_4(\text{HF})^-$	= -42.3
	$\text{SbCl}_6^- + \text{HCl} \rightleftharpoons \text{SbCl}_6(\text{HCl})^-$	= 1017.7
	$\text{SbF}_6^- + \text{HF} \rightleftharpoons \text{SbF}_6(\text{HF})^-$	= -4.05
	$\text{AlCl}_4^- + \text{HCl} \rightleftharpoons \text{AlCl}_4(\text{HCl})^-$	= -5.4
E)	$\text{BCl}_3 + 2\text{HCl} \rightleftharpoons \text{BCl}_4^- + \text{H}_2\text{Cl}^+$	= 716.1
	$\text{BF}_3 + 2\text{HF} \rightleftharpoons \text{BF}_4^- + \text{H}_2\text{F}^+$	= 734.3
	$\text{SbCl}_5 + 2\text{HCl} \rightleftharpoons \text{SbCl}_6^- + \text{H}_2\text{Cl}^+$	= 455.8
	$\text{SbF}_5 + 2\text{HF} \rightleftharpoons \text{SbF}_6^- + \text{H}_2\text{F}^+$	= 770.4
	$\text{AlCl}_3 + 2\text{HCl} \rightleftharpoons \text{AlCl}_4^- + \text{H}_2\text{Cl}^+$	= 579.5
F)	$\text{BCl}_3 + \text{Cl}^- \rightleftharpoons \text{BCl}_4^-$	= -117.9
	$\text{BF}_3 + \text{F}^- \rightleftharpoons \text{BF}_4^-$	= -309.0 (exp.-297.1 ^a)
	$\text{SbCl}_5 + \text{Cl}^- \rightleftharpoons \text{SbCl}_6^-$	= -256.7
	$\text{SbF}_5 + \text{F}^- \rightleftharpoons \text{SbF}_6^-$	= -235.9
	$\text{AlCl}_3 + \text{Cl}^- \rightleftharpoons \text{AlCl}_4^-$	= -254.5
G)	$\text{B}_2\text{F}_7^- + \text{HF} \rightleftharpoons \text{B}_2\text{F}_7(\text{HF})^-$	= -16.5
	$\text{Sb}_2\text{Cl}_{11}^- + \text{HCl} \rightleftharpoons \text{Sb}_2\text{Cl}_{11}(\text{HCl})^-$	= -34.2
	$\text{Sb}_2\text{F}_{11}^- + \text{HF} \rightleftharpoons \text{Sb}_2\text{F}_{11}(\text{HF})^-$	= 314.4
	$\text{Al}_2\text{Cl}_7^- + \text{HCl} \rightleftharpoons \text{Al}_2\text{Cl}_7(\text{HCl})^-$	= 6.31
H)	$2\text{BF}_3 + 2\text{HF} \rightleftharpoons \text{B}_2\text{F}_7^- + \text{H}_2\text{F}^+$	= 683.1
	$2\text{SbCl}_5 + 2\text{HCl} \rightleftharpoons \text{Sb}_2\text{Cl}_{11}^- + \text{H}_2\text{Cl}^+$	= 17.4
	$2\text{SbF}_5 + 2\text{HF} \rightleftharpoons \text{Sb}_2\text{F}_{11}^- + \text{H}_2\text{F}^+$	= 611.6
	$2\text{AlCl}_3 + 2\text{HCl} \rightleftharpoons \text{Al}_2\text{Cl}_7^- + \text{H}_2\text{Cl}^+$	= 509.7
I)	$\text{HBF}_4 + \text{BF}_3 \rightleftharpoons \text{HB}_2\text{F}_7$	= 19.2
	$\text{HSbCl}_6 + \text{SbCl}_5 \rightleftharpoons \text{HSb}_2\text{Cl}_{11}$	= -729.1
	$\text{HSbF}_6 + \text{SbF}_5 \rightleftharpoons \text{HSb}_2\text{F}_{11}$	= 1169
	$\text{HAlCl}_4 + \text{AlCl}_3 \rightleftharpoons \text{HAl}_2\text{Cl}_7$	= not determined
J)	$\text{B}_2\text{F}_7^- + \text{F}^- \rightleftharpoons 2\text{BF}_4^-$	= -257.8
	$\text{Sb}_2\text{Cl}_{11}^- + \text{Cl}^- \rightleftharpoons 2\text{SbCl}_6^-$	= 181.7
	$\text{Sb}_2\text{F}_{11}^- + \text{F}^- \rightleftharpoons 2\text{SbF}_6^-$	= -77.1
	$\text{Al}_2\text{Cl}_7^- + \text{Cl}^- \rightleftharpoons 2\text{AlCl}_4^-$	= -184.7 (exp.-108.4 ^b)
a	reference 15	
b	reference 7	

NMR Calculations

The CSGT and IGAIM methods of magnetic susceptibility, at the BVWN/6-311++G(3df, 3pd) level of theory, gave the most accurate ^1H and ^{13}C shieldings for methane and so were considered the most reliable for calculating shielding tensors for HCl_2^- , H_2Cl^+ and HCl . The results are collected in Table 2. The values are within 2 ppm and 1.5 ppm of the experimental ones for HCl_2^- (7) and HCl (18) in solution, respectively.

Table II

^1H NMR Absolute Shieldings for HCl , H_2Cl^+ and HCl_2^- Using BVWN/6-311++G(3df,3pd) {experimental values are given in parentheses}

<u>Species</u>	<u>Absolute Shielding</u>		
TMS	(31.06 ppm ^a)		a reference 16
HCl	31.6 ppm	(30.4 ppm ^b)	b reference 17
		(29.5-30.2 ppm ^c)	c reference 18
H_2Cl^+	24.8 ppm		
HCl_2^-	15.2 ppm	(17.2 ppm ^d)	d reference 7

Fujuvara *et al.* (16) also found that gas-phase calculations resulted in a 1-2 ppm extra shielding for HX molecules relative to the experimental values for inert solutions. The ^1H NMR resonance of H_2Cl^+ is expected at ~6 ppm. Such a resonance is not seen for the $\text{SbCl}_5\text{:HCl}$ system nor for the Lewis acidic chloroaluminate melts. Values for the latter range up to only 1.6 ppm (18) and thus are consistent with chloroaluminate:HCl adduct formation.

CONCLUSIONS

1. HCl dissolves in SbCl_5 to give unionized solutions. ^1H NMR indicates the formation of one species up to ~10% HCl with solubility proportional to HCl partial pressure. Over the 10-24 mol % HCl range an additional protic species formed.

2. Calculations for systems involving BCl_3 and BF_3 suggest that the as yet unknown adducts $\text{BCl}_4(\text{HCl})^-$, $\text{BF}_4(\text{HF})^-$ and $\text{B}_2\text{F}_7(\text{HF})^-$ should be stable and agree with the stability of the recently made B_2F_7^- . ΔG_f° values for HBF_4 and HB_2F_7 were small and positive.

3. ^1H NMR calculations agree with the experimental assignments for HCl_2^- and HCl and suggest the signal for H_2Cl^+ should be sought at ~ 6 ppm.

REFERENCES

1. J.W. Shuppert and C.A. Angell, *J. Chem. Phys.*, **67**, 3050 (1977).
2. J.L. Campbell, K.E. Johnson and J.R. Torkelson, *Inorg. Chem.*, **33**, 3340 (1994).
3. M. Ma and K.E. Johnson, *J. Am. Chem. Soc.*, **117**, 1508 (1995).
4. R.J. Gillespie and K.C. Moss, *J. Chem. Soc. (A)*, 1170 (1966).
5. B. Bonnet and G. Mascherpa, *Inorg. Chem.*, **19**, 785 (1980).
6. G.P. Smith, A.S. Dworkin, R.M. Pagni and S.P. Zingg, *J. Am. Chem. Soc.*, **111**, 525 (1989).
7. J.L. Campbell and K.E. Johnson, *Inorg. Chem.*, **32**, 3809 (1993).
8. J.L. Campbell and K.E. Johnson, *J. Am. Chem. Soc.*, **117**, 7791 (1995).
9. W.D. Chandler, K.E. Johnson and J.L. Campbell, *Inorg. Chem.*, **34**, 4943 (1995).
10. W.D. Chandler, J.L. Campbell and K.E. Johnson. To be submitted for publication.
11. M.J. Frisch, G.W. Trucks, H.B. Schlegel, P.M.W. Gill, B.G. Johnson, M.W. Wong, J.B. Foresman, M.A. Robb, M. Head-Gordon, E.S. Replogle, R. Gomperts, J.L. Andres, K. Raghavachari, J.S. Binkley, C. Gonzalez, R.L. Martin, D.J. Fox, D.J. Defrees, J. Baker, J.J.P. Stewart and J.A. Pople, Gaussian 92/DFT, Revision G.4, Gaussian, Inc., Pittsburgh, PA, 1993.
12. M.J. Frisch, G.W. Trucks, H.B. Schlegel, P.M.W. Gill, B.G. Johnson, M.A. Robb, J.R. Cheeseman, T.A. Keith, G.A. Petersson, J.A. Montgomery, K. Raghavachari, M.A. Al-Laham, V.G. Zakrzewski, J.V. Ortiz, J.B. Foresman, J. Cioslowski, B.B. Stefanov, A. Nanayakkara, M. Challacombe, C.Y. Peng, P.Y. Ayala, W. Chen, M.W. Wong, J.L. Andres, E.S. Replogle, R. Gomperts, R.L. Martin, D.J. Fox, J.S. Binkley, D.J. Defrees, J. Baker, J.P. Stewart, M. Head-Gordon, C. Gonzalez and J.A. Pople, Gaussian 94, Revision B.2, Gaussian, Inc., Pittsburgh, PA, 1995.
13. V.G.P. Lutschinsky, *Z. anorg. allg. Chem.*, **223**, 210 (1935).
14. M. Van der Puy, D. Nalewajek, G.A. Shia and W.J. Wagner, *Aldrichimica*, **28**, 36 (1995).
15. J.A. Phillips, M. Canagaratna, H. Goodfriend, A. Grushow, J. Almlof and K.R. Leopold, *J. Am. Chem. Soc.*, **117**, 12549 (1995).
16. F.Y. Fujiwara and J.S. Martin, *J. Chem. Phys.*, **56**, 4091 (1972).
17. W.G. Schneider, H.J. Bernstein and J.A. Pople, *J. Chem. Phys.*, **28**, 601 (1958).
18. P.C. Trulove and R.A. Osteryoung, *Inorg. Chem.*, **31**, 3980 (1992).

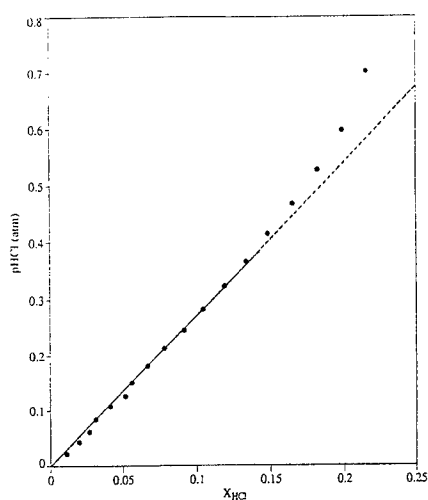


Figure 1 Pressure-Composition isotherm for a 21.5 mol% HCl-in-SbCl₃ solution (Isotherm A)

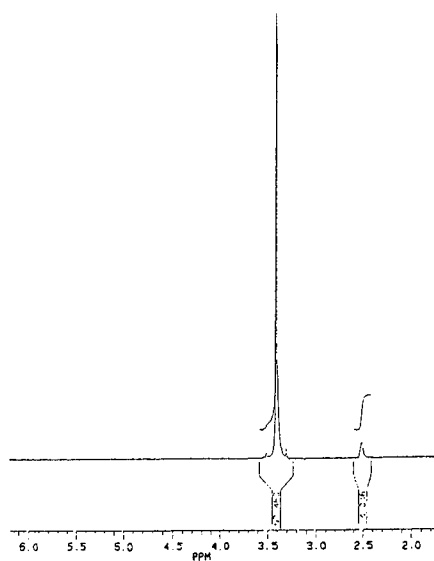


Figure 2 ¹H NMR spectrum for 100 mol% SbCl₃ corresponding to isotherm A

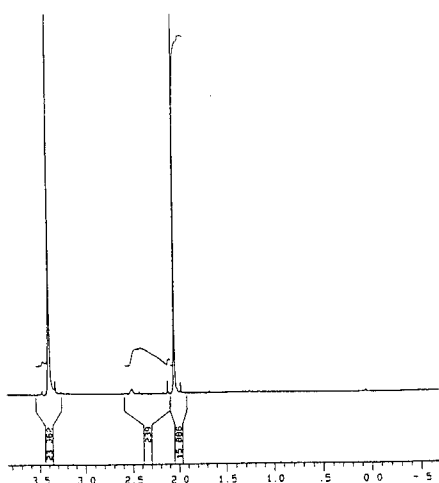


Figure 3 ^1H NMR spectrum for a 5.3 mol% HCl-in-SbCl_5 solution

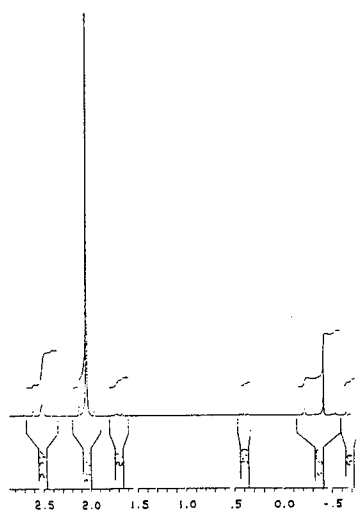


Figure 4 ^1H NMR spectrum for a 5.3 mol% HCl-in-SbCl_5 solution

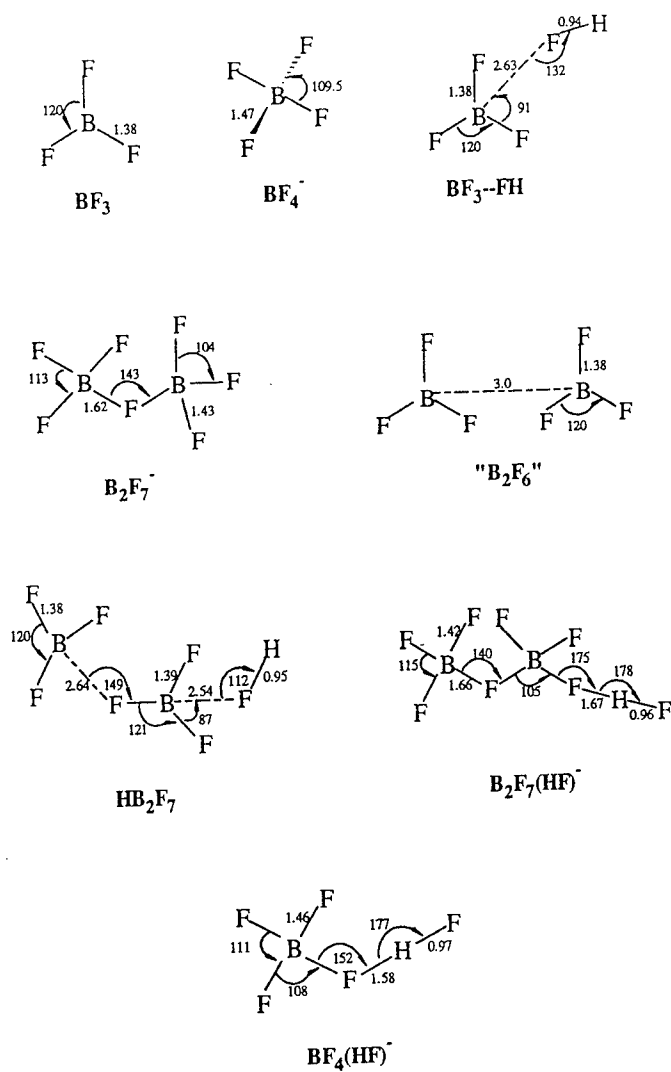


Figure 6 Structures of species from the $\text{BF}_3\text{:HF:MF}$ system calculated using BVWN/3-21+G** {Note: bond lengths are given in Angstroms}

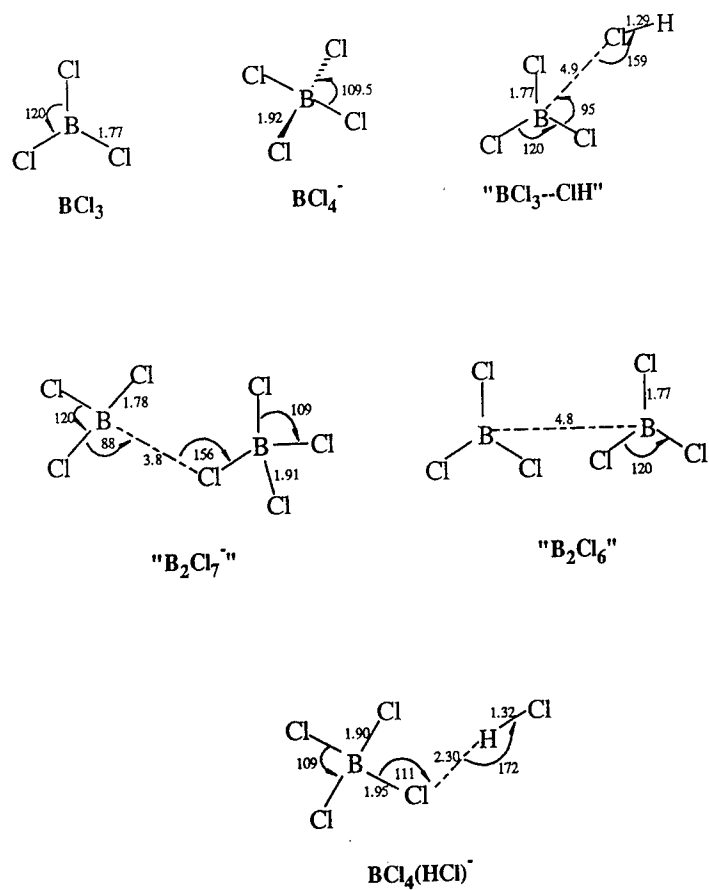


Figure 5 Structures of species from the $\text{BCl}_3\text{:HCl:MCl}$ system calculated using BVWN/3-21+G** (Note: bond lengths are given in Angstroms)

GUTMANN ACCEPTOR PROPERTIES OF LiCl, NaCl, AND KCl BUFFERED AMBIENT-TEMPERATURE CHLOROALUMINATE IONIC LIQUIDS

Robert A. Mantz, Paul C. Trulove[†], Richard T. Carlin[†], Robert A. Osteryoung*
Department of Chemistry
North Carolina State University
Raleigh, NC 27695-8204

[†]Chemistry Department
United States Naval Academy
572 Holloway Road
Annapolis, MD 21402-5026

*Covalent Associates, Inc.
10 State Street
Woburn, MA 01801

ABSTRACT

Gutmann acceptor numbers have been determined using ³¹P NMR for AlCl₃ / EMIC melts, where EMIC is 1-ethyl-3-methylimidazolium chloride, as well as LiCl, NaCl, and KCl neutral buffered melts. Functions have been determined that allow the prediction of the acceptor number for AlCl₃ / EMIC melts and LiCl, NaCl, and KCl neutral buffered melts. The binary melts observed acceptor numbers are due to an equilibrium between a triethylphosphine oxide / AlCl₃ monoadduct and a triethylphosphine oxide / 2 AlCl₃ diadduct. The neutral buffered melts observed acceptor numbers are linear with respect to melt initial mole ratio of AlCl₃:EMIC prior to buffering. The lithium cation appears to be the most Lewis acidic followed by sodium and potassium.

INTRODUCTION

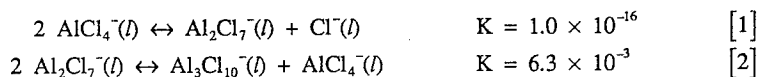
Ambient-temperature chloroaluminate ionic liquids are an important class of non-aqueous solvents; they have been used for a wide variety of chemical and electrochemical studies (1-4). In addition, they show promise as electroplating baths for industrial aluminum electroplating as well as electrolytes in high energy density batteries (5-7).

Gutmann acceptor numbers are a non-thermodynamic measure of Lewis acidity of a solvent. They give a description of solvent Lewis acidity that can be used to compare disparate solvents and to predict the chemistry of different solutes in these systems (8-10). Work conducted by Zawodzinski and Osteryoung described the Gutmann donor and acceptor number parameters for ethylmethylimidazolium and N-butylpyridinium based chloroaluminate melts (11). However, since that time neutral-buffered chloroaluminate

melts have emerged. These new ternary melts provide researchers with new tunable systems that allow additional control of the melt properties. The acidity of these new melts is unknown and Gutmann acceptor numbers provide a way to make comparisons between the neutral buffered melts as well as between the neutral buffered melts and ethylmethylimidazolium based melts.

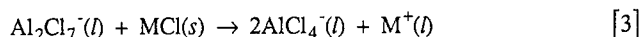
The chloroaluminate ionic liquids we are studying are comprised of mixtures of 1-ethyl-3-methylimidazolium chloride (EMIC) and aluminum chloride (AlCl_3). The two solids react over a wide range of stoichiometries to yield room-temperature molten salts (12). The melts are defined as acidic, basic, or neutral if the mole ratio of AlCl_3 to EMIC is greater than, less than, or equal to unity. The chemistry observed in the melts is strongly affected by melt composition. This change in chemistry is due to the change in anionic speciation of the melt with composition.

Melt anion composition is controlled by two equilibria the first of which is analogous to the auto-protolysis of water (13)



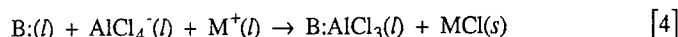
In basic melts, added aluminum chloride is neutralized by reaction with the chloride anion. As the mole ratio of the two components approaches 1.0:1.0 the Cl^- concentration drops until the melt contains only the AlCl_4^- anion. Beyond mole ratios of 1.0:1.0 the anions AlCl_4^- , Al_2Cl_7^- , and perhaps $\text{Al}_3\text{Cl}_{10}^-$ are present in the melt. Just beyond a mole ratio of 1.0:1.0 the Al_2Cl_7^- mole fraction is increasing and the AlCl_4^- mole fraction is decreasing. However, if the mole ratio is increased to 1.6:1.0 or higher the AlCl_4^- mole fraction continues to drop and the Al_2Cl_7^- mole fraction rolls over as the $\text{Al}_3\text{Cl}_{10}^-$ mole fraction grows in.

Neutral-buffered chloroaluminate melts are prepared by the addition of alkali metal chlorides (MCl) to an acidic melt (13,14). The following reaction takes place when MCl is added to an acidic melt:



The melt that results does not contain Al_2Cl_7^- so it is no longer described as acidic but contains only the AlCl_4^- anion making the melt neutral. The electrochemical window of these neutral buffered melts is essentially the same as that of the neutral unbuffered melt. The melts are considered buffered because if an acidic species is added to the melt more MCl dissolves and reacts to bring the melt back to neutrality. If a basic species is added to the melt the dissolved M^+ reacts to form MCl which is insoluble in a neutral melt and precipitates out of solution. The neutral-buffered melts have another property which we have termed "latent acidity" (15,16). This is demonstrated when a weak Lewis base (B:) is added to a neutral-buffered melt. If the M^+ concentration exceeds the base concentration then all of the base forms an AlCl_3 adduct. This occurs because the M^+ reacts with the Cl^-

liberated when the AlCl_4^- becomes an AlCl_3 adduct:



When the base concentration exceeds the M^+ concentration the adduct is only formed up to the M^+ concentration; the excess base does not form an AlCl_3 adduct (16).

This work further characterizes this unique chloroaluminate melt system by comparing the LiCl, NaCl, and KCl neutral buffered melts to the binary AlCl_3 / EMIC melts and determining the Gutmann acceptor numbers and how they vary with melt composition for the four systems.

EXPERIMENTAL

The preparation of EMIC has been described elsewhere (12,17). The AlCl_3 was Fluka purissimo and was purified as described elsewhere (1). All melt preparation and handling was carried out in a helium-filled Vacuum Atmospheres drybox with oxygen and water levels less than 5 ppm. Melts were prepared by combining weighed portions of AlCl_3 to EMIC in Quorpak bottles to yield a slightly basic melt (0.99:1.00). The melts were filtered with 1 μm glass acrodisk filters. Proton impurity was removed using vacuum (4×10^{-5} Torr) (18). Oxide was removed by exposing the melt to phosgene twice and proton was removed again under vacuum (4×10^{-5} Torr) (19). A weighed amount of AlCl_3 was then added to a portion of the basic melt to yield the desired composition. LiCl (Aldrich, 99.994%), NaCl (Aldrich, 99.999%), and KCl (Aldrich, 99.999%) were dried at 400 °C under vacuum (1×10^{-3} Torr) for at least 3 days. Buffered melts were prepared by addition of 150 weight percent of the required metal chloride to the acidic melt. The weight percent of metal chloride required to buffer the melt was determined from the Al_2Cl_7^- concentration in the unbuffered melt. The melt was then allowed to stir for at least 24 hours while being warmed on a stirrer hot plate (≈ 60 °C). Triethylphosphine oxide (TEPO) (Alfa Chemical) was sublimed under vacuum (1×10^{-3} Torr) from room temperature to a 0 °C trap prior to use (9). NMR tubes were prepared by first soaking in 50% HNO_3 heated to 90 °C, rinsing with deionized water, soaking in a solution of the tetrasodium salt of EDTA for 12 hours at room temperature, and again rinsing with deionized water. ^{31}P NMR spectra were obtained with a Bruker AC-300 NMR spectrometer operating at 121.50 MHz. The probe temperature was maintained at 31.0 °C and each sample was allowed to equilibrate while rotating at 10 Hz for at least 5 minutes prior to spectra being taken. Spectra consisted of 64 scans with a sweep width of 128.6 ppm and a relaxation delay of 2.0 seconds. An exponential multiplication with a line broadening of 2.0 Hz was applied to the acquired free induction decay (FID). The chemical shift was externally referenced to an 85% phosphoric acid in water sample (0 ppm) whose spectrum was obtained using identical acquisition and processing parameters.

Experiments were conducted to determine the change in chemical shift of the triethylphosphine oxide (TEPO) versus the concentration of the TEPO in the melt. Four melts were prepared, a 1.30:1.00 melt, a 1.15:1.00 LiCl buffered melt, a 1.30:1.00 NaCl

buffered melt, and a 1.30:1.00 KCl buffered melt. Each melt was divided into six portions and TEPO was added to make 5, 10, 25, 50, 100, and 300 mM solutions. The solutions were allowed to stir for 24 hours at $\approx 60^\circ\text{C}$ to ensure complete dissolution of the TEPO. After stirring for 24 hours the samples were allowed to cool to room temperature. The resultant solution was filtered through a $0.1\ \mu\text{m}$ PTFE (Whatman) filter disk (13 mm diameter) using a 5 mL syringe (B&D tuberculine, polyethylene, natural rubber latex) into a 9 inch long 10 mm Wilmad NMR tube that had been constricted at 8 inches. For the buffered melts a tip-off manifold was placed on each tube and the sealed assembly was removed from the dry box and flame sealed under vacuum ($\approx 1 \times 10^{-2}$ Torr). The unbuffered melts were capped and sealed with parafilm. ^{31}P spectra were obtained for each sample.

Experiments were conducted to determine the change in chemical shift of the TEPO versus the melt composition. Melt compositions of the unbuffered and of LiCl, NaCl, and KCl buffered melts were made which corresponded to initial AlCl_3 :EMIC mole ratios of, 1.05:1.00, 1.10:1.00, 1.15:1.00, 1.20:1.00, 1.30:1.00, 1.40:1.00, 1.50:1.00, 1.70:1.00, and 1.90:1.00. In addition an unbuffered melt with a mole ratio of 0.99:1.00 was prepared. To each melt TEPO was added to make 10 mM solutions. The solutions were prepared as described above. ^{31}P spectra were obtained for each sample.

Volume magnetic susceptibilities were determined using a variation of Beccensal's method (20,21). Samples were prepared by first flame sealing benzene- d_6 in the inner coaxial tube from a Wilmad 10 mm coaxial tube pair. In the outer tube was placed the melt of interest to which approximately 5% by weight of benzene- d_6 had been added. The inner coaxial tube was slid into the 10 mm NMR tube and the entire apparatus was then capped and sealed with Parafilm. These samples were analyzed in both a Bruker AC-300 (75.47 MHz) and a JEOL FX-90Q (22.48 MHz) using ^{13}C NMR. The probe on each spectrometer was maintained at 31°C . Samples were allowed to equilibrate for at least 5 minutes while being rotated at 10 Hz in the Bruker and 15-20 Hz in the JEOL prior to spectra being taken. Each spectrometer was locked on the benzene- d_6 in the sample. Spectra on the Bruker AC-300 consisted of 16 scans with a sweep width of 161.6 ppm and a relaxation delay of 2.0 seconds. An exponential multiplication with a line broadening of 2.0 Hz was applied to the acquired FID. Spectra on the JEOL FX-90Q consisted of 64 scans on the JEOL FX-90Q with a sweep width of 111.0 ppm and a relaxation delay of 2.0 seconds. An exponential multiplication with a line broadening of 1.0 Hz was applied to the acquired FID. The volume magnetic susceptibility was then calculated from the differences in ^{13}C chemical shifts with the two different field axis between the benzene- d_6 in the inner and annular region of the coaxial pair.

Safety Note

Phosgene is an extremely toxic gas which should be used with extreme caution (22). A phosgene detector, Matheson Toxic Gas Detector Model 8014LA, is used to test for leaks in the apparatus employed to remove oxide impurities and the apparatus is assembled in a laboratory hood (23).

RESULTS AND DISCUSSION

^{31}P NMR spectra of pure solutions of triethylphosphine oxide (TEPO) in all melts generally consisted of a single line and did not change in the course of several days. Before we could use the ^{31}P NMR data to determine the acceptor number we needed to correct the data. Two corrections were applied to the ^{31}P NMR chemical shift data. The first correction is the extrapolation of ^{31}P chemical shift to infinite dilution of TEPO in the melt. The second correction is for the contribution made to the observed ^{31}P chemical shift by the volume bulk magnetic susceptibility (χ_v).

The effect of TEPO concentration on the ^{31}P chemical shift was determined for all four melt types. The resultant data were fitted to a linear equation and the least squared fit used to extrapolate to infinite dilution (Figure 1 and Table I). Since the TEPO concentration used to determine the acceptor numbers was only 10 mM the correction by extrapolating to infinite dilution of TEPO is only ≈ 0.005 ppm.

Correction for magnetic susceptibility effects required additional experiments as mentioned above but did result in a much larger chemical shift correction, approximately 1 ppm. The magnetic susceptibility was measured and the data fit to a linear function (Figure 2 and Table II). This resultant function was then used to determine the chemical shift correction necessary for each melt composition.

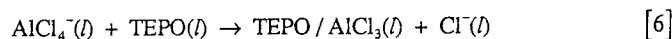
Experiments were conducted in which the melt composition was varied and the buffering alkali metal chloride was varied as well. After applying both corrections to the observed chemical shift data the data were converted into Gutmann acceptor numbers using equation 5:

$$\text{AN} = 2.348 \times (\delta_{\text{CORR}}) \quad [5]$$

δ_{CORR} is the ^{31}P chemical shift using TEPO in hexane as the zero reference chemical shift (Figures 3 and 4). It should be noted that the melt ratio in the neutral buffered cases is the original melt ratio prior to addition of alkali halide. After buffering the only anion present is AlCl_4^- and the alkali metal composition is equal to the original Al_2Cl_7^- composition.

Binary AlCl_3 / EMIC Melts

The results for the binary AlCl_3 / EMIC melts have been interpreted based upon Zawodzinski and Osteryoung's earlier results (11). They demonstrated the observed acceptor number in binary AlCl_3 / EMIC was a function of melt composition. Our results for the binary melts are in agreement with their prior work. In basic and neutral melts the acceptor number is a constant 95.8 for an AlCl_3 monoadduct and does not change. This appears to be due to solvent leveling (equation 6).



In melts with acidic compositions the acceptor numbers change due to the formation of an $\text{TEPO} / 2 \text{AlCl}_3$ diadduct due to the strong Lewis acidity of Al_2Cl_7^- .



In order to quantitate this observed phenomenon the equilibrium based on the above equation and the anionic mole fraction was calculated for each melt composition. The monoadduct and diadduct species are in fast equilibrium on the NMR timescale, because only a single ^{31}P NMR peak is observed, so contributions from both sides of the equilibrium (equation 7) must be considered. The observed chemical shift is a weighted average of the concentration of the two species multiplied by their respective chemical shifts. The acceptor number is directly related to the ^{31}P NMR chemical shift (equation 5). Because significant contributions from $\text{Al}_3\text{Cl}_{10}^-$ are present only in melt compositions above $\approx 1.7:1.0$ ($\text{AlCl}_3:\text{EMIC}$), melt compositions were calculated neglecting the $\text{Al}_3\text{Cl}_{10}^-$ contributions and only AlCl_4^- and Al_2Cl_7^- contributions were considered. Fitting the results to equation 8 results in an equilibrium constant, K for equations 7 and 8 of 0.158 ± 0.008 , an acceptor number of the diadduct of 108.1 ± 0.3 , and R^2 of 0.9993 (Figure 3).

$$\text{AN} = \frac{95.8}{\frac{\text{Equilibrium Constant} \times [\text{Al}_2\text{Cl}_7^-]}{[\text{AlCl}_4^-]} + 1} + \frac{\text{Diadduct Acceptor Number}}{\frac{[\text{AlCl}_4^-]}{\text{Equilibrium Constant} \times [\text{Al}_2\text{Cl}_7^-]} + 1} \quad [8]$$

Fitting the data to a function that does contain the $\text{Al}_3\text{Cl}_{10}^-$ contributions simply results in greater uncertainty for the equilibrium constants and the diadduct acceptor number. It should be noted that given the data above the maximum acceptor number that would be theoretically possible would be ≈ 108 and it should also be noted that the magnitude of K shows that even at large Al_2Cl_7^- concentrations there is only a small amount of diadduct formed. In the presence of a weak base such as the TEPO / AlCl_3 monoadduct Al_2Cl_7^- does not act as a strong AlCl_3 donor. This is indicative of how weak a base the TEPO / AlCl_3 monoadduct is.

To calculate the Gutmann acceptor number (AN) of a binary melt of known composition first the $[\text{AlCl}_4^-]$ and $[\text{Al}_2\text{Cl}_7^-]$ anionic mole fractions must be calculated from the melt ratio (13). Taking these values and simply substituting into equation 9 gives the expected Gutmann acceptor number for the melt.

$$\text{AN} = \frac{95.8}{\frac{0.158 [\text{Al}_2\text{Cl}_7^-]}{[\text{AlCl}_4^-]} + 1} + \frac{108.1}{\frac{[\text{AlCl}_4^-]}{0.158 [\text{Al}_2\text{Cl}_7^-]} + 1} \quad [9]$$

Neutral Buffered Melts

The determination of the acceptor numbers for the alkali metal neutral buffered

melts was completed in the same fashion as those for the binary melts using equation 5. Attempts to model the neutral buffered melts using a method analogous to the binary melts have been unsuccessful. However, the plot of acceptor number versus the melt ratio of AlCl_3 :EMIC prior to buffering is linear. It is important to remember the melt ratio prior to buffering corresponds to the alkali metal cation concentration in the buffered melt. The linear functions result in very good fits R^2 of 0.9981, 0.9982, and 0.9888 for the LiCl, NaCl, and KCl buffered melts respectively (Figure 4 and Table III). Using the linear functions for each of the three types of buffered melts the acceptor numbers can be predicted.

CONCLUSIONS

These results characterize the Gutmann acceptor numbers of the AlCl_3 / EMIC melts as well as their alkali metal neutral buffered counterparts. The binary AlCl_3 / EMIC melts have been fitted to the equilibrium expression derived from the model in which triethylphosphine oxide forms an AlCl_3 diadduct with an acceptor number of 108.1. This expression allows us to predict the Gutmann acceptor number of binary AlCl_3 / EMIC melts.

The alkali metal chloride neutral buffered melts Gutmann acceptor number can be predicted using a linear fit. The LiCl neutral buffered melts show the greatest Lewis acidity followed by the NaCl and then the KCl buffered melts. This data indicates the potassium chloride neutral buffered melt is more Lewis acidic than its binary counterpart up to an AlCl_3 :EMIC mole ratio of 1.3:1.0; for the sodium chloride neutral buffered melt this ratio is 1.6:1.0 while for the lithium chloride it is 1.7:1.0. These results provide insight into the differences between the unbuffered and alkali metal buffered melts as well and between the different alkali buffered melts themselves.

ACKNOWLEDGMENT

This work was supported in part by the Air Force Office of Scientific Research.

TABLE I. ^{31}P NMR Chemical Shift Dependence on TEPO Concentration

^{31}P NMR Shift (ppm) = $M \times [\text{TEPO (mM)}] + B$		
Melt	M	B
Unbuffered	$-4.4 \times 10^{-4} \pm 2 \times 10^{-5}$	82.798 ± 0.003
LiCl Buffered	$-5.3 \times 10^{-4} \pm 3 \times 10^{-5}$	82.781 ± 0.003
NaCl Buffered	$-4.4 \times 10^{-4} \pm 2 \times 10^{-5}$	82.989 ± 0.002
KCl Buffered	$-5 \times 10^{-4} \pm 1 \times 10^{-4}$	82.90 ± 0.01

TABLE II. Volume Bulk Magnetic Susceptibility of Melts

Magnetic Susceptibility ($\times 10^6$) = $M \times \text{Melt Ratio} + B$		
Melt	M	B
Unbuffered	-0.034 ± 0.003	-0.759 ± 0.004
LiCl Buffered	-0.051 ± 0.003	-0.745 ± 0.004
NaCl Buffered	-0.031 ± 0.006	-0.769 ± 0.008
KCl Buffered	-0.09 ± 0.06	-0.69 ± 0.06

TABLE III. Gutmann Acceptor Numbers of Alkali Metal Chloride Neutral Buffered Melts

$\text{AN} = M \times \text{Melt Ratio} + B$			
Buffering Agent	M	B	R^2
LiCl	4.97 ± 0.08	90.8 ± 0.1	0.9981
NaCl	3.70 ± 0.06	92.28 ± 0.08	0.9982
KCl	2.5 ± 0.1	93.4 ± 0.1	0.9888

REFERENCES

1. R. J. Gale and R. A. Osteryoung, in *Molten Salt Techniques*, Vol 1, D. G. Lovering and R. J. Gale, Editors, p. 55, Plenum: New York (1983).
2. C. L. Hussey, in *Advances in Molten Salt Chemistry*, Vol 5, G. Mamantov, Editor, p.185, Elsevier Science Publishers, Amsterdam (1983).
3. R. A. Osteryoung, in *Molten Salt Techniques*, Vol 202, G. Mamantov and R. Marassi, Editors, p. 329, NATO ASI Series C; Reidel: Dordrecht, The Netherlands (1986).
4. C. L. Hussey, *Pure Appl. Chem.*, **60**, 1763 (1988).
5. J. S. Wilkes, J. A. Levisky, R. A. Wilson and C. L. Hussey, *Inorg. Chem.*, **21**, 1263 (1982).
6. A. A. Fannin, Jr., D. A. Floreani, L. A. King, J. S. Sanders, B. J. Piersma, D. J. Stech, R. L. Vaughn, J. S. Wilkes and J. L. Williams, *J. Phys. Chem.*, **88**, 2614 (1984).
7. D. Floreani, D. Stech, J. Wilkes, J. Williams, B. Piersma, L. King and R. Vaughn, in *Proc. 30th Power Sources Symp.*, p. 84, The Electrochemical Society: Pennington NJ (1982).
8. V. Gutmann, *The Donor-Acceptor Approach to Molecular Interactions*; Plenum Press, New York, (1978).
9. U. Mayer, V. Gutmann and W. Gerger, *Mh. Chem.*, **106**, 1235 (1975).
10. V. Gutmann, *Electrochimica Acta.*, **21**, 662 (1976).
11. T. A. Zawodzinski, Jr. and R. A. Osteryoung, *Inorg. Chem.*, **28**, 1710, (1989).
12. J. S. Wilkes, J. A. Levisky, R. A. Wilson and C. L. Hussey, *Inorg. Chem.*, **21**, 1263 (1982).
13. T. J. Melton, J. Joyce, J. T. Maloy, J. A. Boon and J. S. Wilkes, *J. Electrochem. Soc.*, **137**, 3865 (1990).
14. C. Scordilis-Kelley, J. Fuller, R. T. Carlin and J. S. Wilkes, *J. Electrochem. Soc.*, **139**, 694 (1992).
15. I. C. Quarmby and R. A. Osteryoung, *J. Am. Chem. Soc.*, **116**, 2649 (1994).
16. I. C. Quarmby, R. A. Mantz and R. A. Osteryoung, *Anal. Chem.*, **66**, 3558 (1994).

17. P. C. Trulove and R. A. Osteryoung, *Inorg. Chem.*, **31**, 3980 (1992).
18. T. A. Zawodzinski, Jr., R. T. Carlin and R. A. Osteryoung, *Anal. Chem.*, **59**, 2639 (1987).
19. I. W. Sun, E. H. Ward and C. L. Hussey, *Inorg. Chem.*, **26**, 4309 (1987).
20. J. K. Becconsal, G. D. Daves, Jr. and W. R. Anderson, Jr., *J. Am. Chem. Soc.*, **92**, 430 (1970).
21. E. D. Becker, *High Resolution NMR: Theory and Chemical Applications*, 2nd ed., p. 59, Academic Press, New York, (1980).
22. *The Merk Index*, 11th ed., S. Budavari, M. J. O'Neil, A. Smith and P. E. Heckelman, Editors, p. 1165, Merk & Co., Rahway, NJ (1989).
23. M. A. Noël, P. C. Trulove and R. A. Osteryoung, *Anal. Chem.*, **63**, 2892 (1991).

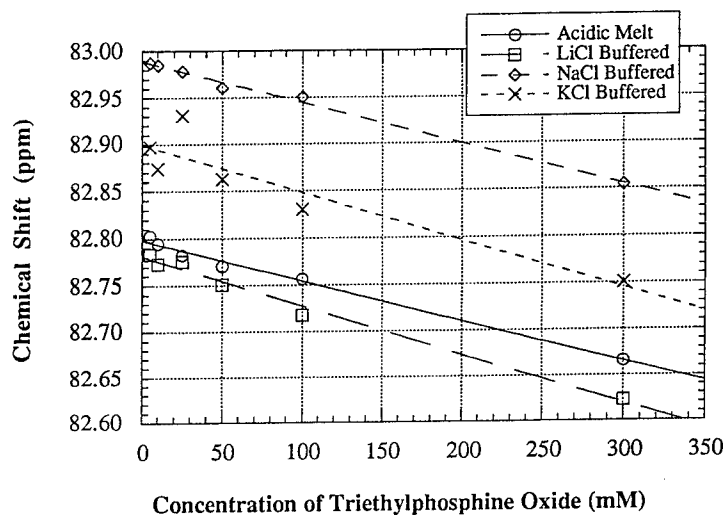


Figure 1. ^{31}P NMR chemical shift dependence of triethylphosphine oxide upon the concentration of triethylphosphine oxide in the melt.

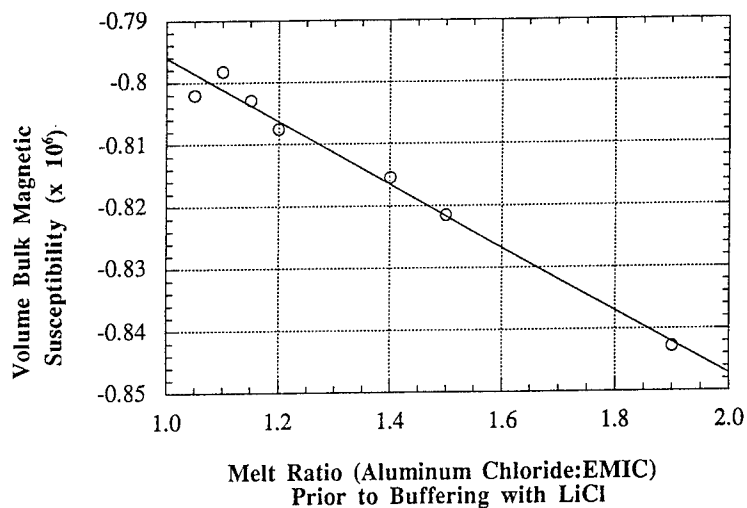


Figure 2. Volume bulk magnetic susceptibility of LiCl neutral buffered AlCl_3 / EMIC ionic liquid.

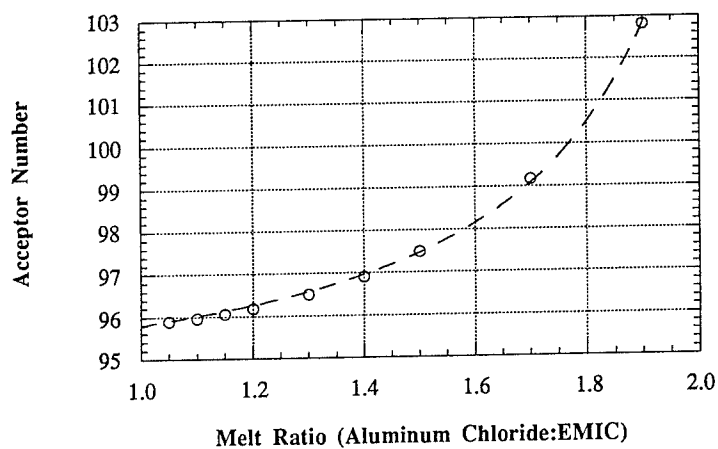


Figure 3. Dependence of the Gutmann acceptor number for binary melts upon the mole ratio of AlCl_3 to EMIC. Points are experimental data while the line is the fit from equation 9.

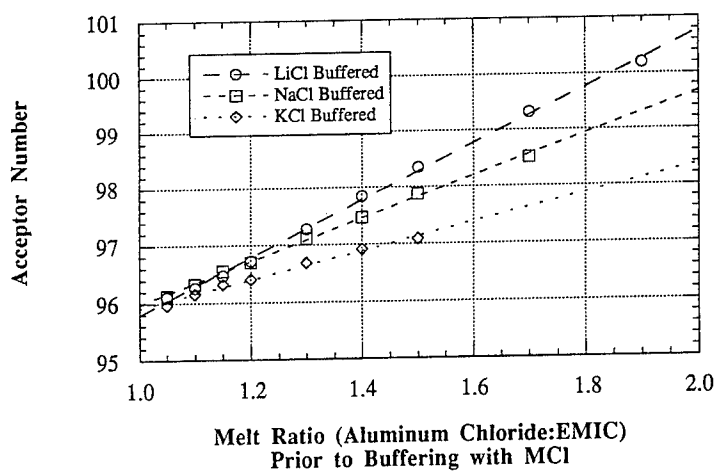


Figure 4. Dependence of the Gutmann acceptor number for alkali metal chloride neutral buffered melts upon the mole ratio of AlCl_3 to EMIC. (Note: This is the mole ratio prior to buffering. During buffering the Al_2Cl_7^- anions react with an equal number of alkali metal chlorides.)

ELECTROCHEMICAL STUDIES OF ACYL HALIDE REDUCTION IN A ROOM-TEMPERATURE MOLTEN SALT

Graham T. Cheek
Chemistry Department, Stop 9b
United States Naval Academy
572 Holloway Road
Annapolis MD 21402-5026

ABSTRACT

The electrochemical reduction of benzoyl chloride has been studied in both the aluminum chloride : EMIC molten salt and the acetonitrile / LiAlCl_4 solvent systems. In both systems, electrolysis at mercury cathodes results in the formation of low (<10%) yields of benzaldehyde, similar to behavior seen in acetonitrile/tetraalkylammonium perchlorate systems. Filming behavior was evident at mercury in the molten salt system by observation of maxima in the voltammograms.

INTRODUCTION

The electrochemical reduction of acyl halides in nonaqueous solvents has been the subject of extensive investigation recently. From initial reports of ester products formed at mercury (1) and carbon (2) electrodes, more detailed investigations revealed other pathways leading to aldehyde formation (3). The initial electrochemical event in these reductions involves elimination of chloride from the reduced acyl halide, followed by various reactions leading to the observed products. This chloride elimination during the reduction process lends itself to study in room-temperature chloroaluminate systems, in which the chloride level can be varied over many orders of magnitude (4). The aluminum chloride : 1-ethyl-3-methylimidazolium chloride (EMIC) system has been specifically chosen as a useful molten salt system in which to carry out these investigations.

EXPERIMENTAL

The melt components, EMIC and AlCl_3 , were prepared and purified as described elsewhere (5). Experiments in acetonitrile (AN) were carried out in solutions prepared by addition of LiAlCl_4 (Lithco) to AN (Burdick and Jackson) which was dried by passage through alumina.

All electrochemical experiments were carried out in a Vacuum Atmospheres drybox under argon. Cyclic voltammetric scans were performed using a PAR 174A Polarographic

Analyzer, with a BAS CV27B as waveform generator. A PARC 273 instrument was used for preparative electrolyses.

Products formed in electrolysis experiments in the molten salt were isolated by extraction in the drybox with pentane to extract neutral compounds from the melt, and by hydrolyzing the melt with water outside the drybox followed by extraction with benzene for other products. Similar procedures were used for the AN/LiAlCl₄ system. Structures of electrolysis products were determined by GC/MS or liquid chromatography.

RESULTS AND DISCUSSION

Experiments in EMIC System

As mentioned in the Introduction, the elimination of chloride ion during reduction of acyl halides invites study in chloroaluminate molten salt systems. The high concentrations of chloride available in basic systems may enhance the stability of the initially formed anion radical. Pure EMIC, which provides the highest molar concentration of chloride in this system, can be used as a solvent at 100°C (above its melting point). Figure 1 presents a cyclic voltammogram of benzoyl chloride in pure EMIC at 100 mV/s. As can be seen, the reduction process is not reversible, there being no current on the return sweep in the -1.35 V region. The acyl radical is apparently so short-lived that, even with chloride ions several angstroms away, no current due to oxidation back to benzoyl chloride is observed on the return sweep. A product is apparently formed, as indicated by the peak at -2.0 V. This is similar to the situation in acetonitrile (2), in which diester products were formed. Due to electrode filming problems, no further studies were carried out in this medium.

In the aluminum chloride:EMIC molten salt system, initial studies were carried out in the basic melt (0.8 : 1.0 composition), giving results similar to those obtained in pure EMIC. Following reduction at -1.35 V (E_p), the product peak at -2.0 V appears again (although smaller), as shown in Figure 2, and filming was also observed after passage through the reduction process. In an attempt to make the system more acidic, aluminum chloride was added to the basic melt, resulting in the immediate formation of a bright violet color, changing to gray after approximately an hour. After all of the aluminum chloride had dissolved, a cyclic voltammogram revealed very little activity; however, addition of more benzoyl chloride resulted in the appearance of a peak at -0.35 V. These observations suggest that benzoyl chloride reacts by direct contact with the aluminum chloride as it dissolves, and that benzoyl chloride is relatively stable in the acidic melt, in which Al₂Cl₇⁻ is the acidic species. The shift in reduction potential (1.15 V) is consistent with that seen for other carbonyl compounds as they undergo complexation by aluminum chloride in the acidic melt (6). It appears, then, that benzoyl chloride can undergo complexation at the carbonyl oxygen, and that the acidic melt is not sufficiently acidic to

cause the removal of chloride from the molecule. The reduction of benzoyl chloride in the acidic melt, as in the basic melt, is irreversible.

In order to identify the products formed in benzoyl chloride electrolysis, a preparative electrolysis at vitreous carbon was attempted, but filming of the electrode soon resulted in very low currents. Initial studies at mercury proved promising, so it was used in preparative electrolyses of benzoyl chloride. Cyclic voltammograms at a hanging drop mercury electrode (HMDE) at concentrations below 15 mM showed a reduction process at -1.35 V similar to that seen at vitreous carbon (Figure 3). For concentrations above this point, however, fluctuations in current began to appear in the voltammograms, in a manner consistent with maxima of the third kind (7). In such cases, sections of an adsorbed film undergo movement across the electrode surface, generating motion in the adjacent solution layer and increasing the current level as a result. From these observations, it is evident that filming occurs at mercury, at least above 15 mM, but it does not appear to completely passivate the surface.

Preparative electrolysis of benzoyl chloride (40 mM) at a mercury pool electrode was carried out at -1.35 V (foot of the reduction process), providing sustained currents sufficient to allow completion of the electrolysis in 2 hours. Coulometric measurements gave an *n*-value of 1.1 for benzoyl chloride reduction. Pentane extraction of the electrolysis melt gave very little material, and extraction of the hydrolyzed melt with benzene gave a 7% yield of benzaldehyde and approximately the same amount of benzyl alcohol (by GC/MS). Liquid chromatography was used to confirm that the diesters commonly produced in other solvents are not formed in this case.

Experiments in Acetonitrile / LiAlCl₄ System

Similar studies were carried out in acetonitrile / LiAlCl₄ mixtures, which also provide a chloroaluminate solvent system. Very little work has been carried out using these systems as solvents, but previous work has shown that aluminum chloride reacts with acetonitrile (AN) to produce an acidic species Al(AN)₃Cl²⁺ and AlCl₄⁻ ions (8). In the present work, the basic solvent regime has been employed by adding LiAlCl₄ (with a slight excess of LiCl) to AN. In this way, it is hoped that the effects of interaction with Lewis acids can be studied in an experimentally more convenient system.

Figure 4 shows cyclic voltammograms for benzoyl chloride (17 mM) reduction in the AN / LiAlCl₄ system, at both vitreous carbon and mercury electrodes. It is apparent that the pathway here is different from that in the molten salt above, there being little evidence of a product wave in the voltammograms. As in the molten salt, a preparative electrolysis at vitreous carbon was halted because severe filming soon produced very low current levels. A preparative electrolysis at a mercury pool, however, proved to be very interesting, resulting in a period of high current density followed by the breakup of the

mercury pool into smaller droplets. At this point, the current decreased substantially and the electrolysis mixture was investigated for product identification. GC/MS of the solution still showed some benzoyl chloride with a small amount of benzaldehyde as product. Perhaps the most interesting aspect of this electrolysis was discovered upon contacting the mercury pool with water during workup. Upon contact, the mercury droplets soon coalesced into a single pool, implying that some surface product had reacted, thereby reducing surface tension and allowing the pool to reform. Benzene extract of the aqueous solution showed that benzil (overall yield, 1%) was present. Considering that benzil is soluble in acetonitrile, it is likely that the adsorption of the reduced form of benzil, or its lithium or aluminum salt, is responsible for the strange behavior of the mercury pool during the electrolysis. This finding is significant because benzil has been proposed as an intermediate in benzoyl chloride reduction in other solvents, in which it immediately reacts with benzoyl chloride to form ester products. Its reduced form is apparently stabilized in the present system because of complexation by either lithium or aluminum ions in the solvent. Further studies are planned to ascertain which cation is responsible for this behavior.

CONCLUSIONS

The results of electrolyses in the molten salt system can be compared with other work carried out at mercury in acetonitrile / tetraalkylammonium perchlorates (9). In the latter system, similar yields of benzaldehyde (6 - 17%) were observed, depending on electrolysis potential and supporting electrolyte. The remaining product mixture is dominated by stilbenediol dibenzoate diesters, which are apparently not formed in the molten salt system. It is possible that complexation of intermediates potentially leading to diester formation causes their destruction to indeterminate products in the molten salt. It is interesting that the amount of benzaldehyde is similar in both systems. This result implies that abstraction of a proton (or hydrogen radical) from the solvent system to form benzaldehyde has the same importance in both systems relative to coupling reactions between benzoyl radicals.

In the acetonitrile / LiAlCl_4 system, formation of benzaldehyde also occurs to a minor extent. The most interesting observation here is that the pathway to diester production can be stopped at the initial coupling product (benzil formation), although this product, in some form, is adsorbed on the mercury electrode surface. This behavior may be due to complexation of a benzil reduction product by either aluminum or lithium ions, causing it to precipitate from solution onto the electrode surface.

REFERENCES

1. A. Guirado, F. Barba, C. Manzanera, and M.D. Velasco, *J. Org. Chem.*, **47**, 142 (1982).
2. G.T. Cheek and P.A. Horine, *J. Electrochem. Soc.*, **131**, 1796 (1984).
3. M.S. Mubarak, *J. Electroanal. Chem.*, **394**, 239 (1995) and references therein.
4. A.A. Fannin, Jr., L.A. King, J.A. Levisky, and J.S. Wilkes, *J. Phys. Chem.*, **88**, 2609 (1984).
5. M.A.M. Noel, P.C. Trulove, and R.A. Osteryoung, *Anal. Chem.*, **63**, 2892 (1991).
6. G.T. Cheek, in Eighth International Symposium on Molten Salts, R.J. Gale, G. Blomgren, and H. Kojima, PV 92-16, p. 426, The Electrochemical Society Softbound Proceedings Series, Pennington, NJ (1992).
7. B.-L. Johansson and B. Persson, *Anal. Chim. Acta*, **102**, 121 (1978).
8. J.A.K. Howard and L.E. Smart, *J. Chem. Society Chem. Commun.*, **1976**, 477.
9. G.A. Urove, M.S. Mubarak and D.G. Peters, in R.D. Little and N.L. Weinberg (Eds.), *Electroorganic Synthesis*, Marcel Dekker, New York, 1991, pp. 91-98.

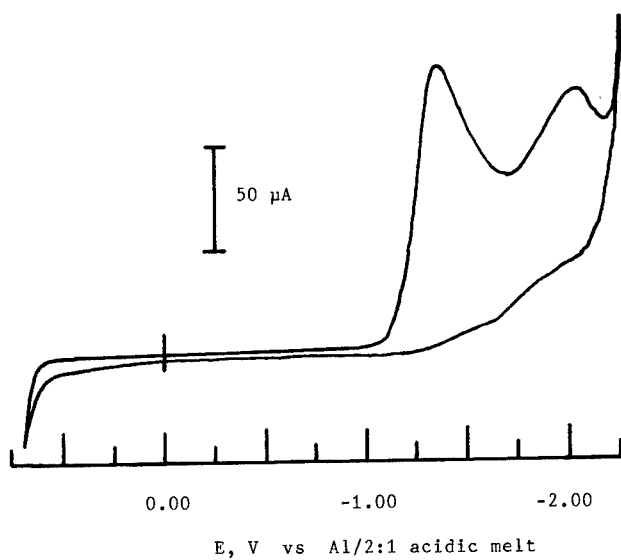


Figure 1. Cyclic voltammogram of 71 mM benzoyl chloride in molten EMIC at vitreous carbon.
Scan rate = 100 mV/s Temperature 100°C

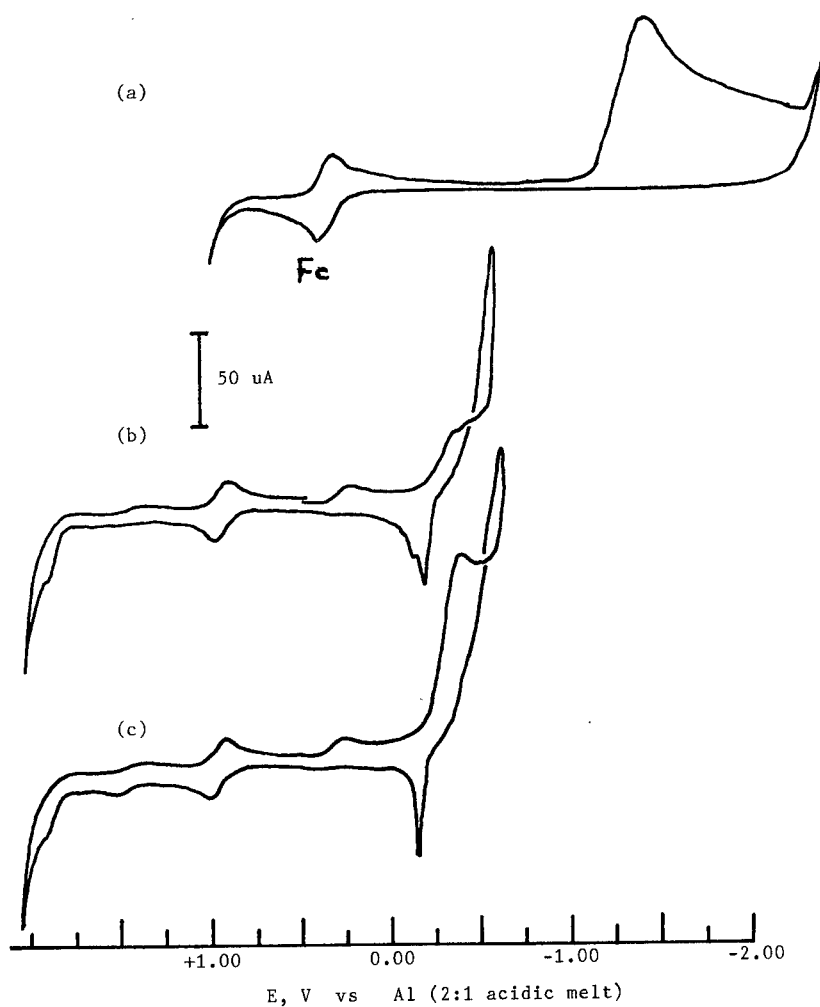


Figure 2. Cyclic voltammograms in AlCl_3 : EMIC molten salt.
Scan rate = 100 mV/s Temperature 25°C

- (a) 18 mM benzoyl chloride in 0.8 : 1.0 basic melt
- (b) addition of AlCl_3 to solution (a)
- (c) 15 mM benzoyl chloride in acidic melt

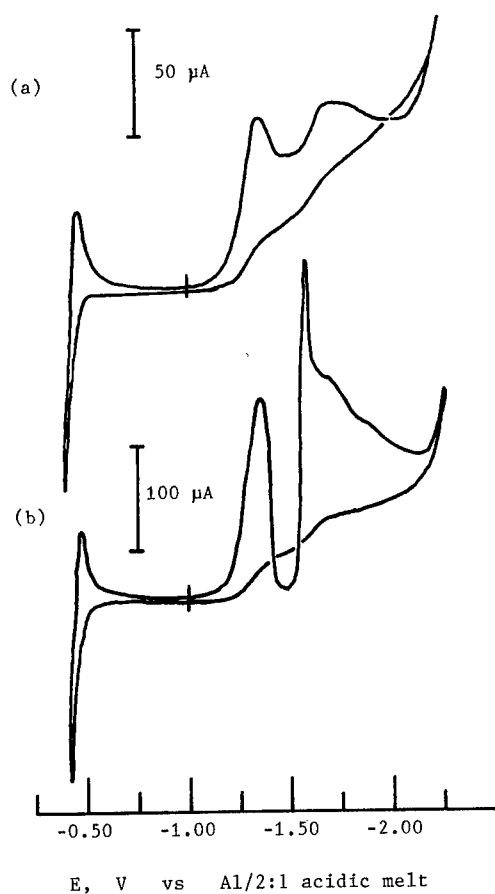


Figure 3. Cyclic voltammograms of benzoyl chloride in 0.8 : 1.0 basic melt, at mercury drop (1 μL). Scan rate = 100 mV/s Temperature = 25°C

- (a) 7.5 mM benzoyl chloride
- (b) 25 mM benzoyl chloride

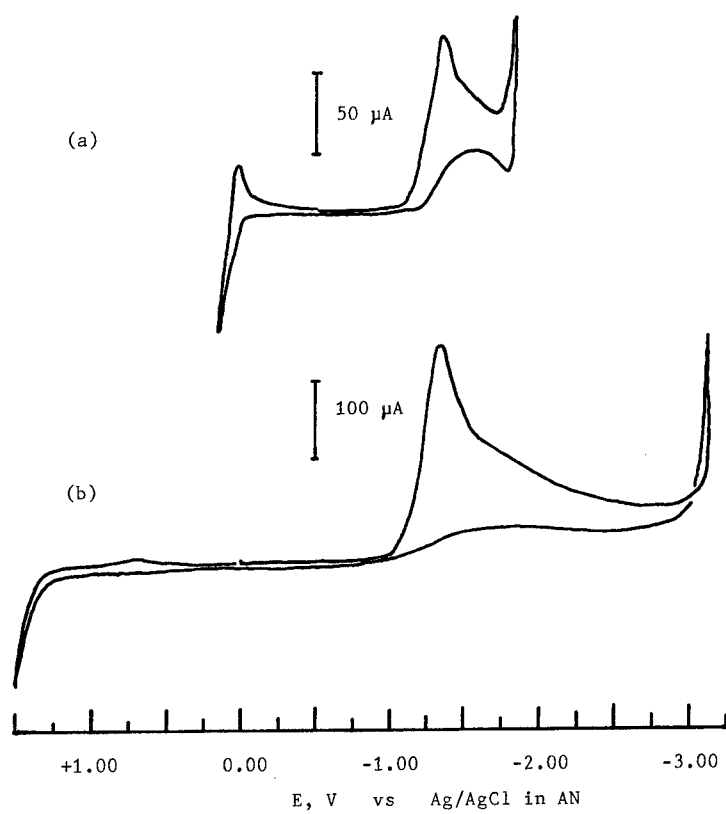


Figure 4. Cyclic voltammograms of benzoyl chloride (14 mM) in 0.1 M LiAlCl_4 solution.
Scan rate = 100 mV/s Temperature = 25°C

- (a) at mercury drop (1 μL)
- (b) at vitreous carbon

A Study of Binary Molten Pyridinium Salts

A. J. S. Carmo, M. E. Elias and A. M. Elias

Department of Chemistry and Biochemistry,
Lisbon University, Campo Grande, C1 piso 5
Centro de CiTecMat, FCUL,
1700 Lisbon, Portugal.

ABSTRACT

Electrical conductivity, viscosity, density of binary mixtures of pyridinium and α -picolinium chlorides (PyHCl and α -PicHCl) were measured isothermally as a function of temperature at fixed compositions, transition phase temperatures, T_g and T_m were measured by DSC and IR spectra were obtained. The system shows glass formation in the range $x = 0.3$ -1.0 α -PicHCl. T_g values slightly increase with the content in α -picolinium chloride. Arrhenius behaviour and thermal stability show that these binary mixtures are fragile. The analysis of cohesion energy and the similarity of the two components support the existence of pre-polymer-in-salt electrolyte in both upper and lower limits of the range of compositions, without segmental motion. The fragility of the systems increases as α -PicHCl is added to the pure organic salt without ring-CHs. This corroborates the presence of ionic species like $[\text{PirH} \dots \text{Cl} \dots \text{HPir}]^+$, $[\alpha\text{-PicH} \dots \text{Cl} \dots \text{HPic-}\alpha]^+$ and higher bonding systems.

INTRODUCTION

Pyridinium and α -picolinium chlorides which are salts formed from Lowry-Bronsted acid-base reaction between pyridine or α -picoline and hydrogen chloride are utilized in a study of chloride ion and proton transfer equilibria. The binary molten chloride systems containing two common components which have low melting points, supercools readily, and functions as good chloride donors. This combination of properties maximises the stability and definition of

any complex grouping which form in the binary systems. Also, these media can be seen as a precursor (lower limit) of the "pre-polymer-in-salt" electrolyte (1) since these components are assumed to exist as dimers, when isolated, despite the differences in the electrical conductivity. α -Picolinium chloride differs from the pyridinium chloride only by the addition of a methyl group in the α -ring position. The modification lowers the melting point considerably (from 144°C to 90.5°C) and thereby confers very useful glassforming ability both on the pure salt and on wide composition ranges of its binary solutions.

PyrHCl and α -picHCl function as strong Lewis base solvents with many inorganic salts and with HCl. In this case, it seems that the compound formation might be due to hydrogen bonding between the extra HCl and the π -cloud of the pyridinium cation. As will be seen, PyrHCl is also soluble in pyridine. There is a variety of possible molecule-molecule and ion-molecule interactions in this system.

Hence, in molten PyrHCl itself, the proton exchange freely between Pyr and Cl^- entities, and contributes much of the high electrical conductivity of this liquid. This is less effective in the case of α -PicHCl because of steric hindrance to rotation by the α - CH_3 group in the organic chloride, and may be sufficient to explain the difference in conductivity between the two hydrochlorides at 146.5 °C, with $\Delta\sigma = 0.0576 \text{ S cm}^{-1}$.

Also, the Arrhenius behaviour and thermal stability of these organic systems in addition with its glass forming features permit to conclude that these binary mixtures are fragile (2).

EXPERIMENTAL

α -PicHCl was prepared and purified as before (3), for PyrHCl the method of Audrieth was followed by the same purification as the methylic compound. The binary mixtures were prepared under inert conditions. Electrical conductivity and viscosity were measured isothermally as a function of temperature at fixed compositions. Density was measured isothermally and determined (4) for each composition. The instrumental methods to measure transport properties were previously reported and all transfer operations were performed in inert atmosphere of dry nitrogen (5). Transition phase temperatures, T_g and T_m were measured by DSC and IR spectra.

RESULTS and DISCUSSION

The temperature range of the measurements was 50-185 °C. From the density data, the molar volumes of the binary mixtures were calculated. The molar volumes V_m is defined by $V_m = (\sum x_i M_i)/\rho$, where M_i and x_i are the molar mass and fraction respectively of component "i". Figure 1 and figure 2 show the variation of molar volume with temperature and composition respectively.

Figure 3 and figure 4 present Arrhenius behavior and isotherms of electrical conductivity. The Arrhenius plot and isotherms for viscosity are shown in figures 5 and 6.

The phase diagram plotted in figure 7, present a simple eutectic. This point occurs for the composition $X=29\%$ pyrHCl and $T=48^\circ\text{C}$. Comparing with the binary systems QHCl and γ -picHCl in α -picHCl(6), the diagram is similar to those with an intermediate value of that eutectics. In figure 7, is also shown glass transition temperature T_g , and values of the ideal glass transition temperature T_o . For each system the conductivity - temperature and viscosity - temperature data were fitted to equations, by the method of least squares. The computer program did a linear least squares fit to the logarithm form of the VTF equation

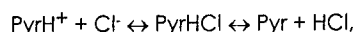
$$\ln W = A - (B/(T-T_o))$$

for a given value of T_o , in a range of temperatures, given the increments for successive T_o values. W is a transport property and A and B are constants. The value of T_o which corresponds to the minimum in the root mean square deviation is adopted for each property and each system.

Hence, T_g and T_o for the present system show monotonic decrease as we add PyrHCl. However, for values above 70% of pyridinium chloride, T_g collapse but the extrapolate value is $-46,5^\circ\text{C}$. Comparing with the quinolinium chloride containing system both glass transition temperatures, T_g and T_o present a minimum for composition 5,3% and then a systematic increase up to the pure QHCl, but below 40% in α -PicHCl, the binary system does not show T_g values. The pyridinium chloride, quinolinium chloride, β - and γ -picolinium chloride are nonglass forming systems (6).

The system shows glass formation in the range $x = 0.3-1.0$ α -PicHCl. T_g values slightly increase with the content in α -picolinium chloride, contrasting with the structural changes in the case of the system in which α -picolinium chloride is added to quinolinium chloride(6). Here the addition of α -picolinium chloride makes a decrease in T_g , revealing different effect on cohesion energy of the system. This is in agreement with the values of T_o . The analysis of cohesion energy and the similarity of the two components support the existence of pre-polymer-in-salt electrolyte in both upper and lower limits of the range of compositions, without segmental motion.

A PMR investigation of the system pyridinium chloride (PyrHCl) + HCl showed that there exists a strong hydrogen bonding interaction between the PyrH^+ cation and Cl^- anion in molten PyrHCl (7). The $>\text{NH}^+$ signals in both pure PyrHCl and α -PicHCl were observed as sharp singlets, -13.45 ppm and -13.35 ppm respectively. α -PicHCl, did seem to have a temperature dependence of $.0016\text{ppm}/^\circ\text{C}$ over the temperature range $89-150^\circ\text{C}$, but PyrHCl no. Also, to support the melt as ionic, and it must be, they (7) suggest a mobile equilibrium, described formally as



and



The free proton exchange involved suggests a large protonic contribution to the electrical conductivity, by Grotthus and/or by hopping mechanism. Unusually high electrical conductivity of the PyrHCl when compared with related organic salts like α -picHCl. In addition, an interesting contribution of Cl^- is also to be considered. Figure 9 shows the IR spectra of α -picHCl and three different samples.

Which concerns to the IR spectra of the binary system we have a common anion in both compounds, in addition, α -PicHCl has the $-\text{CH}_3$ group and the pyridinium ion has the extra hydrogen atom not present in pyridine, the species should have additional fundamentals in the IR spectrum. This ion gives a band at approximately 1540 cm^{-1} which is not present in pyridine and involves the N-H^+ deformation. However, α -PicHCl spectrum does not show this band but is present in all samples spectra. The band at 1540 cm^{-1} along with the band near the 1640 cm^{-1} and the very intense band which varies in $1470\text{-}1485\text{ cm}^{-1}$ range and present in all samples, indicates proton acidity in pyridinium and α -picolinium ion (8). Of greater interest is the band which is described as a N-H stretching vibration. It shows a large variation in intensity, band width, and frequency since is almost non-existing for α -PicHCl, and broad, intense band at 2440 cm^{-1} as the PyrHCl concentration increases.

All the spectra show a striking similarity in this region for mixtures of the compounds studied. Four bands of remarkable constancy in frequency and intensity located near 1640 , 1620 , 1540 and 1480 cm^{-1} and all are $\nu_{\text{C-C}}$. However, not present in α -picolinium chloride. The Raman spectrum also shows the 1640 and 1610 cm^{-1} bands to be depolarized, and 1480 cm^{-1} band probably polarized (9). The region 1020 to 640 cm^{-1} will contain the ring-breathing and -bending modes as well as the characteristic out-of plane hydrogen-deformation vibrations. However, the assignments are important in determining intermolecular effects(10) is the case with $1010(m)$, $970(w)$, $905(w)$, $770(vs)$, $720(w)$ and $690(m)$ bands. The band at 1010 cm^{-1} is assigned to $\nu_{\text{C-C}}$, the totally symmetric ring-breathing mode and band at 970 cm^{-1} assigned to $\nu_{\text{C-H}}$. The presence of organic complex is shown by $2100(m)$, $2025(w)$ and $1990(w)\text{ cm}^{-1}$ bands. Hence, the set of spectra and those bands along with the bands in region 1020 to 640 cm^{-1} permit to understand the mixtures from the point of view of the IR interactions and the presence of organic complex.

The fragility of this system is apparent from fig. 8. This fragility is related to the facility with which the molecular order can reorganize particularly in the intermediate distance order. The fragility of the systems increases slightly as pyrHCl is added to the pure organic salt with ring- CH_3 . However, decreases for the most concentrate sample.

In the case of QHCl containing ionic liquids (6), fragility increases with quinolinium chloride content due to the shift, in the reduced-Arrhenius plot for viscosity, toward the center of general pattern in accordance with the complex formation decrease for $X < 94.7$ α -PicHCl in the glass-forming range.

This corroborates the presence of ionic species like $[\text{PirH}\dots\text{Cl}\dots\text{HPir}]^+$, $[\alpha\text{-PicH}\dots\text{Cl}\dots\text{HPic-}\alpha]^+$ and higher bonding systems of the kind $[\text{PirH}\dots\text{Cl}\dots\text{H}\alpha\text{-Pic}]^+$. Hence, hydrogen bonding have a strong influence in the transport properties (11), species involved, melt structure and these are responsible for the "pre-polymer-in-salt" electrolyte characteristics.

The mechanism for ionic conductivity in polymer electrolytes is strongly linked to the polymer segmental mobility and therefore to η of the system and to increase the conductivity (12) we may mix low and high molecular weight chains, and the present study shows a good system of the first type. Also, the low glass transition temperature, T_g and T_o , derived in $X=0.50\text{-}0.65$ pyrHCl range, allow that polymer systems remain rubbery at room temperature while keeping conductivity and high electrochemical stability.

REFERENCES

1. C. A. Angell, C. Liu and E. Sanchez, *Nature*, **362**, 137 (1993).
2. C. A. Angell, in *Relaxation in Complex Systems*, (Proceedings of the Workshop on Relaxation Processes, Blacksburg, VA., July 1983); K. Ngai, G. B. Smith, Eds.; National Technical Information Service, US Department of Commerce, Washington DC, 1985; p. 3.
3. C. A. Angell and A. M. Elias, *J. Phys. Chem.*, **87**, 4707 (1983).
4. A. M. Elias and M. H. Pereira, *Rev. Port. Quím.*, **15**, 6 (1973).
5. C. A. Angell and A. M. Elias, *J. Chem. and Eng. Data*, **33**, 1 (1988).
6. A. M. Elias and M. E. Elias, in *Proceedings of the Joint Symposium on Molten Salts*, Honolulu 1987; G. Mamantov, C. Hussey, M.-L. Saboungi, M. Blander, C. Mamantov, J. S. Wilkes, Eds.; The Electrochemical Society, Inc., Pennington (1987), p. 305.
7. C. A. Angell and J. W. Shuppert, *J. Phys. Chem.*, **84**, 538 (1980).
8. P. Parry, *J. Catalysis*, **2**, 371 (1963).
9. G. Kotowycz, T. Schaefer and E. Bock, *Can. J. Chem.*, **42**, 2541 (1964).
10. J. Rozière, J. M. Williams, E. Grech, Z. Malarski and L. Sobczyk, *J. Chem. Phys.*, **72**(11), 6117 (1980).
11. W. Nadler and T. Krausche, *Phys. Rev. A*, **44**(12), 7888 (1991).
12. P. G. Bruce and C. A. Vincent, *J. Chem. Soc., Far. Trans.*, **89**, 3187 (1993).

ACKNOWLEDGMENT: We thank Eng. M. M. Nunes for performing IR spectra

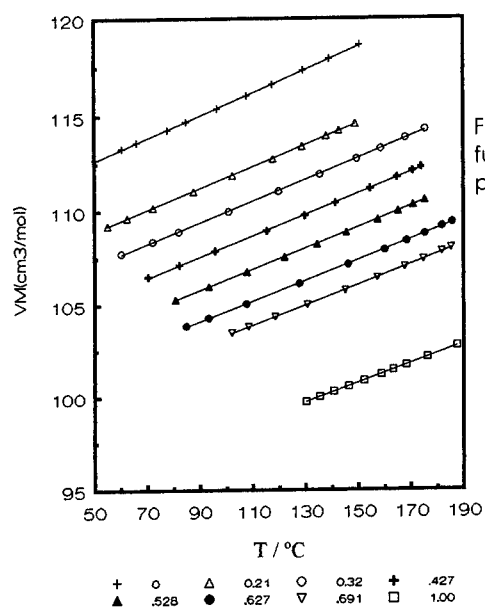


Figure 1. Molar volume as a function of temperature for $\text{pyrHCl} + \alpha\text{-picHCl}$ system.

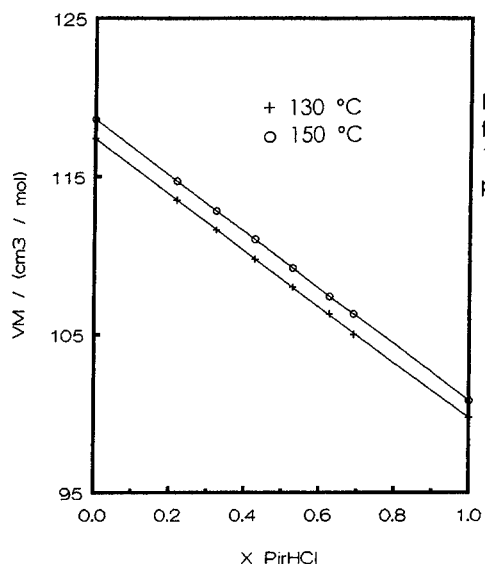


Figure 2. Molar volume as a function of mole fraction for 130 and 150 $^\circ\text{C}$ for $\text{pyrHCl} + \alpha\text{-picHCl}$ system.

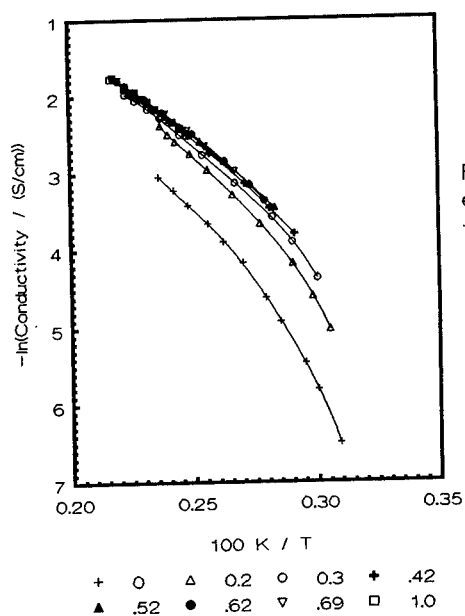


Figure 3. Arrhenius plot of electrical conductivity for pyrHCl + α-picHCl system.

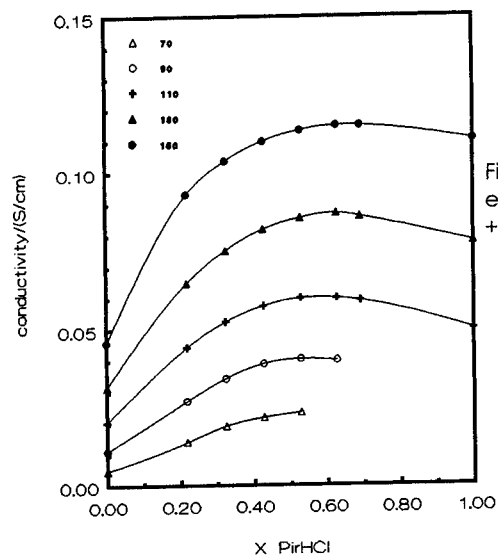


Figure 4. Isothermal plot of electrical conductivity for pyrHCl + α-picHCl system.

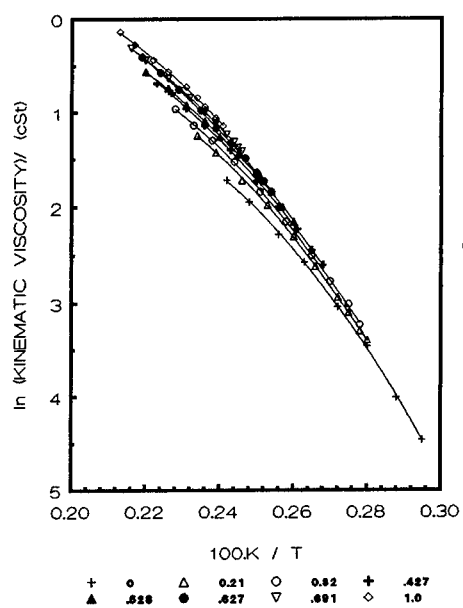


Figure 5. Arrhenius plot of kinematic viscosity for pyrHCl + α-picHCl system.

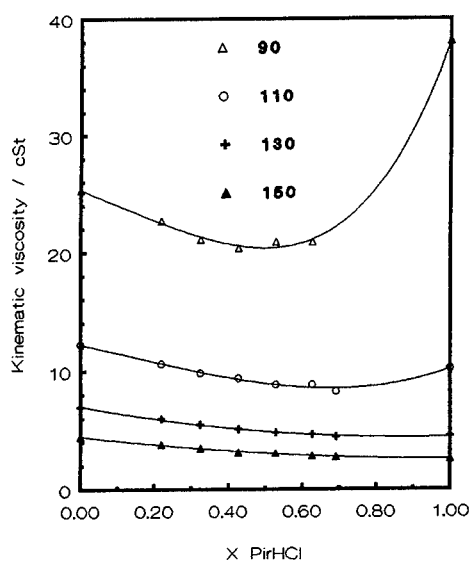


Figure 6. Isothermal plot of kinematic viscosity for pyrHCl + α-picHCl system.

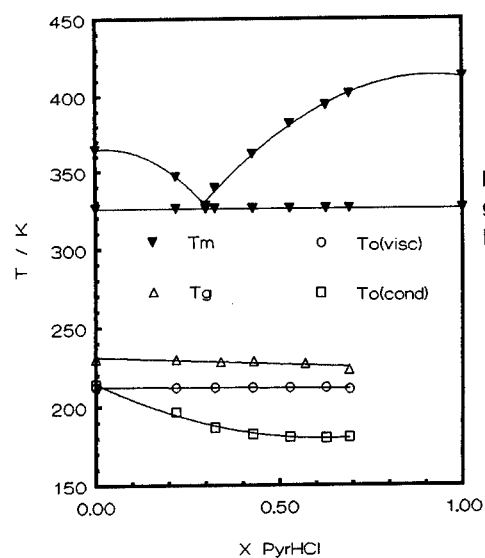


Figure 7. Phase diagram and glass transition temperatures for pyrHCl + α -picHCl system.

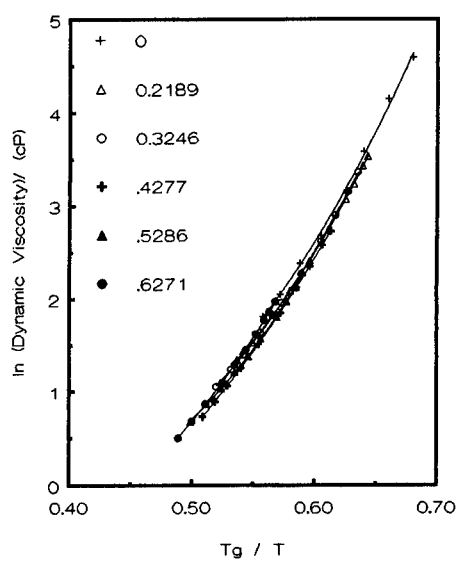


Figure 8. T_g -reduced Arrhenius plot of viscosity for pyrHCl + α -picHCl system.

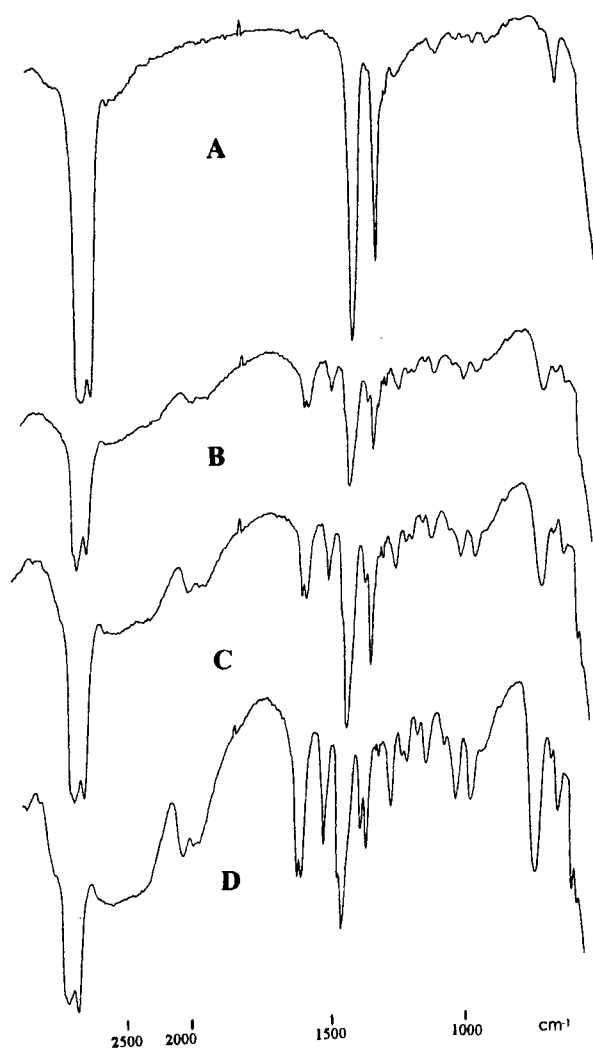


Figure 9. Infrared spectra for A - α -picHCl, B - $X=0.3296$, C - $X=0.5286$ and D - $X=0.6271$ pyrHCl of α -picHCl+pyrHCl system.

MEASURING THE RATES OF SOLID STATE REACTIONS BETWEEN AlCl_3 AND $\text{C}_5\text{H}_6\text{NCl}$ USING DIFFERENTIAL SCANNING CALORIMETRY

David S. Newman, Jennifer Rosinski and Kathleen S. Leis
Department of Chemistry
Bowling Green State University
Bowling Green, OH 43403

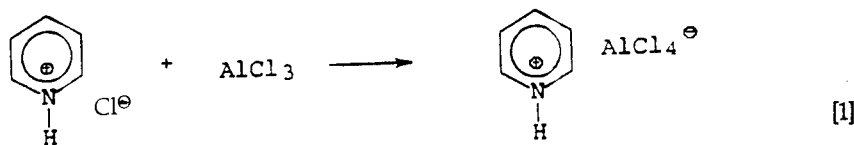
ABSTRACT

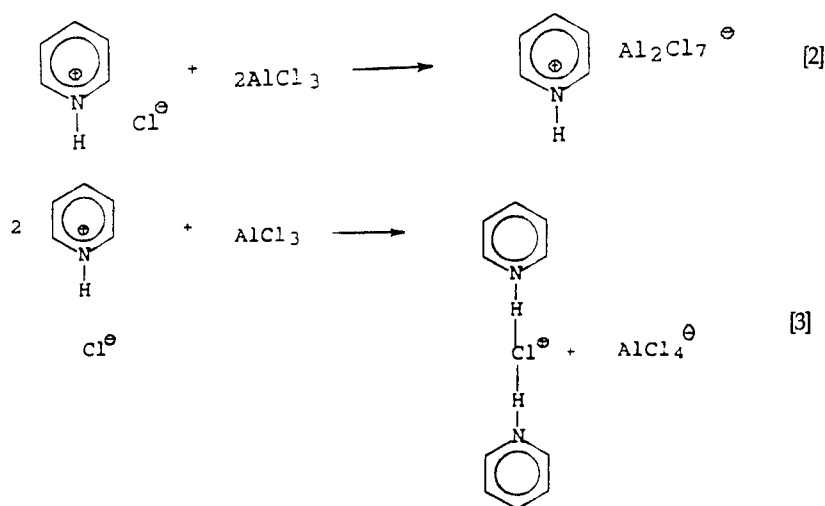
Differential Scanning Calorimetry was used to measure the rates and heats of the solid state reactions between aluminum chloride and pyridinium chloride. It was found that the three reactions studied followed the same rate law derived from a two dimensional diffusion mechanism. The integrated form of this rate law is $(1-\zeta)\ln(1-\zeta) + \zeta = kt$ where ζ is the degree of transformation, k is the specific rate constant and t is the time. The rate constant for the neutralization reaction was measured at several temperatures and from these data the energy of activation was calculated. From the measured rate law, inferences about the reaction mechanism and energy transfer were made.

INTRODUCTION

Despite the fact that almost all materials of interest are solids and there is a pressing need to understand homogeneous solid state reactions, relatively little is known about the kinetics and mechanisms of solid state reactions because it is difficult to design experiments that will generate useful information. For this reason we have begun a series of experiments using differential scanning calorimetry (DSC) to measure the rates of solid state reactions (1). The reason we are using DSC is that for any exothermic reaction, heat begins to evolve at the beginning of the reaction and stops when the system equilibrates, so that the rate of the reaction is proportional to the rate at which heat is evolved. If the heat is generated quickly enough for the reaction to be followed by DSC, useful information about the kinetics of solid state reactions might be obtained.

We have selected the series of reactions between AlCl_3 and chloride salts such as NaCl (2), pyridinium chloride (3), methylethylimidazolium chloride (4), or *n*-butylpyridinium chloride (5) to explore the feasibility of using DSC to study solid state kinetics. These reactions are highly exothermic, very rapid for solid state reactions, have interesting Lewis acid-base chemistry and generally form products that have lower melting points than either of the reactants. They are also of particular interest to the molten salt community because, in the liquid state, the chloroaluminates formed are useful as solvents for interesting reactions and unusual species and as electrolytes in energy generating devices. The reactions whose kinetics we report on here are between pyridinium chloride, $\text{C}_5\text{H}_6\text{NCl}$, and AlCl_3 and are shown below.





Each product is a congruently melting compound. The melting point of $\text{C}_5\text{H}_6\text{NAlCl}_4$ is approximately 120 °C, the melting point of $\text{C}_5\text{H}_6\text{NAl}_2\text{Cl}_7$ is approximately 24 °C and the melting point of $(\text{C}_5\text{H}_6)_2\text{ClAlAlCl}_4$ is approximately 91 °C (6).

THEORETICAL BACKGROUND

A differential scanning calorimeter can be used to measure both isothermal and dynamic (temperature changing) processes and in the present study, an isothermal mode was used. This means changes as a function of time, keeping temperature constant, were recorded. Since a differential scanning calorimeter is designed, in effect, to maintain a zero temperature differential between a standard and a test sample, any heat evolved during the reaction (the test sample) will be supplied by the instrument to the reference sample and is therefore the quantity measured. If we define a quantity ζ as the degree of transformation, $\zeta = 0$ at the beginning of the reaction when the heat begins to evolve and $\zeta = 1$ when the system equilibrates and heat stops being evolved. Therefore, the rate of the reaction is $d\zeta/dt$.

For the solid state reaction,

$$A = C + \Delta H \quad [4]$$

A is the solid at the start of the reaction, C is the material after the reaction has equilibrated, and ΔH is the heat evolved during the reaction. In general,

$$\zeta = \Delta H_{\text{(partial)}} / \Delta H_{\text{(reaction)}}. \quad [5]$$

That is, the entire area under the experimental Q vs. time curve gives ΔH for the reaction and an area corresponding to a particular time less than t_{reaction} , $(\Delta Q/\Delta t) \times \Delta t$, gives $\Delta H_{\text{(partial)}}$ for that elapsed time. Dividing $\Delta H_{\text{(partial)}}$ by $\Delta H_{\text{(reaction)}}$ yields the value of ζ corresponding to that rate. The process is repeated for several times at each of several temperatures. In order to ensure that the reaction has not proceeded to any significant extent before data is collected, the reactants and pans are cooled to as low a temperature as is practical prior to being loaded into the calorimeter. This concept is illustrated in Fig. 1 (7) which shows a three dimensional plot of ζ against time and temperature, T, for a generalized solid state reaction. It is apparent from the diagram that as T approaches 260 °C, ζ approaches zero.

For first, second, or third order reactions, the temperature dependence of the reaction rate is given by the familiar Arrhenius equation so that the rate law for the reaction becomes

$$d\zeta/dt = k(1-\zeta)^n = A_0[\exp - E_a/RT](1-\zeta)^n \quad [6]$$

In linear form, this equation becomes

$$\ln(d\zeta/dt) = \ln A_0 - E_a/RT + n\ln(1-\zeta). \quad [7]$$

A_0 , E_a , n and k are obtained from experimental values of $d\zeta/dt$, $1/T$, and $(1-\zeta)$. However, most solid state reactions do not follow a simple ordered rate law and for these reactions, the rate law is derived for various possible model reaction mechanisms. The experimental ζ vs t curves are then compared with the model ζ vs t curves and the best fit selected to obtain the overall reaction rate law. From the rate law, inferences about the reaction mechanism can be made. Unfortunately, differences in the ζ vs. t curves corresponding to different mechanisms are often quite small so that very precise measurements are needed.

EXPERIMENTAL DETAILS

The experiments were performed on a Perkin-Elmer DSC-4 with a thermal analysis data station (TADS). Data were collected in the isothermal mode using a special isothermal program. Because the reactions between C_5H_6NCl and $AlCl_3$ were fairly rapid at elevated temperatures, both reactants were cooled on dry ice in a nitrogen filled glove box (moisture content less than 10 ppm), to ensure that the reaction did not proceed to any great extent prior to being placed in the calorimeter. The desired mole fractions of the reactants were prepared by weighing stoichiometric quantities of each compound that had been ground and sieved through a 40 Mesh screen, directly into a large stainless steel pan (0.7 cm diameter) inside the glove box and then sealing the pan. This conceptually simple procedure proved to be quite difficult in practice and took quite a bit of preparation time. The temperature of the sealed pans was further reduced before removing them from the glove

box. The best mixing procedure seemed to be simply holding the sealed pan with a tweezers and gently shaking it for a few seconds. The cold pans were then placed in the calorimeter and brought to a high enough temperature for the reaction to occur fairly rapidly.

$\Delta H_{\text{(partial)}}$ and $\Delta H_{\text{(reaction)}}$ were calculated by first enlarging the measured thermogram, transferring it to heavy cardboard, cutting out the area under the curve with a sharp scissors and weighing it on an analytical balance. A square with known dimensions of the same cardboard was used to calibrate the area. The precision of this technique was better than 1%.

The melting and freezing points of the products were obtained by switching to the normal dynamic mode of the instrument. This was done to further ensure that a true product was actually produced. Sublimation, decomposition, and vaporization all produce endothermic thermograms similar to melting so that obtaining an exotherm is fairly good evidence that a reaction has occurred. Since all reactants and products are very hygroscopic, all transfer reactions were done in the controlled atmosphere glove box.

RESULTS AND DISCUSSION

Fig. 2 shows a typical thermogram obtained from our calorimeter for Eq[3] at 50 °C. The dashed line represents the baseline extrapolation procedure. Since we are operating the instrument in the isothermal mode, the abscissa represents time and not temperature. A temperature range of 10 °C is actually a time of one minute so the time for this reaction is slightly longer than two minutes. All thermograms had the same general shape as Fig. 2. Fig. 3, 4, and 5. show typical isothermal ζ vs t plots for Eq.[1], Eq.[2], and Eq.[3] respectively. Table I lists the average $\Delta H_{\text{(reaction)}}$ and temperature range for the reactions studied. Although there is considerable error in each of the ΔH measurements shown in Table I, the general trends are all in the expected direction and the data are self consistent. For example, it must be the case that the enthalpy of reaction for Eq.[2] is considerably larger than the enthalpy of reaction for Eq.[1] because an AlCl_3 molecule is being added to pyridinium tetrachloroaluminate. The difference between the heats of reaction for Eq.[1] and Eq.[2] should equal ΔH_{rxn} for the reaction:



Although the measurement for this reaction proved extremely difficult, our preliminary data indicate that, within experimental error, $\Delta H_{[8]} = \Delta H_{[2]} - \Delta H_{[1]}$.

The ζ vs. t curves indicate that Eq. [1-3] all follow a rate law derived from a two dimensional diffusion mechanism (8):

$$d\zeta/dt = k[-\ln(1-\zeta)]^{-1} \quad [9]$$

where k is the specific rate constant. The integrated form of this rate law is:

$$f(\zeta) = (1-\zeta)\ln(1-\zeta) + \zeta = kt \quad [10]$$

so that if the rate law is correct for a particular reaction, a plot of $f(\zeta)$ vs. t would give a straight line with slope k . Fig. 6 shows a plot of $f(\zeta)$ vs. t for Eq.[1] at each of three temperatures and all three are linear, the 50 °C plot having a correlation coefficient of 0.999. Special care was taken in each of these reactions to fill the pan with exactly (to three significant figures) 1×10^{-4} moles of each reactant. Fig. 7 shows an Arrhenius plot for Eq.[1] using the results of these experiments plus two additional experiments. The data are fairly linear yielding an E_a of 16 kJ/mol. The theoretical interpretation of an Arrhenius plot for inherently heterogeneous solid state reactions is open to question, but the relative linearity of the graph and the value of E_a is useful for purposes of comparison and to verify internal consistency of the data. Fig. 8 and Fig. 9 are the $f(\zeta)$ vs. t plots for Eq.[2] and Eq.[3] respectively and again, each of these graphs is quite linear indicating a two dimensional diffusion mechanism.

The salient features of all of these reactions is their extreme rapidity and the fact that, within experimental error, they all follow the same rate law indicating a similar mechanism. The heterogeneous reactions probably proceed evenly over two contiguous crystal surfaces. On a microscopic level, for the neutralization reaction, this can be pictured as the Cl^- ions from the surface of a crystal of $\text{C}_5\text{H}_6\text{NCl}$ hopping to the surface of an AlCl_3 crystal followed by the formation of pyridinium tetrachloroaluminate nuclei which then grow. Details of how these nuclei grow are unclear (9) as are the details of energy transfer. The heat generated by one group of molecules reacting with another generates the activation energy for a subsequent reaction producing a kind of energy wave moving through the crystal. It is also probable that enough heat is generated in this process to cause eutectic mixtures to melt locally forming a molten salt and thus significantly increasing the reaction rate. Freezing eventually occurs and the system appears to always be in the solid state. It is also possible that these reactions are vapor driven. That is, there is a high enough vapor pressure of each reactant in the sealed pan so that a gas phase reaction occurs. The reaction product is well below its melting point and eventually precipitates causing either a eutectic to form locally or, allowing more unreacted material to vaporize and drive the reaction.

SUMMARY

Differential Scanning Calorimetry has been shown to be a useful technique for measuring the rates of exothermic solid state reactions. The extent of reaction, ζ , is obtained from the thermogram and is then fitted to known rate laws derived for different possible solid state reaction mechanisms. From these rate laws inferences as to the microscopic details of the solid state reaction may be drawn.

ACKNOWLEDGMENT

We wish to thank the NSF REU program at Bowling Green State University for their support. We also wish to thank Jimmie Edwards for his helpful discussions.

LIST OF REFERENCES

1. D.S. Newman and J. Rosinski., The Proceedings of the Ninth International Symposium on Molten Salts. G. Mamantov, C.L. Hussey, D.S. Newman, Y. Ito, Editors, Pennington, New Jersey, The Electrochemical Society Soft Bound Proceedings Series, 1994, pv.94 -13, pp 633-637.
2. L.G.Boxall, , H.L. Jones, and R.A. Osteryoung. *J. Electrochem. Soc.* **120**, 223 (1973), 1973, .
3. .C.A. Angell, J.W. Shuppert. *J. Phys. Chem.* **84**, 538 (1980) .
4. J.S. Wilkes, J.A. Levisky, R. A. Wilson, and C. L. Hussey. *Inorg. Chem.* **21**, 1263 (1982)
5. C. Nanjundiah, K. Shimizu, and R.A. Osteryoung, *J. Electrochem. Soc.* **129**, 2474 (1982)
- 6.K.S. Leis, MS Thesis, Department of Chemistry, Bowling Green State University, Bowling Green, OH, 1995
7. M.E. Brown, C.A.R. Philpotts , *J. Chem. Ed.*, **55**, 556 (1978)
8. Michael L. Brown, Introduction to Thermal Analysis. Chapman and Hall, New York, 1988, pp 127-151.
9. V.V. Boldyrev, M. Bulens, and B. Delmon. The Control of the Reactivity of Solids. Elsevier Scientific Publishing, Amsterdam, 1979, Vol. 2.

TABLE I

Average Heats of Reaction and Temperature Range for the Solid State Reactions between AlCl_3 and $\text{C}_5\text{H}_6\text{NCl}$

<u>Reaction</u>	<u>$\Delta H_{av}(\text{kJ/mol})$</u>	<u>Temperature Range ($^{\circ}\text{C}$)</u>
$\text{C}_5\text{H}_6\text{NCl} + \text{AlCl}_3$	- 53 +/- 6	50 - 100
$2\text{C}_5\text{H}_6\text{NCl} + \text{AlCl}_3$	- 76 +/- 1	50
$\text{C}_5\text{H}_6\text{NCl} + 2\text{AlCl}_3$	- 120 +/- 14	22 - 33
$\text{C}_5\text{H}_6\text{NAlCl}_4 + \text{AlCl}_3$	- 63	25

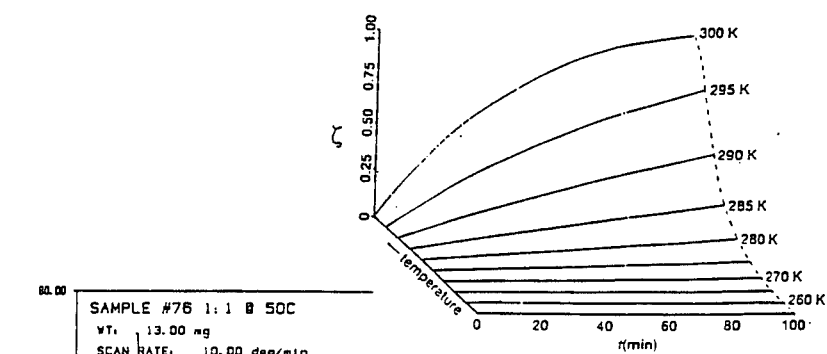


FIG. 1

A series of isothermal ζ vs. time curves at different temperatures.

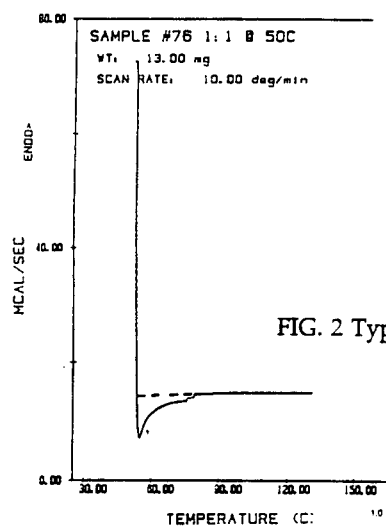


FIG. 2 Typical DSC Thermogram.

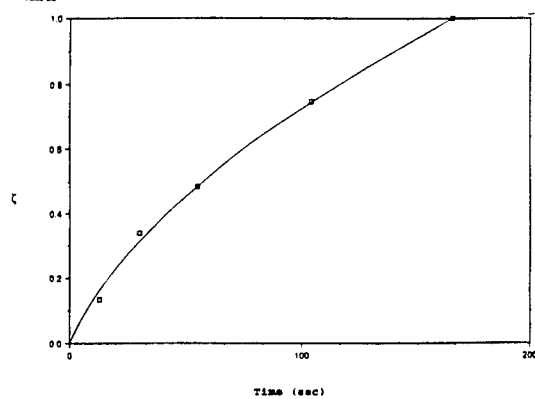


FIG. 3 Isothermal ζ vs. time for Eq. [1].

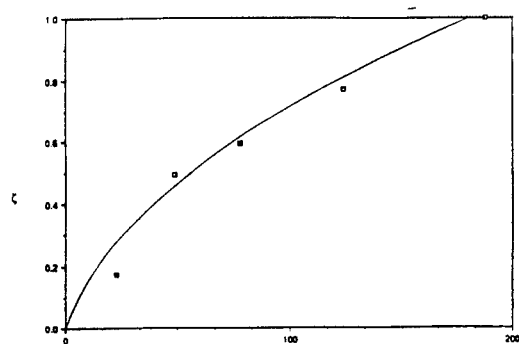


FIG. 4
Isothermal ζ vs.
time for Eq. [2].

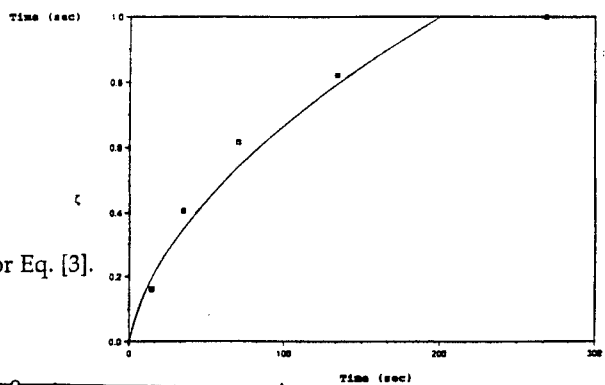


FIG. 5
Isothermal ζ vs. time for Eq. [3].

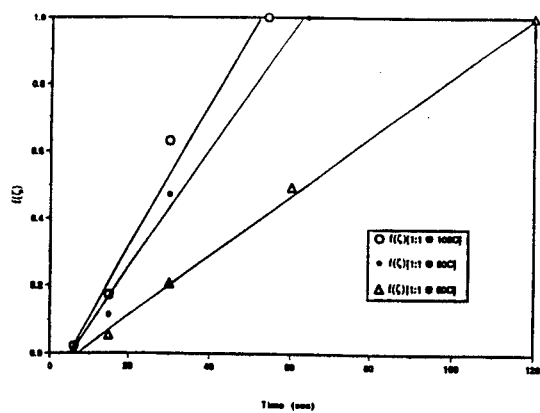


FIG. 6 $f(\zeta)$ vs. time for Eq. [1] at each
of three temperatures.

FIG. 7 Arrhenius plot for Eq. [1].

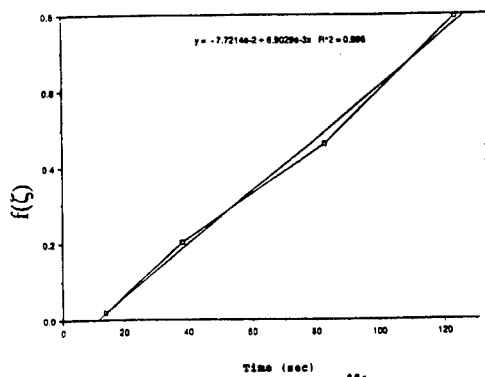
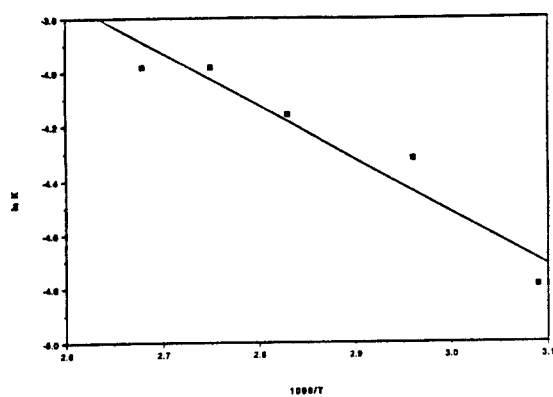


FIG. 8 $f(\zeta)$ vs. time for Eq. [2]

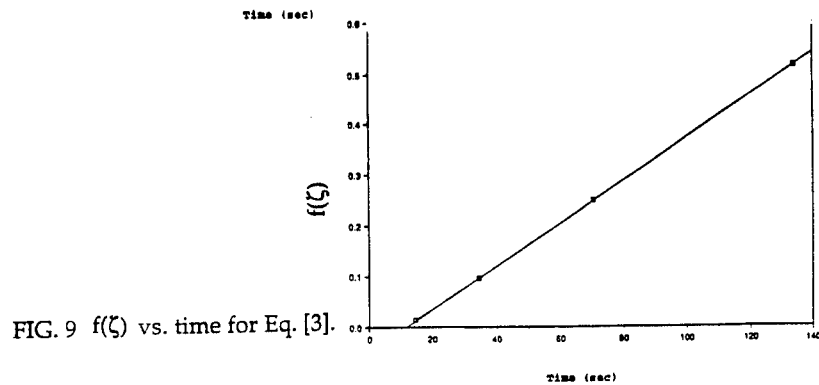


FIG. 9 $f(\zeta)$ vs. time for Eq. [3].

EFFECT OF ALKALI METAL FLUORIDE ON ANODIC REACTION IN A MOLTEN NH_4F -HF SYSTEM

Akimasa TASAKA*, Tomoo KAWAGOE, and Toshinori OSADA

Department of Molecular Science and Technology, Doshisha
University, Miyako-dani 1-3, Tadara, Tanabe-cho, Tsuzuki-gun,
Kyoto 610-03, Japan

ABSTRACT

The current efficiency for NF_3 formation and the consumption of nickel anodes depends on the composition of molten fluoride containing HF and temperature. Trivalent and/or tetravalent nickel compounds were detected on nickel by electrochemical methods and x-ray photoelectron spectroscopy (XPS). The surface was observed by means of a scanning electron microscope (SEM). The addition of LiF to an $\text{NH}_4\text{F} \cdot 2\text{HF}$ melt was the most effective for increasing the NF_3 current efficiency and minimizing the consumption of the nickel anode. A new mechanism for the electrochemical fluorination is proposed. In this mechanism, the starting material reacts at the anode with nickel compounds having high oxidation states.

INTRODUCTION

Pure NF_3 free from CF_4 can be obtained by electrolysis of $\text{NH}_4\text{F} \cdot 2\text{HF}$ when a nickel anode is substituted for a carbon anode. However, corrosion of the nickel anode is troublesome, and it corresponds to current losses of 3 ~ 5% under operating conditions. NiF_2 and NH_4NiF_3 are deposited on the anode and the cell bottom. Although the addition of CsF into the electrolyte minimizes nickel anode consumption, and lowers the vapor pressure of the melt, it is inapplicable to the practical cell because CsF is expensive. Fluorination of NH_4^+ to NF_3 and other species such as N_2 , N_2F_4 , N_2F_2 , and N_2O is also a problem. In addition, oxygen is generated even if water in the electrolyte is low. Water in the melt lowers the current efficiency for the NF_3 formation and increases the consumption of nickel anode.

This paper deals with the effects of alkali metal fluorides added into the melt on the current efficiency for the NF_3 formation and to the anode corrosion. The effect of temperature on the current efficiency for the NF_3 formation is also discussed.

EXPERIMENTAL

A cylinder-type nickel cell (1.5 dm³) was equipped with a nickel sheet anode (24 cm²) at the center for production experiments. The cell wall was used as the cathode. A skirt was provided to separate the anode gas from hydrogen generated at the cathode. The cell bottom was insulated by a PTFE sheet to avoid hydrogen evolution (nickel cell, thereafter). A box-type PTFE cell equipped with the nickel electrode, both anode and cathode, was provided for fundamental studies. A Pt wire was inserted into the nickel cell as a reference electrode while a specially designed electrode was employed for the PTFE cell. However, the potentials in the text are shown by the hydrogen electrode scale in the volts vs. H₂.

NH₄F · 2HF prepared with extra pure HF (99.99%) and NH₄F (99.9%) in a dry box was used. Nitrogen was supplied to the glove box, in which the PTFE cell at 120°C was positioned, to remove moisture from the atmosphere during the experiment. The electrolytic experiments were conducted under constant temperatures at 120, 100, 80, and 60°C.

The PTFE cell was pre-electrolyzed at a low current density with a carbon anode for many hours until NF₃ was generated under steady state conditions, then the potential decay measurements and the corrosion test were performed. The nickel electrode specimen was washed with water followed by methanol rinsing. The current losses caused by nickel dissolution were calculated from the weight losses.

The water content in the nickel cell was high before start-up, but it decreased by electrolysis to less than 0.02 wt% or ca. 21 mmol/dm³.

The anode gas was treated with NaF to eliminate HF before the chromatographic and IR spectroscopic analyses. The current efficiencies for the constituents were evaluated from the results of gas analysis and the flow rate of the anode gas.

For the corrosion test, the nickel anode was electrolyzed in a well dehydrated NH₄F · 2HF melt with and without alkali metal fluoride for 90 minutes under constant voltage at 5 V vs. H₂. The test specimen was washed with anhydrous HF (99.9% HF) and/or 47% HF aqueous solution to remove adhesive melt on the surface and inspected by the XPS and SEM. The nickel concentration in the melt was measured by absorptiometry.

RESULTS AND DISCUSSION

Oxygen was evolved for the first 20 hours of electrolysis followed by gradual formation on NF_3 . The NF_3 current efficiency increased and reached a steady state 80 hours after start-up, depending on the electrolyte composition. The N_2O content in the anode gas decreased with time to a minimum level. The final ratio of N_2O to NF_3 was <0.05 , for example. In these preliminary experiments, we think that the cell was stabilized by electrolysis within 80 hours. Table 1 shows the current efficiencies for the anode gas and its constituents. The current efficiency for hydrogen evolved at the cathode is also listed. The last column is the current losses caused by the dissolution of the nickel anode. The current efficiency for the NF_3 formation in the electrolyte containing LiF was high compared with others. Also, the Ni dissolution was decreased by the addition of LiF . The NF_3 current efficiency varied slightly with CsF content while the anode gas and the cathodic hydrogen as well as the Ni dissolution were unchanged except in the case of the CsF content of 6.7 mol%. In the case of an $\text{NH}_4\text{F} \cdot 2\text{HF}$ melt with KF , the current efficiencies for the anode gas, NF_3 , and cathodic hydrogen were low and the anodic consumption increased with the increase of the KF content. Hence, KF was detrimental to the Ni anode. The addition of NaF into $\text{NH}_4\text{F} \cdot 2\text{HF}$ increased both the NF_3 current efficiency and the anode consumption slightly.

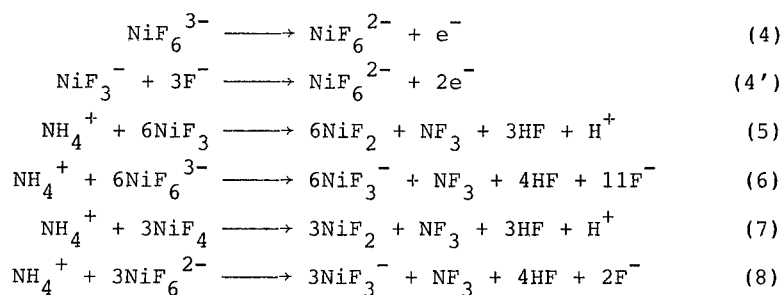
Figure 1 shows the XPS spectra of $\text{Ni } 2p_{3/2}$, $\text{O } 1s$, and $\text{F } 1s$ of the nickel anode electrolyzed in the melt of $\text{NH}_4\text{F} \cdot 2\text{HF}$ at 25 mA/cm^2 and 100°C for 100 hours. Specimens were washed with 99.9% HF (solid) and 47% HF aqueous solution (dotted curves). Large peaks at 858 eV and 685 eV correspond to NiF_2 ($\text{Ni } 2p_{3/2} = 857.7 \text{ eV}$ and $\text{F } 1s = 685.0 \text{ eV}$). Small peaks at 531 and 533 eV of the $\text{O } 1s$ spectrum are NiO and Ni_2O_3 , respectively [1]. A new shoulder at 861 eV of the $\text{Ni } 2p_{3/2}$ spectrum and a new peak at 688 eV of the $\text{F } 1s$ spectrum were observed on the specimen washed with 99.9% HF . These peaks correspond to trivalent and/or tetravalent nickel compounds such as NiF_3 and NiF_4 ($\text{Ni } 2p_{3/2} = 861.2 \text{ eV}$ and $\text{F } 1s = 687.8 \text{ eV}$) [2]. In contrast, no new peak was observed on the specimen staying at a potential less noble than 0.5 V vs. H_2 in the open circuit after electrolysis at 25 mA/cm^2 for 100 hours, as shown in Fig. 2. With these results, it is considered that the oxide layer is composed of NiF_2 with a small amount of both oxides having multiple oxidation states of Ni and fluorides of trivalent and/or tetravalent oxidation states of Ni . The surface layers on the anode

electrolyzed in $\text{NH}_4\text{F} \cdot 2\text{HF}$ melts with CsF , NaF , and KF contained cesium, sodium, and potassium compounds, respectively.

Figure 3 shows the potential decay curves of the nickel anode electrolyzed at 25 mA/cm^2 and a few temperatures of 60, 80, and 100°C in an $\text{NH}_4\text{F} \cdot 2\text{HF}$ with and without alkali metal fluoride. When the polarization current was switched off, the potential dropped steeply to ca. 2 ~ 2.4 V, stayed at this potential for 1 ~ 10 minutes depending on temperature and the composition of melt, and moved to 0.5 V, which was close to the static potentials for NiO (0.18 ~ 0.20 V) and Ni_3O_4 (0.53 ~ 0.55 V). A stagnation at ca. 2 ~ 2.4 V is due to the coexistence of highly oxidized species. NiF_3 and NiF_4 (or M_3NiF_6 and M_2NiF_6 ; $\text{M} = \text{Cs, K, Li}$). The time of its stagnation decreased with increasing temperature and its time observed in the melt containing KF was long compared with that in $\text{NH}_4\text{F} \cdot 2\text{HF}$. On the other hand, the time the potential remained unchanged in the melts with LiF and CsF was almost the same as that in the melt of $\text{NH}_4\text{F} \cdot 2\text{HF}$ at 100°C and almost the same as that in the melt containing KF at 60°C . This means that the highly oxidized species in the oxide layer was stabilized by coexistence of alkali metal compounds and that the consumption rate of highly oxidized species increased with increasing temperature.

Figure 4 shows the effect of temperature on the current efficiency for the NF_3 formation in galvanostatic electrolysis at 25 mA/cm^2 , i.e., the rate of NF_3 formation. The rate of NF_3 formation increased with increasing temperature, and hence the time of stagnation at ca. 2 ~ 2.4 V is due to the rate of the reaction of ammonia with the highly oxidized species on the surface of film. That is, the faster the rate of the fluorination of ammonia with trivalent and/or tetravalent nickel compounds, the shorter the stagnation time at ca. 2 ~ 2.4 V. From these results, we propose a new mechanism of electrochemical fluorination in addition to the mechanism proposed in the previous papers [3, 4] as follows.





REFERENCES

- [1] A. Tasaka, K. Miki, T. Ohashi, S. Yamaguchi, M. Kanemaru, N. Iwanaga, and M. Aritsuka, *J. Electrochem. Soc.*, **141**, 1460 (1994).
- [2] C. A. Tolman, W. M. Riggs, W. J. Lim, C. M. King, and R. C. Wendt, *Inorg. Chem.*, **12**, 2770 (1973).
- [3] A. Tasaka, K. Mizuno, A. Kamata, and K. Miki, *J. Fluorine Chem.*, **57**, 121 (1992).
- [4] A. Tasaka, H. Kobayashi, M. Negami, M. Hori, T. Osada, K. Nagasaki, T. Ozaki, H. Nakayama, and K. Katamura, *Proceedings Volume 94-13*, p. 601 (1994); *J. Electrochem. Soc.*, Submitted.

Table 1 Effect of alkali metal fluorides added in the melt on current efficiencies of anode and cathode gases and current loss caused by Ni dissolution (Q_d/Q_c) in electrolysis at $25 \text{ mA} \cdot \text{cm}^{-2}$ and 120°C (393K) for 100 hours.

Melts	Current efficiencies of anode and cathode gases / %							Current loss caused by Ni dissolution (Q_d/Q_c) / %	
	NF ₃	N ₂	O ₂	N ₂ F ₄	N ₂ F ₂	N ₂ O	Overall		
NH ₄ F·2HF ^{a)}	49.2	20.1	9.26	4.83	1.47	7.18	92.0	92.9	2.51
NH ₄ F·2HF ^{b)}	45.2	23.1	4.22	4.16	1.32	5.21	83.2	87.2	2.45
NH ₄ F·2HF+0.1mol%LiF ^{b)}	53.0	19.9	4.46	5.56	0.77	3.51	87.2	88.1	1.47
NH ₄ F·2HF+0.3mol%LiF ^{a)}	68.3	12.6	3.41	4.25	0.54	4.56	93.7	94.6	1.37
NH ₄ F·2HF+0.3mol%LiF ^{b)}	53.3	24.1	6.15	3.22	0.67	1.15	88.6	88.7	1.37
NH ₄ F·2HF+0.9mol%LiF ^{b)}	54.8	18.4	8.70	2.98	1.14	1.24	87.3	87.7	1.36
NH ₄ F·2HF+6.7mol%CsF ^{a)}	59.0	19.1	0.61	5.75	1.15	7.75	93.4	95.3	2.85
CsF·3NH ₄ F·8HF(8.3mol%) ^{b)}	49.8	21.9	4.43	7.26	1.66	3.38	88.4	89.1	1.59
CsF·2NH ₄ F·6HF(11.1mol%) ^{b)}	55.5	22.1	4.31	3.13	0.65	3.33	89.0	89.7	1.46
CsF·NH ₄ F·4HF(16.7mol%) ^{b)}	36.1	33.7	8.52	3.61	0.80	2.69	85.4	90.1	1.39
NH ₄ F·2HF+0.3mol%NaF ^{a)}	57.9	11.1	6.79	6.57	0.92	8.86	92.1	92.9	2.01
NH ₄ F·2HF+6.7mol%NaF ^{a)}	56.9	25.3	2.11	4.24	0.85	2.72	92.1	94.0	3.14
NH ₄ F·2HF+0.3mol%KF ^{a)}	52.1	18.0	7.15	2.99	1.51	6.79	88.5	89.5	2.79
NH ₄ F·2HF+6.7mol%KF ^{a)}	48.0	30.7	1.21	3.55	0.49	5.84	89.8	92.6	3.40
KF·3NH ₄ F·8HF(8.3mol%) ^{b)}	39.8	35.9	3.91	0.66	0.21	2.73	83.2	83.2	3.81
KF·2NH ₄ F·6HF(11.1mol%) ^{b)}	40.4	35.2	2.11	0.49	0.14	4.50	82.8	81.3	4.12
KF·NH ₄ F·4HF(16.7mol%) ^{b)}	37.8	32.1	6.01	0.42	0.67	3.14	80.1	80.2	5.16

The cell was equipped with a nickel anode. Anode area = 24 cm^2 , Current density = $25 \text{ mA} \cdot \text{cm}^{-2}$.

a) Nickel cell, Time of line= 100 hours.

b) Nickel cell, Time of line= 80 hours.

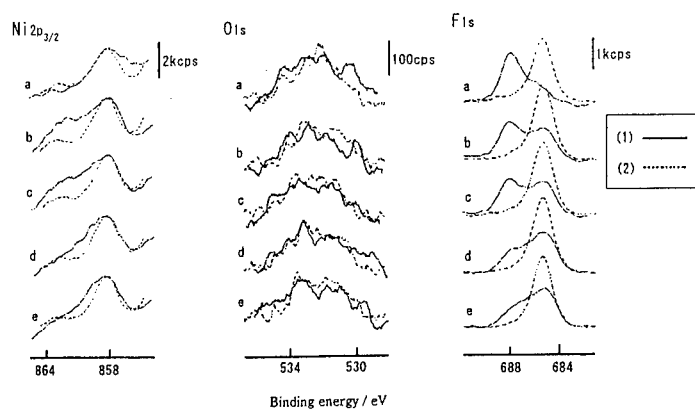


Fig. 1 X-ray photoelectron spectra of Ni $2p_{3/2}$, F $1s$, and O $1s$ levels on the nickel anode after electrolysis at 25 mA/cm^2 and 100°C for 100 hours in $\text{NH}_4\text{F} \cdot 2\text{HF}$. Specimens were washed with anhydrous HF (99.9%; solid line) and 47% HF aqueous solution (dotted line). (a) Outermost surface, (b) Exposed to Ar^+ beam for 30 seconds*, (c) Exposed to Ar^+ beam for 1 minute, (d) Exposed to Ar^+ beam for 10 minutes, (e) Exposed to Ar^+ beam for 30 minutes.

* Beam current = 20 mA at 2 kV.

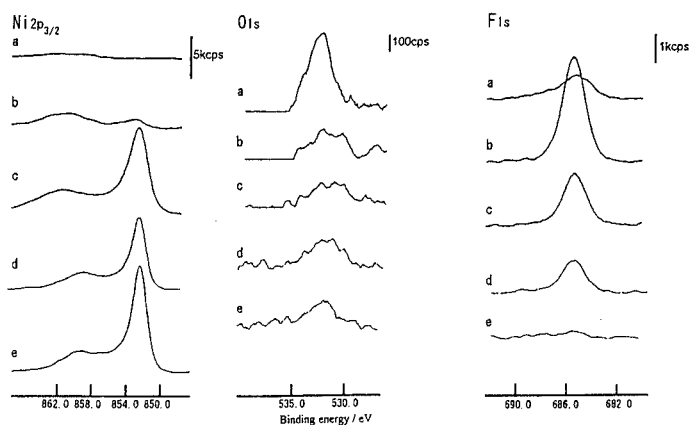


Fig. 2 X-ray photoelectron spectra of Ni $2p_{3/2}$, F $1s$, and O $1s$ levels on the nickel anode staying at a potential less noble than 0.5 V vs. H_2 in the open circuit after electrolysis at 25 mA/cm^2 and 100°C for 100 hours in $\text{NH}_4\text{F}\cdot 2\text{HF}$. Specimen was washed with anhydrous HF (99.9%). (a) Outermost surface, (b) Exposed to Ar^+ beam for 30 secs.*, (c) Exposed to Ar^+ beam for 1 min., (d) Exposed to Ar^+ beam for 10 mins., (e) Exposed to Ar^+ beam for 30 mins.

* Beam current = 20 mA at 2 kV.

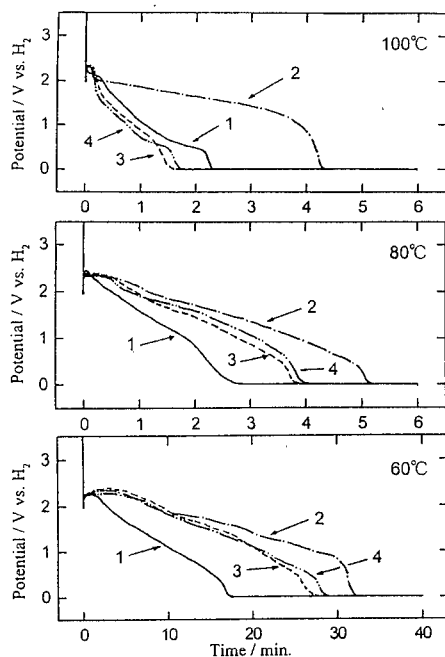


Fig. 3 Potential decay curves of a nickel anode polarized at 5 V vs. H_2 and temperatures of 60, 80, and 100°C for 90 minutes in well dehydrated melts.

Curve 1; $\text{NH}_4\text{F}\cdot 2\text{HF}$,
Curve 2; $\text{KF}\cdot 2\text{NH}_4\text{F}\cdot 6\text{HF}$,
Curve 3; $\text{CsF}\cdot 2\text{NH}_4\text{F}\cdot 6\text{HF}$,
Curve 4; $\text{NH}_4\text{F}\cdot 2\text{HF} + 0.3\text{mol}\% \text{LiF}$.

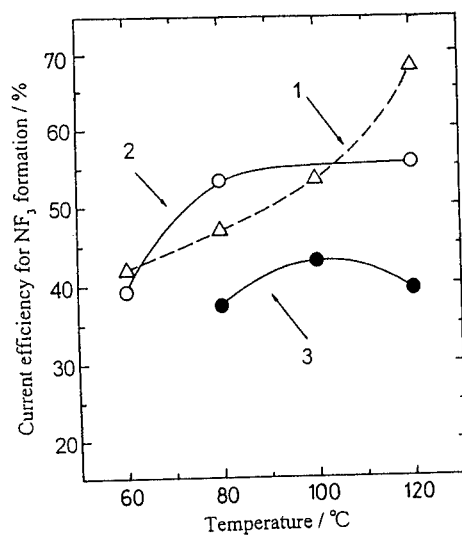


Fig. 4 Effect of temperature on current efficiency for the NF_3 formation in electrolysis at 25 mA/cm^2 in molten $\text{LiF-NH}_4\text{F-HF}$ and $\text{CsF-NH}_4\text{F-HF}$ systems.

- 1 (Δ); $\text{NH}_4\text{F} \cdot 2\text{HF} + 0.3\text{mol}\% \text{LiF}$, 2 (\circ); $\text{CsF} \cdot 2\text{NH}_4\text{F} \cdot 6\text{HF}$,
 3 (\bullet); $\text{CsF} \cdot \text{NH}_4\text{F} \cdot 4\text{HF}$.

Spectroscopic Investigation of Effect of Lewis Basicity on the Valent-State Stability of an Uranium(V) Chloride Complex in Ambient Temperature Melts

Sheng Dai,^a L. M. Toth,^a G.D. Del Cul,^a G. R. Hayes,^b and J.R. Peterson^{b,c}

^aChemical Technology Division, Oak Ridge National Laboratory, P.O. Box 2008, Oak Ridge, TN 37831-6181

^bDepartment of Chemistry, University of Tennessee, Knoxville, TN 37996-1600

^cTransuranium Research Laboratory, Oak Ridge National Laboratory, P.O. Box 2008, Oak Ridge, TN 37831-6375, USA

Abstract

The visible and NIR absorption spectrum of uranium(V) chloride in room temperature acidic melts has been measured. This spectrum was obtained by the direct dissolution of an uranium(V) chloride compound into a room-temperature melt. Changing the acidic melt to a basic melt by adding EMIC caused the gradual disappearance of the U(V) spectrum and the concomitant appearance of a new set of bands. The absorption spectrum recorded in the basic melt of composition $\text{AlCl}_3\text{:EMIC} = 45\text{:}55$ is identical to that from the uranium(IV) hexachloride complex in the same melt. This conversion of U(V) to U(IV) establishes that the uranium(V) chloride complex underwent a reduction reaction to form the uranium(IV) hexachloride complex. The stoichiometric ratio of U(total) : U(IV) in this redox process was experimentally determined to be 1:1. This suggests that the formation of uranium (IV) hexachloride in the basic melt is not via the disproportionation reaction of U(V).

Although the UV-visible and near-IR(NIR) spectra of uranyl(VI) and uranium(IV) chloride complexes in molten chloride melts have been widely investigated,¹⁻⁴ Adams *et al.*⁵ and Wenz *et al.*⁶ have found the formation of UO_2^+ in the dissolution of UO_3 in high-temperature molten KCl-MgCl_2 . Later, Dewaele *et al.* suggested the formation of an uranium(V) complex during the electrolytic oxidation of uranium(IV) in room-temperature acidic melts.⁷ In the present note, the visible and NIR absorption spectrum of uranium(V) chloride in room temperature acidic melts is reported. This spectrum was obtained by the direct dissolution of an uranium(V) chloride compound into the melts. An unusual dependence of the chemical stability of the uranium(V) chloride complex on the Lewis basicity has been found.

The preparation and purification of uranium(IV) tetrachloride has been reported previously.^{4,8} The UCl_4 was purified by loading the nominally pure starting material in a silica tube and pumping it down to $\sim 20\text{ }\mu\text{m Hg}$ at $650\text{ }^\circ\text{C}$ to remove any moisture or HCl .

The tube was then sealed, and UCl_4 was sublimed at 510°C from one end of the tube to the other. The uranium trioxide was prepared according to the standard literature procedure.⁹ The preparation of $\text{UCl}_5 \cdot \text{SOCl}_2$ was also according to the literature.¹⁰ Briefly, $\text{UCl}_5 \cdot \text{SOCl}_2$ was obtained by refluxing UO_3 with excess SOCl_2 for two weeks, followed by removal of excess SOCl_2 by distillation. The procedure for the purification of AlCl_3 has been described previously.¹¹ 1-Ethyl-3-methyl-imidazolium chloride (EMIC) was synthesized according to the procedure of Smith *et al.*¹² All molten salt solutions were prepared under helium atmosphere in a drybox with <1 ppm moisture. Visible and NIR spectra were measured at room temperature with a Cary 14H scanning spectrophotometer converted by On-Line Instrument Systems (OLIS) for data acquisition and analysis by a PC computer. Samples were loaded into a quartz cuvette (1 cm pathlength) with a threaded glass cap.

The spectrum of $\text{UCl}_5 \cdot \text{SOCl}_2$ dissolved in an acidic melt ($\text{AlCl}_3:\text{EMIC} = 62:38$) is given in Figure 1. (An acidic melt is defined to contain a molar excess of AlCl_3 relative to the organic salt, while a basic melt contains a molar excess of the organic salt relative to AlCl_3 . The excess aluminum chloride in acidic melts can then act as a Lewis acid.) As can be seen from the Figure 1, the spectrum consists of many peaks with the characteristic narrow vibronic bands around 1500 nm. This spectrum is almost identical to that recorded from the UCl_6^- complex prepared by dissolving $\text{UCl}_5 \cdot \text{SOCl}_2$ into other non-aqueous solvents.¹³ Accordingly, we assigned the spectrum in Figure 1 to that of the uranium(V) hexachloride complex. The formation of the uranium(V) hexachloride complex in the acidic melt implies that the affinity of UCl_5 to Cl^- ion is greater than that of AlCl_3 to Cl^- ion.

It is well known that visible and NIR absorption spectra of uranium(V) complexes result from the f-f transitions in U^{5+} ion. Because these f-f electronic transitions are Laporte forbidden, the observed bands arise from the relaxation of the selection rule via either a static or a vibronic interaction. Our previous studies^{14, 15} of UCl_4 in similar melts and crystal-host matrices have indicated that the electronic transition selection rule can be relaxed via a static mechanism such as hydrogen bonding between the uranium(IV) chloride complex and the organic cation (EMI^+). The observation of a strong vibronic origin transition is usually an indication of the selection-rule relaxation by a static mechanism.¹⁴ According to Selbin and Ortego,¹³ the band around 1478 nm in Figure 1 is due to the electronic transition from Γ_7 ($^2F_{5/2}$) to Γ_7' ($^2F_{7/2}$). As seen clearly from the inset in Figure 1, the origin transition is the strongest of the transitions in this band. This is consistent with our expectation that the f-f transitions of the uranium(V) hexachloride complex in the room-temperature molten salt are mainly induced by the relaxation of the selection rule via a static mechanism. The peaks located symmetrically around the origin transition are vibronic transitions induced by *odd* vibrational modes. The peaks on the high energy side of the origin are non-hot bands, whose transition frequencies can be expressed as $\nu_0 + \nu$, where ν_0 and ν are the electronic origin transition frequency and odd vibrational transition frequency, respectively. Similarly, the peaks on the low energy side of the origin are equal to $\nu_0 - \nu$. Because these vibronic transitions are well resolved, it is possible to make assignments of vibrational modes in octahedral UCl_6^- species from the

vibronic spectrum. As already pointed out above, the odd vibrational modes are expected to couple most strongly with the electronic transitions. In our case, these odd vibrational modes are ν_3 , ν_4 , and ν_6 of the octahedral complex. (The nomenclature follows the assignments by Nakamoto.¹⁶) The ν_6 mode (T_{2g} symmetry) involves only angle deformations, whereas the ν_3 and ν_4 modes involve uranium-halogen bond stretching. A comparison of the vibrational frequencies observed in our system and those in the literature¹³ is given in Table 1.

Changing the above acidic melt to a basic melt by adding EMIC caused the gradual disappearance of the U(V) spectrum and the concomitant appearance of a new set of bands. The absorption spectrum recorded in the basic melt of composition $\text{AlCl}_3:\text{EMIC} = 45:55$ is given in Figure 2a. This spectrum is identical to that from the uranium(IV) hexachloride complex in the same melt (Figure 2b). This conversion of U(V) to U(IV) establishes that the uranium(V) chloride complex underwent a reduction reaction to form the uranium(IV) hexachloride complex. Because the molar extinction coefficient of uranium(IV) hexachloride in the basic melt has been determined previously,^{3,14} the stoichiometric ratio of U(total) : U(IV) in this redox process was experimentally determined to be 1:1. This suggests that the formation of uranium (IV) hexachloride in the basic melt is not via the disproportionation reaction of U(V), i.e., $2\text{UCl}_5 \rightarrow \text{UCl}_6 + \text{UCl}_4$. Therefore, we conclude that the uranium(IV) species is formed as a result of the oxidation of one or more components of the basic melt by the uranium(V) hexachloride complex. Clearly, the redox chemistry of uranium(V) in molten salts is very different from that in aqueous solutions, where the disproportionation is a dominant process. Hussey and his coworkers have found a similar reduction reaction in the dissolution of MoCl_5 in the same kind of basic melt.¹⁷ In their case, a total reduction of MoCl_5 to MoCl_6^{2-} was observed.

In conclusion, the optical spectrum of an uranium(V) chloride complex obtained by the dissolution of $\text{UCl}_5 \cdot \text{SOCl}_2$ in an acidic chloroaluminate melt has been measured. The characteristic fine vibronic structure is consistent with uranium(V) hexachloride complex. The dependence of the stability of this uranium(V) complex on the Lewis acidity of the melt has been demonstrated. The formation of an uranium(IV) hexachloride complex from the initial uranium(V) hexachloride complex as the melt becomes basic is facilitated by the oxidation of the melt components not the result of disproportionation reaction of the uranium(V) hexachloride complex.

Acknowledgement: This work was supported by the Division of Chemical Sciences, Office of Basic Energy Sciences, U.S. Department of Energy, under contract No. DE-AC05-84OR21400 with Lockheed Martin Energy Systems. The authors thank Prof. K.R. Seddon (Bristol University, UK) for pointing out reference 17.

References

1. Gruen, D.M. and McBeth, R.L., *J. Inorg. Nucl. Chem.*, **1959**, *9*, 290.
2. Morrey, J.R., *Inorg. Chem.*, **1963**, *2*, 163.
3. Anderson, C. J., Deakin, M. R., Choppin, G. R.; D'Olieslager, W.; Heerman, L.;

- and Pruett, D. J., *Inorg. Chem.*, **1991**, *30*, 4013.
4. Dai, S.; Toth, L.M.; Del Cul, G.D.; and Metcalf, D.H., *Inorg. Chem.*, **1995**, *34*, 412.
 5. Adams, M.D.; Wenz, D. A.; and Steunenberg, R. K., *J. Phys. Chem.*, **1963**, *67*, 1939
 6. Wenz, D. A; Adams, M.D.; and Steunenberg, R. K., *J. Inorg. Nucl. Chem.* **1964**, *3*, 989.
 7. Dewaele, R.; Heerman, L.; and D'Olieslager, W., *J. Electroanal. Chem.*, **1982**, *142*, 137.
 8. Toth, L. M.; Felker, L. K.; Hunt, R. D.; Brunson, R. R.; and Loghry, S. L., *Separation Science and Technology*, **1993**, *28*, 781.
 9. Hoekstra, H. R. and Siegel, S., *J. Inorg. Nucl. Chem.*, **1961**, *18*, 154.
 10. Bradley, D. C.; Chakravarti, B. N.; and Chatterjee, A. K., *J. Inorg. Nucl. Chem.*, **1957**, *3*, 367
 11. Marassi, R.; Chambers, J. Q.; and Mamantov, G., *J. Electroanal. Chem. Interfacial Electrochem.*, **1976**, *69*, 345.
 12. Smith, G. P.; Dworkin, A. S.; Pagni, R. M.; and Zingg, S. P., *J. Am. Chem. Soc.*, **1989**, *111*, 525.
 13. Selbin, J. and Ortego, J. D., *Chem. Rev.*, **1969**, *69*, 657.
 14. Dai, S.; Toth, L. M.; Del Cul, G. D.; and Metcalf, D. H., *Proceedings of the Ninth International Symposium on Molten Salts*, C. L. Hussey, D. S. Newman, G. Mamantov, and Y. Ito, Editors, p. 308, Electrochemical Society, Pennington, NJ, 1994.
 15. Dai, S.; Toth, L. M.; Del Cul, G. D.; and Metcalf, D. H., *Chem. Phys.*, in press.
 16. Nakamoto, K., *Infrared and Raman Spectra of Inorganic and Coordination Compunds*, New York: Wiley, 1986.
 17. Scheffler, T. R.; Hussey, C. L.; Seddon, K. R.; Kear, C. M.; and Armitage, P. D., *Inorg. Chem.*, **1983**, *22*, 2099.

Table 1. Vibrational frequencies of octahedral uranium(V) hexachloride complexes obtained from the respective vibronic absorption spectra.

Vibrational Mode	Vibrational Freq. (cm ⁻¹ , this work)	Vibration Freq. (cm ⁻¹ , literature) ¹³
ν_3	312.0	315.0
ν_4	122.0	122.0
ν_6	91.0	92.0

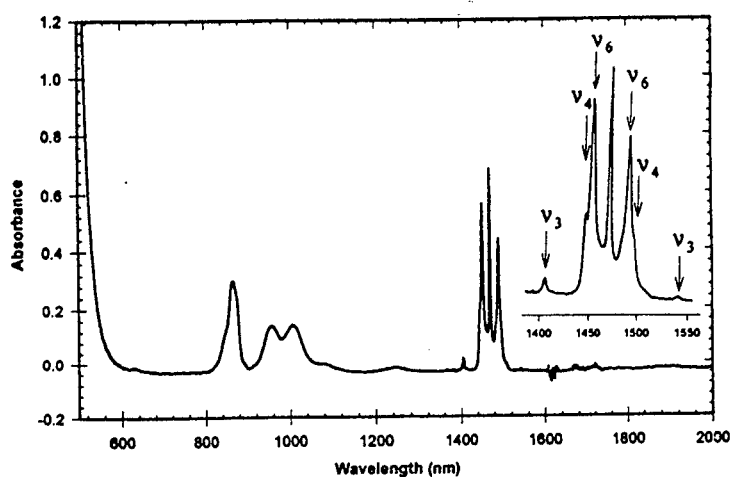


Figure 1. UV-visible spectrum from an uranium(V) hexachloride complex in an acidic melt ($\text{AlCl}_3\text{:EMIC} = 62\text{:}38$) at room temperature.

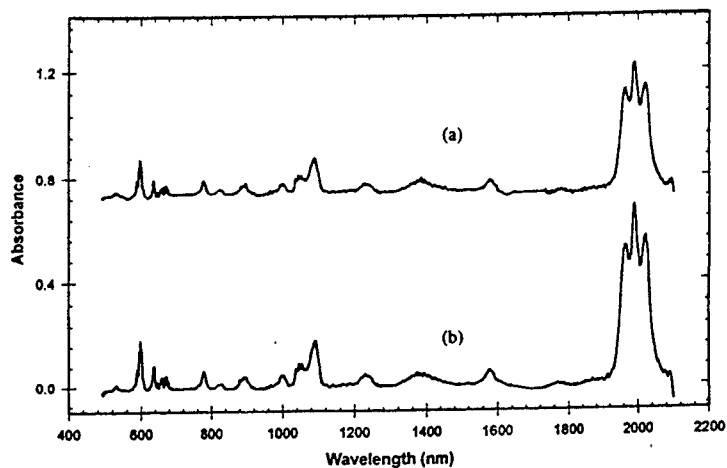


Figure 2. UV-visible spectrum recorded at room temperature from (a) an uranium(IV) hexachloride complex in a basic melt ($\text{AlCl}_3\text{:EMIC} = 45\text{:}55$) prepared by the direct dissolution of UCl_4 into the melt; and (b) an uranium(IV) hexachloride complex in a basic melt ($\text{AlCl}_3\text{:EMIC} = 45\text{:}55$) prepared by addition of EMIC to an acidic melt containing uranium(V) hexachloride complex.

ELECTRODEPOSITION OF MAGNESIUM FROM HALIDE MELTS

B. Børresen, G.M. Haarberg, R. Tunold,
A. Kiszka* and J. Kazmierczak*

Department of Electrochemistry
Norwegian University of Science and Technology
N-7034 Trondheim, Norway

*Institute of Chemistry
University of Wrocław
Wrocław, Poland

SUMMARY

Different aspects of the cathodic deposition of magnesium from molten halides have been investigated. The charge transfer, which was determined by a combined AC impedance/potential relaxation technique, follows a two step mechanism. The first step is rate controlling with a significant effect of melt composition, while the second step is very fast with an exchange cd of 25-30 A cm⁻² at 750°C.

At potentials above a critical nucleation potential, underpotential deposition of a monolayer or a few layers of Mg is observed. In this region the reaction is either controlled by diffusion of reactant, in dilute solutions, or product; ie dissolved magnesium, in pure MgCl₂.

Nucleation seems to be instantaneous in dilute solution and changes from progressive to instantaneous (constant number of nuclei) at high negative potentials in pure magnesium halide melts. Unstable nucleation is found at some conditions and is related to the observation of a fog.

INTRODUCTION

Cathodic deposition of magnesium from various chloride melts on different substrates has been studied by several authors /1-5/. Most of the electrochemical measurements in MgCl_2 containing melts reported in the literature has been performed in dilute solutions of Mg(II) -species, typically 0.1-10 wt %.

In dilute solutions the cathode process has been found to be controlled by diffusion of the reactant. Alloy formation has been observed on platinum, as reported by Tunold /1/ and Duan et al /3/. The rate constant of the charge transfer process on a Mg/Ni electrode in molten $\text{NaCl-CaCl}_2\text{-MgCl}_2$ was reported by Tunold to have a value of about 0.01 cm/s. This author also reported the underpotential deposition of a monolayer on iron electrodes, at potentials approximately 100 mV positive to the Mg deposition potential.

The kinetics of a liquid magnesium electrode in pure molten MgCl_2 has been determined by combining ac-impedance spectra and galvanostatic relaxation transients, by Kiszka et al /6/. These authors concluded that the charge transfer is a two step process and that the rate determining step is the reduction of a Mg(II) species to a Mg(I) species with an exchange cd of about 2.5 A cm^{-2} at 750°C whereas the second charge transfer step is very fast with an exchange cd of about 25 A cm^{-2} at the same temperature. The charge transfer process could be preceded by the slow dissociation of a polynuclear magnesium complex.

The present authors reported earlier that the deposition process was found to be unstable under certain circumstances. The instability was observed as an oscillating current during potentiostatic deposition of magnesium on glassy carbon from pure MgCl_2 /7/.

Raman spectroscopic studies of molten magnesium chloride and alkali chloride-magnesium chloride mixtures have been reported by Balasubramanyam /8/, Capwell /9/ and Huang and Brooker /10/. There is a general agreement that molten magnesium chloride to a certain extent retains the polynuclear structure found in the solid state, also in the liquid state. Huang and Brooker /10/ observed peaks which were assigned to tetrahedral MgCl_4^{2-} -species also in pure MgCl_2 .

The reported measurements are part of an extensive study of the cathode process in pure and dilute molten magnesium halides.

EXPERIMENTAL

Anhydrous MgCl_2 was prepared by drying magnesium hexahydrate (Merck, p.a) in HCl(g) during slow heating to 450°C and subsequently distilled under vacuum ($p < 0.1$ Pa). MgF_2 , NaCl and KCl were dried under vacuum at temperatures slowly increasing up to 600°C . LiCl was treated by dry HCl gas at temperatures slowly increasing up to 400°C and then melted under vacuum and filtered. MgCl_2 is very hygroscopic and all handling of the salts was carried out in a glove box with dry argon atmosphere. During measurements the experimental cell was also purged with dry argon.

The working electrodes were rods of glassy carbon (Tokai, GC30S), iron (Johnson Matthey, specpure) or molybdenum (Riedel-DeHaen AG, 99.8%) pressed into graphite. The counter electrode was either a graphite or a glassy carbon rod, while the reference electrode was either magnesium metal contained in an oxide tube in direct contact with the melt or a platinum wire acting as a quasi-reversible reference electrode.

RESULTS AND DISCUSSION

Charge transfer kinetics in the binary system MgCl_2 - NaCl

The rate of charge transfer of metallic electrodes in molten binary mixtures as a function of composition is not determined frequently due to lack of methods for studying fast electrode reactions. In this case the combination of impedance spectroscopy and potential relaxation after current interruption has been used. This combination method is developed by Kiszka /11,12/ and has been used for the determination of very high exchange cds, up to 200 A cm^{-2} , as in the pure NaCl melt /13/.

In the present work kinetic parameters for the Mg electrode in the system MgCl_2 - NaCl were determined in the concentration range from 20 to 100% MgCl_2 and in the temperature range from 540° (for some compositions) to 820°C .

The analysis of the data shows that the reduction of the Mg(II) species is a two step charge transfer process. The values of i_0 for the high frequency step at different compositions and temperatures are tabulated in Table 1. The results correspond to a step with very high charge transfer rate. The rate of this step increases with temperature, but does not change very much with composition, with only a shallow maximum around $x_{\text{MgCl}_2} = 0.75$.

The exchange cd of the low frequency step as a function of composition at 755°C is shown in Fig 1. The rate of this step increases sharply with decrease in x_{MgCl_2} from 2.7 A cm^{-2} in pure MgCl_2 to 11.6 A cm^{-2} at 75 mol% MgCl_2 and then decreases continuously to about 3.0 A cm^{-2} at 20 mol% MgCl_2 .

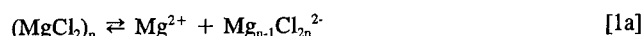
Table 1. Values of the exchange current density (A/cm²) of the high frequency second step for different melts at various temperatures.

x_{MgCl_2}	1.0	0.88	0.75	0.63	0.50	0.33	0.2
T°C							
725	20.6	25.2	26.0	25.6	26.7	25.9	19.8
740	(28.3)	27.4	29.5	28.3	28.9	27.7	20.9
755	24.7	29.7	33.3	31.3	31.2	29.6	22.1
770	26.7	32.1	37.4	34.4	33.6	31.5	23.3
785	34.7	34.6	41.9	37.8	36.2	33.5	24.5

The mechanism of the charge transfer

In pure molten MgCl_2 polynuclear complexes exist which retain parts of the structure in solid MgCl_2 , as shown by Raman spectroscopy /10/. When alkali chlorides are added, more mobile structures are created with the subsequent formation of very stable tetrahedral MgCl_4^{2-} complex ions. When adding NaCl to MgCl_2 the availability of "free" Mg(II) -species increases. In Fig 1 is also drawn the activity vs composition curve for MgCl_2 as determined potentiometrically by Ikeuchi and Krohn /14/. The figure shows a very interesting correlation between a_{MgCl_2} and the exchange cd for the low frequency step in the range of 75 to 20% MgCl_2 . These results reveal that the rather slow low frequency step most probably is the first, composition dependent step whereas the fast high frequency and composition independent step is the second one in the total charge transfer process.

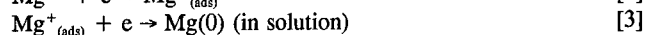
The primary step probably consists of breaking up of a polynuclear species. In pure or nearly pure MgCl_2 it might formally be written in the following way:



The addition of NaCl increases the availability of "free" Mg^{2+} . At higher concentrations of alkali chloride the tetrahedral complex is formed, which dissociates according to:



The next two steps can then be formulated as follows /13/:



The very high rate of the second charge transfer step probably means that the monovalent species are very unstable and exist only at the interface. The dimeric form of the monovalent species, Mg_2^{2+} , is probably more stable as proposed by van Norman and Egan /15/. The two electrons which are transferred into the homogeneous solution are strongly trapped by the magnesium species. No measurable electronic conductivity due to mobile electrons is observed in the Mg-MgCl_2 system /16/.

UNDERPOTENTIAL DEPOSITION AND DIFFUSION

A typical voltammogram obtained on glassy carbon (GC) electrodes in pure molten MgCl_2 is given in Fig 2. Similar voltammograms were obtained in molten $\text{MgCl}_2\text{-MgF}_2$. The magnesium deposition is observed as wave (A). By reversing the potential scan, peak (B), which is typical for stripping of a deposit, is recorded. The chlorine evolution is observed as wave (C). The peaks D and D' are most likely due to the formation and dissolution of an adsorbed layer of reduced magnesium species equivalent to an underpotential deposition (UPD). The charge of the cathodic prepeak (D) corresponds to 1-3 monolayers while the charge corresponding to the anodic peak (D') in general is somewhat higher and typically amounts to 3-8 monolayers. This means that the charge involved in the UPD increased during normal deposition of Mg. The difference between the peak potential of the underpotential deposition on glassy carbon and the potential of the magnesium reference electrode was found to be 50 to 100 mV, which corresponds to an energy difference of 10 to 20 kJ/mol. Such underpotential deposition was also observed on metallic electrodes (Fe, Mo), but the observed peaks (due to the UPD process) were less reproducible on these electrodes. This could be due to problems related to removal of all magnesium deposited in the UPD process between each potential scan. There also exists the possibility of a very small alloy formation with the metallic substrates, even if molybdenum is not known to alloy with magnesium and iron alloys to an insignificant extent.

By applying cathodic potential pulses a hump due to UPD was observed, as shown in Fig 3. The charge associated with this hump was found to be 0.5-0.6 mC/cm^2 at temperatures above the melting point of magnesium and 0.1-0.3 mC/cm^2 at 647°C, which is below the melting point of Mg (650°C). The theoretical charge required to form a dense monolayer of magnesium atoms is about 0.8 mC/cm^2 . Consequently the obtained data indicate that the electrode becomes only partly covered by this layer during the initial period (~ 0.15 ms). By comparing this information with the estimated charge from corresponding peaks in the voltammogram, it seems that the layer formation takes place on a more extended time scale than indicated by the hump in the current transients. The charge of this layer was not found to depend significantly on the applied potential in the region studied (+ 50 mV to - 30 mV vs Mg). Similar values have been obtained also on iron electrodes in the pure MgCl_2 system. To study this UPD further current transients were plotted as $\log i$ versus $\log t$. The slopes of these plots were expected to be close to

one, which would indicate the nucleation of a two dimensional adsorption layer /17/. The calculated slopes, however, were much lower (0.01-0.05) for the iron electrode in MgCl_2 as well as the glassy carbon electrode in the MgCl_2 - MgF_2 mixture. This can be explained by more than one process in parallel in the actual time range. These processes are likely to be charge transfer followed by nucleation at the surface and/or diffusion of dissolved magnesium away from the electrode surface.

From the voltammogram in Fig 2 a small limiting cd is observed at potentials anodic (positive) to the UPD. In this potentials range also diffusion controlled transients following the Cottrell equation were recorded, both for pure MgCl_2 and MgCl_2 - MgF_2 melts. Since Mg(II) -species are the only cations in these melts the mass transfer controlled process most likely corresponds to diffusion of the product, which is metal going into homogeneous solution in the melt and diffusing away from the electrode interphase to the bulk electrolyte.

NUCLEATION AND PHASE FORMATION OF Mg

Nucleation of magnesium from various halide melts was studied by classical electrochemical techniques. In order to compare the behaviour in concentrated and dilute systems, both pure MgCl_2 and MgCl_2 - MgF_2 and mixtures of alkali chlorides with small amounts of MgCl_2 , were investigated. The phenomenon with the formation of so called metal "fog" was studied by visual observations and electrochemical oxidation.

At potentials negative to a critical nucleation potential, nucleation and formation of a Mg phase started. This critical potential was determined to be about - 15 mV for Mo electrodes and about - 20 mV for electrodes of Fe and GC. Potentiostatic current transients for nucleation and growth during deposition of Mg on GC from a melt of 5 wt% MgCl_2 in NaCl-KCl at 750°C are shown in Fig 4. Log/log plots of the rising parts of the same transients where overlap of the single nuclei are not prevailing, are shown in Fig 5. The slopes of these plots vary from 0.3 to 0.5 with a slight increase with decreasing potential. Similar log/log plots are shown in Fig 6 for pure MgCl_2 at 750°C.

Nucleation mechanisms

The transients of nucleation have different shapes depending on which type of nucleation kinetics are prevailing. In the following we have summarized the ideal theoretical time dependency of the rising part of the current for different rate controlling steps at short times /18,19/.

Two dimensional (monolayer):

$$\begin{array}{ll}\text{Instantaneous:} & i \sim K_1 \cdot t \\ \text{Progressive:} & i \sim K_2 \cdot t^2\end{array}$$

Three dimensional nucleation:

$$\begin{array}{ll}\text{Instantaneous:} & i \sim K_3 \cdot t^2 \\ \text{Progressive:} & i \sim K_4 \cdot t^3\end{array}$$

Three dimensional with diffusion control:

$$\begin{array}{ll}\text{Instantaneous:} & i \sim K_5 \cdot t^{1/2} \\ \text{Progressive:} & i \sim K_6 \cdot t^{3/2}\end{array}$$

In dilute melts we obtained exponents varying between 0.3 and 0.5. This points to instantaneous nucleation; i.e. (nearly) all nuclei form from start (instantaneously) and grow with diffusion control. In the pure melt it seems that the nucleation could be instantaneous at low cathodic overpotentials with an exponent of about 0.7. At high cathodic overpotentials the mechanism seem to change from progressive to instantaneous, where the number of nuclei becomes constant, corresponding to a decrease in the exponent from 1.6 to 0.4-0.5. Possible mechanisms are either control by diffusion of homogeneously dissolved metal in supersaturation or that small nuclei are growing under the control of migration of magnesium cations. These two types of transport should be governed by similar laws. The mechanism then depends on the site of the charge transfer.

In "oxide free" melts (see later) nucleation seemed to be dependent on the substrate. On Mo electrodes nucleation was always stable with a rather constant current vs time behaviour. It seemed that the nucleation was very fast on this material with a high number of, probably, two dimensional nuclei that continued to grow like a two dimensional film, layer by layer.

In most cases the iron electrodes exhibited "normal" behaviour with a falling, diffusion controlled transient followed by a rising portion, as discussed above.

With nearly all the GC electrodes at high cathodic potentials and some of the totally fresh iron electrode surfaces, unstable nucleation took place in "oxide free" melts.

Stability of nuclei, effect of substrate and oxide content

The oxide content in the melt could be varied qualitatively from a very low level in "oxide free" melts to saturation. In the "oxide free" melts a Pt wire was used as the reference electrode. In this way all ceramic materials, including the ceramic tube containing the Mg-reference electrode, could be omitted. The Pt electrode was rather stable but is not thermodynamically defined. As can be observed in Fig 7, which shows transients on GC electrodes in an "oxide free" pure MgCl_2 melt, the current suddenly changed from cathodic to anodic giving rise to an oscillatory behaviour. The interpretation of these transients is as follows: In the first period of time nucleation occurs. In the second period nucleation stops and all, or part of the nuclei, seem to dissolve anodically giving rise to an anodic current. Subsequent nucleation and dissolution periods are following. One reason for this could be that the reference electrode is exposed to a wave of dissolved chlorine from the anode reaction. This then would bring the potentials of the reference electrode and thereby the working electrode, in the anodic direction. This explanation seem not to be valid, however, since instability on GC electrodes were also found with a Mg reference electrode surrounded by a MgO tube.

Another possible explanation is connected with the "fog" formation, which is a phenomenon observed when producing molten metals from melts. The nature of this fog is not clear but one possible explanation is that the fog consists of very small molten particles nucleated homogeneously from a melt, supersaturated with dissolved metal. The necessity of a certain supersaturation is well known for all types of nucleation processes. Consequently the melt is supersaturated with respect to dissolved metal when magnesium nucleates at the electrode. The degree of critical supersaturation will depend on the interfacial interaction between the metal, the melt and the substrate. In a very cathodic potential pulse the supersaturation becomes very high with the possibility of an abrupt homogeneous nucleation and growth to tiny droplets in the melt adjacent to the electrode. This would then lead to a sudden reduction in the concentration of dissolved metal in the interphase with a corresponding instability of the smallest magnesium nuclei attached to the electrode with subsequent electrochemical dissolution.

A high level of oxide in the melt seems to stabilize the nuclei, probably by changing the surface energy of magnesium. The same is true for nucleation of solid Mg. No instability was found below the melting point of Mg.

Fog formation

Optically one could observe the fog formation at the electrode/electrolyte interphase immediately (within 2-3 s) after applying a cathodic pulse. The particulate nature of this fog is indicated by the voltammogram in Fig 8, obtained in a dilute melt with

5 wt% MgCl_2 + 3% MgF_2 in NaCl-KCl. After cathodic deposition the anodic oxidation wave shows small narrow peaks over the whole anodic potential range superimposed on a general oxidation wave. If one presume that each peak is associated with the oxidation of one tiny Mg-particle (droplet), then the diameter of these peaks varies between 40 and 120 μm . Similar results have been obtained in pure MgCl_2 .

CONCLUSIONS

The total process in the deposition of magnesium from halide melts consists of several steps, diffusion of reactants in dilute melts, charge transfer, diffusion of metal dissolved in the melt from the interphase and nucleation and growth of a Mg phase.

The charge transfer follows a two step process with a composition dependent slower first step and a composition independent very fast second step.

Underpotential deposition and nucleation are observed. Nucleation kinetics vary with substrate and potential. The stability of nuclei also depends on substrate and on the oxide level in the melt.

REFERENCES

1. R. Tunold, Light Metals, 109th AIME Annual Meeting, 949 (1980).
2. G.M. Rao, J. Electroanal. Chem., **16**, 775 (1986).
3. S. Duan, P.G. Dudley and D. Inman, Proc. fifth Int. Symp. Molten Salts, The Electrochem. Soc., **86-1**, 248 (1986).
4. S.Y. Yoon, "A Spectroelectrochemical Study of Aluminium and Magnesium Electrolysis in Molten Chlorides", Ph.D.thesis, MIT, 1987.
5. Z. Youngjin and L. Liangming, J. Cent.-South Inst. Min.metal, **22** (5), 529 (1992).
6. A. Kiszka, J. Kazmierczak, B. Børresen, G.M. Haarberg and R. Tunold, J. Appl Electrochem., **25**, 940 (1995).
7. B. Børresen, G.M. Haarberg, R. Tunold and O. Wallevik, J. Electrochem. Soc., **140** (6), L99 (1993).
8. K. Balasubrahmanyam, J. Chem. Phys., **44** (3), 443 (1972).

-
9. R.J. Capwell, *Chem. Phys. Letters*, **12** (3), 443 (1972).
 10. C.H. Huang and M.H. Brooker, *Chem. Phys. Letters*, **43** (1), 180 (1976).
 11. A. Kiszka, *Polish J. Chem.*, **67**, 885 (1993).
 12. A. Kiszka, *Polish J. Chem.*, **68**, 613 (1994).
 13. A. Kiszka, J. Kazmierczak, B. Børresen, G.M. Haarberg and R. Tunold, *J. Electrochem. Soc.*, **142**, 1035 (1995).
 14. H. Ikeuchi and C. Krohn, *Acta Chem. Scand.*, **23**, 2230 (1969).
 15. J.D. van Norman and J.J. Egan, *J. Phys. Chem.*, **67**, 2460 (1963).
 16. J.J. Egan, private communication.
 17. E. Budevski, *Progress in Surface and Membrane Science*, Eds. D.A. Cadenhead and J.F. Daniell, Academic press, **11**, 71 (1976).
 18. R.D. Armstrong, M. Fleischmann and H.R. Thirsk, *J. Electroanal. Chem.*, **11**, 205 (1966).
 19. *Instrumental Methods in Electrochemistry*, ed Southampton Electrochemistry Group, Ellis Harwood, London (1990).

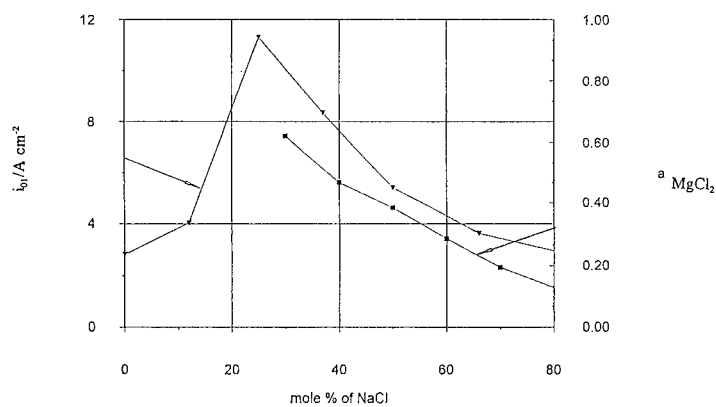


Fig 1. The exchange cd of the first step in the discharge of Mg(II) species in the system MgCl_2 -NaCl as a function of composition and compared with activity data for MgCl_2 .

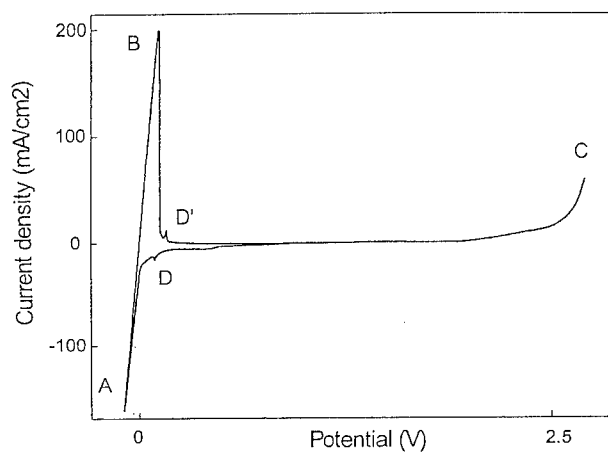


Fig 2. Cyclic voltammogram on a glassy carbon (GC) electrode in molten MgCl_2 at 725°C , sweep rate 100 mVs^{-1} .

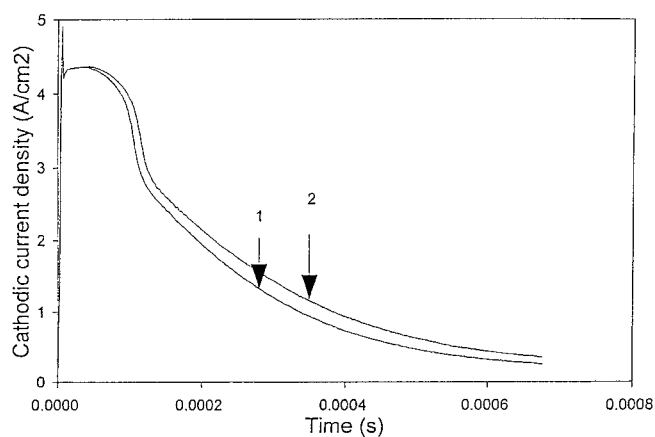


Fig 3. Cathodic current transients on GC electrode in $\text{MgCl}_2\text{-MgF}_2$, $T = 656^\circ\text{C}$. Applied potential 1) + 20 mV, 2) + 10 mV vs $E_{\text{Mg}(\text{dep})}$.

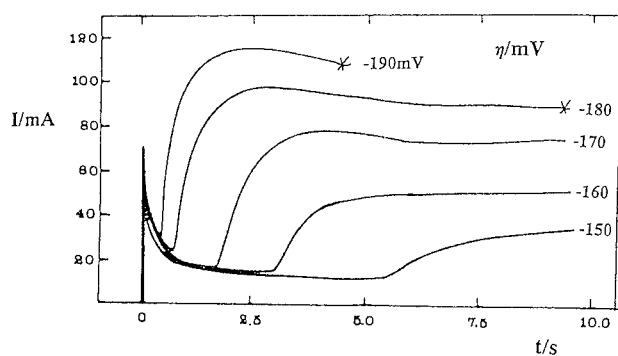


Fig 4. Cathodic current transients at different overpotentials on GC electrode in $\text{NaCl-KCl} + 5 \text{ wt\% MgCl}_2$, $T = 750^\circ\text{C}$.

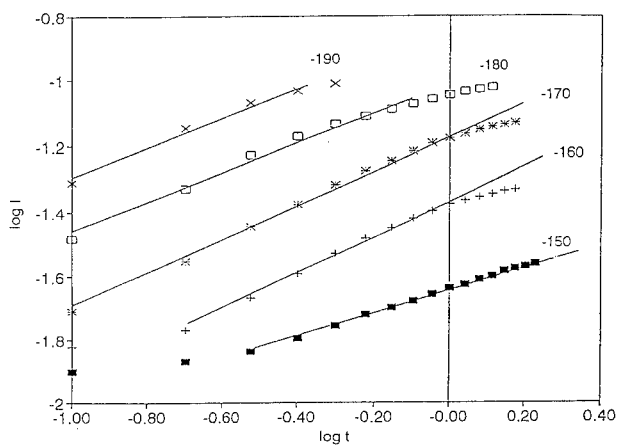


Fig 5. The transients from Fig 4 plotted as $\log I$ vs $\log t$.

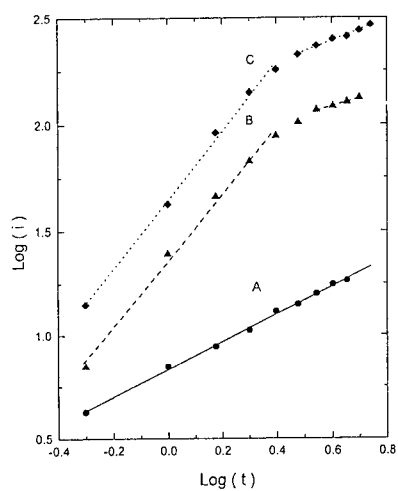


Fig 6. Cathodic transients on GC electrode in pure MgCl_2 plotted as $\log i$ vs $\log t$, $T = 750^\circ\text{C}$.
A) $\eta = -150 \text{ mV}$; B) $\eta = -180 \text{ mV}$; C) $\eta = -290 \text{ mV}$

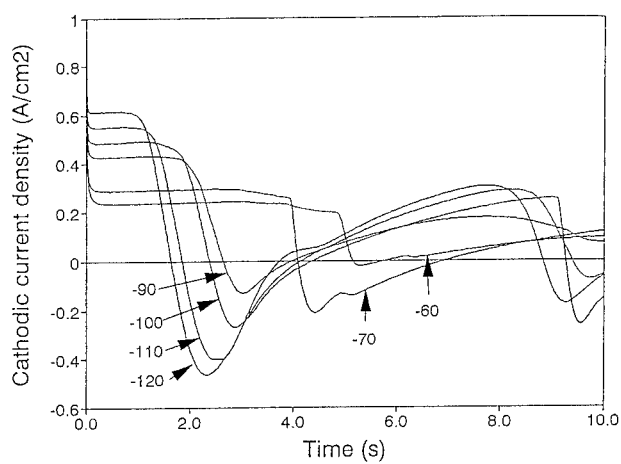


Fig 7. Potentiostatic current transients on GC electrode in pure MgCl_2 at different overpotentials showing instability of nuclei.

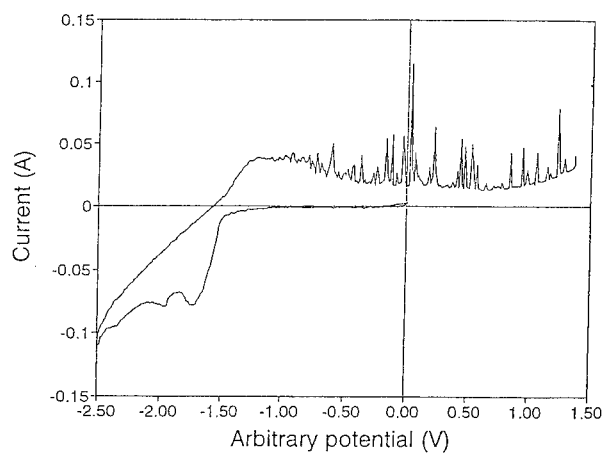


Fig 8. Cyclic voltammogram on GC in $\text{NaCl-KCl} + 5 \text{ wt\% MgCl}_2$, $T = 680^\circ\text{C}$, $v = 5 \text{ mVs}^{-1}$.

EFFECT OF ADDITIVES ON TI ELECTROREFINING IN MOLTEN CHLORIDE

Toshihide Takenaka, Akihisa Sugimoto, Yuki Yoshi Mitani and Masahiro Kawakami

Department of Production Systems Engineering,
Toyohashi University of Technology
Hibarigaoka 1-1, Tempaku-cho, Toyohashi 441, Japan

ABSTRACT

The effect of fluoride addition on Ti electrorefining in a NaCl-KCl melt has been investigated at 973K. The dominant Ti ion and its electrode reaction changed with the fluoride addition. In a melt where the molar ratio of F ion to Ti ion, $[F/Ti]$, was below 1, the dominant Ti ion was Ti^{2+} and the electrode reaction was $Ti \rightleftharpoons Ti^{2+} + 2e$ under our experimental condition. In a melt of $[F/Ti] > 6$, the dominant ion was Ti^{3+} and the electrode reaction was $Ti \rightleftharpoons Ti^{3+} + 3e$. The contents of impurities in the Ti metal deposit on the cathode also depended strongly upon $[F/Ti]$. The contents of Cr and Mn, which could not be eliminated completely in a pure chloride melt, decreased immediately with fluoride addition. However, the content of Al increased gradually with fluoride addition.

INTRODUCTION

Titanium of high purity is used for electric devices. The electrorefining is one of the most general procedures to produce high purity Ti. Many works on Ti electrorefining in molten salts were reported(1), and A.Girginov et al. summarized the electrode reactions of Ti recently(2). We also have been studying the Ti electrorefining in a chloride melt.

It is well-known that the electrode reaction of Ti in a chloride melt changes with fluoride addition(2). Some researchers have reported that the purification effect also depended upon the presence of fluoride in a melt(3). However, most of these studies were carried out in the melts in which the fluoride ion concentration was relatively high. In this work, we focused on Ti electrorefining in a melt of low fluoride ion concentration, and discussed the effect of fluoride addition.

EXPERIMENTAL

The schematic diagram of our experimental apparatus is shown in Figure 1. Titanium chloride was synthesized in an equimolar NaCl-KCl melt by the reaction of $TiCl_4$ with Ti metal in the quartz glass apparatus, and the mixture was solidified. A Ni crucible with the prepared salt was set in an airtight container under high purity Ar flow. The container itself

was set in the electric furnace in the Ar-filled glove box. The apparatus was heated to 973K, and the electrolysis was carried out. The fluoride ion concentration was controlled by the succeeding additions of an equimolar NaF-KF mixture. The thermocouple with a pure alumina sheath was soaked in a pure chloride melt. However, it was pulled out before fluoride addition to prevent the alumina sheath from dissolving.

A strip (~2mm×30mm×1mm) of high purity Ti was used as a cathode. The anode was a Ti rod (commercial grade, 10mmφ), and a Ni or Ti wire was used as a quasi-reference electrode. The electrolysis was performed as the cathodic overpotential became constant. To eliminate the impurities in a melt, the pre-electrolysis was carried out thoroughly before fluoride addition. After this treatment, the average valence of Ti ion in the melt became about 2.

The electrodeposit on the cathode was rinsed and weighed. The cathodic current efficiency was calculated from the amount of electricity and the weight of deposit. The content of impurity in a deposit was measured by ICP. Small amounts of melt were occasionally sampled by collecting the melt in a quartz tube. The Ti ion concentration and its valence in the sampled melt were evaluated by chemical analysis.

The effect of fluoride addition should be controlled not so much by the fluoride ion concentration itself as by the molar ratio of fluoride ion to Ti ion in a melt. Therefore, we present our experimental results by this ratio, and it is represented by $[F/Ti]$ in this paper. The ratio $[F/Ti]$ was calculated from the measured Ti ion concentration and the added amount of NaF-KF.

RESULT AND DISCUSSION

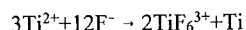
Change in Ti Ion in Melt

The color of the melt changed with fluoride addition. The color was green in a melt of $[F/Ti]=0\sim 1$, while it was purple in a melt of $[F/Ti]>6$. In a melt of $[F/Ti]=1\sim 5$, the color was black though it changed to green after solidification. The rest potential of Ti metal changed gradually to the positive with fluoride addition when $[F/Ti]<2$, and then shifted sharply toward the positive at $[F/Ti]=2\sim 3$. The rest potential did not change in a melt of $[F/Ti]>4$.

The total Ti ion concentration and the average valence of Ti ion in a melt were affected by fluoride addition. The changes in the average valence of Ti ion and in the compensated Ti amount in a melt are shown in Figure 2. Because the amount of sampled melts and the amount of added NaF-KF were not negligible, the compensated Ti amount for both of them was plotted instead of the Ti ion concentration. The average valence of Ti ion before fluoride addition was about 2, and increased with $[F/Ti]$. It was almost constant, ~3, in a melt of $[F/Ti]>3$. The Ti amount in a melt decreased with fluoride addition in a melt of $[F/Ti]<4$, and did not change in a melt of $[F/Ti]>4$. The Ti amount in a melt of $[F/Ti]>4$ was about 70% of that in the pure chloride melt.

The color of melt and the result of chemical analysis showed that the dominant valence

of Ti ion was Ti^{2+} in a melt of $[F/Ti]<1$ and Ti^{3+} in a melt of $[F/Ti]>6$. The decrease in the total amount of Ti in a melt suggested that the chemical reaction as follows occurred;



The actual Ti ion concentration was very important information, but it was hard to compensate the effect of sampled melts completely. In our experiments for electrolysis, therefore, the melt sampling was held to a minimum; just before the first fluoride addition and at the end of experiments. The ratio $[F/Ti]$ was calculated from the Ti ion concentration before the first fluoride addition.

Dependence of Morphology and Current Efficiency

The cathodic current efficiencies strongly depended upon $[F/Ti]$ as shown in Figure 3. In a melt of $[F/Ti]=0\sim 1$, the electrodeposit was dendritic and its size became smaller with the increase in $[F/Ti]$. The cathodic current efficiency suggested that the cathodic reduction was $Ti^{2+} + 2e^- \rightarrow Ti^0$. In a melt of $[F/Ti]=2\sim 5$, an electrodeposit could not be obtained, or a small amount of black material attached on the cathode surface was observed. In a melt of $[F/Ti]>6$, the electrodeposit was dendritic but its size was smaller than that in a melt of $[F/Ti]=0\sim 1$. The cathodic current efficiency was less than that in a melt of $[F/Ti]=0\sim 1$, and suggested that the cathodic reduction of Ti was $Ti^{3+} + 3e^- \rightarrow Ti^0$.

The dependence of cathodic current efficiency on the cathodic overpotential is shown in Figure 4. The current efficiency was affected strongly by the overpotential in a pure chloride melt, while it did not depend clearly on the overpotential in a melt of $[F/Ti]>6$. The morphology of electrodeposit changed with overpotential in the pure chloride melt, but it did not change in a melt of $[F/Ti]>6$.

The anodic current efficiency was measured by polarizing a strip of Ti metal toward the positive from its rest potential. The dependence of the anodic current efficiency on $[F/Ti]$ is shown in Figure 5. The results suggested that the anodic dissolution of Ti was $Ti \rightarrow Ti^{2+} + 2e^-$ in a melt of $[F/Ti]<2$ and $Ti \rightarrow Ti^{3+} + 3e^-$ in a melt of $[F/Ti]>6$. The anodic current efficiency decreased with $[F/Ti]$ in a melt of $[F/Ti]=2\sim 5$. The dependence of anodic current efficiency on the anodic overpotential was not clear irrespective of the $[F/Ti]$ values.

The results on the electrode reaction consisted well with the dominant Ti ion shown by the analysis of the melts. Moreover, in a melt of $[F/Ti]<1$ or $[F/Ti]>6$, the cathodic reactions suggested by our results agreed well with those by some researchers(2)(4). The behavior in a melt of $[F/Ti]=2\sim 5$ was unique. The Ti ion under this condition might exist as a more complicated form.

Dependence of Purification

The typical impurity contents in the electrodeposits are shown in Table 1. In a pure chloride melt, $[F/Ti]=0$, Ti was purified very effectively even in our beaker scale experiment, but Cr and Mn could not be eliminated completely. In a melt of $[F/Ti]>6$, the contents of Cr and Mn in the deposit were less than those in a chloride melt. On the other hand, the content

of Al was always larger than that in a chloride melt, especially in the case when an alumina tube was immersed in a melt. The content of Ni seemed not to depend directly on the presence of fluoride ion. However, the surface of the Ni crucible exposed to a melt deteriorated when the melt included fluoride. The Ni content in a deposit became larger in the next experiment using such a crucible again, though its surface was polished thoroughly before each experiment.

The dependence of impurity content in the electrodeposit on $[F/Ti]$ is shown in Figure 6. Chromium and Mn were eliminated very effectively by the addition of a small amount of fluoride. The content of Al increased gradually with $[F/Ti]$. The contents of most impurity were usually high in the deposits obtained in a melt of $[F/Ti]=2\sim4$.

The elimination factor of impurities depended not on the impurity concentration in a melt itself but on the ratio of the impurity concentration to the Ti concentration. Most of the impurity concentrations were too low to be measured. The Al concentration in a melt increased with $[F/Ti]$ as shown in Figure 7, and was consistent with the change in the Al content in deposits. Because the Ti anode did not contain Al, Al in the Ni crucible might dissolve in the melt with fluoride.

The Ti anode after electrolysis was covered with a porous layer. The measurement by means of EPMA showed that the main ingredient was Ti, and that Fe and Ni were concentrated in it. In a melt of $[F/Ti]>6$ Cr seemed to be concentrated in this layer, while there was no indication that Cr was concentrated in the anode surface in a pure chloride melt.

CONCLUSION

The addition of fluoride to a chloride melt caused the change in a dominant Ti ion from Ti^{2+} to Ti^{3+} , and strongly affected the Ti electrorefining. The electrodeposit was obtained in a melt of $[F/Ti]<1$ or $[F/Ti]>6$, but was not obtained in a melt of $[F/Ti]=1\sim5$. Chromium and Mn were eliminated more effectively in a melt with fluoride than in a pure chloride melt. However, the content of Al and Ni became larger with fluoride addition.

ACKNOWLEDGEMENTS

The authors wish to acknowledge the support of Toho Titanium Co., Ltd., Chigasaki, Japan.

REFERENCES

1. H.Miyazaki, Y.Yamagoe and Y.Shindo, *Materia Japan*, **33**, 51 (1994).
2. A.Girginov, T.Z.Tzvetkoff and M.Bojinov, *J. Appl. Electrochem.*, **25**, 993 (1995).
3. Y.Shindo and H.Miyazaki, Japan Patent, H6-173065.
4. C.Guang-Sen, M.Okido and T.Oki, *J. Appl. Electrochem.*, **18**, 80 (1988).

Table 1 Typical values of impurity content of Ti electrodeposit.

Melt condition		η / V	Content of impurity / ppm							
[Ti]/wt% *)	[F/Ti]		Fe	Ni	Cu	Al	Cr	Mn	Ca	Si
3.55	0	-0.2	4	<1	<1	27	17	5	<1	<1
	6.76	-0.3	4	1	1	184	<1	1	44	4
2.63	0	-0.2	2	41	1	1	40	5	<1	1
	9.13	-0.3	<1	140	3	32	1	1	2	4
Ti anode			600	160	-	-	140	20	-	-

*) Ti concentration in melt before fluoride addition.

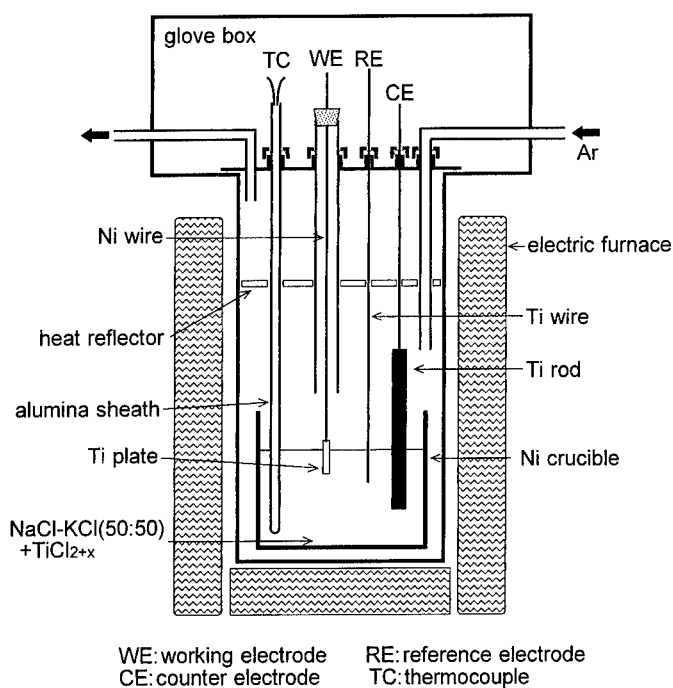


Fig.1 Experimental apparatus.

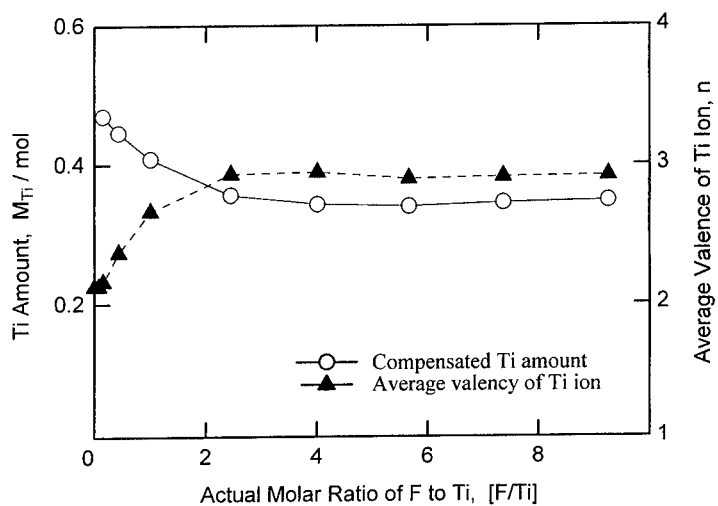


Fig.2 Changes in amount of Ti ion and average valence of Ti ion with fluoride addition.

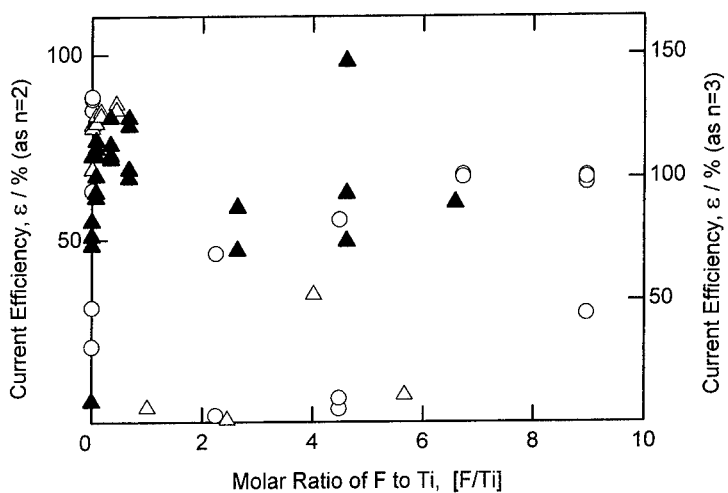


Fig.3 Dependence of cathodic current efficiency on molar ratio of F to Ti.
initial Ti ion concentration in melt;
○: 2.83wt%, △: 2.86wt%, ▲: 3.04wt%

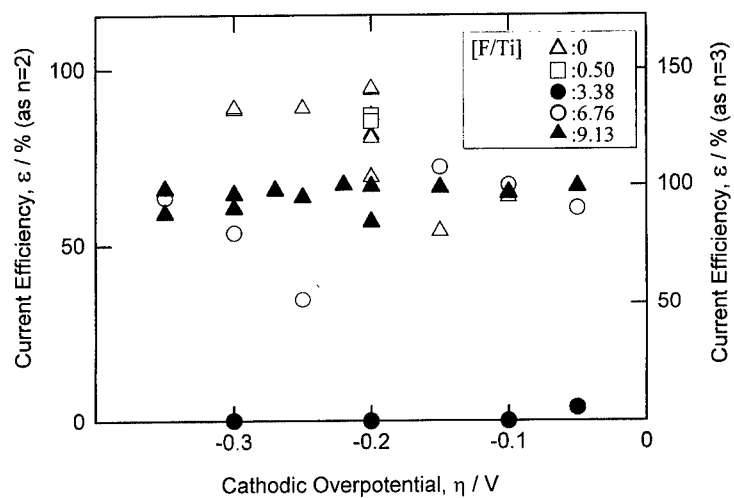


Fig.4 Dependence of cathodic current efficiency on cathodic overpotential.

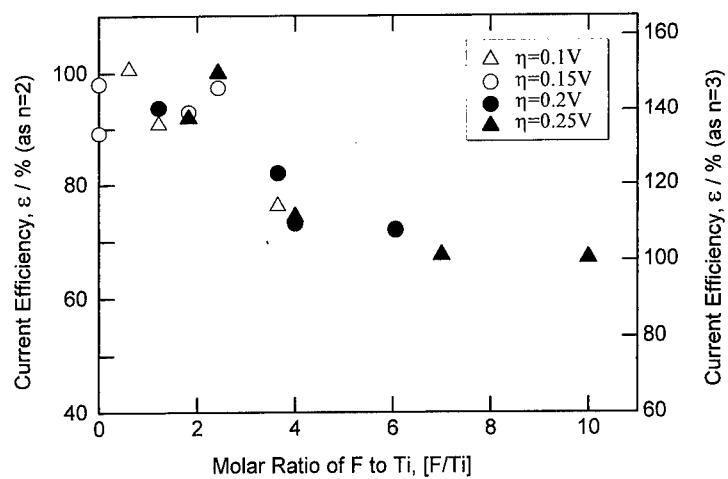


Fig.5 Dependence of anodic current efficiency on molar ratio of F to Ti.

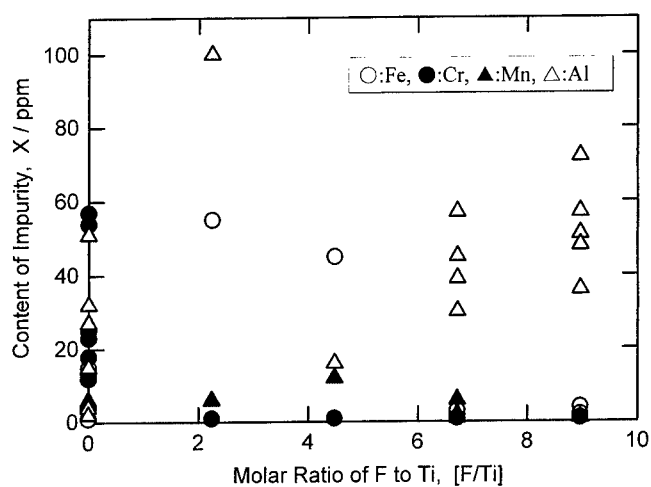


Fig.6 Dependence of impurity contents of Ti deposit on molar ratio of F to Ti.

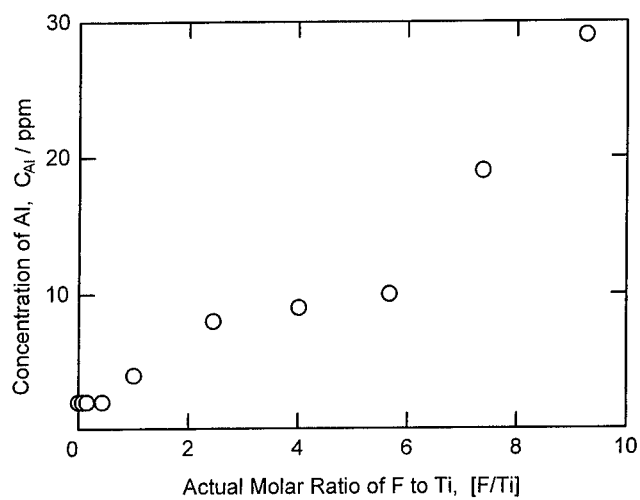


Fig.7 Change in Al concentration in melt with fluoride addition.

CATHODIC BEHAVIOR OF THE DEPOSITION OF Nb AND Al IN NaCl-AlCl₃ MELT

Yuzuru Sato, Katsuyuki Iwabuchi, Nobuaki Kawaguchi, Hongmin Zhu,
Mamoru Endo, Tsutomu Yamamura and *Sakae Saito

Department of Metallurgy, Tohoku University, Sendai 980-77, Japan.

**Department of Mechanics, Ashikaga Institute of Technology, Ashikaga 326, Japan.*

ABSTRACT

The deposition of Nb and Al from an acidic NaCl-AlCl₃ melt was studied by using the cyclic voltammetry and EPMA observation of the deposit in order to get a Nb-Al alloy which is a candidate of next generation superconductor. Nb sources used were niobium chlorides, NbCl₅ and Nb₃Cl₈, and anodically dissolved niobium. No deposit was obtained for NbCl₅ due probably to a disproportionation reaction. The deposit obtained for Nb₃Cl₈ was an alloy although the Nb content was considerably lower than the stoichiometric composition of superconductive Nb₃Al. For the anodically dissolved Nb, almost an equimolar deposit was obtained.

INTRODUCTION

Intermetallic compound, Nb₃Al found in Nb-Al system, is promising material as a superconductive material and a high temperature structural material. Nb₃Al has a very high T_c and J_c and is more practical than the oxide superconductors. It also exhibits excellent mechanical strength at higher temperatures. However, it is difficult to process the compound to fine wire or thin sheet by using conventional metallurgical method because of its very high melting temperature and its brittle nature.

In this work, molten salt electrolysis was adopted to produce Nb-Al alloys from an acidic NaCl-AlCl₃ melt containing niobium chlorides. Nb-Al alloys are expected to be deposited on the cathode even if the niobium ion concentration is low because niobium has more positive standard potential than aluminum in the chloride melt.

EXPERIMENTAL

Apparatus

Cyclic voltammetry and constant potential electrolysis were carried out using a Hokuto HA-305 potentiostat and a HB-104 function generator for studying the cathodic

behavior. Figure 1 shows the electrochemical cell. The cell has four threaded connectors for the electrodes and the thermocouple, and is placed in an electric furnace which is on a hot plate with magnetic stirrer to agitate the melt.

Electrodes used are shown in Fig.2. The working electrode is an end surface of polished tungsten wire of 0.5mm diameter sealed in Pyrex tube. The reference electrode is an aluminum wire, welded to tungsten wire sealed in Pyrex tube, immersed in a NaCl-55mol%AlCl₃ melt which is separated from the electrolyte with b-Al₂O₃. The counter electrodes are an aluminum plate which is also welded to tungsten wire in Pyrex tube and a spiral niobium wire of 0.5mm diameter which was sealed in Pyrex tube.

For SEM observations and chemical analysis of the electrodeposits, a Shimadzu EPMA-8705 electron probe micro analyzer was used.

Chemicals

AlCl₃ in the form of large colorless transparent single crystals was purified by sublimation method after first drying under vacuum(1). NaCl was purified by dry HCl bubbling into the melt(1). NbCl₅ was synthesized directly from 99.9% metallic niobium and dry chlorine gas. Nb₃Cl₈ was also synthesized by chemical transport reaction from NbCl₅ and metallic niobium(2). Nb₃Cl₈ was expected to be suitable as a source of niobium because of its low valence and less hygroscopic property.

Electrolyte for the electrolytic cell and NaCl-55mol%AlCl₃ for the reference electrode were prepared by co-melting the purified NaCl and AlCl₃ sealed in the Pyrex tube under vacuum.

Procedure

The experiment was carried out for the four electrolytes. The first was the NaCl-52mol%AlCl₃ melt. Second and third electrolytes are the melt containing NbCl₅ and Nb₃Cl₈ which was premixed with the electrolyte, respectively. Fourth electrolyte is the melt into which metallic niobium is anodically dissolved just before the measurement.

The cyclic voltammetry and controlled potential electrolysis were carried out for above melts and the deposits were analyzed by EPMA.

The atmosphere in the cell is dry nitrogen from the dry box. Experimental temperature was 473K for all the experiments.

RESULTS AND DISCUSSION

Figure 3 shows the cyclic voltammogram obtained for niobium free electrolyte. No cathodic peaks are obtained at the potential higher than 0V and a large cathodic peak

appears near to -0.1V. This means that the tungsten electrode is stable and has wide electrochemical window at higher potential. The peak is considered to be assigned to aluminum deposition by the reaction shown in equation[1] in the acidic melt.



Figure 4 shows the SEM image of the deposit on the tungsten electrode obtained at -0.2V. Crystals of aluminum are observed although the amount is small.

Cyclic voltammogram for the electrolyte containing 1mol%NbCl₅ is shown in Fig.5. Three cathodic peaks are observed at the potentials of 1.15V, 0.5V and 0.3V, respectively. Current densities are plotted against square root of the scan rate in Fig.6. The figure indicates that the peaks are linear diffusion controlled reaction due to their good linear relations. The number of electrons, *n* for the peaks was calculated by equation [2].

$$|E_p - E_{p/2}| = 2.2 RT / nF \quad [2]$$

The *n* obtained, by averaging the data of different scan rate of 0.05~1.0V · s⁻¹, for the peaks was 0.2, 1.0 and 0.6, respectively. It is considered that Nb(V) is not reduced to metal because the total electron number is about 2 in the potential range higher than that where Al(III) is reduced, although the co-deposition of Nb with Al may be expected at negative potential. Therefore, the electrodeposition was attempted at -0.2V. However no deposit was found by EPMA observation. The reason of no deposit is considered as follows; The potential is sufficiently negative for the deposition of metals, Nb or Al. Then the reduction of ions to metals is blocked by highly oxidative Nb(V) species. Namely the disproportionation reactions may occur due to the presence of higher valence NbCl₅.

Figure 7 shows the cyclic voltammogram for the electrolyte containing Nb₃Cl₈ which was fed as a form of Nb₃Cl₈ · 4NaCl because Nb₃Cl₈ · 4NaCl has lower melting temperature than Nb₃Cl₈(3) and was expected to dissolve easily. However its concentration seemed very low because the melt showed only light color and black condensates were found on the bottom, and it was difficult to analyze the concentration. A new weak peak appeared near 0V. The electrolysis was then performed at -0.2V. Fig.8 shows the SEM image of the deposit obtained. Island like deposits smaller than 10mm were found on the tungsten substrate. Figure 9 shows the concentration map of niobium and aluminum obtained by EPMA. The ordinate indicates relative intensity to the pure metal. Deposit contains both aluminum and niobium, but the sum of relative intensities does not reach to 100% because of island like morphology. The composition of niobium in the deposit is 37~42wt%. This concentration of niobium, although it is comparable with composition reported(4), is considerably low compared with the superconductive Nb₃Al, 91.2wt%Nb. The standard decomposition potentials of solid Nb₃Cl₈ and liquid AlCl₃ calculated based on the thermodynamic data(5) are 1.73V and 2.02V at 473K, respectively. This difference is

considerably large and is corresponding to nine order of the ionic concentration by simply assuming both ions of trivalent niobium and aluminum equilibrated with the pure metals. It is considered that the main reason of low content of niobium is low solubility of Nb_3Cl_8 in the melt other than the disproportionation reaction between the niobium species.

Anodic dissolution of metallic niobium into the melt was tried based on above results. A spiral niobium electrode shown in Fig.1 was used and 250C was passed through the electrode anodically at 2.0V. The charge is corresponding to about 0.1mol% of NbCl_5 in the melt. Cyclic voltammogram for the electrolyte containing anodically dissolved niobium is shown in Fig.10. Relatively large peak is found at around 0.4V. Electrolysis was carried out at the potential of 0.0V. The deposit obtained consist of fine grains as shown in Fig.11 and the concentration map for the deposit is shown in Fig.12. The niobium concentration is quite high, almost 75~80wt%, corresponding to an equimolar composition of niobium and aluminum. These results suggest that the anodic dissolution of metallic niobium is an effective niobium source to increase the niobium concentration and/or that the species dissolved may be in a low valence state.

CONCLUSION

Cathodic behavior of Nb-Al alloy deposition was studied in NaCl -52mol% AlCl_3 electrolyte containing niobium chlorides. The goal of this study was to produce the superconductive Nb_3Al alloy electrochemically. The niobium chlorides used were NbCl_5 , Nb_3Cl_8 and anodically dissolved niobium. No deposit was obtained for NbCl_5 . The reason is considered to be due to the disproportionation of niobium compound. For Nb_3Cl_8 and anodically dissolved niobium, the deposits of Nb-Al alloy were obtained and their niobium content were 37~42wt% and 75~80wt%, respectively. The low content of niobium in the alloy may be due to low solubility of Nb_3Cl_8 in the melt. Anodically dissolved niobium is an effective niobium source for obtaining alloys with high niobium content.

REFERENCES

1. Y.Sato and T.Ejima, in Molten Salts/1983, M.Blander, D.S.Newman, G.Mamantov, M.-L.Saboungi and K.Johnson, Editors, **PV 84-2**, p121, The Electrochemical Society Proceedings Series, Pennington, NJ(1994).
2. Y.Sacki, M.Yanai and A.Sofue, *Denki Kagaku*, **40**, 816 (1972).
3. Y.Sacki, T.Suzuki and S.Yamaki, *Denki Kagaku*, **33**, 656 (1965).
4. N.Koura, T.Kato and E.Yumoto, *J.Surface Finishing Soc.Jpn*, **45**, 805 (1994).
5. I.Barin, *Thermochemical Data of Pure substances*: VCH, Germany (1989).

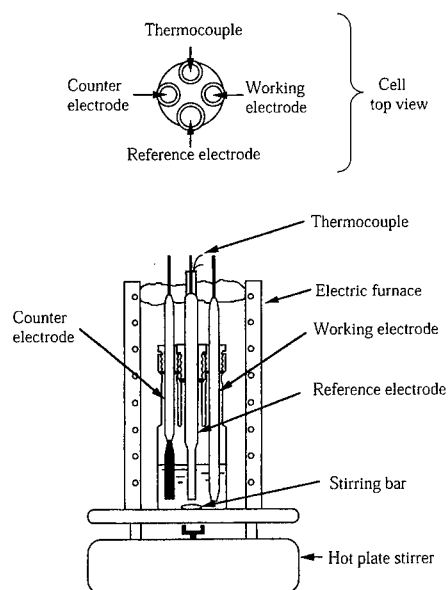


Fig.1 Schematic diagram of the apparatus used for electrochemical measurement.

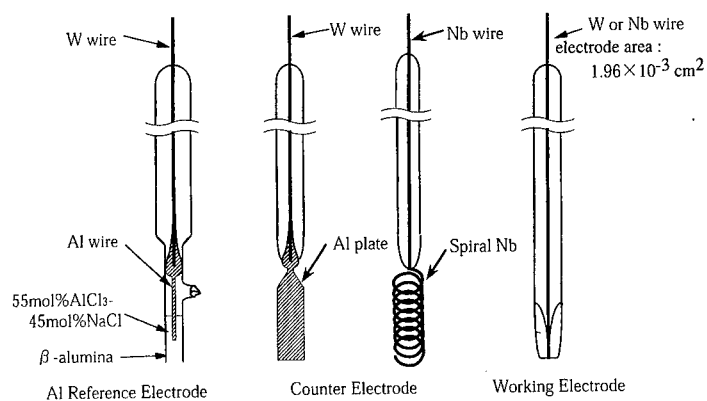


Fig. 2 Schematic diagram of the electrodes used.

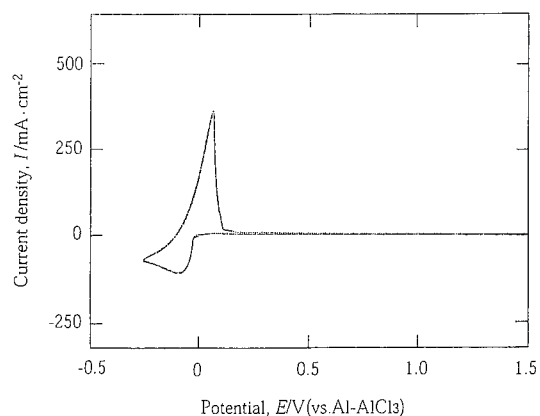


Fig. 3 Cyclic voltammogram for NaCl-AlCl₃ melt.

Temp. : 473K
 Scan rate : 100mV · s⁻¹
 W.E. : Tungsten
 Electrolyte : NaCl-52mol%AlCl₃



Fig. 4 SEM image of Al deposited onto tungsten electrode.

Temp. : 473K
 Potential : -0.1V(vs. Al-AlCl₃)
 Total charge : 3.75×10^{-2} C
 Electrolyte : NaCl-52mol%AlCl₃

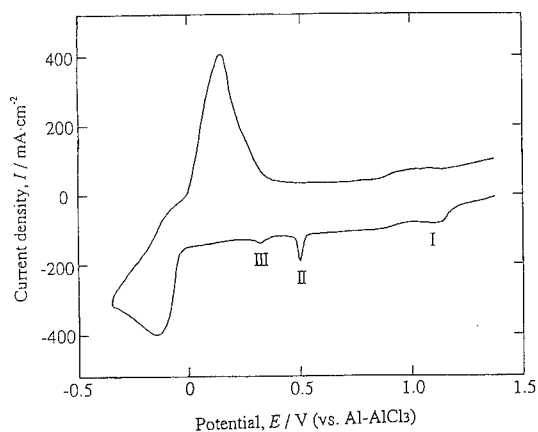


Fig. 5 Cyclic voltammogram for NaCl-AlCl₃ melt containing 1mol% NbCl₅.

Temp. : 473K
 Scan rate : 300mV · s⁻¹
 W.E. : Tungsten
 Electrolyte : NaCl-52mol%AlCl₃

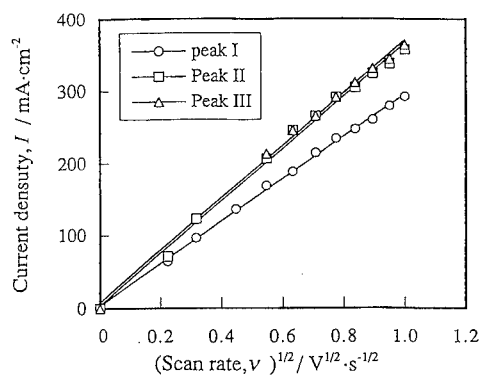


Fig. 6 Relation between peak current density and scan rate.

Temp. : 473K
 W.E. : Tungsten
 Electrolyte : NaCl-52mol%AlCl₃
 Solute : 1mol% NbCl₅

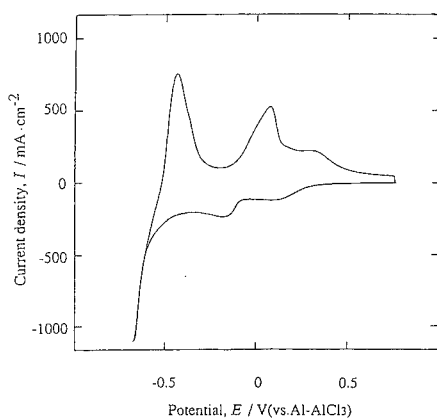


Fig. 7 Cyclic voltammogram for NaCl-AlCl₃ melt containing Nb₃Cl₈.

Temp. : 473K
 Scan rate : 1.0V · s⁻¹
 W.E. : Tungsten
 Electrolyte : NaCl-52mol%AlCl₃
 Solute added : Nb₃Cl₈ · 4NaCl

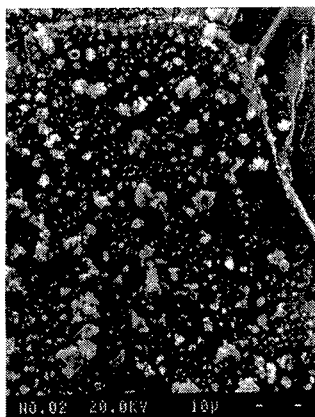


Fig. 8 SEM image of Nb-Al alloy deposited onto tungsten from the melt containing Nb₃Cl₈.

Temp. : 473K
 Potential : -0.2V(vs. Al-AlCl₃)
 Total charge : 5.0C
 Electrolyte : NaCl-52mol%AlCl₃
 Solute added : Nb₃Cl₈ · 4NaCl

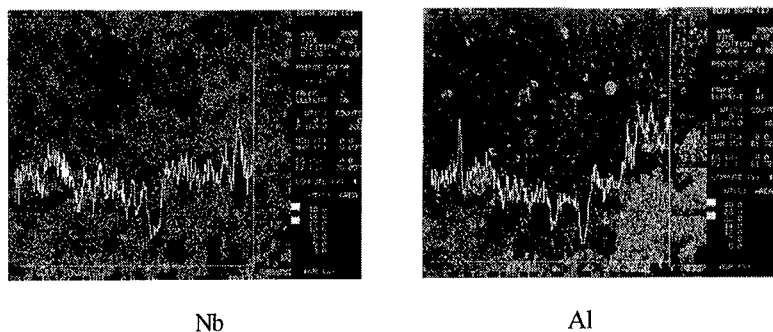


Fig. 9 Concentration map of the deposit obtained from the melt containing Nb_3Cl_8 .

Temp. : 473K
 Potential : -0.2V(vs. Al- AlCl_3)
 Total charge : 5.0C
 Electrolyte : NaCl-52mol% AlCl_3
 Solute added : $\text{Nb}_3\text{Cl}_8 \cdot 4\text{NaCl}$

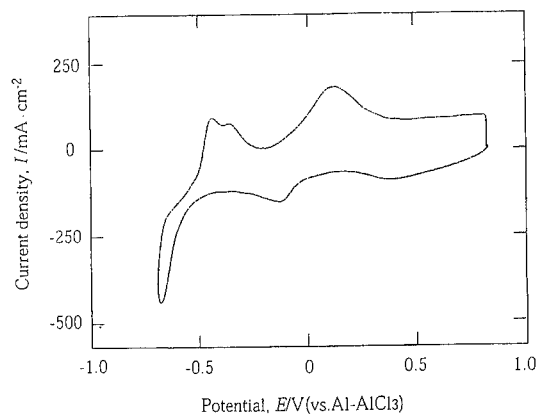


Fig. 10 Cyclic voltammogram for NaCl- AlCl_3 melt containing anodically dissolved Nb.

Temp. : 473K
 Scan rate : $1.0\text{V} \cdot \text{s}^{-1}$
 W.E. : Tungsten
 Electrolyte : NaCl-52mol% AlCl_3
 Solute : anodically dissolved Nb

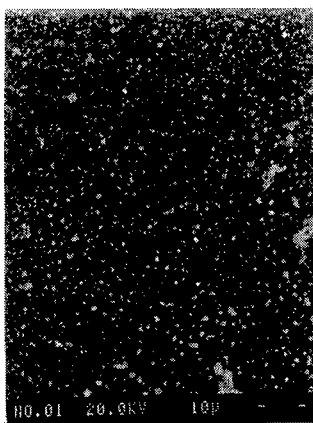
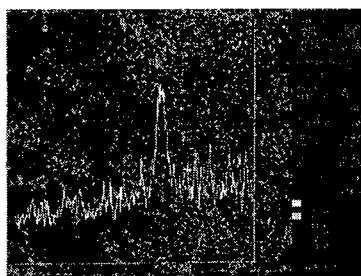
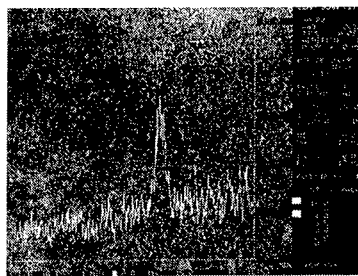


Fig. 11 SEM image of Nb-Al alloy deposited onto tungsten from the melt containing anodically dissolved Nb.

Temp. : 473K
 Potential : -0.2V(vs. Al-AlCl₃)
 Total charge : 11.2C
 Electrolyte : NaCl-52mol%AlCl₃
 Solute : anodically dissolved Nb



Nb



Al

Fig. 12 Concentration map of the deposit obtained from the melt containing anodically dissolved Nb.

Temp. : 473K
 Potential : -0.2V(vs. Al-AlCl₃)
 Total charge : 11.2C
 Electrolyte : NaCl-52mol%AlCl₃
 Solute : anodically dissolved Nb

ELECTROCHEMICAL PROPERTIES OF Nb_3Cl_8 IN THE $\text{MgCl}_2\text{-NaCl}$ EUTECTIC AT 471°C

Mohamed Mohamedi, Nobuaki Kawaguchi, Yuzuru Sato and Tsutomu Yamamura

Department of Metallurgy, Faculty of Engineering,
Tohoku University, Sendai, 980-77, Japan

ABSTRACT

The electrochemical properties of solutions of Nb_3Cl_8 in the fused eutectic $\text{MgCl}_2\text{-NaCl}$ eutectic were examined at 471°C by means of cyclic voltammetry and convolution voltammetry. The reduction of Nb_3Cl_8 to the metal showed a complicated behavior. It was shown that the reduction proceeds mainly via two steps: one electron irreversible step Nb(III)/Nb(II) and two electron reversible step Nb(II)/Nb(0) .

INTRODUCTION

The electrochemistry of niobium has been greatly studied in both molten chlorides, chloride-fluoride and fluoride melts. From the literature reviews (1-2) it can be seen that in spite of the numerous studies for obtaining niobium by electrolytic means, the proposed mechanisms still divergent and niobium metal has been obtained essentially in the form of powders or dendrites in molten chlorides with complications due to:

- numerous difficulties due to the low solubility of certain niobium chlorides,
- numerous problems due to electrolyte stability because of volatilization of niobium chlorides of higher oxidation state as well as the disproportionation of intermediate valence niobium chlorides,
- according to the experimental conditions, temperature and current density, the anodic oxidation of niobium metal does not yield the same niobium chlorides.

Considering these problems encountered in molten chlorides, in order to stabilize certain oxidation states of niobium, the latter were complexed with fluoride ions, or the operating temperature was increased. Production of deposits which are coherent and closely adherent has been demonstrated in fluoride melts (3). However the disadvantage of fluorides is that the systems are generally toxic, corrosive and require high working temperatures.

The present paper is concerned with the mechanism of the reduction of Nb_3Cl_8 solution to the metal in MgCl_2 - NaCl melt in which, to our knowledge, the electrochemistry of niobium has not been investigated. This binary melt presents eutectic at 445°C with 41.5 mol%(MgCl_2)- 58.5 mol%(NaCl) composition (4).

EXPERIMENTAL

Salt preparation

$\text{MgCl}_2 \cdot 6\text{H}_2\text{O}$ was purified according to the procedure described in ref(5). NaCl was purified under dry HCl bubbling into the melt(6). Nb_3Cl_8 was synthesized by chemical transportation reaction from NbCl_5 and metallic niobium(7).

Electrochemical cell and procedure

A three-electrode Pyrex cell arrangement was used for the electrochemical experiments. The Pyrex crucible($\Phi=45\text{mm}$) served as an electrolyte container. We have chosen to use the cross section of tungsten wire($\Phi=0.5\text{mm}$) sealed in Pyrex tube as a working electrode. Before use, the working electrode was first mechanically polished on emery paper, was washed with distilled water and acetone and then dried. The silver-silver chloride equilibrium was used as the reference for the measurement of the electrode potential. The electrode arrangement was a silver wire($\Phi=1\text{mm}$) dipped into a silver chloride solution in the MgCl_2 - NaCl eutectic half cell built with a thin Pyrex bulb junction. The silver chloride concentration used was 5mol%. All the potentials are reported to this reference. The counter-electrode was a graphite rod of 5 mm diameter. The cell containing the crucible and the electrodes was assembled in the dry box. At this stage, the solvent mixture was introduced into the crucible which was returned to the main cell. Then the cell is removed from the dry-box and placed in a Pyrex transparent furnace and dried completely by heating under vacuum. The temperature in the cell was measured with a Chromel-Alumel thermocouple and kept within 2°C . Atmosphere in the cell was dry argon. The melted mixture was conditioned at the selected temperature for several hours before adding the solute as blocks of frozen Nb_3Cl_8 -4 NaCl mixture through an air-lock chamber.

Instrumentation

The electrolytic reduction of Nb_3Cl_8 solution has been mainly studied by means of cyclic voltammetry and convolution voltammetry. The data acquisition system was composed of a potentiostat/galvanostat HA305, a function generator HB104, an intelligent recorder INR141A for recording transients and a personal computer for data processing. The convolution voltammetry or semi-integral $m(t)$ is defined by the integral :

$$m(t) = \frac{d^{-1/2}}{dt^{-1/2}} I(t) = \frac{1}{\pi^{1/2}} \int_0^t \frac{I(\tau)}{\sqrt{t-\tau}} d\tau \quad [1]$$

Where $I(\tau)$ is the current measured at the time τ . The convolution treatment of $I(t)$ transients was carried out on the basis of Oldham's G1 and G2 algorithms(8).

RESULTS AND DISCUSSION

Electrochemical window of the solvent

The theoretical electrochemical span of the solvent could be computed from thermodynamic data (9). However, the real electrochemical stability domain of $\text{MgCl}_2\text{-NaCl}$ was examined by means of voltammetric experiments. A cyclic voltammogram obtained at a tungsten electrode is reported in Fig.1. The reduction of magnesium ions is easily observed at a potential equal to $-1.5\text{V}/\text{Ag}/\text{AgCl}$ (wave E) which is quite close to the theoretical one ($-1.47\text{V}/\text{Ag}/\text{AgCl}$). Peak E' which is typical for a stripping of deposit, is observed in the reverse scan. On the anodic side chlorine evolution is seen (wave F).

After the addition of Nb_3Cl_8 , Fig.2 shows a series of voltammograms recorded for different cathodic reversal potential E_λ . Within the narrowest potential window $+0.2\text{V}$ and -0.9V , two cathodic peaks were observed with no relevant anodic peaks. The peaks noted A and B are located at -0.35V and -0.77V respectively. As the reversal potential became more cathodic ($E_\lambda = -1.1\text{V}$) a new redox couple C/C' was observed at $-1\text{V}/+0.11\text{V}$. For $E_\lambda = -1.3\text{V}$ the same cathodic processes remained visible, however, a new peak C'' appeared at $+0.14\text{V}$. The peak A was not visible for $E_\lambda > -1.4\text{V}$ and a new redox couple D/D' was evolved at $-1.4\text{V}/-1.35\text{V}$. The shape of the curve D, and particularly the sharp increase in current is characteristic of the formation of a substance of a constant activity. The cathodic limit E/E' corresponds to magnesium deposition.

Analysis in the $+0.2\text{V}$ and -1.4V potential range

On the Fig.3, we report the cathodic evolution of the voltammetric curves as a function of the potential sweep rate recorded in the $+0.2\text{V}$ and -1.4V potential range. Peculiar features of these voltammograms (Table I and Fig4-6) lie in the following:

- Only one reduction peak is observed (Peak G).
- The cathodic peak potential E_{pG} is dependent upon the potential sweep rate logarithm $\log v$ (Fig.4), i.e., an increase in the potential sweep rate shifts the E_{pG} towards negative potentials.
- Figure 5 shows that the dependence of the cathodic peak current I_{pG} is also complicated

in that I_{pG} is not proportional to the square root of the potential sweep rate. Then values of $I_{pG}/v^{1/2}$ were measured to check for possible chemical reactions coupled to the charge transfer. Constancy of $I_{pG}/v^{1/2}$ would indicate charge transfer with no chemical complication(10). Table I shows that the parameter $I_{pG}/v^{1/2}$ increases as the potential sweep rate increases. This increase can not be due to the ohmic drop since that would tend to decrease the $I_{pG}/v^{1/2}$ parameter(11). When I_{pG} is plotted against the potential sweep rate(Fig.6), a linear relation is obtained between the two parameters and the plot passes through the origin.

Table I - Characteristics of the voltammograms presented in Fig.3						
E_{pG} V	$E_{pG/2}$ V	$E_{pG}-E_{pG/2}$ V	$I_{pG} \times 10^4$ A	v Vs ⁻¹	$I_{pG}/v^{1/2} \times 10^4$ A/(V ^{1/2} s ^{-1/2})	$I_{pG}/v \times 10^4$ A/(Vs ⁻¹)
-0.96	-0.66	-0.30	-3.0	0.2	-6.70	-1.50
-1.07	-0.73	-0.34	-6.1	0.5	-8.60	-1.22
-1.10	-0.75	-0.35	-8.6	0.7	-10.3	-1.23
-1.10	-0.77	-0.33	-11	0.9	-11.0	-1.22
-1.14	-0.80	-0.34	-12	1.0	-12.0	-1.20
-1.20	-0.85	-0.35	-25	2.0	-17.6	-1.25

$E_{pG/2}$ = half peak potential at $0.5I_{pG}$.

The theoretical study of an adsorption step coupled to a charge transfer(10), shows that the reduction current of the adsorbed species becomes predominant at high potential sweep rates, yielding thus an increase of the $I_{pG}/v^{1/2}$ parameter.

Note that the marked constancy of the quantity I_{pG}/v for potential sweep rate $>0.2V/s$ is an inherent feature for adsorption(12-13). In addition the dependence of the peak potential upon the potential sweep rate logarithm suggests that the process is not reversible(12-13).

Laviron(12) indicates, in the case of a totally irreversible adsorption process, that the peak potential varies with the logarithm of the potential sweep rate v according to the equation :

$$E_{pG} = E^{0'} + \frac{2.3RT}{\alpha n_{\alpha}F} \log \frac{RTk^0}{\alpha n_{\alpha}Fv} \quad [2]$$

where k^0 is the standard rate constant, n the overall number of electron transferred, α the transfer coefficient, n_α the number of electrons transferred in the rate determining step and the others symbols have their usual meaning. From the slope of Fig.4, the product αn_α evaluated was found to be equal to 0.62. Assuming $\alpha = 0.5$ this yields to 1.24 electron number.

The peak current is expressed following(12)

$$I_{pG} = \frac{n\alpha n_\alpha F^2 A v \Gamma_0^*}{2.718 RT} \quad [3]$$

where Γ_0^* is the initial superficial concentration in mol.cm^{-2} . This expression was established assuming the potential sweep rate so large that the amount of molecules brought to the electrode by diffusion during the potential sweep is negligible compared to the amount adsorbed, and that the electrode area A can be regarded as constant.

Γ_0^* determined from the slope of Fig.6 and using equation 3 was found to be equal to $1.46 \times 10^{-6} \text{ mol.cm}^{-2}$.

Analysis by semi-integration

The Fig.7 represents a calculated semi-integral of a voltammogram from Fig.3, hysteresis is noticed between the forward and the backward sweeps of the semi-integral. We can therefore conclude that the process is not reversible(14). Furthermore, the return curve crosses the horizontal axis, indicating the formation of an insoluble substance at the electrode(15). Fig.8 shows several cathodic semi-integration curves deduced from the voltammograms of Fig.3. The following facts are established:

- the occurrence of a plateau in the region of cathodic potentials indicates that the diffusion is controlling the process(16). The value of this plateau increases when the potential sweep rate increases.

In the case of a charge transfer under diffusion control when the concentration of the electroactive species at the electrode surface is diminished to virtually zero, the semi-integral function $m(t)$ tends to a limiting value independent of the potential sweep rate, this limiting value is expressed by the following equation:

$$m^* = nFAC_i^* \sqrt{D_i} \quad [4]$$

This equation is valid whether or not the electrochemical system is reversible(16) and demonstrates the proportionality between the initial concentration C_i^* of the electroactive species. We have observed that m^* depends on the potential sweep rate(Fig.8). To our knowledge, this kind of mechanism has not been treated by semi-integration, but we think that the increase of the plateau value with the potential sweep rate is due to the intervention of the adsorption step.

Analysis in the -0.2V and -1.5V potential range

Figure 9 shows a typical voltammogram recorded in the -0.2V and -1.5V range. On this figure we recognize the peaks D/D'(see Fig.2) and in addition the peak G(see Fig.3) appears as a shoulder on peak D.

The variations of the anodic and cathodic peak currents D/D' I_{pa} and I_{pc} with the square root of the potential sweep rate $v^{1/2}$ shown in Fig.10 are straight lines through the coordinate origin, indicating that the processes are under diffusion-controlled.

The cathodic peak potential slightly moves towards a negative direction with increasing potential sweep rate. It indicates that the cathodic reduction of niobium ions is very close to a reversible process. The electron number can be calculated using the peak potential E_{pc} and the half peak potential $E_{pc/2}$ separation relation in the case of a reversible electrodeposition reaction(17) :

$$|E_{pc} - E_{pc/2}| = 0.77 \frac{RT}{nF} \quad [5]$$

By applying this equation to peak D, $n=2.14$ was obtained.
 $E_{pc}-E_{pc/2}$ was determined by extrapolating the plot of $E_{pc}-E_{pc/2}$ to $v=0$.

The insolubility and the adherence to the electrode of a deposit can be verified on the voltammogram by the fact that the anodic peak current is less than the cathodic one. The peak current ratio I_{pa}/I_{pc} is lower than unity and assumed the value between 0.5 and 0.57. This is confirmed by the semi-integral curve presented on Fig.11. It can be seen that the reverse semi-integral transient do not cross the abscissa as expected for soluble/insoluble electron transfer(15).

Discussion

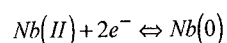
The plurality of cathodic and anodic peaks observed during the reduction of Nb_3Cl_8 to the metal(Fig.2) shows the high intricacy of the whole electrochemical process. This is the reason why the mechanism could not be elucidated completely. In order to simplify we will consider only the main steps G and D.

According to Safonov *et al.*(18-19) niobium dichloride disproportionates on heating

to niobium tetrachloride and metallic niobium. K. Zhou *et al.*(20) concluded that in molten LiCl-KCl that Nb_3Cl_8 dissociates to Nb(II) and Nb(III) ions, and they are reduced by the steps $Nb(III) \rightarrow Nb(II) \rightarrow Nb(0)$.

Lantelme *et al.*(21) concluded that during the reduction of Nb(III) to the metal an intermediate step occurs during this reaction involving Nb(II) which forms a thin electroactive layer of insoluble cluster compounds at the electrode surface. This agrees with our results, since the cyclic voltammetry and convolution voltammetry confirmed the existence of an adsorption reaction. The electron number involved during step G was found equal to 1.24, thus we can suggest the reduction of Nb(III) ions resulted from the dissociation of Nb_3Cl_8 to Nb(II) electroactive layer adsorbed on the electrode surface.

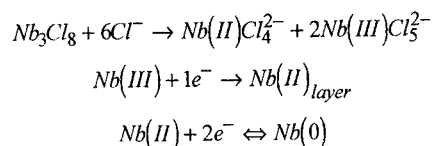
The main cathodic peak D is attributed to the formation of niobium metal. The electron exchange during this step was found to be 2.14, it will therefore be assumed that the reaction along the cathodic peak D is:



It is however certain that the process D/D' corresponds to a superimposition of several processes. This was confirmed by semi-integration which showed the character apparently soluble of the product formed during step D, cyclic voltammetry also showed that the anodic charge involved during step D' was half of the cathodic step D. This suggests that deposited niobium may be dissolved in the melt through a disproportionation reaction.

CONCLUSION

The cathodic behavior of Nb_3Cl_8 was studied by cyclic voltammetry and convolution voltammetry. The results suggest that the mechanism is mainly two reduction steps, the first step is irreversible and the second is close to reversible charge transfer, the following mechanism is then proposed:



ACKNOWLEDGEMENT

One of the authors (M.M) is gratefully indebted to Japan Society for the Promotion of Science(JSPS) for the assistance of a post-doctoral fellowship. The authors would like to acknowledge Dr. Zhu and Mr. Kariya for helpful discussions and assistance during the course of the investigation.

REFERENCES

1. L. Arurault, J. Bouteillon and J. C. Poignet, *J. Electrochem. Soc.*, **142**, 3351, (1995).
2. E. G. Polyakov, L.P. Polyakova and I. R. Elizarova, *Russ. J. Electrochem.*, **31**, 457, (1995).
3. G. W. Mellors and S. Senderoff, *J. Electrochem. Soc.*, **112**, 266, (1965).
4. E. M. Levin, C. R. Robbins and H. F. McMurdie, *Phase Diagrams for Ceramists*, The American Ceramic Society, (1964).
5. T. Ejima, Y. Sato, A. Ando and T. Asakawa, *J. Jpn. Inst. Metals*, **45**, 368, (1981).
6. Y. Sato and T. Ejima, in *Molten Salts/1983*, M. Blander, D. S. Newman, G. Mamantov, M-L. Saboungi and K. Johnson, Editors, **PV 84-2**, p121, The Electrochemical Society Proceedings Series, Pennington, NJ(1984).
7. Y. Saeki, M. Yanai and A. Sofue, *Denki Kagaku*, **40**, 816, (1972).
8. K. B. Oldham, *J. Electroanal. Chem.*, **121**, 341, (1981).
9. I. Barin, *Thermochemical Data of Pure substances*, VCH, (1989).
10. R. H. Wopschal, I. Shain, *Anal. Chem.*, **39**, 1514, (1967).
11. J. C. Imbeaux, J. M. Saveant, *J. Electroanal. Chem.*, **28**, 325, (1970).
12. E. Laviron, *Electroanal. Chem. and Interf. Electrochem.*, **52**, 355, (1974).
13. A. J. Bard and L. R. Faulkner, *Electrochemical Methods: Fundamentals and applications*, John Wiley & Sons, New York (1980).
14. J. M. Saveant and D. Tessier, *J. Electroanal. Chem.*, **65**, 57, (1975).
15. D. Renaud, Ph.D Thesis, INP, Grenoble (1985).
16. M. Grenness and K. B. Oldham, *Anal. Chem.*, **44**, 1121, (1972).
17. P. Delahay, *New Instrumental Methods in Electrochemistry*, Interscience, New York (1954).
18. V.V. Safonov, B. G. Korshunov and A.A. Yarovoi, *Russ. J. Inorg. Chem.*, **11**, 918, (1966).
19. V.V. Safonov, B. G. Korshunov and S.N. Steblovskaia, *Russ. J. Inorg. Chem.*, **11**, 1148, (1966).
20. K. Zhou, T. Takenaka, N. Sato and M. Nanjo, *Denki Kagaku*, **59**, 981, (1991).
21. A. Salmi, Y. Berghoute and F. Lantelme, *Electrochimica Acta*, **40**, 403, (1995).

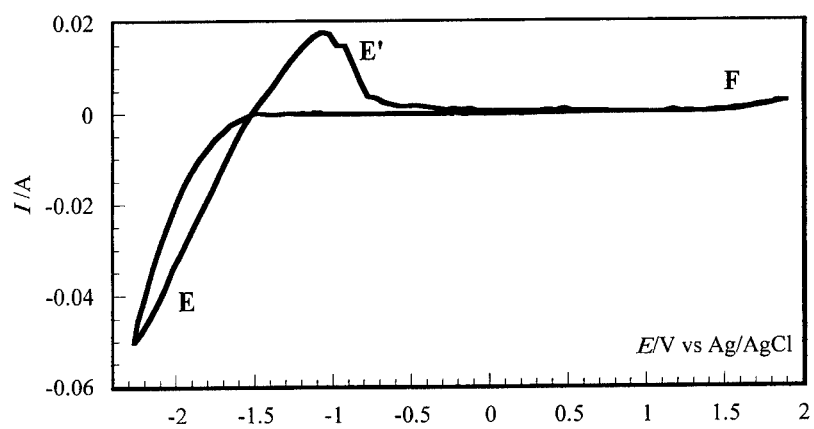


Fig.1 Cyclic voltammogram obtained on tungsten electrode at 1V/s in molten MgCl_2 -NaCl eutectic at 471°C. Electrode area: $1.96 \times 10^{-3} \text{ cm}^2$

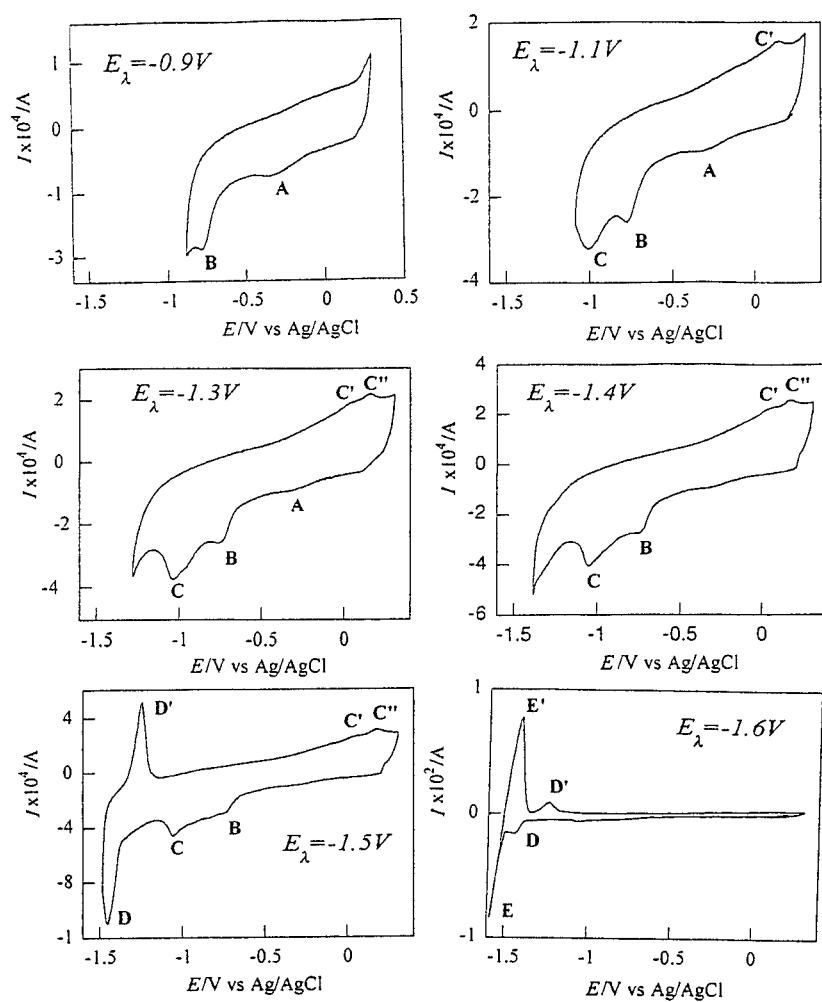


Fig. 2 Cyclic voltammograms for different cathodic reversal potential at tungsten electrode in $\text{MgCl}_2\text{-NaCl-Nb}_3\text{Cl}_8$ ($<0.07\text{mol}\%$). $T=471^\circ\text{C}$, $v=0.2\text{V/s}$
electrode area= $1.96 \times 10^{-3}\text{cm}^2$

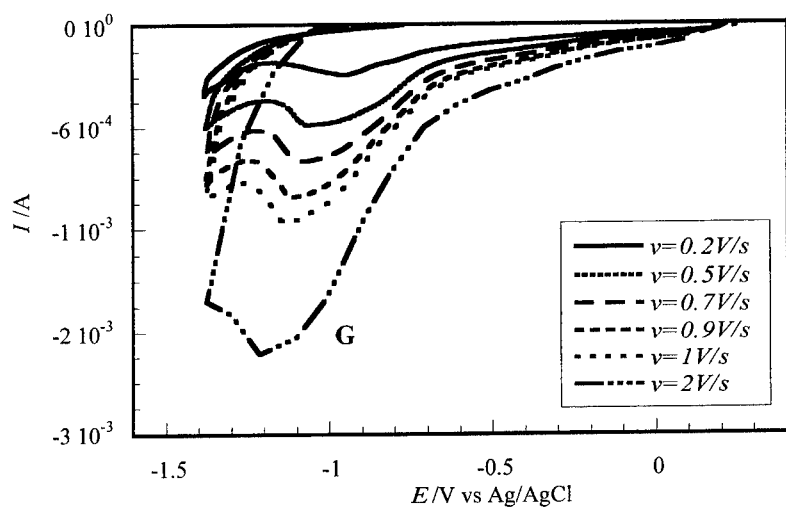


Fig.3 Cathodic voltammograms recorded at tungsten electrode in the $\text{MgCl}_2\text{-NaCl-Nb}_3\text{Cl}_8$ system at various potential sweep rate.

$T=471^\circ\text{C}$, $[\text{Nb}_3\text{Cl}_8]<0.07\text{ mol\%}$, $A=0.00396\text{cm}^2$.

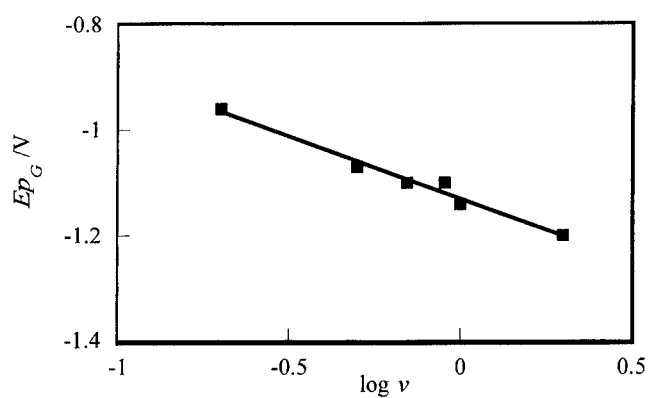


Fig. 4 Relation between the E_{p_G} and the logarithm of the potential sweep rate for the voltammograms of Fig.3.

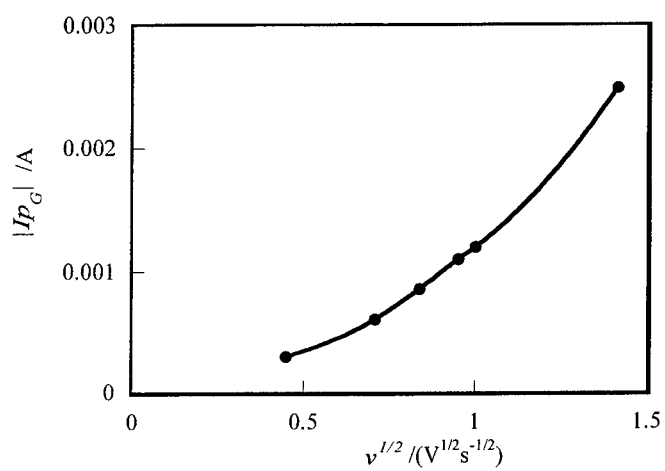


Fig.5 Variation of the I_{p_G} versus $v^{1/2}$ in the same system as Fig. 3.

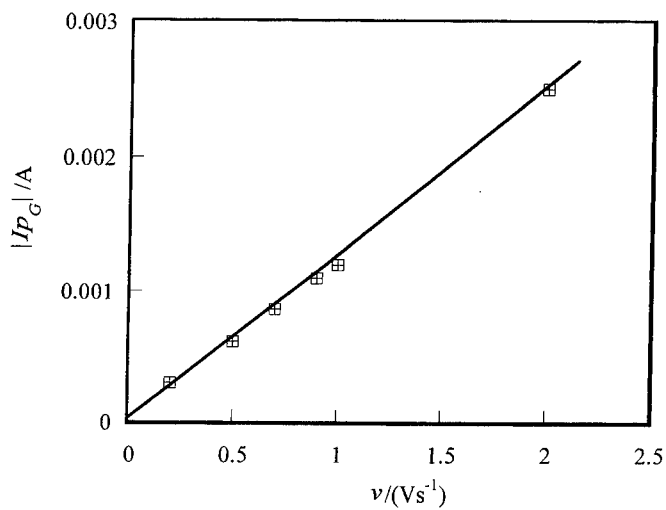


Fig.6 Dependence of the I_{p_G} on the potential sweep rate for the same system as in Fig.3.

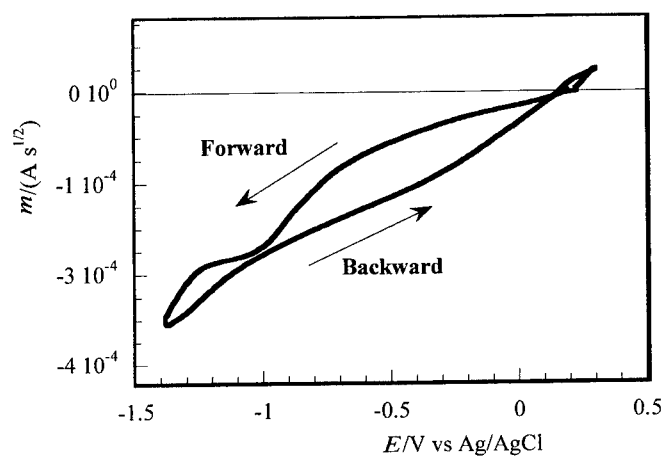


Fig.7 Semi-integral curve related to a voltammogram from Fig. 3.
 $v=0.2\text{V/s}$

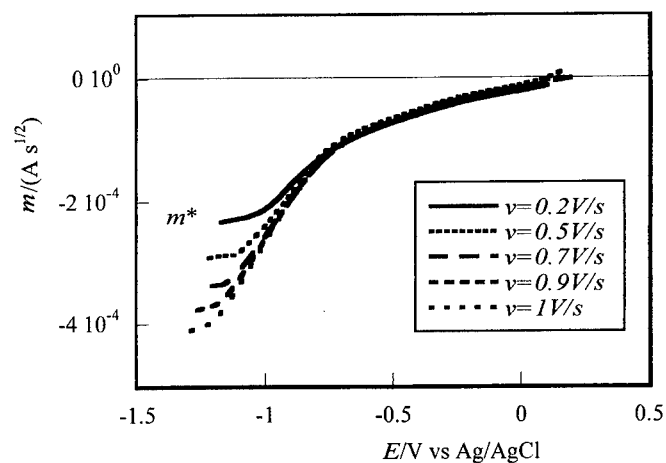


Fig.8 Cathodic semi-integral curves related to the voltammograms of Fig.3 for various potential sweep rates.

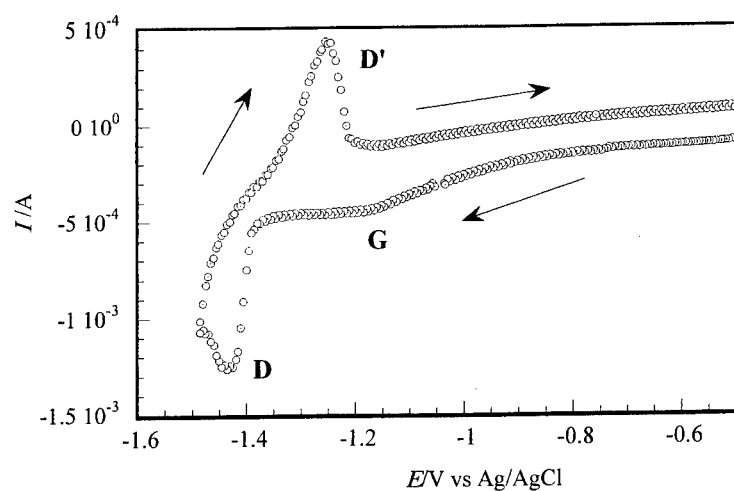


Fig. 9 Cyclic voltammogram for the reduction of Nb_3Cl_8 (<0.07mol%) in the MgCl_2 - NaCl eutectic at 471°C . Potential range -0.2V to -1.5V.

Electrode Area: $1.96 \times 10^{-3} \text{ cm}^2$, $v = 0.1 \text{ V/s}$

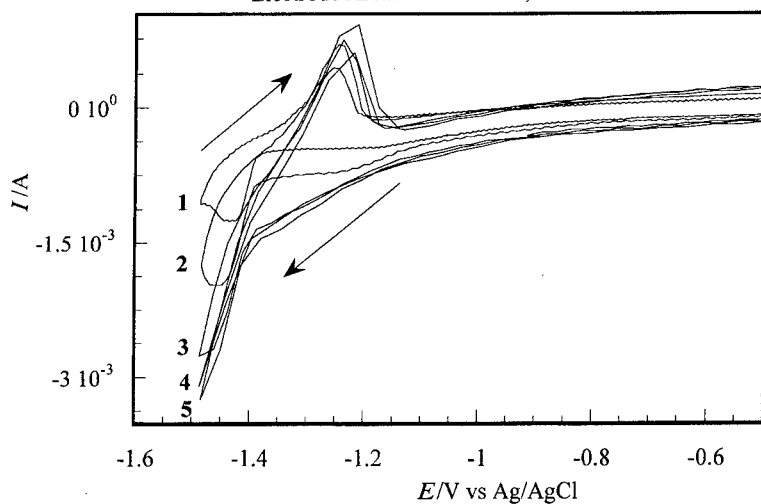


Fig. 10 A series of voltammograms for various sweep rates :1,0.1; 2,0.2; 3,0.5; 4,0.7 and 5, 0.8V/s. $[\text{Nb}_3\text{Cl}_8] < 0.07 \text{ mol\%}$, Electrode area : $1.96 \times 10^{-3} \text{ cm}^2$

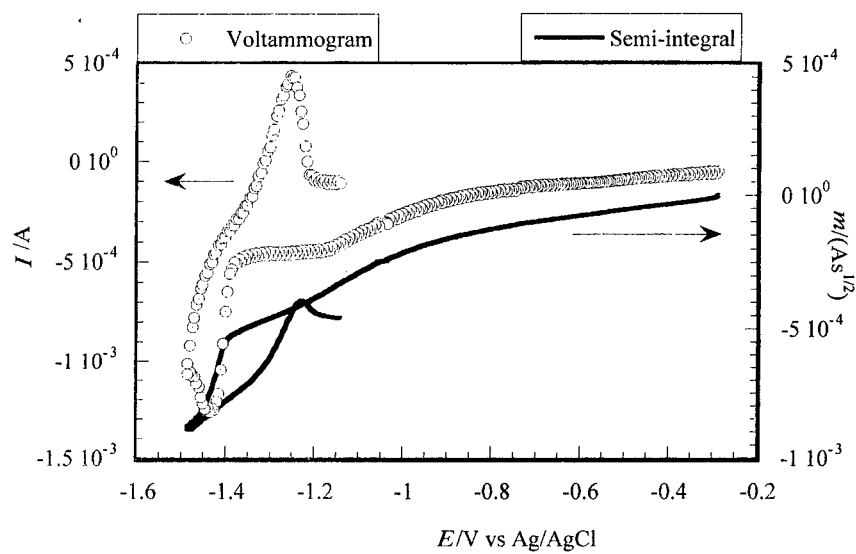


Fig. 11 Cyclic voltammogram and its corresponding semi-integral.
Electrode area= $1.96 \times 10^{-3} \text{ cm}^2$, $v = 0.1 \text{ V/s}$

DEMONSTRATION EXPERIMENT OF URANIUM METAL PRODUCTION SYSTEM

Toru Suzuki, Takeshi Sakata, Haruaki Tsuchiya
Metal Mining Agency of Japan
Tokiwa Bldg. 1-24-14 Toranomon, Minato-ku, Tokyo 105, Japan

Kazuaki Ota, Yutaka Takasawa, Naoki Teramae, Sumio Yamagami
Naka Energy Research Center, Mitsubishi Materials Corporation
1002-14 Mukoyama, Nakamachi, Nakagun, Ibaraki 311-01, Japan

Kazuhiro Endo
Nuclear Energy Business Center, Mitsubishi Materials Corporation
Koishikawa Daikoku Bldg. 1-3-25 Koishikawa, Bunkyo-Ku, Tokyo 112, Japan

ABSTRACT

Demonstration experiments of uranium metal production system have been carried out in order to verify its technical feasibility. Uranium metal is produced from its oxides by molten salt electrolysis and continuously cast into an uranium ingot by Vacuum Melting and Pressurized Upward Continuous Casting (VMCC) method. Current efficiency of electrolysis was around 50%, which was higher value than those reported in earlier experiments. A rod of uranium metal, which is 80 cm in length and 1cm in diameter, was obtained with high purity (>99.7%) through the production system. Major impurities in the metal were B, C, Cr, Fe, Mn, Mo, Ni, O and W, which are from its oxide raw material, cell materials and salt impurities.

INTRODUCTION

The atomic vapor laser isotope separation (AVLIS) will be a promising uranium enrichment technology for the next generation because of its high cost performance and high enrichment efficiency. In this AVLIS enrichment process, uranium metal or uranium metal alloy will be used as feed material. Today, commercial production of uranium metal in the world is done by thermite reduction of UF_4 with magnesium ⁽¹⁾. In this thermite process, large amount of MgF_2 contaminated with uranium is produced as a byproduct simultaneously.

Considering cost performance, minimization of waste production and continuous process concept, an electrolytic process for producing uranium metal directly from uranium oxide will offer potential advantages over the existing commercial process ⁽²⁾.

Metal Mining Agency of Japan has carried out a feasibility study on metallic uranium production systems for AVLIS feed materials since fiscal 1989. In this study, uranium metal

production from uranium oxide by molten salt electrolysis has been examined to get basic characteristics of electrolysis and design data for scale-up^(3, 4), and system component technologies such as molten salts electrolysis for uranium metal production and continuous casting have been developed.

Process Concept

A process flow sheet of uranium metal production and a future concept of apparatus is shown in Fig.1 and Fig.2, respectively. Uranium oxide (UO_2) was directly reduced into uranium metal by electrolysis in molten fluoride melts. The molten uranium metal is transferred to VMCC stage, and cast into a uranium ingot (Rod). In this conceptual process, uranium oxide will be directly converted into uranium metal rod. In this study, however, electrolysis and casting experiments were carried out separately to confirm its technical feasibility.

EXPERIMENT

Electrolysis

Reagent - Mixture of BaF_2 , LiF and UF_4 salts was used as electrolyte. Its composition was $\text{BaF}_2\text{-LiF-UF}_4$ (74-11-15 wt.%). Uranium tetrafluoride acts as solvent for uranium oxide in this electrolysis. Lithium fluoride acts to increase the electrical conductivity of electrolyte. These salts were reagent grade chemicals. Uranium tetrafluoride was produced by a reaction of UO_2 with HF at about 400°C . These fluorides were mixed and premelted before experiment. In most cases, UO_3 produced by fluidized bed denitration was used as starting material. Uranium trioxide was also treated in a vacuum furnace to remove remaining acidic moisture at 450°C . Triuranium octoxide (U_3O_8) was prepared by calcination of UO_3 in the N_2 atmosphere at 650°C . Uranium dioxide was prepared by reduction of UO_3 with hydrogen at 600°C .

Apparatus - A schematic feature of an electrolytic apparatus and an outline of the apparatus are shown in Fig.3 and Table 1, respectively. The electrolytic cell made of graphite has a size of 20cm inner diameter and 35cm in height. The present cell concept is a neutral hearth with a rod type cathode, which is different from the Hall process. The anode is made of graphite which has a cylindrical shape with slits as a standard case. The cathode rod is made of tungsten. It is considered to act as uranium electrode under electrolysis because the tungsten surface is covered with liquid uranium. A graphite uranium metal receiver covered with boron nitride has a capacity for 3 kg uranium metal and is set just below the cathode. The electrolytic cell is enclosed in a quartz tube with steel flanges so that a gas tight enclosure was achieved. Argon gas with high purity is used as purge gas in the cell. Off gas is introduced to gas mass spectrometer (UTI Instruments Co., ISS-325A), for the measurement of gas components such as CO , CO_2 and CF_4 with electrolysis. Direct current generator for electrolysis has a capacity of 0~20V and 0~500A. Induction heating which has a maximum heating capacity of 1400°C (Fujidenpa Kogyo Co. Ltd., 440V-50Hz, 3-Phase, 280kVA) is used to bring the cell to the experiment temperature of about 1200°C and maintain it during the experiment.

Procedure - Mixture of LiF, BaF₂ and UF₄ was pretreated in a vacuum at 400°C and in Ar at 800°C for 30 minutes in order to evacuate volatile species and moisture, then heated up to about 1200°C, which is well over the melting point of LiF-BaF₂-UF₄ electrolyte and the melting point of uranium metal (1132°C). The electrodes and uranium receiver assembly were immersed slowly into the electrolyte to a desired depth. All of the experiments were carried out by constant current mode. Before melting, all of the uranium oxides were fed into the cell. And off-gas composition was analyzed continuously with electrolysis. Direct current, cell voltage, temperature, and induction heating power were also recorded continuously. After electrolysis, cathode and anode electrodes assembly, and uranium metal receiver were removed upward in order to minimize back-reaction of the metal with the electrolyte. After cooling, uranium metal was removed from the receiver and was weighed. Electrolysis experiments were repeated 5 times in an optimum condition in order to confirm its reproducibility.

Uranium Metal Rod Production

In order to confirm the production of uranium metal rod by continuous casting and to minimize the scrap of uranium metal, an availability of Vacuum Melting and Pressurized Upward Continuous Casting (VMCC) ⁽⁵⁾ method was examined. A summary of the experimental conditions is listed in Table 2.

Uranium Material - The uranium metal produced by electrolysis mentioned above is used for this casting experiment. In order to remove the salts on the metal, the uranium metal was immersed in nitric acid (reagent grade) and rinsed by both distilled water and acetone (reagent grade).

Apparatus - A schematic diagram of VMCC experimental apparatus is shown Fig.4. The containment vessel is made of stainless steel and has a size of 120cm I.D. and 120cm in height, and a total volume is 1.1m³. The inner wall of the cell is cooled by water. The cell is enclosed so tightly that air contamination cannot be brought into the cell. First, the air in the tank is degassed by a oil-diffusion pump, and the pressure can be achieved 1×10^{-5} Torr within 60 minutes. Then, the cell is filled with high purity Ar gas (>99.999%). A crucible for melting uranium made of graphite has a size of 15cm inner diameter and 18cm in height. This graphite crucible is heated by induction heating (Max. 60kW, 1500°C). A nozzle is attached to a copper jacket cooled by water in order to cast molten uranium metal into a rod.

Procedure - Initially, uranium metal (~16 kg) was charged into the graphite crucible. The cell was enclosed. Under a pressure of 1×10^{-4} Torr, the metal was heated up to a temperature of about 100~200°C higher than the melting point of U (1132°C). Keeping a vacuum under 3×10^{-4} Torr for a couple of hours, salt impurities such as Ba, F and Li volatile during this period. And then Ar gas of high purity was purged into the cell up to a pressure of 2.5×10^5 Pa. A tip of the nozzle was dipped into molten uranium bath, and a cylindrical rod was cast upward continuously.

RESULTS AND DISCUSSION

Electrolysis

Uranium Metal - Five electrolytic experiments were carried out. The typical cell voltage and current chart are shown in Fig.5. A summary of the results are listed in Table 3. Uranium metal was obtained in three forms of "ingot", "shot" and "powder". Considering this uranium is transferred to the casting experiments, it is better to produce uranium metal as an "ingot". Thus, experimental conditions were optimized to produce this required metal, as well as to achieve higher current efficiency. Except for Test 1, more than 1kg uranium metal were produced as aggregate form.

In this electrolysis process, uranium ion was reduced to uranium metal on the surface of the tungsten cathode, and liquid uranium metal will flow downward into the graphite crucible under the cathode. And then uranium metal was coalesced making "metal pool" in the crucible. In our experiments, metal coalescence tends to become poorer with higher oxide ion (O^{2-}) concentration in the melts.

Off-Gas Analysis - During electrolysis off-gas from the cell was introduced to the gas mass spectrometer, and the concentrations of CO , CO_2 and CF_4 gas were analyzed. The typical off gas (CO , CO_2 and CF_4) chart data is shown in Fig.6.

During electrolysis, CO , CO_2 and CF_4 gas were continuously detected. In addition to the oxidation of O^{2-} in the melts, F^- were simultaneously oxidized at the surface of the anodes. Though CF_4 gas was evolved, a sudden increase in cell voltage such as "anode effect" was not observed all through the experiments.

Current Efficiency - Current efficiencies of each experiment were calculated by the off-gas volume of CO , CO_2 and CF_4 , and by weight of uranium metal produced. From Test 2 to Test 5, both of the CE values are consistent and around 50%. These values seem to be higher compared with other electrolytic oxide processes. However, these relatively low values might be attributed to several side reactions such as;



Uranium Metal Rod Production

To confirm the reliability of the apparatus and the reproducibility of the casting, five casting experiments are conducted. In all tests, uranium metal were cast in a form of a rod (49~80cm in length, 1cm-O.D.). The length of the rod was restricted by a usable uranium metal weight. The defects in the rods were not observed. But it is necessary to improve the surface of the rod and the casting speed. Through five tests, there was not observed any operational problem. The casting conditions and the results are summarized in Table 4.

Impurities Behavior in the Process

Impurities in each uranium formed in this process are analyzed and shown in Table 5.

These analyzed values were deviated depending on sampling points.

Uranium metal rods in the final product have impurities such as B, C, Cr, Fe, Mn, Mo, Ni, O and W.

It was found that B, Mo and W in the uranium metal were from cell assembly materials such as BN insulator, Mo rod, W cathode and Mo induction insulation sheet. And Cr, Fe, Mn and Ti which were impurities in uranium oxide were reduced and condensed in the uranium metal. Na, Ca and P were not transferred to the metal and remained in the electrolyte. Ba, Li and F were contaminants from the salt and were easily separated by volatilization or mechanical settlement of liquid.

After melted in vacuum atmosphere and cast, it appeared that the concentration of volatile species such as Ba, C, F, N, Na, Li and O decreased but that heavy metals such as Cr, Fe, Mo and W still remained in uranium metal.

CONCLUSION

Demonstration experiments of uranium metal production system has been carried out. Uranium metal was produced from its oxides by molten salt electrolysis and cast into an uranium ingot by Vacuum Melting and Pressurized Upward Continuous Casting (VMCC) method. For the electrolysis, current efficiency obtained was around 50%, which was higher value than reported in earlier experiments. A rod of uranium metal, which is 80 cm in length and 1cm in diameter, was produced with high purity (>99.7%). The origination of the impurities contained in the metal such as B, C, Cr, Fe, Mn, Mo, Ni, O and W were identified.

ACKNOWLEDGEMENT

This work was funded by the Ministry of International Trade and Industry of Japan.

REFERENCES

- (1) C.D.Harrington and A.E.Ruchle, "*Uranium Production Technology*", D.Van Nostrand Co., Inc., Princeton (1959).
- (2) K.O.Laughon, "*Uranium Processing for the AVLIS Enrichment Process*", Uranium Seminar '89 (1989)
- (3) Y. Takasawa, K. Ota, T. Onoue, S. Yamagami, H. Ikeda, H. Kubota, K. Nakamura and K. Endo, in "*Proceedings of the Ninth International Symposium on Molten Salts*", Charles L. Hussey, David S. Newman, Gleb Mamantov and Yasuhiko Ito, Editors, PV 94-13, pp. 665-672, The Electrochemical Society, Pennington, NJ (1994).
- (4) H. Ikeda, H. Kubota, K. Nakamura, K. Ota, Y. Takasawa, T. Onoue, S. Yamagami, and K. Endo, in "*Proceedings of the Ninth International Symposium on Molten Salts*", Charles L. Hussey, David S. Newman, Gleb Mamantov and Yasuhiko Ito, Editors, PV 94-13, pp. 673-680, The Electrochemical Society, Pennington, NJ (1994).
- (5) Y. Mae and R. Iwai, "*Development of the vacuum melting pressurized upward continuous casting process.*" in "*Proceedings of the Ninth International Vacuum*

Metallurgy Conference on Special Melting. pp. 223-231, San Diego, California, April 11-15 (1988).

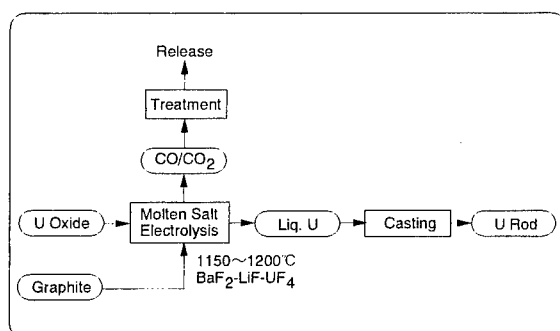


Fig.1 A Process Flow of Uranium Metal Production.

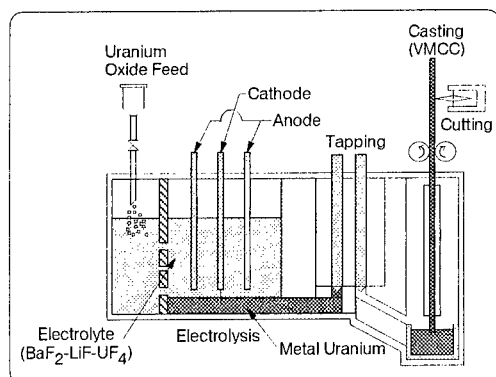


Fig.2 A Future Concept of Apparatus.

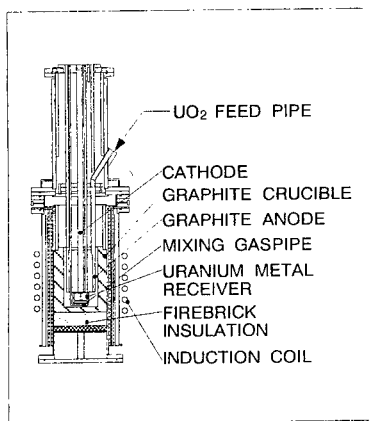


Fig.3 Schematic Diagram of Electrolytic Experimental Apparatus.

Table 1 Typical Operating Data for Electrolytic Reduction of Uranium Oxides to Uranium Metal.

Cell size	20cm ID × 33cm high
Electrolyte	BaF ₂ -LiF ₂ -UF ₄ (74-11-15 wt.%)
Temperature	1150°C
Anode type	Graphite
Anode shape	Rods
Cathode type	Tungsten rod (22 mm OD)
Current	200 A
Anode current density	0.635-0.667 A/cm ²
Cathode current density	2.05-2.31 A/cm ²
Feed material	UO ₂
Uranium metal receiver	Graphite crucible surrounded with BN insulation
Heating	Induction coil heating

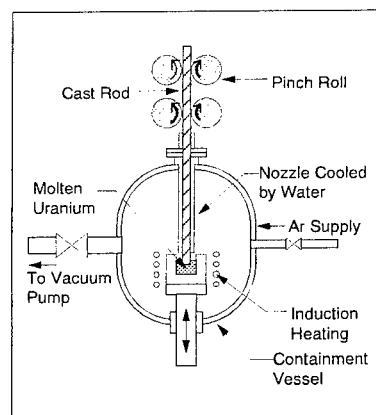


Fig.4 A schematic diagram of VMCC experimental apparatus.

Table 2 A summary of the experimental conditions. (VMCC)

Cell Size	120cm-OD × 120 cm High
Cell Volume	1.1 m ³
Uranium Charged	14-20 kg/Batch
Crucible	Graphite (15 cm-ID × 18 cm high)
Nozzle	Graphite or Y ₂ O ₃
Heating	Induction Heating
Temperature	1250-1350 °C
Pressure	1.5-2.5 × 10 ⁵ Pa
Casting Speed	3-30 mm/min
Cast Rod Shape	Cylindrical
Rod Size	10 mm-OD

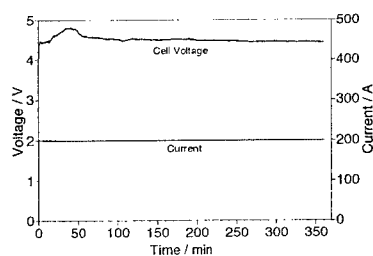


Fig.5 The typical cell voltage and current chart during electrolysis. (Test 4)

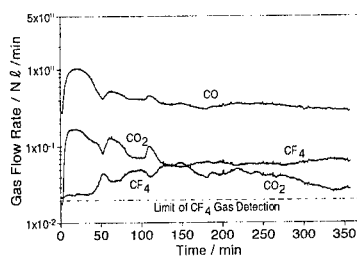


Fig.6 The typical off gas (CO, CO₂ and CF₄ gases) chart during electrolysis. (Test 4)

Table 3 Summary of the Electrolytic Experiments.

	Test 1	Test 2	Test 3	Test 4	Test 5
Temperature of electrolyte	1110-1152°C	1104-1153°C	1103-1186°C	1101-1153°C	1097-1152°C
Anode Current Density	0.635 A/cm ²	0.667 A/cm ²	0.667 A/cm ²	0.667 A/cm ²	0.667 A/cm ²
Cathode Current Density	2.05 A/cm ²	2.14 A/cm ²	2.31 A/cm ²	2.31 A/cm ²	2.31 A/cm ²
Cell Voltage	3.59-4.21 V	3.95-4.36 V	3.93-4.38 V	4.19-4.58 V	3.81-4.45 V
U (ingot)	197 g	1082 g	1231 g	1295 g	1253 g
U (shot)	251 g	63 g	51 g	67 g	75 g
U (powder)	245 g	47 g	47 g	34 g	42 g
CE (Calculated by metal weighed)	44 %	53 %	50 %	52 %	51 %
CE (Calculated by off-gas volume)	64 %	52 %	50 %	49 %	48 %

Table 4 The casting conditions and the results.

	Test 1	Test 2	Test 3	Test 4	Test 5
Pressure	2.5×10^5 Pa	2.5×10^5 Pa	2.5×10^5 Pa	2.5×10^5 Pa	2.5×10^5 Pa
Temperature	1336-1340°C	1361-1368°C	1363-1367°C	1354-1362°C	1355-1358°C
Casting Speed	8 mm/min	8 mm/min	8 mm/min	8 mm/min	8 mm/min
Cast Rod Size	1cm ^{OD} × 80 cm ^L	1cm ^{OD} × 54 cm ^L	1cm ^{OD} × 49 cm ^L	1cm ^{OD} × 59 cm ^L	1cm ^{OD} × 61 cm ^L
Crack	Some	Some	Some	Some	Some
Inside Defect	None	None	None	None	None

Table 5. Analytical Results of Impurities of Uranium Oxide, Fluoride Salts, Uranium Metal and Uranium Ingot.

Impurities Elements	UO ₂ as Feed Material	Salts before Electrolysis	Metal U (5 Tests Averaged)	Salts after Electrolysis	U ingot by VMCC
Ag	<2	<2	<2	<2	<2
B	<0.4	1	164	<0.4	100
Ba	<2	-	1830	-	2
Be	<2	<2	<2	<2	<2
Bi	<1	<1	<1	<1	<1
Ca	<5	<5	9	33	<5
Cd	<0.4	<0.4	<0.4	<0.4	<0.4
Co	<2	<2	<2	<2	<2
Cr	<5	<5	15	<5	150
Cu	1	<1	2	<1	3
Fe	15	20	244	<10	300
In	<1	<1	<1	<1	<1
Li	<2	-	108	-	<2
Mg	<1	<1	<1	<1	<1
Mn	<1	<1	11	<1	22
Mo	1	>4000	>4000	290	1100
Na	<1	87	3	240	<1
Ni	<5	<5	5	<5	26
P	<50	2200	50	7000	<50
Pb	<1	<1	<1	<1	<1
Si	<10	<10	13	<10	10
Sn	<1	<1	<1	<1	<1
Ti	<4	9	25	<4	6
V	<1	1	5	<1	1
W	<50	<50	170	<50	400
Zn	<10	<10	<10	<10	<10
C	-	-	777	-	279
N	-	-	33	-	3
O	-	-	807	-	141
F	400	-	584	-	5

**A STUDY OF PRODUCTION PROCESS OF URANIUM METAL BY
MOLTEN SALT ELECTROLYSIS USING ZINC CATHODE
---A STUDY OF URANIUM CHLORIDE PRODUCTION STEP---**

Haruaki Tsuchiya¹⁾, Takeshi Sakata¹⁾, Toru Suzuki¹⁾
Jun-ichi Takahashi²⁾, Takahiro Fukamachi²⁾, Yoshio Kijima³⁾, Keiji Toyabe²⁾

1) Technical Development Department, Metal Mining Agency of Japan
Tokiwa BLDG., 1-24-14 Toranomon, Minato-ku, Tokyo, Japan

2) Research and Development Center, Energy and Environment Business Division,
Sumitomo Metal Mining Co., LTD.

2600 Ishigamitokujuku, Tokai-mura, Ibaraki-ken, Japan

3) Energy and Nuclear Power Department, Energy and Environment Business Division,
Sumitomo Metal Mining Co., LTD.

5-11-3 Shinbasi, Minato-ku, Tokyo, Japan

ABSTRACT

The production process of uranium tetrachloride powder by a single reaction of uranium oxide reduction and chlorination with chlorine gas in the presence of carbon as a reductant was investigated. This process is aimed at the production of high purity uranium metal for the ^{235}U isotopic enrichment process by Atomic Vapor Laser Isotope Separation (AVLIS). Direct production of uranium tetrachloride became possible by using a vertical type chamber. A high reaction temperature and low chlorine potential are necessary for uranium tetrachloride production. UO_2 , U_3O_8 and UO_3 had no significant difference as starting uranium oxides.

INTRODUCTION

The AVLIS (Atomic Vapor Laser Isotope Separation) technology for the enrichment of ^{235}U has been studied intensively in Japan, USA and France. The magnesium thermite method has been widely adopted to produce the uranium metal which is the starting material for the AVLIS process. However, a large amount of magnesium fluoride slag is produced as solid waste containing trace amounts of uranium. The molten salt electrolysis method has been developed for uranium metal production in Japan to avoid this problem⁽¹⁾⁻⁽³⁾. The authors have been studying the uranium metal production process by molten salt electrolysis of UCl_4 using a molten zinc cathode. Fig.1 illustrates the overall flow sheet of the process. The present report is concerned with the authors studies of UCl_4 direct production by Cl_2 gas with carbon as a reductant.

Experiments were carried out by the following three scales;

- 1. 30g-U scale:** study on the influence of reaction temperature, amount of reductant and chlorine gas volume
- 2. 300g-U scale:** study on the influence of chamber type, reaction temperature, starting oxide, carrier gas and contamination of impurities
- 3. 1kg-U scale:** study on factors in larger-scale experiments

EXPERIMENTAL

30g-U scale experiment(horizontal type chamber)

A schema of the reaction chamber is illustrated in Fig.2. The starting material was a mixture of uranium dioxide powder and graphite powder as a reductant. Uranium chloride was produced by chlorine gas, then vaporized uranium chloride was condensed in the cooling part in a quartz cell. Experimental conditions are listed in Table 1. Chlorine and uranium in the chloride were analyzed by titration and ICP respectively.

300g-U scale experiment(vertical type chamber)

A schema of the reaction chamber is illustrated in Fig.3. The starting material was a pelletized mixture of uranium oxide and graphite powder. Ar or N₂ was used as carrier gas. The other experimental procedures were basically the same as the 30g-U scale experiment. Experimental conditions are listed in Table 2.

1Kg-U scale experiment

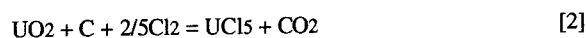
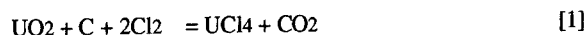
The size of the experimental apparatus was twice the diameter of the 300g-U scale. Experimental procedures were the same as the 300g-U scale. Experimental conditions are listed on Table 4.

RESULTS AND DISCUSSION

30g-U scale experiment(horizontal type chamber)

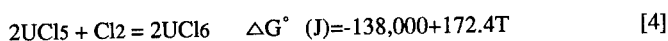
The results are listed in Table 1. All of the uranium dioxide was chlorinated under all the experimental conditions except 1hr chlorination. Cl/U molar ratios were around 6. This means that the produced uranium chlorides were UCl₆.

[1],[2],[3] are the equations of Cl₄,Cl₅,Cl₆ formation from UO₂, respectively.





If UCl₆ was produced directly from UO₂, the reaction proceeded according to eq.[3]. However, from a thermodynamic point of view, it is hardly considered that direct UCl₆ formation proceeded under these conditions. Fig.4 shows the potential diagram of the U-O-Cl ternary system at 1173K. Considering that carbon was saturated and the inlet gas was only Cl₂, it is reasonable to assume that logp_{O2} is -15~-20(atm) and logp_{Cl2} is 0. Given these potentials, the governing equation has to be [2]. On the other hand, as shown in eq.[4], ΔG° is negative under 800K. This means that UCl₅ is possibly chlorinated to UCl₆ at lower temperature whenever Cl₂ pressure is high enough. That is to say, it is speculated that UCl₅ was produced in the furnace then chlorinated to UCl₆ by excess Cl₂ gas at a lower temperature zone.



For producing UCl₄, from this speculation, it is necessary not only to raise the reaction temperature but also to reduce excess Cl₂ gas.

300g-U scale experiment(vertical type chamber)

Vertical type chamber has a structure which allows Cl₂ gas to pass through the pellet zone. That structure is suited to reduce excess Cl₂.

The efficiency of Cl₂ and Cl/U molar ratios are listed in Table 2. The efficiency was much higher than the horizontal chamber and Cl/U ratios of all products were almost 4. This means that the reaction proceeded according to eq.[1] and direct production of UCl₄ from UO₂ became possible by using the vertical type chamber.

Another controlling factor was carrier gas. Chlorine potential was decreased (logp_{Cl2} < -0.3) by introducing Ar gas. Considering that the chlorine potential between UCl₄ and UCl₅ is -0.45 in Fig.4, the numerical value of -0.3 is low enough for tetrachloride production.

Temperature: The yield of uranium chloride(calculated value into weight of uranium in chloride) at 1073K was much less than that of 1173K. Operation at 1173K was preferable to 1073K.

Carrier gas: Ar and N₂ had no significant difference on the chloride products. Production cost will be reduced by using N₂ gas instead of Ar gas.

Starting oxide: UO₂, U₃O₈ and UO₃ had no significant difference on the

treatment efficiency. From a thermodynamic point of view, this result is reasonable as far as O₂ and Cl₂ potentials are low enough. Production cost will be possible to be reduced by using U₃O₈ or UO₃ instead of UO₂.

Impurities: The impurities in uranium chloride are listed in Table 4 with Pre-AVLIS requirement data. Product had less impurity than Pre-AVLIS requirement. As for the uranium oxy-chloride, no evidence of its existence was observed in any of the experiments.

1Kg-U scale experiment

The results are listed in Table 3. Cl/U molar ratio were almost 4. Recovery of uranium was high(>96%). These results show that this method was able to be adopted to a larger size uranium tetrachloride production process.

CONCLUSIONS

1. The vertical type chamber is very suitable for the UCl₄ production process.
2. The influences of fundamental parameters were confirmed as follows;
(1)reaction temperature;1173K was preferable to 1073K
(2)carrier gas ;there are no differences between Ar and N₂
(3)starting oxide ;there are no differences among UO₂, U₃O₈ and UO₃
(4)impurities ;the percentage of impurities in the product was low enough
3. This method is possible to be adopted to a larger size uranium tetrachloride production process.

ACKNOWLEDGMENT

This work was funded by the Ministry of International Trade and Industry of Japan.

REFERENCES

1. T. Kuroda: Electrochemistry Handbook, 2nd Edition, Maruzen, p1055(1964).
2. T. Kuroda: Denki Kagaku, 33, p116(1965).
3. T. Mukaibo and M. Kanno: J. Atomic Energy Society Japan, 7[8], p410(1965).
4. P. A. Haas, D. D. Lee and J.C.Mailen: "Reaction of Uranium Oxides with Chloride and Carbon Monoxide to Prepare Uranium Chlorides" ORNL / TM - 11792 (1991)

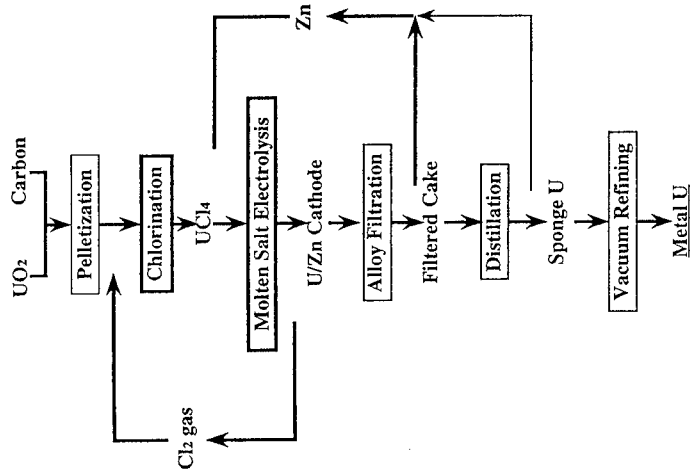


Fig.1 Flowsheet of Uranium Metal Production Process

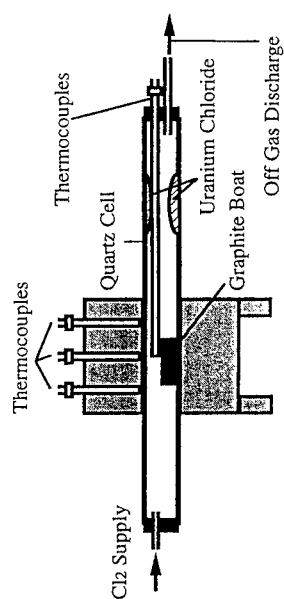


Fig.2 Schema of Horizontal Type Chamber

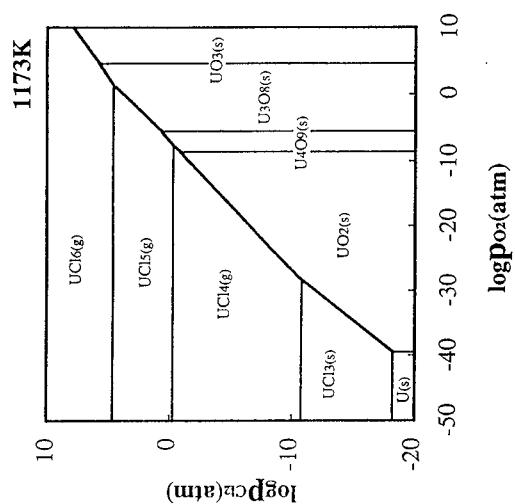


Fig. 4 Potential Diagram of U-O-Cl Ternary System

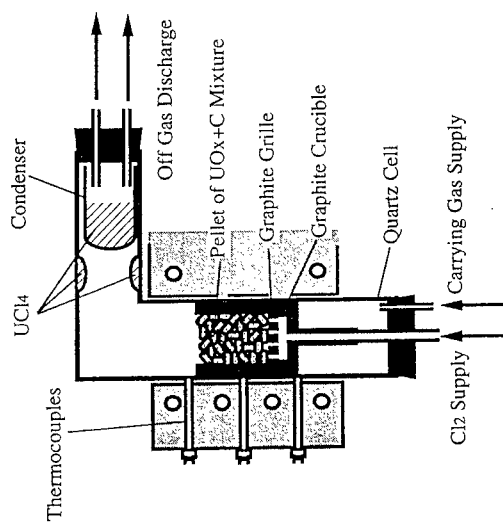


Fig.3 Schema of Vertical Type Chamber

Table 1 Experimental conditions and results of the 30g-U scale experiments

Starting Oxide	UO ₂	UO ₂	UO ₂	UO ₂	UO ₂	UO ₂	UO ₂	UO ₂	UO ₂	UO ₂	UO ₂	UO ₂	UO ₂
Weight of Uranium Oxide (g)	30	30	30	30	30	30	30	30	30	30	30	30	30
Weight of Uranium in Oxide (g)	26.3	26.3	26.3	26.3	26.3	26.3	26.3	26.3	26.3	26.3	26.3	26.3	26.3
Weight of Carbon Reductant (g)	1.99	1.99	1.99	1.99	1.99	1.99	1.99	1.99	1.99	1.33	1.99	2.66	
Equivalent Value of Carbon	1.5	1.5	1.5	1.5	1.5	1.5	1.5	1.5	1.5	1	1.5	2	
Temperature (K)	973	973	973	973	1073	1173	1223	1073	1073	1073	1073	1073	
Rate of Chloride Gas Supply (l/min)	0.2	0.2	0.2	0.2	0.2	0.2	0.2	0.2	0.2	0.2	0.2	0.2	
Reaction Time(min)	60	120	180	240	120	120	120	120	120	120	120	120	
Efficiency of Chloride Gas	13%	33%	19%	15%	30%	30%	31%	31%	31%	31%	30%	31%	
Cl/U Molar Rate	6.2	6.5	5.6	6.0	5.9	5.9	6.0	6.1	6.1	5.9	6.0	6.0	
Yield of Uranium (g-U)	6	26	26	26	26	26	26	26	26	26	26	26	
Recovery of Uranium	21%	100%	100%	100%	100%	100%	100%	100%	100%	100%	100%	100%	

Table2 Experimental conditions and Results of the 300-g-U scale experiments

Starting Oxide	UO2		UO2		UO2		UO2		U3O8		U3O8		U3O8		UO3	
	Ar		Ar		Ar		N2		N2		N2		N2		N2	
	1173	1173	1073	1073	1073	1173	1173	1173	1173	1173	1173	1173	1173	1173	1173	1173
Carrier Gas	Ar		Ar		Ar		N2		N2		N2		N2		N2	
Temperature (K)	1173		1073		1073		1173		1173		1173		1173		1173	
Rate of Chloride Gas Supply (l/min)	0.1		0.2		0.1		0.2		0.2		0.2		0.1		0.1	
Rate of Chloride Gas Supply (l/min)	0.2		0.2		0.2		0.2		0.2		0.2		0.2		0.2	
Reaction Time (min)	100		50		100		50		50		100		200		200	
Efficiency of Chloride Gas	91 %		89 %		90 %		93 %		90 %		89 %		77 %		92 %	
CUTU Molar Rate	3.9		4.0		4.1		3.8		4.1		3.8		4.0		4.1	
Yield of Uranium (g-U)	29		27		8		8		21		16		16		23	

Table 3 Experimental conditions and results
of the 1kg-U scale experiment

Starting Oxide	UO ₂	UO ₂	UO ₂
Weight of Uranium Oxide (g)	1134	1134	1134
Carrier Gas	Ar	Ar	Ar
Temperature (K)	1173	1173	1173
Rate of Chloride Gas Supply (U/min)	0.8	0.8	0.8
Rate of Chloride Gas Supply (U/min)	0.8	0.8	0.8
Reaction Time (min)	449	402	422
Cl/U Molar Rate	4.1	4.2	4.1
Yield of Uranium Tetrachloride (g)	1571	1554	1563
Recovery of Uranium (%)	98	96	97

Table 4 The list of impurity in Uranium Tetrachloride

Element	Al	B	Ca	Cr	Cu	Fe	K	Mg	Na	Ni	Si	Y	Zn
PRE-AVLIS(ppm)	<50	<50	<50	<200	<200	<200	<50	<50	<50	<200	<100	<50	<50
This Result(ppm)	<20	<20	<20	<10	<5	<10	<20	<10	<20	<10	22	<5	<10

CORROSION BEHAVIORS OF MATERIALS USED IN URANIUM METAL PRODUCTION

Yasushi Hoshino, Kazuaki Ota, Sumio Yamagami, Kazuhiro Endo
Naka Energy Research Center, Mitsubishi Materials Corporation
1002-14 Mukoyama, Naka-machi, Naka-gun, Ibaraki 311-01, Japan

Haruaki Tsuchiya, Takeshi Sakata, Toru Suzuki
Metal Mining Agency of Japan
Tokiwa Bldg. 1-24-14 Toranomon, Minato-ku, Tokyo 105, Japan

ABSTRACT

Corrosion behaviors of materials used in molten uranium or fluoride were studied in order to predict life spans of the materials and know contamination levels of uranium by the materials. By means of compatibility tests, materials, such as Y_2O_3 to molten uranium, graphite and W also to molten uranium to some extent, graphite and Mo to molten fluoride, are proved to be corrosion resistance materials, and their corrosion behaviors are discussed. Furthermore, the materials were used in electrolysis operation, and evaluated by comparing their corrosion behaviors with those observed in the compatibility tests. The result is that each material shows quite similar corrosion behavior in both cases.

INTRODUCTION

There is a process which electrolyze uranium oxides directly to metal in fluoride electrolyte among the electrolysis processes. In this process, uranium metal electrodeposited is dealt with in liquid phase because of its high electrolysis temperature (around 1200°C). Both molten uranium and fluoride are so corrosive that it is important to find corrosion resistance materials to select apparatus materials. Furthermore, it is important to know life spans of the materials and contamination of uranium from the materials by making their corrosion behaviors clear.

Though studies on corrosion resistance materials to molten uranium or fluoride were, if anything, done energetically so far ⁽¹⁾⁻⁽²⁵⁾, they are not always available for the selection of apparatus materials for mass production. There are many things which have not been revealed yet, for example, long-term corrosion resistance at high temperature

around 1200°C, corrosion behaviors in electrolysis apparatus, effects of degradation in density of materials for higher cost performance etc.

From such background, first, candidate materials listed in Table 1 were chosen by means of literature review ⁽¹⁾⁻⁽²⁵⁾. In choosing them, workability and possibility of mass production, etc., were taken account of as well as corrosion resistance. Properties of the candidate materials were also shown in Table 1. Then, compatibility tests were carried out on those materials. On the basis of results of the compatibility tests, corrosion resistance materials were selected. The corrosion behaviors of those materials were also investigated by both the compatibility tests and electrolysis operation.

EXPERIMENT

Compatibility Tests

Selection of corrosion resistance materials. Preliminary compatibility test were carried out between the candidate materials, and molten uranium or fluoride. Each material was formed to a crucible shape whose outer diameter and height were about 30mm by machining, sintering and plasma spray. Fifty grams of uranium metal or 7 grams of fluoride (74wt%BaF₂-11wt%LiF-15wt%UF₄) was then filled in the material crucibles. Uranium metal was pickled and fluoride was dried at 100°C in advance. Chemical compositions of uranium metal and fluoride used in the tests were shown in Table 2. The material crucibles filled with uranium metal or fluoride were placed in a furnace, and heated on the conditions listed in Table 3. After heating, the outside appearances of material crucibles were observed, then the material crucibles were cut for analyses. Cross sections of the interfaces between materials and uranium metal or fluoride were also observed and analyzed, using XRD, EPMA, etc.

Long-term compatibility test. Compatibility test extended to from 96 hours to 936 hours were carried out on materials which showed good corrosion resistance in the test within 32 hours. Heating temperature was mainly set to 1240°C, here. Some of the materials needed covers on the crucibles in order to prevent molten uranium or fluoride creeping out because of their high wettabilities.

Corrosion evaluation of Materials in Electrolysis Operation

The materials which showed good corrosion resistance in the compatibility tests (including exceptional materials) were used in apparatuses of electrolysis or related experiments, and checked their corrosion behaviors. Details of the electrolysis and related experiments are described in the another paper of this proceedings volume. Each material was used repeatedly at around 1200°C in the experiments. Total use times of the materials changed from several hours to several tens of hours according to parts of apparatuses where the materials were used. Every material, except a few materials, experienced heat

cycles between room temperature and around 1200°C more than 5 times. After the experiments, components of the apparatuses were taken apart, and specimens for analyses were sampled. The specimens were analyzed by the same methods as the compatibility tests.

Corrosion behaviors of materials in the electrolysis process were evaluated by comparing results obtained with those of the compatibility tests.

RESULTS AND DISCUSSION

Compatibility Tests

Selection of corrosion resistance materials. Result of the preliminary compatibility test is summarized in Table 4. Yttrium oxide showed good corrosion resistance to molten uranium regardless of the decrease in density, the difference between sintered body and plasma-splayed one. Tungsten, graphite, UO₂ and CaAl₄O₇ showed corrosion resistance to molten uranium to some extent. On the other hand, graphite (regardless of the degradation in both purity and density), amorphous carbon and Mo showed good corrosion resistance to molten fluoride. Tungsten and BN did not show any reaction with molten fluoride, but embrittlement by recrystallization in the case of W and infiltration of molten fluoride in the case of BN were observed.

Selected materials by the test were as follows. Materials for molten uranium were Y₂O₃, W and graphite (W and graphite were selected because of their functions as a conductor or corrosion resistance to molten fluoride). Materials for molten fluoride were graphite (including amorphous carbon) and Mo.

Long-term compatibility test. Result of the long-term compatibility test was qualitatively same as that of preliminary compatibility test but degree of the corrosion was greater except in the case of graphite to molten fluoride. Graphite to molten fluoride did not show any corrosion.

Corrosion behaviors of selected materials

Corrosion behaviors revealed by the compatibility tests were as follows.

Y₂O₃ to molten uranium. When the temperature was 1240°C, slight amount of UO₂ was formed at the interface between Y₂O₃ and molten uranium, and slight color change of Y₂O₃ was observed only in the vicinity of the interface even after 936 hours contact. On the other hand, when the temperature was 1400°C, remarkable color change of Y₂O₃ from white to black was observed after 96, 936 hours contact, and UO₂ layer was formed (~ 100 μ m thick after 96 hours). In every condition, Yttrium was not

detected in uranium metal. The color change is considered to be those caused by oxygen defects because only Y_2O_3 can be the oxygen source of the UO_2 layer. Therefore, it is considered that the corrosion behaviors of Y_2O_3 are formation of the oxygen defects and the oxidation of molten uranium forming UO_2 .

Graphite to molten uranium. It was observed that UC layer was formed at interface between graphite and molten uranium by reaction of $\text{C} + \text{U} \rightarrow \text{UC}$. Uranium Carbide was formed not only at the interface but in molten uranium region as UC dendrite. The UC dendrite soaked up molten uranium while growing up along the surface of graphite crucible, hence it was observed that molten uranium crept up on the inner wall of graphite crucible. Weight increases of UC, estimated from width of the UC layer and carbon content of uranium containing the UC dendrite, are plotted in Fig. 1. The formation rate of UC decreases with time. The slope of line within 8 hours is in between 0.5 and 1.0. On the contrary, the slope of line over 8 hours is about 0.5 or less. This indicates that the rate determining step may change from reaction-diffusion to diffusion (or slower step than diffusion) with time. Therefore, it is suggested that the UC layer may be protective to some extent.

W to molten uranium. It was observed that grain boundaries of W were dissolved preferentially and some amounts of grains were floating in uranium metal. Tungsten contents in uranium metal after the test at 1240°C are shown in Fig. 2. The W contents are almost constant regardless of their heating time. Figure 2 indicates that W dissolves quickly in molten uranium and no more dissolution do not occur after W content reaches its solubility (within 3 hours). The grains of W grew up by recrystallization with the heating time, and W embrittled remarkably especially in the case of 936 hours. Wettability of W with molten uranium also increased with the heating time, and molten uranium crept out from the W crucible in the case of 936 hours. This creeping is considered to be caused by the coarse surface of recrystallized W and its capillarity.

Graphite to molten fluoride. Graphite heated with molten fluoride did not show any corrosion, and no increase of carbon content in fluoride was observed. The carbon content changes with time were also shown in Fig. 2. Hence, it can be said that graphite is a good corrosion resistance material to molten fluoride. The only change observed in the compatibility tests was slight infiltration of molten fluoride when graphite was degraded in purity and density.

Mo to molten fluoride. Molybdenum recrystallized with time but its embrittlement was slight compared to W. Neither reaction layer nor increase of Mo content in fluoride was observed. Therefore, Molybdenum is good corrosion resistance material to molten fluoride. However, it was suggested that the Mo content in fluoride was effected by moisture content of fluoride before heating. When Mo was heated with fluoride which had experienced premelting, Molybdenum was not detected in fluoride. On the contrary, when Mo was heated with fluoride powder which was only dried at 100°C , Molybdenum was

detected. This results indicate that Mo is corroded only when moisture exists in the fluoride.

Y₂O₃ to molten fluoride. Yttrium oxide is not a corrosion resistance material to molten fluoride but it is so good corrosion resistance material to molten uranium that its compatibility with molten fluoride is tested. As the result, existence of $Y_2O_3 + UF_4 \rightarrow YOF + UO_2 + YF_3$ reaction was suggested. This reaction progressed quickly and UO₂ layer was formed at the interface while a part of Y₂O₃ changed to YOF. Many cracks were introduced both in area of YOF (including remaining Y₂O₃) and UO₂ layer. Yttrium was detected in fluoride by analysis.

Corrosion evaluation of Materials in Electrolysis Operation

Result of corrosion evaluation of materials is summarized in Table5. Part names of apparatus where materials were used and their histories are also written in Table 5. Every material functioned normally as a corrosion resistance material during its service. Especially Y₂O₃ to molten uranium, and graphite to molten fluoride showed similar results to the compatibility tests even though they were heat cycled at least 5 times. Graphite and W to molten uranium were cracked at the vicinity of the interface between graphite and uranium. Those cracks are considered to be caused by stronger effects of differences of thermal expansion between materials and uranium metal when their size become bigger. Therefore, it is desirable that graphite and W do not experience any heat recycling when they are used as corrosion resistance materials to molten uranium. It was clear that Mo corroded in electrolyte initially because Mo was detected in electrolyte contacted with Mo parts. However, the corrosion considered to be that occurred by moisture initially included in raw fluoride because Mo content decrease drastically after the series of electrolysis experiments. Boron nitride was used as an insulator in the electrolyte, but infiltration of fluoride was observed in the same way with the compatibility test. Hence, possibility of electrical short was suggested in the long run.

CONCLUSION

Corrosion resistance material to molten uranium is Y₂O₃, and both graphite and tungsten show corrosion resistance to some extent. On the other hand, corrosion resistance materials to molten fluoride are graphite and Mo. Yttrium oxide corrodes slowly by molten uranium, and Mo also corrodes by molten fluoride in the presence of moisture content. Corrosion behaviors of these materials in electrolysis operation are similar to those observed in compatibility tests. However, introduction of cracks by heat cycling is recognized in the case of Graphite and W to molten uranium. These results are quite useful to design further experiments for prediction of life spans of the materials and contamination of uranium by the materials in the electrolysis process for uranium metal production.

ACKNOWLEDGMENTS

This study was funded by Metal Mining Agency of Japan.

REFERENCES

1. T. Shibata et al., *Shinku*, **32**, 277 (1989)
2. M. Kuznietz et al., *J. Nucl. Mater.*, **160**, 69 (1988)
3. A. B. Macintosh and K. Q. Bagley, *J. Inst. Metals*, **84**, 251 (1955-1956)
4. R. J. Ackerman and E. G. Rauh, *High Temp. Sci.*, **4**, 496 (1972)
5. M. Kuznietz et al., *J. Nucl. Mater.*, **152**, 235 (1988)
6. M. Kuznietz et al., *High Temperatures-High Pressures*, **18**, 665 (1986)
7. J. S. Huang et al., *Scripta Metallurgica*, **23**, 103 (1989)
8. M. Kuznietz and C. Cotler, *J. Nucl. Mater.*, **196** (1988)
9. N. Morioka et al., *Oyo-Butsuri*, **55**, 249 (1989)
10. J. B. Condon and C. E. Holcombe, Jr., *Crucible Materials to Contain Molten Uranium*, Y-2084 (1977)
11. H. M. Feder et al., *Interaction of Uranium and its Alloys with Ceramic Oxides*, ANL-5765 (1957)
12. B. Blumenthal, *Trans. AIME, J. Metals*, 1199 (1955)
13. N. C. Jessen, Jr. et al., *Application of Metal Oxide Refractories of Melting and Casting Reactive Metals*, Y/DA-8225 (1979)
14. I. L. Jenkins and N. J. Keen, *J. Less-Common Metals*, **4**, 387 (1962)
15. E. D. Eastman et al., *J. Am. Ceram. Soc.*, **34**, 128 (1951)
16. O. H. Krikorian and P. G. Curtis, *High Temperatures-High Pressures*, **20**, 9 (1988)
17. C. E. Holcombe and G. L. Powell, *J. Nucl. Mater.*, **49**, 238 (1973-1974)
18. L. W. Niedrach et al., *J. Electrochem. Soc.*, **105**, 353 (1958)
19. T. A. Henrie, *J. Metals*, **16**, 978 (1964)
20. R. D. Piper, *Laboratory Development of the Uranium Electroreduction Process*, MCW-1500 (1966)
21. R. D. Piper, *Electrochem. Technol.*, **5**, 147 (1967)
22. D. S. Poa et al., *Laboratory-Scale Study of Electrolytic Reduction of Uranium Oxides*, ANL-88-29 (1988)
23. J. W. Koger et al., *Compatibility of Molybdenum-Base Alloy TZM with LiF-BeF₂-ThF₄-UF₄ at 1100°C*, ORNL/TM-2724 (1969)
24. J. R. Keiser, *Compatibility Studies of Potential Molten-Salt Breeder Reactor Materials in Fluoride Salts*, ORNL/TM-5783 (1987)
25. A. K. Misra et al., *Fluoride Salts and Container Materials for Thermal Energy Storage Applications in the Temperature Range 973 to 1400 K*, NASA/TM-89913

Table 1 List of candidates for corrosion resistance materials to molten uranium or fluoride chosen by literature review

Molten uranium		Molten fluoride	
Candidates	Properties	Candidates	Properties
W	W>99.95%, 99.6%TD	W	W>99.95%, 99.6%TD
Ta	Ta>99.83%, 100.0%TD	Ta	Ta>99.83%, 100.0%TD
Graphite	a. Ash<0.001%, 82.3%TD b. Ash<0.1%, 77.8%TD	Mo	Mo>99.93%, 98.7%TD
Y ₂ O ₃	a. Y ₂ O ₃ >99.9%, 100.3%TD b. Y ₂ O ₃ >99.9%, 70.0%TD c. Plasma-sprayed	Graphite	a. Ash<0.001%, 82.3%TD b. Ash<0.1%, 77.8%TD
UO ₂	UO ₂ >99.9%, 97.7%TD	Carbon**	Ash<0.5%, 1.48g/cm ³
ZrO ₂ *	ZrO ₂ :92.76%, 5.96g/cm ³	Y ₂ O ₃	Y ₂ O ₃ >99.9%, 100.3%TD
ZrSiO ₄	ZrO ₂ :65.87%, SiO ₂ :32.58%, 3.79g/cm ³	AlN	AlN>99.4%, 100.9%TD
CaAl ₂ O ₇	Al ₂ O ₃ :80.0%, CaO:19.5%, 2.14g/cm ³	BN	BN>99.5%, 83.8%TD

ZrO₂*: partially stabilized by 4.60wt%Y₂O₃
Carbon**: amorphous carbon

Table 2 Uranium and fluoride used in the compatibility tests

Uranium / ppm	Uranium		Fluoride	
	Elements	Contents	Elements	Contents
	Al	< 10	In	< 1
	B	< 0.4	Mg	< 1
	Ba	< 1	Mn	9
	Ca	< 5	Mo	< 10
	Cd	0.5	Na	< 1
	Co	< 2	Ni	28
	Cr	5	Pb	< 1
	Cu	12	Si	32
	Fe	78	Sn	< 1
			S	< 10
Fluoride / wt%	Constituents		Purities	
	BaF ₂	> 98		74
	LiF	> 98		11
	UF ₄	> 99		15

Table 3 Conditions of compatibility tests

Items	Tests	Selection of corrosion resistance materials	Long-term compatibility test
Atmosphere		Ar gas, 1 atm	Ar gas, 1 atm
Temperature		1240, 1400°C	1240°C (Y ₂ O ₃ :1400°C)
Time		3, 8, 32 hrs	96, 936 hrs
Heating and cooling rate		300°C/min	300°C/min

Table 4 Result of preliminary compatibility test

Corrosives	Candidates	Remarks	Compatibilities	Corrosion behaviors
Molten uranium	W		Fair	Solution of grain boundary, Embrittlement by recrystallization
	Ta		Poor	Solution of grain boundary
	Graphite	a, b table1	Fair	Formation of UC layer
	Y ₂ O ₃	a - e table1	Good	Formation of very thin UO ₂ layer
	UO ₂		Fair	Formation of thin UO ₂ layer
	ZrO ₂		Poor	Formation of UO ₂ layer
	ZrSiO ₄		Poor	Formation of UO ₂ +U ₃ Si ₃ layer and porous ZrO ₂ layer
Molten fluoride	CaAl ₂ O ₇		Fair	Formation of thin UO ₂ layer
	W		Fair	Embrittlement by recrystallization
	Ta		Poor	Fluorination
	Mo		Good	Recrystallization
	Graphite	a table1 b table1	Good Good	Slight infiltration
	Carbon		Good	Slight infiltration
	Y ₂ O ₃		Poor	Embrittlement, Formation of YOF and UO ₂ layer
	AlN		Poor	Embrittlement, Formation of U-rich layer
	BN		Fair	Infiltration

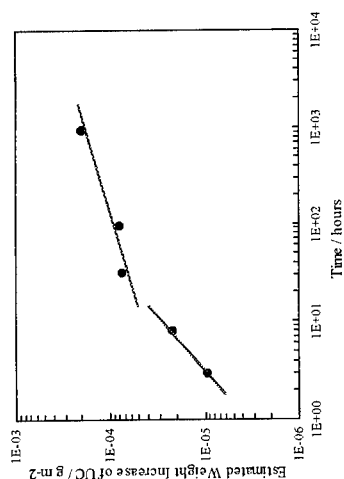


Fig. 1 Weight increase of UC estimated from width of UC layer and carbon content of uranium containing UC dendrite at 1240°C

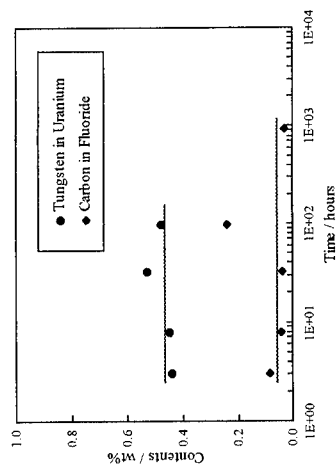


Fig. 2 Tungsten content of uranium contacted with W crucible, and C content of fluoride contacted with graphite crucible at 1240°C

Table 5 Corrosion evaluation of materials by using them in electrolysis operation

Corrosives	Materials	Part names of apparatus (Experiment)	Histories of use a. temperature b. total time c. number of heat cycles	Differences from the compatibility tests, Heat cycle resistance
Molten uranium	Y ₂ O ₃	Stopper rod (Transport experiment of molten uranium)	a. 1220-1260°C b. 4 hrs c. 5	No difference Show heat cycle resistance
	Graphite	Container of molten uranium (Electrolysis experiment)	a. 1150°C b. 6 hrs c. 1	Small difference Crack was introduced by cooling
	W	Cathode (Electrolysis experiment)	a. 1100-1300°C b. 68 hrs c. 15	Small difference Crack was introduced by heat cycles
Molten fluoride	Graphite	Electrolytic cell (Electrolysis experiment)	a. 1100-1190°C b. 27 hrs c. 5	No difference Show heat cycle resistance
	Mo	Purge tube of stirrer gas (Electrolysis experiment)	a. 1100-1190°C b. 27 hrs c. 5	No difference Show heat cycle resistance
	BN	Insulator in electrolyte (Electrolysis experiment)	a. 1150°C b. 6 hrs c. 1	No difference

DEVELOPMENT OF TRANSURANIUM ELEMENT RECOVERY FROM HIGH-LEVEL RADIOACTIVE LIQUID WASTE.

Yoshie Akai and Reiko Fujita
Nuclear Engineering Laboratory, Toshiba Corporation
4-1 Ukishima-cho, Kawasaki-ku, Kawasaki 210, Japan

ABSTRACT

In order to confirm experimentally the new partitioning process composed of oxalate precipitation with electrorefining, the simulated transuranium elements (TRUs) are separated from KCl-LiCl eutectic by electrorefining. The simulated TRUs are cerium (Ce) and the simulated rare earth elements are lanthanum (La). Separation factor is defined as La/Ce concentration ratio in KCl-LiCl eutectic and La/Ce concentration ratio on cathode. Separation factor increases in accordance with increasingly negative electrolytic potential. Separation factor is about 5 in La/Ce ratio in KCl - LiCl eutectic from 1 to 11 under the following conditions : 0.5 wt% Ce in KCl-LiCl eutectic and -1.76 V vs Ag/AgCl(0.1w/o) of electrolytic potential. Separation factor is independent of La/Ce concentration ratio in KCl-LiCl eutectic from 1 to 11. Therefore it is possible to estimate La/Ce ratio on cathode.

INTRODUCTION

High-level radioactive liquid waste (HLW) is produced in the spent fuel reprocessing process. This process generally employs plutonium reduction extraction (PUREX) methods whereby spent fuel is dissolved in nitric acid and then plutonium and uranium are extracted by tributyl phosphate (TBP). HLW is raffinate that consists of alkali elements, alkaline earth elements, noble metals, rare earth elements (REs) and transuranium elements (TRUs). TRUs have long half-life and are α emitters. Therefore, it is necessary for TRUs to be separated from HLW before HLW is disposed in geologic repository.

The separation methods for TRUs from HLW are classified into two categories, that is, the wet processes and dry processes. The wet processes consist of solvent extraction, ion exchange and precipitation. The methods of TRU recovery such as the TRUEX process⁽¹⁾ and the OXAL process⁽²⁾ have been developed and an advanced partitioning process has been investigated by Japan Atomic Energy Institute (JAERI)⁽³⁾. The dry process composed of four steps, that is, conversion, dissolution, reduction and electrorefining, has been developed by Central Research Institute of Electric Power Industry (CREPI)⁽⁴⁾. Though the dry process is a simple process, such pretreatment as conversion of HLW to chloride is necessary before electrorefining. Therefore, it is desirable to develop a partitioning process that achieves simplicity and high separation without pretreatment.

Figure 1 shows a new partitioning process combining oxalate precipitation and electrorefining developed by Toshiba Corporation. This partitioning process is characterized by oxalate precipitation yielding high TRU recovery and electrorefining achieving high TRU separation from REs. This process is composed of three steps. In the first step, TRUs, REs and alkaline earth elements whose oxalates have smaller solubility are recovered from HLW by the addition of oxalic acid. In the second step, these oxalates are converted to chlorides with hydrochloric acid and hydrogen peroxide. In the final step, TRUs are recovered on cathode by electrorefining after these chlorides have been dissolved in KCl-LiCl eutectic. In order to confirm the new partitioning process experimentally, it was investigated whether the simulated TRUs are separated from REs by potentiostatic electrolysis.

EXPERIMENTAL

Table 1 shows redox potential of REs and TRUs. Electrorefining satisfies the requirement of TRUs' separation from REs in KCl-LiCl eutectic. In general, TRUs' redox potential is more positive than that of REs. The most negative element in TRUs is Am and the most positive element in REs is Gd. The difference of redox potential between Am and Gd is almost 51 mV. If Am were separated from Gd, it is possible that TRUs would be separated from REs. Therefore the simulated TRUs are used for Ce and the REs are La. The difference of redox potential between Ce and La is almost 67 mV. This potential difference between Am and Gd is simulated.

The electrodes and electrolyte were contained in a cylindrical alumina crucible to isolate the cell electrically. The alumina crucible has an outer diameter of 60 mm, a depth of 100 mm and a wall thickness of 3 mm. This crucible was placed in an argon atmosphere glove box. The oxygen and moisture content in the glove box was maintained below 10 ppm during the operation. Three electrodes were used for all the measurements. The working electrode for cyclic voltammetry was molybdenum rod, 1.3 mm in diameter and that for potentiostatic electrolysis was low carbon steel rod, 3 mm in diameter. The counter electrode was glassy carbon rod produced by Tokai Carbon, 3 mm in diameter. The reference electrode was Ag/AgCl(0.1w/o). KCl-LiCl(99.99% purity) was obtained from Anderson Physics Laboratory. The operation temperature is 773K. After KCl-LiCl, CeCl₃ and LaCl₃ were added in the alumina crucible, the experiment of cyclic voltammetry and potentiostatic electrolysis was carried out. During the experiment, Ce concentration was raised in increments from 0.5 to 1.5 w/o and that of La was from 0.5 to 5.5 w/o. Separation factor may be defined as Eq.[1].

$$\text{Separation factor} = \frac{\text{La/Ce concentration ratio in KCl-LiCl}}{\text{La/Ce concentration ratio on cathode}} \quad [1]$$

RESULT AND DISCUSSION

Cyclic voltammetry

Figure 2 shows the cyclic voltammogram of LaCl_3 in KCl-LiCl at 773K. La concentration is 0.22 wt%. The potential scan rate is varied from 20 to 200 mV/s. Two waves are observed for both cathodic and anodic scan. Wopschall⁽⁵⁾ investigated whether the product is strongly adsorbed and found that separation adsorption peak may occur prior to normal peak. The reaction of La on electrode is shown by Eq.[2],



Because La is deposited on electrode, La is strongly adsorbed. Assuming that La adsorption is subject to the Langmuir isotherm, the free energy of adsorption, ΔG , is calculated by experimental result. The surface concentration, Γ_R , may be defined as Eq.[3],

$$\Gamma_R = \Gamma_R^S C_R / (K_R + C_R) \quad [3]$$

where Γ_R^S is the saturation value at maximum surface coverage and C_R is the solution concentration. K_R may be defined by ΔG as Eq.[4],

$$-RT \cdot \ln K_R = \Delta G^0 + \alpha (E - E_a^0) = \Delta G \quad [4]$$

where R is gas constant, T is absolute temperature and E_a^0 is the adsorption redox potential. Adsorption peak potential is defined as E_{pc1} and normal peak potential is E_{pc2} . If E can be approximately E_{pc1} , K_R is approximately C_R and Co is Co^* . It is shown by Eq.[5] that potential is related to solution concentration.

$$Co / C_R = \exp [(nF / RT) (E - E_0)] \quad [5]$$

By combination of Eq.[4] and Eq.[5].

$$Co^* / K_R^0 = \exp [- (\alpha / RT) (E_{pc1} - E_a^0) - (nF / RT) (E_{pc1} - E_{12})] \quad [6]$$

Assuming that the adsorption obeys the Langmuir isotherm, E_{pc1} is equal to E_a^0 . Thus it is shown by Eq.[7] that potential is related to solution concentration and the Langmuir isotherm parameter K_R^0 .

$$Co^* / K_R^0 = \exp [- (nF / RT) \Delta E_p] , \quad \Delta E_p = E_{pc1} - E_{12} \quad [7]$$

The value of ΔE_p is 0.1 V. Thus ΔG^0 is calculated to be 9.2 kcal/mol.. Figure 3 shows the effect of the square root of potential scan rate on the normal peak current density. The peak current density is in direct proportion to the potential scan rate. Therefore La electrode reaction is diffusion-controlled.

Figure 4 shows the cyclic voltammogram of CeCl_3 in KCl-LiCl at 773K. Ce concentration is 0.22 wt%. The potential scan rate is varied from 20 to 200 mV/s. One wave is observed for cathodic scan and three waves for anodic scan. The shape of cathodic wave indicates that the product is not strongly adsorbed. Figure 5 shows the effect of the square root of the potential scan rate on the normal peak current density. The peak current density is in direct proportion to potential scan rate. Therefore Ce electrode reaction is diffusion-controlled.

Effect of electrolytic potential on separation factor

Figure 6 shows the effect of electrolytic potential on separation factor when La and Ce was 1.5 wt% in KCl-LiCl. Electrolytic potential varied from -1.76 to -1.825 V vs Ag/AgCl(0.1w/o). Separation factor is about 6 at electrolytic potential from -1.76 to -1.8 V vs Ag/AgCl(0.1w/o). But separation factor is about 3 at -1.825 V vs Ag/AgCl(0.1w/o). The proportion of La deposition on cathode decreases when electrolytic potential is more negative than La redox potential. On the other hand, the proportion of Ce deposition on cathode increases as this electrolytic potential is more positive than Ce redox potential. Therefore separation factor increases in accordance with increasingly negative electrolytic potential.

Effect of initial La/Ce concentration ratio in KCl-LiCl eutectic on separation factor

Figure 7 shows the effect of initial La/Ce concentration ratio in KCl-LiCl eutectic on separation factor when initial La/Ce concentration was from 1 to 11. La concentration varied from 0.5 to 5.5 wt% and Ce concentration is 0.5 wt%. Electrolytic potential is -1.76 V vs Ag/AgCl(0.1w/o). Separation factor is about 5 in La/Ce concentration ratio from 1 to 11. Separation factor is constantly independent of La/Ce concentration ratio.

In general, REs and TRUs are diffusion-controlled in molten salt. La and Ce are diffusion-controlled by cyclic voltammetry. As electrode reaction is diffusion-controlled, the current density may be defined as Eq.[8],

$$i = nFD (C^o - C) / \delta \quad [8]$$

where i is the current density, n is the number of electron, F is the Faraday constant, D is the diffusion coefficient, C^o is the bulk concentration of oxidant, C is the electrode surface concentration of oxidant and δ is the thickness of diffusion layer. As La concentration in molten salt is m times, the current density may be defined as Eq. [8-1],

$$i_m = nFD (mC^o - C_m) / \delta \quad [8-1]$$

where i_m is the current density of La and C_m is the La electrode surface concentration. If concentration relation satisfies Eq.[9], i_m/i is approximately determined by Eq.[9-1].

$$C^0 \gg C_m > C \quad [9]$$

$$i_m / i = m \quad [9-1]$$

If La concentration in molten salt is doubled, La cathodic current is doubled. La cathodic current is equal to La deposition. Separation factor may be defined as La/Ce concentration ratio in KCl-LiCl and La/Ce concentration ratio on cathode. Therefore separation factor is constant at La/Ce concentration ratio from 1 to 11. It is possible to estimate La/Ce ratio on cathode by separation factor.

CONCLUSION

It was confirmed experimentally the new partitioning process composed of oxalate precipitation with electrowinning. Ce was separated from La by potentiostatic electrolysis. Separation factor is about 5 under the following conditions : 0.5 wt% Ce in KCl-LiCl eutectic and -1.76 V vs Ag/AgCl(0.1w/o) of electrolytic potential. Separation factor is independent of La/Ce concentration ratio in KCl-LiCl eutectic from 1 to 11. It is possible to estimate La/Ce ratio on cathode. Therefore TRUs were separated from REs.

REFERENCES

1. G.F. Vandergriff, ANL-84-45 (1984).
2. L.Cecille, IAEA-SM-246/22, p573 (1980).
3. M.Kubota, Joint Int. Waste Management Conf/1989, 537 (1989).
4. T.Inoue, Nucl. Technol., **93**, 206 (1991).
5. R.H.Wopschall, Anal. Chem., **39** 1514 (1967).

Table 1 Redox potential

	Element	Redox potential ¹⁾	Potential difference	Simulated
TRUs	Pu/Pu ³⁺	-1.494 V	0.157 V 0.051	
	Am/Am ³⁺	-1.600		
	Gd/Gd ³⁺	-1.651		
REs	Nd/Nd ³⁺	-1.744	0.090 0.062	TRUs
	Ce/Ce ³⁺	-1.772		
	La/La ³⁺	-1.834		
				REs

1) vs Ag/AgCl(0.1M)

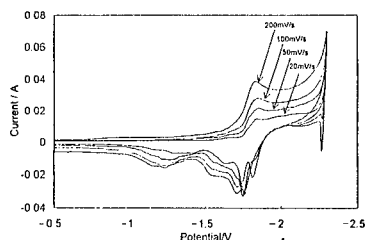


Fig.4 Cyclic voltammogram of CeCl₃

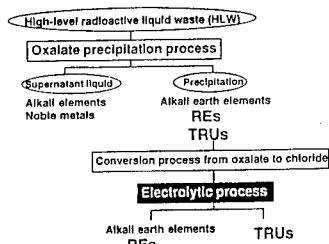


Fig.1 Process flow of a new partitioning process

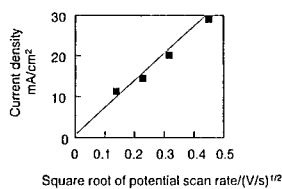


Fig.5 Effect of the square root of the potential scan rate on Ce peak current density

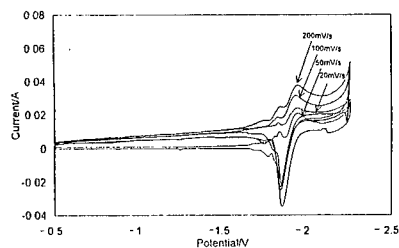
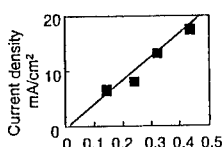


Fig.2 Cyclic voltammogram of LaCl₃



Square root of potential scan rate $((V/s)^{1/2})$

Fig.3 Effect of the square root of the potential scan rate on La normal peak current density

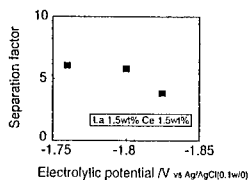


Fig.6 Effect of electrolytic potential on separation factor

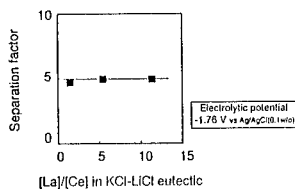


Fig.7 Effect of La/Ce concentration ratio in KCl-LiCl eutectic on separation factor

Characteristics of Cathodic Reactions in BaCl_2 -NaCl Melts Containing AlF_3 Components

Mikito UEDA, Shoichi KONDA, Takeshi SASAKI
and Tatsuo ISHIKAWA

Research Group of Interface Control Engineering,
Graduate School of Engineering, Hokkaido University,
Kita-13, Nishi-8, Kita-ku Sapporo, 060, Japan

Abstract

For electrorefining of Al from scrap aluminum using a bipolar electrode system, characteristics of BaCl_2 -NaCl melts, less corrosive for cell materials than fluoride melts, were investigated. First, methods for introducing aluminum components into BaCl_2 -NaCl melts were examined in terms of their solubilities. Only melts fed with double salts of AlF_3 -NaF were available for the electrolysis bath. Next, characteristics of cathodic reactions in the melts with various concentrations of aluminum components were investigated. Plateau currents were observed at 0.35 and 0.75 A/cm² in 2.5 and 5 mol% melts, respectively, whereas no plateau current was found in 10 mol% melts.

Introduction

A novel method for electrorefining of Al from scrap aluminum using a bipolar electrode system has been proposed for electric-energy saving and high productivity.[1-3] This method requires new melts which are less corrosive for the cell material because, in this system, it is impossible to form a frozen layer on the inner wall of the cell for protection of the material. We selected an equimolar BaCl_2 -NaCl melt as the base melt for the system. This had low corrosivity against the cell material composed of oxides and a higher density than liquid Al.

In this report we describe a method to introduce aluminum components into the base melt and the characteristics of the cathodic reaction in melts with various concentrations of aluminum components.

Experimental

The apparatus for measurement of polarization curves is illustrated in Fig. 1. The cell consisted of a graphite crucible placed in a quartz vessel and an alumina tube inserted into the crucible. The anode was a 40 wt% Cu-Al alloy pool settled in the bottom of the graphite crucible, where a Ni rod was embedded to improve electric contact. A graphite cathode was arranged 4 cm from the top of the anode pool with an alumina spacer.

After melting an equimolar BaCl_2 -NaCl salt in the crucible at 750°C, we added a fixed amount of 40 mol% AlF_3 -NaF double salts. Next, using graphite electrodes instead of

the anode and cathode electrodes, we pre-electrolyzed the melt at cell voltages less than 2.2V for about 2 hours to remove impurities. After the refinement of the melt the graphite electrodes were replaced with the test graphite cathode. A pure aluminum rod inserted into an alumina tube was used as a reference electrode.

Polarization curves were measured galvanostatically in the range from 0.1 to 1.2 A/cm² in melts with three concentrations of Al components, 2.5, 5 and 10mol%, at 750°C.

Results and Discussion

As sublimated AlCl₃ was added to the BaCl₂-NaCl melt at 750°C, time variations in the Al concentration in the melt were followed. The results are presented in Fig. 2. The figure shows that the introduction of gaseous AlCl₃ corresponding to 6mol% achieved only 2mol% in the melt and AlCl₃ was still continuously evaporating. This indicated that a sufficient concentration of aluminum components could not be attained by supplying gaseous AlCl₃ because of its high vapor pressure at this temperature. The addition of AlF₃ powder to the base melt resulted in a melt with fine white particles suspended in it.

Melts containing about 10mol% AlF₃ were obtained by addition of co-melted AlF₃-NaF with a rather narrow range of compositions (shown by the hatched area in Fig. 3) to the base melt. When the melts with concentrations outside the hatched area were supplied to the base melt, the white particles, probably due to AlF₃, remained undissolved. In this procedure no significant differences were recognized between the additions of co-melted AlF₃-NaF salts in a liquid state and a solid state (double salts). The density of the melt containing 10mol% AlF₃ showed $2.52 \pm 0.04 \text{ g/cm}^3$, whereas the density of aluminum is given by the following equation[4];

$$\rho_{\text{Al}} = [2.382 - 0.000272(t - 658)] \text{ g/cm}^3.$$

Although the density of the melt was larger than that of liquid aluminum (2.36g/cm³ at 750°C), it was smaller than that of Gadeau melt (2.6g/cm³) and seemed to be unavailable for electrorefining. To raise the density we increased the BaCl₂ component in the base melt to 55mol%BaCl₂-45mol%NaCl and proposed a new melt for electrorefining of Al. The composition is listed together with those of Hoopes and Gadeau baths in Table 1. The atomic ratios of Cl to F in the melts are also presented in the last column.

As shown in the table, the proposed melt was mainly composed of chlorides and suggestive of less corrosivity against oxides of the cell material. Corrosion tests actually showed that the corrosivity of the melt was one-twentieth that of the Gadeau melt. The density of the proposed melt was $2.67 \pm 0.03 \text{ g/cm}^3$.

Time variations in the concentrations of Al components in the proposed melt are shown Fig. 4. As shown in the figure, the concentrations of Al components stayed constant for over one day. This suggested that Al components existed stably in this melt.[5]

To investigate the characteristics of the cathode reactions, polarization curves were measured in three melts with different concentrations of Al components. The compositions of the melts are listed in Table 2. Because we had to add double salts, AlF₃ and NaF, to the base melt for increments in aluminum components as mentioned above, the atomic ratios of Cl to F and the atomic fractions of Na were not necessarily obvious. Thus, they are

presented in the last two columns.

Polarization curves obtained in the three melts are depicted in Fig. 5, where polarization curves in the anodic region are also plotted together with cathodic curves. The cathodic curves in the figure show linear relations; the curves in the 2.5 and 5mol% melts are composed of two linear parts. This indicated that the main parts of the measured potentials were due to ohmic potential drops in the electrolytes. The gradients of the curves increased with the increase in Al components and this suggested that the conductivities of the melts increased with the increase in Al components because the conductivities were directly proportional to the gradients.

Coordinating F^- and Cl^- , Al and Ba ions formed big complex anions in these melts. Since the complex ions could hardly move through electric fields, the electric conductance of the melts was, therefore, predominantly supported by Na ions in the melts. The conductivities of the melts were estimated to increase with increases in aluminum components, since the Na fractions increased with them as shown in the last column in Table 2. The cathodic polarization curves reflect the conductivities of the melts.

The potentials determined by extrapolating the curves to $i=0$ should indicate the reversible potential of the cathodic reaction. As shown in the figure the extrapolations of the three curves in low current regions converged at 0V, which corresponds to the reversible potential of Al. On the other hand, the extrapolated lines in high current regions in the 2.5 and 5mol% melts came together at about -0.4V, and the potential is regarded as a reversible potential of Ba.[6] Plateau currents observed in the 2.5 and 5mol% melts were at 0.35 and 0.75A/cm², respectively, and the values were directly proportional to the concentration of Al components; this relation supports the hypothesis that the plateau currents correspond to the limiting current densities due to the diffusion of Al components.

The results mentioned above suggested that in the 2.5 and 5mol% melts, the Al deposition reaction occurred in the current density regions under the plateaus and that in the regions over the plateaus the main cathodic reaction became Ba deposition. In the 10mol% melt, the cathodic reaction was Al deposition in all current ranges in the experiment.

In the anodic region three curves nearly coincided with others, though they showed mostly linear relations. This suggested that the main part of the observed potentials could be attributed to an overvoltage at the electrode/electrolyte interfaces. The overvoltage was probably related to surface activity of Al in the alloy, but the mechanism is remains unclear at present.

After 6-hour electrolysis, the compositions of cathodic deposits and the Cu-Al pool were analyzed with EPMA. The results showed no evidence of copper deposition in cathodic deposits, whereas condensation of copper in the anode pool was observed. This confirmed that the melt proposed in this report might be available for electrorefining Al from scrap aluminum, and that a concentration over 5mol% of Al components was preferable to apply the current density of 0.6A/cm² as in the Hoopes and Gadeau processes.

Conclusions

The equimolar BaCl₂-NaCl melt fed individually with AlCl₃ or AlF₃ is not applicable for electrorefining melts, because a desired amount of aluminum components can not exist stably in the melt, and the melts supplied with co-melted and double salts of about

40mol%AlF₃-NaF are available for the electrolysis bath. The melts did not cause the cell material to corrode. In the polarization curves in the cathodic region plateau currents were observed at 0.35 and 0.75A/cm² in the melts with 2.5 and 5mol% aluminum components, respectively. In 10mol% melts, plateau current was not observed. A concentration over 5mol% of Al components is preferable to gain productivity as in the Hoopes and Gadeau processes.

References

1. T. Ishikawa, S. Konda, Proc. 1st Int. Sympo. Molten Salt Chem. and Tech., 5 (1983).
2. T. Ishikawa, S. Konda and T. Narita, Proc. 6th Int. Sympo. Molten Salt, **PV87-7**, p. 734 (1987).
3. M. Ueda, S. Konda, T. Sasaki, T. Ishikawa; Proc. of the 25th Symposium on Molten Salt Chemistry, Kobe, p. 115, (1993).
4. K. Grjotheim, Aluminum Electrolysis, Aluminum-Verlag GmbH · Dusseldorf, 109 (1977).
5. M. Ueda, S. Konda, T. Sasaki, T. Ishikawa; *Denki Kagaku*, **63**, p. 664, (1995).
6. M. Ueda, S. Konda, T. Sasaki, T. Ishikawa; Proc. of the 26th Symposium on Molten Salt Chemistry, Sapporo, p. 59, (1994).

Table 1 Compositions of the proposed melt and Hoopes and Gadeau baths(mol%).

Electrolyte	AlF ₃	NaF	BaF ₂	BaCl ₂	NaCl	Cl : F
Hoopes bath	31.3	53.6	15.1	—	—	0 : 100
Gadeau bath	28.1	41.7	—	30.2	—	33 : 67
Proposed melt	5.0	7.5	—	48.1	39.4	86 : 14
	10.0	15.0		41.3	33.7	72 : 28

Table 2 Compositions of the melts used for polarization curve measurements (mol%).

AlF ₃	NaF	BaCl ₂	NaCl	Cl : F	Na component(%)
2.5	3.8	51.5	42.2	93 : 7	46.0
5.0	7.5	48.1	39.4	86 : 14	46.9
10.0	15.0	41.3	33.7	72 : 28	48.7

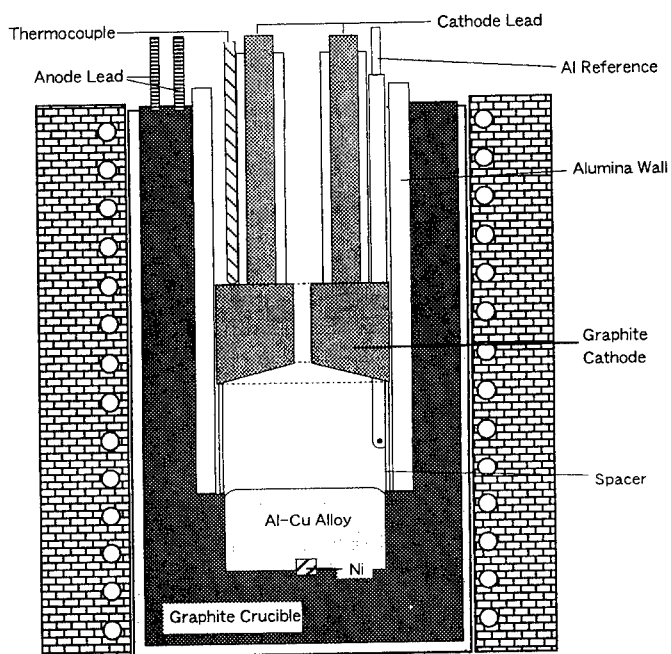


Fig.1 Apparatus for polarization curve measurements.

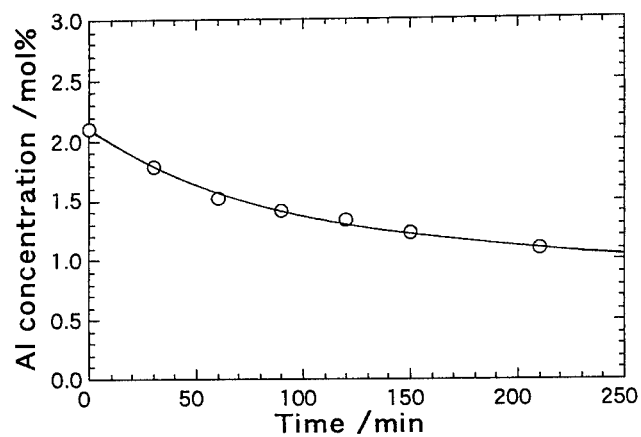


Fig. 2. Time variations in concentration of Al in an equimolar BaCl_2 -NaCl melt.

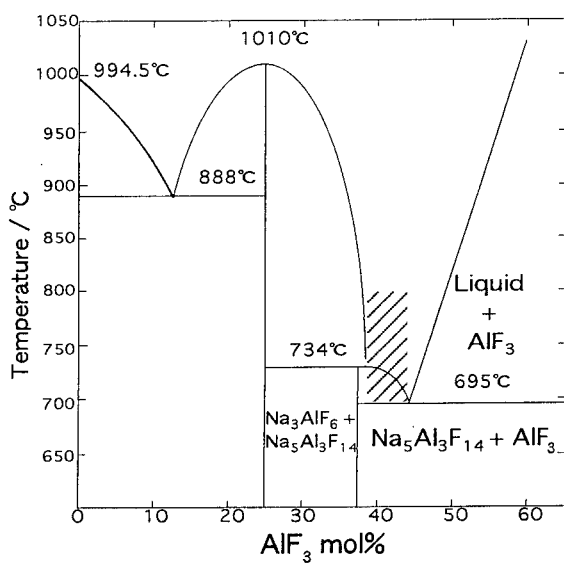


Fig. 3 Phase diagram of AlF_3 - NaF system.

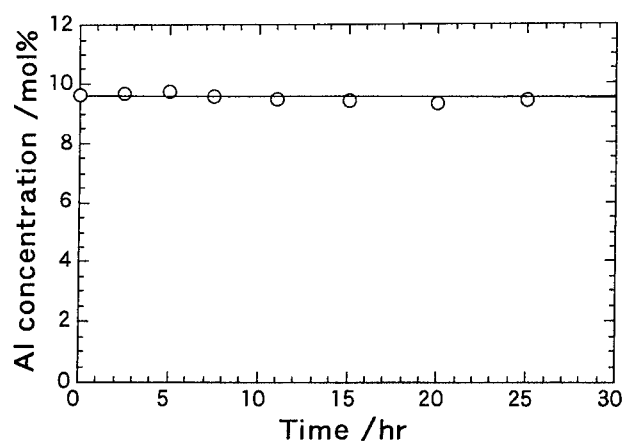


Fig. 4 Time variations in concentration of Al in the BaCl_2 - NaCl - AlF_3 - NaF melt.

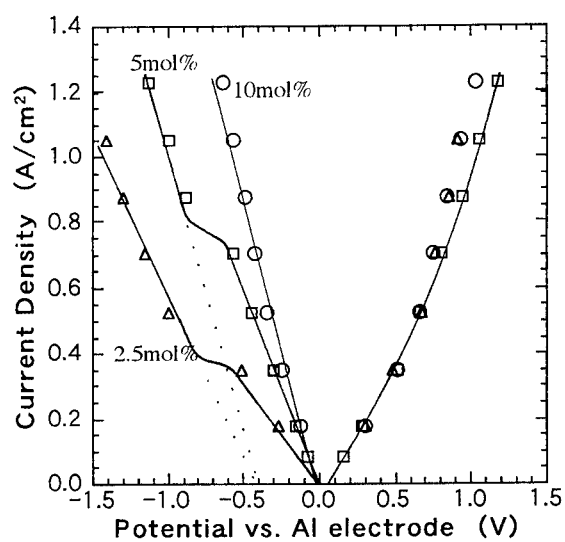


Fig. 5 Polarization curves in 55mol% BaCl₂-NaCl melts containing Al components.
Concentrations of Al components (mol%),
△ : 2.5, □ : 5, ○ : 10.

ELECTROCHEMICAL BEHAVIOR OF GLASSY CARBON AND SOME METALS IN A ZnCl_2 -NaCl MELT

Y. Okano* and A. Katagiri**

**Graduate School of Human and Environmental Studies, and **Faculty of Integrated Human Studies, Kyoto University, Sakyo-ku, Kyoto 606, JAPAN*

Stability and reactivity of glassy carbon, nickel, platinum, and tungsten in ZnCl_2 -NaCl (60-40 mol%) melt at 450°C were investigated by cyclic voltammetry and constant-potential electrolysis. Glassy carbon was stable in the potential range of 0.23-1.8 V vs. Zn in ZnCl_2 -NaCl(saturated). Nickel was oxidized and partially passivated around 0.8-0.9 V. X-ray diffraction analysis revealed the formation of β_1 -NiZn alloy at 0.3-0.35 V and γ -NiZn alloy at 0.2-0.25 V. Platinum was oxidized and partially passivated around 1.7-1.8 V, formed δ -PtZn alloy at 0.35-0.4 V, γ_1 -PtZn alloy at 0.4 V, and γ -PtZn alloy at 0.2-0.25 V. Voltammograms from a rotating tungsten disk electrode suggested the formation of a poorly soluble compound in an anodic process.

INTRODUCTION

Stability and reactivity of metals in molten salts are important in considering their use in electrolytic processes. We have been interested in ZnCl_2 -NaCl and ZnBr_2 -NaBr melts which have characteristics such as low melting point and low halide activity (1, 2). In previous papers (3, 4) we reported that the electrodeposition of tungsten occurred on nickel and glassy carbon substrates in these melts. Voltammetric studies of some tungsten compounds were performed on platinum and glassy carbon electrodes (5, 6). For interpreting the obtained results, it is necessary to know the electrochemical behavior of these electrode materials. Furthermore, the dissolution of tungsten anode is important in an electroplating cell. With these objectives in mind, a voltammetric study and constant-potential electrolysis were performed on glassy carbon, nickel, platinum, and tungsten in a ZnCl_2 -NaCl (60-40 mol %) melt at 450°C.

EXPERIMENTAL

Voltammetric experiments were carried out in a Pyrex cell. Platinum (0.5 mm in diameter), nickel (0.5 mm in diameter), and tungsten wires (0.8 mm in diameter) and a glassy carbon rod (Tokai Carbon, GC-20, 3 mm in diameter) were used as the working electrode. The effective area of the glassy carbon electrode was a circular section (0.071 cm^2) of the rod sealed in a Pyrex tube. For constant-potential electrolysis, nickel and platinum plates (0.5 mm in thickness) were used. A rotating tungsten disk electrode was made of a tungsten rod (3 mm in diameter) and a Pyrex tube. The counter electrode was

a glassy carbon rod, which was separated from the main compartment by a glass frit. The reference electrode (RE) was molten zinc in ZnCl_2 -NaCl(saturated) which was separated from the bulk electrolyte by a small piece of sodium β -alumina. Potential values were expressed in V vs. RE.

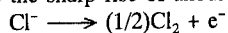
Zinc chloride (Wako) was dried at 250°C under vacuum, and then sublimed at 450°C. Sodium chloride (Wako) was dried at 350°C under vacuum. ZnCl_2 -NaCl (60-40 mol%) melt was prepared at 350°C in a Pyrex tube and then cooled and pulverized. The cell was loaded with appropriate materials under a nitrogen atmosphere in a Mecaplex Model GB80 glove box equipped with a Vacuum/Atmospheres HE-493 purifier. The moisture level in the box was monitored with a Shaw Model OEM-2 dew point meter; it was typically below 4 ppm. The cell was heated and maintained at 450°C in an electric furnace which had a window for visual observation. The inside of the cell was kept under a nitrogen atmosphere at slightly positive pressure in order to avoid atmospheric oxygen and moisture. Nitrogen gas was occasionally bubbled through the melt for stirring.

Cyclic voltammetry was performed by using a Hokuto Denko Model HA-501 potentiostat and Model HB-104 function generator. X-ray diffraction was performed with a JEOL Model JDX-8F diffractometer using CuK_α radiation.

RESULTS AND DISCUSSION

Glassy Carbon

Cyclic voltammetry was performed to examine the stability of glassy carbon as the working electrode in ZnCl_2 -NaCl (60-40 mol%) melt at 450°C. Voltammograms shown in Fig. 1 was very reproducible. Cathodic (C1) and anodic (A1) currents occurring around 0.23 V can be ascribed to the deposition and dissolution of metallic zinc (liquid), since a separate experiment showed that the potential of zinc in an identical melt was 0.23 V at open circuit. An anodic current (A2) was observed above 1.8 V and gas bubbles were generated at 1.9 V. The corresponding cathodic current was not observed, indicating that the reaction at A1 was irreversible. Lantratov and Alabyshev (7) measured the electromotive force (EMF) of the cell $\text{Zn}/\text{ZnCl}_2\text{-NaCl}/\text{Cl}_2(1 \text{ atm})/\text{graphite}$ and reported the value of 1.63 V for the melt composition of 60 mol% ZnCl_2 at 450°C. Assuming that the equilibrium potential of Zn/Zn^{2+} in ZnCl_2 -NaCl (60-40 mol%) melt is 0.23 V vs. RE, the equilibrium potential of $\text{Cl}^-/\text{Cl}_2(1 \text{ atm})$ is calculated to be $1.63 + 0.23 = 1.86$ V vs. RE. Therefore the sharp rise of anodic current (A2) is due to the reaction

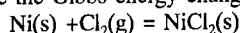


Glassy carbon is a good electrode material within the potential window of 0.23-1.8 V.

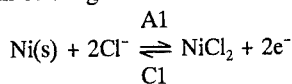
Nickel

Figure 2 shows cyclic voltammograms obtained for a nickel electrode in different modes of potential scanning. Anodic (A1) and cathodic (C1) peaks on curves a and d seem to represent the oxidation of nickel and the reverse reaction (reduction) of the product, which is presumably solid NiCl_2 (see below). The anodic peak A1 exhibits the characteristics of passivation which is also suggested by the fact that the anodic current due to the evolution of Cl_2 did not occur at potentials as high as 1.86 V.

Chemical potential data at 723 K, which are calculated from the literature (8) and listed in Table I, give the Gibbs energy change $\Delta G^0 = -195.8$ kJ/mol for the reaction



at 723 K. Therefore, the EMF of the cell $\text{Ni(s)}/\text{NiCl}_2(\text{s})/\text{Cl}_2(\text{g})$ is $-\Delta G^0/2F = 1.014$ V. Since the equilibrium potential of $\text{Cl}_2(\text{g})/\text{Cl}^-$ in $\text{ZnCl}_2\text{-NaCl}(60\text{-}40\text{ mol}\%)$ is 1.86 V vs. RE, the potential of $\text{Ni(s)}/\text{NiCl}_2(\text{s})/\text{ZnCl}_2\text{-NaCl}(60\text{-}40\text{ mol}\%)$ is calculated to be $1.86 - 1.014 = 0.85$ V vs. RE, which is in the middle of the peaks A1 and C1. Therefore the following reaction can be assigned:



Comparison of voltammetric curves **a**, **b**, and **c** suggests that the anodic peaks A2 and A3 are coupled with the cathodic peaks C2 and C3, respectively. Since it was considered that the formation of nickel-zinc alloys (9, 10) might occur, constant-potential electrolysis was carried out with a nickel electrode, and X-ray diffraction analysis of the deposit was performed. Published data of X-ray powder diffraction (11) were used for identification. As shown in Table II, different types of Ni-Zn alloys were formed depending upon the potential. Figure 3 shows X-ray diffraction patterns obtained for different duration of electrolysis at 0.250 V. It can be seen that the diffraction due to the nickel substrate decreases in the course of electrolysis, whereas the diffraction due to the γ -NiZn alloy increases. The results of Table II suggest that the currents C2 and C3 represent the formation of β_1 -NiZn and γ -NiZn alloys, respectively. Although the increase of cathodic current (C4) below 0.23 V might be associated with the deposition of pure zinc, the corresponding anodic current was not observed, and only γ -NiZn alloy was found in constant-potential electrolysis at 0.200 V. It seems that the deposited zinc (liquid) quickly reacted with the nickel substrate to yield γ -NiZn alloy.

In order to interpret the voltammetric results, thermodynamic activity data of Ni-Zn alloys obtained from vapor pressure measurements (12) were used. Table III shows the Zn activity a_{Zn} at 450°C, in mole fraction scale, which was calculated from experimentally obtained activity parameters (12). Table III includes the corresponding equilibrium potentials referred to Zn/Zn^{2+} in $\text{ZnCl}_2\text{-NaCl}(60\text{-}40\text{ mol}\%)$ and to RE:

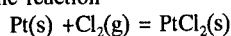
$$E [\text{V vs. Zn}/\text{Zn}^{2+} \text{ in } \text{ZnCl}_2\text{-NaCl}(60\text{-}40\text{ mol}\%)] = -(RT/2F)\ln a_{\text{Zn}}$$

$$E [\text{V vs. RE}] = -(RT/2F)\ln a_{\text{Zn}} + 0.23$$

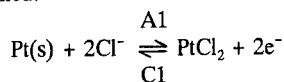
It can be seen, for example, that γ -NiZn alloy is thermodynamically stable in the potential range 0.235–0.299 V vs. RE. Figure 4 shows the relationship between the alloy composition and the equilibrium potential, together with the relevant voltammograms (reproduced from Fig. 2). The vertical broken lines are the boundaries which separate the regions of thermodynamically stable phases (α , β_1 , etc). Figure 4 confirms that the currents C2 and C3 represent the formation of β_1 - and γ -NiZn alloys, respectively. The anodic current A2 and A3 correspond to the oxidation of zinc in β_1 - and γ -NiZn alloys, respectively, to Zn^{2+} . The anodic current A5 may represent the dissolution of zinc in α -NiZn alloy.

Platinum

Similar experiments were performed for a platinum electrode. Figure 5 shows cyclic voltammograms obtained in different modes of potential scanning. The anodic peak A1 on curve a seems to represent the oxidation of platinum. In the reverse scan, current oscillation occurred (A1'), which indicates the alternation of passivation and reactivation, that is, the repeated formation and dissolution of a passive film. The cathodic current C1 may be due to the reduction of the oxidation product, which is presumably solid PtCl_2 . Thus, chemical potential data (8), shown in Table I, give the Gibbs energy change $\Delta G^0 = -16.3 \text{ kJ/mol}$ for the reaction



at 723 K. Therefore, EMF of the cell $\text{Pt(s)}/\text{PtCl}_2(\text{s})/\text{Cl}_2(\text{g})$ is $-\Delta G^0/2F = 0.084 \text{ V}$. The potential of $\text{Pt(s)}/\text{PtCl}_2(\text{s})/\text{ZnCl}_2\text{-NaCl}(60\text{-}40 \text{ mol}\%)$ is calculated to be $1.86 - 0.084 = 1.776 \text{ V}$ vs. RE, which is in the middle of the peaks A1 and C1. Therefore the following reaction can be assigned:



Comparison of voltammetric curves b, d and e suggest that the anodic currents A2 and A3 are coupled with the cathodic currents C2 and C3, respectively. In order to investigate the formation of platinum-zinc alloys, constant-potential electrolysis was carried out with a platinum electrode, and X-ray diffraction analysis was performed. As shown in Table IV, different types of Pt-Zn alloys (10, 13) were formed depending upon the potential. The results of Table IV suggest that the current C2 represents the formation of $\delta_1\text{-PtZn}$ alloy. γ - and $\gamma_1\text{-PtZn}$ alloys are formed by the cathodic current C3. Thermodynamic activity data on Pt-Zn alloys (14) are not sufficient for detailed discussion.

Tungsten

Figure 6 shows cyclic voltammograms obtained for a tungsten wire electrode. Cathodic and anodic currents due to the deposition and dissolution of metallic zinc were observed at 0.23 V. Anodic current occurred above 0.7 V with no indication of passivation. Evolution of gas bubbles was seen at 1.2 V. Since the equilibrium potential of $\text{Cl}_2(1 \text{ atm})/\text{Cl}^-$ has been estimated to be 1.86 V, the gas may not be chlorine but volatile chloride of tungsten. Chemical potential data (Table I) yield the following values of equilibrium potentials (V vs. RE):

$\text{WCl}_2(\text{s}) + 2\text{e}^- = \text{W} + 2\text{Cl}^-$	0.958 V
$\text{WCl}_4(\text{s}) + 4\text{e}^- = \text{W} + 4\text{Cl}^-$	1.215 V
$\text{WCl}_5(\text{g}) + 5\text{e}^- = \text{W} + 5\text{Cl}^-$	1.277 V
$\text{WCl}_6(\text{g}) + 6\text{e}^- = \text{W} + 6\text{Cl}^-$	1.353 V
$\text{WCl}_5(\text{g}) + 3\text{e}^- = \text{WCl}_2(\text{s}) + 3\text{Cl}^-$	1.489 V
$\text{WCl}_6(\text{g}) + 4\text{e}^- = \text{WCl}_2(\text{s}) + 4\text{Cl}^-$	1.551 V

It is probable that WCl_5 and WCl_6 are formed at higher potentials.

In order to investigate the anodic behavior more closely, a rotating tungsten disk electrode was used. The obtained voltammograms (Fig. 7) show complex phenomena

occurring at potentials 1.1–1.4 V. Thus, anodic current decreased as the potential increased, and that to greater extent at higher rotation rates. Such observations suggest that poorly soluble product was formed which was facilitated by the forced convection in the melt. Although the situation is not clear yet, anodic behavior of tungsten seems important in designing a tungsten electroplating cell.

REFERENCES

1. H. Hayashi, K. Uno, Z. Takehara, and A. Katagiri, *J. Electrochem. Soc.*, **140**, 386 (1993).
2. M. Matsunaga and K. Hosokawa, *Rep. Asahi Glass Found. Ind. Technol.*, **41**, 255 (1982).
3. H. Hayashi, K. Uno, N. Hayashi, A. Katagiri, and Z. Takehara, *Denki Kagaku*, **56**, 40 (1988).
4. A. Katagiri, M. Suzuki, and Z. Takehara, *J. Electrochem. Soc.*, **138**, 767 (1991).
5. A. Katagiri, *Materials Science Forum*, Vol. 73–75, 415 (1991).
6. A. Katagiri, *Denki Kagaku*, **61**, 1025 (1993).
7. M. F. Lantratov and A. F. Alabyshev, *J. Appl. Chem. USSR*, **27**, 685 (1954).
8. O. Knacke, O. Kubaschewski, and H. Hesselmann, "Thermochemical Properties of Inorganic Substances," 2nd Ed., Springer-Verlag, Berlin (1991).
9. "Gmelin Handbook of Inorganic Chemistry," System No. 57, Nickel, Vol. B1, Verlag Chemie, Weinheim (1965).
10. Massalski, "Binary Alloy Phase Diagrams," Vol. 3.
11. "Powder Diffraction File," No. 6–580, No. 6–0604, No. 6–619, Joint Committee on Powder Diffraction Standards.
12. R. P. Anantamula and D. B. Masson, *Metall. Trans.*, **5**, 605 (1974).
13. "Powder Diffraction File," No. 12–612, Joint Committee on Powder Diffraction Standards.
14. H. J. Hsiao, Y. A. Chang, and H. Ipser, *J. Electrochem. Soc.*, **124**, 1235 (1977).

Table I. Chemical potential at 723K

Substance	Phase	μ^0 (kJ/mol) at 723K
Cl ₂	gas	-168.9
Ni	solid	-27.9
NiCl ₂	solid	-392.6
Pt	solid	-35.9
PtCl ₂	solid	-221.1
W	solid	-29.1
WCl ₂	solid	-372.1
WCl ₄	solid	-616.0
WCl ₅	gas	-732.9
WCl ₆	gas	-829.2

Table II. Deposits on Ni substrate in constant-potential electrolysis

Potential	Deposit	Crystal structure	Atomic percent Zn*
0.200 V	γ -NiZn alloy	Body-centered cubic	73-85 %
0.250 V	γ -NiZn alloy	Body-centered cubic	73-85 %
0.300 V	β_1 -NiZn alloy	Tetragonal, CuAu type	45-52 %
0.350 V	β_1 -NiZn alloy	Tetragonal, CuAu type	45-52 %
0.500 V	No deposits		

*Estimated from the phase diagram in Ref. 10

Table III. Logarithm of activity of zinc a_{Zn} in Ni-Zn alloys and the corresponding equilibrium potential E in the ZnCl_2 -NaCl (60-40 mol %) melt at 450°C

X_{Zn} *	Phase	$\log_{10} a_{\text{Zn}}$ **	$E(\text{V})$ **
0.0507	α	-10.125	0.545
0.1005	α	-9.125	0.514
0.1502	α	-8.612	0.498
0.2493	α	-7.332	0.458
0.2890	α	-6.787	0.441
0.4575	β	-6.787	0.441
0.4750	β	-6.197	0.423
0.4900	β	-5.452	0.400
0.5000	β	-3.978	0.354
0.5190	β	-2.201	0.299
0.7390	γ	-2.201	0.299
0.8020	γ	-1.534	0.278
0.8260	γ	-0.963	0.260
0.8380	γ	-0.786	0.254
0.8500	γ	-0.155	0.235
1	pure Zn	0.000	0.230

*Mole fraction of zinc in alloy

**Obtained from vapor pressure measurements (12)

***Referred to the potential of zinc in ZnCl_2 -NaCl_{sat}

Table IV. Deposits on Pt substrate in constant-potential electrolysis

Potential	Deposit	Crystal structure	Atomic percent Zn*
0.200 V	γ -PtZn alloy	Cubic	77-81 %
0.250 V	γ -PtZn alloy	Cubic	77-81 %
0.300 V	γ_1 -PtZn alloy	Cubic	74-76 %
0.350 V	δ -PtZn alloy	Tetragonal, CuAu type	32-50 %
0.400 V	δ -PtZn alloy	Tetragonal, CuAu type	32-50 %

*Estimated from the phase diagram in Ref. 10

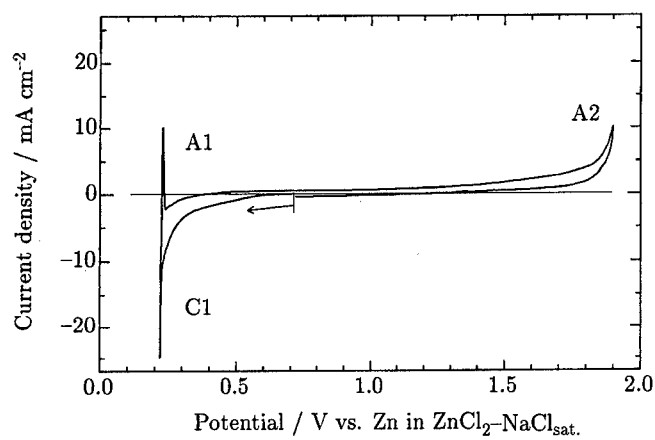


Fig. 1 Cyclic voltammogram of a glassy carbon electrode in a $\text{ZnCl}_2\text{-NaCl}$ (60-40 mol %) melt. Temperature, 450°C ; scan rate, 0.05 V/s.

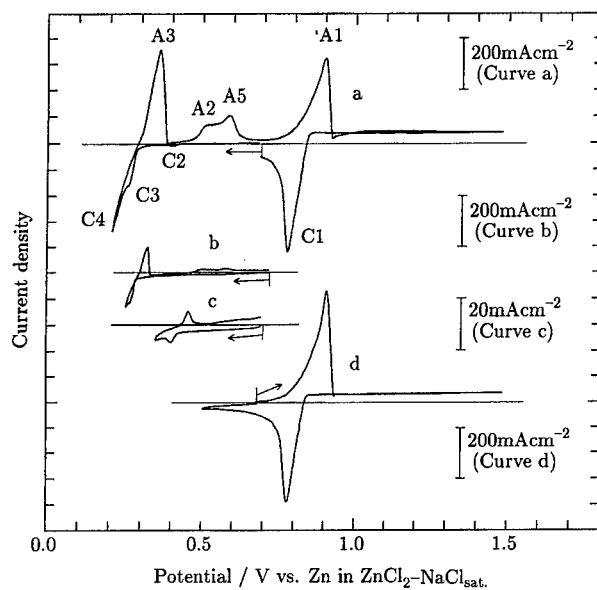


Fig. 2 Cyclic voltammograms of a nickel electrode in a $\text{ZnCl}_2\text{-NaCl}$ (60-40 mol %) melt. Temperature, 450°C ; scan rate, (a) 0.2, (b) 0.05, (c) 0.05, (d) 0.2 V/s.

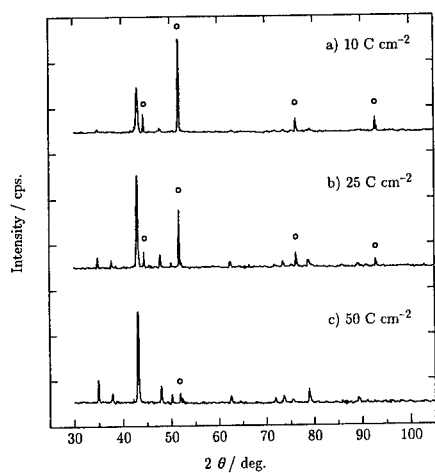


Fig. 3 X-ray diffraction patterns of deposits obtained in constant-potential electrolysis on nickel substrates. Potential, 0.250 V vs. RE; amount of electricity, (a) 10, (b) 25, (c) 50 C/cm². ○, Ni; other peaks, γ -NiZn.

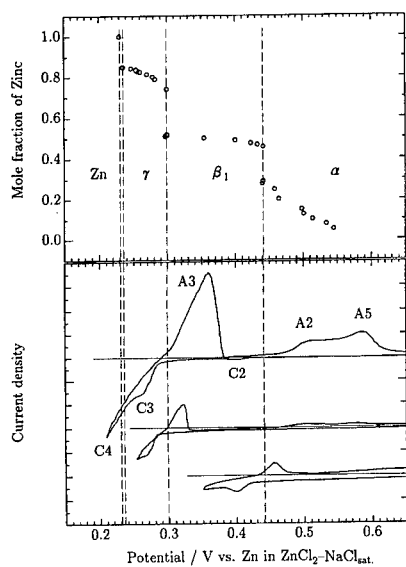


Fig. 4 Alloy composition-potential relationship and cyclic voltammograms of the nickel electrode in a ZnCl₂-NaCl (60-40 mol %) melt. Temperature, 450°C.

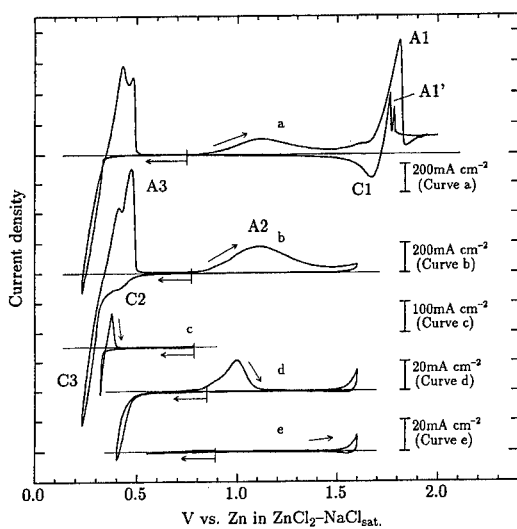


Fig. 5 Cyclic voltammograms of a platinum electrode in a $\text{ZnCl}_2\text{-NaCl}$ (60-40 mol %) melt. Temperature, 450°C ; scan rate, 0.05 V/s .

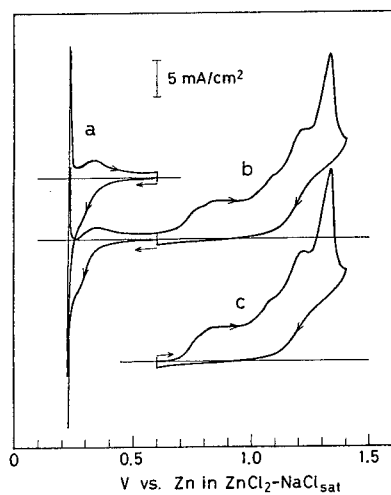


Fig. 6 Cyclic voltammograms of a W electrode in a $\text{ZnCl}_2\text{-NaCl}$ (60-40 mol %) melt. Temperature, 450°C ; scan rate, 0.05 V/s .

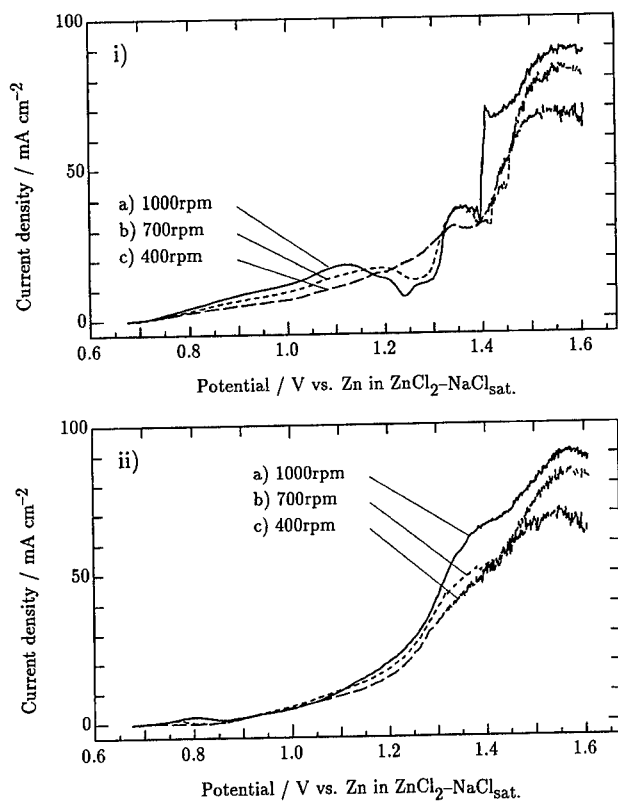


Fig. 7 Cyclic voltammograms of a rotating tungsten disk electrode in a $\text{ZnCl}_2\text{-NaCl}$ (60-40 mol %) melt. Temperature, 450°C ; scan rate, 0.002 V/s ; with (i) increasing and (ii) decreasing potential.

**A NEW EXPERIMENTAL APPROACH TO MEASURE ELECTRICAL
CONDUCTIVITY OF MOLTEN FLUORIDE ELECTROLYTES**

Xiangwen Wang and Ray D. Peterson

3326 East Second Street
Manufacturing Technology Laboratory
Reynolds Metals Company
Muscle Shoals, AL 35661-1258

Abstract

A method was developed for measuring the electrical conductivity of highly corrosive cryolite-based electrolytes and other molten fluoride systems. A pyrolytic boron nitride tube with a constant diameter was used to construct a conductivity cell, which in conjunction with a movable Pt-disc electrode constitutes a unique conductivity cell system. The electrical conductivity was determined from measuring a set of cell resistance versus a programmed linear variation of cell constant. The method, independent of the applied frequency and wiring contact resistance, was demonstrated to have distinct advantages over classic techniques in measuring the electrical resistance of highly corrosive fused fluoride electrolytes.

Introduction

Electrical conductivity of molten salts has been one of the fundamental research areas in molten salt physical chemistry.^[1,2] Because of its theoretical and technical importance, the electrical conductivity of molten fluoride systems has also received intensive attention in the past research.^[3 to 7] The molten fluoride system has several unique qualities, i.e., high melting temperature, high conductivity, and high corrosiveness to most commonly used materials which the conductivity cells are constructed with. These qualities require special experimental techniques to accurately determine the electrical conductivity of the fused fluoride systems.^[8] Measuring the electrical conductivity of a molten fluoride system can therefore be rephrased as a search for proper techniques and suitable materials to construct the conductivity cells.^[9,10]

A shortcoming associated with the traditional techniques in measuring electrical conductivity of molten salts is the dependence of the cell resistance on the applied frequency of the measuring current. Lack of proper materials also limited construction of a high cell-constant conductivity cell which could counter the highly corrosive nature and high conductivity of the melts. A number of articles have been published which have critically reviewed experimental techniques and electrical conductivity results.^[3,7,8] A comprehensive survey for the measurements of the electrical conductivity in the molten fluorides was published by Robins.^[7] Most measurements had been carried out either by using high cell-constant capillary-type cells which were made either from hot pressed boron nitride (BN)^[9,10] or from single-crystal magnesium oxide,^[11] or were made by using low cell-constant cells which made of platinum^[12] and Pt-Rh^[13] alloys. Due to either the limitation of the materials or experimental techniques, the reported results of the electrical conductivity bear a degree of uncertainty.

Significant progress has been seen both in the availability of advanced materials for conductivity cells and in experimental technique development for fused fluoride systems. A pyrolytic tube-type conductivity cell was reported for use in measuring electrical conductivity of cryolitic electrolytes.^[10] This material is immune to the molten fluoride attack and has a high thermal stability. The small inner diameter of the tube offers a greater cell constant. However, since a graphite crucible was used to hold a relatively small amount of fused electrolyte, it was difficult to hold the composition constant. Also, the technique did not overcome the applied frequency effect as in the conventional methods.

Investigation of the electrical conductivity is important to industries producing metals through electrolytic processes. More reliable data would help the aluminum industry by allowing us to predict with greater certainty those areas of the cryolitic system which may improve smelter efficiency. Consequently, old literature data has to be experimentally reviewed and new data generated. On the other hand, the availability of state-of-the-art engineering material which can resist the highly corrosive environment of the fused fluorides, make it possible to construct reliable conductivity cells. These aspects provided us an opportunity to develop new techniques for electrical conductivity measurements.

This paper presents an experimental approach designed for measuring electrical conductivity of fused fluoride salts. Unlike the traditional methods, the present technique uses the principle of linearly varying the cell constant and at the same time, continuously measuring the circuit resistance to determine the conductivity. The newest commercially-available material was used to construct the conductivity cell to counter the salt corrosion attack. The technique also employs a relatively large electrolyte pool to minimize variation in the electrolyte composition during measurements. The measured electrical conductivity is independent of the applied frequency and the effect of wire contact resistance.

Theoretical Background

In the measurement of electrical conductivity, the total impedance of the circuit may be expressed by:

$$Z = R_m + X_L + X_C \quad (1)$$

where Z is the impedance of the circuit, R_m is the real component (resistance) of the circuit, X_L is the inductive component of the impedance, and X_C is the capacitive component of the impedance. The real component of the impedance, R_m , is of interest in this study and it may be expressed as follows:

$$R_m = R_0 + R_f + \Delta R \quad (2)$$

where R_0 is the ohmic resistivity of the electrolyte, R_f is the polarization resistance of the electrolyte, and ΔR is the contact resistance between wires and electrodes. Equation (2) may be also expressed as:

$$R_m = \gamma \cdot \frac{L}{S} + F(f) + \Delta R \quad (3)$$

where γ is specific resistivity of electrolyte. L is the length of conductivity cell, S is the cross-sectional area of the conductivity cell, and f is the applied frequency. The specific resistivity, γ , equals the reciprocal of the specific electrical conductivity, k :

$$\gamma = \frac{1}{k} \quad (4)$$

The traditional methods (either high or low cell-constant conductivity cells) have been based on applying very high frequencies. At a sufficiently high frequency, the polarization resistance of the electrolyte, R_f , which is usually a function of $1/f$, decreases to a minimal value and can be omitted when compared with the magnitude of R_0 :

$$R_f = k f^{-1/2} \rightarrow 0 \quad \text{as } f \rightarrow \infty \quad (5)$$

The principle of the current technique is based on a continuously varying cell-constant, and at the same time measuring the real component of the circuit, R_m , at a fixed frequency. Continuously varying the cell-constant is realized by linearly varying the length of the conductivity cell, L , while keeping the cell cross-sectional area, S , constant. Differentiation of equation (3) with respect to L and substituting in equation (4), will result in:

$$\frac{dR_m}{dL} = \frac{1}{k} \cdot \frac{1}{S} \quad (6)$$

The polarization resistance, R_f , and the contact resistance, ΔR are constants and are independent of L . Thus by measuring R_m while linearly varying L , the electrical conductivity of the electrolyte, k , can be obtained from:

$$k = 1 / [S \cdot \frac{dR_m}{dL}] \quad (7)$$

The electrical conductivity, derived from equation (7) through a set of precisely measured cell distance increments, is free of the effects of applied frequency and wire contact resistance.

Experimental

1. Conductivity Cell Design

The system assembly is shown in Figure 1. A graphite crucible was used as a molten electrolyte reservoir. It had 3.0 cm inner diameter (I.D.) and was able to hold over 100 grams of electrolyte sample. The graphite crucible was also used as a counter electrode which was connected to a LCR Impedance Meter via a thermocouple Inconel protection sheath. The thermocouple was screwed into the wall of the graphite crucible and was used to monitor the bath temperature. The graphite crucible also had a 3.8 cm I.D. concentric positioning hole at the open end for centering the pyrolitic BN tube-type conductivity-cell. The tube-type conductivity-cell was centered vertically in the graphite crucible by a BN disc which fit in the bigger diameter hole of the graphite crucible.

A schematic of the conductivity cells used in the tests is shown in Figure 2. The pyrolitic BN tube with a consistent I.D. was obtained from Union Carbide. The material was dense and electrically non-conductive. It was also able to resist the corrosion attack by the molten fluorides. One end of the tube was fixed on a BN disc holder through the center. A Inconel rod was connected to the BN disc via threads. At least 5.5 cm of the tube was immersed in the molten electrolyte during the measurement. A Pt disc electrode was connected to 0.16 cm Pt wire by threads. The other end of the Pt wire

was also threaded to connect with a 0.64 cm Inconel rod which was then connected to the arm of a positioner for the test. The Pt rod was covered with a BN insulating tube.

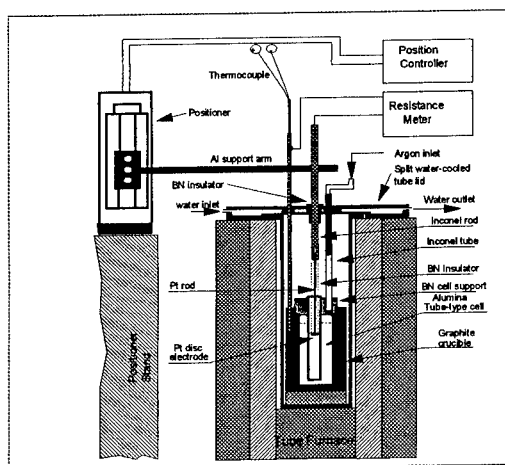


Figure 1 Schematic view of the electrical conductivity measurement system for the fused fluoride systems.

The electrode positioner used in this study was an Unidex Model X1 from AeroTech, which was vertically mounted on a vibration-free stand. It could vertically move the Pt-disc electrode in the conductivity-cell with a positional accuracy of ± 0.001 cm via the extension arm. The positioner was controlled by a programmable position controller.

An Electro Scientific Industries SP2596 impedance Meter with a fixed frequency of 1 kHz was used in most of the tests. All three components of the measuring circuit, i.e., real component (resistance), capacity, and induction, could be measured. In the study of the frequency effect, a HP 4274A Multifrequency LCR meter was employed. The LCR meter had a frequency range from 100 Hz to 100 kHz with 11 intervals and measured resistance from milliohms to megohms with 5 significant digits.

2. Experimental Procedures

2.1 Calibration of Conductivity Cell: It was shown in equation (7) that to measure the electrical conductivity of an electrolyte, the inner cross-sectional area, S , of the tube-type cell has to be known. For the pyrolytic tube-type conductivity-cell, its cross-sectional area or I.D. is determined through measuring the conductivity of a 1.00 Molar KCl aqueous solution and back calculating the area from the published conductivity data

at ambient temperatures.^[14] It is assumed that the thermal expansion of the tube I.D. due to an increase of the temperature can be neglected and was not taken into account. This was verified with molten KCl at 780°C.

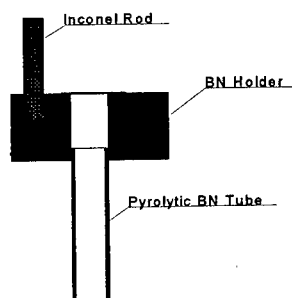


Figure 2 Schematic view of a pyrolytic BN electrical conductivity cell used for fused fluoride systems.

Calibration or determination of the cell inner cross-sectional area was conducted in a 400 ml Beaker. An Inconel coil was placed on the bottom and used as the counter electrode. The fabricated tube-type cell was centrally suspended in the KCl solution via a clamp. The Pt electrode was centered in the cell through the positioner arm. Then the resistance versus the distance the Pt electrode moved was recorded. After completing the calibration, the conductivity cell and Pt electrode were fully rinsed with distilled water before being put into a 110°C oven for over-night drying.

2.2 Electrical Conductivity Measurement: A pre-treated graphite crucible loaded with about 100 grams of electrolyte sample was placed in a temperature stabilized furnace. Once the electrolyte sample was melted, the tube-type conductivity-cell with its support was positioned on the graphite crucible via the Inconel rod. About 5.5 cm of pyrolytic tube was immersed in the molten bath. Then the Pt-disc electrode was carefully loaded into the furnace and centered in the conductivity cell via the Inconel rod, which was then fixed on the positioner's arm. The Pt-disc electrode was moved down and immersed in the molten bath by the position controller. The electrode position on the surface of the bath electrolyte was determined by the resistance reading suddenly becoming unmeasurable (Pt-disc electrode out of the electrolyte) when the electrode was moved up. Once the bath temperature was stabilized, the measurement began by moving down the Pt-disc electrode via the positioner one step at a time. The movement of the Pt-disc electrode in the conductivity cell was incremented by 0.2000 cm per each step. One set of measurements was made when the electrode was moved in the conductivity cell from the just below the surface of the bath to the lower open end of the conductivity cell and another set was made by moving back up. At least two sets of the measurements were conducted for each experimental condition, i.e., one bath

composition at one desired temperature. The measured values were same when the electrode was moved either up or down. Electrolyte samples were taken from the crucible for compositional analysis after measurement of each experimental condition.

Results and Discussion

1. KCl Aqueous Electrolyte

Two representative sets of resistance versus Pt-disc electrode moved distance in the 1.0 M KCl solution at ambient temperature are shown in Figure 3. The results were used to determine the conductivity-cell I.D. by referring to the literature data for KCl solutions^[14]. The correlation coefficient, R-square, between the resistance and the distance moved had a value higher than 0.9999 for both sets of data. This high correlation coefficient means a high accuracy for the conductivity value of the electrolyte. The linear function verified the feasibility of the continuously-varying cell-constant method.

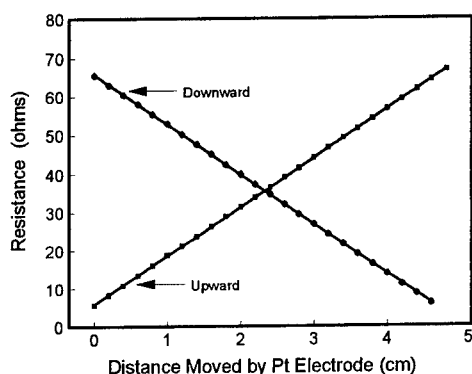


Figure 3 Electrical resistance versus the distance moved by the Pt-disk electrode in the conductivity cell for 1.0M KCl electrolyte.

2. Molten NaCl and KCl

Molten NaCl and KCl systems were selected for the evaluation of the technique for higher temperature applications. Molten NaCl has a relatively high electrical conductivity ($3.65 \text{ S}\cdot\text{cm}^{-1}$ at 815°C ^[15]) and is ideal for use in evaluating this measurement technique. Molten KCl has an electrical conductivity value ($2.25 \text{ S}\cdot\text{cm}^{-1}$

at 800°C^[15]) closer to most fused fluoride systems such as cryolitic electrolyte used in aluminum production.

Figure 4 shows two of four sets of measurements conducted in pure KCl. A close-to-perfect linear relationship was obtained between the circuit resistance and the distance moved by the electrode. The results of the electrical conductivity measurement for molten NaCl and KCl are presented in Table I.

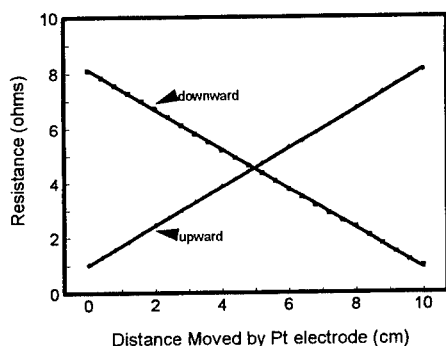


Figure 4 Electrical resistance versus distance moved by the Pt electrode in the conductivity cell for molten KCl.

Table I. Electrical Conductivity of Molten NaCl and KCl

Test Set	Lin. Rgrn. R ²	Slope (Ohm·cm ⁻¹)	Electrical Conductivity Measured (S·cm ⁻¹)	Reference (S·cm ⁻¹)	Temperature (°C)
NaCl					
Down 1st	0.9998	0.4214	3.8162	3.6722	821.4
Down 2nd	0.9999	0.4192	3.8368	3.6714	821.1
Up 1st	0.9997	0.4232	3.8003	3.6714	821.1
Up 2nd	0.9994	0.4223	3.8081	3.6712	821.0
KCl					
Down 1st	0.9999	0.7248	2.2188	2.2129	790.7
Down 2nd	0.9997	0.7267	2.1231	2.2087	789.1
Up 1st	0.9999	0.7139	2.2528	2.2126	790.6
Up 2nd	0.9999	0.7225	2.2259	2.2065	788.3

The measured electrical conductivity is higher by an average of 4.9% than the literature values for the pure NaCl at the temperatures measured, even though the correlation between the resistance recorded and the distance moved by the electrode is over 0.999. The error may be attributed to the possible impurities in the NaCl used. For the pure KCl, the average error is only 0.79% when compared with the literature values. The error is much lower than that for the molten NaCl. It should also be noted that the

equation from the literature has $\pm 1\%$ uncertainty. From the high correlation coefficient ($R^2 > 0.999$), and close match to literature data, it can be concluded that this technique can be used with high accuracy for measuring electrical conductivity of molten salts.

Figure 5 shows the measured electrical conductivity of KCl as a function of temperature. Literature data are also provided for comparison. Again, less than 1.0% relative error was obtained for all of the data points in the temperature range. The literature data were calculated by a regression equation which has a $\pm 1\%$ uncertainty for quite a large temperature range. The system proved to be sensitive to the temperature changes of the KCl bath.

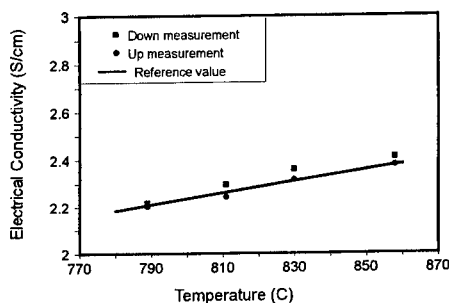


Figure 5 Electrical conductivity of KCl as a function of electrolyte temperature.

3. Frequency Effect

To examine the possible frequency effect, a series of frequencies from 100 Hz to 100 kHz were applied and the corresponding resistance readings were recorded for each step of movement by the Pt-disc electrode. The tests were conducted in four types of electrolytes:

- Pure KCl at 818°C;
- Pure cryolite (Na_3AlF_6) at 1022°C;
- Cryolitic melt with a molar ratio ($\text{MCR} = \text{N}_{\text{NaF}}/\text{N}_{\text{AlF}_3}$) equal to 2.2 containing 3.0 % Al_2O_3 , and 5.0 % CaF_2 at 959°C;
- Cryolitic melt with $\text{MCR} = 2.5$ containing 3.0 % Al_2O_3 , 3.0 % LiF , 4.0 % CaF_2 , and 2.0 % MgF_2 at 959°C.

Figure 6 shows the test results in a cryolitic melt with MCR equal to 2.5 containing 3.0 % Al_2O_3 , 3.0 % LiF , 4.0 % CaF_2 , and 2.0 % MgF_2 at 945°C. At all the testing frequencies, the resistance of the measuring circuit responded linearly with the distance moved by the electrode. When the test frequency was increased, the resistance non-linearly decreased (shifted downward), but the slopes remained parallel. The changing resistance of the measuring electrolyte as a function of test frequency has been reported in the literature.^[16,17] To overcome this resistance dependence on the applied

frequency, traditional techniques extrapolate the frequency to an infinite value or use a sufficiently high frequency in order to obtain an accurate electrical conductivity.

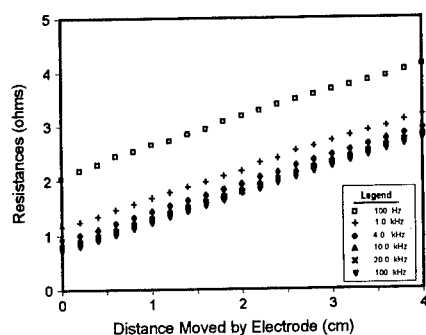


Figure 6 Electrical resistance reading versus distance moved by the Pt electrode in the conductivity cells when varying frequency. Cryolitic electrolyte: MCR=2.5 with 3.0% Al_2O_3 , 3.0% LiF, 4.0% CaF_2 , and 2.0% MgF_2 at 945°C .

A very important aspect shown in Figures 6 is that the slopes of the resistance versus the distance moved by the electrode are same and independent of the applied frequencies. The same behavior was obtained for all four molten salts. Our experimental technique uses the slope to derive electrical conductivity rather than a single resistance reading at a high applied frequency. And the very same slope implies the same derived electrical conductivity value no matter what frequency is employed in the measurement.

Figure 7 shows the typical resistance responses for the four electrolytes at an electrode distance of 3.6 cm when the applied frequency was increased from 100 Hz to 100 kHz. When the frequency increased, the resistance readings tended to decrease to constant values as the polarization resistance R_f decreased to zero. It is also shown in Figure 7 that the resistance of the molten chloride salt KCl was the most frequency-dependent while the pure cryolite was the least dependent. For pure cryolite, its electrical conductivity at 100 kHz was measured to be $2.756 \text{ S}\cdot\text{cm}^{-1}$, which agrees with the accepted literature value.^[3] However, its apparent electrical conductivity value at 1.0 kHz was measured to be $2.305 \text{ S}\cdot\text{cm}^{-1}$, only 83.6% of its accepted conductivity value.

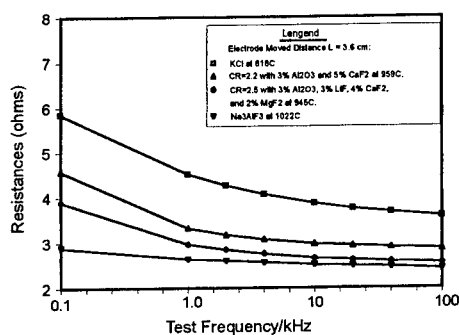


Figure 7 Effect of applied frequency on the resistance readings for electrolytes with varied electrical conductivity. Cell constant $L=3.6$ cm.

Figure 8 shows the conductivity results as a function of the applied frequency. Lines in the graph represents the average electrical conductivity. No variations of the conductivity values were observed versus the applied frequencies from 100 Hz to 100 kHz. This proves that the technique is independent of the applied frequency unlike the conventional methods.

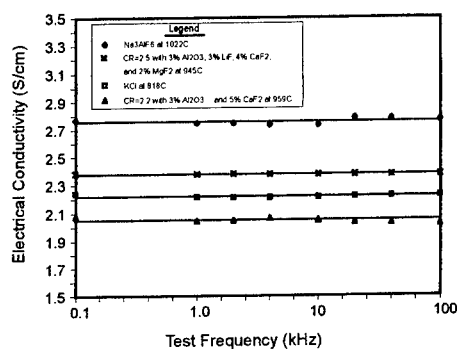


Figure 8 The measured electrical conductivity of electrolytes when varying applied frequency.

5. Applications

The present technique was specially designed for measuring electrical conductivity of cryolitic melts even though it can be used for other fused fluoride systems. It can be used for all types of electrolytes from aqueous at ambient

temperatures to molten salts at high temperatures. It has proved to be efficient and accurate in measuring electrical conductivity.

Figure 9 shows the results of the electrical conductivity measurements for analytically pure cryolite (99.5%) as a function of temperature in the range from 1020 to 1070°C. Some literature data are also presented in the Figure.

As seen from the Figure 9, the measured electrical conductivity increased from 2.82 S·cm⁻¹ at 1020°C to 2.98 S·cm⁻¹ at 1070°C, which agrees with that reported by Yim and Feinleib,^[9] Matiasovisky et al,^[18] and Edward.^[8] Other literature data for pure cryolite conductivity are quite scattered from very high values around 3.4 S·cm⁻¹ by Batashev^[19] to low values around 2.7 S·cm⁻¹ as reported by Abramov.^[20] The commonly accepted value for the pure cryolite conductivity is around 2.8 S·cm⁻¹ as reported by Yim and Feinleib.^[9]

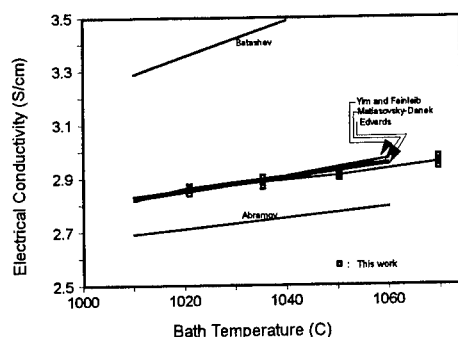


Figure 9 Electrical conductivity of pure cryolite as a function of temperature.

Figure 10 presents an example of the LiF concentration effect on conductivity in cryolitic melts. The base electrolyte was started with weight cryolite ratio (WCR) and bath ratio (BR) equal to 1.44 in a melt containing 5.0 % CaF₂ and 3.0 % Al₂O₃. A discussion of WCR and BR as used in the aluminum industry can be found in Richards.^[21] The effect of the LiF addition on the conductivity was measured under both constant bath temperature and constant superheat.

The electrical conductivity of the base electrolyte was measured to be 2.5716 S·cm⁻¹ at 985°C and 2.5880 S·cm⁻¹ at 992.8°C. At WCR = 1.44, when the LiF concentration increased up to 8.0 %, the conductivity correspondingly increased up to 2.9458 S·cm⁻¹, a 14.6% of increase from the base electrolyte at an isothermal temperature of 985°C. For the same LiF concentration increase, only about 3.2% increase in the conductivity over the base electrolyte was observed at 15°C superheat above the solidus temperature. For the cryolitic electrolytes maintained at BR=1.44 (which was achieved by addition of AlF₃), no variation of the electrical conductivity values was observed at the isothermal temperature of 985°C while a 7.1% decrease in

electrical conductivity was measured at 15°C superheat when the LiF concentration increased from 0 to 8.0 %. These conductivity results helped us to understand and adjust bath chemistry of Hall cells for the purposes of maximizing current efficiency and minimizing energy consumption in conjunction with other physicochemical parameters.

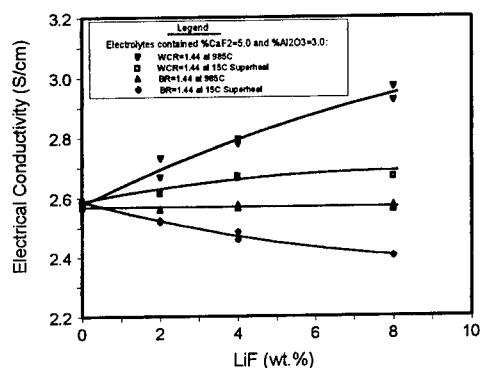


Figure 10 Measured electrical conductivity of cryolitic electrolytes as a function of LiF concentration.

Summary

Development of the present technique takes advantage of pyrolitic BN material for the conductivity cells. In conjunction with a high-precision positioner which controls the Pt-disc electrode movement in the conductivity cell, the technique measures the electrical conductivity by determining the slope of the resistance of the measuring circuit versus the linear cell-constant variation. The technique was specially designed for conductivity measurements in fused fluoride systems which can cause difficulties when using conventional techniques. The technique was tested with aqueous electrolytes and high temperature molten chloride salts. It was then used for the high temperature cryolitic electrolytes. Important findings from this work include:

1. The electrical conductivity of high temperature electrolytes can be determined through the slope of a set of resistance versus a linear cell-constant variation.
2. The measured conductivity value is independent of the test frequency and measuring circuit contact resistance.
3. Pyrolitic BN material, which resists the corrosive attacks by high temperature fused fluoride salts, was employed to construct electrical conductivity cells.
4. A relatively large amount of electrolyte pool insures the electrolyte composition remains unchanged during the conductivity measurement.

5. The technique was successfully used for the measurement of electrical conductivity in cryolitic systems. The technique verified reported literature values and generated new data for modern bath chemistries used in Hall cells.

Acknowledgment

Authors wish to thank Mr. John Cook who fabricated this experimental apparatus and help make the technique work.

References

1. M. Blander (ed): *Molten Salt chemistry*, John Wiley & Sons, Inc., New York (1966).
2. I. K. Delimarskii and B. F. Markov (ed): *Electrochem. of Fused Salts*, Trans in English by R. E. Wood, The Sigma Press, Publishers, Washington, D. C., 1961.
3. Grojtheim et al (ed): *Aluminum Electrolysis*, Aluminium-Verlag, Dusseldorf, 1982.
4. G. Choudhary: *J. Electrochem. Soc.*, Vol. 120, No. 3, p381-383, 1973.
5. G. J. Janz and R. D. Reeves: *Molten Salt Electrolytes -- Transport Properties* in "Adv. in Electrochem. and Elec. Eng.", Vol.5, C. W. Tobias (ed), John Wiley & Sons, Inc., New York, 1967.
6. B. R. Sundheim : *Transport Properties of Liquid Electrolytes* in "Fused Salts", B. R. Sundheim (ed), McGraw-Hill Book Co., New York, 1964.
7. G. D. Robbins: *J. Electrochem. Soc.*, Vol.116, No.6, pp 813-817, 1969.
8. J. D. Edwards, C. S. Taylor, A. S. Russell, and F. Marvanvill: *J. Electrochem. Soc.*, Vol. 99, No. 10, p527, 1952.
9. E. W. Yim and M. Feinleib: *J. Electrochem. Soc.*, Vol. 104, No.10, pp622-626, 1957.
10. R. D. Peterson: *Conductivity Measurements in Cryolitic Baths*, Presented at Electrolyte Workshop, Light Metals Prod., Res, Group, Carnegie-Mellon Univ., Pittsburg, 1986.
11. H. R. Bronstein and M. A. Bredig: *J. Am. Chem. Soc.*, Vol.80, p2077, 1953.
12. J. Bajcsy, M. Malinovsky, K. Matiasovsky: *Electrochim. Acta*, Vol.7, p543, 1962.
13. J. D. Mackenzie: *J. Chem. Phys.*, vol.32, p1150, 1960.
14. J. A. Dean et al., ed. *Lange's Handbook of Chemistry*, (12th ed., New York, McGraw-Hill Book Co., 1979), 5-29..
15. G. J. Janz et al (ed): *Physical Properties Data*, Compilations Relevant to Energy Storage, II. Molten Salts, NSRDS-NIBS 61, Part II, p50, 1979.
G. J. Janz: *J. Phys.Chem. Ref. Data*, Suppl. 2, 1988, Vol. 17, p232.
16. K. Matiasovsky, M. Malinovsky, and V. Danek: *Electrochim Acta*, Vol. 15, pp25-32, 1970.
17. J. Thonstad et al: *CIM* Vol.26, No.5, pp219-228, 1987.
18. K. Matiasovsky, et al: *Electrochim Acta*, Vol.17, p463, 1972.

-
19. K. P. Batashev: *Legkie Metally*, Vol.10, p48, 1936.
 20. G. A. Abramov, et al: *Metallurgizdat*, Moscow, 1953.
 21. R.E. Richards, et al., *Light Metals*, p379, 1983.

TITRATION OF REFRACTORY METAL COMPOUNDS IN MOLTEN SALTS BY SQUARE WAVE VOLTAMMETRY

P. CHAMELOT, B. LAFAGE and P. TAXIL
Université Paul-Sabatier,
Laboratoire de Génie Chimique et Electrochimie,
URA CNRS 192, 118, route de narbonne,
31062 Toulouse Cedex, France

ABSTRACT

In this paper, an electrochemical methodology is attempted for the quantitative analysis of molten fluoride solutions, used for the electrodeposition of refractory metals (Ta, Nb). Both oxidation state of the bath and oxygenated compounds degree, critical for the issue of the process may be measured by square wave voltammetry rather than cyclic voltammetry. Firstly the accuracy and the sensitivity of the method are evidenced in the case of Ta electrodeposition bath. Further a titration method of tetravalent niobium ions is performed, using the statement of the mass balance of niobium species after each addition of solute.

INTRODUCTION

Refractory metals (namely Ta, Nb, Ti, Zr, Hf...) are now of great importance in various fields of high technology owing to their attractive surface properties (1); their high cost often leads to expect their use only as thin coatings on usual materials.

Among the main techniques available for surface coatings, electrodeposition in molten salts can be considered as suitable for industrial processing: classically, the electrodeposition is performed in molten alkaline fluorides, containing electroactive ionic compounds (K_2TaF_7 , K_2TiF_6 ...) (2).

The management of the industrial process requires an efficient tool for the on-line control of the electrolyte composition, specially concerning the following points: (i) the oxidation state of polyvalent ions (Nb, Ti ions...); (ii) the content of low valency metal ions producing the coating; (iii) the content in oxycomplexes which has to be as low as possible.

Preferable to the spectroscopic methods, electrochemical ones and particularly Square Wave Voltammetry (SWV) are available for analysis of high temperature ionic liquids (3,4). SWV was attempted in this work for the titration of Ta and Nb electrodeposition baths.

EXPERIMENTAL PART

The cell:

The electrolysis cell has been described in detail in a earlier paper (5).

The electrolytic bath consisted of an eutectic mixture of LiF-NaF (60-40% m/m) initially dehydrated by heating in a vacuum (2×10^{-2} mmHg) up to the melting point (650°C). Fusion was performed in a neutral argon atmosphere (U quality) and then the bath was raised to the working temperature of 780°C .

The Nb and Ta ions were introduced into the bath in the form of pellets of respectively $NbCl_5$ and K_2TaF_7 . The oxyfluoride compounds were prepared *in situ* by means of controlled additions of sodium oxide, Na_2O . All the additions were made via an argon atmosphere lock.

The electrodes:

The analytical electrochemical techniques used (cyclic and square wave voltammetry) require a three-electrode set-up:

- the working electrode was a tungsten wire with a diameter of 1 mm, plunged approximately 1 cm into the bath.
- the reference electrode was a wire with a diameter of 1 mm, plunged into the molten solution. Tungsten was used in the case of niobium solutions, and tantalum was used in the case of tantalum solutions. The first electrode acts as a $\text{Nb}^{\text{V}}/\text{Nb}^{\text{IV}}$ red ox electrode, whereas the second is indicative of $\text{Ta}^{\text{V}}/\text{Ta}$ system.
- the auxiliary electrode was a rod of vitreous carbon (Carbone Lorraine, V25 quality) with a diameter of 3 mm, with an immersed surface area of more than 2 cm^2 .

The electrochemical analysis methods:

For a first qualitative approach we used cyclic voltammetry; then for quantitative analysis the square wave voltammetry (SWV) technique was proved to be preferable.

This technique gives for each electrochemical reaction a peak shaped signal modeled by Ramaley and Krause (6). From this model, we recall here the following equations adapted both to qualitative and quantitative analysis of electrochemical systems:

(i) the width of the half peak $W_{1/2}$ depends on the number of electrons n exchanged and on the temperature. According to Osteryoung et al (7), the appropriate equation is:

$$W_{1/2} = 3.52 \frac{RT}{nF} \quad (\text{I})$$

with $W_{1/2}$ in V; R: ideal gas constant in $\text{J.mol}^{-1}.\text{K}^{-1}$; T: absolute temperature (K); F: Faraday constant (A.s.mol^{-1}).

(ii) the peak current δI_p is linear with the concentration of the electroactive species and with the square root of the frequency f according to the equation:

$$\delta I_p = nFA C_0 \frac{1-\Gamma}{1+\Gamma} \sqrt{\frac{Df}{\pi}} \quad (\text{II})$$

with

$$\Gamma = \exp\left(\frac{nF}{RT} \frac{\Delta E}{2}\right) \quad (\text{III})$$

and δI_p in A; ΔE (V): amplitude of the square wave potential; A: surface area of the electrode (cm^2); D: diffusion coefficient of the electroactive species ($\text{cm}^2.\text{s}^{-1}$); C_0 : Bulk concentration of the electroactive species (mol.cm^{-3}).

In the case of a multicomponent system with interfering waves, the resulting differential current $\delta I(E)$ is formally expressed as follows:

$$\delta I(E) = \sum_{j=1}^N \delta I_p^j f_j(E) \quad (\text{IV})$$

N is the number of components in the system, $f_j(E)$ is a function that depends, in particular, on the number of electrons and their individual equilibrium potentials. If these parameters are not known precisely, trial and error fitting of the values has to be performed to match the model's voltammogram and the experimental data. In this way it is possible to separate the wave components.

Instrumentation:

The square wave voltammograms were obtained using an EGG PAR 273 potentiostat controlled by a microcomputer.

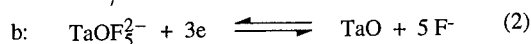
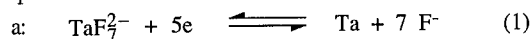
For cyclic voltammetry, an EGG PAR 371 potentiostat, controlled by an EGG PAR 175 signal generator, was used. It was connected to a Kipp and Zonen (Y,Y) BD plotting table.

RESULTS AND DISCUSSION

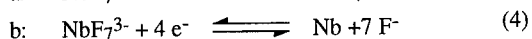
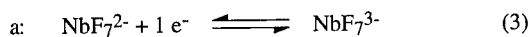
Cyclic voltammetry

Fig 1 and 2 show respectively the cyclic voltammogram of K_2TaF_7 and $NbCl_5$ in molten $LiF-NaF$ in the 750-850°C temperature range.

Comment of fig.1: According to earlier literature, the peak noted a is associated with the Ta electrowinning reaction (8), whereas the peak b is produced by the reduction of an oxyfluoride compound, generated by reaction with the melt of very active oxide ions remaining in the molten solution after the fusion process. So, the following reactions are proposed for each peak:

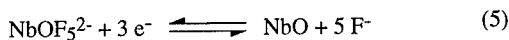


Comments on fig.2: The dissolution of $NbCl_5$ in the fluoride melt gives rise to the complexed form, NbF_7^{2-} . It is now stated that the reduction of pentavalent niobium ions in molten fluoride media proceed in two successive steps (9,10):



These two steps, very close to each other in terms of potential respectively contribute, to the slow increase of current noted a and the peak b in fig.2.

The third event on this figure marked by c was attributed to the reduction of a niobium oxyfluoride, according to reference (11).



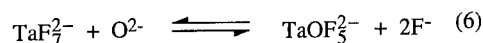
The preceding results are thus in agreement with previous papers related to the reduction mechanism of niobium ions in molten fluorides but they don't allow the titration of each specie involved in this system to be performed, since the waves related to these species are greatly interfering.

Square wave voltammetry

On fig 3 and 4, we present the square wave voltammograms of the respective mixtures $LiF-NaF-K_2TaF_7$ and $LiF-NaF-NbCl_5$ mixtures in the same range of temperature and potential as fig. 1 and 2.

The deconvolution of the overall signal, according to the procedure indicated above (eq. IV and following comment) allows each electrochemical reaction to be associated on these figures to a gaussian peak.

Due to the high sensitivity of the method, any variation of the content in each electrochemical specie can be detected: in fig.5, we observe the consequence on the SW voltammogram of fig.3, of the addition of oxide ions in the form of Na_2O , that produces the following reaction:



The mutual evolution of peaks a and b, observed on fig. 5 is consistent with the shift of reaction (6) in the right sense, respectively decreasing $[\text{TaF}_7^{2-}]$ and increasing $[\text{TaOF}_5^{2-}]$, taking into account the linear relationship between the peak current and the content in electroactive species (eq. II)

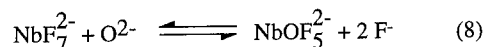
Quantitative analysis of niobium electrodeposition baths.

Chemical analysis of niobium electrodeposition is considered to be somewhat complexe, due not only to the two step reduction mechanism of Nb^{V} ions (instead of one step for tantalum system) as stated above, but also to the following disproportionation reaction occurring in the transient phases after each change in composition of the bath:



In order to prevent this reaction, a niobium rod must be kept into the bath, to ensure that the content in pentavalent ions is at the lowest value.

The reaction of oxide ions on Nb^{V} ions, similar to equation (6) for tantalum, is expressed as below:



Quantitative analysis of this system has to take into account the shift of the equilibrium (7) and (8) when compounds such as NbCl_5 and / or Na_2O are introduced in the melt.

When the differential current peak is plotted versus the niobium content in the bath on fig. 6, a linear relationship is observed for both Nb^{IV} peak (curve 1) and NbOF_5^{2-} (curve 2); in each case, the straight line does not pass through the origin, that can be explained by the initial presence of oxide ions in the molten salt solvent.

This correction of intercept of curve 1 is possible if we assume that, when Na_2O is introduced in the bath, the oxide ions react with Nb^{V} ions, according to equation (8). So, using the dosed addition method, the initial concentration in oxide ions and consequently the loss of niobium in the form of oxifluoride compound can be estimated (12).

Afterwards, the slope of the straight line (1) has to be corrected since only one part of NbCl_5 introduced is converted in Nb^{IV} species (cf equation 7).

It is possible to determine the equilibrium constant of equation (7), using the difference in potential of peaks (a) and (b) of fig. 4, related to the respective Nb^{V} and Nb^{IV} species, and knowing that a peak potential in SWV is close to the half wave potential of the involved electrochemical species (13). We found that this constant is $K = \frac{[\text{Nb}^{\text{IV}}]}{[\text{Nb}^{\text{V}}]^4} = 198$

This data allows the mass balance of the total amount of niobium species to be performed and therefore to calculate, in particular, the effective content in Nb^{IV} after each addition of the solute.

Taking into account these corrections, it was possible in fig.7, to build up a calibration curve giving the height of peak (b) of fig. 4 versus the true content in tetravalent niobium.

This curve must be expected to be an efficient tool for the control on line of the electrolyte during the electrodeposition of niobium, since the metal is produced by the one step reduction of tetravalent niobium and therefore the content in this species must be continuously optimized.

CONCLUSION

This study has made it possible to show that square wave voltammetry is a powerful analysis method both from the qualitative and quantitative viewpoints for ionized media at high temperatures. The calibration curves established using this method should make it possible to measure in real time the concentration of the Nb^{IV} species leading to the metallic deposition, and the niobium's oxyfluoride compound content. Any drift in these two parameters can therefore be easily detected, which will therefore make it possible to consider controlling the bath during the electrolysis process.

This technique is all the more sensitive and precise as the number of electrons exchanged during the electrochemical reaction concerned is high, as is the case for the electrolytic deposition of refractory metals such as Ta, Hf, Nb, Zr in a molten alkaline fluoride media. We have seen in this paper that it was adapted to tantalum and niobium systems. We are now evaluating its suitability to the hafnium system.

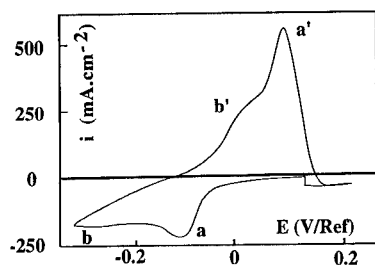


Figure 1: Cyclic voltammetry of a solution of K_2TaF_7 in molten LiF-NaF (2.5 mass percent) at 790°C ; Working Electrode: Mo (area = 0.31 cm^2); electrode of comparison: Ta; Counter electrode: Vitreous carbon; Potential scan rate: 100 mV/sec .

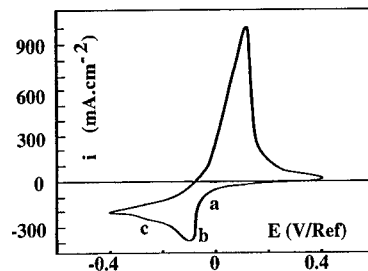


Figure 2: Typical cyclic voltammogram of NbCl_5 in LiF-NaF containing oxide ions O^{2-} : $[\text{NbCl}_5] = 3.7 \text{ mass percent}$, working electrode: tungsten (area = 0.31 cm^2), electrode of comparison: tungsten, counter electrode: vitreous carbon, $T=780^\circ\text{C}$, scanning potential rate = 200 mV.s^{-1} .

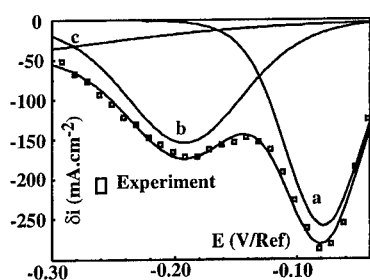


Figure 3: Square wave voltammogram of a solution of K_2TaF_7 in molten $LiF-NaF$ (5.0 mass percent) at $790^\circ C$; Working Electrode: Mo (area = 0.31 cm^2); electrode of comparison: Ta; Counter electrode: Vitreous carbon; Pulse frequency: 36 Hz; Potential scan rate: 72 mV/sec . \square : experimental points; full line: curve obtained by modeling

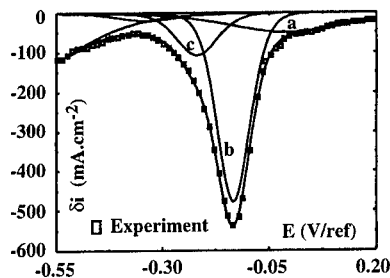


Figure 4: Typical square wave voltammogram of $NbCl_5$ in $LiF-NaF$. $[NbCl_5] = 3.3$ mass percent, working electrode: tungsten (area = 0.31 cm^2), electrode of comparison: tungsten, counter electrode: vitreous carbon, pulse frequency: 25 Hz, scanning potential rate: 75 mV.s^{-1} , $\theta = 780^\circ C$.

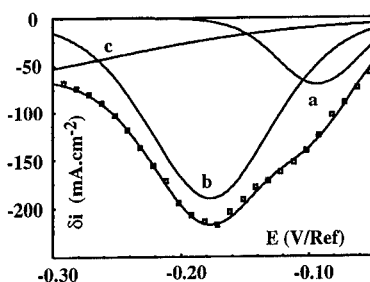


Figure 5: Square wave voltammogram of a solution of K_2TaF_7 in molten $LiF-NaF$, supplemented with sodium oxide, at $790^\circ C$. Composition of the bath: 5.0 mass percent K_2TaF_7 ; 0.2 mass percent Na_2O . Working Electrode: Mo (area = 0.31 cm^2); electrode of comparison: Ta; Counter electrode: Vitreous carbon. \square : experimental points; full line: curve obtained by modeling

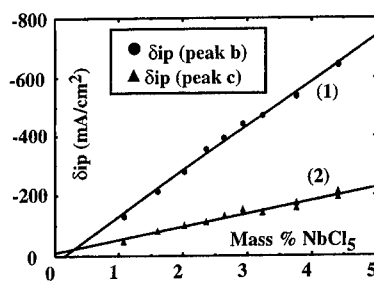


Figure 6: Linear relationships of reduction peaks differential current densities for Nb^{IV} (1) and $NbOF_5^{2-}$ (2) species versus the concentration of $NbCl_5$ added (in mass percent).

Working electrode: tungsten (area: 0.31 cm^2), electrode of comparison: tungsten, pulse frequency: 25 Hz, scanning potential rate: 75 mV.s^{-1} , $\theta = 780^\circ C$.

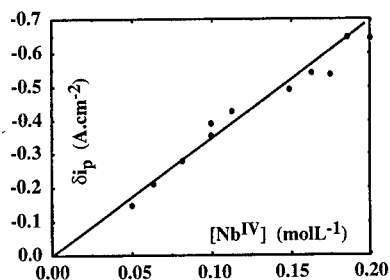


Figure 7: Linear relationship of reduction peak differential current density for Nb^{IV} species versus its real concentration in the bath.

Working electrode: tungsten (area: 0.31 cm²),
 electrode of comparison: tungsten, pulse frequency:
 25 Hz, scanning potential rate: 75 mV.s⁻¹,
 θ = 780°C.

AKNOWLEDGMENTS

The authors express their thanks to the company CRV Pechiney, and in particular to S. Bouvet, A. P. Lamaze and Y. Bertaud for their collaboration and financial support for this research.

REFERENCES

- (1): Refractory Metals and their applications, Ed. E. Smallwood, ASTM STP 849, New Orleans, 1982.
- (2): S. Senderoff and G.W. Mellors, *Science* **153**, 1475 (1966)
- (3): C. Russel: *Phys. Chem. Glasses*, **32**, 138, (1991)
- (4): B. Lafage and P. Taxil, *J. Electrochem. Soc.* **140**, 3089, (1993)
- (5): P. Chamelot, B. Lafage and P. Taxil, *Electrochim. Acta*, **39**, 2571 (1994).
- (6): L. E. Ramaley and M.S. Krause, *Anal. chem.* **41**, 1362 (1969)
- (7): J. J. O'Dea, J. G. Osteryoung and R. A. Osteryoung, *Anal. Chem.*, **53**, 695 (1981).
- (8): P. Taxil, J. Mahenc, *J. Appl. Electrochem* **17**, 261, (1987)
- (9): Q. Zhiyu and P. Taxil, *J. Appl. Electrochem.*, **15**, 259 (1985).
- (10): P. Chamelot, Thesis, Toulouse (1994).
- (11): J.H. Von Barner; E. Christensen; N.J. Bjerrum; B. Gilbert, *Inorg. Chem*, **30**, 561, (1993)
- (12): P. Chamelot, B. Lafage and P. Taxil, to be published.
- (13): J. G. Osteryoung and R. A. Osteryoung, *Anal. Chem.*, **57**, 101A (1985).

EQCM Studies of Aluminum and Aluminum Alloys in Room Temperature Molten Salts

H. C. De Long[†] and P. C. Trulove[‡]
Surface Chemistry Branch
Chemistry Division
Naval Research Laboratory
Washington DC

ABSTRACT

Room-temperature molten salts composed of aluminum chloride (AlCl_3) and 1-ethyl-3-methylimidazolium chloride (EMIC) are well suited to studying the electrodeposition of aluminum (Al) and as a codeposit with other metals (Al-M_x).¹ We have employed an Electrochemical Quartz Crystal Microbalance (EQCM) to investigate, *in situ*, the deposition and stripping behavior of Al and Al-M_x in acidic AlCl_3 :EMIC molten salts. The EQCM provides both mass and charge data during electrodeposition and stripping processes. This information can be used to determine codeposited metal composition and to model deposition and/or stripping processes.

INTRODUCTION

Our interest lies in the electrodeposition of various combinations of metals with aluminum. This grows from the planned use of these metal combinations to make thin multilayers and bulk deposits. These multilayers are being investigated for their various properties^{2,3} such as their utility as magnetic thin layered films as in the case of aluminum with cobalt, iron, or nickel. In order to understand these systems, their growth and film properties need to be investigated. A first step in this process is the growth of these films from room temperature molten salts. Application of room temperature molten salts to the deposition of various metals arises from their known use as an electroplating medium for aluminum production. Previous work with cobalt and nickel indicate that the growth of these films is by a underpotential deposition (UPD) mechanism, that is tempered by a three dimensional nucleation phenomena. The focus of the present work is the examination of the EQCM behavior of these aluminum metal combinations and the characterization of the resulting films produced by the above method.

EXPERIMENTAL

Purification of $\text{AlCl}_3\text{:EMIC}$ melt components was performed as previously described.⁴ Protonic impurities were removed by vacuum treatment at 1×10^{-5} Torr for several days.⁵ Polycrystalline gold disk electrodes were made by vapor deposition of approximately 2000 Å of gold onto approximately 50 Å of chromium. The support material was AT-cut 5 MHz Quartz crystals, which were highly polished and 1.0 inch in diameter. The electrochemically active area is 0.34 cm^2 and the piezoelectrically active area is 0.28 cm^2 . The counter electrode was a 0.5 mm diameter platinum wire coil, and the reference electrode consisted of an Al wire immersed in $N=0.60 \text{ AlCl}_3\text{-EMIC}$ melt contained in a sealed glass compartments built into a homemade EQCM cell using a platinum wire connection to the built-in luggin capillary. Melt preparation and handling was performed in a nitrogen filled Vacuum Atmospheres two man drybox. All EQCM measurements were conducted using the air-tight glass electrochemical cells which were set up inside the drybox, then used outside the drybox. EQCM cyclic voltammetry was performed with an Intertech Systems HB-111 Analog Function Generator and a PS151 Potentiostat/Galvanostat controlled by the Asyst 4.01 software environment using a GTSI 486DX/33MHz computer. Data acquisition was done with a Data Translation DT-2801A D/A converter board and a DT-707 screw board. The oscillator circuit used was for a 5 MHz crystal in the normal mode⁶ powered by a Hewlett Packard 20 volt power supply. All data collected in the above system was converted into Microsoft Excel 5.0 worksheets for data analysis by Microsoft Excel or Origin software.

RESULTS AND DISCUSSION

We have recently demonstrated the use of the EQCM in room-temperature molten salts.⁷ Room-temperature molten salts are significantly more viscous than aqueous solutions. The acidic molten salts used in these studies had viscosities in the range of 15-20 centipoise. (This is comparable to the viscosity of ethylene glycol). The higher viscosity of the melts tends to slow down the EQCM indicated response time causing a separation to occur between the forward and reverse scans. However, we can somewhat compensate for this by slowing down the scan rate, which allows for the reaction to proceed to completion before scan reversal.

The nature of the EQCM frequency data can be evaluated by mathematically converting it to current response data; this gives a calculated cyclic voltammogram which can be compared with the experimental voltammogram. Differences between the two voltammograms may be an indication of solvent occlusion, mixed transport of ions, or the presence of other species (i.e. proton) which are electroactive in the region of interest. Consequently, these studies were performed on clean proton free acidic melts to minimize these problems.

The first effort in looking at the use of EQCM in room temperature molten salts involved an examination of the UPD of aluminum. The nature of the response would give us a good indication of the utility the EQCM would have in this relatively viscous medium. The answer to that question lies in the analysis of the data presented in Table I. The second column reports both the frequency and current data converted into grams per centimeter squared to give areal mass. The areal mass data indicates that the results of the frequency and current data don't have amplification (positive or negative) due to viscoelastic effects from the viscous electrolyte. The film remains a rigid layer as far as the system can detect with no indicated variable damping of the resonance frequency of the quartz crystal. The data representing the calculated and actual frequencies achieved indicate that this EQCM method is sensitive enough to detect monolayer amounts of material in the molten salt used for this study. Furthermore, this data indicates the viability of using EQCM as a tool to study rigid layers in this room temperature molten salt.

EQCM measurements give simultaneous current and frequency data as a function of potential. By making certain assumptions, the frequency data can be converted to mass data. Figure 1 shows the staircase cyclic voltammogram of aluminum and chromium electrodeposited from a $N=0.52$ acidic melt. The corresponding frequency verses potential plot for the staircase cyclic voltammogram in Figure 1 is shown in Figure 2. As stated earlier, the frequency is proportional to the mass, and as Figure 2 clearly shows, there is a significant mass increase as the potential is scanned negative of zero volts. This corresponds to the first reduction wave in Figure 1. This mass increase continues through the rising part of the second reduction wave and also upon scan reversal out to approximately 0.25 V. At that point, the process is reversed and all the mass is stripped off. This corresponds to the two oxidation waves observed upon scan reversal in Figure 1. This is important because this indicates that nothing is left on the surface and no stripping of the electrode surface is occurring either.

Similar results to figures 1 and 2 are seen in figures 3 and 4, when the voltage is scanned only out through the first reduction wave. This gives a better look at the voltammetry of the first wave. Of interest is to figure out what component, the Al or Cr, is the main contributor to the electrochemical events taking place.

Also present is a secondary frequency change seen in both figures 2 and 4. This secondary frequency change at 0.8 to 1.5 V is hypothesized to be from the Cr^{+2} to Cr^{+3} transition which formed an insoluble compound. This compound precipitates out to give a frequency decrease which indicates an increased mass is sensed. The process is reversible and the material is completely removed.

EQCM measurements can be used to ascertain the composition of the deposited material. If we assume a uniform codeposit, analysis of mass and current data can be used to characterize deposition and stripping processes.⁶ The total mass change during deposition or stripping (ΔW_{Total}) is equal to the sum of the masses of the individual metals; ΔW_{Mx} is

the weight for added metal (other than aluminum) and ΔW_{Al} is the weight for aluminum (equation 1).

$$\Delta W_{Total} = \Delta W_{Mx} + \Delta W_{Al} \quad [1]$$

$$\Delta Q_{Total} = \Delta Q_{Mx} + \Delta Q_{Al} \quad [2]$$

The total charge (ΔQ_{Total}) is equal to the charge from the added metal (ΔQ_{Mx}) and from Al (ΔQ_{Al}) (equation 2). Conversion of charge to weight and substitution of equation 2 into equation 1, gives equation 3. K_1 and K_2 are constants for Al and M_x , respectively.

$$\Delta W_{Mx} = (\Delta Q_{Total} - K_1 \Delta W_{Total}) / (K_2 - K_1) \quad [3]$$

Once the ΔW_{Mx} is known, it is substituted back into equation 1 to get ΔW_{Al} . From the ratio of the mass changes we can calculate the composition of the deposit. In addition, the mass changes can be plotted against the potential to determine mass loss and charge loss, upon stripping, of the codeposited Al and M_x and individual metals.

Using the data from the frequency-potential plot shown in figure 4, we calculated the mass versus potential using the above equations for both Cr and Al. The data are plotted in figure 5 as moles of Cr and moles of Al. The plots for the Al and Cr are almost superimposable indicating that for the first reduction wave Al and Cr are deposited simultaneously and in similar molar quantities.

SUMMARY

We have concluded several issues from the above discussed work.

1. EQCM is a viable technique to use in a medium such as the room temperature EMIC- $AlCl_3$ molten salts.
2. The UPD of aluminum can be measured in this electrolyte system and the results are fairly close to the expected values.
3. Aluminum and chromium can be codeposited from the room temperature EMIC- $AlCl_3$ molten salts even though the potential at which they deposit occurs after normal bulk aluminum deposition.
4. EQCM can give us insight into the deposition and stripping behavior of metal deposits.

REFERENCES

- [†] Air Force Office of Scientific Research, Directorate of Chemistry and Life Sciences, Bolling AFB, DC 20332-8080
- [‡] Chemistry Department, U.S. Naval Academy, Annapolis, MD 21402-5026

1. R. T. Carlin, P. C. Trulove, H. C. De Long, J. Electrochem. Soc., 143, (1996) in press.
2. R. T. Carlin, H. C. De Long, P. C. Trulove, Abs. 652, p. 981, The Electrochemical Society Extended Abstracts, Reno, NV, May 21-26, 1995.
3. C. L. Hussey, In *Chemistry of Nonaqueous Solvents*, G. Mamantov, A. I. Popov, eds., VCH, 1994, p. 227.
4. J. S. Wilkes, J. A. Levisky, R. A. Wilson, C. L. Hussey, *Inorg. Chem.* **21**, 1263 (1982).
5. M. A. M. Noel, P. C. Trulove, and R. A. Osteryoung, *Anal. Chem.*, **63**, 2892 (1991).
6. Oscillator circuit diagram from D. A. Buttry, University of Wyoming.
7. H. C. De Long, R. T. Carlin, Abs. 647, p. 974, The Electrochemical Society Extended Abstracts, Reno, NV, May 21-26, 1995.

Table I EQCM data of the underpotential deposition of aluminum.

Scan	Q vs Freq (g/cm ²)	Frequency Expected	Frequency Actual
1	6.5/5.5x10 ⁻⁸	3.6 Hz	3.8 Hz
2	5.4/5.8x10 ⁻⁸	3.6 Hz	4.0 Hz
3	6.8/6.1x10 ⁻⁸	3.6 Hz	4.2 Hz

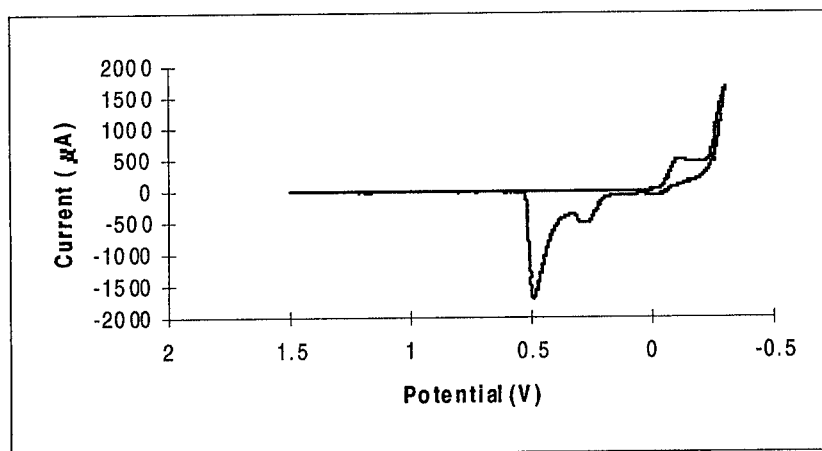


Fig. 1 Staircase cyclic voltammogram of aluminum and chromium electrodeposited from $N=0.52$ room temperature EMIC- AlCl_3 molten salt using an aluminum wire in $N=0.60$ EMIC- AlCl_3 as a reference electrode.

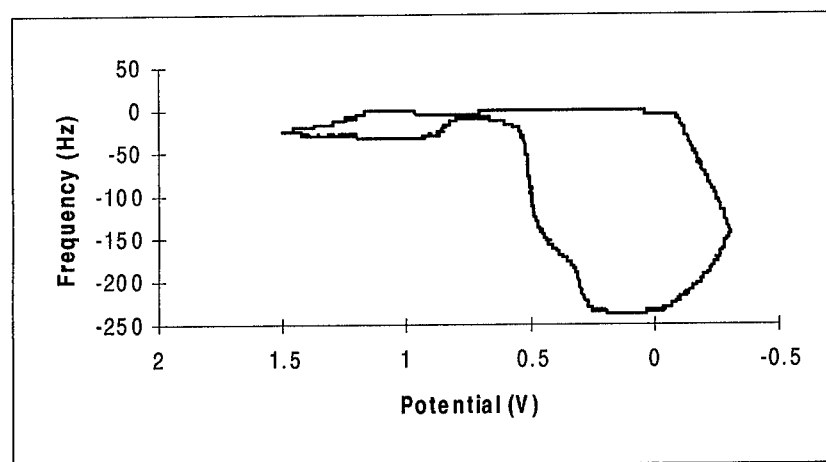


Fig. 2 The accompanying frequency data of Aluminum and Chromium electrodeposited during the EQCM experiment depicted in figure 1.

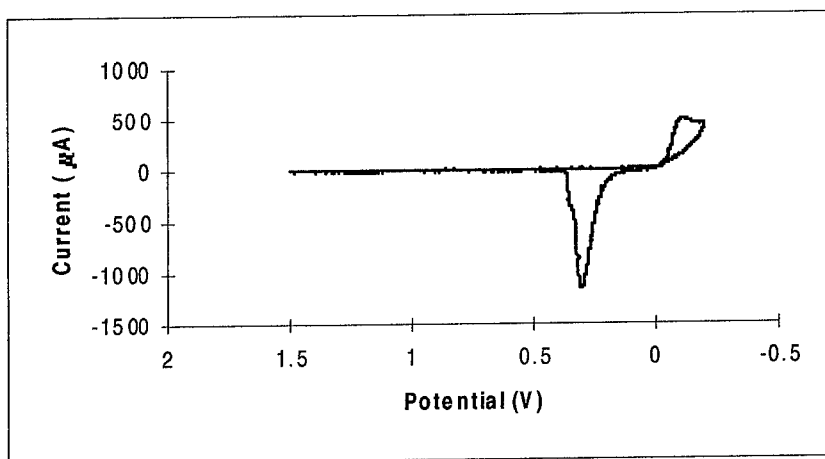


Fig. 3 Staircase cyclic voltammogram of first peak from aluminum and chromium electrodeposited out of a $N=0.52$ room temperature EMIC- AlCl_3 molten salt using an aluminum wire in $N=0.60$ EMIC- AlCl_3 as a reference electrode.

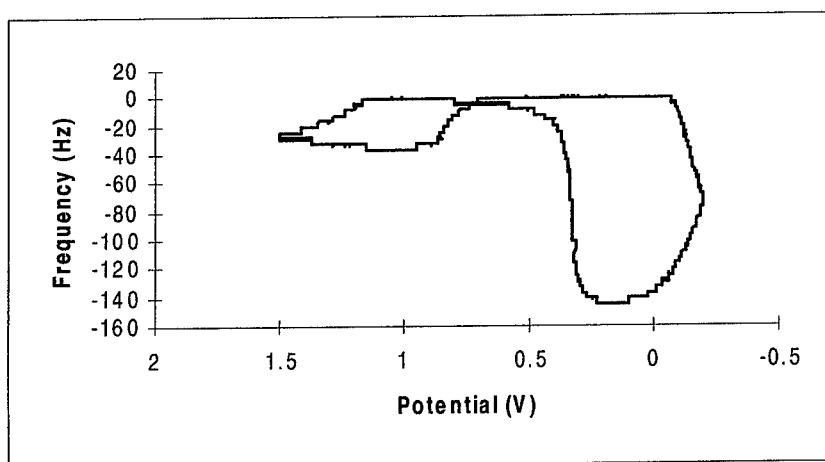


Fig. 4 The accompanying frequency data of aluminum and chromium electrodeposited during the EQCM experiment depicted in figure 3.

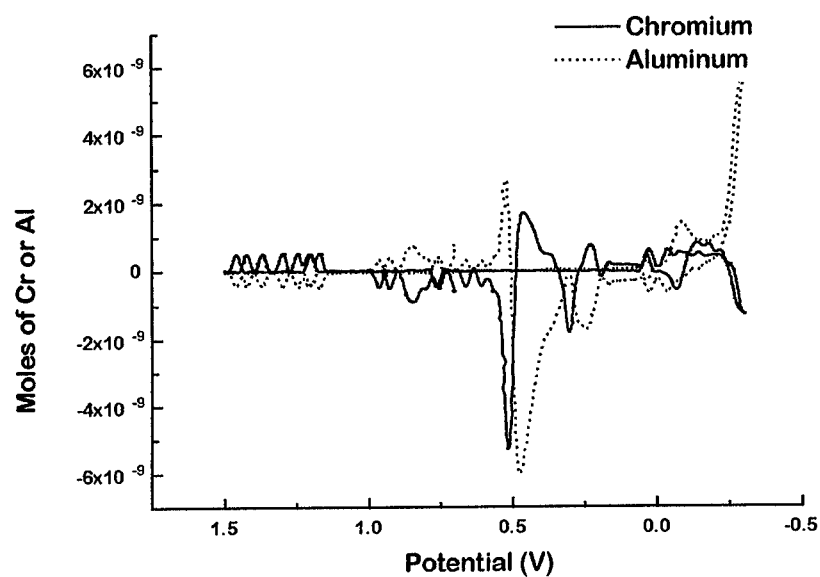


Fig 5 The modeled frequency and charge data for chromium and aluminum. Depicted are curves for the moles of aluminum or chromium present during the electrochemical events.

EQCM Measurements of Cobalt-Aluminum Alloys

H. C. De Long

Air Force Office of Scientific Research
Bolling AFB DC 20332

R. T. Carlin

Covalent Associates
Woburn, MA

ABSTRACT

Electrochemical quartz crystal microbalance (EQCM) measurements were made *in situ* on cobalt-aluminum alloy deposition and stripping in room-temperature molten salts. The room-temperature molten salt was AlCl_3 -rich (acidic) AlCl_3 :EMIC (EMIC = 1-ethyl-3-methylimidazolium chloride). In these melt systems, the cobalt-aluminum alloys are electrodeposited between the two metal redox couples of cobalt and aluminum. Cobalt metal is deposited at potentials positive of + 0.4 V, while the CoAl_x alloys are produced at potentials negative of +0.4. The value of x in CoAl_x gradually increases up to a value of 2 as the electrodeposition potential ($E_{\text{deposition}}$) decreases; however, plots of x vs. $E_{\text{deposition}}$ exhibit sloping plateaus and indicate preferential formation of alloys having integral compositions of CoAl_1 and CoAl_2 . The formation of these alloys can be interpreted as a UPD-based process or as a free energy of alloy formation. Upon oxidation of the alloys, EQCM data indicates that aluminum is stripped out of the alloy matrix separately from the cobalt.

INTRODUCTION

The room-temperature AlCl_3 :EMIC molten salts (EMIC = 1-ethyl-3-methylimidazolium chloride) have proven to be useful solvents for electrochemical and chemical investigations.^{1,2} Most importantly, aluminum can be reversible electrodeposited from acidic melt compositions (AlCl_3 :EMIC molar ratio > 1).³⁻⁹ The molten salts are excellent solvents for both ionic and molecular species; thus, a great many transition metal salts are soluble in the acidic melts. The room-temperature molten salts are also excellent electrochemical solvents: they possess a wide electrochemical window; they are purely ionic, so they have high intrinsic conductivities (*ca.* $10^{-2} \text{ ohm}^{-1} \text{ cm}^{-1}$); and they are liquid and thermally stable over a very wide temperature range (-60 to 250°C). Unlike conventional electroplating baths, the AlCl_3 :EMIC molten salts have very low dielectric constants. This fact, coupled with their low operating temperature, appears to promote

preferential orientation of electrochemical deposits, thus making possible epitaxial growth of metals and alloys.¹⁰

We have demonstrated that EQCM experiments can be effectively performed in these AlCl_3 :EMIC molten salts by examining the electrodeposition of aluminum onto a gold EQCM electrode.¹¹ The viscosity of the molten salt is comparable to that of ethylene glycol, but does not dampen the frequency change of the rigid layer. By examining the underpotential deposition (UPD) of aluminum on gold/chromium coated quartz crystals, it was possible to get monolayer measurements in this viscous medium which agreed with the expected frequency change for an Al monolayer. Further tests with UPD of PbCl_2 confirmed the applicability of EQCM in these melt electrolytes.

Earlier, we reported the UPD-induced electrodeposition of Co-Al alloys in the AlCl_3 :EMIC room-temperature molten salts.^{11,12} In these studies, we used microelectrodes and energy dispersive spectroscopy (EDS) to analyze the composition of these alloys.¹² We discussed the electrodeposition behavior (*e.g.*, nucleation mechanism) of Co-Al alloys at platinum macroelectrodes and the role of UPD (both Co-on-Pt and Al-on-Co) in the overall deposition process.¹⁰ We also presented EDS analyses of the Co-Al electrodeposits and scanning electron microscopy (SEM) images of alloy thin films, showing unusual surface morphologies.

In this paper, we employ an electrochemical quartz crystal microbalance to investigate the mass changes occurring during film formation and growth during electrodeposition and the selective dealloying of these materials during anodization.

EXPERIMENTAL

Purification of AlCl_3 :EMIC melt components has been previously described.^{13,14} Protonic impurities were removed by vacuum treatment at 1×10^{-5} Torr for several days.^{15,16} The analyte melt used in this investigation had a AlCl_3 :EMIC molar ratio of $N = 0.55$ (N = mole fraction of AlCl_3) and contained 70 mM Co(II) added as anhydrous CoCl_2 . Polycrystalline gold disk electrodes were made by vapor deposition of approx. 2000 Å of gold onto approximately 50 Å of chromium. The support material was AT-cut 5 MHz Quartz crystals, which were highly polished and 1.0 inch in diameter. The electrochemically active area was 0.34 cm^2 and the piezoelectric active area was 0.28 cm^2 . The counter electrode was a platinum coil, and the reference electrode consisted of aluminum wire immersed in $N = 0.60$ AlCl_3 :EMIC melt contained in separate fritted or Vycor glass compartments.

All experiments were performed in glass-constructed cells sealed under a UHP Helium atmosphere in a Vacuum Atmospheres dry box at room temperature. Cyclic voltammetry was performed with an Intertech Systems HB-111 Analog Function Generator and a PS151 Potentiostat / Galvanostat controlled by the Asyst 4.01 software

environment using a GTSI 486DX/33MHz computer. Data acquisition was performed with a Data Translation DT-2801A D/A board and a DT-707 screw board. The oscillator circuit was a 5 MHz crystal operating in the normal mode.¹⁷

RESULTS AND DISCUSSION

Cyclic voltammetry for cobalt, aluminum, and its alloys in a $N = 0.55$ AlCl_3 :EMIC melt is represented in Fig. 1. Data are plotted with reduction proceeding to the left. Starting from the right side of the voltammogram and scanning to less positive potentials, one sees an initial peak at +0.5 V corresponding to the electrodeposition of Co metal, a plateau at +0.3 V due to formation of a 1:1 Co-Al alloy, a plateau at +0.1 V corresponding to a 1:2 Co-Al alloy, and finally the electrodeposition of bulk aluminum at -0.1 V. The presence of the two preferred alloys compositions CoAl_1 and CoAl_2 has been verified by SEM-EDS and microelectrode work,^{10,12} although all compositions from CoAl_x with $x = 0$ to 2 are accessible. This earlier work led to the use of EQCM to obtain further data on the electrodeposition and oxidative stripping of these unusual alloys.

The acidic chloroaluminate room-temperature molten salts have a viscosity of approximately 15-20 centipoise which is about the same as ethylene glycol. This tends to slow the EQCM response time and necessitates the use of slower scan rates. From the weight changes and a knowledge of the material electrodeposited the frequency data from the EQCM can be converted to a current response dataset. This calculated dataset should agree with the current response data taken from the cyclic voltammetry experiments. Deviations from a perfect match in the data often indicates the uptake of solvent or a mixed transport phenomenon. To eliminate the possibility of mixed transport, limitation of transportable species is achieved and the number of different redox events are limited. In the case of molten salts, it is possible to get solvent entrapment on roughened surfaces by occlusion.

Upon obtaining simultaneous current and frequency data as a function of potential, standard EQCM analysis provides the total weight change as a function of potential. To differentiate the weight changes assigned independently to Co and to Al during electrodeposition and stripping, it is necessary to combine the changes in total weight (ΔW_{total}) and the changes in the total charge (ΔQ_{total}) according to the formulations below.

Assuming assuming total weight and charge are from Co and Al deposition and stripping only, then Eqns. 1 and 2 are valid.

$$\Delta W_{\text{Total}} = \Delta W_{\text{Co}} + \Delta W_{\text{Al}} \quad [1]$$

$$\Delta Q_{\text{total}} = \Delta Q_{\text{Co}} + \Delta Q_{\text{Al}} \quad [2]$$

Using the constants $K_1 = (3 \cdot F)(\text{Atomic Mass Al})^{-1}$ and $K_2 = (2 \cdot F)(\text{Atomic Mass Co})^{-1}$ to convert charge to weight, Eq. 2 is substituted into Eq. 1 to give Eq. 3.

$$\Delta W_{\text{Co}} = (\Delta Q_{\text{Total}} - K_1 \cdot \Delta W_{\text{Total}}) / (K_2 - K_1) \quad [3]$$

Then, ΔW_{Co} is substituted back into Eq. 1 to calculate ΔW_{Al} . Finally both weight changes are converted to micromoles and plotted (see Figure 2) against potential to determine the selective material gain or loss during deposition or stripping, respectively, of the metals and alloys.

In Fig. 2, both Co and Al are seen to deposit in the alloy forming region during the negative potential sweep; however, the deposition peaks are not clearly defined, and so the cathodic currents are not discussed in this study. On the other hand, the oxidation currents display well resolved stripping peaks for both Al and Co, which are used to examine the selective dealloying processes during alloy oxidation. From the pronounced stripping peaks of only Al at +0.2 and +0.5 V, it appears that Al is selectively stripped from the alloys before Co. Cobalt oxidation appears to take place in two steps at +0.6 and +0.95 V -- potentials positive of the Co metal reduction potential. Importantly, Al deposits before its reduction potential to form an alloy with Co via a UPD mechanism, and it strips from the alloy first. The formation of Co-Al alloys in this system is supported by EDS¹⁰ results that do not show any discrete islands of individual metal forming on the surface.

Finally, Fig. 2 also shows that only Al is depositing in the Al bulk deposition region. This serves as a test of the model used to derive Eq. 3, because only a large micromolar change in Al should be seen in the bulk Al deposition region.

SUMMARY

From this EQCM study the following conclusions can be made:

1. The composition of the Co-Al alloy can be changed dramatically by adjusting the plating potential. This results in a range of CoAl_x alloys where x is predominantly 1 or 2.
2. Aluminum can be selectively stripped out of the CoAl_x structure (dealloying), leaving behind a cobalt superlattice. The remaining Co can then be stripped from the surface at potentials positive of the Co reduction potential.
3. At more negative potentials, it is possible to plate bulk Al on top of the predeposited alloy underlayer.

ACKNOWLEDGEMENTS

The authors would like to thank the Air Force Office of Scientific Research, Bolling AFB DC, for funding this work.

REFERENCES

1. C. L. Hussey, In *Chemistry of Nonaqueous Solvents*, A. Popov and G. Mamantov, Editors, Chapter 4, VCH Publishers, New York (1994).
2. R. T. Carlin and J. S. Wilkes, in *Chemistry of Nonaqueous Solvents*, A. Popov and G. Mamantov, Editors, Chapter 5, VCH Publishers, New York (1994).
3. H. L. Chum and R. A. Osteryoung, in *Ionic Liquids*, D. Inman, and D. G. Lovering, Editors, p. 407, Plenum, New York (1981).
4. R. J. Gale and R. A. Osteryoung, in *Molten Salt Techniques*, D. G. Lovering, and R. J. Gale, Editors, p. 55, Plenum, New York (1983).
5. C. L. Hussey, *Adv. Molten Salt Chem.*, **5**, 185 (1983).
6. R. A. Osteryoung, in *Molten Salt Chemistry*, G. Mamantov, and R. Marassi, Editors, p. 329, D. Reidel Publishing, New York (1987).
7. J. S. Wilkes, in *Molten Salt Chemistry*, G. Mamantov, and R. Marassi, Editors, p. 217, D. Reidel Publishing, New York (1987).
8. C. L. Hussey, *Pure Appl. Chem.*, **60**, 1763 (1988).
9. G. Mamantov, C. L. Hussey, and R. Marassi, in *Techniques for Characterization of Electrodes and Electrochemical Processes*, R. Varma, and J. R. Selman, Editors, p. 471, Wiley, New York (1991).
10. R. T. Carlin, P. C. Trulove, and H. C. De Long, *J. Electrochem. Soc.* **143**, (1996) in press.
11. H. C. De Long and R. T. Carlin, Abs. 647, p. 974, The Electrochemical Society Extended Abstracts, Reno, NV, May 21-26, 1995.
12. R. T. Carlin, H. C. De Long, and P. C. Trulove, Abs. 652, p. 981, The Electrochemical Society Extended Abstracts, Reno, NV, May 21-26, 1995.
13. T. J. Melton, J. Joyce, J. T. Maloy, J. A. Boon, J. S. Wilkes, *J. Electrochem. Soc.* **137**, 3865 (1990).
14. J. S. Wilkes, J. A. Levisky, R. A. Wilson, C. L. Hussey, *Inorg. Chem.* **21**, 1263 (1982).
15. T. A. Zawodzinski, Jr., R. T. Carlin, and R. A. Osteryoung, *Anal. Chem.*, **59**, 2639 (1987).
16. M. A. M. Noel, P. C. Trulove, and R. A. Osteryoung, *ibid.*, **63**, 2892 (1991).
17. Oscillator circuit diagram from D. A. Buttry, University of Wyoming.

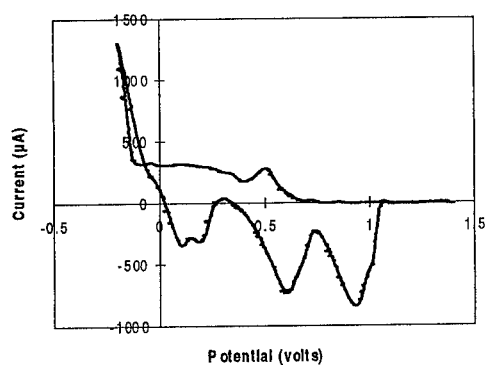


Figure 1. Cyclic voltammogram at 0.34-cm^2 Au EQCM electrode in $N = 0.55$ AlCl_3 :EMIC containing 70 mM Co(II) .

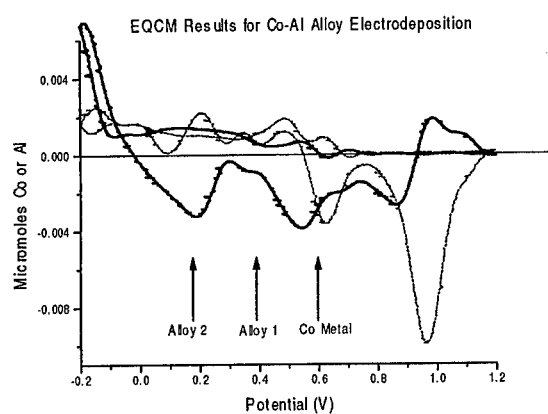


Figure 2. Plot of ΔW_{Co} (dotted line) and ΔW_{Al} (solid line) in micromoles versus potential. Arrows indicate the approximate potentials where the electrodeposition of Co metal, CoAl_1 (alloy 1), and CoAl_2 (alloy 2) begin.

ELECTRODEPOSITION AND NUCLEATION OF LEAD FROM CHLORIDE MELTS

T. Støre, G. M. Haarberg, T. E. Jentoftsen and R. Tunold

Norwegian University of Science and Technology
Department of Electrochemistry
N-7034 Trondheim, NORWAY

The electrodeposition of lead from molten KCl-LiCl eutectic at 400°C has been studied by cyclic voltammetry and chronoamperometry. The nucleation was shown to be progressive with diffusion controlled growth of nuclei. No nucleation overpotential was observed. The saturation number density of nuclei, calculated from potentiostatic current transients, was of the order of 10^6 nuclei per cm^2 for overpotentials between -15 and -25 mV. The reduction of Pb^{2+} was found to be a reversible process. From cyclic voltammetry, the diffusion coefficient was calculated to $D = 1.5 \cdot 10^{-5} \text{ cm}^2/\text{s}$. This was in poor agreement with the value obtained by analysing the current transients according to a theoretical nucleation model.

INTRODUCTION

The electrochemistry of PbCl_2 in molten chlorides has been studied by a number of authors (1-5). None of these has been concerned about electrochemical nucleation. However, Hussey and Xu (6) have carried out such studies in a mixture of AlCl_3 and 1-methyl-3-ethylimidazolium chloride at 40°C. At this temperature the lead forms a solid deposit. They found that the electrodeposition of lead on glassy carbon exhibited progressive three-dimensional nucleation with diffusion controlled growth.

Gunawardena et al. (7) have developed a nucleation model which is very useful for determining nuclear number densities. It considers three-dimensional growth of nuclei under diffusion control. Each of the randomly distributed nuclei is surrounded by a growing hemispherical diffusion zone. The key assumption is that no new nuclei will appear inside the zones. Since the diffusion zones grow with time, they will eventually overlap, and the only source of material will then be by linear diffusion perpendicularly to the electrode. Consequently, the nucleation process becomes arrested and the nuclear

number density approaches a final limiting value. A summary of the model will be outlined in the following.

For an instantaneous nucleation process, the current density is given by

$$i = \frac{zFD^{1/2}c^\infty}{\pi^{1/2}t^{1/2}} [1 - \exp(-N\pi k_i Dt)] \quad [1]$$

where

$$k_i = (8\pi c^\infty M/\rho)^{1/2} \quad [2]$$

D and c^∞ are the diffusion coefficient (cm^2/s) and bulk concentration (mol/cm^3) of the depositing species, respectively. M and ρ are the molecular weight (g/mol) and density (g/cm^3) of the deposit. N is the number density of nuclei (cm^{-2}), and the other symbols have their usual meaning.

The corresponding expressions for progressive nucleation are

$$i = \frac{zFD^{1/2}c^\infty}{\pi^{1/2}t^{1/2}} [1 - \exp(-AN_\infty\pi k_p Dt^2/2)] \quad [3]$$

and

$$k_p = \frac{4}{3} (8\pi c^\infty M/\rho)^{1/2} \quad [4]$$

where A is the steady state nucleation rate per site (s^{-1}) and N_∞ is the number density of available sites (cm^{-2}).

The transients [1] and [3] pass through a maximum, i_m , at a certain time, t_m . Equating the time derivatives of these expressions to zero gives

instantaneous nucleation

$$t_m = \frac{1.2564}{N\pi k_i D} \quad [5]$$

$$i_m = 0.6382zFc^\infty (k_i N)^{1/2} \quad [6]$$

progressive nucleation

$$t_m = \left\{ \frac{4.6733}{AN_\infty \pi k_p D} \right\}^{1/2} \quad [7]$$

$$i_m = 0.4615 z F D^{3/4} c^\infty (k_p AN_\infty)^{1/4} \quad [8]$$

Both mechanisms predict that the product $i_m^2 t_m$ should be constant:

instantaneous $i_m^2 t_m = 0.1629 (z F c^\infty)^2 D \quad [9]$

progressive $i_m^2 t_m = 0.2598 (z F c^\infty)^2 D \quad [10]$

In principle, these expressions could be used to identify the nucleation mechanism in a particular experiment. This, however, would require a rather accurate value for the diffusion coefficient. Scharifker and Hills (8) have suggested a better method in which the experimental current transients are presented in non-dimensional form and compared with the following theoretical expressions:

instantaneous $\frac{i^2}{i_m^2} = \frac{1.9542}{t/t_m} \left\{ 1 - \exp \left[-1.2564 (t/t_m) \right] \right\}^2 \quad [11]$

progressive $\frac{i^2}{i_m^2} = \frac{1.2254}{t/t_m} \left\{ 1 - \exp \left[-2.3367 (t/t_m)^2 \right] \right\}^2 \quad [12]$

One further point should be mentioned. Normally, the number density of nuclei in progressive nucleation is expected to approach the total number of available sites, N_∞ , at long times. This, however, is not the case for a diffusion controlled process. Gunawardena et al. (7) have shown that because of the growth of the diffusion zones, the number density reaches a limiting value, the so-called saturation number density, given by

$$N_{sat} = (AN_\infty / 2k_p D)^{1/2} \quad [13]$$

EXPERIMENTAL

All chemicals were of analytic grade. KCl and LiCl were dried under vacuum at 500°C for about 6 hours, while PbCl₂ was vacuum-distilled. A eutectic mixture of KCl and LiCl was used as solvent with a PbCl₂ concentration of 0.030 M (about 0.1 mol%). The molten electrolyte was contained in a glassy carbon crucible (Le Carbone-Lorraine, V25) placed inside a quartz tube.

The working electrode was a 3 mm diameter glassy carbon rod (Tokai, GC-20S) sealed with pyrex, giving an active electrode area of 0.071 cm². A pool of liquid lead inside an open quartz tube served as reference, and a graphite rod (Ultra Carbon) was used as counter electrode. The experimental cell was assembled in a dry-box before being transferred to the furnace. During the experiments, the temperature was kept constant at 400°C, and the cell was purged with argon to prevent any oxygen or moisture to enter.

Electrochemical measurements were performed with a Radiometer VoltaLab 32 potentiostat with integrated software. Linear sweep voltammetry and potential step chronoamperometry were used to study the lead deposition process.

RESULTS AND DISCUSSION

A cyclic voltammogram of lead at a glassy carbon electrode is shown in figure 1. When the potential is swept in the negative direction, a reduction wave with $E_p = -61$ mV is observed. The steep leading edge of this peak indicates that the reduced species forms an insoluble deposit on the electrode. The sharp 'stripping peak' on the reverse scan confirms this. Between the lead deposition and the chlorine evolution starting at about +1.5 V, practically no current is observed.

To study the cathodic process closer, the potential was swept at a rate of only 1 mV/s. In figure 2, lead deposition starts at -19 mV, while the curve crosses the potential axis at -23 mV on the reverse scan. These exact values were easily reproduced. There was no sign of a 'cross-over' on the reverse scan, which would have indicated that the process involves a nucleation overpotential. No explicit value for the nucleation overpotential is reported by Hussey and Xu (6), but from a 50 mV/s cyclic voltammogram, it can be estimated to something like 60 mV. This is not very surprising if one considers the difference in the two processes. Deposition of a metal below its melting point includes a lattice incorporation step which is probably responsible for most of the nucleation overpotential.

As seen from figure 3, the cathodic peak current was found to be a linear function of the square root of sweep rate, with intercept at the origin. The process therefore behaves reversibly for sweep rates up to 500 mV/s. The diffusion coefficient of Pb^{2+} -ions can be evaluated using the following equation (9):

$$i_p = 0.610 \frac{(zF)^{3/2}}{(RT)^{1/2}} c^\infty D^{1/2} v^{1/2} \quad [14]$$

i_p is the cathodic peak current density (A/cm^2) and v is the sweep rate (V/s). From the slope in figure 2 one obtains $D = 1.5 \cdot 10^{-5} \text{ cm}^2/\text{s}$. This is in reasonable agreement with an empirical equation for the temperature dependence of D reported by Yurinskii and Makarov (4), which gives a value of $1.3 \cdot 10^{-5} \text{ cm}^2/\text{s}$.

Chronoamperometry is probably the best method for studying nucleation processes quantitatively. A constant potential was applied to the electrode for 50 s, and the current was recorded as a function of time. Figure 4 shows a family of such current transients. The initial part of each transient, which represents double layer charging, is not shown in the figure. After a certain potential dependent time delay, the current reaches a minimum value. The following rising part of the curves is due to an increase in the electro-active area, as a result of the birth and growth of nuclei. With potentials less cathodic than -20 mV, no current maxima were observed within the 50 s timescale, while the maxima occurred before 0.5 s when potentials more cathodic than -36 mV were applied. It is interesting to notice the relatively large shift of the current maxima on the time axis resulting from a decrease in the electrode potential of only a few millivolts. In similar experiments in aqueous solution, it is often necessary to apply several tens of millivolts to achieve the same effect.

The classical way to treat nucleation processes is to plot $\log i$ against $\log t$. This is supposed to give a linear relation at short times, with a slope from which the nucleation mechanism can be deduced. An attempt to do so is shown in figure 5. The only linear portion of these S-shaped curves seems to be in the middle section. Moreover, the slope increases steadily from 0.68 to 2.14 as the potential becomes more cathodic. Obviously, no conclusions regarding the nucleation mechanism can be drawn.

Consequently, the transients were plotted in non-dimensional form as described in the introduction. Two such curves are shown in figure 6. Note that the non-dimensional plots only represent the transients after the current minimum. This minimum is redefined as the origin to which all following time and current values are referred. This is necessary for comparing experimental data with theory, since the model does not account for neither double layer charging nor any delay in the nucleation process.

The experimental data show a remarkable agreement with the theoretical curve for progressive nucleation, especially in the rising part. The irregularity beyond the maximum in figure 6a is attributed to the effect of natural convection, which becomes important at long times. The timescale of the transients in figure 6a and b is 10 s and 2 s, respectively. All transients showed proof of progressive nucleation in a similar manner.

These non-dimensional plots are only a qualitative tool for deciding whether the nucleation is spontaneous or progressive. Once this has been established, the maximum values, t_m and i_m , are used in a quantitative treatment of the process. Table I contains these values for each applied potential.

Table I. Analysis of current transients for calculation of nuclear number densities.

E [mV]	t_m [s]	$10^3 i_m$ [A/cm ²]	$10^6 i_m^2 t_m$ [A ² cm ⁻⁴ s]	$10^{-6} AN_\infty$ [s ⁻¹ cm ⁻²]	$10^6 D$ [cm ² /s]	$10^{-6} N_{int}$ [cm ⁻²]
-20	38.8	0.209	1.70	0.0314	0.195	0.706
-21	26.3	0.258	1.74	0.0666	0.200	1.01
-22	17.5	0.412	2.97	0.0879	0.341	0.892
-23	11.8	0.556	3.64	0.159	0.418	1.09
-24	8.90	0.682	4.14	0.244	0.476	1.26
-25	5.24	1.01	5.36	0.544	0.616	1.65
-26	3.62	1.32	6.30	0.968	0.724	2.03
-27	2.66	1.66	7.33	1.54	0.842	2.38
-28	2.03	2.09	8.83	2.20	1.01	2.59
-29	1.46	2.33	7.93	4.73	0.911	4.00
-30	1.22	2.55	7.87	6.88	0.904	4.85
-31	1.05	3.09	9.99	7.33	1.15	4.44
-32	0.875	3.32	9.67	10.8	1.11	5.48
-33	0.808	3.17	8.14	15.1	0.935	7.05
-34	0.602	4.57	12.6	17.6	1.44	6.14
-35	0.556	5.02	14.0	18.4	1.61	5.94
-36	0.500	6.03	18.2	17.6	2.09	5.10
-37	0.484	5.70	15.7	21.7	1.81	6.08
-39	0.394	6.72	17.8	29.0	2.04	6.62

It is not possible to determine the nucleation rate explicitly, only the product AN_∞ . Gunawardena et al. (7) state that this could be accomplished using either of equations [7] or [8]. Since an accurate value of the diffusion coefficient is not always available in advance, it is better to eliminate D by combining these two equations. This results in the following expression:

$$AN_{\infty} = \frac{0.3864(zFc^{\infty})^2}{i_m^2 t_m^3 k_p} \quad [15]$$

When AN_{∞} is determined, D can be evaluated from [7] or [8]. These values are inserted in [13] for calculation of the saturation number density, N_{sat} .

According to equation [10], the product $i_m^2 t_m$ is supposed to be independent of potential. As can be seen from table I, this is far from being true. Instead, there is a one order of magnitude increase down the column. Furthermore, the calculated diffusion coefficient shows the same trend, as well as being unreasonably low. One could ask what is wrong here, and the answer is very simple.

In general, the current density at an electrode is proportional to the gradient $(c^{\infty} - c^{\sigma})$, where c^{∞} and c^{σ} are the bulk and surface concentrations of the reactant, respectively. However, the model is based on total diffusion control, and c^{σ} is therefore neglected in equation [3] and all other current density expressions. This assumption is valid for sufficiently large overpotentials. When the electron transfer is fast, the surface concentration of the reactant is given by the Nernst equation, from which the following expression is obtained:

$$c^{\sigma} = c^{\infty} \left\{ \exp\left(\frac{zF\eta}{RT}\right) \right\} \quad [16]$$

Table II contains calculated surface concentrations. Even at the highest overpotential, c^{σ} is more than 40% of the bulk concentration. This fact obviously has to be corrected for. Use of equation [16] requires a knowledge of the reversible potential. No steady state measurements were carried out in this work, but earlier experiments with single $PbCl_2$ gave a reversible potential of -14 mV against the same reference electrode. As it turned out, this value gave the most consistent result. From a re-examination of the voltammogram in figure 2, it follows that the nucleation overpotential is at most 5 mV.

Replacement of c^{∞} with $(c^{\infty} - c^{\sigma})$ in the current density expressions corresponds to multiplication by $(1 - c^{\sigma}/c^{\infty})$. It is then expected that the quantity $i_m^2 t_m / (1 - c^{\sigma}/c^{\infty})^2$ should be independent of potential. Table II shows that this is indeed the case. According to equation [15], AN_{∞} should be corrected in the same fashion.

As before, the diffusion coefficient is found by inserting AN_{∞} in equation [7]. There is some variation in the calculated values in table II, but no general trend is observed. An

estimate of the diffusion coefficient is obtained by using the average $D_{avg} = 5.8 \cdot 10^{-6} \text{ cm}^2/\text{s}$. This value seems too low, being only 39% of that calculated from cyclic voltammetry. On the other hand, the latter method is probably not very reliable when electrochemical nucleation is involved. Hills et al. (10) studied the electrodeposition of Ag on a Pt electrode from molten $\text{KNO}_3\text{-NaNO}_3$. The diffusion coefficient of Ag^+ was determined with three different methods. The value calculated from chronopotentiometry was only 40% of that from cyclic voltammetry, and the authors claimed that the former method gave the most reliable result.

To our knowledge, there is no well established method for calculation of D that takes into account the increase in electro-active area which accompanies nucleation processes. The variation of the data in table II indicates that D cannot be determined from one single potentiostatic current transient. Although the average value may be a better estimate of the true diffusion coefficient than the one obtained from cyclic voltammetry, other methods, such as chronopotentiometry, probably give more reliable results.

Table II. Analysis of current transients, with the correction that $c^0 \neq 0$ at lower overpotentials.

η [mV]	t_m [s]	$10^3 i_m$ [A/cm ²]	c^0/c^∞	$10^6 i_m^2 t_m / (1 - c^0/c^\infty)^2$ [A ² cm ⁴ s]	$10^{-6} A N_\infty$ [s ⁻¹ cm ⁻²]	$10^6 D$ [cm ² /s]	$10^{-6} N_{sat}$ [cm ⁻²]
-6	38.8	0.209	0.813	48.5	0.00110	5.57	0.0247
-7	26.3	0.258	0.786	37.9	0.00306	4.35	0.0466
-8	17.5	0.412	0.759	51.1	0.00511	5.87	0.0519
-9	11.8	0.556	0.733	51.1	0.0113	5.87	0.0773
-10	8.90	0.682	0.708	48.7	0.0207	5.59	0.107
-11	5.24	1.01	0.684	53.8	0.0542	6.18	0.165
-12	3.62	1.32	0.661	54.9	0.111	6.31	0.233
-13	2.66	1.66	0.639	56.2	0.201	6.45	0.310
-14	2.03	2.09	0.617	60.2	0.322	6.92	0.379
-15	1.46	2.33	0.596	48.6	0.771	5.59	0.653
-16	1.22	2.55	0.576	43.8	1.24	5.03	0.872
-17	1.05	3.09	0.556	50.8	1.44	5.83	0.874
-18	0.875	3.32	0.538	45.2	2.31	5.19	1.17
-19	0.808	3.17	0.519	35.2	3.48	4.04	1.63
-20	0.602	4.57	0.502	50.6	4.37	5.81	1.52
-21	0.556	5.02	0.485	52.8	4.89	6.07	1.58
-22	0.500	6.02	0.468	64.3	4.98	7.38	1.44
-23	0.484	5.70	0.452	52.5	6.50	6.03	1.82
-25	0.394	6.72	0.422	53.3	9.67	6.12	2.21

The saturation number density of nuclei increases by two orders of magnitude with a 20 mV increase in overpotential. With η between -15 and -25 mV, N_{sat} is of the order of 10^6 cm^{-2} . It is interesting to compare these results with a similar process in aqueous solution.

Gunawardena et al. (7) studied the electrochemical nucleation of Hg on carbon from a 0.05 M $\text{Hg}_2(\text{NO}_3)_2$ solution. They found that it was necessary to apply an overpotential of -260 mV for N_{sat} to exceed 10^6 cm^{-2} .

CONCLUSION

The model developed by Gunawardena et al. (7) has been used to study the electrodeposition of lead on glassy carbon. It was necessary to take into account the nonzero surface concentration of Pb^{2+} at lower overpotentials.

The nucleation was shown to be progressive with diffusion controlled growth of nuclei. Liquid Pb nucleates easily on glassy carbon, as no nucleation overpotential was observed. Moreover, the current maximum appeared before 0.5 s with an overpotential of only -23 mV. The saturation number density of nuclei was of the order of 10^6 cm^{-2} with η between -15 and -25 mV.

The diffusion coefficient calculated from an analysis of the nucleation process was not consistent with the value obtained from cyclic voltammetry. While the former method suffers somewhat from lack of reproducibility, the latter does not take into account the effects of nucleation at all.

REFERENCES

1. R. B. Stein, J. Electrochem. Soc., **106**, 528 (1959).
2. S. Sternberg, T. Visan, N. Bonciocat and A. Cotarta, Rev. Roum. Chim., **32**, 883 (1987).
3. M. E. Lima and J. Bouteillon, J. Appl. Electrochem., **21**, 824 (1991).
4. V. P. Yurinskii and D. V. Makarov, Russ. J. Appl. Chem., **67**, 1132 (1994).
5. G. M. Haarberg, T. Støre, B. Børresen and R. Tunold, in Molten Salts/1994, C. L. Hussey, D. S. Newman, G. Mamantov and Y. Ito, Editors, **PV 94-13**, p. 463, The Electrochemical Society Proceedings Series, Pennington, NJ (1994).
6. C. L. Hussey and Xiaohong Xu, J. Electrochem. Soc., **138**, 1886 (1991).

7. G. Gunawardena, G. Hills, I. Montenegro and B. Scharifker, *J. Electroanal. Chem.*, **138**, 225 (1982).
8. B. Scharifker and G. Hills, *Electrochim. Acta*, **28**, 879 (1983).
9. T. Berzins and P. Delahay, *J. Am. Chem. Soc.*, **75**, 555 (1953).
10. G. J. Hills, D. J. Schiffrin and J. Thompson, *Electrochim. Acta*, **19**, 657 (1974).

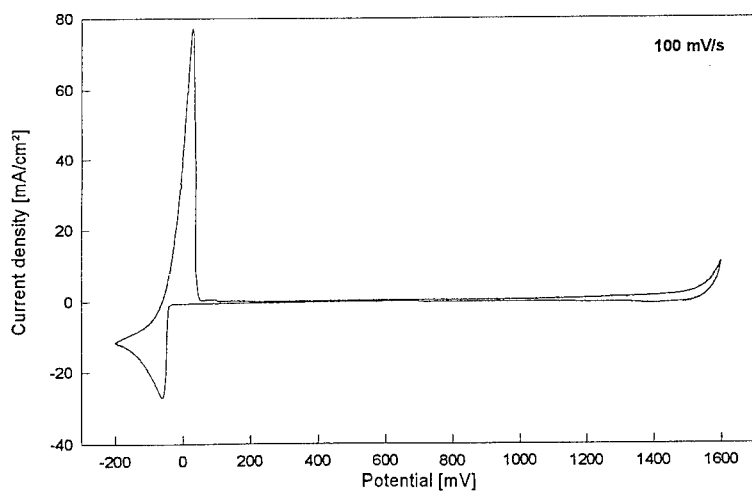


Figure 1. Cyclic voltammogram for 0.030 M PbCl_2 in KCl-LiCl eutectic at a glassy carbon electrode. All potentials are referred to the lead reference electrode. $T = 400^\circ\text{C}$. Sweep rate 100 mV/s.

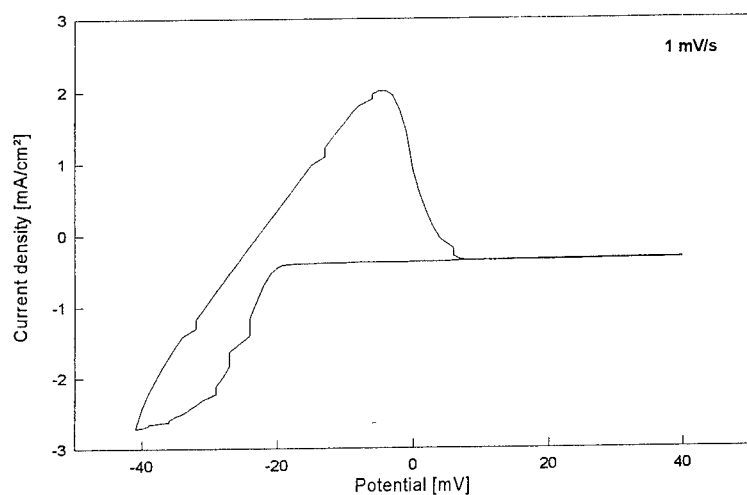


Figure 2. As figure 1, but with sweep rate 1 mV/s.

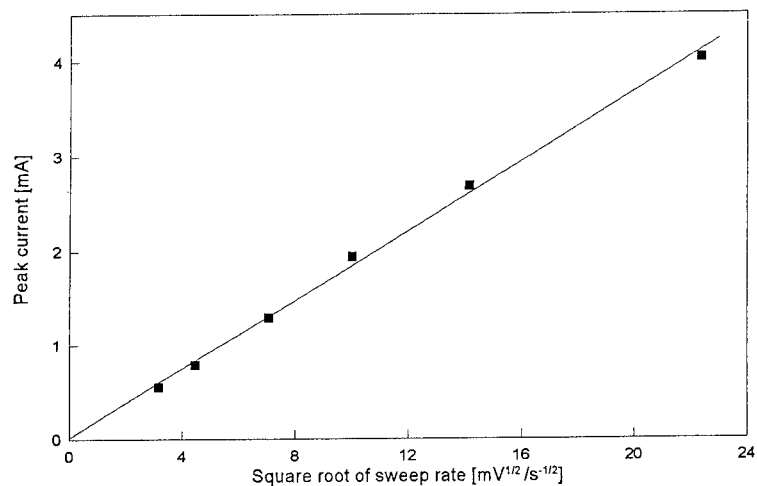


Figure 3. Plot of cathodic peak current against square root of sweep rate. Data from cyclic voltammograms for 0.030 M PbCl_2 in KCl-LiCl eutectic at a glassy carbon electrode. $T = 400^\circ\text{C}$. Electrode area 0.071 cm^2 .

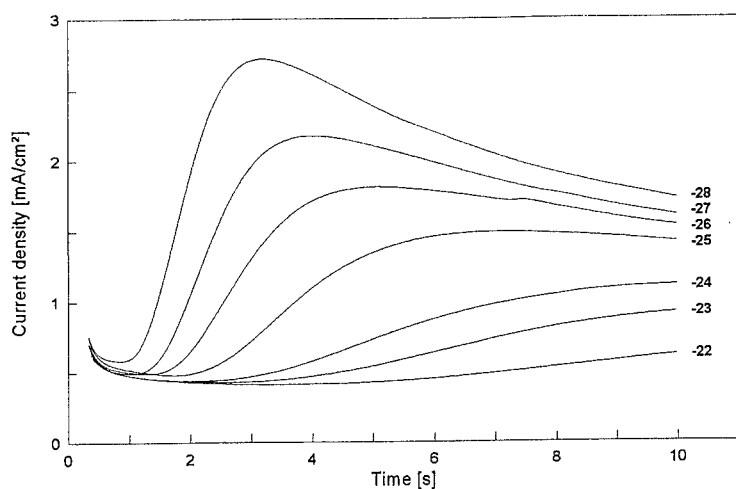


Figure 4. Potentiostatic current transients for 0.030 M PbCl_2 in KCl-LiCl eutectic at a glassy carbon electrode. Applied potentials (mV) are indicated in the figure. $T = 400^\circ\text{C}$.

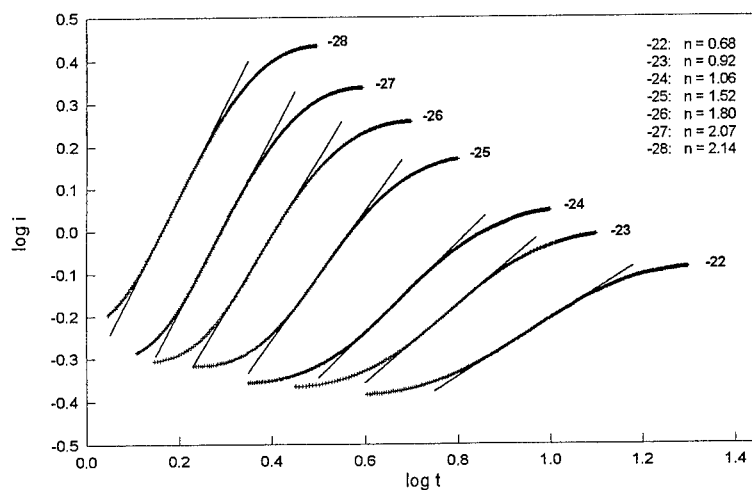


Figure 5. The same transients as in figure 4 plotted as $\log i$ against $\log t$. The numbers in the legend refer to the slope of the linear fits.

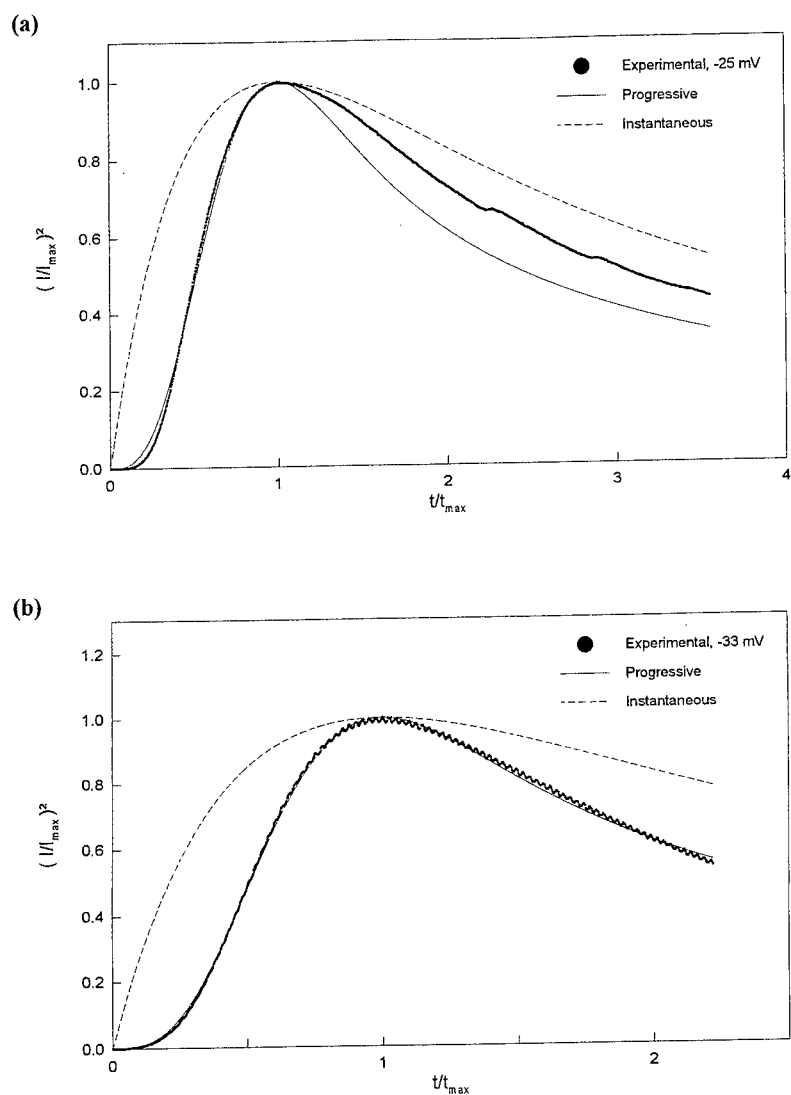


Figure 6. Comparison of experimental non-dimensional current transients with theory for determination of nucleation mechanism. Potential : (a) -25 mV and (b) -33 mV.

HIGH TEMPERATURE ELECTROCHEMICAL SYNTHESIS OF ZIRCONIUM DIBORIDE FROM CHLORO-FLUORIDE MELTS

V.P. Lugovoi*, S.V. Deviatkin**, G. Kaptay**, S.A. Kuznetsov***

* Institute of General and Inorganic Chemistry
Academy of Sciences of Ukraine
Palladin pr. 32-34, Kiev-142, Ukraine

**The University of Miskolc
Department of Physical Chemistry
Miskolc 3515 Hungary

***Institute of Chemistry KSC RAS
Apatity, Russia

Thermodynamic calculation of the possibility of electrochemical synthesis of Zirconium Diboride is performed in chloride, fluoride and oxide melts. Voltammetric measurements have been carried out in the NaCl-KCl-KBF₄-K₂ZrF₆-NaF system. Dense coatings of Zirconium Diboride have been obtained on glassy carbon cathodes by electrolysis with additions of Boron Oxide in order to reduce cathodic passivation.

Metal-like refractory compounds in a form of both coatings and powder can be produced by high-temperature electrochemical synthesis [1]. Diborides of different transition metals have been obtained in this way by different research groups [2-10]. Electrochemical synthesis of Zirconium Diboride was also studied in some detail [2,6-8]. First, Zirconium Diboride was obtained by electrochemical synthesis from oxide-fluoride melts in the temperature interval of 1173-1273 K by Andrieux [2]. However, the interpretation of experimental results given in [2], according to which first a alkali metal is deposited, and then this alkali metal reduces both oxides of Boron and Zirconium, seems to be controversial. The Zirconium Diboride powder has been synthesized by Anthony and Welch [6] from the KBF₄-K₂ZrF₆-B₂O₃ system at 873 K. Dense coatings of Zirconium Diboride on cathodes made of Copper, Nickel and Graphite were obtained by Mellors and Senderoff [7] from NaF-KF-LiF-ZrF₄-B₂O₃ at 1023-1073 K. Powders of Zirconium Diboride were obtained by Gomes et al. [8] from Na₂B₄O₇-NaOH-Na₃AlF₆-NaCl-ZrSiO₄(ZrO₂) system at 1323 K. The electrochemical behavior of the FLINAK-KBF₄-K₂ZrF₆ system at 973 K has been studied by Wendt et al [9]. Authors [9] show, that deposition of Zirconium and Boron from the FLINAK is taking place in one step, with an immediate formation of the diboride.

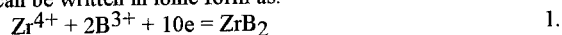
The goal of this work was to study the possibility of and conditions for electrochemical synthesis of Zirconium Diboride from the NaCl-KCl(50-50 %mol.)-KBF₄-K₂ZrF₆

system, as this system has the following technological advantages compared to the systems studied before:

- i. this system is less aggressive compared to FLINAK;
- ii. this system avoids the formation of anodic gases that oxidize the cathodic product, like O₂, CO and CO₂ in the oxide-fluoride melts;
- iii. the system allows one to easily wash out easily the quenched salts from the cathodic product, giving more precise analysis.

Thermodynamic Calculations

The electrochemical synthesis can be written in ionic form as:



The chemical formation of the compound from the elements can be written as:



The criteria for carrying out the electrochemical synthesis of Zirconium Diboride according to reaction 1 in the so called "quasi-equilibrium", or "stable-stoichiometry", way can be derived as [10]:

$$\left| E_{\text{Zr}^{4+}/\text{Zr}} - E_{\text{B}^{3+}/\text{B}} \right| < - \frac{\Delta G_{R2}^{\circ}}{nkF} \quad 3.$$

where $\left| E_{\text{Zr}^{4+}/\text{Zr}} - E_{\text{B}^{3+}/\text{B}} \right|$ is the difference of equilibrium potentials of Zirconium and

Boron ions from the melt at the given temperature and composition;

ΔG_{R2}° is the change of standard Gibbs energy of reaction 2;

n and k are the stoichiometric coefficient and number of transferred electrons in the electrochemical act for the more electronegative component of the compound ($n_{\text{Zr}} = 1$, $k_{\text{Zr}} = 4$, $n_{\text{B}} = 2$, $k_{\text{B}} = 3$);

F is the Faraday constant.

Results of calculation are given in Table 1. Thermodynamic properties of pure phases are taken from handbooks [11, 12].

Table 1. Results of thermodynamic calculations

Salt	T	$E_{\text{Zr}^{4+}/\text{Zr}}$	$E_{\text{B}^{3+}/\text{B}}$	$E_{\text{Zr}^{4+}/\text{Zr}} - E_{\text{B}^{3+}/\text{B}}$	nk	$-\frac{\Delta G_{R2}^{\circ}}{nkF}$	way of synthesis
	K	V	V	V		V	
chloride	973	-1.85	-1.10	0.75	4	0.79	?
fluoride	973	-4.08	-3.55	0.53	4	0.79	"stable"
oxide	1273	-2.11	-1.66	0.45	4	0.75	"stable"

As one can see, comparing columns 5 and 7 of Table 1, the two sides of Eq.3 are practically the same for the chloride melts; therefore, we cannot definitely state whether the synthesis of Zirconium Diboride from chloride melts will go in the "stable stoichiometric", or in the "unstable stoichiometric" way, i.e. if the stoichiometry of the compound will be stable, or will be an undefined function of current density and other variables. For fluoride and oxide melts, however, we can state with confidence, that synthesis of Zirconium Diboride is taking place in the "stable stoichiometric" way, i.e. the stoichiometry of the compound will be stable (1:2) at any value of current density below the limiting current density due diffusion limitations in the melt. Finally we can conclude, that in order to obtain stable stoichiometry compounds from the chloro-fluoride melt, the activity of fluoride ions should be increased. Calculations, as well as further experiments, proved that the addition of 10 w% of NaF in the equimolar NaCl-KCl melt will ensure the synthesis of Zirconium Diboride in the "stable-stoichiometry" way, and also will stabilize KBF_4 in the melt.

Experimental Procedures

Linear voltammetry in the wide range of sweep rates (from 20 mV/s to 10 V/s) was applied at 973 K. Experiments were carried out in an atmosphere of purified Argon against a $\text{Pb/KCl-2\%mol PbCl}_2$ reference electrode. Glassy carbon was used as the crucible, which also served as the counter-electrode. Cylindrical glassy carbon with a surface area of $S = 0.5\text{-}0.7\text{ cm}^2$ was used as the working electrode. Ions of Zirconium and Boron were added to the equimolar NaCl-KCl+10 w% NaF melt in form of compounds K_2ZrF_6 and KBF_4 .

Electrolysis experiments were carried out in the hermetic quartz crucible, in the atmosphere of purified Argon. A graphite crucible, also serving as anode, was used. Cylindrical glassy carbon served as cathode for electrolysis. Current was applied to the anode and cathode by cylindrical Mo and W. The cathodic product was washed after the electrolysis in water and HF solutions.

Results of the Voltammetric Experiments

On the cathodic part of the voltammogram obtained from the NaCl-KCl- K_2ZrF_6 -NaF system (Fig. 1.) the wave more electropositive than the wave corresponding to deposition of the alkali metals has been observed. This wave corresponds to the one-step, irreversible deposition of Zirconium:



This result is in agreement with results of [9,14]. Similarly, in the NaCl-KCl- KBF_4 -NaF system (Fig. 2.) one cathodic wave was observed (at more electropositive potentials than the potential of alkali metal reduction), which obviously corresponds to the one-step, irreversible deposition of Boron:



The results of Fig.2. are in agreement with data of [15]. Comparing Figs 1 and 2, one can find, that the deposition of Boron is taking place at more electropositive potential than the deposition of Zirconium by about 150 -200 mV.

The results of voltammetry in the complex melt $\text{NaCl-KCl-K}_2\text{ZrF}_6\text{-KBF}_4\text{-NaF}$ are given in Fig.3. Again, one very sharp cathodic wave is observed, at a potential more electropositive than for Zirconium (by about 300 mV) and for Boron (by about 100 - 150 mV). Potentiostatic electrolysis was performed at this potential. As proven by X-ray analysis, Zirconium Diboride has been formed. As one can see on the anodic part of the curve, the electrochemical synthesis of Zirconium Diboride is taking place irreversibly.

Finally, based on the analysis of Figures 1, 2 and 3 we can conclude, that the electrochemical synthesis of Zirconium Diboride from $\text{NaCl-KCl-K}_2\text{ZrF}_6\text{-KBF}_4\text{-NaF}$ melt at 973 K takes place in one irreversible step.

Results of Electrolysis Experiments

First, electrolysis was carried out in $\text{NaCl-KCl}(50\text{-}50\text{ \%mol.})\text{-KBF}_4(5\text{-}10\text{ w\%})\text{-K}_2\text{ZrF}_6(5\text{-}10\text{ w\%})\text{-NaF}(10\text{ w\%})$ melt at 973-1073 K in the range of current densities of 0.05-0.5 A/cm^2 on the glassy carbon cathode. It was impossible to obtain dense coatings in these experiments. In our opinion, this was due to passivation of the cathodic surface by low-valent, low-soluble Zirconium compounds, like KZrF_4 [16], or ZrF [17]. Obviously, this is the same reason coatings were not obtained in experiments by Wendt et al [18].

In order to reduce the passivation of the cathode surface, 5 w% of B_2O_3 was added to the melt. In this $\text{NaCl-KCl}(50\text{-}50\text{ \%mol.})\text{-KBF}_4(5\text{-}10\text{ w\%})\text{-K}_2\text{ZrF}_6(5\text{-}10\text{ w\%})\text{-NaF}(10\text{ w\%})\text{-B}_2\text{O}_3(5\text{ w\%})$ melt, coatings of Zirconium Diboride have been obtained in the interval of current densities 0.05-0.5 A/cm^2 . The thickness of the coating obtained was 15-20 μm . The structure of the coatings is layered, probably due to some passivation of the surface of the grains [13]. Morphology of the coatings are given in Fig.4. Photography of the microsection is shown in Fig.5.

At high current densities of 0.3-1.0 A/cm^2 in the system $\text{KCl-KF-KBF}_4(15\text{ w\%})\text{-K}_2\text{ZrF}_6(15\text{ w\%})\text{-NaF}(10\text{ w\%})$ at 923 K, powders of Zirconium diboride have been obtained. Powders obtained at 0.5 A/cm^2 are shown in Fig. 6.a and 6.b. As seen, crystals have no defined form, and a size of 20-60 μm . Comparing them to the crystals of metallic Zirconium obtained from electrolysis of $\text{KCl-KF-K}_2\text{ZrF}_6(15\text{ w\%})$ at 923 K (see Fig. 6.c and 6.d), one can see a definite difference between them. Crystals of Zirconium metal are mostly dendritic with a length of 800- 1000 μm and width of 60-80 μm .

Conclusions

Based on thermodynamic calculations and voltammetric and electrolysis experiments, we can conclude, that the electrochemical synthesis of Zirconium Diboride from chloro-fluoride melts takes place in an one-step, irreversible electrochemical process. Zirconium Diboride of stable stoichiometry can be obtained in a wide range of current densities. From chloro-fluoride melts, however, only Zirconium Diboride in form of powders can be obtained, due to passivation of cathodic surface by low-soluble, low-valent Zirconium compounds. In order to obtain Zirconium Diboride coatings, Boron Oxide should be added to eliminate passivation.

References

1. V.N. Gurin, *Uspekhi Khimii* (in Russian), **41**, 616 (1972).
2. L. Andrieux, *Chim. et. ind.*, **27**, 411 (1932).
3. D. Schlain, F.X. Mecawley, and Ch. Wiche, *J. Electrochem.*, **116**, 1227 (1969).
4. Deviatkin S.V., Kaptay G., Shapoval V.I. and Berecz E., *Proc. of the Int. Symp. on Molten Salts Chemistry and Technology*, v. 93-9, p.584, The Electrochemical Society Proceedings Series, Pennington, NJ (1990).
5. Kh. B. Kushkhov, V.V. Malyshev, A.A. Tishchenko, V.I. Shapoval, *Poroshkovaya Metallurgiya*, **1**, 8 (1993).
6. K.E. Anthony and B.J. Welch, *Aust. J. Chem.*, **22**, 1593 (1969).
7. G.W. Mellors and S. Senderoff, *J. Electrochem. Soc.*, **118**, 220 (1971).
8. J.M. Gomes, K. Uchida, M.M. Wong, *United States Department of the Interior. Bureau of Mines*, **8053**, 14 (1975).
9. H. Wendt, K. Reuhl, V. Schwarz, *Electrochimica Acta*, **37**, 237 (1992).
10. V.I. Shapoval, G. Kaptay, S.V. Deviatkin, *High-temperature Electrochemical Synthesis of Intermetallides of Titanium in Molten Salts - in: Electrochemical Technology: Innovation and New Developments*, Chapter 18., pp 361-378, Kodansha Scientific Ltd., Tokyo, 1996.
11. V.P. Glushko, *Termodinamicheskie svoistva individual'nykh veshchestv* (in Russian), , Nauka, Moscow (1978).
12. M.W. Chase and al., *JANAF Thermochemical Tables (Third Edition)*, *J. Phys. Chem. Data*, **14**, Suppl.1 (1985).
13. A.N. Baraboshkin, *Elektrokristallizatsiya metallov iz rasplavlennykh solei* (in Russian), p. 280, Nauka, Moscow (1976).
14. M. Steinberg, M. Sibert and E. Wainer, *J. Electrochem. Soc.*, **101**, 63 (1954).
15. V.I. Taranenko, I.V. Zarutskii, V.I. Shapoval, M. Makyta and K. Matiasovsky, *Electrochem. Acta*, **37**, 263 (1992).
16. L.E. Ivanovskii and O.S. Petenev, *Trudy Inst. Elektrokhimii UFAN USSR*, **2**, 71 (1961).
17. L.P. Polyakova, E.G. Polyakov and P.T. Stangrit, *Rasplavy*, **1**, 54 (1991).
18. H. Wendt, K. Reuhl, V. Schwarz, *J. of Applied Electrochemistry*, **22**, 161 (1992).

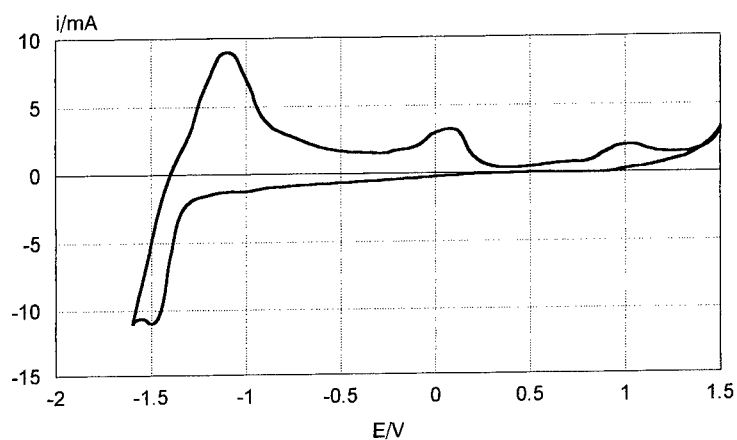


Fig. 1. Cyclic voltammogram measured in the system NaCl - KCl - $\text{K}_2\text{ZrF}_6(10^{-4} \text{ mol cm}^{-3})$ -NaF($7 \times 10^{-4} \text{ mol cm}^{-3}$) at the scan rate of 0.1 V/s at 973 K.

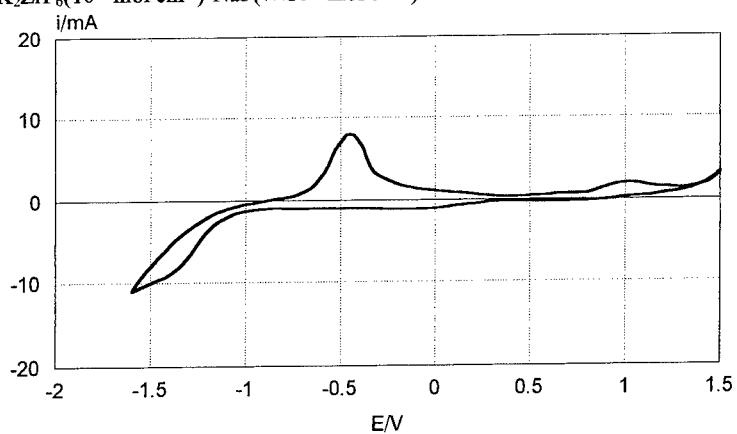


Fig. 2. Cyclic voltammogram measured in the system NaCl - KCl - $\text{KBF}_4(2 \times 10^{-4} \text{ mol cm}^{-3})$ -NaF($6 \times 10^{-4} \text{ mol cm}^{-3}$) at the scan rate of 0.1 V/s at 973 K.

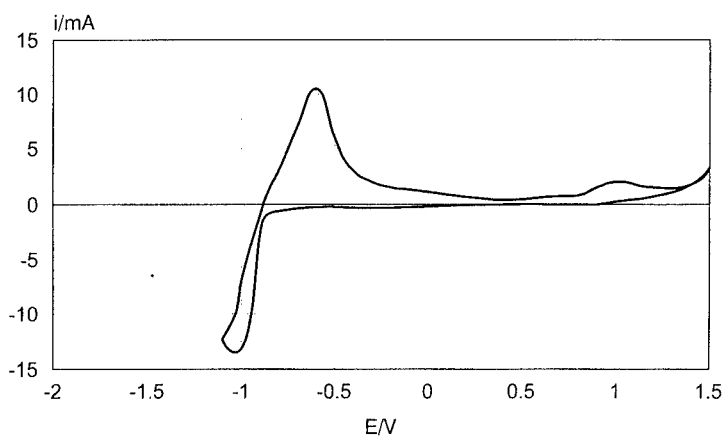


Fig. 3. Cyclic voltammogram measured in the system $\text{NaCl-KCl-K}_2\text{ZrF}_6(6.3 \times 10^{-5} \text{ mol cm}^{-3})$ - $\text{KBF}_4(9.3 \times 10^{-4} \text{ mol cm}^{-3})$ - $\text{NaF}(6.3 \times 10^{-4} \text{ mol cm}^{-3})$ at the scan rate of 0.1 V/s at 973 K.

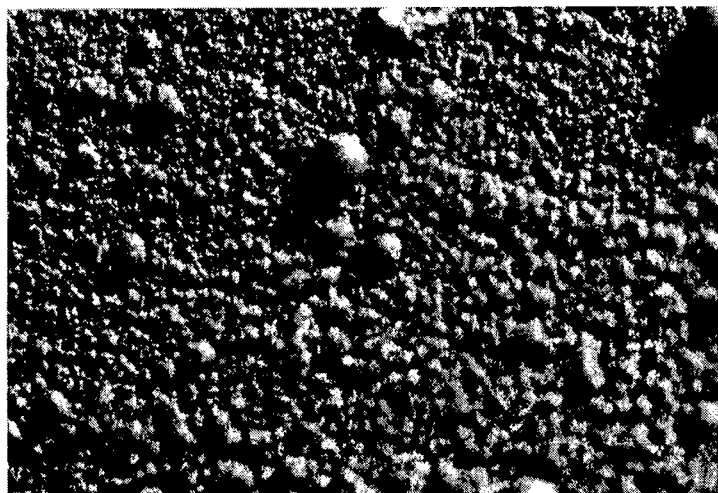
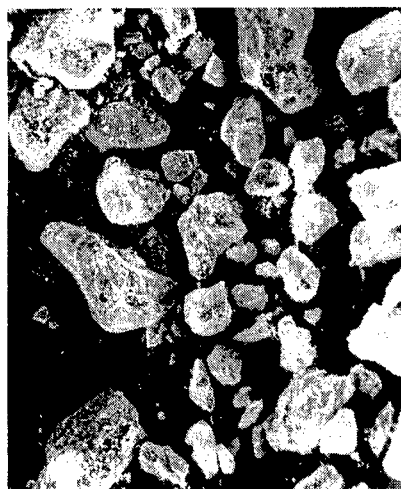


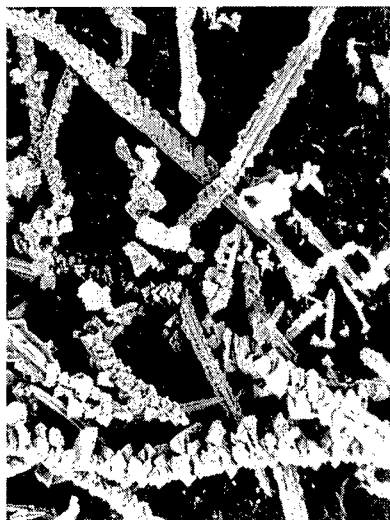
Fig. 4. Microphotograph of the surface of the electrochemically deposited ZrB_2 on glassy carbon ($\times 30$).



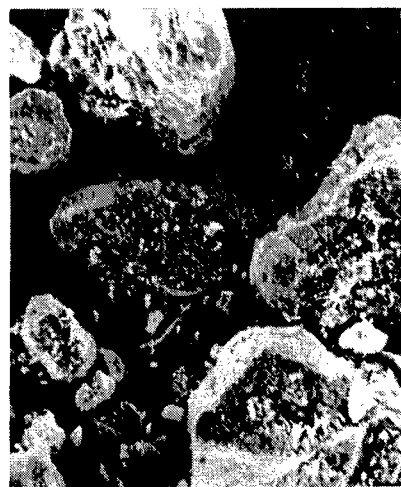
Fig. 5. Microsection of the electrochemically deposited ZrB_2 on glassy carbon ($\times 1500$).



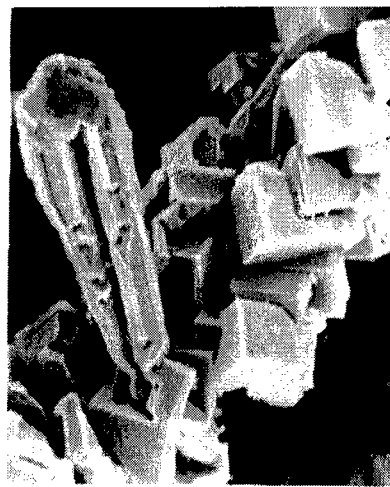
6.a.



6.c.



6.b.



6.d.

Fig. 6. Powders obtained by electrolysis: a) ZrB_2 ($\times 200$), b) ZrB_2 ($\times 500$), c) Zr ($\times 200$), d) Zr ($\times 500$).

HIGH TEMPERATURE INTERACTION OF BORON OXIDE WITH ALUMINUM FLUORIDE

Deviatkin S.V.*, Arsenin K.I.***, Kaptay G.*

*University of Miskolc, Dep. Phys. Chem.
Egyetemvaros, Miskolc, 3515 Hungary

***Institute of General and Inorg. Chemistry
32-34 Palladin pr., Kiev-142, Ukraine

High-temperature interaction of Boron Oxide with Aluminum Fluoride has been studied by infrared spectroscopy and derivatography. The formation of volatile Boron Fluoride, and some complex Aluminum-Boron Oxides has been found, which have a stabilizing effect on Boron at a molar ratio of Boron Oxide to Aluminum Fluoride 1:2 and lower.

For production of Aluminum pre-alloys in-situ by electrolysis of cryolite melts, oxides of the alloying elements (SiO_2 , TiO_2 , B_2O_3 ,...) are added to the melt [1]. However, oxides of Boron and Silicon interact with Aluminum Fluoride with a formation of volatile fluorides BF_3 and SiF_4 [2,3]. In the present work, we studied in detail the interaction of Boron Oxide with Aluminum Fluoride by derivatography of the B_2O_3 - AlF_3 system. Infrared spectra of the rapidly quenched B_2O_3 - AlF_3 salts heated to different temperatures were also taken. Information obtained can also be used for developing an in-situ electrochemical synthesis method for producing Titanium Diboride cathodic layer from cryolite based melts.

Thermodynamic Calculations

Thermodynamic calculations are performed for exchange reactions between Boron Oxide and Aluminum Fluoride, with formation of simple Al_2O_3 and also with formation of complex Aluminum-Boron oxides with different molar ratios of B_2O_3 to Al_2O_3 (hereinafter called "complex molar ratio" or CMR) of 1:2 and 2:9. Thermodynamic properties of phases are taken from handbooks [4,5]. Results of calculations are given in Table 1. As Table 1 shows, the change of standard Gibbs energies of the exchange reactions are positive at low temperatures, and become negative at higher temperatures (the temperature at which the standard Gibbs energy becomes zero is called hereinafter as "zeroG temperature"). As activities of all the solid and liquid phases given in Table 1 can be taken as approximately 1, the vapor pressure of the product Boron Fluoride will reach the outside pressure of 1 bar at the zeroG temperature. Hence, at this temperature, massive losses of Boron in the form of Boron Fluoride are expected. As shown in Table 1, the zeroG temperature is 850 K when the complex oxide product has the highest complex molar ratio (1:2), and becomes higher at lower complex molar ratios, being 910 K

for a complex molar ratio of 2:9, and 970 K for a complex molar ratio of 0:1 (actually for simple Al_2O_3).

Table 1. Change of standard Gibbs energy of possible reactions in the B_2O_3 - AlF_3 system at different temperatures

Reaction	T/K	$\Delta G^\circ/\text{kJ}$
reaction A $2\text{AlF}_3(\text{s}) + \text{B}_2\text{O}_3(\text{l}) = \text{Al}_2\text{O}_3(\text{s}) + 2\text{BF}_3(\text{g})$	773	95
	873	40
	970	0
	973	-2
	1073	-33
reaction B $4\text{AlF}_3(\text{s}) + 3\text{B}_2\text{O}_3(\text{l}) = \text{Al}_4\text{B}_2\text{O}_9(\text{s}) + 4\text{BF}_3(\text{g})$	773	53
	850	0
	873	-8
	973	-51
reaction C $18\text{AlF}_3(\text{s}) + 11\text{B}_2\text{O}_3(\text{l}) = \text{Al}_{18}\text{B}_4\text{O}_{33}(\text{s}) + 18\text{BF}_3(\text{g})$	773	385
	873	98
	910	0
	973	-185
	1023	-324

Experimental Techniques

Chemically pure H_3BO_3 and AlF_3 were used for experiments. The amounts of the two components were taken such, that the molar ratio of B_2O_3 (to be formed at higher temperature from the originally used H_3BO_3) to AlF_3 was 2:1, 1:1 and 1:2 (this ratio is called hereinafter "experimental molar ratio", or EMR). The sample powders were carefully mixed before experiments. Derivatograms were taken on a derivatograph OD-102 with a heating rate of $10^\circ\text{C}/\text{min}$, to the maximum temperature of 1000°C . Pure alumina was used as reference material in the derivatograph. Other samples were heated to different temperatures (up to 950°C), kept at the given temperature for 30 minutes, then quenched. Quenched samples were pressed into disks made of Potassium Bromide. Infrared spectra of the samples were measured on a spectrometer SPECORD M-80 in a range of 200 - 4000 cm^{-1} . Characteristic frequencies for some molecules of importance for this study are given in Table 2.

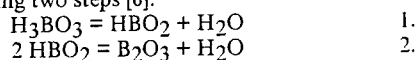
Table 2. Characteristic frequencies for some molecules (cm^{-1})

Molecule	ν_1	ν_2	ν_3	ν_4	Literature
H_3BO_3	1060	668-648	1490-1428	545	8
B_2O_3	-	-	1330-1310	-	9
BF_3	888	718	1505	482	8
AlF_3	-	544	665	360	7
Al_2O_3	860	786	660-620	462	12

Results of Experiments and Discussion

Derivatograms of mixtures with three different experimental molar ratios are given in Fig.1. Mass losses in % found from low-temperature and high-temperature parts of the derivatograms are given in Table 3 (columns 3 and 5). Infrared spectra of the quenched samples previously heated to different temperatures are given in Fig.2.

The low temperature parts of all three derivatograms are identical. One can observe two endothermic processes accompanied by some mass loss at 170 and 236 °C on each derivatogramm. These two low-temperature processes are obviously due to loss of water by H_3BO_3 in the following two steps [6]:



In columns 2 and 3 of Table 3 the low temperature mass losses are given as calculated for reaction 1 and 2, and as measured from derivatograms of Fig.1. As follows from comparison of calculated and measured data, the calculated and measured mass losses are identical for low B_2O_3 content. For high B_2O_3 content, however, there is a higher mass loss measured than expected, probably due to some extra water content of the initial salts. The nature of low-temperature mass losses can also be understood from comparison of spectrum in Fig.2.1 (taken without pre-heating) with other spectra (taken with high-temperature pre-heating), showing the disappearance of peaks corresponding to the OH- group and H_3BO_3 . It should be noted, that the peaks disappear only, if the B_2O_3 is complexed at high temperatures (see details below). Finally we can conclude, that above 236 °C the sample does not contain any more H_3BO_3 and therefore all the processes above 236 °C refer to interaction between B_2O_3 and AlF_3 .

Table 3. Calculated and measured mass losses in % for 3 derivatograms (Fig.1.) ("low T" is calculated from Reactions 1, 2; measured values taken as average between 250 and 600 °C; "high T" is calculated based on Table 4.; measured values taken as the difference between mass at 900 °C and mass at 600 °C; "high T diff." is a difference between measured and calculated data)

EMR	low T, calc.	low T, meas.	high T, calc.	high T, meas.	high T diff.
2:1	-24,4 %	-30 ± 2 %	-23,0 %	- 27 ± 4 %	- 4 ± 4 %
1:1	-19,0 %	-21 ± 1 %	-35,8 %	-37 ± 2 %	- 1 ± 2 %
1:2	-13,2 %	-13 ± 1 %	-49,6 %	-36 ± 2 %	+ 14 ± 2 %

At higher temperatures (above 650 °C) on derivatograms of Fig.1. one can observe one (for Fig.1.1.), or several (Fig. 1.2. and 1.3.) endothermic peaks, accompanied by mass loss. Those peaks obviously correspond to chemical reactions listed in Table 1, leading to formation of gaseous Boron Fluoride. As a simplest

case, amounts of products are calculated in Table 4 supposing reaction A of Table 1 is totally shifted to the right, and no complex formation between Al_2O_3 and B_2O_3 is taking place (i.e. no reaction B or C of Table 1). The high-temperature mass loss calculated based on this simplified model is given in column 4 of Table 3. Column 5 of Table 3 presents the experimental values of high temperature mass losses, measured from derivatograms of Fig.1. between temperature range of 600 and 900 °C. In the last column of Table 3 the difference between measured and calculated high-temperature mass losses are given. One can see, that for experimental molar ratios of 2:1 and 1:1 the difference is negligible, hence probably indeed reaction A is taking place. This is obvious also from the fact that the first high-temperature endothermic peaks on Figs 1.1. and 1.2 appear at 703 and 700 °C accordingly, while the zeroG temperature of reaction A appears practically at the same temperature (970 K = 697 °C - see Table 1). However, for an experimental molar ratio of 1:2, the measured weight loss is less by 14 % than expected from reaction A (see last column, last row of Table 3). Recalculating the 14 % to the weight of B_2O_3 in the sample, one can find, that about 40 % of B_2O_3 is remaining in the system against 0 % predicted by Reaction A (see last row of Table 4). Then, the molar ratio of remaining oxides in the sample is 1:1.5, which is between the complex molar ratios 1:2 [4] and of 1:1 [11], or single Al_2O_3 . Hence, obviously a mixture of complexes (and also pure alumina) is formed, i.e. instead of the single reaction A, in fact, some complex processes involving reaction A, B and C are taking place. This is also obvious from the fact that the first high-temperature peak in Fig.1.3. appears at 675 °C, which is between the zeroG temperatures of reaction A, B and C.

Table 4. Calculation of the products of reaction supposing only reaction A of Table 1 is active and is shifted totally to the right

EMR	reactants	products	CMR
2:1	$2 \text{ B}_2\text{O}_3 + 1 \text{ AlF}_3$	$1.5 \text{ B}_2\text{O}_3 + 0.5 \text{ Al}_2\text{O}_3 + 1 \text{ BF}_3$	3:1
1:1	$1 \text{ B}_2\text{O}_3 + 1 \text{ AlF}_3$	$0.5 \text{ B}_2\text{O}_3 + 0.5 \text{ Al}_2\text{O}_3 + 1 \text{ BF}_3$	1:1
1:2	$\text{B}_2\text{O}_3 + 2 \text{ AlF}_3$	$0 \text{ B}_2\text{O}_3 + 1 \text{ Al}_2\text{O}_3 + 2 \text{ BF}_3$ (*)	0:1

*- in reality, about $0.4 \text{ B}_2\text{O}_3 + 0.6 \text{ Al}_2\text{O}_3 + 1.2 \text{ BF}_3 + 0.8 \text{ AlF}_3$ is formed (see Table 3, last column, last row), hence the real CMR is 1:1.5.

The above conclusions based on derivatograms are also verified by infrared spectra. For an experimental molar ratio of 2:1 the spectra are shown in Fig 2.2. and 2.3 for 760 and 950 °C heat treatment. Comparing Fig. 2.2 with Fig.2.1. (received without heat treatment), one can see the followings:

- the low frequency peak at 360 cm^{-1} of Fig.2.1. corresponding to AlF_3 disappears;
- the high frequency peak above 3000 cm^{-1} , corresponding to OH- group of H_3BO_3 , is still present, although with slightly lower intensity;
- the peak at 1450 cm^{-1} , corresponding to H_3BO_3 , is still present, although with lower intensity;
- there is a poorly defined peak between 400 and 900 cm^{-1} , corresponding probably to Al_2O_3 that may be partly complexed by B_2O_3 .

The spectra for the experimental molar ratio of 2:1 with a heat treatment at 950 °C (Fig.2.3) is quite different from the spectra of the same system preheated to 760 °C (Fig.2.2). Before listing differences it should be noted, that there is no peak for AlF_3 in Fig.2.3. either, i.e. the two experiments are identical for the AlF_3 disappearance from the system. Fig.2.3. differs from Fig.2.2. in the following: in Fig.2.3

- i. there is no peak for the OH- group;
- ii. there is no peak for H_3BO_3 ;
- iii. there are new, very well defined peaks at around 600, 800, and 1300-1350 cm^{-1} frequency regions, which probably correspond to deformed peaks of Al_2O_3 and B_2O_3 .

Hence, at higher temperatures just 0.5 mole of Al_2O_3 seems to stabilize all the 1.5 mole of B_2O_3 . This result is surprising, because the well known phases between Boron oxide and Aluminum oxide have complex molar ratios of 1:2 and 2:9 [4], but not 3:1. On the Al_2O_3 - B_2O_3 phase diagram given in [11] one more compound with complex molar ratio of 1:1 is also given (so called "eremeevit"). Therefore, based on our results, we can conclude, that there should be a high-temperature phase with the B_2O_3 to Al_2O_3 molar ratio of 3:1, which might be metastable at room temperature (and therefore not seen on phase diagrams), but still is able to stabilize B_2O_3 if rapidly quenched.

For an experimental molar ratio of 1:1, the spectra are shown in Fig 2.4, 2.5 and 2.6 for 720, 760 and 950 °C heat treatment. As seen from infrared spectrum of Fig.2.4, at 720 °C the reaction A is not shifted totally to the right, as a medium intensity peak of AlF_3 can still be observed. At slightly higher temperature 760 °C (Fig.2.5) the peak of AlF_3 has practically disappeared. The 0.5 mole of Al_2O_3 formed might form a 1:1 complex oxide with the remaining amount of 0.5 mole of B_2O_3 . At higher temperature this 1:1 complex can dissociate to the 3:1 complex (see above) and 1:2 or 2:9 complexes (see [4] and Table 4). The total complex formation of the remaining salt can be well seen in the spectrum (Fig 2.6) of the salt preheated up to 950 °C.

For an experimental molar ratio of 1:2 the spectra are shown in Fig 2.7, 2.8, and 2.9 for 760, 900 and 950 °C heat treatment. As was shown before, in this case the complex formation between Al_2O_3 and B_2O_3 will partially prevent the formation of gaseous Boron Fluoride. The formation of complexes can be well seen on the spectra.

Conclusions

1. The gaseous Boron Fluoride is formed at about 700 °C, or at lower temperature in excess of Aluminum Fluoride.
2. The high-temperature complex oxide phase is found with molar ratios of Boron Oxide to Aluminum Oxide 3:1, which forms at about 900 °C, and is metastable at lower temperatures.

3. The formation of complex Aluminum-Boron oxides can partially prevent Boron losses due to Boron Fluoride formation in excess Aluminum Fluoride. When the Aluminum Fluoride to Boron Oxide molar ratio is 2:1, about 40 % of Boron Oxide is kept in the system in form of complex oxides up to 950 °C.

Acknowledgements

This work has been supported by COPERNICUS 1171 and OTKA T016903.

References

1. A.I. Belyaev, *Metallurgiya legkikh metallov*, p.543, Metallurgiya, Moscow (1944).
2. A.P. Krymov, V.V. Bugaenko, V.V. Nerubashchenko and R.V. Chernov, *Elektrokhimicheskie i termodinamicheskie svoistva ionnykh rasplavov*, p.69, Naukova Dumka, Kiev (1977).
3. D.V. Pruttskov, *Ionnye rasplavy i tverdye elektrolity*, 1, 70 (1986).
4. I.h. Barin, *Thermochemical Data of Pure Substances*, VCH, Weinheim (1993).
5. M.W. Chase et al., *JANAF Thermochemical Tables (Third Edition)*, J. Phys. Chem. Data, 14, Suppl.1 (1985).
6. H. Remy, *Lehrbuch der Anorganischen Chemie*, p.334, AVG&P, Leipzig (1960).
7. E.N. Jurtchenko, G.N. Kustova, S.S. Batsanov, *Kolebatel'nye spektry neorganicheskikh soedinenii*, p.19, Nauka, Sibirskoe otdelenie, Novosibirsk (1981).
8. K. Nakamoto, *Infrared Spectra of Inorganic and Coordination Compounds*, p. 98, Wiley-Interscience, Second Edition, New York (1970).
9. V.N. Pavlikov and al., *Russ. J. Inorg. Chem.*, 19, 1597 (1974).
10. P. Ramdohr, H. Strunz, *Lehrbuch der Mineralogie*, p. 564, Ferdinand Enke Verlag, Stuttgart (1967).
11. P.J.M. Gielisse and W.R. Foster, *Nature*, 195, 69 (1962).
12. V.A. Florinskaya, *Infrakrasnye spektry neorganicheskikh stekol i kristallov*, p. 113, Khimiya, Leningrad (1972).

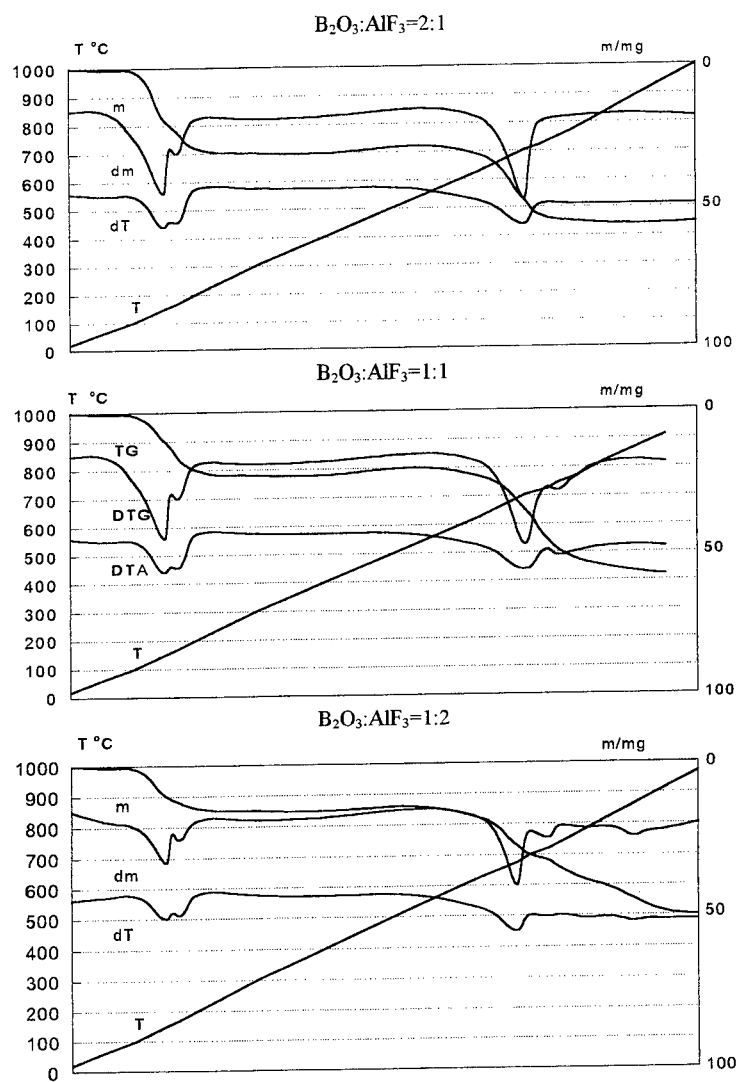


Fig. 1. Derivatograms of $B_2O_3-AlF_3$ systems.

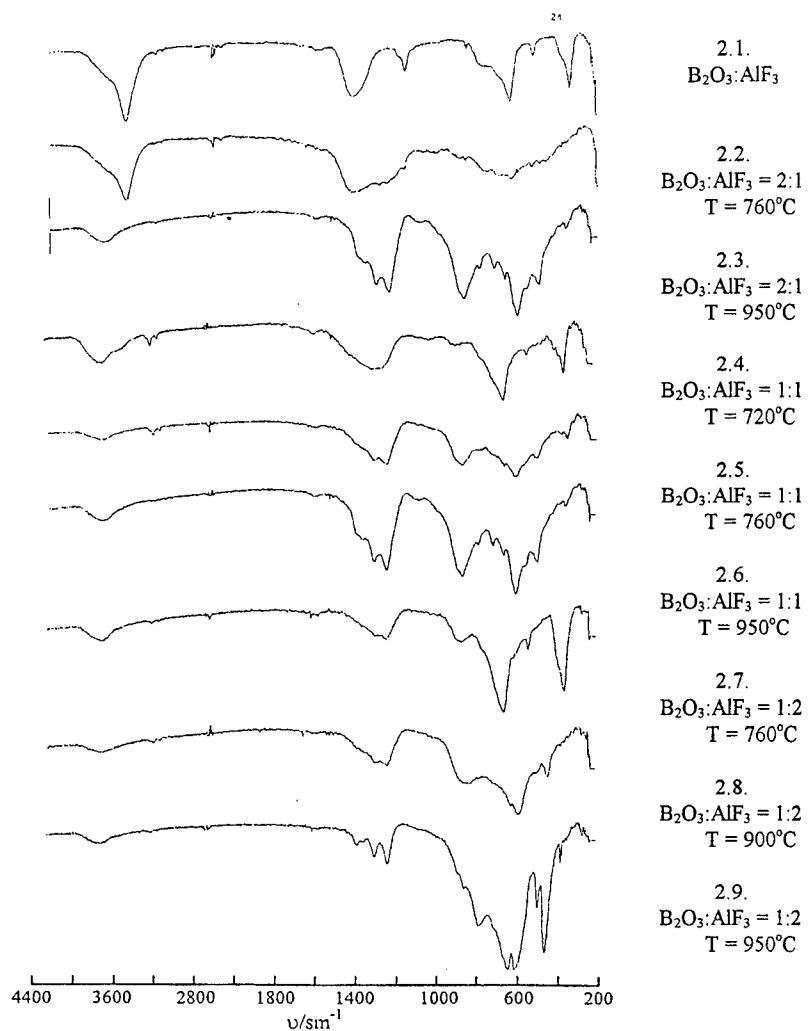


Fig. 2. Infrared spectra of rapidly quenched salts of the $\text{B}_2\text{O}_3:\text{AlF}_3$ system.

FORMATION OF LaNi_5 FILM ON NI SUBSTRATE BY ELECTROLYSIS IN MOLTEN CHLORIDE AND ITS HYDROGEN ABSORPTION PROPERTY

M.OKIDO*, R.ICHINO** and R.TAMURA***

* Center for Integrated Research in Science and Engineering, Nagoya University

** Department of Materials Science and Engineering, School of Engineering,
Nagoya University

*** Graduate student, School of Engineering, Nagoya University
Furo-cho, Chikusa-ku, Nagoya, 464-01, Japan

Lanthanum - nickel alloy films can be formed on a nickel substrate by electrolysis in eutectic KCl - LiCl molten salts with both 1.5 mol% La_2O_3 and 18 mol% NH_4Cl or in eutectic KCl - NaCl molten salts with 10 mol% $\text{LaCl}_3 \cdot 7\text{H}_2\text{O}$. An alloy film of 30 μm thickness was obtained by this electrolysis at 923 K for 1 hour. The composition of the alloy films depends on the temperature, consisting of LaNi_3 , La_2Ni_7 and LaNi_5 at less than 923 K and LaNi_5 at more than 923 K. The vickers hardness of the alloy films obtained by this method was less than that of the commercial LaNi_5 ingot specimen. The alloy films show better hydrogen absorption behavior in the early stage, better charge - discharge behavior and less pulverization compared to the LaNi_5 ingot.

INTRODUCTION

Nickel - Hydrogen absorbing alloy batteries, with an electromotive force the same as Ni - Cd batteries, have higher energy density by 1.5 - 2 times than the latter battery. Moreover, since the reaction product is only water, Nickel - Hydrogen absorption alloy batteries are excellent in terms of low environmental impact.

A LaNi_5 alloy is used as an active material for a negative electrode in Nickel - hydrogen

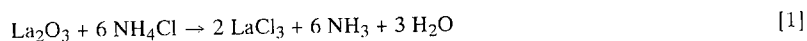
batteries. The degradation due to the brittleness of expansion with hydrogen absorption, however, decays the battery properties. Recently, partial substitution of Al, Co or Mn for Ni is found to have good charge - discharge properties and to inhibit this degradation (1),(2).

Though LaNi_5 source can be commercially mass-produced in a high frequency-induced furnace because of high melting points of La and Ni, lanthanum is rare and noble mineral resource and refining of La metal is too expensive. Substitution of other elements for La is carried out in practice. Misch metal, cheaper than La, is used instead of La for good cost performance. On the other hand, it is considered that the use of thin film reduces the amount of LaNi_5 needed, and the material diffusion in films occurs better.

Electrolysis, electroplating and electrodeposition are usual methods in surface modification technique for metallic materials. As the temperature for electrolysis in molten salts is much higher than that in aqueous solutions, the deposited metal can be sometimes alloyed with the substrate. The capability for forming alloys depends on the affinity between metals and the temperature. In this paper, La - Ni alloy phases were formed onto Ni sheets under controlled cathodic currents in molten salts. Formed films were tested for their hydrogen absorption property, charge - discharge behavior, hardness, structure and the effect of the condition of electrolysis.

EXPERIMENTAL

Two electrolysis in molten salts were prepared. One was eutectic KCl - NaCl molten salts with 10 mol% $\text{LaCl}_3 \cdot 7\text{H}_2\text{O}$, denoted as bath (a). The other was eutectic KCl - LiCl molten salts with both 1.5 mol% La_2O_3 and 18 mol% NH_4Cl , bath (b). All chemicals were commercial high purity. The latter bath was heated for 4 hours at 623 K after pre-drying for 24 hours at 353 K, in order to form a LaCl_3 as in the following reaction(3);



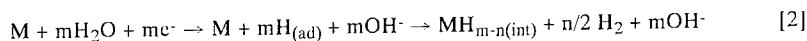
The electrolysis is carried out after preheating at 1073 K for 1 hour to remove moisture in the molten salts. Cathodic polarization curves are measured for the Ni electrode in the molten salts. The counter electrode is a carbon rod, and a reference electrode is an Ag

electrode in equimolar NaCl - KCl with 0.1 M AgCl in a mullite tube.

In electrolysis, a Ni sheet in the size of 15 mm square with a thickness of 0.1 mm is used as a cathode electrode. Before La electrolysis, every Ni cathode is preheated in the molten salts for 30 min. to remove the stress in the Ni electrode. Pre-electrolysis is performed by using another Ni cathode at - 1.5 V for 20 min. to remove contaminations and water from the molten salts. Then, lanthanum is deposited in the potential region between - 1.2 V and - 2.0 V with a total charge of 32 C. Lanthanum - Nickel alloy films were electrolyzed at 0.1 Acm⁻² in bath (a) at 923 K - 1073 K for 400 s to estimate the effect of temperature on the films. Every electrolysis was carried out under argon atmosphere. Deposits were analyzed by X-ray diffraction (XRD), EPMA, SEM observation and a microvickers hardness test.

Hydrogen absorption into alloys during charge, and hydrogen desorption during discharge, were evaluated in 30 % KOH solution at 298 K for comparison with commercial LaNi₅ ingot. They were performed under galvanostatic condition with cathodic and anodic current densities of 10 mAcm⁻².

Hydrogen gas evolved on the cathode was collected in a buret. Absorbed hydrogen, equal to the charging electricity, Q_c (C), was calculated by the following equations.



$$Q_c = zF(m-n) = it-2FPV/RT \quad [3]$$

M:LaNi₅, Q_c:amount of absorbed hydrogen, z:valence, F:Faraday constant, i:current, t:time, P:pressure, V:volume of hydrogen collected in the buret, R:gas constant, T:temperature

Charge - discharge characteristics in alkaline solution were evaluated, in the unit of coulomb by calculating the ratio, Q_c / Q_d, where Q_d (C) corresponds to the amount of desorbed hydrogen during discharging.

RESULTS AND DISCUSSIONS

Formation of LaNi₅

The cathodic polarization curves for a nickel electrode in molten salts of bath (a) with 10 mol% LaCl₃·7H₂O, bath (b) with 1.5 mol% La₂O₃ and 18 mol% NH₄Cl and (c) without La ions at 973 K are shown in Fig. 1. In the molten salts with La ions, cathodic current peaks appear in the potential region from -1.7 V to -2.0 V. These peaks correspond to the deposition of La. In XRD results on the Ni surface electrolyzed at -2.0 V in bath (b), LaNi₅ was detected on the surface. The plateau at potentials between -1.7 V and -2.0 V in bath (b) results from the diffusion limitations of La ion because of the lower concentration of La ions, 3 mol%, versus bath (a), 10 mol%.

Figure 2 shows an alloy phase of La and Ni in the cross section of the nickel film cathode with a thickness of 100 μm, electrolyzed with a current density of 0.02 Acm⁻² for 1 hour in bath (b). This film thickness is less dependent on the temperature and duration of electrolysis and is approximately constant at 25 - 30 μm below 923 K. The EPMA line analysis of La and Ni shows the constant content of La and Ni in the alloy layer, corresponding to LaNi₅. The alloy film formed at 773 K is LaNi₃ from XRD results. The result that the Ni content in alloy films electrolyzed at 923 K is richer than that at 773 K is caused by the temperature dependence of the diffusion rate in the solid alloy film. Figure 2(3) shows the result of EPMA for a deposit which was electrolyzed at 923 K for 1 hour and then cooled rapidly from 923 K to 473 K in the rapid Ar gas flow. Lanthanum content in the surface region is higher than that in the layer. This behavior shows that La diffusion takes place at the beginning of electrolysis and continues until low temperatures during cooling after electrolysis. However, in the case of rapid cooling, since La diffusion cannot have occurred sufficiently, La content in the surface region is high. Moreover, the difference in formation between LaNi₅ and LaNi₃ can also be caused by the difference between the liquid state and the solid state. Since the melting point of LaNi₃ is lower than that of LaNi₅, from the La - Ni binary phase diagram (3), LaNi₃ can be removed and depart from electrode surface at high temperature easily while LaNi₅ remains on the electrode surface at high temperature.

Figure 3 shows XRD analysis for La - Ni alloy films electrolyzed in bath (a) at different temperatures for 400 s. All diffractograms show LaNi₅, Ni and LaOCl diffraction peaks. LaOCl is due to the oxidation products from LaCl₃ with H₂O and/or O₂ during drying the molten salts, and it may be included in films during electrolysis and/or may be produced from LaCl₃ with H₂O and O₂ in Ar gas during cooling in the cell after electrolysis.

Lanthanum and nickel contents in films formed in bath (a) at 923 K - 1073 K are shown in Fig. 4. The La contents are approximately constant and the profiles of La in films are similar to Fig. 2. Lanthanum contents on the surface evaluated by EDX were 28 at%, 20 at%, 18 at% and 12 at%, respectively. Lanthanum content in the film electrolyzed at 1073 K was less than the stoichiometric value of 16.7 at% in LaNi_5 . Since LaNi_3 formed at 773 K and LaNi_5 formed at 923 K, as shown in Fig. 2, mutual diffusion velocities of La and Ni are slow at low temperature, it seems that the excess La over LaNi_5 exists on the surface at the temperature less than 1023 K.

Current efficiencies calculated from weight gain, using the alloy thickness, for the alloys electrolyzed at 923 K, 973 K, 1023 K and 1073 K in bath (a) were 10.3, 38.5, 9.7 and 4.3, respectively. The low values of current efficiency are mainly contribute to La remelting into the molten salts in the style of La - Ni alloy. The melting point of La - Ni alloy containing Ni between 10 at% and 40 at% is about 900 K (4), which is lower than electrolysis temperature. Moreover, La_2Ni_3 , $\text{La}_2\text{Ni}_4\text{O}$ and La_2O_3 were detected by XRD in the molten salts after electrolysis. This evidence shows that La remelts into the molten salts. Therefore the thickness of alloy films is less, and the current efficiencies are low.

Surface morphology of alloy films formed at 923 K, 973 K, 1023 K and 1073 K for 400 s in bath (a) were shown in Fig. 5. Maximum grain size formed at 1073 K was about 8 μm and the grain size reduced with decreasing in electrolytic temperature. Therefore, the grain size depends on cooling history and grains grew during cooling in cell. Deposits formed at higher temperature than 1023 K showed brightness. On the other hand, deposits at lower temperature showed dark and non-bright feature because of fine grains.

Hydrogen absorption property

Cathodic charge for reduction of hydrogen ion at a current density of 10 mAcm^{-2} in 30 % KOH solution was compared for Ni sheets electrolyzed in bath (a), LaNi_5 ingot and raw Ni sheet without any activation pretreatment. The result is shown in Fig. 6. The solid lines, noted 0 % charge, corresponds to the case where all cathodic current is used for hydrogen gas evolution. The dotted line, noted 100 % charge, corresponds to the absorption of hydrogen into the electrode without any gas evolution, in other words, the current efficiency for forming a hydride alloy is 100 %.

The amount of absorbed hydrogen for alloy films deposited at 923 K and 1073 K shows constant values of 2 C and 0.8 C, respectively. This shows saturation with absorbed hydrogen in these films because they are thinner than any other films. Alloy films deposited at 973 K and 1023 K show better absorption properties, nearly 100 % charged, until a cathodic electricity of 3 C compared to LaNi₅ ingot. Because the alloy films have finer grains, hydrogen is more easily able to absorb into alloy films than into LaNi₅. The lines of charge efficiency deviates from the 100 % charge line at over 3 C, because the films become saturated with absorbed hydrogen.

The amount of absorbed hydrogen in LaNi₅ electrolyzed at 923 K in bath (a) was evaluated from the saturated charge electricity of hydrogen, Q_c , i.e. approximately 2.2 C in Fig. 6. If the volume of the alloy phase is assumed to be $2.0 \times 10^{-4} \text{ cm}^3$, it is found that the atomic ratio of hydrogen to LaNi₅ is 5.80, i.e. LaNi₅H_{5.80}. In the same way, that for films electrolyzed at 923 K in bath (b) is 5.76, i.e. LaNi₅H_{5.76}. The theoretical value of the ratio of hydrogen is 6, i.e. LaNi₅H₆. Therefore, the Ni - La films formed by this electrolysis in molten salts can absorb much hydrogen and there are almost no differences in the ratio of hydrogen between bath (a) or bath (b).

Figure 7 shows the result of discharging tests, performed in 30 % KOH solution at 298 K after charging for 30 min. All potential curves show a shoulder, and the potential increases rapidly until each shoulder. As each charged alloy electrode begins to discharge at the potential of the shoulder, the lower this potential is, the more easily hydrogen discharges. Dehydrogenation takes place in the plateau region after each shoulder, and the width of the plateau region depends on the amount of charged electricity, in other words, the film thickness. Hereby, alloy films produced by this molten salts technique have good charge - discharge properties in comparison with LaNi₅ ingot. The discharged electricity for LaNi₅ electrolyzed at 973 K was approximately 3 C, which was half of the charged electricity since this sample was charged with 6 C.

Charge - discharge characteristics in cycle test

Figure 8 shows the dependence of the ratio for the hydrogen discharge to the hydrogen charge on cycling test in alkaline solution. This test was performed under the condition of cathodic current density of 10 mA cm^{-2} for 200 s, charging, and remaining still in the solution

for 10 min., before the anodic current density of 10 mAcm^{-2} , discharging. The time for anodic discharge is determined by reaching the potential of -0.6 V . Nickel hydroxide may form over this potential, and the discharge is regarded to have ended. All alloy films, except that deposited at 1073 K , shows effective discharge properties at approximately 10 cycles, *i.e.* discharged electricity is as same as charged electricity. The charge - discharge ratio for alloys electrolyzed at 923 K and 973 K rapidly decreases after 20 and 10 cycles, respectively. This ratio for films electrolyzed at 1023 K is more than 0.8 after 10 cycles, and for films electrolyzed at 1073 K , it has a constant value of 0.2. This low value for the latter may come from the film thickness. On the other hand, the commercial LaNi_5 ingot shows slight cycle dependency and remains at about 0.2 after 20 cycles. Consequently, alloy films prepared by this method, especially electrolyzed at 1023 K , show better charge - discharge characteristics than commercial LaNi_5 ingot. Some powders with dark gray color were observed at the bottom of cell for all films and the LaNi_5 ingot after cycle tests. The amount of powder decreased and powder was fine and roundish with increasing in electrolyzing temperature. As for the LaNi_5 ingot, powders with brightness and large powders were observed.

The surface morphology for the film electrolyzed at 1023 K after cycle testing and for the LaNi_5 ingot before and after cycle testing are shown in Fig. 9. The morphology for alloy film after cycle testing is similar to that before cycle test in Fig. 5(3). The white angular colored part is Ni and the part which looks like lichen is $\text{Ni}(\text{OH})_2$. As for the other films using different temperatures, similar behavior was shown. In the case of LaNi_5 ingot, the morphology shows a fibrous structure with certain orientation after some grains parted from surface and fell down onto the bottom of the cell.

The hardness for alloy films measured by microvickers hardness tester was about 300 Hv and that for LaNi_5 ingot was about 650 Hv. This hardness of LaNi_5 ingot causes much of the powdering in cycle testing.

There were large cracks in the LaNi_5 ingot and small ones with network in electrodeposited alloy films in Fig. 9. The cracks, which were generated during charge - discharge cycles, caused grains to break and separate into parts. This behavior made the stress of grains relaxed and small and net work crevasse released it better than large one. Hereby, powdering of the alloy surface was inhibited. Hence charge - discharge characteristics of films were better than LaNi_5 ingot.

CONCLUSIONS

Lanthanum - Nickel alloy film phase can be formed on Ni thin films by electrolysis in chloride molten salts baths containing La ion. The LaNi_5 film was formed over 923 K. The current efficiency for electrolysis was mainly 10 %, maximum is 38.5 % at 973 K in this study because of melting of La and La - Ni alloy into the molten salts. The LaNi_5 films show less powdering, good hydrogen absorption and charge - discharge characteristics in alkaline solution compared to LaNi_5 ingot.

REFERENCES

1. M.Latroche, A.Percheron-Guegan, Y.Chabre, J.Bouet, J.Pannetier and E.Ressouche, J. Alloys and Compounds, **231**, 537(1995).
2. H.Kaiya and T.Ookawa, J. Alloys and Compounds, **231**, 598(1995).
3. Y.Y.Pan and P.Nash, in Binary Alloy Phase Diagrams 3, T.B.Massalski, Editor-in-chief, p.2406, ASM International, Metal Park(1990).
4. C.Guang-sen, M.Okido and T.Oki, J. Appl. Electrochem., **20**, 77(1990).

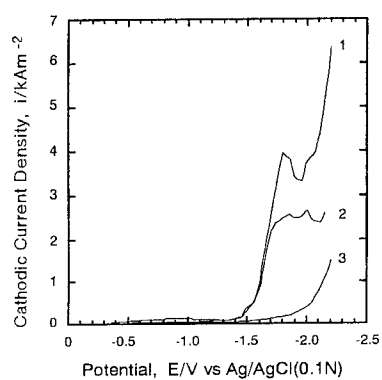


Fig. 1 Cathodic polarization curves for reduction of La^{3+} on Ni electrode at 973K. 1 in bath (a), 2 in bath (b) and 3 without LaCl_3 .

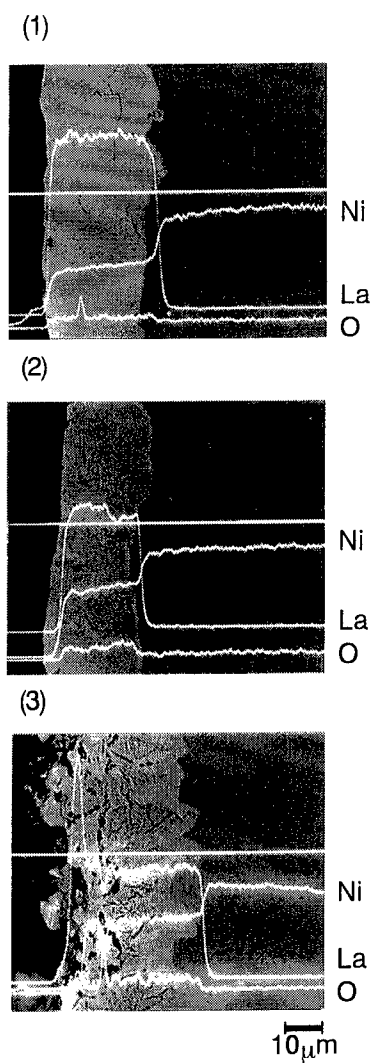


Fig.2 EPMA line analysis of La-Ni alloy layers electrodeposited in bath (b) at (1) 723 K, (2) and (3) 923 K. (1) and (2) slow cooling in the furnace, (3) rapid cooling by Ar gas after electrolysis.

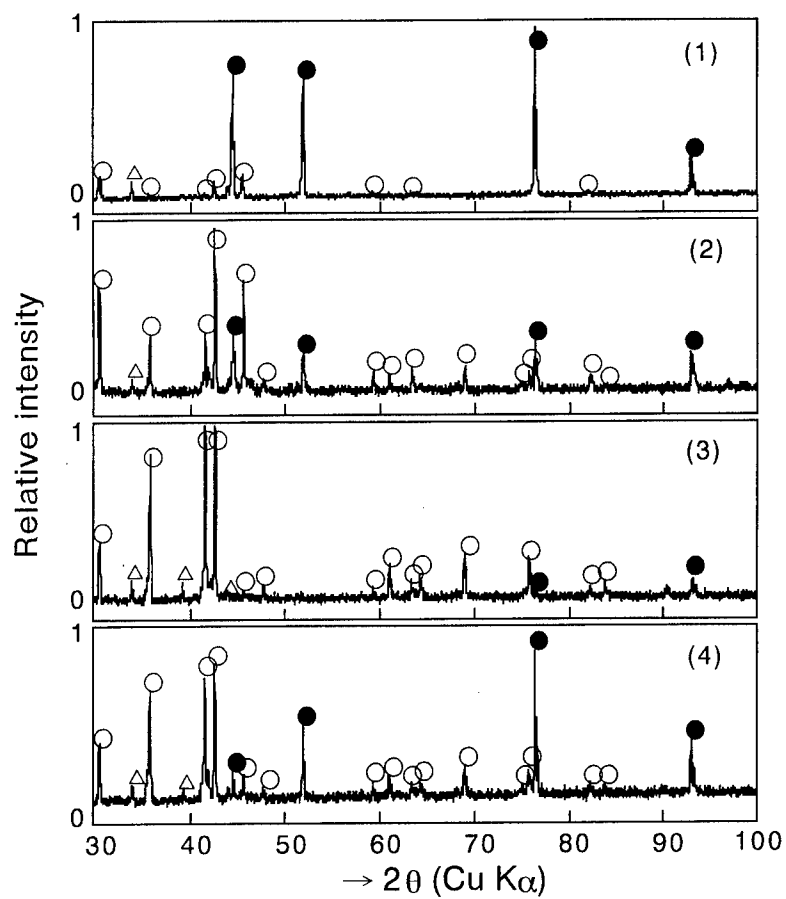


Fig.3 X-ray diffraction patterns of La-Ni alloy electrodeposited in bath (a) at (1) 923 K, (2) 973 K, (3) 1023 K and (4) 1073 K.

○ LaNi_5 ● Ni △ LaOCl

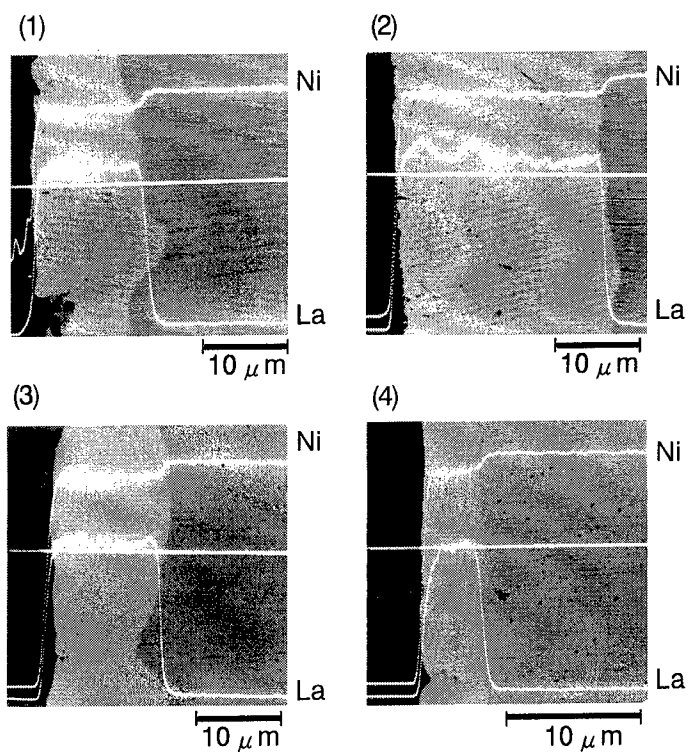


Fig.4 EPMA line analysis of La-Ni alloy layers electrodeposited in bath (a) at (1) 923 K, (2) 973 K, (3) 1023 K and (4) 1073 K.

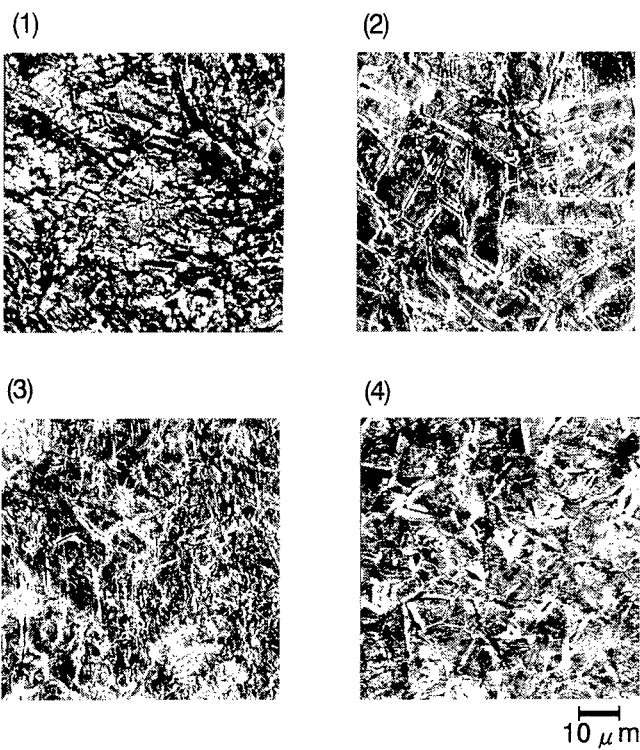


Fig.5 SEM photographs of La-Ni alloy surface electrodeposited in bath (a) at (1) 923 K, (2) 973 K, (3) 1023 K and (4) 1073 K.

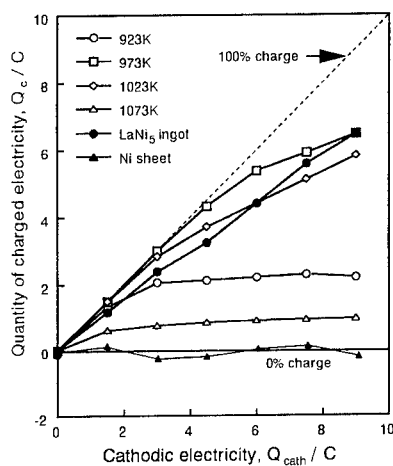


Fig. 6 Charge performance of LaNi_5 ingot, Ni sheet and LaNi_5 electrodeposited in bath (a) at various temperature in 30 wt% KOH solution at 298 K.

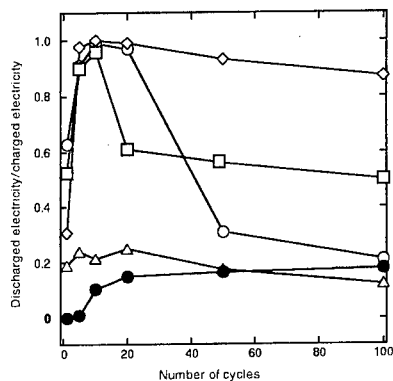


Fig. 8 Change in discharged electricity/charged electricity with cycle number on LaNi_5 ingot and LaNi_5 electrolyzed in bath (a) at various temperature.
○ 923K, □ 973K, ◇ 1023K, △ 1073K and ● LaNi_5 ingot

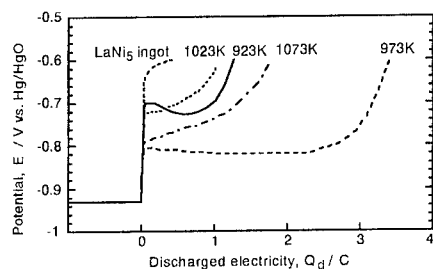


Fig. 7 Discharge performance of LaNi_5 ingot and LaNi_5 electrodeposited at various temperature in bath (a), after charging.

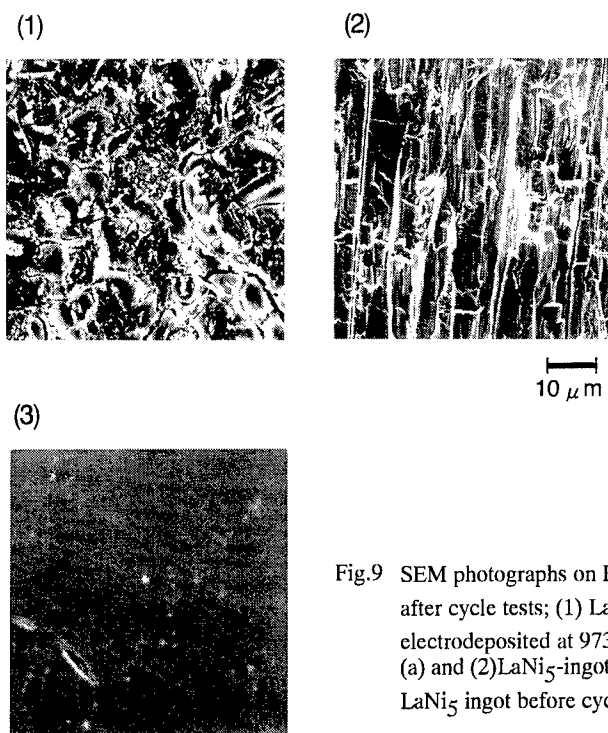


Fig.9 SEM photographs on LaNi_5 surface after cycle tests; (1) LaNi_5 electrodeposited at 973K in bath (a) and (2) LaNi_5 -ingot. (3) is LaNi_5 ingot before cycle tests

ELIMINATION OF PRIMARY SILICON PHASE IN HYPER-EUTECTIC AL-SI ALLOY BY MOLTEN SALT PROCESS

Tetsuo INOUE^{*1}, Hideyuki KANEMATSU^{*1}, Yoshihiko
KUNIEDA^{*1}, Shigeo HAYASHI^{*2} and Takeo OKI^{*3}

^{*1} Department of Materials Science and Engineering,
Suzuka College of Technology, Suzuka,
510-02, JAPAN

^{*2} Mie Prefectural Ceramics Research Institute,
Yokkaichi, 510, JAPAN

^{*3} Department of Materials Science and Engineering,
Nagoya University, Nagoya 464-01, JAPAN

ABSTRACT

The detrimental effects arising from the presence of nonmetallic inclusions in aluminum are well known. On the other hand, aluminum is one of the materials with high recyclability among many metals, and over 60 percent of aluminum alloys are recycled and reused in Japan. Unfortunately, the application of recycled aluminum is limited to use for some purposes since the recycled aluminum contains several different phases, e.g., inclusions, precipitates etc. Therefore, the elimination of nonmetallic inclusions, particularly silicon phases in hyper-eutectic Al-25Si alloy, using molten equimolar KCl-NaCl salts system was investigated experimentally. The amount of silicon in hyper-eutectic Al-Si alloy was gradually reduced to about 15% with the cycle number of treatment in molten equimolar KCl-NaCl salts. X-ray diffraction and fluorescent X-ray analysis indicate that the silicon in aluminum alloy is transferred to the molten salts.

INTRODUCTION

Aluminum and its alloys have high recyclability. Since we are face-to face with an energy and resource crisis at the turn of the century, their recycling is now being investigated and developed(1,2). However, it is very difficult for the current techniques to eliminate impurities melting in matrices, since aluminum is one of the very active metals. Therefore, scraps containing high level impurities are recycled by blending primary metals and/or scraps of low level impurities together. And in addition, various other techniques e.g the method using the difference in affinities for oxygen and for nitrogen, and the process using the difference of the specific weight between aluminum and impurities are also being developed. However, all of these are not enough to overwhelm the other recycling techniques and more effective new process are required now(3). In the present study, we investigated the elimination of the primary silicon phase from Al-Si alloys using equimolar KCl-NaCl molten salts and discuss the effectiveness and possibility of the process as the practical recycling technique.

EXPERIMENTAL

The specimens used were hyper-eutectic Al-25Si alloy whose composition is Si=24.6, Cu<0.1, Mg<0.2, Fe=0.2, and the residual part is aluminum. The salts used consist of NaCl and KCl basically. Several percentages of sodium fluorides were added to remove the surface oxide films on specimens. Prior to treating, the mixed salts were heated to 1033K and maintained at this temperature for about an hour in order to reduce the moisture in the salts.

Each specimen(15g) was immersed into molten salts at the adequate temperatures(1033K and 923K for 0.9ks-9ks). The experimental procedure is shown in Fig.1. The molten salts in mullite crucibles were agitated intermittently during the treatment in the electric furnace. After immersion treatment, the salts containing a specimen were slowly cooled to room temperature in the furnace, and then the specimen and salts were mechanically separated. During the operation, the atmosphere in the furnace was not regulated,

since the molten salts acted as protection against the ambient atmosphere. The primary silicon phase in the specimens was confirmed by optical microscope, and the silicon contents were measured by fluorescent X-ray analysis (FLX). In order to confirm the separated silicon phase, the salts were examined by X-ray diffraction analysis(XRD) and the extent of elimination of Si phases was measured.

RESULTS AND DISCUSSION

Fig.2 shows the correlation between the amount of residual silicon in specimens and the dehydration time prior to treatment of salts. The specimens were heated to the temperature which coexistence region of solid silicon phase and liquid aluminum phase in equilibrium phase diagram. Although the non-treated hyper eutectic Al-Si alloy contained about 25% Si, the amount of the residual silicon in the specimen after the 1st. cycle treatment was less than 20%. Fig.2 also indicates that the silicon in specimens was eliminated gradually in the following 2nd. and 3rd. cycle treatments, respectively.

Fig.3 shows the correlation between the amount of the residual silicon in specimens and treatment time, when molten salts were dehydrated for 7.2ks; other conditions were the same as described above. For the specimen in the 1st. cycle for 0.9ks, there was little difference between the amount of silicon for the non-treated specimen and that for the treated one.

However, the following 2nd. and 3rd. treatments decreased the silicon content in specimens down to 20% and 18% , respectively.

On the other hand, the silicon in the specimen treated in the 1st. cycle for 3.6ks was eliminated to an amount less than 20%. These results suggest that the elimination process needs an adequate time for contacting both solid and liquid phases during treatment.

Fig.4 shows variations of the amount of residual silicon in treated specimens with the number of times for agitation. The amount of residual silicon in treated specimen has a

tendency to decrease to a certain extent by agitation in KCl-NaCl molten salt.

This suggests that during agitation in molten salts solid silicon comes into contact with the liquid molten salt, resulting in the transfer of silicon from hyper-eutectic Al-Si alloy to the molten salt. There is little difference between the amount of residual silicon in the specimen after the 1st. cycle of treatment by agitating, no agitating, and that by agitating four times. These results suggest that the solid silicon phase was thoroughly miscible with the liquid molten salt by agitation.

Fig.5 shows the XRD spectrum for residual materials in the treated salt. These salts were washed with water and filtrated after treatment and submitted to XRD. The two silicon peaks at 28 and 47 deg./ 2θ were observed for the treated salt. These peaks indicate the presence of silicon that was transferred from the treated specimen. This result suggests that this process using molten salts makes it possible to eliminate the primary silicon phase from the hyper-eutectic Al-Si alloy.

Fig.6 shows the variation of the amount of residual silicon in the treated specimen with the difference of the treatment temperatures. The sample is on the liquidus line at 1033K, and it is in the coexisting region of both the solid and liquid phase at 923K. A part of primary silicon phase exists as a solid phase at 923K, though almost all phases of specimen are more liquid at 1033K. So, solid silicon particles can more easily contact the molten salt during the 923K treatment than at 1033K. Consequently, it has been considered that the amount of residual silicon in the 923K treated specimen is less than that of the 1033K treated one. Nevertheless, the silicon was eliminated by this molten salt process and the amounts of residual silicon in treated specimen decreased with increasing treatment numbers of cycle at either condition.

The precise mechanism for the elimination process has not been clarified yet. However, all these results confirm that the primary silicon phase can be eliminated from hyper-eutectic Al-Si alloy by using the molten salt. Although the mechanism has not been clear yet, part of the explanation can

be deduced from earlier experiments.(4,5,6)

CONCLUSIONS

The elimination process of primary silicon phases in hyper-eutectic Al-Si alloys was investigated by using a KCl-NaCl molten salts system, and the following results were obtained.

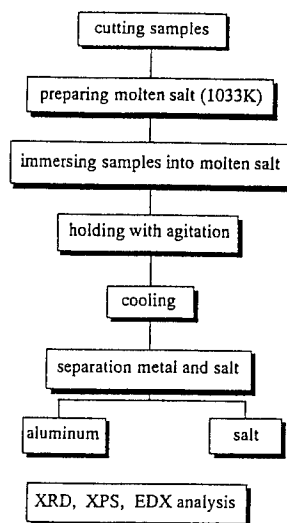
- (1) The primary silicon phase in hyper-eutectic Al-Si alloy transferred from the melting alloy to molten salts by treatment at adequate temperatures.
- (2) Application of this process will makes it possible to eliminate the impurities contained in the recycled aluminum alloy.

ACKNOWLEDGMENT

The authors would like to thank the Research Foundation for the Electrotechnology of Chubu for supporting this foreign voyage(Nagoya). The major part of this work was supported by the Okasan-Kato Foundation(Tsu) .

REFERENCES

- (1) T.Nakamura,"RECYCLING PROCESSES OF METALS", Molten salts, 35 (1992),p81-94
- (2) M.Nanjoh and N.Sato,"RECYCLING OF MATERIALS", Jour. Min. Mat. Proc. Inst. Jpn., 105(1989), p17-22
- (3) R.Yamamoto:"THE PRESENT AND FUTURE PROSPECT ON ALUMINUM RECYCLING", Jour. of Min. Proc. Inst. Jpn. 107 (1991) p95-102
- (4) T.Choh and T.Oki,"WETTABILITY FOR FABRICATION OF METAL MATRIX COMPOSITE", Bull. of Jpn. Inst. of Metals, 28(1989),p285-293
- (5) T.Inoue, H.Kanematsu and T.Oki:"SEPARATION AND RECOVERY OF ALUMINUM FROM ALUMINUM COMPOSITE MATERIALS BY MOLTEN SALT PROCESS", Proc. Intern. Conf. on Processing Materials and Properties, p755-758, TMS & MMIJ,1993.
- (6) T.Inoue, H.Kanematsu and T.Oki:"THE ELIMINATION OF COMPONENT MATERIALS FROM ALUMINUM MATRIX COMPOSITE BY MOLTEN SALT PROCESS AND THE MECHANISM OF THIS PROCESS ", Proc. of 9th Intern. Sympo on Molten salts, p646-653, ECS,Inc.,1994 .



analytical conditions

XRD : Cu anode, 40kV, 20mA, 8deg./ min.

XPS : 7kV, 30mA

EDX : 20kV, 2×10^{-10} A, W.D. 15mm

Fig.1 Flowchart of experimental procedures

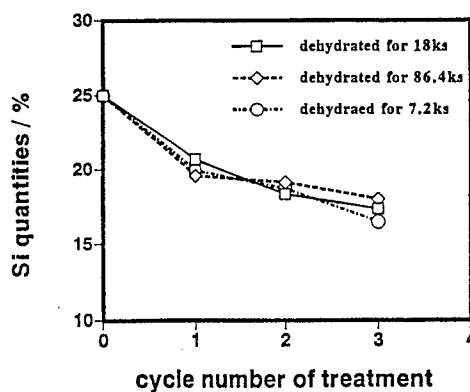


Fig.2 Changes of the amount of residual Si in the treated specimens for 3.6ks at 1033K in KCl-NaCl molten salt

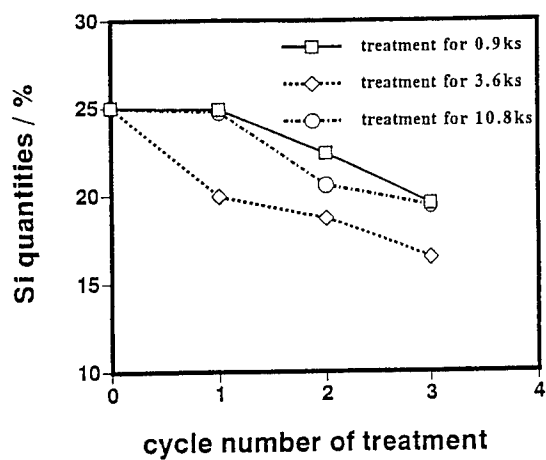


Fig.3 Changes of the amount of residual Si in the treated specimens at 1033K in KCl-NaCl molten salt

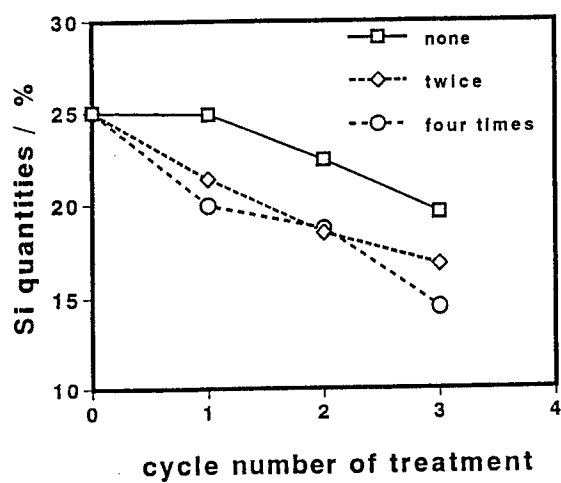


Fig. 4 Changes of amount of residual Si in the treated specimen by agitation times in KCl-NaCl molten salts

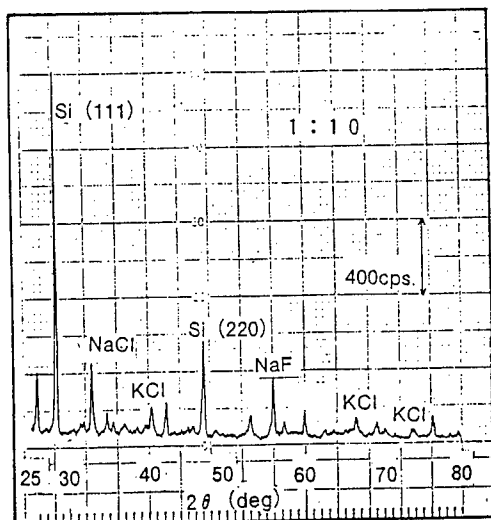


Fig. 5 XRD spectra for residual materials in the treated salt for 3.6ks at 1033K : (sample/salt=1/10)

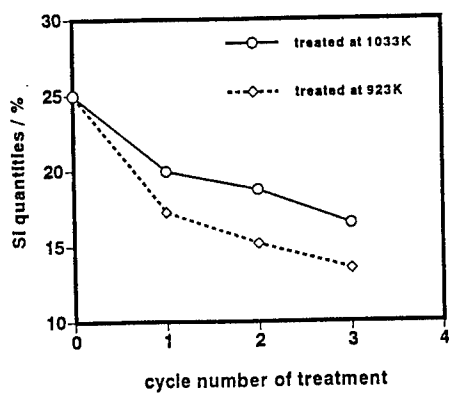


Fig.6 Changes of the amount of residual Si in the treated specimens for 3.6ks in KCl-NaCl molten salt

MODIFICATION OF LiCl-LiBr-KBr ELECTROLYTE FOR LiAl/FeS₂ BATTERIES

T. D. Kaun, A. N. Jansen,
G. L. Henriksen, and D. R. Vissers
Argonne National Laboratory
Chemical Technology Division
9700 South Cass Avenue
Argonne, IL 60439

ABSTRACT

The bipolar LiAl/FeS₂ battery is being developed to achieve the high performance and long cycle life needed for electric vehicle application. The molten-salt (400 to 440°C operation) electrolyte composition for this battery has evolved to support these objectives. An earlier change to LiCl-LiBr-KBr electrolyte is responsible for significantly increased cycle life (up to 1000 cycles). Recent electrolyte modification has significantly improved cell performance; approximately 50% increased power, with increased high rate capacity utilization. Results are based on power-demanding EV driving profile test at 600 W/kg. The effects of adding small amounts (1-5 mol%) of LiF and LiI to LiCl-LiBr-KBr electrolyte are discussed. By cyclic voltammetry, the modified electrolytes exhibit improved FeS₂ electrochemistry. Electrolyte conductivity is little changed, but high current density (200 mA/cm²) performance improved by approximately 50%. A specific feature of the LiI addition is an enhanced cell overcharge tolerance rate from 2.5 to 5 mA/cm². The rate of overcharge tolerance is related to electrolyte properties and negative electrode lithium activity. As a result, the charge balancing of a bipolar battery configuration with molten-salt electrolyte is improved to accept greater cell-to-cell deviations.

INTRODUCTION

The LiAl/FeS₂ bipolar battery is being developed to achieve the high performance and long cycle life needed for electric vehicle batteries. The electrolyte used in this molten-salt battery has a major impact on cell performance and cycle life. The initial development of the LiAl/FeS₂ cell, with LiCl-LiBr-KBr electrolyte (25-37-38 mol%), enhanced cycle life dramatically (from 100 to about 1000 cycles) without severely compromising performance. The lower temperature cell operation (400-425°C) increased cycle life [1]. The phase diagram of the LiCl-LiBr-KBr (Fig. 1) has a broad liquidus range of composition related to ion content. Its liquidus range of 1.25 to 2.6 Li⁺/K⁺ ratio at 400°C is of particular interest to the dynamic conditions of electrode operation at high current density. Melting point and

cooling curve determinations at APL [6] indicated a melting point of $312 \pm 1^\circ\text{C}$, but once liquid, this molten salt exhibits a lower freezing point of $296 \pm 4^\circ\text{C}$. For LiCl-KCl, the liquidus range at 400°C is only 1.2 to 1.81 Li⁺/K⁺ ratio. The melting point of the LiCl-KCl electrode is 354°C . Thus, the local lithium content of the LiCl-LiBr-KBr electrolyte can deviate from that in the bulk electrolyte without experiencing localized salt freezing.

A number of electrolyte characteristics must be juggled to achieve an overall improvement in cell performance: lithium conductivity, liquidus range, and cell operating temperature. In the past, the LiCl content of the LiCl-LiKBr-KBr electrolyte has been increased with concomitant increase in cell performance. Electrolyte-starved cells with 34 mol% LiCl salt gave cell impedances comparable to flooded cells. The off-eutectic composition, with its increased lithium conductivity, compensated for the reduced electrolyte volume in the electrolyte-starved, MgO powder separator used in the FeS₂ cell. Historically, increased lithium content produces increased cell performance, but usually at the expense of cycle life, as with LiF-LiCl-LiBr at 465°C . Analyses with cyclic voltammetry has showed improved kinetics in FeS₂ electrodes using the electrolytes with higher lithium-ion content. The charge/discharge reversibility also improves with higher lithium-ion content, as had been observed earlier with LiCl-LiBr-KBr at a given temperature when compared to the 58 mol% LiCl-KCl electrolyte [2]. FeS₂ cells have 34 mol% LiCl-32.5 mol% LiBr-33.5 mol% KBr electrolyte, which has a liquidus transition at 360°C . Adding LiF to LiCl-LiBr-KBr has also been examined, but smaller increases in ionic conductivity were obtained. Based on the LiF-LiBr-KBr phase diagram [3], the eutectic composition contains only a few mole percent LiF.

We set general guidelines for modifying the LiCl-LiBr-KBr (34-33-33 mol%) electrolyte with other lithium halides: (1) The lithium-ion content should be raised without raising the electrolyte liquidus temperature. (2) The liquidus range of the lithium-ion content at 425°C should not be diminished. (3) The relatively lower ionic conductivity of some lithium halides (e.g., LiI compared to LiF) should be minimized.

BACKGROUND

Three lithium-ion-containing molten salts have been employed in lithium/sulfide battery development: LiCl-KCl, LiCl-LiBr-KBr, and LiF-LiCl-LiBr [4]. We have determined conductivities as a function of temperature for their eutectic compositions using the AC impedance technique. The results are plotted in Fig. 2. Each of these molten salts has unique properties that affect cell development. The LiCl-KCl eutectic has a 354°C melting point, while cells are operated at 450°C where the conductivity is 1.4 S cm^{-1} [5]. Although the LiCl-KCl electrolyte was the baseline electrolyte for primary thermal batteries and secondary batteries, it is being replaced by the three-component salts. The LiF-LiCl-LiBr (all lithium electrolyte) has the highest conductivity, about 3.0 S cm^{-1} at 450°C [6]. On the other hand, the LiCl-LiBr-KBr electrolyte, with its low melting point of 320°C and broad liquidus region, allowing large Li/K ion ratio deviations from that of the eutectic, provides

a stable operating environment at 400°C for the FeS₂ electrode [2,7]. It has a conductivity of 1.3 S cm⁻¹ at 450°C. The Li⁺ and K⁺ ion activities of these molten salts regulate solubilities of charge/electrode discharge products and electrode kinetics. As will be discussed later, self-discharge rates, cell performance, and cycle-life stability strongly depend upon the electrolyte properties.

Use of LiCl-LiBr-KBr electrolyte allows Li/FeS₂ cell operation at considerably lower temperatures (400-425°C) than do the other electrolytes (LiCl-KCl or LiF-LiCl-LiBr). In general, Li/FeS₂ cells with LiF-LiCl-LiBr are operated at 475°C, where corrosion reactions are more likely to limit cycle life. Also, thermal management of the Li/FeS₂ battery operated at 475°C requires an active heating and cooling system, whereas at 425°C greater temperature fluctuations can be tolerated to ease requirements of the thermal management system.

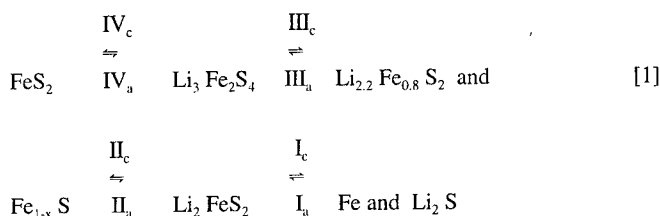
A variation of this electrolyte, an LiCl-rich composition, was identified as the electrolyte of choice for use in "electrolyte-starved" cells (i.e., cells that contain only a limited quantity of electrolyte in the pores of the MgO powder separator). The LiCl-rich composition of LiCl-LiBr-KBr (34-33-33.5 mol %) possesses a 25% higher ionic conductivity (1.7 S cm⁻¹) than the LiCl-LiBr-KBr eutectic at 425°C (Fig. 2). This higher conductivity allows these electrolyte-starved cells to operate with a cell impedance, AS_I, comparable to that of flooded cells that employ the eutectic electrolyte [11].

The addition of LiI (5 mol%) to LiCl-LiBr-KBr was found to lower the eutectic electrolyte melting point 10°C. The increased lithium content of the modified electrolyte due to the LiI addition does not anticipate higher conductivity because the Li⁺ conductivity of LiI is lower than that of the other lithium halides. Therefore, the two effects counterbalance. Any addition of LiI should also be minimized due to its high density and high affinity for water. A small addition is sufficient to improve cell kinetics. As discussed earlier, the liquidus range of the electrolyte has proven to be an important property to support high performance. The effect of LiI addition to the LiCl-LiBr-KBr electrolyte is suggestive of an extended range of liquidus composition of the cell operating temperature.

Electrochemistry of the FeS₂ Electrode

The electrochemistry of FeS₂ in LiCl-LiBr-KBr was examined previously using cyclic voltammetry and compared to LiCl-KCl [2]. The LiCl-LiBr-KBr electrolyte exhibits improved reversibility. The cyclic voltamograms are generated at a low sweep rate of 0.02 mV/s on a 75-mg sample of FeS₂. Under these conditions, summed areas of either anodic or cathodic peaks exceed 80% of theoretical capacity. LiAl/FeS₂ are only operated in the upper voltage plateau of the FeS₂ electrode. As such, the potential sweep is approximately 1.6 to 1.9 volts vs. LiAl reference electrode.

The dominant features of these voltammograms, Fig.3a, are consistent with those of FeS_2 in LiCl-KCl eutectic, which were reported by Preto et al. [8]. Roman numerals label the peaks, with "a" for anodic and "c" for cathodic. The corresponding sequence of phases at the various states of charge are assigned according to the work of Tomczuk et al. [9] as follows:



These are equilibrium phases and do not imply reaction mechanisms. Of particular interest for this study is the separation of the anodic and cathodic high-voltage peaks (IVa and IVc), which indicates the reversibility of this reaction. A notable difference between the cyclic voltammograms of FeS_2 in LiCl-LiBr-KBr and those of FeS_2 in LiCl-KCl is that this peak separation (difference in leading edge potentials, LEP) is less: 95 mV vs. 120 mV, respectively. (The lower plateau capacity of reaction peak I is not shown). Also, the leading edge of peak IVa does not exhibit the shoulder found for FeS_2 in LiCl-KCl [2]. These differences indicate improved reversibility from a molten salt with a higher Li^+ ion activity.

The emf for the $\text{FeS}_2 \rightarrow \text{Li}_3\text{Fe}_2\text{S}_4$ phase transition has been reported by Tomczuk et al. [10], as

$$\text{emf} = 1.542 + 0.0005231 T (^\circ\text{C}) \quad [2]$$

The differences between the equilibrium potentials of the reaction peaks with their leading-edge potentials (LEPs) for peaks IVa and IVc indicate the over potentials for these reactions. The cathodic over potentials are quite small (4-14 mV), while the anodic overpotential of peak IVa is about 85 mV at 400°C. Most significantly, the overpotential of charging the high voltage reaction of FeS_2 (IVa) in LiCl-LiBr-KBr at 450°C is 20 mV less than it is in LiCl-KCl eutectic.

The cyclic voltammograms indicate good stability of FeS_2 in LiCl-LiBr-KBr. At 425°C, soluble polysulfides are not generated, as evidenced by the lack of activity in the voltage region 1.95 to 2.10 V vs. LiAl. Generation of soluble polysulfides would lead to electrode capacity loss. Unlike FeS_2 , CoS_2 and NiS_2 generate Li_2S in charging their high voltage reaction, which can be further oxidized to soluble Li_2S_2 [2].

Electrolyte modifications are also assessed by cyclic voltammetry, Fig. 3. Adding LiF is a unique approach to improving FeS₂ electrochemistry. For the most part, the LiF remains as a separate solid phase in molten LiCl-LiBr-KBr (as indicated by differential thermal analysis). The liquidus point and the liquidus range of lithium-ion content are largely unaffected. Only about 1 mol% LiF solubilizes, as shown by the LiF-LiBr-KBr phase diagram. [3] As shown in the cyclic voltammograms, Fig. 3b, a dispersion of LiF within the positive electrode can have a significant effect upon FeS₂ electrode reversibility. Reversibility of the positive electrode is assessed by examining the difference in leading-edge potentials (Δ LEP) of the oxidation and reduction reaction peaks (FeS₂ ↔ Li₃Fe₂S₄). As indicated by the cyclic voltammograms in Fig. 3, the Δ LEP of the FeS₂ electrode with the LiF-containing salt is 40 mV, compared to 85 mV for the standard electrolyte LiCl-LiBr-KBr. A local increase in Li⁺ concentration would explain the improved FeS₂ electrode reversibility. The improved reversibility in 2.5-cm-dia cells using the dispersed LiF was indicated by a 20% reduced cell impedance.

The Li-alloy Electrode and Overcharge Tolerance

A "lithium shuttle" mechanism (LSM) was developed to provide lithium/sulfide cells with an overcharge tolerance capability [11-13] by forming a second lithium alloy phase in the negative electrode, as the cell reaches the overcharged state. This second phase possesses a higher lithium activity than the standard $\alpha + \beta$ Li-Al alloy, thereby significantly increasing the concentration of lithium metal dissolved in the electrolyte. Dissolved lithium is free to diffuse across the electrolyte/separator and react chemically at the positive electrode in a self-charge reaction. The higher dissolved lithium concentration produces a higher self-discharge rate and allows electrochemical charging of the cell to proceed at a rate equivalent to the self-discharge rate without causing any net change in the state-of-charge of the cell. The ultimate LSM rate is controlled by the lithium activity of the overcharge alloy, the electrolyte composition, the operating temperature, and the structure and thickness of the separator. Figure 4 illustrates the effects of electrolyte composition and temperature on the LSM rate for a given alloy and separator design. The rates are fit to Arrhenius expressions for the three electrolyte compositions shown. These rate expressions agree well with available physical data for lithium solubility, including dimerization of lithium for the respective molten-salt compositions. That is, Li₂⁺ would form in all lithium (LiF-LiCl-LiBr) electrolyte, whereas LiK⁺ would form in the K⁺-containing molten salts (LiCl-KCl and LiCl-LiBr-KBr). In general, the electrolyte composition establishes a level of lithium solubility to enable the LSM to operate [11].

Modifying the LiCl-LiBr-KBr has directly influenced the LSM rate at a given temperature. Typically, an end-of-charge trickle-charge rate of 2.5 mA/cm² was available to charge/equalize the bipolar Li/FeS₂ battery. This rate was sufficient for extremely well-matched cells having only low-level defects and similar separator characteristics, but it meant that cells with greater than 1 to 2 mA/cm² self-discharge rate would eventually be lost from the battery. The addition of LiF diminished the LMS rate to 1.5 mA/cm², while adding

LiI increased the LSM rate to 5 mA/cm² at 425°C. The extend of lithium solubility in the modified molten-salt explains the changed LSM rates. The lithium content is little changed by the modifications. The LiI addition provides a much-sought-after 50% enhancement of the LSM rate. With the increased LSM rate of 5 mA/cm², a battery developer can accept a greater cell-to-cell deviation and still maintain bipolar battery charge/equalization capability.

A combination of LiF and LiI electrolyte additives is of interest because it increased cell capacity utilization by 23% for 13% increased specific energy. Subsequent tests established that the enhanced overcharge tolerance of LiI addition is retained and overcomes the reduced LSM rate that occurred from the singular LiF addition. The LSM rate for overcharge tolerance with both additives, LiF and LiI, was also determined to be 5 mA/cm² at 440°C. Two consecutive cycles are compared: one charge to a voltage cutoff, a subsequent cycle of charge, followed by a 1.0 A trickle charge. A 2.5 Ah overcharge capacity (without increased discharge capacity) over a 4-h period translates into a 5 mA/cm² trickle charge tolerance rate. An underlying self-discharge rate of 0.3 mA/cm² is taken into account. Another examination of LSM rate submits the cell to 4-h periods of trickle charge at 0.4 to 0.8 A, Fig.5. Again, 0.6 A (or 5 mA/cm²) produces a steady cell voltage during the extended trickle-charge period as it equals the LSM rate for the cell. This rate closely approximates the LSM rates for LiCl-LiBr-KBr with only LiI added.

Cell Performance with Modified Electrolyte

Tests with full-sized bipolar cells were conducted to evaluate performance improvement related to electrolyte modifications. The electrolyte additives indicated a progressive improvement in achieved specific energy. Three cells were operated with the same FeS₂-15 mol% CoS₂ positive electrode of 40 Ah theoretical capacity but different electrolyte (Fig. 6). A 5 mol% LiI addition increased FeS₂ capacity utilization by 13.7% to 78.6% of theoretical capacity. The further addition of a LiF dispersion (4 wt%) further increased FeS₂ capacity utilization by 22.7% to 85% of theoretical capacity. The cell capacity was increased from approximately 28 Ah to approximately 34 Ah at 75 mA/cm² discharge current density. With two additives, cell specific energy at the C/3 rate was increased by 13%, to 189 Wh/kg.

The ultimate evaluation of the electrolyte modification is the cell power capability. Simulated electric-vehicle driving profiles of repetitive power pulsing (DST) as seen in Fig.7 are generally used for performance assessment. By testing a cell under a series of driving profiles having increased power demand (70 to 150 W/cell), a Ragone-type plot can be generated. This new method of testing provides specific energy/specific power tradeoffs to aid battery design. As shown in Fig. 8, the electrolyte modification provided nearly 50% increased power performance at test profiles that achieved similar net specific energy. For example, at 140 Wh/kg, the modified-electrolyte cell supported 600 W/kg power pulses (8-s duration), in comparison to only 400 W/kg for the standard-electrolyte cell.

A further objective of the electrolyte modification studies is to improve battery-level performance. Specifically, for bipolar battery operation, a LSM has been developed to enable equalization of cell capacities in a bipolar stack without hard-wired equalization equipment. The chemistry of each cell is capable of tolerating a trickle charge (5 mA/cm^2). A strong cell can tolerate the trickle charge without destructive overcharging, while a weaker cell would gain in discharge capacity. [11] A 4-cell stack Li/FeS_2 is shown to equalize in state of charge by undergoing a period of trickle charge after a normal charge to a battery voltage cutoff, Fig.9. During two trickle-charge periods shown (125 to 127 h and 135.5 to 137.5 h) the voltage of the weaker cell (02) increases in voltage and subsequent discharge capacity, while the remaining three cells safely tolerate a 0.6A trickle-charge period of 2 h. The weak cell (02) picks up charge as the trickle charge exceeds its self-discharge rate, while the other cells, closer to full-charge state, have an LSM rate of 5 mA/cm^2 to equal the trickle-charge rate. The electrolyte modification has improved the rate of cell capacity equalization at the battery level through an increased rate of the trickle-charge tolerance. Greater cell-to-cell deviations are tolerated, such that battery cycle life and performance is improved.

SUMMARY

Small additions of LiF and LiI to LiCl-LiBr-KBr electrolyte has produced some significant improvements in bipolar Li/FeS_2 battery performance and bipolar battery operation. Physical property changes, such as lithium content, lithium-ion conductivity, and liquidus range, promote FeS_2 electrode reversibility. The influence of the LiF additive was examined by cyclic voltammetry; it increased reversibility and reduced electrode polarization. A phase diagram for LiF-LiBr-KBr provides insight into the effect of LiF addition, but no comparable diagram is available to gain understanding of the LiI addition. The significant influence of LiI on Li/FeS_2 cell chemistry implies a broadening of the liquidus range for lithium-ion content at 440°C . Likewise, lithium solubility is apparently increased by adding LiI to LiCl-LiBr-KBr to bring about an increase of overcharge tolerance rate at 5 mA/cm^2 . LiF has limited solubility and remains in the FeS_2 electrode as a dispersion of a solid (4 wt% of the positive electrode), whereas the 5 mol% LiI added permeates the cell. These electrolyte modifications increased the FeS_2 electrode capacity utilization by 28%, under a 3 h-rate discharge, 75 mA/cm^2 , rate. Of even greater significance, high power pulse capability is improved by 50% under the power-demanding EV driving profile testing (DST). With the modified electrolyte, specific energy under DST increased by 50%. Specifically, a 155 Wh/kg specific energy is achieved under DST having a repeating demand of over 500 W/kg pulse power (8-s duration). The same cell chemistry can operate at continuous high power of 170 W/kg and deliver 165 Wh/kg specific energy. Finally, the battery operation is improved with the modified electrolyte. Greater cell-to-cell deviation is accepted by an enhanced overcharge tolerance, 5 mA/cm^2 . Bipolar Li/FeS_2 battery can be charge/equalized with a faster rate of battery-level trickle charging.

ACKNOWLEDGMENTS

The authors gratefully acknowledge the support of Dr. K. M. Myles. SAFT America (G. Chagnon) provided 13-cm-dia pressed pellets to ANL's specifications. M.C. Hash contributed DTA analysis of electrolytes. Co-op students S. Nied, G. Steinkoenig, and R. Selepa, contributed to cell testing. This work was supported by the USABC and U.S. Department of Energy, B. Heinrich, R. Sutula, and K. Heitner, Project Managers.

REFERENCES

1. T. D. Kaun, T. F. Holifield, and W. H. DeLuca. in *Proceedings of the Materials and Processes for Lithium Batteries Symp.*, Electrochem. Soc., Pennington, NJ, Vol. 98-4, p. 373 (1989).
2. T. D. Kaun in *Proceedings of Joint International Symposium on Molten Salts.*, Electrochemical Society, New Jersey, Vol 87-7, p. 621 (1987).
3. C. Margheritis, G. Flor, and C. Sinistri, *Z. Naturforsch* **280**, 1329 (1973).
4. D. R. Vissers, L. Redey, and T. D. Kaun, *J. Power Sources* **26**, 37 (1989).
5. E. P. Van Artsdalen and G. Jaffe, *J. Phys. Chem.* **59**, 119 (1955).
6. T. D. Kaun, in *Proceedings of the Symposium on Rechargeable Lithium Batteries*, Ed., S. Subbaro, Electrochemical Society, New Jersey, Vol. 90-5, p. 274 (1990).
7. T. D. Kaun, *J. Electrochem. Soc.* **132**, 3063 (1986).
8. S. K. Preto, Z. Tomczuk, S. Von Winbush, and M. F. Roche, *J. Electrochem. Soc.* **130**, 264 (1983).
9. Z. Tomczuk, B. Tani, N. C. Otto, M. F. Roche, and D. R. Vissers, *J. Electrochem. Soc.* **129**, 925 (1982).
10. Z. Tomczuk and D. R. Vissers, *J. Electrochem. Soc.* **133**, 2504 (1986).
11. T. D. Kaun and P. A. Nelson, *Proceedings of Lithium Batteries Symposium*, Electrochemical Society, New Jersey, Vol. 94-4, pp. 63-74 (1994).
12. L. Redey, *J. Electrochem. Soc.* **136**, (1989).
13. T. D. Kaun, T. F. Holifield, M. F. Nigohosian, and P. A. Nelson, in *Proceedings of the Materials and Processes Symposium*, Eds., K. M. Adams and B. B. Owens, Electrochemical Society, New Jersey, Vol. 89-4, p. 383 (1989).

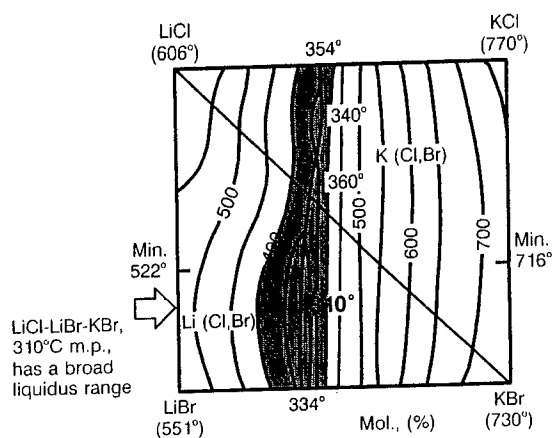


Fig. 1. Phase Diagram of LiCl-BiCl-LiBr-KBr Molten-Salt.

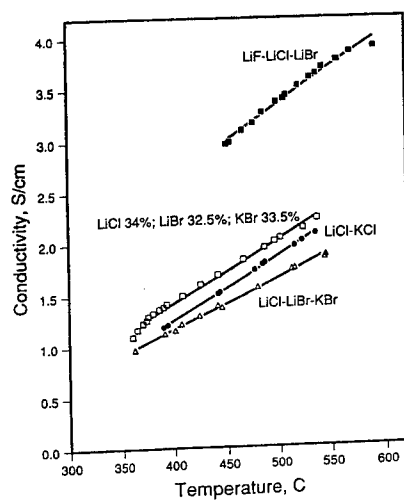
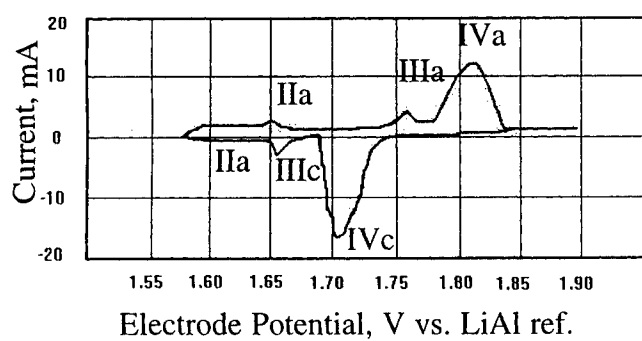


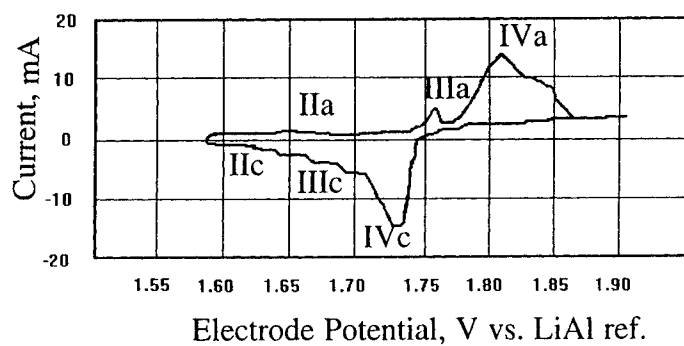
Fig. 2. Conductivities of Molten Salts for Rechargeable Lithium Batteries. The data for the three eutectic compositions are compared to a LiCl rich composition of LiCl-LiBr-KBr.

(a) LiCl-LiBr-KBr



$\Delta\text{LEP} \approx 85 \text{ mV}$

(b) LiCl-LiBr-KBr with LiF solid dispersion



$\Delta\text{LEP} \approx 40 \text{ mV}$

Fig. 3. Cyclic voltammograms of FeS_2 electrode in LiCl-LiBr-KBr exhibiting improved kinetics with a LiF dispersion.

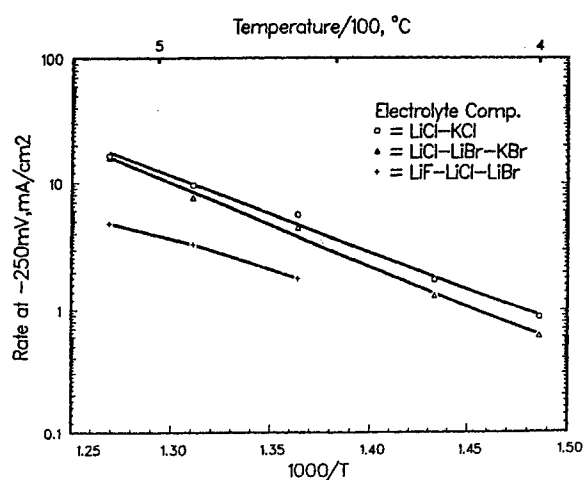


Fig. 4. Effect of Temperature Upon Lithium Shuttle Rates at about -250 mV vs. Li-Al Reference Electrode in Three Molten-Salt Electrolytes.

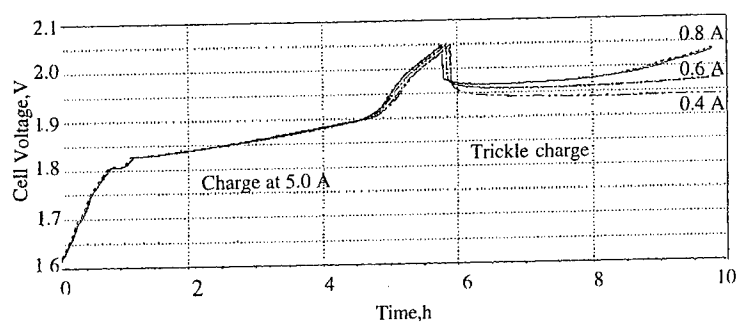


Fig. 5. Rate of overcharge tolerance determined at 5.0 mA/cm² under varied trickle-charge rates.

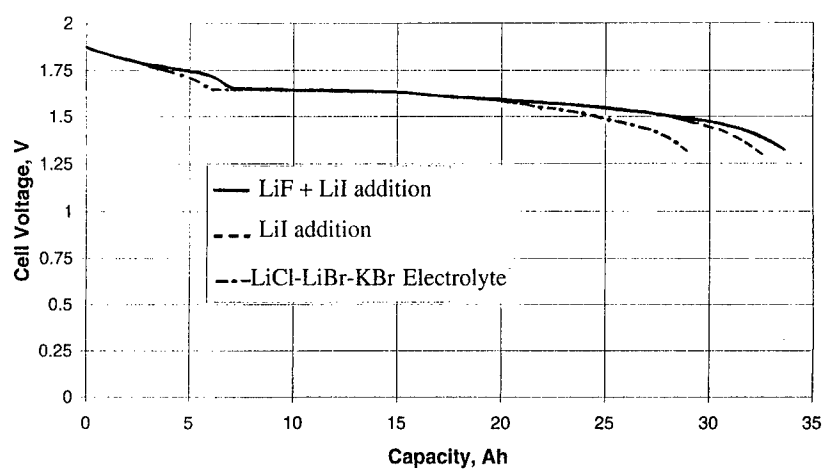


Fig. 6. Improved cell capacity as a result of LiCl-LiBr-KBr electrolyte modification.

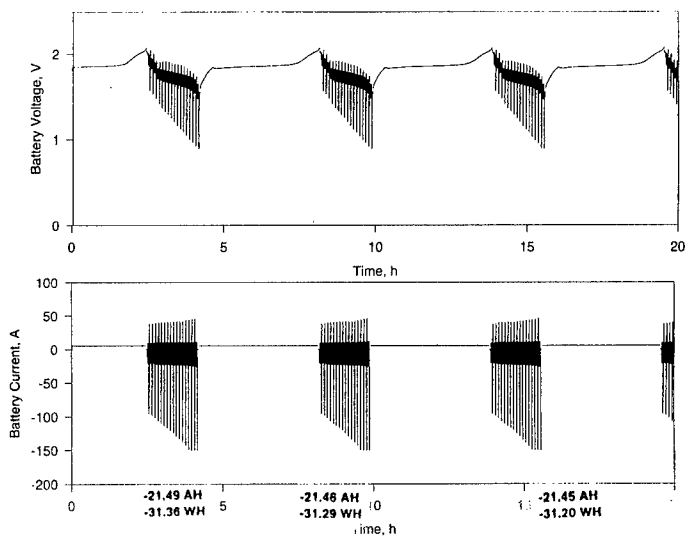


Fig. 7. Driving profile voltage and current for improved Li/FeS₂ cell, 0.275 kg.

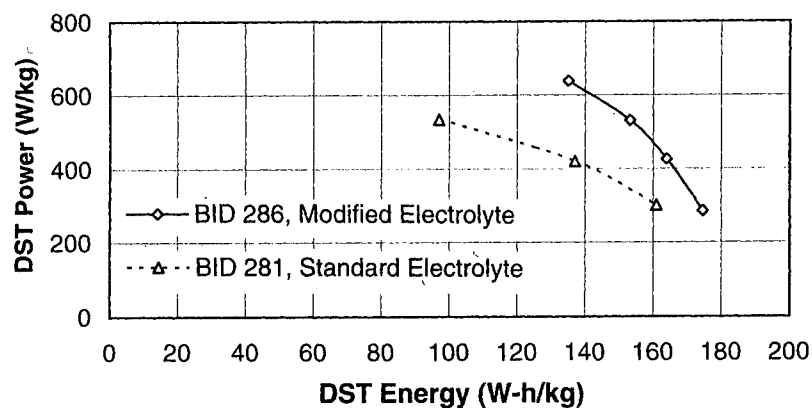


Fig. 8. The Lil modified electrolyte increases power capability for simulated driving profile tests (DST Ragone).

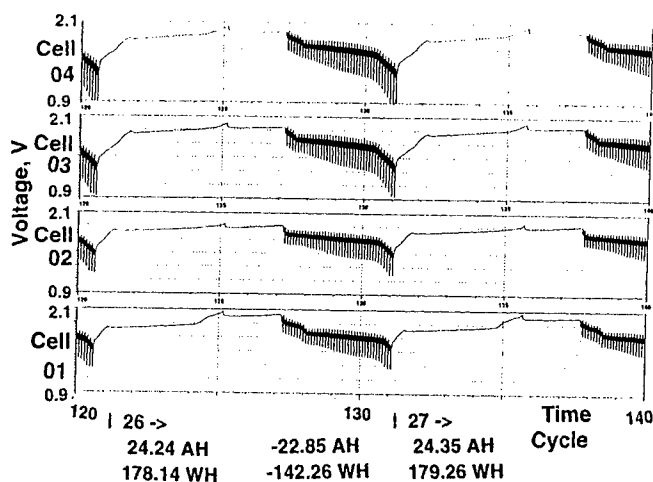


Fig. 9. Voltage of 4 cells in a bipolar Li/FeS₂ stack exhibiting charge/equalization during trickle charge.

POLARIZATION PHENOMENA AT β'' -ALUMINA/MOLTEN SALT INTERFACE

M. Matsunaga, K. Minamoto, and M. Morimitsu
Department of Applied Chemistry, Faculty of Engineering,
Kyushu Institute of Technology,
1-1 Sensui-cho, Tobata-ku, Kitakyushu 804, Japan

ABSTRACT

The polarization at the interface between β'' -alumina solid electrolyte and AlCl_3 -NaCl melt has been studied at 473 K by ac impedance spectroscopy, using cells equipped with a β'' -alumina disk. Impedance spectra at the interface were observed at frequencies lower than 400 Hz. The melt composition influences a little on the impedance spectra in the cell with a dried β'' -alumina disk. The damped surface of the β'' -alumina obstructs the movement of sodium ions from the melt into the damped layer of the β'' -alumina. The damped layer induces quite high polarization at the interface, when the acidic melt is utilized.

INTRODUCTION

Sodium batteries designated as sodium/ β'' -alumina/molten salt have been studied for electric vehicle and load leveling applications. Several kinds of this type batteries were proposed such as Na/SbCl₃(1), Na/SCl₄ (2,3), Na/SeCl₄ (4-7), Na/NiCl₂(8,9), Na/FeCl₂ (10). These cells usually utilize AlCl_3 -NaCl melts. The pretreatment of the β'' -alumina often influences on the charge-discharge behavior of these cells, especially when the acidic chloroaluminate melt is utilized.

The polarization at two interfaces, between β'' -alumina and liquid sodium and between β'' -alumina and the molten salt, should be reduced to improve the charge and discharge properties (11-13). In this paper, the effects of the surface conditions of β'' -alumina and the acidity of molten salt have been studied by ac impedance spectroscopy to clarify the polarization mechanism at the interface between β'' -alumina and AlCl_3 -NaCl melts.

EXPERIMENTAL

An experimental cell, type-I, composed of Pyrex glass compartments filled with AlCl_3 -NaCl melts as shown in Fig.1. Two identical compartments were separated by means of a Li_2O -doped β'' -alumina disk (16 mm diameter and 2 mm thickness) produced by Mitsubishi Heavy Industry Company. The β'' -alumina disk was sealed with Schott 8338 glass, of which the expansion coefficient is similar to that of β'' -alumina.

The sealed β'' -alumina disk was connected to Pyrex glass with two kinds of sealing glass tubes. Each compartment was equipped with a whirlpool aluminum electrode, which was located at a distance of ca. 6 mm from the β'' -alumina surface. This cell was washed with organic solvents in an ultrasonic cleaning equipment, and was dried under vacuum at 723 K for one week prior to use. Another cell without the β'' -alumina disk, type-II, was used to study the electrode reaction of aluminum. This cell was equipped with a 99.999% pure aluminum microelectrode as the working, a coiled aluminum wire as the counter and an aluminum reference electrode.

Melt preparation and most experimental procedures have been described previously (6,7). Impedance spectrum was measured in frequency range from 0.1 Hz to 100 kHz by using a Solatron Instruments Model 1260 impedance/gainphase analyzer, Model 1287 potentiostat, and a Toyo Technica CAP-1 electrochemical software. The impedance data were recorded and analyzed with a NEC Model PC-9801 personal computer.

RESULTS AND DISCUSSION

Impedance Spectra at β'' -Alumina/Molten Salt Interface

A well-defined impedance spectrum could be measured with the type-I cell. Figure 2 depicts typical spectra for the cell containing basic AlCl_3 -NaCl melts in both compartments. The current density is calculated as a value for unit surface area of the β'' -alumina disk. The impedance spectrum consists of two overlapped arcs; i.e., arcs-A and -B in Fig.2. The value of dc bias influence little on the arc-A. On the other hand, the higher the current flows, the smaller the size of the arc-B becomes. Considering the cell configuration, an equivalent circuit for this cell, as shown in Fig.3, consists of the aluminum electrode impedance, the melt resistance R_m , the impedance at β'' -alumina/molten salt interface Z_i , and the β'' -alumina impedance caused by grain boundary Z_{gb} , and grain bulk Z_b . It was reported that the impedance of the grain boundary and grain bulk of the β'' -alumina appeared at quite high frequency such as several MHz (14). Therefore, the arc-A and arc-B in Fig.2 correspond to the electrode reactions of aluminum electrodes and the interfaces between β'' -alumina and molten salt.

The impedance spectra for the aluminum electrode reaction in the basic AlCl_3 -NaCl melts were measured by using the β'' -alumina-free cell (type-II), in order to separate it from the impedance at the interface. A typical Nyquist plot for the aluminum deposition displays a quite small arc-C at high frequencies and a large arc-D at low frequencies as shown in Fig.4. The impedance spectrum for the anodic dissolution of aluminum is similar to that for the deposition. The time constants for these circles were compared, in order to separate the impedance at the β'' -alumina/melt interface from that of the aluminum electrode reactions. The time constant was estimated by complex nonlinear least squares fitting (15). In this study we assume that a depressed arc is caused by a simple parallel circuit consisting of resistance and constant-phase element (CPE). The time constant of the arc-A in Fig.2 is 7.8×10^{-5}

s^{-1} , that is similar to $9.9 \times 10^{-5} \text{ s}^{-1}$ for the arc-C in Fig.4. These results on the time constant suggest the arc-A observed at high frequencies in the type-I cell correspond to the electrode reactions of aluminum. The depressed shape of the arc-C indicates that the rate-determining step may be the charge transfer.

Comparing the impedance spectra at frequencies lower than 10 Hz, the arc-B in Fig.2 is different from the arc-D in Fig.4. The straight-like shape of the arc-D suggests the diffusion process in the electrochemical reaction of aluminum. Therefore, we can conclude that the arc-B corresponds to frequency response from the interface between β'' -alumina and molten salt. It should be, however, noticed that the arc-B involves somewhat the influence of the electrode reaction of aluminum. In the later discussion, the arc-B with dc bias of 0.5 mAcm^{-2} will be used as the reference spectrum to investigate the effects of the melt composition and wet surface of β'' -alumina.

Effects of Melt Composition

Figure 5 depicts the impedance spectra measured in a type-I cell, in which the melt of one compartment was replaced by 63/37 AlCl_3 -NaCl. The positive current in this figure indicates that sodium ions migrate from the acidic to the basic melt. The radius of the arc-B at low frequencies becomes short by replacing the melt to be acidic, although the arc-A at high frequencies changes little. This tendency becomes clearer as shown in Fig.6, when both compartments are filled with the 63/37 melt. These results suggest that sodium ions can move easily from the acidic melt to the β'' -alumina and *vice versa*, comparing to the case of the NaCl saturated melt. Weak Coulomb's force between sodium ion and Al_2Cl_7^- ion may cause the easier transfer of the sodium ion at the interface.

Effects of Water on β'' -Alumina

It is known that the cell resistance becomes quite high especially at charging in sodium/acidic molten salt cells, when moisture remains on the surface of the β'' -alumina. Figure 7 depicts the typical impedance spectra measured in the type-I cell with wet β'' -alumina. The real axis in this figure is compensated to zero to simplify the comparison of the results. One side of the well-dried β'' -alumina disk in the cell was exposed to the atmosphere for three days, before loading the melt. The positive current in this figure indicates that sodium ions migrate from the damped surface to the dried one in the β'' -alumina. The impedance spectrum at the interface depends on the current direction in this cell containing the NaCl saturated melt. The positive current increases the impedance at low frequencies, whereas the arc-B obtained with the opposite direction of the current is similar to the results for the dried β'' -alumina. The moisture adsorbed on the β'' -alumina surface clearly obstructs the movement of sodium ions from the basic melt into the damped layer of the β'' -alumina.

The effects of the damped layer were studied by using the cells washed with water. Figures 8 and 9 show the impedance spectra with these cells containing the basic and acidic melts, respectively. Although the cells were dried under vacuum at

723 K, the polarization became higher in both cells. These figures, however, suggest that the influence of the damped surface depends on the melt composition. While the impedance spectrum changes little with time in the cell containing the NaCl saturated melt, the damped surface layer of β "-alumina induces an increase in the polarization with time for the cell containing the acidic melt. Therefore, the effect of water adsorbed on or absorbed in β "-alumina induces high polarization in the cell utilizing the acidic AlCl_3 -NaCl melt. The mechanism of this difference of melt acidity should be studied in future.

CONCLUSION

The drying of β "-alumina is quite important to reduce the polarization at the β "-alumina/ AlCl_3 -NaCl melt, especially when the cell utilizes an acidic melt. The damped surface of the β "-alumina obstructs the movement of sodium ions from the melt into the solid electrolyte.

ACKNOWLEDGEMENTS

We would like to acknowledge the late Prof. Gleb Mamantov for helpful discussion. The authors would also like to thank the sponsorship from Kyushu Electric Power Ltd. and Ministry of Education, Science and Culture, Japan.

REFERENCES

1. A. M. Chreitzberg, J. W. Consolloy, M. R. Manning and J. C. Sklarcek, *J. Power Sources*, **3**, 201 (1978).
2. G. Mamantov, R. Marassi, M. Matsunaga, Y. Ogata, J. P. Wiaux and E. J. Frazer, *J. Electrochem. Soc.*, **127**, 2319 (1980).
3. J. Caja, T. D. J. Dunstan and G. Mamantov, *Proc. 36th Power Sources Conf.*, p.337 (1994).
4. M. Matsunaga, K. Kitagawa and K. Hosokawa, *Denki Kagaku*, **51**, 847 (1983).
5. M. Matsunaga and K. Hosokawa, *Yoyuen (Molten Salts)*, **30**, 83 (1987).
6. M. Matsunaga, T. Gouda, R. Otagawa and K. Hosokawa, *Nippon Kagaku Kaishi*, **8**, 1466 (1988).
7. M. Matsunaga, M. Morimitsu, S. Obata, K. Hosokawa, K. Rikihisa and K. Adachi, *J. Electrochem. Soc.*, **141**, 2413 (1994).
8. J. Coetzer, *J. Power Sources*, **18**, 377 (1986).
9. R. C. Galloway, *J. Electrochem. Soc.*, **134**, 256 (1987).
10. R. J. Wedlake and A. R. Tilley, *Bull. Electrochem.*, **4**, 41 (1988).
11. M. W. Breiter, B. Dunn and R. W. Powers, *Electrochim. Acta*, **25**, 613 (1980).
12. D. S. Demott, *J. Electrochem. Soc.*, **127**, 2312 (1980).
13. A. Katagiri, J. Hvistenedahl, K. Shimakage and G. Mamantov, *J. Electrochem. Soc.*, **133**, 1281 (1986).

14. A. Hooper, *J. Phys. D; Appl. Phys.*, **10**, 1487 (1977).
15. J. R. Macdonald, *Impedance Spectroscopy*, pp.16-20, pp.180-182, John Wiley & Sons, New York (1987)

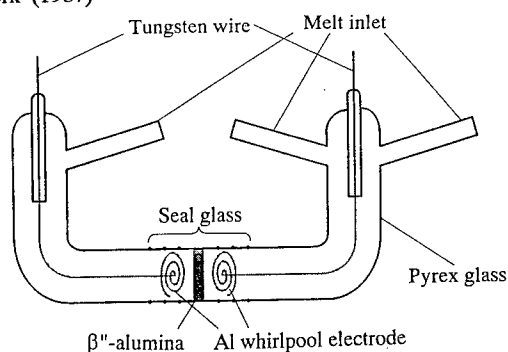


Fig.1 Typical geometry of an experimental cell (type-I).

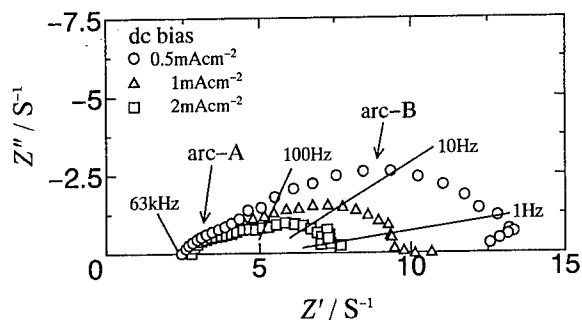


Fig.2 Impedance spectra at 473 K for the type-I cell containing basic melts. AC amplitude is $53 \mu\text{Acm}^{-2}$.

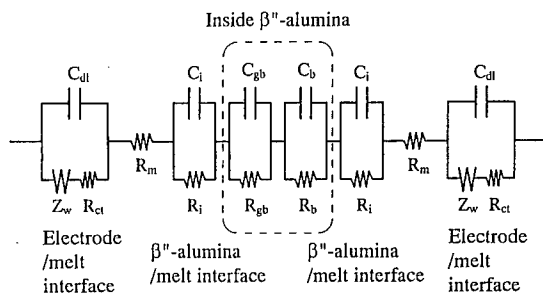


Fig.3 The equivalent circuit of the type-I cell shown in Fig.1.

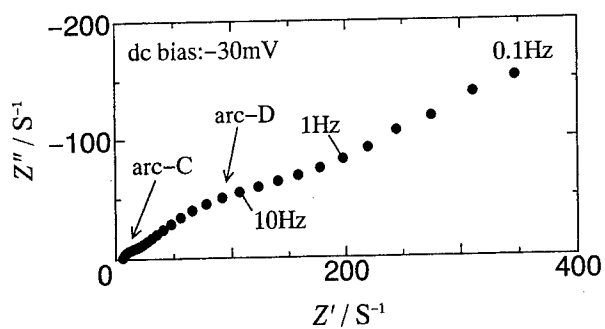


Fig.4 Impedance spectrum for the deposition of aluminum in a NaCl saturated melt at 473 K.

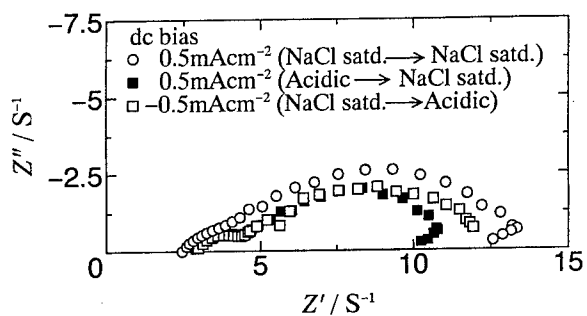


Fig.5 Impedance spectra by replacing the melt of one compartment to 63/37 AlCl_3 -NaCl in type-I cell.

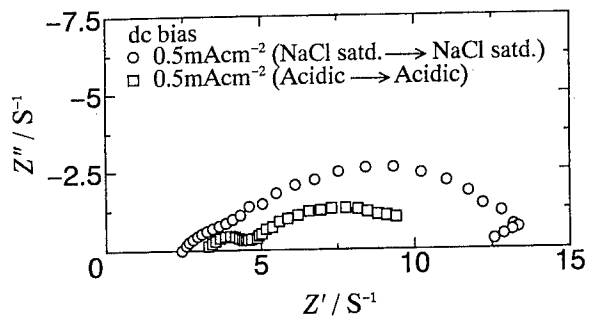


Fig.6 Effects of the melt composition on the impedance spectrum.

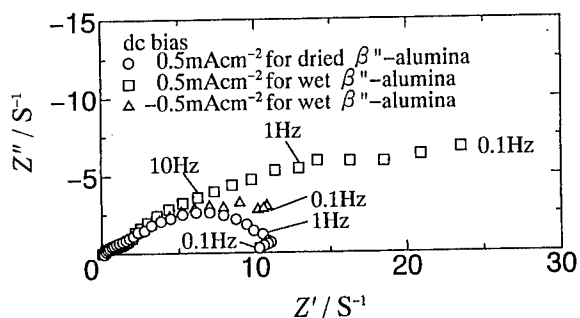


Fig.7 Dependence of the direction of dc current direction on impedance spectra, when the one side of the β'' -alumina disk contains water.

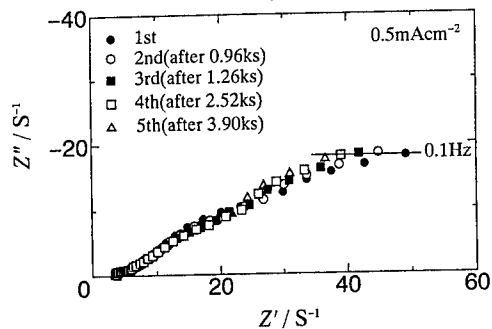


Fig.8 Effects of the damped surface of the β'' -alumina on the impedance spectra. Melt composition is NaCl saturated melt

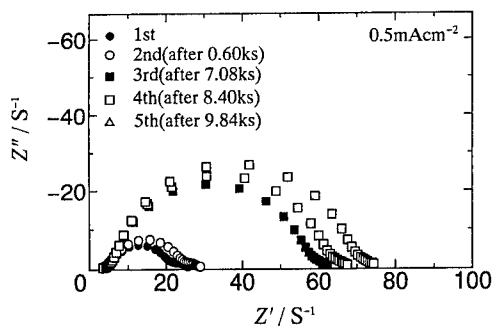


Fig.9 Effects of the damped surface of the β'' -alumina on the impedance spectra. Melt composition is 63/37.

RECHARGEABLE ALKALI METAL AND LI-AL ALLOY ANODES IN IONIC LIQUID ELECTROLYTES

Richard T. Carlin and Joan Fuller
Covalent Associates, Inc.
10 State Street
Woburn, MA 01801

ABSTRACT

The room-temperature molten salts possess a number of unique properties that make them ideal battery electrolytes. In particular, they are nonflammable, nonvolatile, and chemically inert, and they display wide electrochemical windows, high inherent conductivities, and wide thermal operating ranges. Although the ionic liquids have excellent characteristics, the chemical and electrochemical properties of desirable battery electrode materials are not well understood in these electrolytes. In this paper, we present results for rechargeable lithium and sodium anodes in buffered neutral chloroaluminate melts and lithium and lithium-aluminum alloy anodes in a BF_4^- ionic liquid.

INTRODUCTION

Room-temperature molten salts, also termed ionic liquids, are versatile solvents that have been employed in a variety of research applications, including electrochemistry, spectroscopy, gas separations, and homogeneous catalysis (1-5). Most studies have been performed in chloroaluminate room-temperature molten salts comprised of AlCl_3 and an organic cation, either 1-butylpyridinium chloride (BPC) or 1-ethyl-3-methylimidazolium chloride (EMIC) (1,2); however, recent efforts have focused on melts in which the chloroaluminate ions have been replaced with air-stable fluoroanions, such as BF_4^- , CF_3SO_3^- , $(\text{CF}_3\text{SO}_2)_2\text{N}^-$, and $(\text{CF}_3\text{SO}_2)_3\text{C}^-$ (5-8). In addition, other heterocyclic organic cations have been substituted for BPC and EMIC to increase the cathodic end of the electrochemical window and to simplify the preparation of the organic cation (5,8-10).

The room-temperature molten salts possess several properties that make them ideal candidates for battery electrolytes:

- Nonvolatile: The negligible vapor pressure allows the ionic liquid electrolytes to be operated in sealed cells at elevated temperatures without venting. In addition, the lack

of organic vapors eliminates the possibility of vapor ignition, increasing the overall safety of ionic liquid batteries.

- **Nonflammable:** When a direct flame is applied to an ionic liquid soaked in a glass separator, it burns with a flame characteristic of the anion. However, upon removing the flame source, the ionic liquid immediately extinguishes, leaving the remaining electrolyte unaltered. Therefore, a room-temperature molten salt will not ignite and burn as in the case of organic solvents currently used in lithium and lithium-ion batteries.
- **Wide Electrochemical Windows:** The ionic liquid cations and anions are extremely resistant to electrochemical reduction and oxidation, respectively. Therefore, high-voltage anode and cathode materials can be employed in the ionic liquid electrolytes to create cells that operate in excess of 4 V.
- **High Inherent Conductivities:** The ionic liquids are single-component electrolytes that possess ionic conductivities equivalent to the best organic battery electrolytes; therefore, high-power battery systems can be achieved with the ionic liquid electrolytes. Also, the manufacture of these electrolytes is easier than many conventional organic electrolytes that contain both an organic solvent and an ionic salt.
- **Wide Thermal Operating Range:** The room temperature molten salts are thermally stable to greater than 200 °C and, in some cases, maintain liquid electrolyte properties at temperatures well below 0 °C. Therefore, these electrolytes can be safely and reliably employed in batteries intended for operation in harsh, fluctuating temperature environments.
- **Chemically Inert:** The ionic liquid electrolytes are compatible with metals and polymers used in common battery devices; therefore, they do not require any specialized materials of construction or manufacturing technologies.

Although the room-temperature molten salts are exceptional battery electrolytes, the chemical and electrochemical properties of desirable battery electrode materials are not well understood in these liquids. In this paper we will briefly discuss our results on rechargeable lithium and sodium electrodes in chloroaluminate melts containing thionyl chloride and then will present more recent results on lithium and lithium-aluminum alloy electrodes in the (EMI)(BF₄) ionic liquid.

EXPERIMENTAL

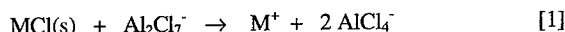
Melt preparations followed standard procedures (1,2,6,7). Unless stated otherwise, all experiments were performed under helium or nitrogen atmospheres inside a Vacuum Atmosphere glove box. Electrochemical experiments were accomplished with an EG&G PARC Model 273 Potentiostat/Galvanostat interfaced to a personal computer using the Model 270 software package. The electrodes and electrochemical cells are described in the appropriate references. Potentials are reported versus an Al/Al(III)

reference electrode (Al wire in 1.5:1.0 AlCl₃:EMIC) in chloroaluminate melts and versus an Al wire quasi-reference electrode in the (EMI)(BF₄) electrolyte.

RESULTS AND DISCUSSION

Lithium and Sodium Rechargeable Anodes

High concentrations of alkali metal ions can be introduced into the chloroaluminate room-temperature molten salts by adding an alkali metal chloride (MCl), usually LiCl or NaCl, to a melt initially containing an excess of Al₂Cl₇⁻. The alkali metal salt effectively neutralizes the Lewis-acidic Al₂Cl₇⁻ via the reaction



Because the alkali metal chloride is not soluble in the resulting melt, the only anion present is the Lewis-neutral AlCl₄⁻ species. The cations are M⁺ and the heterocyclic organic cation, usually EMI⁺. In these melts, any Al₂Cl₇⁻ ions produced by an electrochemical process are neutralized by excess solid MCl, and any chloride ions formed are precipitated as MCl. Therefore, the ionic liquid is maintained in the Lewis-neutral state, and the system is termed a buffered neutral room-temperature molten salt (11). A number of ternary room-temperature melts with compositions AlCl₃-EMIC-MCl (MCl = LiCl, NaCl, KCl, RbCl, and CsCl) have been prepared and studied (10-13).

We have examined the alkali metal couples in the buffered neutral melts and have found that only lithium and sodium with standard reduction potentials of -2.066 (± 0.005) and -2.097 (± 0.050) V vs. Al/Al(III), respectively, can be electrodeposited before reduction of the organic cation (12). Despite these thermodynamic indications, elemental lithium and sodium can not be electrodeposited from the pure buffered neutral melts. Instead, researchers have found it necessary to add a source of hydrogen chloride -- HCl₂⁻ (10,13-15), gaseous HCl (16), or a hydrogen chloride salt (17) -- to the melt before elemental lithium and sodium can be deposited and stripped at an inert substrate electrode. However, because hydrogen chloride volatilizes from the melts, the desired deposition-stripping behavior can only be maintained by adding HCl₂⁻ at regular intervals, controlling the gaseous HCl partial pressure, or introducing a large excess of a hydrogen chloride salt. Therefore, addition of hydrogen chloride is not an ideal method for achieving rechargeable alkali metal anodes in these melts.

More recently we have achieved reversible lithium and sodium deposition-stripping behavior in chloroaluminate ionic liquids by adding small quantities (< 100 mM) of thionyl chloride, SOCl₂, to the electrolyte (18). The cycling efficiencies in the presence of the thionyl chloride solute are > 90%, and the deposited alkali metals exhibit improved stability under open-circuit conditions. In addition, the low volatility of SOCl₂ (b.p. =

75.8 °C) maintains the high cycling efficiencies, even in an open vessel, for extended times. A more detailed discussion of this system is presented in an accompanying paper by Fuller and Carlin in this proceedings.

The dramatic improvements in the cyclability of lithium and sodium in the presence of SOCl_2 have been attributed to the formation of a thin, stabilizing solid-electrolyte interphase (SEI) at the electrode-electrolyte interface. This SEI has been extensively studied for lithium and lithium-ion electrodes in organic solvents (19), but less so for sodium (20,21). The SEI is formed by reaction of the alkali metal with components in the electrolyte to produce inorganic salts, such as LiCl , Li_2O , and Li_2CO_3 . To achieve a stable rechargeable system, the SEI must be a good ionic conductor for the ion of the alkali metal comprising the active electrode. In chloroaluminate ionic liquids containing SOCl_2 , we believe the SEI is composed of LiCl or NaCl , depending upon the alkali metal ion present in the melt. Figure 1 illustrates the formation and function of the SEI at lithium: (A) bare substrate electrode in buffered neutral AlCl_3 -EMIC- LiCl containing SOCl_2 ; (B) electrodeposited Li; (C) reaction of Li with SOCl_2 to produce a protective LiCl SEI layer; (D) Li^+ transport through the SEI during charge and discharge.

Lithium Anodes in (EMI)(BF₄).

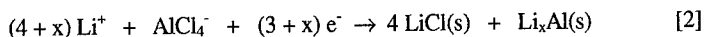
We have recently found that $< 100 \text{ mM H}_2\text{O}$ in $(\text{EMI})(\text{BF}_4) + 0.2 \text{ M LiBF}_4$ promotes the electrodeposition and stripping of lithium metal from this non-chloroaluminate ionic liquid (22). A cyclic voltammogram at Pt (area = 0.02 cm^2), illustrating the deposition-stripping of lithium and the wide electrochemical window afforded by this system ($> 5 \text{ V}$), is shown in Fig. 2. The Li/Li^+ couple found at -3 V is referenced to a quasi-reference electrode. The cycling efficiency in this voltammogram is only 60%; however, this may be improved by future optimizations.

The H_2O is believed to form a Li_2O or LiOH SEI on the electrodeposited lithium metal in a manner similar to the LiCl SEI depicted in Fig. 1. In addition, a number of reduction processes occur at the Pt working electrode before lithium deposition. Figure 3 shows an expanded view of the cathodic portion of Fig. 2 overlaid with additional scans in which the potential was switched before lithium deposition. Several small waves are found in this region and are attributed to direct reduction of water at Pt and/or to electrochemical alloying of lithium with the Pt surface. We believe these initial reduction processes act to passivate the Pt electrode towards reduction of the EMI^+ cation and cause the cathodic window limit of the melt to shift to more negative potentials.

Lithium-Aluminum Alloys in (EMI)(BF₄)

The extraordinary interest in Li-carbon anodes for Li-ion batteries with organic electrolytes prompted us to examine the possibility of using an intercalating lithium-graphite anode in an AlCl_3 -EMIC- LiCl room-temperature molten salt. Initial results

appeared to show a lithium ion intercalation at -1.4 V, but the process assigned as the deintercalation occurred at -0.1 V (23). Subsequent studies in our laboratory have shown that the process at -1.4 V is not the intercalation of lithium into the graphite lattice, but instead, it is the reduction of AlCl_4^- from the buffered neutral melt. This reduction is promoted by the presence of the lithium ion in the melt and results in the formation of an, as yet unidentified, Li-Al alloy phase (Eq. 2).



Unfortunately, the products of Eq. 2 slowly coated the graphite surface with a film of solid LiCl and a black Li_xAl alloy, making it impossible to use the Li-Al alloy as a reversible electrode (24). Also, it eliminates the possibility of using an aluminum current collector in the buffered neutral chloroaluminates melts and precludes the possibility of accessing the $\beta\text{-LiAl}$ phase which should form at +0.35 V from the Li/Li^+ couple (25).

To overcome these limitation inherent to the $\text{AlCl}_3\text{-EMIC-LiCl}$ melts, we have performed preliminary studies of Li-Al alloy formation in an $(\text{EMI})(\text{BF}_4)$ melt containing 0.2 M LiBF_4 . In these studies, an Al wire (area $\approx 1 \text{ cm}^2$) was used as the working electrode and experiments were performed on a lab bench and were exposed to the ambient atmosphere. Cyclic voltammetric scans at the Al wire in $(\text{EMI})(\text{BF}_4) + 0.2 \text{ M LiBF}_4$ are shown in Fig. 4. Formation of a Li-Al alloy at -2.72 V (versus an Al quasi-reference electrode) is clearly present, while the anodic window limit at Al is at *ca.* +2.5 V. The cycling efficiency for the $\beta\text{-LiAl}$ anode was measured consistently at $\geq 90\%$, even under these unoptimized studies.

The potential for alloy formation is compared to the Li/Li^+ reduction potential in Fig. 5 where the Li/Li^+ couple is measured at a Pt electrode in the same melt and under identical experimental conditions. The Li/Li^+ potential is at -3.07 V. Therefore, the reduction potential for the Li-Al alloy is +0.35 V more positive than elemental lithium and is in agreement with the potential expected for the $\beta\text{-LiAl}$ alloy phase (25). This alloy has an electricity storage capacity of 790 Ah kg^{-1} . At this time it is not clear if water is needed for alloy formation; however, preliminary data indicates that water is required only to shift the EMI^+ reduction to more negative potentials, discussed above, and not to form an SEI on the alloy surface.

Finally, chronopotentiometric experiments were performed in the $(\text{EMI})(\text{BF}_4) + 0.2 \text{ M LiBF}_4$ ionic liquid at an Al wire as the $\beta\text{-LiAl}$ anode substrate and at a commercial Li_xCoO_2 cathode material. The charge and discharge chronopotentiometric curves for these two electrode materials are shown in Fig. 6. The $\beta\text{-LiAl}$ electrode is well behaved with charge and discharge potentials (0.5 mA cm^{-2}) of -2.81 and -2.52 V, respectively. The Li_xCoO_2 electrode displays charge and discharge potentials of 1.46 and 1.05 V with

an open-circuit potential of *ca.* 1.34 V. Therefore, a properly engineered β -LiAl | (EMI)(BF₄) + LiBF₄ | Li_xCoO₂ cell is expected to have an operating voltage of *ca.* 4 V.

ACKNOWLEDGMENTS

This work was supported by the Air Force Office of Scientific Research. Opinions, interpretations, conclusions, and recommendations are those of the authors and are not necessarily endorsed by the United States Air Force.

REFERENCES

1. C. L. Hussey, in *Chemistry of Nonaqueous Solvents*, A. Popov and G. Mamantov, Editors, Chapter 4, VCH Publishers, New York (1994).
2. R. T. Carlin and J. S. Wilkes, in *Chemistry of Nonaqueous Solvents*, A. Popov and G. Mamantov, Editors, Chapter 5, VCH Publishers, New York (1994).
3. G. P. Pez, R. T. Carlin, D. V. Laciak, and C. Sorenson, "Method for Gas Separation," U. S. Patent No. 4,761,164, issued 2 August 1988. Proprietary research performed at Air Products and Chemicals, Inc.
4. R. T. Carlin and J. S. Wilkes, *J. Mol. Catal.*, **63**, 125 (1990).
5. Y. Chauvin and H. Olivier-Bourbigou, *CHEMTECH*, **25** (9), 26 (1995).
6. J. Fuller, R. T. Carlin, H. C. De Long, and D. Haworth, *J. C. S., Chem. Comm.*, 299 (1994).
7. R. T. Carlin, H. C. De Long, J. Fuller, and P. C. Trulove, *J. Electrochem. Soc.*, **141**, L73 (1994).
8. V. R. Koch, C. Nanjundiah, G. Battista Appetecchi, and B. Scrosati, *J. Electrochem. Soc.*, **142**, L116 (1995).
9. R. Gifford and J. B. Palmisano, *J. Electrochem. Soc.*, **134**, 610 (1987).
10. C. Scordilis-Kelley and R. T. Carlin, *J. Electrochem. Soc.*, **141**, 873 (1994).
11. T. J. Melton, J. Joyce, J. T. Maloy, J. A. Boon, and J. S. Wilkes, *J. Electrochem. Soc.*, **137**, 3865 (1990).
12. C. Scordilis, J. Fuller, R. T. Carlin, and J. S. Wilkes, *J. Electrochem. Soc.*, **139**, 694 (1992).
13. C. Scordilis Kelley and R. T. Carlin, *J. Electrochem. Soc.*, **140**, 1606 (1993).
14. T. L. Riechel and J. S. Wilkes, *J. Electrochem. Soc.*, **139**, 977 (1992).
15. T. L. Riechel, M. J. Miedler, and E. R. Schumacher, in *Proceedings of the Ninth International Symposium on Molten Salts*, C. L. Hussey, D. S. Newman, G. Mamantov, and Y. Ito, Editors, PV 94-13, p. 491, The Electrochemical Society Proceedings Series, Pennington, NJ (1994).
16. G. E. Gray, P. A. Kohl, and J. Winnick, *J. Electrochem. Soc.*, **142**, 3636 (1995).

-
17. B. J. Piersma, in *Proceedings of the Ninth International Symposium on Molten Salts*, C. L. Hussey, D. S. Newman, G. Mamantov, and Y. Ito, Editors, PV 94-13, p. 415, The Electrochemical Society Proceedings Series, Pennington, NJ (1994).
 18. J. Fuller, R. A. Osteryoung, and R. T. Carlin, *J. Electrochem. Soc.*, **142**, 3632 (1995).
 19. E. Peled, *Proceedings of the Symposium on Lithium and Lithium-Ion Batteries*, S. Megahed, B. M. Barnett, and L. Xie, Editors, PV 94-28, p. 1, The Electrochemical Society Series, Pennington, NJ (1994) and references therein.
 20. Y. Ma, M. M. Doeff, S. J. Visco, and L. C. De Jonghe, *J. Electrochem. Soc.*, **140**, 2726 (1993).
 21. M. M. Doeff, S. J. Visco, Y. Ma, M. Peng, L. Ding, and L. C. De Jonghe, *Electrochim. Acta*, **40**, 2205 (1995).
 22. J. Fuller, R. A. Osteryoung, and R. T. Carlin, "Lithium Anode Studies in a Tetrafluoroborate Molten Salt Electrolyte," The Electrochemical Society, Spring Meeting, Reno, Nevada, May 21-26, 1995.
 23. R. T. Carlin, J. Fuller, and M. Hedenskoog, *J. Electrochem. Soc.*, **141**, L21 (1994).
 24. R. T. Carlin, J. Fuller, Kevin Kuhn, M. J. Lysaght, and P. C. Trulove, *J. Applied Electrochem.* (in press).
 25. J. N. Reimers and J. R. Dahn, *Phys. Rev. B*, **47**, 2995 (1993).

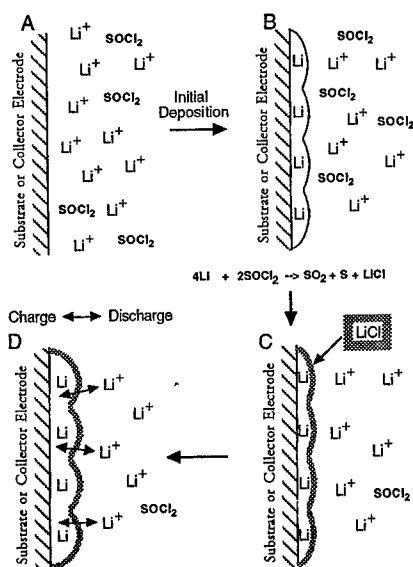


Figure 1. SEI formation and function at lithium. See text for description.

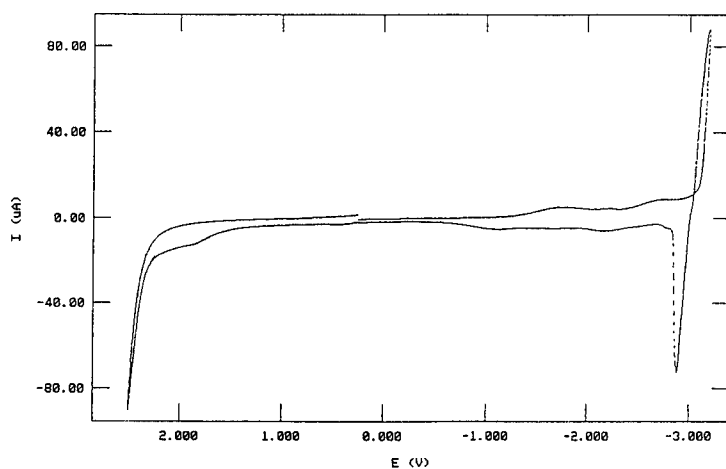


Figure 2. Cyclic voltammetry at Pt (area = 0.02 cm²) in (EMI)(BF₄) containing 0.2 M LiBF₄ and < 100 mM H₂O.

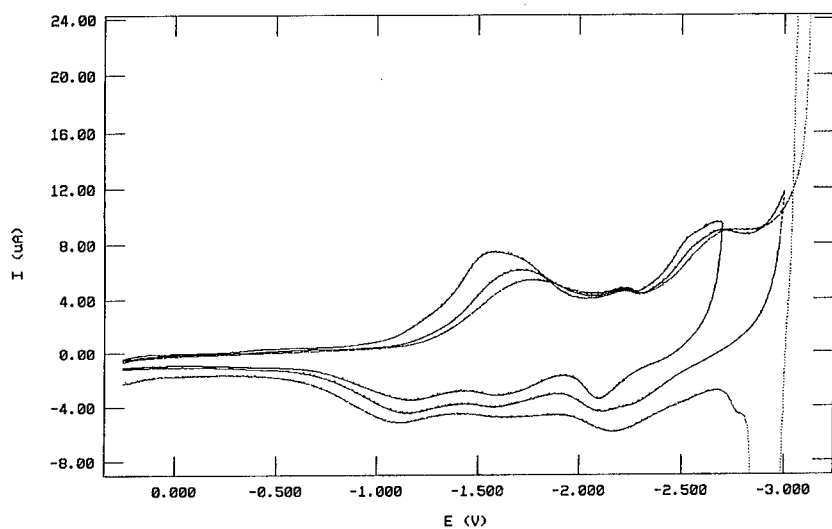


Figure 3. Expanded view of the cathodic portion of Fig. 2.

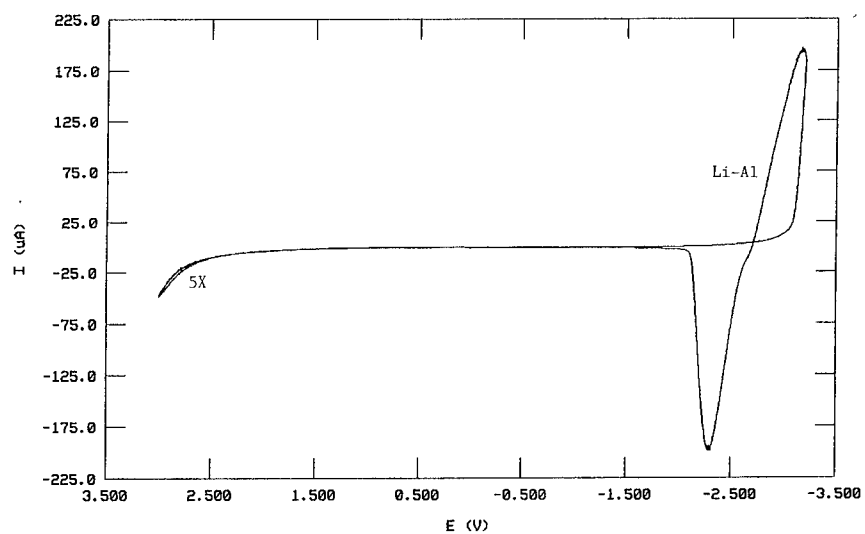


Figure 4. Cyclic voltammograms at an Al wire in (EMI)(BF₄) + 0.2 M LiBF₄.

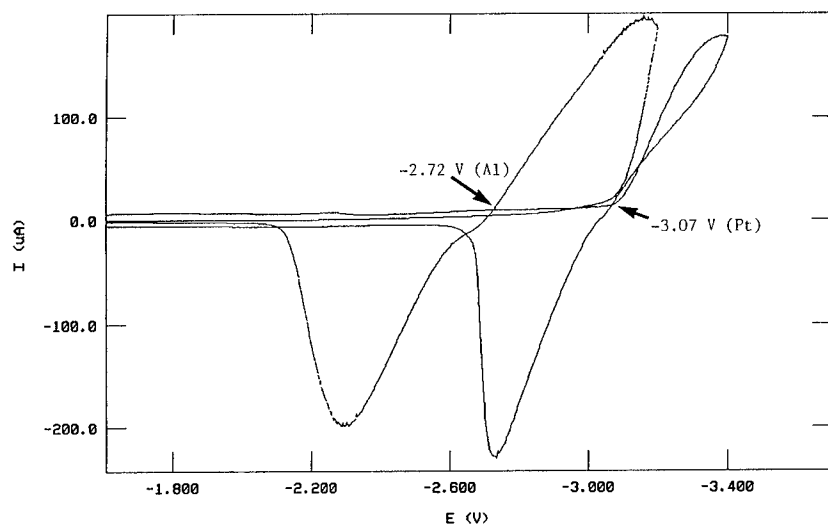


Figure 5. Cyclic voltammograms at Al (curve A) and at Pt (curve B) in $(\text{EMI})(\text{BF}_4) + 0.2 \text{ M LiBF}_4$.

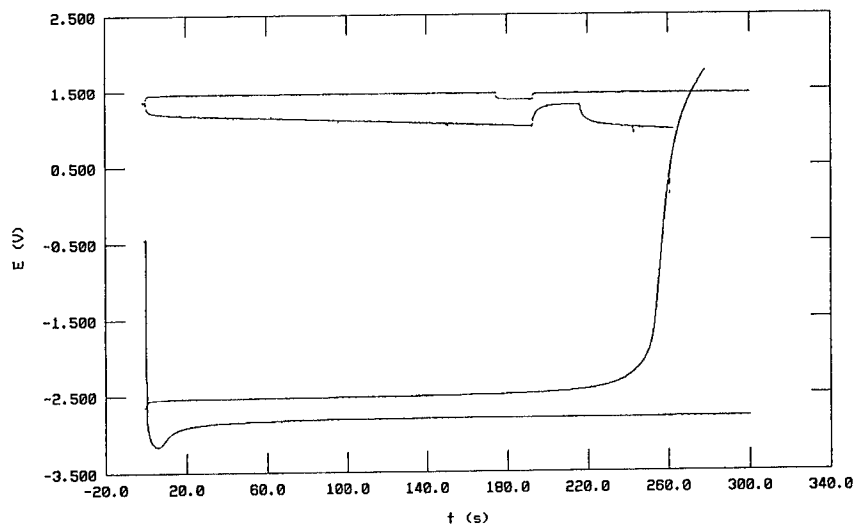


Figure 6. Chronopotentiometry at an Al wire anode (charge A; discharge B) and at a Li_xCoO_2 cathode (charge C; discharge D) in the $(\text{EMI})(\text{BF}_4) + 0.2 \text{ M LiBF}_4$.

MORPHOLOGY OF LITHIUM AND SODIUM ELECTRODEPOSITS IN ROOM-TEMPERATURE MOLTEN SALTS

Joan Fuller and Richard T. Carlin
Covalent Associates, Inc.
10 State Street
Woburn, Massachusetts 01801

ABSTRACT

We have recently demonstrated that the addition of small amounts of SOCl_2 in both sodium and lithium buffered chloroaluminate molten salts promotes the reversible stripping behavior of lithium and sodium metal with cycling efficiencies between 80-90% (1). In addition to determining cycling efficiencies, we have performed a series of optical studies in conjunction with electrochemical experiments at varying SOCl_2 concentrations in both the lithium and sodium melts. The lithium deposit appears to be dendritic in nature and does not form a uniform film on the tungsten electrode. Repeated deposition and stripping experiments (without cleaning the electrode between cycles) results in additional dendritic growth with a steady decay in the cycling efficiency. The sodium deposit is a flat uniform film on the tungsten electrode with little or no dendritic growth. Repeated deposition and stripping experiments continue without the formation of dendritic sodium metal and the cycling efficiencies remain constant.

INTRODUCTION

Room-temperature chloroaluminate molten salts have been investigated as electrolytes for high energy density batteries employing elemental lithium and sodium anodes (1-9). The primary molten salts used in these studies are prepared by adding an excess of solid LiCl or NaCl to AlCl_3 -EMIC melts (EMIC = 1-ethyl-3-methylimidazolium chloride) having AlCl_3 :EMIC molar ratios greater than 1.0, termed acidic melts. The solid alkali metal chloride reacts with the Lewis acid Al_2Cl_7^- species in the acidic melts, forming the Lewis neutral AlCl_4^- anion and introducing a high concentration of the corresponding alkali melt cation into the melt. Because the excess alkali metal chloride is insoluble in the final melt, it acts to maintain the neutral state through dissolution and precipitation reactions. Therefore, these systems have been termed buffered neutral chloroaluminate molten salts (10). The high concentration of alkali metal cations in these melts and the negative value of the alkali metal reduction potentials make the buffered neutral melts feasible electrolytes for rechargeable high energy density batteries (1-9).

In this article, we present findings on reversible lithium and sodium deposition-stripping behavior in buffered neutral melts promoted by the addition of measured quantities of thionyl chloride (SOCl_2). The cycling efficiencies in the presence of the

thionyl chloride solute are >90%, and the deposited alkali metals exhibit improved stability under open-circuit conditions (1). In addition, the low volatility of SOCl_2 (b.p. = 75.8 °C) maintains the high cycling efficiencies, even in an open vessel for extended times.

Although, the role of SOCl_2 in these systems is not certain, we believe that this system behaves in a similar fashion to the conventional organic electrolytes used to study many rechargeable lithium anodes in which "precursor" additives such as SO_2 , CS_2 , POCl_3 , and SOCl_2 are in low concentrations to the electrolyte. These additives are instrumental in the formation of a passivating film on the surface of the alkali metal anode and thus prevent further reaction between the organic electrolyte and the active metal (10).

To better understand the nature of the alkali metal deposition / passivation process, we have performed a series of electrochemical experiments in conjunction with optical studies of the electrode surface at various thionyl chloride concentrations for both LiCl and NaCl buffered melts. This allows us to correlate electrochemical experiments (cyclic voltammetry, chronoamperometry, and open circuit monitoring) with the thionyl chloride concentration in the melt and the morphology of the metal deposit.

EXPERIMENTAL

The melts were prepared under a purified helium atmosphere in a Vacuum Atmosphere dry box at ambient temperature (ca. 20 °C). Acidic melts having the molar composition 1.1:1.0 AlCl_3 :EMIC were initially prepared by the addition of sublimed AlCl_3 to EMIC while stirring. The EMIC was prepared and purified as previously described. The buffered melts were then prepared by the addition of a 50 to 100% excess of LiCl (99.99%, Aldrich) or NaCl (99.999%, Aldrich) to the 1.1:1.0 acidic melt. The melts were stirred for one week at room temperature. The melts were filtered through 0.5 micron Teflon syringe filters (Millipore). The resulting melt was crystal clear and of suitable quality for the optical microscope studies.

The buffered melt was transferred to a sealed optical microscope electrochemical cell and removed from the drybox. For a more detailed description of the cell please refer to reference 11. The cell was fitted with rubber septa and the thionyl chloride (99+%, Aldrich) was added directly to the melt using an HPLC microsyringe. All electrochemical experiments were performed at a 250 μm tungsten wire electrode, constructed as previously described. The reference and counter electrodes were aluminum wires inserted directly into the melt. An aluminum wire, used as a reference electrode, in these systems has been shown to be relatively stable over the time scale of these experiments. We did observe an approximate 100 mV shift more negative in the reduction potential of the alkali metal deposit as the concentration of SOCl_2 was increased in the melt. We are unsure at this time if this was due to a possible reaction between the aluminum wire and the SOCl_2 in solution or if it is potential shift of the alkali metal couple.

A Nikon Epiphot metallurgical inverted microscope equipped with bright-field / dark-field optics and with an attached 35 mm camera was used for optical observations and photographs. In addition, all experiments were recorded using a Sony VCR system for archival purposes. All electrochemical experiments were performed using an EG&G Princeton Applied Research Model 273 Potentiostat / Galvanostat controlled with the PAR Model 270 software package.

RESULTS AND DISCUSSION

Thionyl chloride electrochemical reduction

Figure 1a shows the electrochemical behavior at a 1.6 mm Pt electrode in a 1.1:1.0:0.1 $\text{AlCl}_3\text{:EMIC:NaCl}$ molten salt. The broad reduction waves starting at +0.4 V are assigned to the reduction of protonic species (12-13). Following addition of ca. 50 mM SOCl_2 , a new reduction wave is seen in Fig. 1b at Pt, starting at +0.7 V and peaking at -0.1 V. At a 250 μm tungsten electrode, the SOCl_2 -containing melt shows a single irreversible reduction process with a peak potential of +0.65 V (Fig. 2); protons are not efficiently reduced at tungsten electrodes in these melts (13).

Based on the above observations, the electrochemical process starting at ca. +0.7 V is assigned to the irreversible reduction of SOCl_2 . At this time, we will not speculate on the mechanism of SOCl_2 reduction in these melts; however, the symmetric peak shapes in Fig. 1b and 2 indicate the reduction is dominated by surface electrochemistry or a passivation process. No additional features are observed more negative of the potential assigned to SOCl_2 until the reduction of the alkali metal Fig. 2. Almost identical behavior has been seen for SOCl_2 reduction at microelectrodes in a $\text{SOCl}_2\text{-LiAlCl}_4$ battery electrolyte (14). The reduction of SOCl_2 at an inert electrode in this system is believed to form a passivating LiCl film on the electrode surface (15). Also, the passivation of lithium metal by chemical reaction with SOCl_2 , forming a solid-electrolyte interphase (SEI), is a critical factor in primary Li/SOCl_2 batteries (16). In the room-temperature molten salt electrolytes studied here, a similar electrochemically formed passive film may be responsible for the negative shift in the reduction potential for the EMI^+ cation which allows the lithium and sodium reductions to be so clearly resolved (see figures 3b and 4b).

It has been proposed that a thin film of LiCl or NaCl forms on the alkali metal surface and acts to protect the metal from additional attack of the molten salt. Due to the nature of the buffered melt, the alkali chloride salt would have extremely low solubility in the melt and would thus provide a sufficient passivating film. In addition to the formation of a stable SEI, it is advantageous if the alkali metal deposit is non-dendritic and uniform.

In Situ Optical Observations of Alkali Metal Deposits

Before SOCl_2 was added to the buffered neutral LiCl melt the lithium was irreversibly reduced at -1.7 V, Fig. 3a. Immediately following the addition of 10 μL SOCl_2 reversible behavior was observed with efficiencies greater than 90%, Fig. 3b.

Thionyl chloride was subsequently added in 10 μL increments to the buffered LiCl melt. A staircase cyclic voltammogram (100 mV sec^{-1} at 250 μm tungsten) was recorded after each addition to monitor any change in the cycling efficiency. The electrochemical experiments were visually monitored, and the lithium deposit was photographed after each SOCl_2 addition. The electrode was cleaned before each experiment by scanning to +3.0 V, into the chloride oxidation wave, to remove any residual film remaining on the tungsten surface.

The efficiencies obtained from the cyclic voltammetry results for each SOCl_2 concentration are tabulated in Table I for both LiCl and NaCl buffered melts. While staircase cyclic voltammetry is not the most quantitative electrochemical technique, it is a good method to qualitatively observe film behavior. In a previous paper, we have reported quantitative data on the cycling efficiencies of both lithium and sodium deposits (1).

The SOCl_2 concentration was steadily increased from 23 mM to 167 mM in the LiCl buffered melt. No apparent benefit was observed in the stability of the film at higher SOCl_2 concentrations, Table I. The recovery of lithium remained near 90% for all concentrations. During the electrochemical scan the electrode remained "clean" until the reduction of the lithium metal. The lithium metal was dark in color and appeared to be rough and nodular, forming an uneven film on the electrode surface. During stripping the lithium deposit darkened further and appeared to detach from the substrate electrode as the potential became more positive. At the end of the scan, some of the deposit was still visible on the electrode surface. This material was easily removed by sweeping anodically to +3.0 V.

In the NaCl buffered melt, the SOCl_2 concentration was increased from 18.5 mM to 148 mM. At 18.5 mM no reversible behavior was observed, Fig. 4a. Following the addition of more SOCl_2 to the melt, reversible sodium behavior was observed, Fig. 4b. Cycling efficiencies for sodium remained relatively constant at 85% for concentrations between 48 mM and 148 mM, Table I. At all concentrations above 48 mM, the sodium deposit appeared flat and grainy with no dendritic growth. The sodium film exhibited some coloration immediately following the deposition and darkened during discharge. This observation of color could be due to the reaction of the sodium metal with the organic cation or with the thionyl chloride. Although the sodium deposit stripped cleanly from the tungsten surface, the electrode was anodically cleaned before each experiment.

Chronopotentiometry

Using a LiCl buffered melt, chronopotentiometric experiments were performed at 1 μA (2 mA cm^{-2}) for 600 sec at each SOCl_2 concentration. The results are tabulated in Table II. *In situ* observation of the growth of the lithium film under dark field illumination revealed the formation of a rough and dendritic surface. The presence of the dendritic lithium was prevalent and seemed independent of SOCl_2 concentration. Growth of the

dendrites from the edges was more excessive at longer deposition times. During the stripping at 2 mA cm^{-1} , the lithium deposit appeared to disconnect from the tungsten electrode and seemed to "float" near the surface. Stripping efficiencies remained reasonably constant through all SOCl_2 concentrations. Repeated cycling of the deposition/stripping experiments without cleaning the electrode resulted in a steady decay in efficiencies; 85.6%, 80.7%, 70.6%, and 69% for four runs, respectively. This decrease in efficiency is further evidence of "dead" lithium on or near the electrode surface.

Using a NaCl buffered melt, chronopotentiometric experiments were performed at $1 \mu\text{A}$ (2 mA cm^{-2}) for 600 sec at each SOCl_2 concentration. The results are tabulated in Table III. *In situ* observation of the growth of the sodium film under dark field illumination revealed the formation of a rough but non-dendritic surface. Stripping efficiencies remained reasonably constant through all SOCl_2 concentrations. Efficiencies obtained from repeated cycling of the deposition/stripping experiments without cleaning the electrode were relatively constant at 85% for four sequential runs.

CONCLUSIONS

Lithium and sodium deposition-stripping studies performed in buffered neutral chloroaluminate molten salts show high cycling efficiencies in the presence of a low concentration of SOCl_2 . The role of SOCl_2 in these systems is not certain; however, it may produce a stabilizing SEI layer in a similar manner as in primary Li- SOCl_2 batteries. Optical observations indicate that the lithium deposit is dendritic in nature at all SOCl_2 concentrations studied. The sodium deposit is flat and non-dendritic at all SOCl_2 concentrations. Future studies will investigate the passivating film and attempts will be made to "flatten" the lithium deposit through the use of other additives.

REFERENCES

1. J. Fuller, R. A. Osteryoung, and R. T. Carlin, *J. Electrochem. Soc.*, **142**, 3632 (1995).
2. C. Scordilis-Kelley and R. T. Carlin, *J. Electrochem. Soc.*, **141**, 873 (1994).
3. G. E. Gray, J. Winnick, and P. A. Kohl, Abstract 140, p. 220, The Electrochemical Society Extended Abstracts, Vol. 94-2, Miami Beach, FL, October 9-14, 1994.
4. T. L. Riechel, M. J. Miedler, and E. R. Schumacher, in *Proceedings of the Ninth International Symposium on Molten Salts*, C. L. Hussey, D. S. Newman, G. Mamantov, and Y. Ito, Editors, PV 94-13, p. 491, The Electrochemical Society Proceedings Series, Pennington, NJ (1994).
5. B. J. Piersma, in *Proceedings of the Ninth International Symposium on Molten Salts*, C. L. Hussey, D. S. Newman, G. Mamantov, and Y. Ito, Editors, PV 94-13, p. 415, The Electrochemical Society Proceedings Series, Pennington, NJ (1994).
6. G. E. Gray, J. Winnick, and P. A. Kohl, in *Proceedings of the Symposium on Batteries and Fuel Cells for Stationary and Electric Vehicle Applications*, A. R. Landgrebe and Z. Takehara, Editors, PV 93-8, p. 134, The Electrochemical Society Series, Pennington, NJ (1993).

7. G. E. Gray, J. Winnick, and P. A. Kohl, in *Proceedings of the Intersociety Energy Conversion Engineering Conference*, 28th, Vol. 1, p. 1139 (1993).
8. C. Scordilis-Kelley and R. T. Carlin, *J. Electrochem. Soc.*, **140**, 1606 (1993).
9. T. L. Riechel and J. S. Wilkes, *J. Electrochem. Soc.*, **139**, 977 (1992).
10. S. B. Brummer, V. R. Koch, and R. D. Rauh, in *Materials for Advanced Batteries*, D. W. Murphy, J. Broadhead, and B. C. Steele, Editors, p. 128, Plenum Press, New York (1980).
11. R. T. Carlin, W. Crawford, and M. Bersch, *J. Electrochem. Soc.*, **139**, 2720 (1992).
12. M. A. M. Noel, P. C. Trulove, and R. A. Osteryoung, *Anal. Chem.*, **63**, 2892 (1991).
13. S. Sahami and R. A. Osteryoung, *Anal. Chem.*, **55**, 1970 (1983).
14. W. M. Hedges, D. Pletcher, and C. Gosden, *J. Electrochem. Soc.*, **134**, 1334 (1987).
15. Y.-K. Choi, B.-S. Kim, and S.-M. Park, *J. Electrochem. Soc.*, **140**, 11 (1993).
16. E. Peled, in *Lithium Batteries*, J. P. Gabano, Editor, p. 43, Academic Press, New York, NY (1983).

Table I: Cycling efficiencies for lithium and sodium deposits at various thionyl chloride concentrations. 100 mV sec⁻¹ cyclic voltammograms at a 250 μ m tungsten electrode.

LiCl Buffered Melt SOCl ₂ Concentration (mM)	% Efficiency	NaCl Buffered Melt SOCl ₂ Concentration (mM)	% Efficiency
23	90	18.5	0
60	87	48	83
76	91	74	85
106	91	111	84
137	91	148	85
167	91		

Table II: Lithium deposition-stripping at 1 μ A (2 mA cm⁻²) for 600 sec at each SOCl₂ concentration.

SOCl ₂ Conc.	E _{deposition} (V)	E _{stripping} (V)	% Efficiency
0.076M	-2.295	-2.240	88.5
0.106M	-2.310	-2.255	88.2
0.137M	-2.335	-2.285	89
0.167M	-2.360	-2.310	88

Table III: Sodium deposition-stripping at 1 μ A (2 mA cm⁻²) for 600 sec at each SOCl₂ concentration.

SOCl ₂ Conc.	E _{deposition} (V)	E _{stripping} (V)	% Efficiency
0.048M	-2.410	-2.185	83
0.074M	-2.500	-2.220	82.8
0.111M	-2.610	-2.505	82.8
0.148M	-2.665	-2.565	80

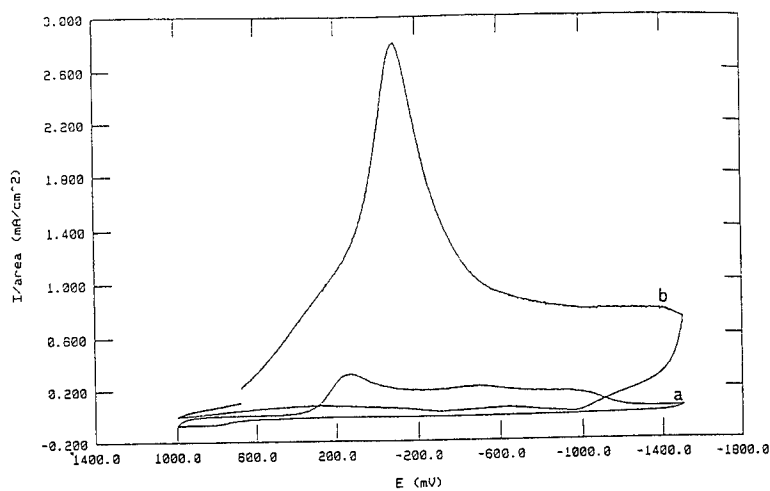


Fig. 1. Electrochemical behavior in 1.1:1.0:0.1 AlCl_3 :EMIC:NaCl at a 1.6 mm Pt electrode (a) without SOCl_2 and (b) after the addition of ca. 50 mM SOCl_2 . Scan rate = 100 mV s^{-1} .

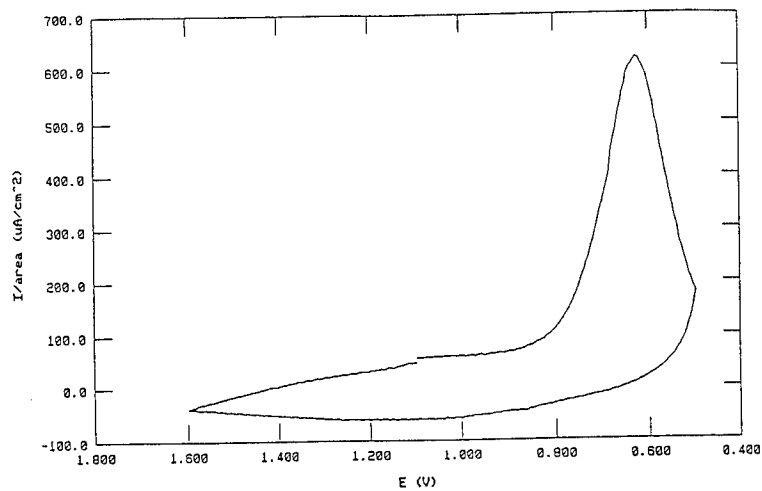


Fig. 2. Cyclic voltammogram showing SOCl_2 reduction in 1.1:1.0:0.1 AlCl_3 :EMIC:NaCl at a 250 μm tungsten electrode. Scan rate = 100 mV s^{-1} .

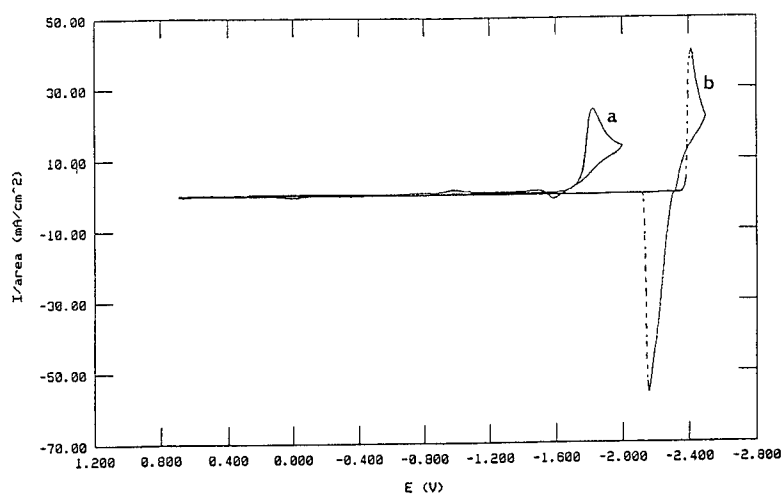


Fig. 3. Lithium electrochemistry in 1.1:1.0:0.1 AlCl_3 :EMIC:LiCl at a 250 μm tungsten electrode (a) without and (b) with addition of 23 mM SOCl_2 . Scan rate = 100 mV s^{-1} .

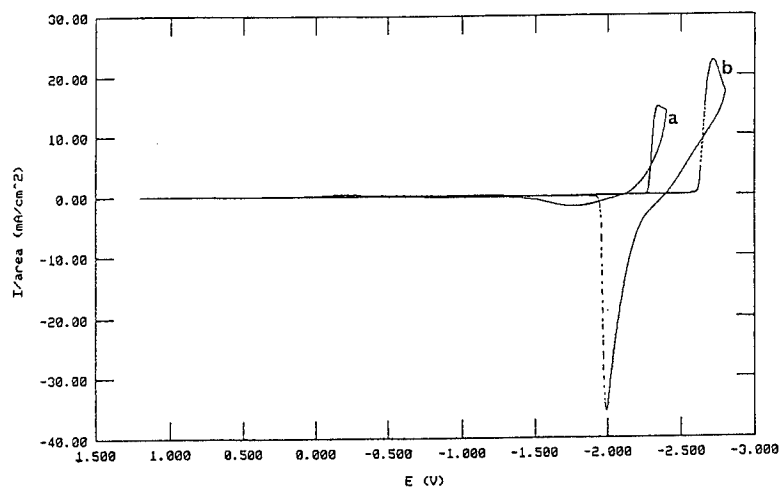


Fig. 4. Sodium electrochemistry in 1.1:1.0:0.1 AlCl_3 :EMIC:NaCl at a 250 μm tungsten electrode (a) with addition of 18.5 mM SOCl_2 and (b) with addition of 48 mM SOCl_2 . Scan rate = 100 mV s^{-1} .

ELECTROCHEMISTRY OF VANADIUM OXIDES IN ROOM TEMPERATURE MOLTEN SALT ELECTROLYTES

David M. Ryan and Thomas L. Riechel
Department of Chemistry
Miami University
Oxford, Ohio 45056

ABSTRACT

The electrochemistry and UV-visible spectroscopy of several high oxidation state vanadium oxides have been investigated in room temperature molten salts formed by mixing 1-methyl-3-ethylimidazolium chloride with AlCl_3 . V_2O_5 , NaVO_3 , Na_3VO_4 , V_2O_4 , and V_2O_3 were studied in acidic, basic, neutral, neutral-buffered, and neutral-buffered-protonated melts. Most of these compounds have limited solubility of about 5mM or less. Cyclic voltammograms of V_2O_5 in the acidic melt show two reduction peaks at 1.7 and 0.5V. Upon reduction of the 1.7V peak a new absorption peak is observed at 510nm in the visible spectrum. This is believed to correspond to a V(IV) species, but comparison to V_2O_4 is difficult because of that compound's low solubility. Neither of the two reduction peaks for V_2O_5 are reversible. The monosodium V(V) salt, NaVO_3 , is more soluble than the trisodium salt, Na_3VO_4 , in all cases. In acidic melt it exhibits peaks similar to those for V_2O_5 , except that the more positive peak is shifted to about 1.3V. V_2O_5 and NaVO_3 are the best candidates for battery cathodes, but neither exhibit reversible electrochemistry as needed for a secondary cell.

INTRODUCTION

Room temperature chloroaluminate molten salts have been considered as electrolytes for primary and secondary batteries [1-3]. Sodium, lithium, and aluminum have been studied as possible battery anodes with these electrolytes, while the electrochemistry and spectroscopy of numerous transition metals have been reported in order to evaluate their use as possible cathodes [4,5]. Only a few vanadium species have been investigated in such systems. An early study examined V_2O_5 in a LiCl-KCl melt at 450°C [6]. Recently a few studies have appeared in which V_2O_5 and other oxides were examined in xerogels [7-9] at or near room temperature. In one case [9] a chloroaluminate melt doped with magnesium chloride was used at 80°C. We report here a survey of the electrochemistry and UV-visible spectroscopy of vanadium oxides in the (III), (IV), and (V) oxidation states studied in acidic, basic, and neutral melts of 1-methyl-

3-ethylimidazolium chloride (MEICl) and AlCl_3 . The purpose is to evaluate the feasibility of using such materials as cathodes in cells incorporating room temperature chloroaluminate molten salt electrolytes.

EXPERIMENTAL

Cyclic voltammetry and controlled potential coulometry were performed using a Bioanalytical Systems (BAS) Model 100A Electrochemical Analyzer. A three electrode cell was employed using BAS Pt, W, and glassy carbon working electrodes for the voltammetry experiments. A Pt mesh electrode was the working electrode for the coulometric experiments. The reference electrode consisted of an Al wire in a 0.6 mole fraction AlCl_3 melt. The auxiliary electrode was a Pt flag. All measurements were made in a Vacuum Atmospheres glove box under a dry nitrogen atmosphere.

Preparation of the acidic, basic, neutral, and neutral-buffered melts of MEICl/ AlCl_3 have been described previously [1-3]. The neutral-buffered-protonated melt was made by adding triethanolamine.HCl to the neutral-buffered melt as given in ref. [3]. The vanadium oxides studied, V_2O_5 , NaVO_3 , Na_3VO_4 , V_2O_4 , and V_2O_3 , were obtained from Aldrich or Alfa/Aesar.

UV-visible spectroscopy was carried out using a Hewlett Packard Model 8452A diode array spectrometer and quartz cuvettes.

RESULTS AND DISCUSSION

Our initial studies focused on the vanadium (V) oxides and V_2O_5 in particular. A Lewis neutral melt ($N=0.5$, the mole fraction of AlCl_3) was made by mixing equal molar amounts of 1-methyl-3-ethylimidazolium chloride with AlCl_3 . The light orange V_2O_5 did not readily dissolve. After heating to 80°C , sonicating, and stirring overnight, a suspension of $<10\text{mM}$ V_2O_5 was obtained. The cyclic voltammogram of this suspension is shown in Figure 1. The rest potential shifted positively from that of the blank melt and two peaks appeared, a reduction peak at 0.5V and an oxidation peak at 1.2V . The oxidation peak only arises after scanning through the reduction peak. Thus, the two peaks are related, although they clearly do not constitute a reversible couple. Because of the small currents observed, the species responsible for these peaks are not certain.

To explore the solubility of V_2O_5 in a Lewis acidic melt, enough V_2O_5 was placed in an $N=0.55$ melt to make a 10mM solution. Although this material also did not dissolve completely even after prolonged stirring, upon filtration to remove the undissolved solid, an orange solution resulted. As shown in Figure 2, the voltammogram of this solution has a rest potential of about 1.9V , which is more positive than that for the suspension of this

reagent in the neutral melt. Furthermore, a new reduction peak appeared at 1.7V. Controlled potential electrolysis was carried out on this solution at 1.55V. After several hours a large residual current remained. The number of coulombs recorded was not useful data because the exact concentration of material was not known. The resulting voltammogram, Figure 3, shows that the species responsible for the 1.7V reduction peak has been consumed. Comparison of UV-visible spectra recorded before and after the electrolysis step also show a significant difference. Figure 4 is the spectrum of V_2O_5 before electrolysis. Three large absorbance peaks are observed below 400 nm, and the rest of the visible spectrum is blank. After electrolysis, the resulting spectrum (Figure 5) shows that of the three peaks below 400 nm only the lowest wavelength peak is still present. (Shoulders for the other two peaks are still evident.) Also, a new peak is present at 510 nm. We believe that this is due to a vanadium (IV) species. Attempts to study V_2O_4 for comparison have been fruitless because this compound is essentially insoluble.

V_2O_5 has also been examined in other melt compositions. In a basic melt ($N=0.45$) solubility is very low and there are no reduction peaks within the voltage window established by Cl^- oxidation. In a neutral melt buffered with NaCl the voltage window is over 4V wide, but no activity is observed. In a neutral buffered melt with protons added (0.060M triethanolamine.HCl, as in ref. [3]) the plating and stripping of sodium was observed, but no redox activity attributable to vanadium was evident.

Two vanadium (V) sodium salts were also investigated. The monosodium salt, $NaVO_3$, dissolved completely at a concentration of 30mM in a neutral melt, but over time deposited a white solid believed to be either NaCl or $NaAlCl_4$. (Both are known to be insoluble in neutral melts.) The voltammogram of this solution is shown in Figure 6. The reduction peak at 0.5V and the oxidation peak at 1.2V appear to be due to the same species as observed for V_2O_5 in neutral melt (Figure 1) but with larger currents as expected. Na_3VO_4 was only slightly soluble in neutral melt, but its voltammograms exhibited the same two peaks.

The solubility of $NaVO_3$ in acidic melt is about 7mM. The voltammogram of such a solution is shown in Figure 7. This voltammogram is similar to that of V_2O_5 in acidic melt (Figure 2) in that there are two reduction peaks in the positive potential range. The more positive peak is shifted to about 1.3V, as compared to 1.7V for V_2O_5 . Because reduction peaks this far positive are not observed in the voltammograms for any of the lower oxidation state vanadium oxides, these peaks are believed to be reduction of vanadium (V).

Results for Na_3VO_4 , V_2O_4 , and V_2O_3 show little because of the very slight solubility of these compounds in the various melts. Further work is underway to identify the dominant vanadium (V) species present in acidic melts of V_2O_5 and $NaVO_3$. Neither of these compounds appear to be useful for reversible cathodes, but may find use in primary cells.

ACKNOWLEDGEMENTS

This work was supported by an Academic Challenge grant to Miami University. DMR thanks the Wright Laboratory, Wright-Patterson Air Force Base, OH, for support while conducting this study.

REFERENCES

1. J. Fuller, R. A. Osteryoung and R. T. Carlin, J. Electrochem. Soc., **142**, 3632 (1995).
2. G. E. Gray, P. A. Kohl and J. Winnick, J. Electrochem. Soc., **142**, 3636 (1995).
3. B. J. Piersma, D. M. Ryan, E. R. Schumacher and T. L. Riechel, J. Electrochem. Soc., **143**, 908 (1996).
4. C. L. Hussey in "Chemistry of Nonaqueous Solutions, Current Progress," G. Mamantov and A. I. Popov, Eds., VCH Publishers, New York, 1994, Chapt. 4.
5. R. T. Carlin and J. S. Wilkes in "Chemistry of Nonaqueous Solutions, Current Progress," G. Mamantov and A. I. Popov, Eds., VCH Publishers, New York, 1994, Chapt. 5.
6. H. A. Laitinen and D. R. Rhodes, J. Electrochem. Soc., **109**, 413 (1962).
7. R. Baddour, J. P. Pereira-Ramos, R. Messina and J. Perichon, J. Electroanal. Chem., **277**, 359 (1990).
8. D. B. Le, S. Passerini, A. L. Tipton, B. B. Owens and W. H. Smyrl, J. Electrochem. Soc., **142**, L102 (1995).
9. P. Novak, W. Scheifele, F. Joho and O. Haas, J. Electrochem. Soc., **142**, 2544 (1995).

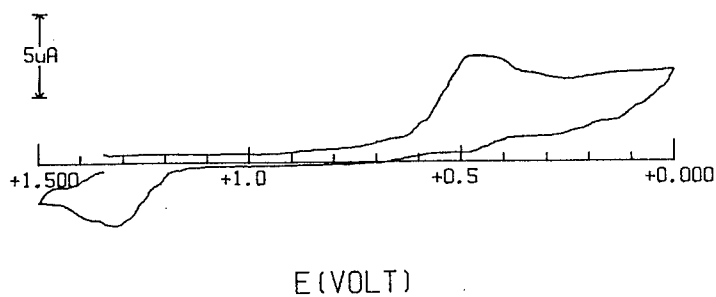


Figure 1. Cyclic voltammogram of a <10mM V_2O_5 suspension in a Lewis neutral $MEICl/AlCl_3$ melt at a Pt working electrode. Scan rate 0.1V/sec.

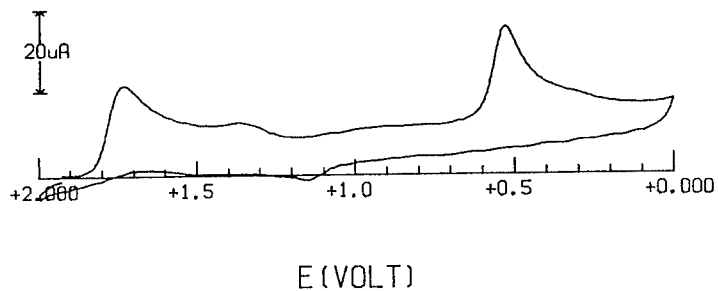


Figure 2. Cyclic voltammogram of a filtered V_2O_5 solution in a Lewis acidic $MEICl/AlCl_3$ melt at a Pt working electrode. Scan rate 0.1 V/sec.

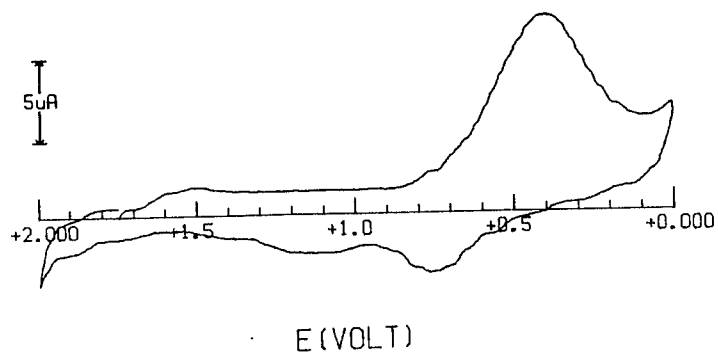


Figure 3. Cyclic voltammogram of the V_2O_5 solution in Figure 2 after controlled potential electrolysis at 1.55V. Scan rate 0.1V/sec.

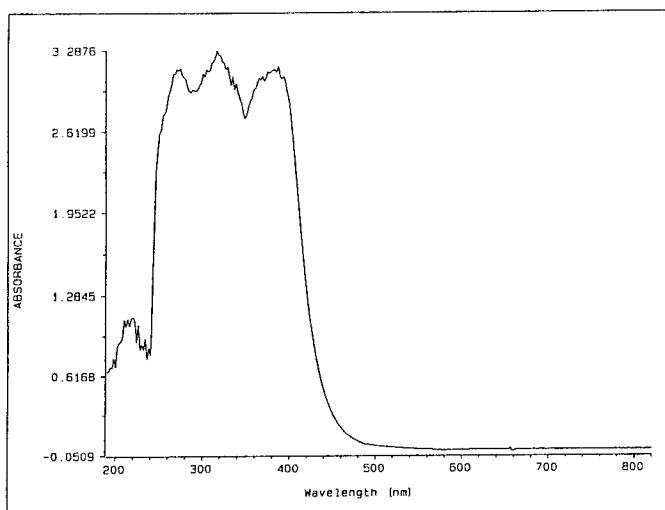


Figure 4. UV-visible spectrum of V_2O_5 in a Lewis acidic MEICl/ $AlCl_3$ melt.

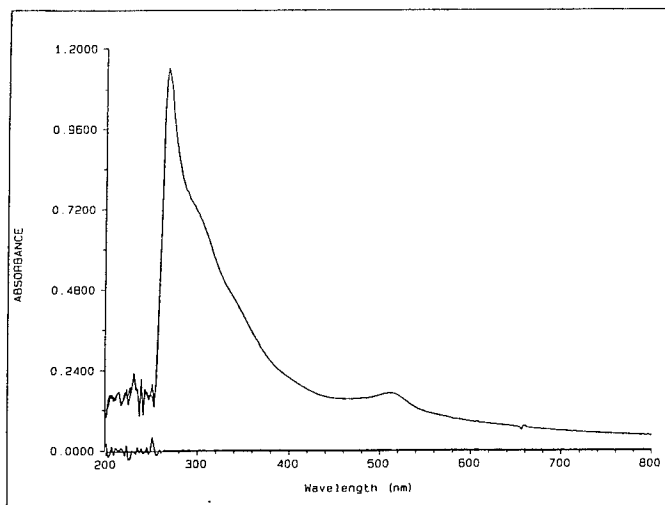


Figure 5. UV-visible spectrum of V_2O_5 in a Lewis acidic MEICl/ $AlCl_3$ melt after electrolysis at 1.55V.

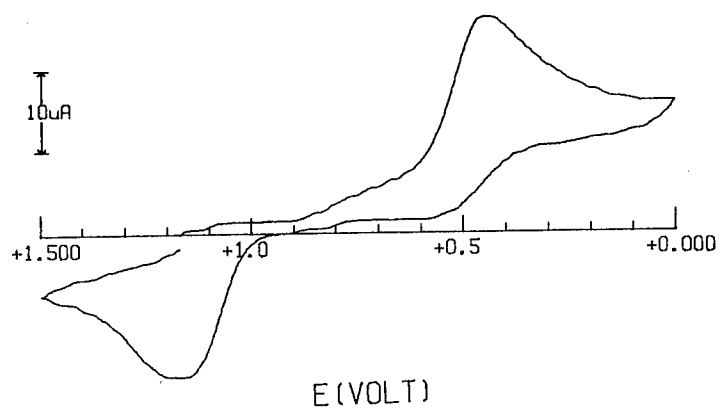


Figure 6. Cyclic voltammogram of 30 mM NaVO_3 in a Lewis neutral $\text{MEICl}/\text{AlCl}_3$ melt at a Pt working electrode. Scan rate 0.1V/sec.

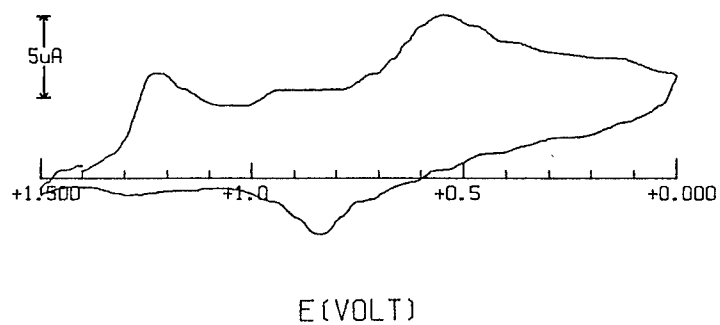


Figure 7. Cyclic voltammogram of 7 mM NaVO_3 in a Lewis acidic $\text{MEICl}/\text{AlCl}_3$ melt at a Pt working electrode. Scan rate 0.1V/sec.

THE ROLE OF MELT CHEMISTRY IN MOLTEN CARBONATE FUEL CELL(MCFC) TECHNOLOGY

J. Robert Selman and M.S. Yazici
Department of Chemical and Environmental Engineering
Illinois Institute of Technology
Chicago, IL 60616

ABSTRACT

An overview is presented of recent developments in MCFC technology that are related to the melt chemistry. The status of chemical and electrochemical aspects of MCFC technology is reviewed, with emphasis on the electrode kinetics, in particular of the cathode, and on the corrosion mechanism of electrode and separator plate materials. Although the current demonstrations of large scale MCFCs all make use of Li-K carbonate eutectic, there is considerable interest in alternative electrolyte compositions. It appears that for the long-term performance of the MCFC, a Li-Na-K carbonate mixture with a composition close to that of the Li-Na eutectic would be advantageous.

Background: requirements for commercialization

This paper aims to give an overview and status report on some chemical and electrochemical issues that relate directly to the performance and stability of molten carbonate fuel cells. The molten carbonate fuel cell(MCFC), after intensive development during recent decades, is approaching commercialization. It is considered a prime candidate for efficient generation of electric power, and cogeneration of heat and power. In 1996 demonstrations of 250 kW-2 MW size MCFC plants will take place in the U.S. and Japan, while several European countries pursue MCFC development programs aimed at developing MW-size plants[1-3].

Cost issues determine the overall direction of current research related to MCFC technology. Whereas a few years ago, chemical and electrochemical questions dominated the research agenda, present emphasis is on new or improved materials, and on system design. However, chemical and electrochemical aspects of "performance"(power density) and "life time"(stability in long-term performance) remain of great importance.

Increasing the power density(presently 1.0-1.25 kW/m²) must be accomplished by improving electrode design and by pressurized operation(below 10 bar). Extending the life time of MCFC stacks(which now rarely exceeds 10,000 h), to at least 20,000 h in pressurized operation, requires a substantial reduction in performance decay[4]. Although much progress has been made recently, the performance decay of scaled-up cells and stacks(now in the range of 2-5 μ V/h) is not completely understood and controllable. Further reduction by new materials and fabrication technologies must be based in insight in MCFC kinetics and corrosion.

Background: fundamental aspects

MCFC technology has almost from the beginning been based on the unique property of molten carbonates to remain invariant in contact with carbonaceous gas, and to be excellent ionic conductors in a temperature range starting at 600 °C, which is reasonably compatible with the operational range of natural gas reformers (optimally at 800 °C). Nevertheless, in spite of these unique properties, there are a number of fundamental difficulties connected with the application of molten carbonates in fuel cells.

1. First of all, the oxygen chemistry in these melts tends to be complicated by the presence of higher oxides (superoxide, peroxide, as well as unstable and adsorbed intermediates, see Table 1). This makes the oxygen reduction process relatively slow, compared, for example, to metal deposition from alkali chloride melts at the same temperature.

2. Furthermore, the capillary properties of molten carbonate are highly dependent on the gas atmosphere, as well as the type of substrate. Wetting angles can vary from close to zero for oxide type surfaces in melts under oxidant gas, to practically 60° at metals under reducing conditions. This exacerbates the "creeping" tendency of carbonates, which is well-known. Whereas creeping of molten salts is usually caused by a temperature gradient as driving force, in molten carbonates creeping is exacerbated by the combination with corrosion of metal surfaces and oxygen reduction at conducting oxide substrate. Nevertheless, in practice the creeping of molten carbonates can be controlled by careful design, in particular by avoiding steep concentration gradients in the gas composition and contact with corrodable materials. The latter, however, is difficult to accomplish, because of the third peculiarity of molten carbonates.

3. As is well-known, molten carbonates are extremely corrosive. This property is well understood in the case of metals, and the thermodynamics of the corrosion processes under various gas atmospheres have been known for some time. Only noble metals such as palladium and gold are resistant to corrosion by molten carbonate under an oxidant atmosphere. Even these noble metals dissolve slowly if the melt is strongly basic, for example in a Li-rich carbonate melt under very low CO₂ partial pressure. Nevertheless, certain alloys such as stainless steels are protected by a passive layer which retards (but does not eliminate) corrosion. However, the corrosion mechanism of alloys in molten carbonate is poorly understood.

Electrode kinetics: effect on power density

Target power densities of 2.0 to 2.5 kW/m² require increasing the current density from 1.65 to 3.0 kA/m² without lowering the present cell voltage (0.75 V). Table 2 shows approximate voltage-loss contributions for single cells at 1.65 kA/m². The ohmic (IR) contribution to overall voltage loss is not insignificant, but cannot be reduced

below a certain minimum level (typically that of a 1 mm thick electrolyte matrix), without causing gas cross-over. To further reduce IR-drop, recent work focuses on using as electrolyte the Li-Na carbonate eutectic, which has a 30% higher conductivity than Li-K eutectic, and also is less volatile[5,6]

It is not clear, however how this would affect the polarization of the cathode, which is the dominant voltage loss contribution. In the standard Li-K eutectic, polarization is due in equal measure to slow electrode kinetics, mass transfer resistance, and ionic-ohmic resistance of the cathode pores[7]. According to recently reported calculations, Li-Na carbonate eutectic would have a smaller cathode polarization than Li-K carbonate[5] (see Figure 1). This is confirmed by some experimental performance data[6]; however, other data are inconclusive, and appear to reinforce arguments that the lower oxygen solubility may limit the cathode performance in Li-Na mixtures (see Table 3).

Thus, there is a practical incentive to investigate the electrode kinetics of Li-Na and Li-Na-K mixtures more closely. It is desirable to review the traditional assumption that the oxygen reduction mechanism in such mixtures involves peroxide ions as primary reactants. Work by Reeves (see Figure 2) on electrode kinetics in Li-K mixtures containing Sr and Ca carbonate as additives[8] points to the inadequacy of existing mechanistic models, as does the discovery by Uchida and coworkers[9] of "spike peaks" presumably due to adsorbed intermediate products.

Corrosion: effect on life time

Recently, the corrosion of iron, nickel and chromium, and various alloys (especially Types 310 and 316 stainless steel) has been investigated systematically[10]. The role of surface layers of LiFeO_2 , which conducts well but is porous, and of LiCrO_2 , which is compact and dense, is becoming increasingly clear (see in this volume, Yazici and Selman, and Yanagida et al.). But the detailed mechanism (kinetics and diffusion) by which these corrosion layers form, and a quantitative correlation with the corrosion rate, in short term and long term operation, still escapes us.

Combining optical observation with electrochemical in-situ techniques and post-test analysis can yield new insights. Recent work at IIT[11,12] has revealed the surprisingly dynamic and non-uniform character of the oxidation of metals such as nickel, which takes place during in-situ oxidation of nickel metal to form a NiO cathode. Figure 3 shows various stages of the oxidation process, which is accompanied by gas evolution.

It appears that also from the viewpoint of NiO dissolution and metal corrosion as a factor in cell life, Li-Na carbonate has advantages (Table 3, Figure 4).

ACKNOWLEDGMENTS

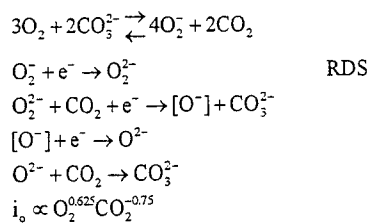
Support by the U.S. Department of Energy, through Morgantown Energy Technology Center(DE-FG21-94MC31078) is gratefully acknowledged. As are helpful conversations with Dr. R.Remick(IGT, Chicago) and Dr. C.Y. Yuh(ERC, Danbury,CT)

REFERENCES

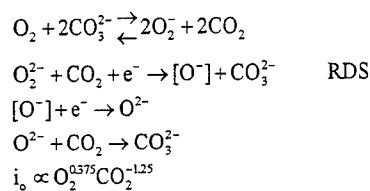
1. Report of the DOE Advanced Fuel Cell Commercialization Working Group(S.S. Penner, Chairman). DOE/ER-0643(March 1995), Section IX-2
2. M.C. Williams, E.L. Parsons and T.J. George, "Status of Molten Carbonate Fuel Cell Technology Development", EA 93-1, The Electrochemical Society Inc.(1993), P. 1500
3. J.R. Selman, "Research, Development and Demonstration of MCFC Systems", in "Fuel Cell Systems"(L. Blomen and M.N. Mugerwa, Eds), NY 1993
4. J.R. Selman, " MCFC Electrode Design and Materials Corrosion in High Current Density Operation", Proc. 2nd IFCC(Kobe, Japan), 1996
5. T. Murahashi, "Li-Na system for MCFC performance and life", U.S.DOE/Japan AIST Fuel Cell Technical Meeting, Dec. 1994
6. R.A. Donado, E.T. Ong, and C. Sishtla, DOE Fuel Cells 95 Mtg, Abstr. P7(1995)
7. G.L. Li, "Dynamic Analysis of MCFC Porous Electrodes" Thesis, I.I.T., Chicago(1992)
8. R.W. Reeve, "A Study of Oxygen Reduction and Related Electrochemistry at the Molten Carbonate Fuel Cell Cathode", Thesis, U. of Essex(UK), 1994
9. T. Nishina, I. Uchida(Tohoku University, Sendai, Japan),Priv. Comm.
10. J. Vossen, "Corrosion of Separator Plate Constituents in Molten Carbonate", T.U. Delft(Netherlands), 1994
11. Y. Izaki and J.R. Selman, "Direct Observation of the Oxidation Process of Nickel in Molten Carbonate", Ms. In preparation(1995)
12. Y. Mugikura and J.R. Selman, "Meniscus Behavior of Metals and Oxides in Molten Carbonate under Oxidant and Reducing Atmospheres" Subm. to J.Electrochem. Soc.(1995)

Table 1. Possible oxygen reduction mechanisms

Superoxide Path



Peroxide Path



Percarbonate Path

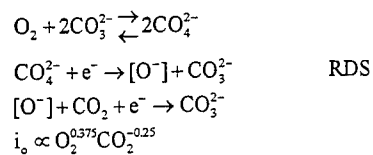


Table 2. Approximate contributions to voltage loss(in mV)of single MCFC cells operating at 1.65 kA/m², 1 bar, 923 K(ref. 1,4)

	State of the art	Future improved design
Cathode	120-80	60-55
Anode	60-10	50-10
Electrolyte matrix	50-55	25-40
"Nernst Loss	65-145	65-145
Total	295-290	200-250

Note: Polarization and Nernst loss depend on specifics of gas composition and utilization

Table 3. Physical properties of molten carbonates at 650 °C

	Li ₂ CO ₃ /K ₂ CO ₃ (62/38)	Li ₂ CO ₃ /Na ₂ CO ₃ (53/47)
O ₂ solubility(mol/cm ³ atm)	3.3x10 ⁻⁷ (50/50)	1.8x10 ⁻⁷
Basicity(pO ⁻)	6.9	6.62
Electrical conductivity (Ω ⁻¹ cm ⁻¹)	1.4~1.6	2.1~2.3
Electrolyte vapor loss (g cm ⁻³)	-32x10 ⁻¹⁰	-3.5x10 ⁻¹⁰

References:

-Advances in Molten Salt Chemistry Vol. 4

-Physical Properties Data Compilations Relevant to Energy Storage

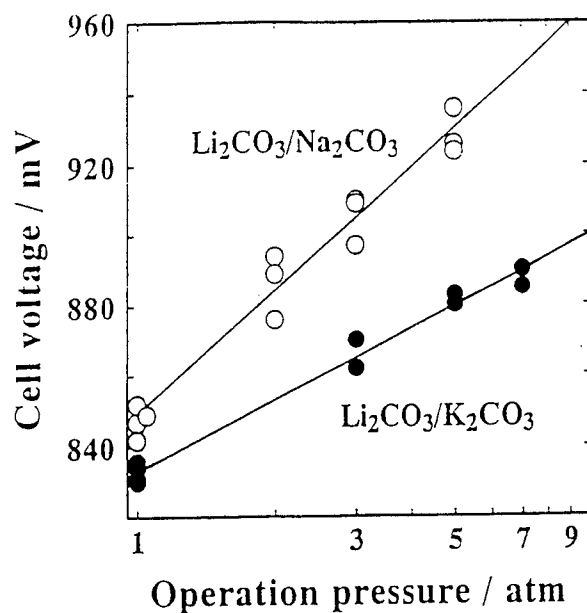


Figure 1. Cell voltage vs. operation pressure with different electrolyte mixtures(ref. 5)

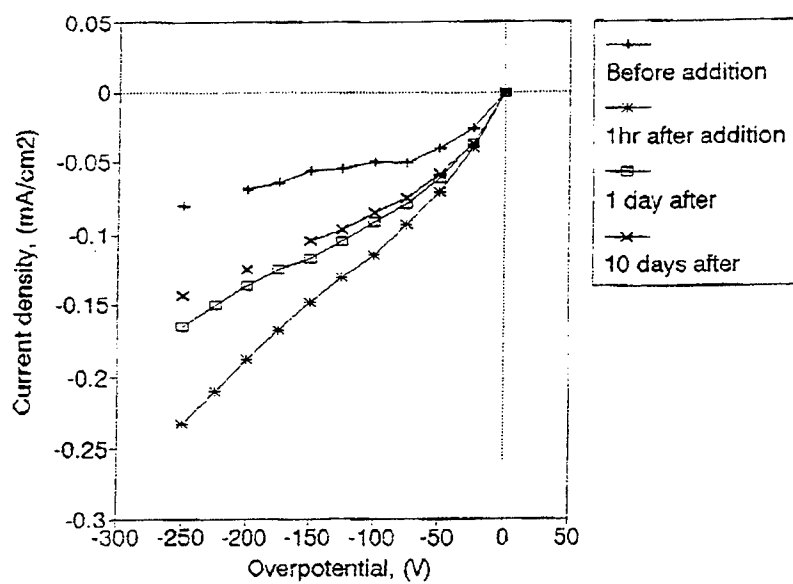


Figure 2. Effect of SrCO_3 on the Steady State Performance in Li/K(50/50) carbonate. $P_{\text{O}_2}=0.33$, $P_{\text{CO}_2}=0.67$, $T=650^\circ\text{C}$.(ref. 8)

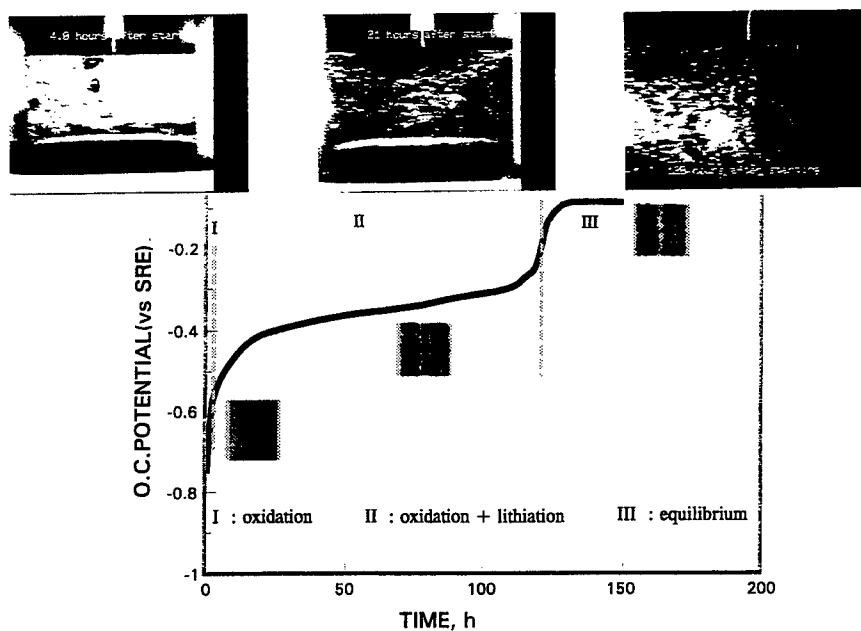


Figure 3. Time development of nickel oxidation under gas evolution in carbonate melt at 650 °C(ref. 11)

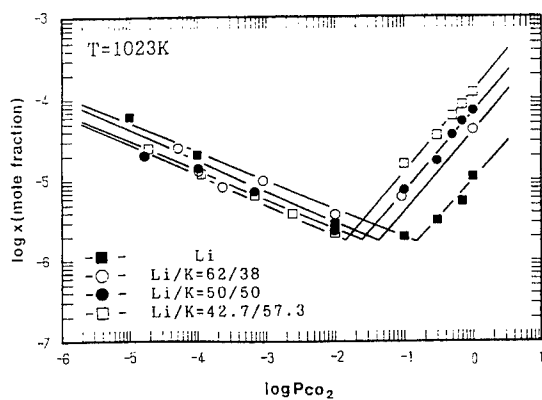


Figure 4. Solubility of NiO in various melts as a function of P_{CO_2} at 1023 K(Ota et.al.,JES,Vol.139, No.3(1992))

MASS TRANSFER AND STEADY STATE CONCENTRATION DISTRIBUTIONS OF BINARY MOLTEN CARBONATE ELECTROLYTES AND ADDITIVES IN MCFCs

Th. Brenscheidt, O. Böhme, H. Wendt
Institut für Chemische Technologie, TH Darmstadt
Petersenstr. 20, D - 64287 Darmstadt, Germany

Abstract

The ionic mobilities of the cations Li^+ , K^+ and Na^+ in alkali carbonate melts is not equal and the small lithium cation is opposite to intuitive assumption but according to the Chemla effect in certain concentration ranges slower than the heavier cations Na^+ and K^+ if the lithium carbonate concentration is below the so-called crossing point. For eutectic lithium/potassium carbonate melts this condition holds and considerable accumulation of potassium over lithium carbonate in the cathode is the consequence under operating condition in MCFCs. This effect limits current densities which could be applied in MCFCs as too high accumulation of potassium might lead to crossing the liquidus/solidus line with the consequence of potassium carbonate precipitation. Ionic additives (La_2O_3) dissolved in the carbonate electrolyte experience either uneven concentration distribution in the fuel cell according to their respective internal mobility or, according to their charge and solubility, even complete transfer and deposition into only one of the two electrodes.

Introduction

Since the early investigation of A. Klemm (1), the demixing of the cations of molten binary salt mixtures with a common anion due to the different mobilities of two different cations had been investigated in numerous experiments and the respective results interpreted in terms of structural features of the melts; see for instance (2) and (3). 1-1 electrolytes had been preferentially investigated, but apart from investigations of molten sulfates Okada also reported investigations on lithium carbonate/potassium carbonate mixtures in the temperature range from 980 to 1070 K, (4).

Charge and mass transfer in the electrolyte of molten carbonate fuel cells is accomplished by the movement of the carbonate anions, which are generated at the cathode and decomposed by release of CO_2 at the anode. Against the steadily moving stream of carbonate anions the cations are migrating - but according to their different mobilities with

different velocities. Under steady state conditions the relatively faster cation would accumulate in the catholyte. Steady state conditions are defined by zero velocities of the summed convective, migrative and diffusive mass transfer - see the schematic of Fig. 1.

Fig. 2 reports results in terms of the so-called internal mobilities b of Li^+ and K^+ vs. the mole fraction of the potassium salt in binary carbonate mixtures determined at 980 K. At $x_K \approx 0,32$ both alkali cations possess equal mobilities and would not separate on prolonged electrolysis, whereas with a higher potassium concentration potassium would be expected to accumulate at the cathode side of an electrolysis cell and with a lower mole fraction than $x_K = 0,32$ the same would be expected to occur for lithium.

Since it is felt, that such demixing of the binary electrolyte in MCFCs might have important consequences in defining limits of operation conditions, limiting applicable current densities in particular, the effect had been investigated in experimental fuel cells. The consequences of migrative mass transfer had been investigated also with respect to added lanthanum oxide, (5), as this oxide was believed to influence the nickel oxide solubility in the cathode but could only act there if it would remain there.

Experimental

Experimental MCFCs were 20 mm in diameter and of the usual tubular design as described for instance in review (6). Anodes, cathodes and electrolyte matrix had been prepared and assembled according the green foil technology and the cells had been formed from the three foil package in-situ as described by one of the authors and his coworkers elsewhere (7). As an example such cells were typically composed of 0,5 mm thick porous nickel oxide cathodes, 0,8 mm thick anodes of sintered and stabilized carbonyl nickel and 1 mm thick 50 % porous and a densely packed LiAlO_2 matrix composed of LiAlO_2 granules of 0,1 to 0,3 μm \varnothing . Fuel cell operation was performed with different current densities for more than 100 h, the cell was chilled and carefully disassembled. The separated anode, cathode and matrix specimens were ground and covered with 10 ml of water/ acetic acid, (1/1) and the carbonate melts dissolved within 3 h. The aqueous solutions were analyzed by atomic absorption spectrometry after adequate dilution. For transference measurements of lanthanum oxide to the cathode foil 20 mole % lanthanum oxide (relative to the nickel contents) was added and the distribution of lanthanum across the cell had been monitored by energy dispersive X-ray fluorescence, (EDX), in a SEM (JEOL - TSM 330A) before and after cell operation of 500 h.

RESULTS

(a) $\text{Li}_2\text{CO}_3/\text{K}_2\text{CO}_3$ -electrolyte

Table 1 collects the chemical analyses of a 340 h experiment performed at 650° C with a steady current density of 100 mA cm^{-2} .

Table 1
Potassium and lithium contents of MCFC operated for 340 h at 100 mA cm⁻²

	anode	matrix	cathode
total K/mg	21,2	175	25
total Li/mg	7,0	58	6,3
thickness/mm	0,8	1,1	0,5

It is evident that the greatest part of the electrolyte is contained in the matrix (75 to 80 %) and that almost equal parts of the remaining electrolyte are contained in both electrodes. The ratio m (K)/m(Li) is almost equal in the matrix and the anode (~3) but it increases to 4 in the cathode.

Table 2 collects the analysis of three experiments - two performed with 100 mA cm⁻² and the third at somewhat enhanced current density of 150 mA cm⁻² - by converting the analytical data of the mean concentrations of Li and K in the melts in the three different cell compartments to mole % of lithium carbonate. Fig. 3 presents a schematic plot of the respective Li-mole fractions in the anode, electrolyte matrix and cathode respectively for the same three experiments.

Table 2
Demixing of 62/38 Li₂/K₂CO₃ electrolyte in MCFC

Operating time /h	c.d./mA cm⁻²	mole % Li₂CO₃		
		anode	matrix	cathode
340	100	64	64	58
147	100	62	61,5	57
160	150	57	56	42

Evidently anode and matrix electrolyte exhibit almost the same chemical composition but the catholyte is seizeably depleted in lithium. This effect becomes much more pronounced at higher current densities. As the current density increases by a factor of 1,5 the concentration difference,

$$\Delta x_{Li_2CO_3} = x_{Li}(matrix) - x_{Li}(cathode)$$

increases by a factor of almost 3, indicating that the current density of a MCFC with Li₂CO₃/K₂CO₃ eutectic melt might become a critical operation parameter.

Li₂CO₃/Na₂CO₃ electrolyte

Transference experiments had also been performed with Li₂CO₃/Na₂CO₃-eutectic (52/48 mole/mole) as this electrolyte is estimated to be a promising alternative to

the lithium/potassium carbonate eutectic. Table 3 lists the analyses of the cell melts in the three different components of a respective lithium-sodium carbonate cell.

Table 3
Demixing of $\text{Li}_2\text{CO}_3/\text{Na}_2\text{CO}_3$ eutectic in MCFC

Operating time /h	c.d./mA cm ⁻²	mole % Li_2CO_3		
		anode	matrix	cathode
139	100	56	51	49
69	150	56	54	53
116	150	53	(57)	48

Obviously also with lithium/sodium carbonate melts (52/48 mole/mole) the accumulation of the heavier sodium cation is observed in the cathode. Therefore also for this binary mixture of carbonates the Chemla effect is prevalent. But the effect is weaker and the concentration gradient seems to be more evenly distributed across the cell than with lithium/potassium carbonate melts.

Transference experiments with La_2O_3 as cathode additive

20 mol % LaNiO_3 dispersed as crystallites of approx. 5 μm diameter had been added to carbonyl-nickel powder (3 to 4 μm). By in-situ reductive sintering which decomposes LaNiO_3 to metallic nickel and La_2O_3 followed by atmospheric oxidation a NiO -cathode doted with La_2O_3 had been formed. A lithiated nickel oxide cathode was formed therefrom by imbibing the electrode with $\text{Li}_2\text{CO}_3/\text{K}_2\text{CO}_3$ electrolyte and was incorporated into an MCFC with Li/K -carbonate electrolyte. After 500 h of operation at 650° C with 100 mA cm² the cell was cooled, disassembled and embedded into a polymer. A cut of the cell, obtained by sawing the polymer block was supplied with a thin gold coating by sputtering and different parts of the cell were examined by EDX for their lanthanum contents. No lanthanum could be detected in the cathode. Fig. 3 depicts the interface between the electrolyte matrix and anode and shows the signal intensity attributed to La at 4,5 eV. Obviously there is no lanthanum present in the electrolyte matrix, but a high lanthanum concentration can be detected in the anode close to the interface and a lower but definitely detectable concentration farther away from the interface.

Discussion

(a) Transport balances of binary salt mixtures

As shown schematically in Fig. 1 the faster cation accumulates in the cathode and correspondingly the slower moving cation must be found in enhanced concentration in the anode and matrix. Under steady state conditions migrative, convective and diffusive mass transport of the cation, i , are adding to zero in any virtual plane parallel to the cell surface:

$$0 = \dot{n}_{(total)} = \dot{n}_{conv.} + \dot{n}_{mig} + \dot{n}_{diff} \quad [1]$$

With t_i equaling the so-called internal transfer number of cation, i , and x_i equaling the mole fraction of the salt $(M_i)_2CO_3$ in the binary mixtures one obtains for the three transport terms

$$\dot{n}_{conv} = -\frac{i}{2F} \cdot x_i; \dot{n}_{mig} = \frac{i}{F} \cdot t_i; \dot{n}_{diff} = -\frac{\partial x_i}{\partial y} \cdot D_i \quad [2]$$

and calculates the steady state balance

$$0 = -\frac{i}{F}(x_i - t_i) - \frac{\partial x_i}{\partial y} \cdot D_i \quad [3]$$

calculating the volumetric concentration c_i by $c_i = x_i \rho / \bar{M}$ with ρ equal to the density of the melt and \bar{M} equal to the mean molar weight of the melt of one arrives at

$$\frac{dx_i}{dy} = -\frac{i}{F}(x_i - t_i) \cdot \frac{\bar{M}}{\rho} \cdot \frac{1}{D_i} \quad [4]$$

t_i as the internal transfer number is, defined by the internal mobilities, b_i and b_j of the two cations and by the mole fractions, x_i and x_j of the two salts in the binary mixture:

$$t_i = \frac{x_i b_i}{x_i b_i + x_j b_j} = \frac{x_i b_i}{x_i(b_i - b_j) + b_j} \quad [5]$$

A closed solution of diff. equ. [4] is impossible, as the b_i , b_j values are not constant as the concentrations of the molten mixture changes. According to equ. [4] the sign of the gradient dx_i/dy depends on the sign of the quantity $(x_i - t_i)$ and its magnitude depends also on the current density, i . For $x_K > 0,32$, as is demonstrated in Fig. 5, the quantity $(x - t)$ becomes negative for potassium and hence the gradient dx_K/dy becomes positive, i.e. the concentration of potassium increases in going from the anode to the cathode, whereas the concentration of lithium decreases correspondingly. Since the eutectic has the composition $x_K = 0,38$ we can definitely predict the accumulation of potassium and the depletion of lithium in the cathode as it is observed in Fig. 3. We expect also, that on the anode side of the cell a limiting potassium concentration will be attained that matches the concentration of crossing point if more and more potassium is dragged into the cathode as would be expected as the current density is increased. Eventually at the anode side the concentration of potassium would become lower than that of the crossing point and lithium starts accumulating in the anode. This prediction is obviously fulfilled at 150 mA cm^{-2} . The mass balance for the experiment with 150 mA cm^{-2} shows, that the total lithium content of the cell is

too low. This is likely to be attributed to lithium losses for instance by lithiation of nickel oxide and corrosion reactions producing LiFeO_2 .

Internal mobilities of the cations in binary lithium carbonate/sodium carbonate mixtures have not yet been published. Therefore in the case of these two cations only some guesses can be made from measurements performed in binary mixtures of lithium and sodium salts with common anions other than carbonate. Okada and Lunden investigated binary mixtures of alkali nitrates [cited in (8)]. In lithium nitrate potassium nitrate mixtures very like in lithium carbonate potassium carbonate melts a crossing point is observed, whereas with mixed lithium sodium nitrate melts a crossing point does not exist and the ratio $b_{\text{Na}^+} / b_{\text{Li}^+}$ stays almost constant (this value is approximately 1,15 at 380°C) across the whole range of melt composition from x_{Li} close to zero to close to one. As the anions NO_3^- and CO_3^{2-} are similar with respect to their geometry, volume and polarizabilities, one would therefore infer, that also for molten Li/Na-carbonate mixtures a crossing point would not exist but the Chemla effect (higher mobility of the heavier cation) would be operative and that the value $(x_i - t_i)$ is positive for the small lithium and negative for the somewhat larger sodium cation. One would therefore anticipate that sodium like potassium accumulates also in the cathode of an MCFC with Li/Na carbonate as electrolyte. This, indeed is actually observed.

(b) Transport of additives

Additives, either dissolved or deposited as little soluble small particles are also influenced by electric field driven transport across the cell as solid state oxides, which are the usual oxides, generate ions if dissolved in the melt. An example is the "acidic" dissolution of nickel oxide in carbonate melts according to equ. [6].



What is valid for the ionic majority species Li^+ and K^+ or Na^+ does hold also for dissolved species of minor concentration. The criterion for their concentration distribution in the cell is still equ. [4] in a modified notation in which mainly the factor \bar{M}/ρ is changed in a way which accounts for the stoichiometry of the dissolution reaction.

Quantitatively still the expression $(x_i - t_i)$ is maintained for cations as decisive. If it is positive, the dissolved species tends to be accumulated at the cathode and vice versa. If, however, the enhanced concentration exceeds the solubility, then almost complete transfer from one side of the cell to the other will occur - as it was observed with La_2O_3 . The same result is affected if the dissolved lanthanum species is anionic and not cationic, e.g. $[\text{La}(\text{CO}_3)_n]^{(2n-3)-}$. Anions move anyway towards the anode, for then the respective term in equ. [5] reads $-(x_{\text{an}} + t_{\text{an}})$ and La_2O_3 will under these conditions precipitate in the anode, provided initially more La_2O_3 had been deposited than can be dissolved in the whole cell electrolyte.

Conclusions

The well known effect of demixing of binary molten carbonates by electrolysis leads in molten carbonate fuel cells, due to the Chemla effect, to the accumulation of the heavier alkali cation (K^+ or Na^+) and depletion of Li^+ at the cathode.

This has several consequences:

- (a) the electrode kinetics of oxygen evolution is affected as the solubility of oxygen in the melts depends on the lithium content.
- (b) The effective volatility of the melt, which is mainly determined by the mole fraction of the more volatile sodium and potassium carbonates respectively is enhanced to some extent according to their increased concentration (9).
- (c) Most serious is the possibility, that at sizeably increased current densities, which are desirable because of the still insufficient power density of MCFCs. The concentration enhancement of potassium cations at the cathode could lead to such enhanced concentrations of lithium in the anode, that there the liquidus/solidus curve is crossed and lithium carbonate begins to precipitate which would certainly destroy the anode. Fig. 6 shows the melting point diagram, which explains that Li_2CO_3 precipitation in the anode is much more likely to occur than K_2CO_3 precipitation in the cathode. In principle this can be avoided only if the whole cell electrolyte is kept at a concentration very close to that of the crossing point of the internal mobilities of two alkali cations.
- (d) As in lithium/sodium carbonate melts the Chemla effect is less pronounced than in lithium/potassium carbonate melts, there exists another reason - additionally to the lower volatility of this binary electrolyte - to use Li/Na carbonate melts instead of Li/K carbonate melts as MCFC electrolyte in the future.

Acknowledgement: The authors are indebted to Siemens AG, MTU Friedrichshafen GmbH and the German Federal Ministry of Research and Development for partial support of this investigation.

References

1. A. Klemm, H. Hinterberger, P. Hoernes, *Z. Naturforsch.* **2a**, 245 (1947)
2. A. Klemm, Ionic Mobilities in G. Mamantov, C.B. Mamantov and I. Braunstein eds., *Advances in Molten Salt Chemistry*, Elsevier, Amsterdam, 1987, Vol. 6, p. 1
3. M. Chemla, I. Okada, *Electrochim. Acta* **35** 1761 (1990)
4. C. Yang, R. Takagi, K. Kawamura, I. Okada, *Electrochim. Acta* **32** (1987) 1607
5. O. Böhme, Grundlagenuntersuchungen zur Karbonatschmelzenzelle, Kathode und Matrix, PhD thesis, TH Darmstadt, 1992
6. J.R. Selman and L.G. Marianowski, "Fuel Cells" in *Molten Salt Technology*, D.G. Lovering ed. Plenum Press, New York and London 1982, p 332
7. O. Böhme, F.-U. Leidich, H.J. Salge and H. Wendt, *Intl. J. Hydrogen Energy* **19** 349 (1994)
8. Cheo-cheng Yang, Rynzo Tagaki, I. Okada, *Z. Naturforsch.* **35a**, 1186 (1980)
9. H. Mohn and H. Wendt, *Zeitschr. f. Physik. Chemie*, **192**, 101 (1995)

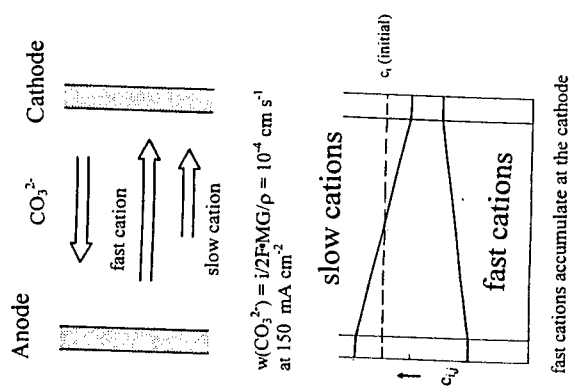


Fig. 1: Schematic of the fluxes of two different cations and carbonate ions in binary molten alkali carbonates in an operating MCFC

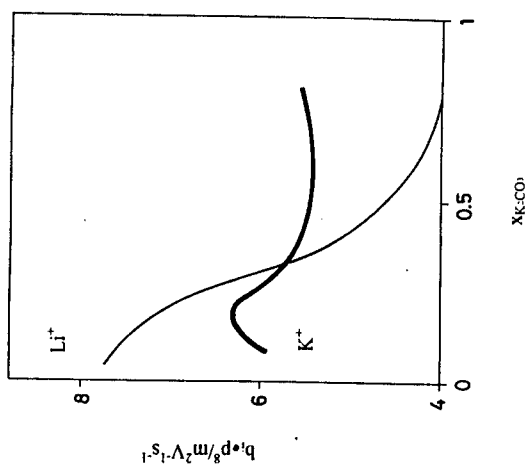


Fig. 2: Intrinsic mobilities of lithium and potassium cations vs. mole fraction of K_2CO_3 in Li/K CO_3 -melts at 707°C (4)

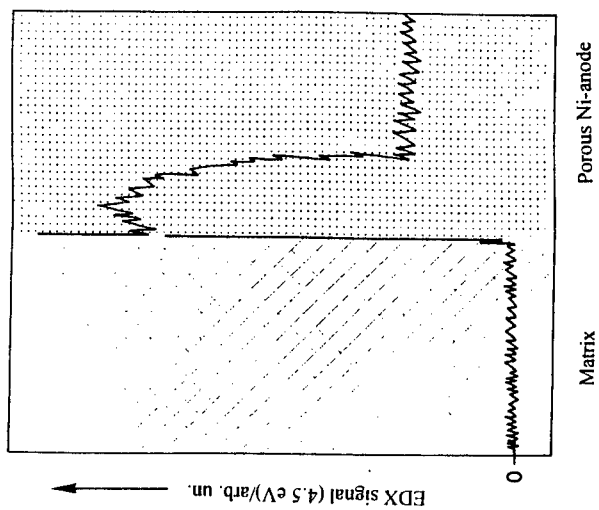


Fig. 4: Distribution of La^{3+} in the matrix and anode of an MCFC after 500 h of operation. The La^{3+} was initially deposited as La_2O_3 in the cathode

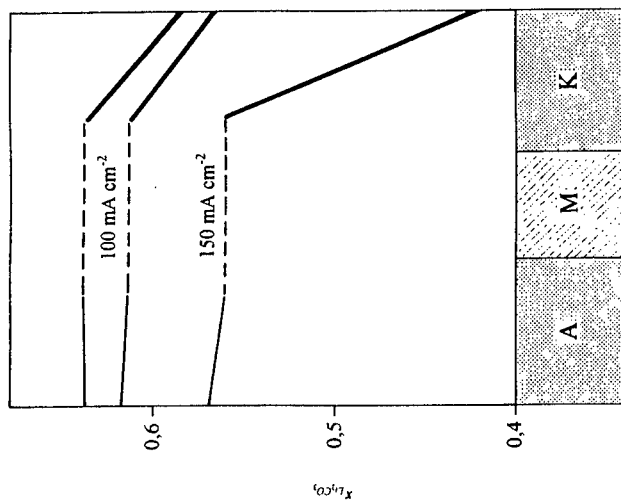


Fig. 3: Experimentally determined concentrations of Li (mole/mole) in an MCFC after 400 h of operation at 100 and 150 mA cm^{-2} at 650°C

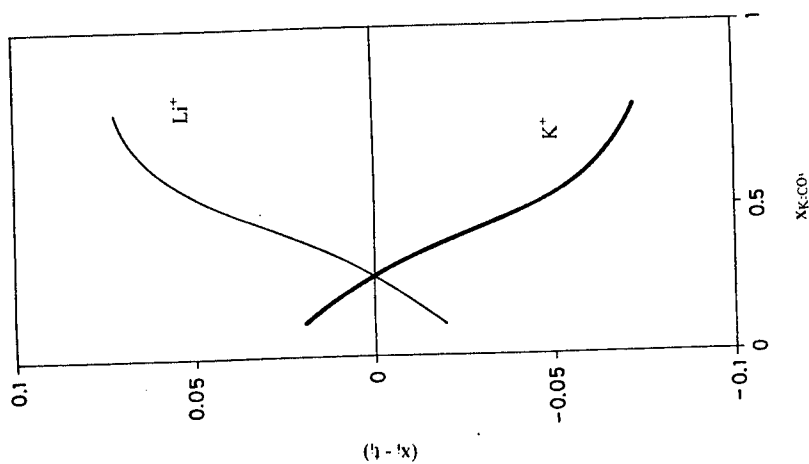


Fig. 5: $(x-t)_{Li}$ and $(x-t)_K$ in molten Li/K carbonates at 707 °C according to the data of Fig. 2, (4)

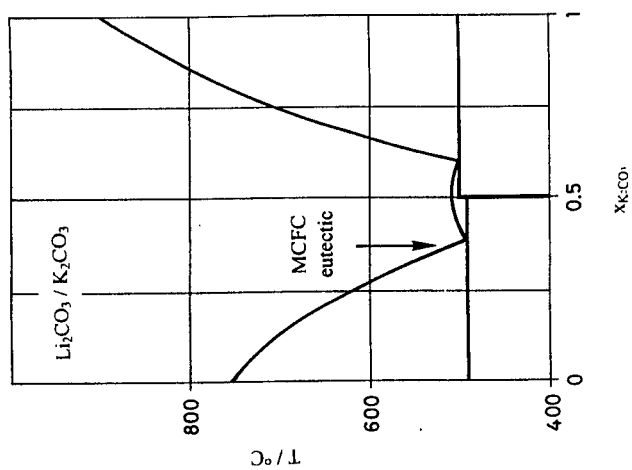


Fig. 6: Melting point composition diagram of Li/K carbonate mixtures

HIGH TEMPERATURE CORROSION OF TANTALUM WITH THE PRESENCE OF MOLTEN CARBONATE

Ken-ichiro OTA, Katsuya TODA, Toru KOJIMA,
Naobumi MOTOHIRA and Nobuyuki KAMIYA
Department of Energy Engineering, Yokohama National University
156 Tokiwadai, Hodogaya-ku, Yokohama 240, JAPAN

ABSTRACT

The high temperature corrosion of tantalum with the presence of molten carbonate has been studied in $\text{CO}_2\text{-O}_2$ atmosphere from 873 K to 1123 K by measuring the weight gain of a specimen. A severe corrosion of tantalum took place with the formation of unprotective Ta_2O_5 at high temperature and the corrosion reaction obeyed the linear rate law. The corrosion rate greatly suppressed with the presence of sufficient molten carbonate. The corrosion reactions obeyed the parabolic rate law if a specimen was in the melt or coated with the coating amount larger than 3 mg/cm^2 . The corrosion rate was very close to that of titanium and much smaller than those of nickel, chromium and iron. If the coating amount was less than 3 mg/cm^2 , the reaction changed from the parabolic rate law to the linear rate law and proceeded the severe corrosion. In order to form a protective scale, a certain amount of molten carbonate was necessary.

INTRODUCTION

Molten salt has been considered for the media of energy conversion or storage since a high energy efficiency or a high reactivity can be obtained. However, the molten salt system has always a problem of a materials durability. The molten carbonate fuel cell (MCFC) has the advantage that a wide variety of fuels, such as hydrogen, hydrocarbons, carbon monoxide, as well as their mixtures (coal gas) can be used. The exhausted heat of the MCFC is more valuable than that of the phosphoric acid fuel cell (PAFC), since the operating temperature is high. The

MCFC can serve as a cogeneration system effectively. However, the durabilities of the components of the MCFC cause problems especially at the long time operation¹⁾.

Several kinds of corrosion of the metallic material in the MCFC are present. The corrosion of anode side of the separator has report to be very severe for stainless steel. However, since the anode side is reducing atmosphere, it is easy to improve the stability and nickel coating on stainless steel is effective to protect the corrosion. On the other hand, the corrosion can be protected by the formation of stable oxide scale at cathode side, since the atmosphere is oxidizing and metal oxide is thermodynamically stable. In another words the corrosion takes place principally and the corrosion rate is reduced by the formation of a stable oxide scale.

With the presence of molten carbonate the stability sometimes decreases since the oxide scale dissolves in the melt. The hot corrosion is the extraordinary corrosion that took place with the presence of thin film of molten salt at high temperature and is usually studied with Na_2SO_4 film²⁾. The hot corrosion associated to molten carbonate has also reported in several papers³⁻⁵⁾. In order to improve the material stability the corrosion characteristics of more variety of metal specimens should be studied as well as the elucidation of the hot corrosion mechanism.

Tantalum is known for a oxidation resistant metal at room temperature similar to titanium. However, the stability of the oxide scale decreases at high temperature and the severe corrosion took place in oxygen or in air⁶⁾. The effect of molten carbonate to the stability of tantalum oxide is worth for studying. In this study the high temperature corrosion of tantalum has been studied with the presence of molten carbonate in oxygen atmosphere.

EXPERIMENTAL

Tantalum specimens were cut into rectangular size (1*6*12 mm or 1*6*6 mm) from 99.95% tantalum sheet. The major impurities of the specimen are given in Table 1. The specimens were polished with #240 - #1500 SiC abrasive paper, followed by degreasing with a neutral detergent, washing with ethanol, drying and weighing before testing. The carbonate was a mixture of alkaline metal carbonate

and were made by the reagent grade chemicals in a nitrogen filled dry box. The standard composition of the melt was $(\text{Li}_{0.62}\text{K}_{0.38})_2\text{CO}_3$. The composition of the carbonate melt was this eutectic melt otherwise notified.

Three kinds of corrosion test were conducted to check the effect of carbonate melt; corrosion without melt, corrosion with the carbonate coating and corrosion in the carbonate melt. For the coating test the carbonate that was made by mixing alkaline carbonate and melting above the melting point was dispersed in ethanol. The carbonate and ethanol mixture was dipped onto the surface of a tantalum specimen and dried. The amount of coating was determined by the weight change of the specimen before and after the coating process. For the corrosion test in the melt a tantalum specimen was fully immersed in the melt. The ratio of melt/metal was about 3 in weight.

The treated specimens were placed in a gold-20% palladium alloy cell. Before starting the corrosion test the cell with the specimen was held at 463 K for 30 min in order to remove remaining moisture. The weight change of the cell with the specimen was measured and monitored continuously by TGA (Shimadzu DT-40). The atmosphere was normally a 67%CO₂-33%O₂ gas mixture at atmospheric pressure. In order to examine the effect of the gas composition, CO₂ and O₂ gas pressure was changed from 0.1 to 0.9 atm. The reaction temperature was varied from 873 to 1123 K. The reaction time was normally 60 h. After the weight measurement, the specimens were analyzed by XRD.

RESULTS AND DISCUSSION

Figure 1 shows the comparison of the weight gain curves for the three kinds of the corrosion test; dry (corrosion without melt), melt coating (corrosion with the melt coating) and immersed (corrosion in the melt). Tantalum corroded severely at high temperature without melt. The corrosion reaction obeyed the linear rate law and the corrosion product was Ta₂O₅. A 1 mm thick tantalum specimen was completely consumed within 20 h at this condition. These results were well corresponded to the previous papers⁶.

The corrosion rate was suppressed greatly with the presence of molten carbonate either coated or immersed. The corrosion reaction obeyed the parabolic rate law and lithiated tantalum oxide was formed on the surface of the corrosion scale. The rate constant was close to those of titanium and stainless steels. The corrosion reaction was suppressed by the formation of lithiated tantalum oxide.

Figure 2 shows the corrosion curves with the different amount of carbonate melt coating. If the amount of carbonate melt on a specimen was larger than 3 mg/cm^2 , the corrosion rate was very small and the reaction obeys the parabolic rate law. Figure 3 shows the dependence of the parabolic rate constant k_p on the amount of coating on the metal. The parabolic rate constant decreased linearly with the increase of coating amount. The thickness of the carbonate melt (amount of coating) affected the corrosion reaction. Since the reaction obeyed the parabolic rate law, in another words the rate determining step of the reaction was the diffusion of the species through the oxide scale, the effect could not be explained directly by the decrease of the oxygen potential at the scale/melt interface. The decrease of oxygen potential would affect the concentration of the diffusion species in the scale.

At Fig. 2 the corrosion reaction changes from the parabolic rate law to the linear rate law and the severe corrosion takes place, if the amount of melt coating is less than 3 mg/cm^2 . The linear corrosion proceeded until the tantalum metal was completely consumed and the major corrosion product was Ta_2O_5 at this stage. The linear rate constant was independent of the amount of coating and close to that without melt. At this stage tantalum is no more stable. The transition time from the parabolic rate law to the linear rate law depend on the amount of coating. When the amount of coating is larger, the transition time delayed.

Figure 4 shows the dependence of $(\text{weight gain})_{tr}$, the weight gain that was obtained at the transition time(parabolic to linear) on the amount of coating. Clearly, $(\text{weight gain})_{tr}$ is proportional to the amount of coating. The transition is directly due to the amount of carbonate melt coating. The carbonate melt is necessary for the formation of lithiated tantalum oxide that can suppress the corrosion reaction. If the carbonate is not enough for covering all the surface of a specimen, the reaction proceeds similar to that without melt after the melt is consumed.

The corrosion reaction depended on temperature. Figure 5 shows the corrosion curves of tantalum with the carbonate melt coating (30 mg/cm^2) at different temperatures. The corrosion reaction obeyed the parabolic rate law below 1073 K and the reaction rate becomes higher at higher temperatures. At the high temperature of 1123 K the reaction did not obey the parabolic rate law any more. The accelerated corrosion takes place at this temperature. The major corrosion product was Ta_2O_5 . The lithiated tantalum oxide that was effective to protect the corrosion is not stable at this temperature.

The dependence of the corrosion reaction on atmosphere was studied with 30 mg/cm^2 melt coating. The reaction was independent of the oxygen pressure at the pressure range from 0.1 to 0.9 atm. Figure 6 shows the corrosion curves of tantalum with carbonate coating at different CO_2 pressure. The corrosion reaction obey the parabolic rate law in each case and depends on the CO_2 pressure. The reaction rate becomes higher at higher CO_2 pressure. Figure 7 shows the dependence of the parabolic rate constant with the carbonate melt coating on CO_2 pressure. The rate constant increases as the CO_2 pressure increases. CO_2 is one of the oxidant in this system. However, the concentration of CO_2 did not directly affect the parabolic rate constant, since the parabolic rate constant expresses the diffusivity of species in the oxide scale. CO_2 affects the basicity of the melt. As the CO_2 pressure increases, the carbonate melt becomes acidic. This change of the basicity of the melt or the CO_2 potential might affect the concentration of the diffusion species in the oxide scale.

Figure 8 shows the dependence of the corrosion reaction with the carbonate melt coating on the melt composition. The corrosion rate decreases if the melt composition is changed from $\text{Li/K}=43/57$ carbonate melt to $62/38$ carbonate melt. The corrosion rate also decreases if the melt is changed from $\text{Li/K}=62/38$ to $\text{Li/Na}=52/48$ carbonate. The melt becomes more basic if the concentration of lithium increases or sodium carbonate is used instead of potassium carbonate⁷⁾. In these cases the CO_2 potential at the surface of the scale did not change, since the CO_2 potential was thermodynamically determined by the atmospheric pressure. The basicity of the melt would affect the diffusion process in the oxide scale. If the melt becomes basic, the rate of the corrosion reaction decreases. Further study is necessary in order to elucidate the diffusion process in the oxide scale that is the key point of the corrosion reaction of tantalum with carbonate melt coating.

CONCLUSION

The high temperature corrosion of tantalum has been studied with the presence of carbonate melt. The corrosion reaction suppressed remarkably if enough carbonate exists and obeyed the parabolic rate law. The parabolic rate constant depended on CO_2 pressure and the melt composition. Figure 9 shows the comparison of the corrosion curves of several metals with the carbonate coating. Tantalum is relatively stable and the corrosion rate is close to that of titanium. However, the severe corrosion took place if the carbonate was insufficient. This point should be counted when tantalum were used at high temperature with the presence of carbonate melt.

ACKNOWLEDGEMENT

The authors express their thanks to the financial support from the MCFC Association of Japan.

REFERENCES

- 1) K. Ota, Corrosion Engineering, 37, 135 (1988)
- 2) R.A. Rapp, in "Selected Topics in High Temperature Chemistry" Φ .Johannesen, A.G.Andersen eds., Elsevier, Amsterdam (1989), p.291
- 3) D.A.Shores, P.Singh, in "Molten Carbonate Fuel Cell Technology" J.R.Selman, T.D.Claar eds., p.271 the Electrochemical Society Proceeding Series PV84-13, Pennington, NJ (1984)
- 4) K.Ota, B. Kim, Y.Abe, H.Yoshitake, N.Kamiya, in "Molten Carbonate Fuel Cell Technology" D.Shores, H.Maru, I.Uchida, J.R.Selman, eds.,p.252,the Electrochemical Society Proceeding Series PV93-3, Pennington, NJ (1993)
- 5) K.Ota, B-u.Kim, H.Yoshitake, N.Kamiya, Bull.Chem.Soc.Japan, 66, 721 (1993)
- 6) P.Kofstad, "High Temperature Oxidation of Metals" John Willy & Sons, (1966) p.190
- 7) K.Ota, S.Mitsushima, S.Kato, S.Asano, N.Kamiya, J.Electrochem.Soc., 139, 667 (1992)

Table 1 Impurities of specimen (wt.ppm)

	W	O	Mo	C	N	Nb	Ni	Si
99.95% Ta	<100	60	<30	<10	10	10	10	10

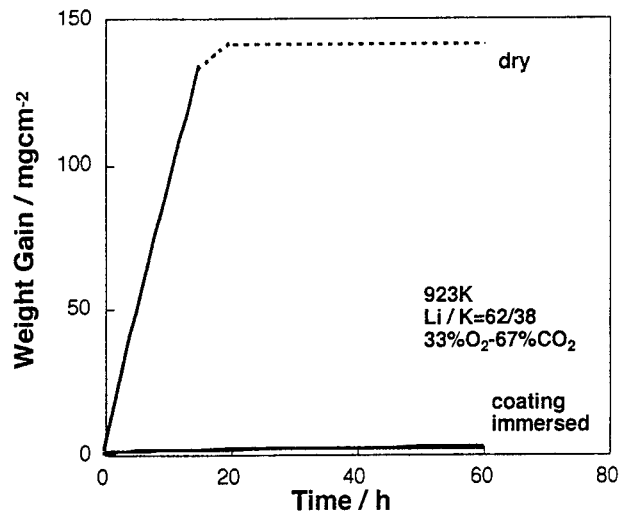


Fig.1 Weight gain curves for the corrosion of Ta with dry, coating and immersed.

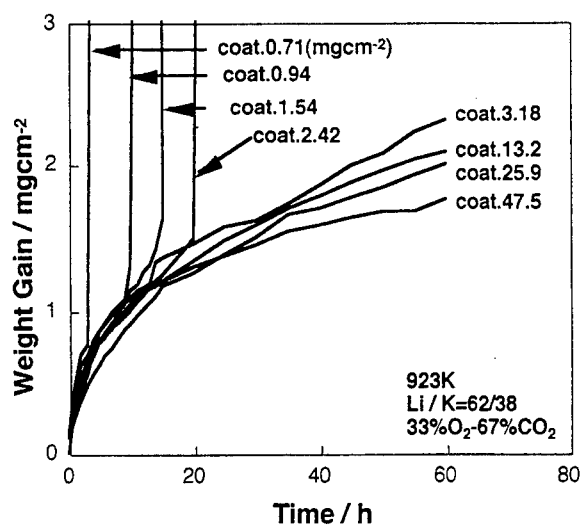


Fig.2 Weight gain curves for the corrosion of Ta with carbonate melt coating.

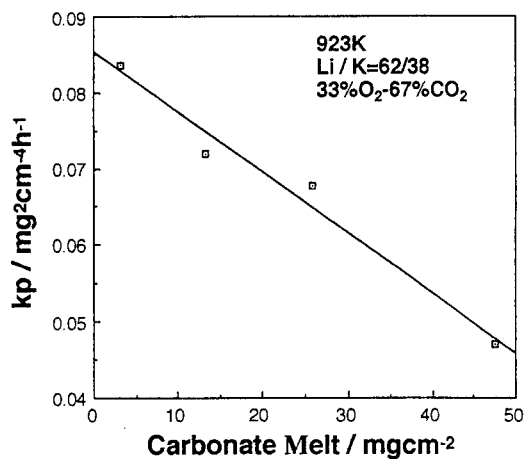


Fig. 3 Dependence of k_p on the amount of carbonate melt.

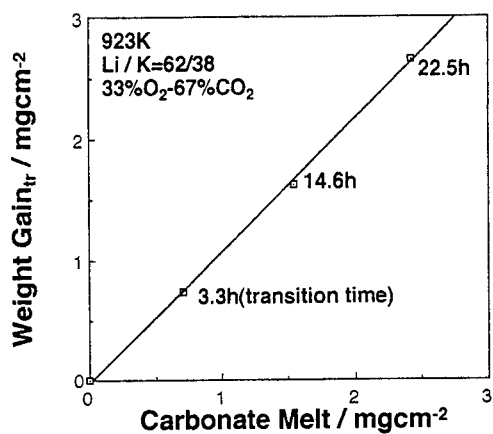


Fig. 4 Relationship between the amount of carbonate melt and the weight gain of transition.

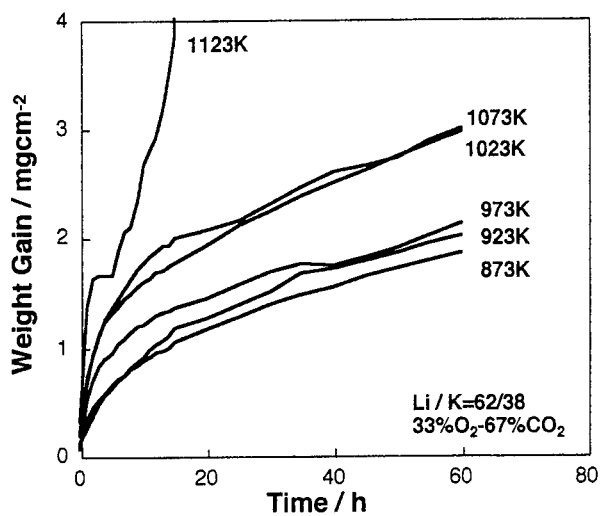


Fig.5 Weight gain curves for the corrosion of Ta with carbonate melt coating (25mg/cm²).

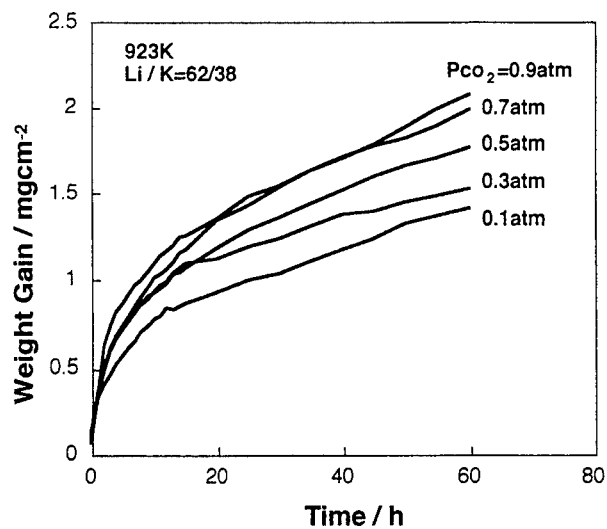


Fig. 6 Effect of Pco₂ for the weight gain curves for the corrosion of Ta with carbonate melt coating (25mg/cm²) at Pco₂=0.1atm.

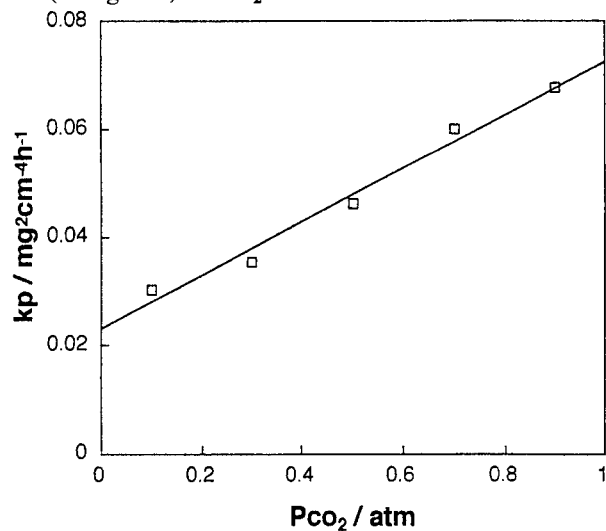


Fig. 7 Relationship between kp and Pco₂ for the corrosion of Ta with carbonate melt coating (25mg/cm²) at Pco₂=0.1atm.

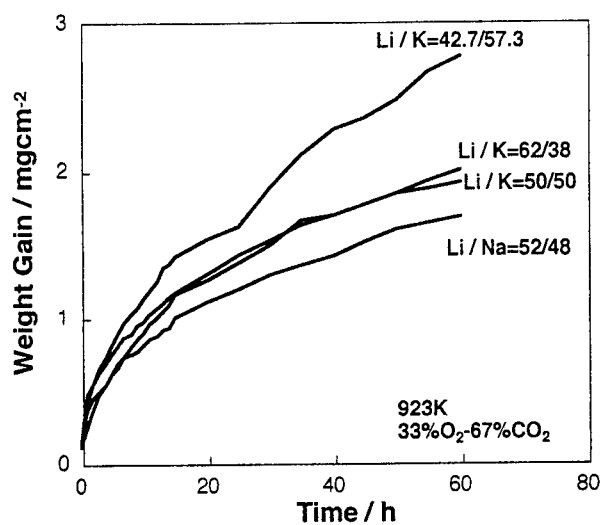


Fig. 8 Weight gain curves for the corrosion of Ta with carbonate melt coating (25mg/cm^2).

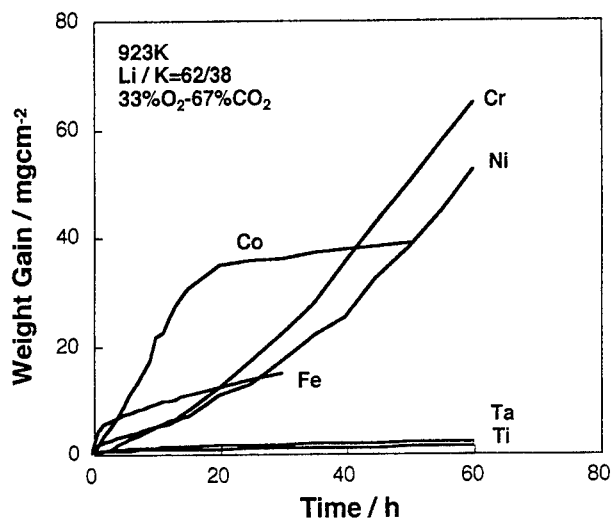


Fig.9 Weight gain curves for the corrosion of metals with carbonate melt coating (30mg/cm^2).

HIGH TEMPERATURE CORROSION OF SEPARATOR MATERIAL IN $\text{Li}_2\text{CO}_3\text{-Na}_2\text{CO}_3$ AND ELECTROLYTE CONSUMPTION FOR MCFC

Masahiro Yanagida, Kazumi Tanimoto, Toshikatsu Kojima,
Yukiko Tamiya, Takasi Asai and Yoshinori Miyazaki

*Fuel Cell Section
Osaka National Research Institute
1-8-31 Midorigaoka, Ikeda, Osaka 563, JAPAN*

Corrosion tests of type 310S stainless steel coated with 5 mg/cm^2 of Li/Na carbonate (52/48 mol%) have been carried out at 873, 923, 973 K under the simulated cathode environment ($\text{CO}_2/\text{O}_2 = 2/1$ (vol%)) of MCFC in out-of-cell test for up to 500 hours. Corrosion products are almost the same under these temperature and consist of two layers of LiFeO_2 as the outer layer and LiCrO_2 as the inner layer. Only Cr dissolved from the specimen into the melt. Though Na content in the melt was independent of the test duration and the temperature, Li content was decreased with increasing the test duration and increasing the temperature. On the other hand, dissolved Cr content in the melt was increased with increasing the test duration and increasing the temperature. Up to 500 hours, amount of Cr dissolution follows parabolic rate law.

INTRODUCTION

The molten carbonate fuel cell (MCFC) is expected to be a high efficiency power generation device with low pollutant emission. Molten carbonate used for its electrolyte separates between anode and cathode gas environment and provides ionic conductivity on MCFC operation. However there are some problems such as NiO cathode degradation and corrosion caused by its electrolyte. In order to reduce the NiO dissolution under cathode environment, some changes of electrolyte have been employed, such as alkaline-earth carbonate addition into the conventional eutectic carbonate mixture (1), using other carbonate mixtures (2). Molten carbonate is very corrosive under MCFC operating condition. And the corrosion behavior of its component materials accompanies with consumption of electrolyte. Therefore, management of electrolyte is one of the important factors of the limiting lifetime and performance of MCFC. From the standpoint of the inventory of the electrolyte in MCFC, we have to

consider that carbonate electrolyte not only distributes to both electrodes and electrolyte supporting material (tile) but also is consumed for corrosion, cathode lithiation and migration.

In this paper, we describe a corrosion behavior of type 310S stainless steel as a separator material and consumption of electrolyte using the another promising carbonate mixture, $(\text{Li}_{0.52}\text{Na}_{0.48})_2\text{CO}_3$, under the simulated cathode environment.

EXPERIMENTAL

A sheet of commercially available type 310S stainless steel (SUS310S), of thickness 1 mm, served as corrosion specimen. Its chemical composition is listed in table 1. The sheet was cut into 10 x 20 mm, polished with wet abrasive paper up to 1000 grit, washed and degreased by acetone, rinsed with distilled water and dried. Chemical reagent grade Li_2CO_3 and Na_2CO_3 , which purity was > 99.0% and > 99.5%, respectively, served for preparation of mixed carbonate after drying at 523 K for 12 hours. The mixed carbonate composed by $\text{Li}_2\text{CO}_3 : \text{Na}_2\text{CO}_3 = 52 : 48$ (mol%) was pre-melted at 923 K under CO_2 environment, quenched and then ground finely. Specimens were coated with 5 mg/cm^2 the carbonate and hung through pure alumina rod in alumina crucible. Corrosion test was carried out under the simulated cathode environment ($\text{CO}_2 : \text{O}_2 = 2 : 1$ (vol%)) at 873, 923 and 973 K in out-of-cell test. After test duration (25, 50, 100, 200, 500 hours), specimens were taken out of the electric furnace and quenched. In order to investigate the carbonate consumption, the residual carbonate with the specimens after the test was dissolved into water and analyzed by inductively coupled plasma atomic emission spectroscopy (ICP-AES). Corrosion products were identified by X-ray diffraction (XRD) and observed by SEM and electron probe micro-analysis (EPMA).

Table 1. Chemical composition in wt.% of SUS310S tested.

C	P	S	O	N	Si	Mn	Ni	Cr	Fe
0.046	0.0012	0.0012	0.0019	0.0316	0.74	1.26	19.01	24.91	Bal.(54)

RESULTS AND DISCUSSION

Results of XRD of the specimen with carbonate after the test showed that the carbonate contained Na_2CrO_4 . Results of XRD of specimens removed carbonate after

test showed that corrosion products on the SUS310S consisted of LiFeO_2 and LiCrO_2 . Except for corrosion products containing $\gamma\text{-LiFeO}_2$ at 873 K due to its stability at the temperature (3), the identified corrosion products were the same under these temperature and duration. No corrosion product containing Na was found in the specimens removed carbonate after test.

The surface observation of the specimens removed carbonate after test by SEM showed that the grain of the corrosion products which had facet grew with the test duration and the temperature. The analysis of the cross section of the specimens by EPMA showed that the corrosion products mainly consisted two layers of outer Fe-rich oxide layer and inner Cr-rich oxide layer. From XRD analysis the outer and inner layer corresponded to LiFeO_2 and LiCrO_2 , respectively. Cr depletion layer of the metal was observed inside of the corrosion products.

Result of each dissolved element ratio at 923 K using ICP-AES is shown in Fig. 1. Cr was only detected in all the melts after the test as the element dissolved from the specimen. Li, Na and Cr were determined as main elements of water soluble products from tested specimens. Amount of Na in soluble products was almost independent of the test duration in melt at 873, 923 and 973 K. Amount of Li in melt, however was decreased with increasing the test duration and temperature. Li was used to produce the corrosion products on the metal and was consumed from about 6 wt.% at 873 K to more than 30 wt.% at 973 K after 500 hours. On the other hand, amount of dissolved Cr in melt was increased with increasing the test duration and temperature. Up to 500 hour duration, it is shown that amount of Cr dissolution follows parabolic rate law in Fig. 2 :

$$x = k_d \cdot \sqrt{t} \quad [1]$$

where x is the Cr dissolution weight into melt (mg), k_d is the parabolic rate constant ($\text{mg/h}^{1/2}$) and t is testing duration (h). The calculated parabolic rate constants of Cr dissolution, k_d , are listed in table 2. Fig. 2 shows that amount of dissolved Cr is increased with the temperature in the range from 873 to 973 K.

Table 2. Calculated parabolic rate constants for Cr dissolution of SUS310S under 67% CO_2 + 33% O_2 with 5 mg/cm^2 $(\text{Li}_{0.52}\text{Na}_{0.48})_2\text{CO}_3$ deposit.

temperature (K)	parabolic rate constant, k_d ($\text{mg/h}^{1/2}$)
873	0.07
923	0.16
973	0.17

Li in carbonate melt reacts with Fe and Cr in the specimen and is fixed in corrosion products of solid phase. On the other hand, Na still exists in carbonate melt of liquid phase due to high solubility of Na_2CrO_4 in Li/Na carbonate. The physical properties of carbonate caused by Cr dissolution into the melt will be changed with the operating time of MCFC. Further, the change of proportion of Li/Na due to consumption of only Li will also change the expected properties of the electrolyte. And it is thought to affect the cell performance and its life.

CONCLUSIONS

Corrosion test of SUS310S coated with 5 mg/cm^2 Li/Na carbonate have been carried out at 873, 923 and 973 K under the simulated cathode environment ($\text{CO}_2/\text{O}_2 = 2/1$ (vol%)) for up to 500 hours in out-of-cell test. Solid corrosion products on the specimens consisted of two layer of the outer LiFeO_2 layer and the inner LiCrO_2 layer. No corrosion product containing Na was found in the solid corrosion products.

Amount of Na in the melt was almost independent of both the test duration and the temperature. Amount of Li in the melt was decreased with increasing test duration and temperature. Cr only detected as dissolved element from the specimen into the melt. Amount of Cr dissolution in the melt was increased with increasing the test duration and temperature and followed parabolic rate law.

REFERENCES

1. K. Tanimoto, Y. Miyazaki, M. Yanagida, S. Tanase, T. Kojima, N. Ohtori, H. Okuyama and T. Kodama, *Denki Kagaku*, **59**, 619 (1991).
2. K. Ota, S. Mitsushima, K. Kato and N. Kamiya, in *The 2nd Symposium on Molten Carbonate Fuel Cell Technology/1990*, J. R. Selman, D. A. Shores, H. C. Maru and I. Uchida, Editors, **PV 90-16**, p.318, The electrochemical Society Proceedings Series, Pennington, NJ (1990).
3. J. C. Anderson and M. Schieber, *J. Phys. Chem. Solids*, **25**, 961 (1964).

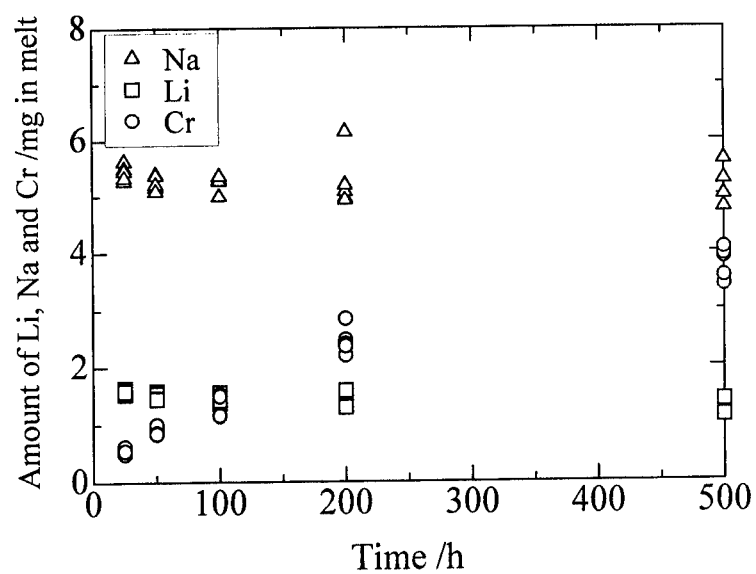


Fig. 1 Amount of Li, Na and Cr in the melt dependence of the test duration at 923 K.

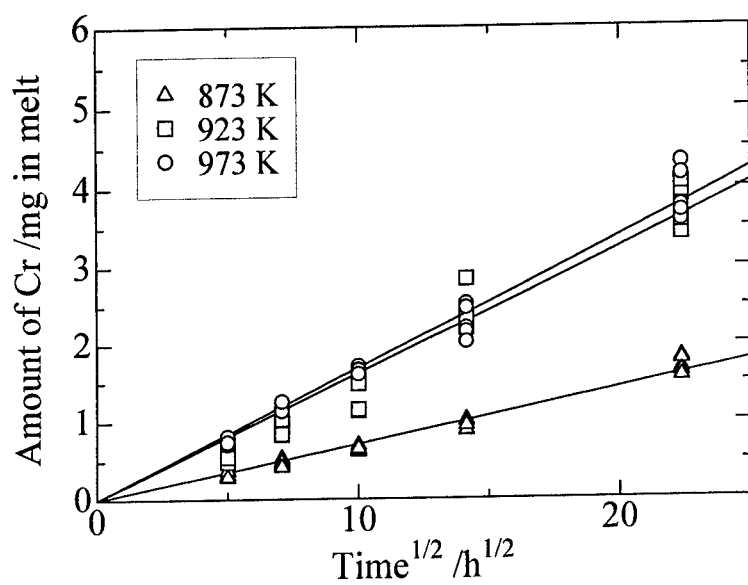


Fig. 2 Amount of Cr dissolved in the melt dependence of the test duration and the temperature.

ELECTROCHEMICAL RESPONSE OF STAINLESS STEELS 310, 316L AND NICKEL-RICH ALLOY IN MOLTEN CARBONATE

M. S. Yazici and J. R. Selman
Department of Chemical and Environmental Engineering
Illinois Institute of Technology
Chicago, IL 60616

ABSTRACT

The corrosion of separator plate/current collector materials in molten carbonate fuel cells is investigated. Although the corrosion resistance of stainless steel Type 310 is better than that of Type 316, the poorly conducting surface oxide layer on Type 310 is a source of significant ohmic resistance in long term operation, where not only corrosion resistant but conductive layer forming materials are needed. A high-nickel content alloy shows better corrosion resistance than 300 series stainless steels. Electrochemical measurements show significant differences in corrosion behavior between completely submerged samples and samples wetted by a carbonate film.

INTRODUCTION

Cathode dissolution leading to electrolyte-matrix shorting, and the corrosion of current collector and separator plate materials are the main life-limiting factors of the state-of-the art MCFC^(1,2). These metallic components are also major contributors to the total system cost. Therefore, it is necessary to minimize hardware corrosion and increase cell life to reduce capital cost.

It is well-known that in the corrosion of stainless steel by molten carbonate chromium forms a protective layer or surface oxide scale which causes the substrate not to be further oxidized. The chromium content of the alloy determines whether it forms an interior layer or an external scale. Low oxide diffusivity in the oxide scale can cause chromium to diffuse to the surface. While chromium is oxidized to form Cr_2O_3 at the metal/oxide interface, an FeO layer also forms and may grow at higher rates. A quantitative explanation of the oxidation behavior of alloy systems requires dealing with multi-component diffusion. In addition, the separator has various contact areas with the carbonate melt, whose different surface to volume ratios lead to differences in character of the corrosion process. The wet-seal area resembles most closely the fully immersed condition. On the other hand, the areas exposed to the gas channels can be dry or covered with a thin film due to creeping of the melt from the porous electrode onto the separator or current collector.

Finally, electrochemical analysis of the multi-component corrosion process becomes difficult when different materials have very close oxidation or reduction potentials. In some cases, it is not possible to find sufficient thermodynamic information for reactions to calculate the required electrode potentials. Therefore, in the following analysis we use a combination of information from different sources such as surface and layer analysis, as well as thermodynamic reference works.

EXPERIMENTAL DETAIL

A series of experiments were carried out on stainless steel Types 310 and 316L, and a nickel-rich alloy, in a specially designed controlled-atmosphere chamber, furnace and cell⁽³⁾. A 62% Li_2CO_3 - 38% K_2CO_3 mixture was used as electrolyte under oxidant gas of 30% CO_2 -70% air compositions. The nickel-rich alloy was also tested in 52% Li_2CO_3 -48% Na_2CO_3 electrolyte. The chemical compositions of the alloys are given in Table 1. The test cell and electrodes are shown in Figure 1. In this half-cell study, two electrodes are compared under open circuit or current load. Potential is measured with reference to a 67% O_2 - 33% CO_2 gas mixture. Three different configurations may be used(Figure 2). The first has the working electrode fully immersed in the melt, in the second the working electrode is partially immersed and in the third, the electrode is mounted on the surface of an alumina tube which provides a very thin film wetting the electrode material. However, electrochemical analysis of the corrosion process at a partially immersed electrode is difficult because it involves too many unknown parameters such as meniscus structure and melt thickness. Therefore, only two(fully immersed and thin-film covered) configurations are examined. These electrodes(immersed and thin-film covered) are subjected to an oxidizing environment at the same time. In the case of the alumina-backed electrode configuration, the electrolyte creeps up very fast on the alumina surface, and fills the crevice at the back of the electrode. The electrolyte starts to slowly creep up to form a thin film on the outer surface of the electrode. A meniscus forms at the interface metal-electrolyte-gas atmosphere.

Steady-state polarization and cyclic voltammetry measurements are performed periodically after the electrode is first in contact with the melt. The experimental set-up allows optical observation and camera recording of the different electrodes to determine the effect of wetting by molten carbonate on the surface reactions.

Table 1. Chemical composition in wt% of alloys used in the study

Alloy/Elements	Fe%	Ni%	Cr%	Al%
SS 316L	69	10	18	
SS 310	55	20	25	
NKK	23	45	30	1

RESULTS AND DISCUSSION

Open Circuit Potential (OCP)

The open circuit potentials of stainless steel Types 310 and 316L and of high-nickel alloy under CO_2 becomes stable around -1000 mV. The stable potential under CO_2 shows roughly 50 mV potential difference between a fully immersed and a mounted electrode. Under CO_2 , these surfaces are indeed stable (i.e., no surface reaction is observed). Steady-state potentials of both immersed and thin-film covered electrodes under CO_2 are given in Figure 3. Table 2 shows corrosion currents and potentials derived from log I-E plots. The data suggest a lower corrosion resistance for thin-film covered electrodes than for immersed electrodes. Stainless steel Type 316L has a lower corrosion resistance than Type 310. High nickel alloy has the lowest corrosion current among these materials.

Table 2. Corrosion currents from steady-state polarization plots under CO_2

sample-(electrolyte)	immersed	immersed	thin-film covered	thin-film covered
	E_{CORR} , mV	I_{CORR} , μA	E_{CORR} , mV	I_{CORR} , μA
SS310-(Li/K)	-1023	4.1	-986	29.6
SS316-(Li/K)	-1040	23	-981	40
NKK-(Li/K)	-991	3.5	-878	5.9
NKK-(Li/Na)	-1058	1.2	-970	5.1

When an O_2/CO_2 mixture is introduced at a partially immersed electrode, most surface reaction is observed on the top portion of the thin-film covered electrode.

The open circuit potential of a thin-film covered electrode under oxidizing gas mixture evolves toward the oxygen reduction potential quickly, i.e., within 2-3 hrs. Figures 4(a) and (b) show open circuit potential decay of stainless steel Types 310 and 316L. If the electrode is wetted by a thin film of carbonate, it easily forms a surface oxide (i.e. FeO and Cr_2O_3). An immersed electrode forms LiCrO_2 under a surface oxide layer. This inner LiCrO_2 layer cannot prevent iron from diffusing out through the outer surface oxide scale. Therefore, the OCP of the immersed electrode cannot reach oxygen equilibrium potential.

As the OCP of a film-wetted electrode evolves, electrolyte intensively moves around the wetted electrode. The forces that drive this movement are generated at the melt/oxide interface, but also appear to accelerate corrosion at the oxide/metal interface. If the thin film on the electrode is rich in lithium, this may affect long-term corrosion behavior because of the more basic character of the film. Due to the low oxygen solubility in the electrolyte layer and the smaller solid-state diffusivities in the alloy, oxygen diffusion from the gas-electrolyte-oxide interface to the metal-oxide interface is slow compared with iron diffusion from the bulk metal to the metal-oxide interface. Thus, the characteristics of the surface oxide layer play an important role. These considerations

also hold for the open circuit potential response of high-nickel alloys. Figures 4(c) and (d) show the potential-time behavior in Li/K and Li/Na electrolytes, respectively. Although, the potential change of thin-film covered electrodes are similar, immersed alloy samples show a response similar to pure nickel⁽⁴⁾. The response of thin-film wetted electrode upon changing oxidizing gas to CO₂ is not explained yet.

Cyclic voltammetry

When the potential is swept repeatedly, the polarization response of the thin-film wetted electrode(FE) is a current increase without peaks. The overall response of an immersed electrode(IE) under CO₂ gas and under oxidizing atmosphere(see Figure 5) does show distinct peaks. The potential window between 0 and -1600 mV contains several oxidation and reduction peaks. Thermodynamic potentials calculated with reference to the oxygen reduction potential under 67% O₂- 33% CO₂ gas are given in Table 3. In the following discussion, expressions in parenthesis will refer to the electrochemical reactions in this table.

The most negative equilibrium potential of the elements forming the alloy is that of chromium, at approximately -1500 mV. Therefore, the first anodic oxidation peak when sweeping anodically from -1400 mV(following a previous cathodic sweep) is apparently due to carbon which may result from carbonate decomposition at such negative potentials, and Cr₂O₃ formation at much more positive potentials than the metal equilibrium potential(C1). LiCrO₂ can also form from chromium at the same potential as Cr₂O₃ formation(C2). Next, iron, starts to be oxidized at a more positive potential than the stable thermodynamic potential(F1). Starting from oxidation of iron metal, current continuously increases by giving peaks. In the potential range of -900 mV, several reactions may take place simultaneously according to Table 3. Metallic iron can react to form lithiated iron oxide(F2) at -953 mV. Around the same potential, FeO is further oxidized to Fe₃O₄(F3). Since formation of Fe₂O₃ from Fe₃O₄ occurs at -550 mV, LiFeO₂ can only be formed from Fe or FeO. Nickel oxidation starts to occur around -800 mV(N1). Participation of nickel in the surface layer reaction depends on the amount of chromium. The potential necessary to cause lithiation of FeO to LiFeO₂ is approximately -700 mV(F4). Since the very negative scan starting potential causes formation of LiCrO₂. This can be oxidized to Li₂CrO₄, which occurs at around -500 mV(C3). This peak is also contributed by lithiation of NiO[4].

Formation of Cr₂O₃ or LiCrO₂ surface layers is a very important step in building the corrosion protection characteristic of Fe-Cr-Ni alloys. Lithium chromite is probably less protective and does not prevent further internal oxidation. Cr₂O₃ is preferable to protect the alloy from further being oxidized. Following the main peak at -500 mV, the current decreases until dissolution of chromium into the melt as CrO₄²⁻ takes place(C4). This process occurs with a lot of bubble formation and color change of the melt. The location of this peak is the same for Types 310 & 316L.

An anodic potential scan causes gas evolution from the surface only at potentials more positive than -600 mV. It is very likely that the anodic current peak above -600 mV is caused by an electrode process which causes CO₂ generation, for example(C3) or (C4).

Table 3. Equilibrium potentials calculated from thermodynamic data

	● (O) $\Rightarrow 1/2\text{O}_2 + \text{CO}_2 + 2\text{e}^- \rightarrow \text{CO}_3^{2-}$
-0.1 --	
-0.2 --	
-0.3 ●	(C4) $\Rightarrow \text{LiCrO}_2 + 2\text{CO}_3^{2-} \rightarrow \text{Li}^+ + \text{CrO}_4^{2-} + 2\text{CO}_2 + 3\text{e}^-$
-0.4 --	
-0.5 ●	(C3) $\Rightarrow \text{LiCrO}_2 + \text{Li}^+ + 2\text{CO}_3^{2-} \rightarrow \text{Li}_2\text{CrO}_4 + 2\text{CO}_2 + 3\text{e}^-$
-0.6 --	
-0.7 ●	(F5) $\Rightarrow \text{FeO} + \text{Li}^+ + \text{CO}_3^{2-} \rightarrow \text{LiFeO}_2 + \text{CO}_2 + \text{e}^-$
-0.8 ●	(F4) $\Rightarrow 2\text{Fe}_3\text{O}_4 + \text{CO}_3^{2-} \rightarrow 3\text{Fe}_2\text{O}_3 + \text{CO}_2 + 2\text{e}^-$
-0.9 ●	(N1) $\Rightarrow \text{Ni} + \text{CO}_3^{2-} \rightarrow \text{NiO} + \text{CO}_2 + 2\text{e}^-$
-1.0 ●	(Co) $\Rightarrow \text{Co} + \text{CO}_3^{2-} \rightarrow \text{CoO} + \text{CO}_2 + 2\text{e}^-$
-1.1 ●	(F3) $\Rightarrow 3\text{FeO} + \text{CO}_3^{2-} \rightarrow \text{Fe}_3\text{O}_4 + \text{CO}_2 + 2\text{e}^-$
-1.2 --	(F2) $\Rightarrow \text{Fe} + \text{Li}^+ + 2\text{CO}_3^{2-} \rightarrow \text{LiFeO}_2 + 2\text{CO}_2 + 3\text{e}^-$
-1.1 ●	(F1) $\Rightarrow \text{Fe} + \text{CO}_3^{2-} \rightarrow \text{FeO} + \text{CO}_2 + 2\text{e}^-$
-1.2 --	(C1) $\Rightarrow 2\text{Cr} + 3\text{CO}_3^{2-} \rightarrow \text{Cr}_2\text{O}_3 + 3\text{CO}_2 + 6\text{e}^-$
	(C2) $\Rightarrow \text{Cr} + \text{Li}^+ + 2\text{CO}_3^{2-} \rightarrow \text{LiCrO}_2 + 2\text{CO}_2 + 3\text{e}^-$
	(C) $\Rightarrow \text{CO}_3^{2-} + 4\text{e}^- \rightarrow \text{C} + 3\text{O}^{2-}$

The reverse cathodic scan starts from 0 mV with carbonate formation(O) and possibly with chromate reduction if it is not removed from the surface. The alloys we are dealing with here consist of three different elements: nickel, chromium and iron, therefore, sometimes peaks related to the oxidation or reduction of two different elements may overlap with each other if their potentials are close. Also, a high valence oxide of iron may become a lower valence oxide at a potential anywhere between -600 to -1200 mV. Between peak(F3) and that assigned to LiFeO₂(F2), the current is very flat over a range of approximately 400 mV. This may be caused by structural changes in the lattice. Removal of lithium or iron(if any higher valence oxide such as LiFe₅O₈ is formed) from the lattice structure reduces the magnitude of the current and keeps it constant until further reduction occurs. If the degree of delithiation does not exceed a certain level, nothing happens until the potential approaches -1100 to -1200 mV. The more clearly defined peak(F1) around -1100 mV is considered to be reduction of FeO and LiFeO₂ to metallic iron. At the end of the cathodic scan, a current increase is caused by metallic chromium formation and cathodic carbonate decomposition.

Optimal resolution of the peaks corresponding to various electrochemical reactions on Type 316L is obtained only at very slow scan rates opposite to type 310. As Figures 5 and 6 show, differences may be due to lower percentages of chromium and nickel in Type 316L.

High nickel alloys show fewer but more distinct peaks compared to stainless steels. These peaks are mainly Ni dominated. The current levels are also lower compared to stainless steels(Figure 7).

Surface-layer analysis

The possible layer products of Types 310 and 316L stainless steel have been determined by Yokokawa⁽⁵⁾ from thermodynamic data. They depend on $\log P_{\text{CO}_2}$, $\log(a_{\text{Cr}}/a_{\text{Fe}})$ and $\log P_{\text{O}_2}$. Yokokawa suggests a layer sequence of $\text{Cr/Cr}_2\text{O}_3/\text{LiCrO}_2/\text{LiFe}_5\text{O}_8/\text{K}_2\text{CrO}_4$ for Type 310 and $\text{Fe,Cr/Cr}_2\text{O}_3/\text{FeCr}_2\text{O}_4/\text{Fe}_3\text{O}_4/\text{Fe}_2\text{O}_3/\text{LiFe}_5\text{O}_8/\text{LiFeO}_2$, for Type 316L.

The corrosion layers found by cross-sectional analysis of Type 310 may be compared for the effect of carbonate contact on the formation of corrosion products. In the case where the electrode is fully immersed in the carbonate mixture, the most inner layer is mainly chromium oxide(positions D & H in Figure 8(a)). These areas are depleted in Fe and Ni. Chromium content gradually decreases from bulk metal to the metal/electrolyte interface. Since Fe diffuses to this interface to form a thick oxide surface layer, the layers below the surface are richer in Cr.

The thin-film wetted electrode forms a compact and thin layer of oxides. The layer thickness at the inner side close to the bulk melt(ceramic facing bottom part) is thicker than at the top which is only slightly wetted by carbonate(Figure 8(b)). Thin-film side which has had less contact with carbonate, shows spreading of chromium oxide at the metal/oxide interface. As electrolyte wetting becomes less and less toward the top of the electrode, this behavior is observed at both sides of the electrode.

Layers formed with a thin-film wetted configuration show concentration differences at the top and the bottom of the electrode, at the gas-facing as well as ceramic-facing side. At the bottom, the most outer layers are continuous and Cr and Fe rich. Below this, a region rich in Fe and Ni occurs. Between this layer and the metal/oxide interface, spreading of chromium oxide is observed. At the top, fewer layers can be distinguished by microprobe analysis. In both gas and ceramic-facing sides, the layer just below the surface is very rich in Cr. At the top of the sample, the overall thickness of the oxide layer becomes less. The more stronger wetted side(ceramic-facing) has a ~ 10% thicker oxide layer than the gas facing side. The thickness are given in Table 4.

Figures 9(a), (b), (c) and (d) show map analyses of oxide layers on thin-film wetted electrodes at the ceramic-facing side. An approximately 8 μ thick iron rich surface layer is observed(b). The region below that is about 6 μ thick and rich in chromium(d). The thickness of the most interior Cr_2O_3 layer is ~ 5 μ and consists mostly of Fe and Ni oxides. Open areas around the dark regions(a) are iron and nickel. Concentration profiles for immersed and thin-film covered electrodes are given in Figures 10(a), (b).

Table 4. Thickness of oxide layers						
condition	thickness, μm		thickness, μm		thickness, μm	
	top		middle		bottom	
	outer	inner	outer	inner	outer	inner
Thin-film wetted	13	15	14	18	19	22
Thin-film wetted	spreading oxide		spreading oxide		spreading oxide	
Immersed			31		25	

Overall, immersed samples have much thicker oxide layers than thin-film wetted ones. In the thin-film wetted electrode configuration, layer thickness decreases from bottom to top as the thickness of the carbonate film decreases.

CONCLUSION

(1). The significant differences observed in this study between immersed and film-wetted electrodes, summarized in (3) and (4) below, suggest that half-cell studies have to mimic actual cell conditions to yield results that are useful for the improvement of materials and long-term performance of the MCFC. However, alloy composition is the primary factor concerning corrosion resistance.

(2). The OCP as well as CV characteristics are affected by the nickel and chromium content of ternary alloys:

(a) The observed OCP decay of alloys suggests that the higher the chromium and nickel content, the faster a protective layer forms. Type 310 stainless steel contains more chromium and nickel than Type 316L. This helps the formation of a more protective, continuous sub-scale. In Type 316L, iron may diffuse outward and break the thin Cr_2O_3 protective scale. Thereby, lithium may more easily diffuse into the alloy and Fe or Cr cations may diffuse toward the oxide/electrolyte interface, facilitating corrosion.

(b) Since the alloys consist of three or four different elements, CV peaks related to the oxidation or reduction of one element may overlap with oxides of the other two elements. This makes interpretation of CV's much more difficult than in pure-metal corrosion. Nevertheless, in combination with OCP and surface layer analysis, CV's can give insight in the sequence of corrosion processes.

(3). A compact(thin) and dual-structured oxide layer is required for good corrosion protection by any candidate material, and this is affected by the degree of wetting:

(a) The film-wetted alloy forms a much more compact layer, due to the passive surface oxide layer formed under high oxygen activity, than the same alloy immersed in a deep layer of carbonate. The corrosion layer thickness close to the bulk melt is thicker than at the top of the sample where it is only slightly wetted.

(b) One other distinction is that a surface contacting a thin carbonate film forms a spreading Cr_2O_3 layer while a deeply immersed surface forms a continuous inner layer of Cr_2O_3 much more slowly and less reliably.

(4). The corrosion protection provided by the film wetted electrode is related to convection at the melt/oxide interface(via the meniscus) and to gas access(via the film):

(a) When Types 310 and 316L are wetted by a thin film of carbonate, the potentials of both alloys approach the oxygen reduction potential within a few hours. This is explainable by easy access of oxygen to the metal/electrolyte interface. A protective scale forms before lithium ions penetrate and can take part in the corrosion process. When electrodes are fully immersed, the diffusion of lithium into, and cations(Fe, Ni and Cr ions) out of the alloy, overtakes the oxide layer formation process. Alloy inter-diffusion coefficients, therefore, are an important consideration in comparing and understanding the corrosion behavior of stainless steels and alloys.

(b) The lithium content of the electrolyte film appears to determine the corrosion rate by making the electrolyte film more basic. If porous oxide layers are filled with carbonates, it causes internal lithiation of oxide products. This process lowers the lithium concentration and increases potassium concentration. However, when the surface layer is stable and inner layers form a spinel, then these stable oxides do not allow lithium to diffuse into the inner structure. In this case, a gradual lithium gradient is established to a certain thickness. Beyond that critical thickness, oxides are not lithiated.

(5). These results suggest that pre-oxidation can be a solution to obtain a compact oxide layer. Adding Al to alloy leads to a very stable oxide layer, but increases its resistivity. Alloy behavior under continuously polarized conditions has to be investigated for more realistic corrosion predictions.

ACKNOWLEDGMENTS

This work was supported by the U.S. Department of Energy, via Morgantown Energy Technology Center(METC). High Ni-alloy samples provided by the NKK Corporation(Kawasaki, Japan) under sponsorship of NEDO(Japan) are gratefully acknowledged.

REFERENCES

- (1) J. Vossen, "Corrosion of Separator Plate Constituents in Molten Carbonate", Ph.D.Thesis, T.U. Delft the Netherlands. 1994
- (2) C. Yuh, R. Johnsen, M. Farooque and H. Maru, "Carbonate Fuel Cell Endurance: Hardware Corrosion and Electrolyte Management Status", Proc. Third Int. Symp. Carbonate Fuel Cell Technology, ECS, Vol.93-3, p. 158-170(1993)
- (3) M. Matsumura and J.R. Selman, *J. Electrochem. Soc.*, 139, p. 1255-1261(1992)
- (4) M.S. Yazici and J. R. Selman, "Investigation of wetting phenomena and oxidation/lithiation behavior of nickel in molten carbonate", Proceedings Fuel Cells '94 Contractors Review Meeting, p. 93-102(1994)
- (5) H. Yokokawa, N.Sakai, T.Kawada, M.Dokiya and K.Ota, *J. Electrochem. Soc.*, Vol.140, No.12, p.3565-3577(1993).

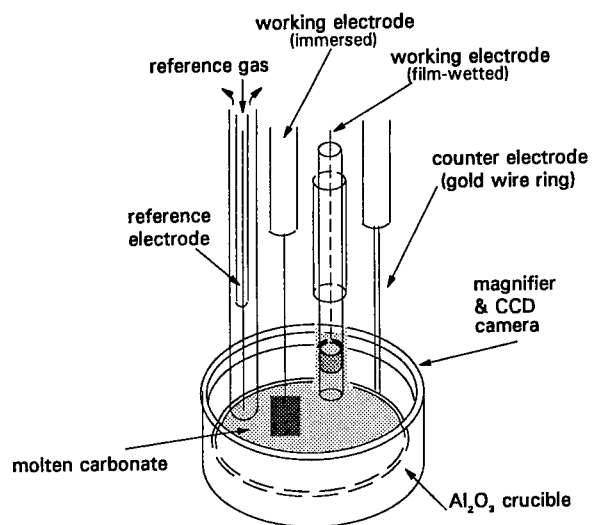


Figure 1. Detail of cell and electrode configuration showing immersed and thin-film covered electrodes

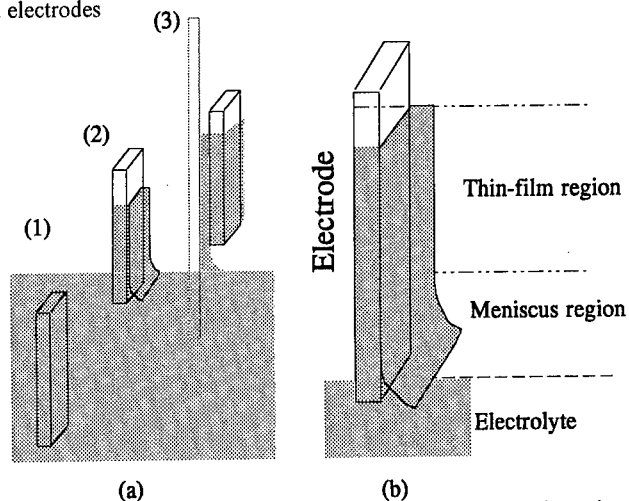


Figure 2. (a) Schematics of possible electrode configurations in the electrolyte: (1) fully immersed, (2) partially immersed and (3) thin-film wetted, (b) detail of partially immersed electrode configuration

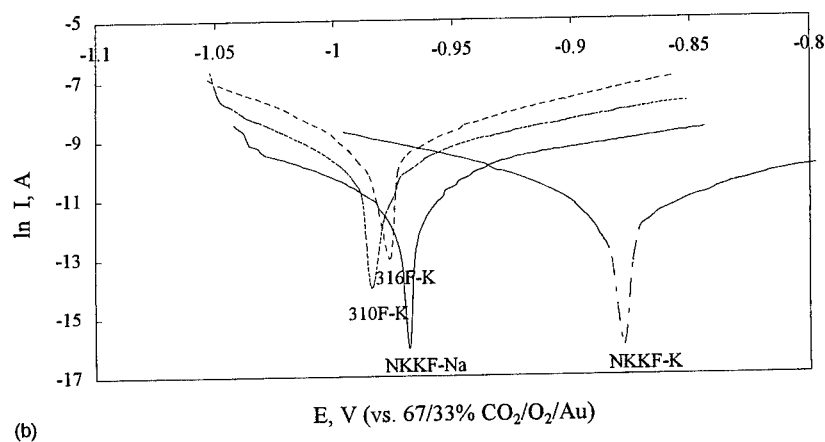
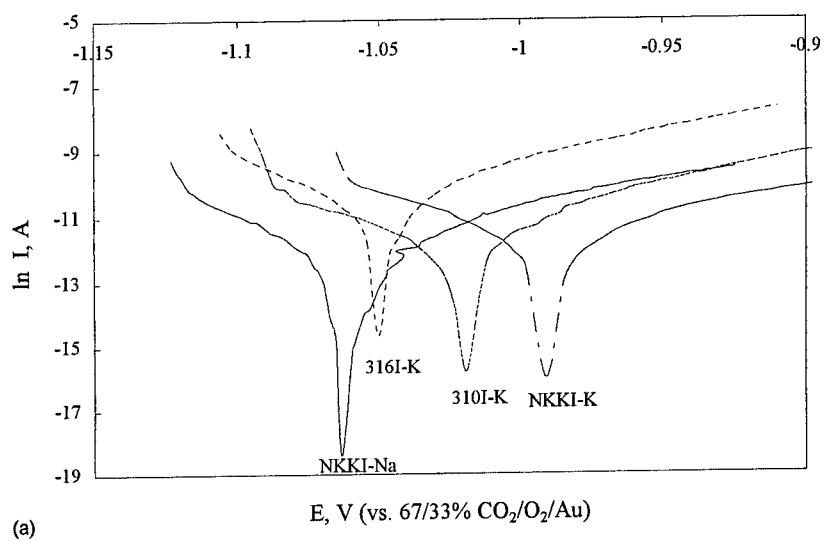


Figure 3. Steady-state polarization curves on (a) immersed and (b) thin-electrolyte-film covered electrodes. NKKI-K stands for (I)mmersed NKK alloy in Li-(K) carbonate, and NKKF-Na stands for (F)ilm-covered electrode in Li-(Na) carbonate electrolyte

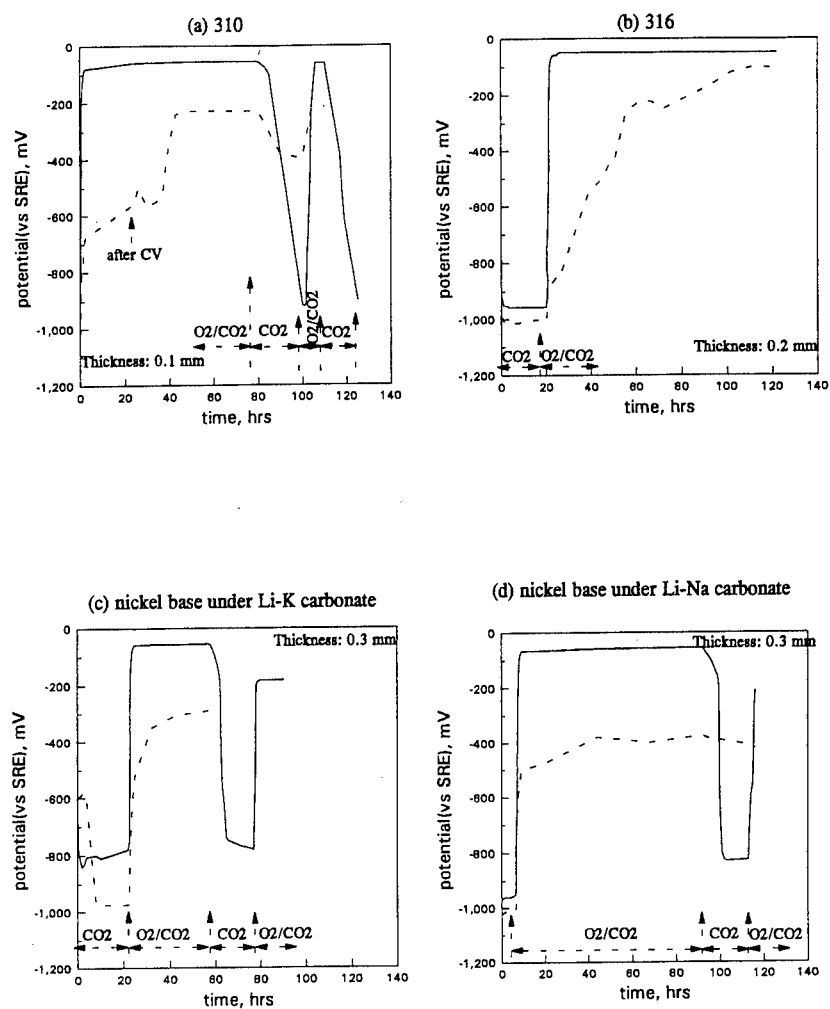


Figure 4. OCP response of stainless steel (a) 310, (b) 316L in Li-K electrolyte and high nickel alloy in (c) Li-K and (d) Li-Na electrolytes. Solid line: wetted electrode, dashed line: immersed electrode

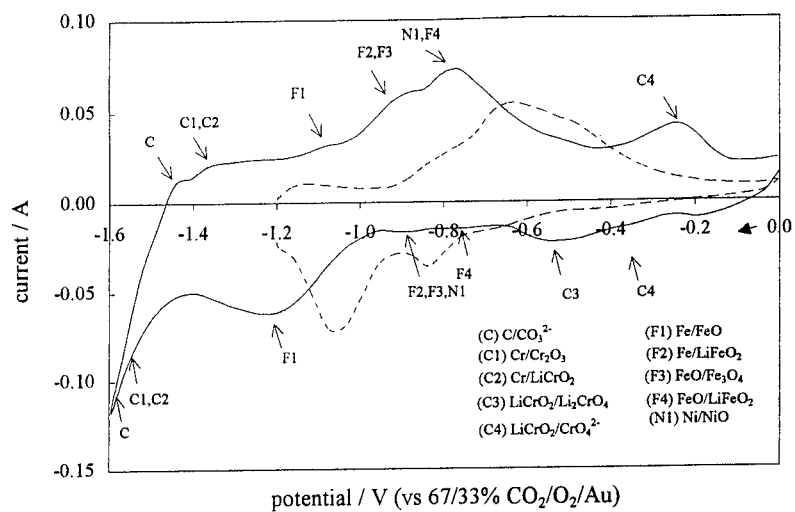


Figure 5. Polarization response of an immersed stainless steel Type 310 under 15% O₂-30% CO₂(solid line) and 100% CO₂(dashed line) at 100 mV/s scan rate

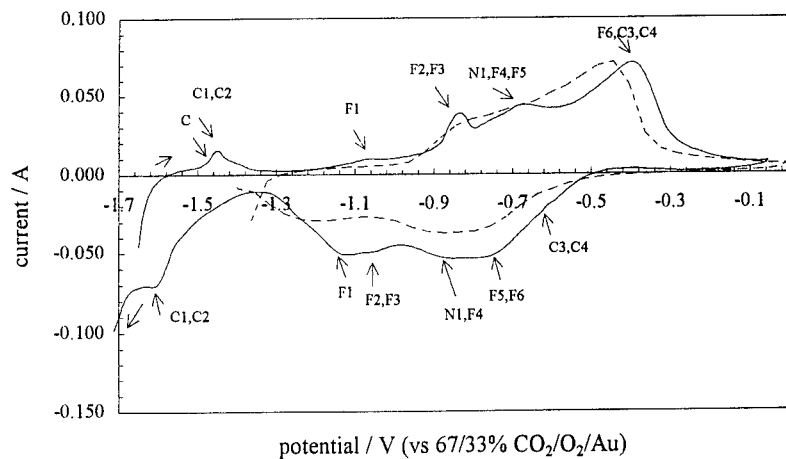


Figure 6. Polarization response of immersed stainless steel Type 316 under 15% O₂-30% CO₂(solid line) and 100% CO₂(dashed line) at 1 mV/s scan rate

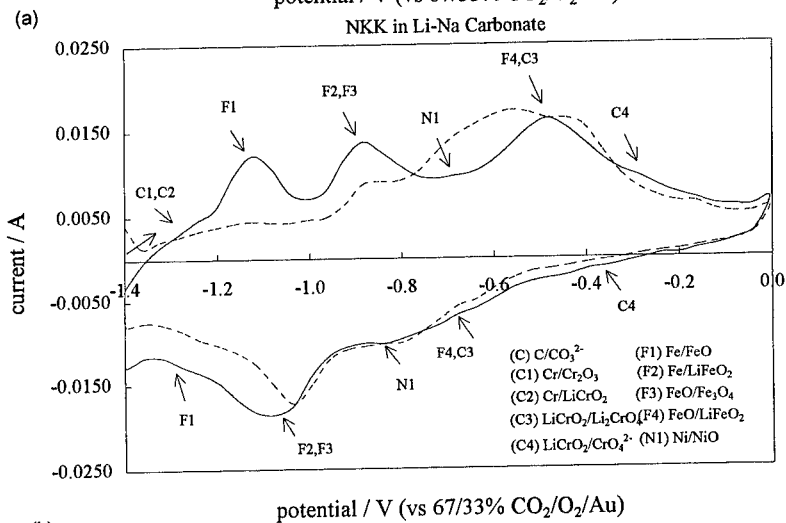
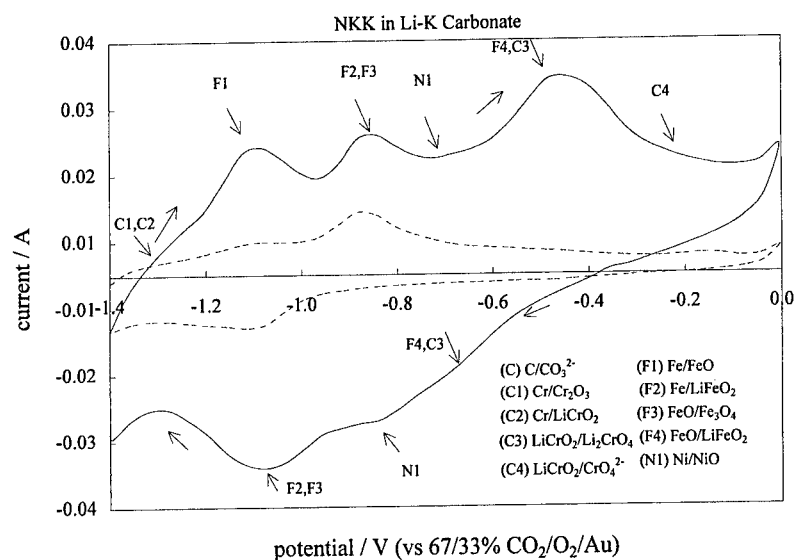


Figure 7. Polarization response of immersed high-nickel alloy under 15% O₂-30% CO₂ (solid line) and 100% CO₂ (dashed line) at 100 mV/s scan rate in (a) Li-K, (b) Li-Na carbonate

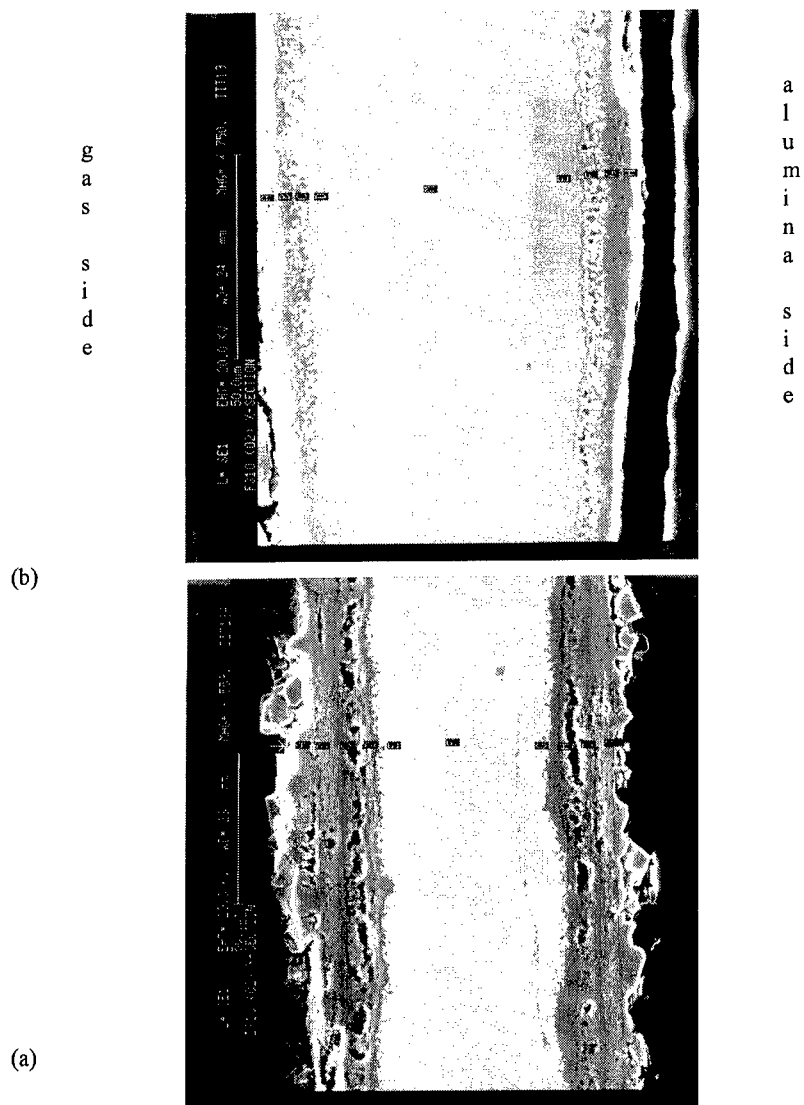


Figure 8. Cross-section of (a) immersed and (b) thin-film covered SS 310

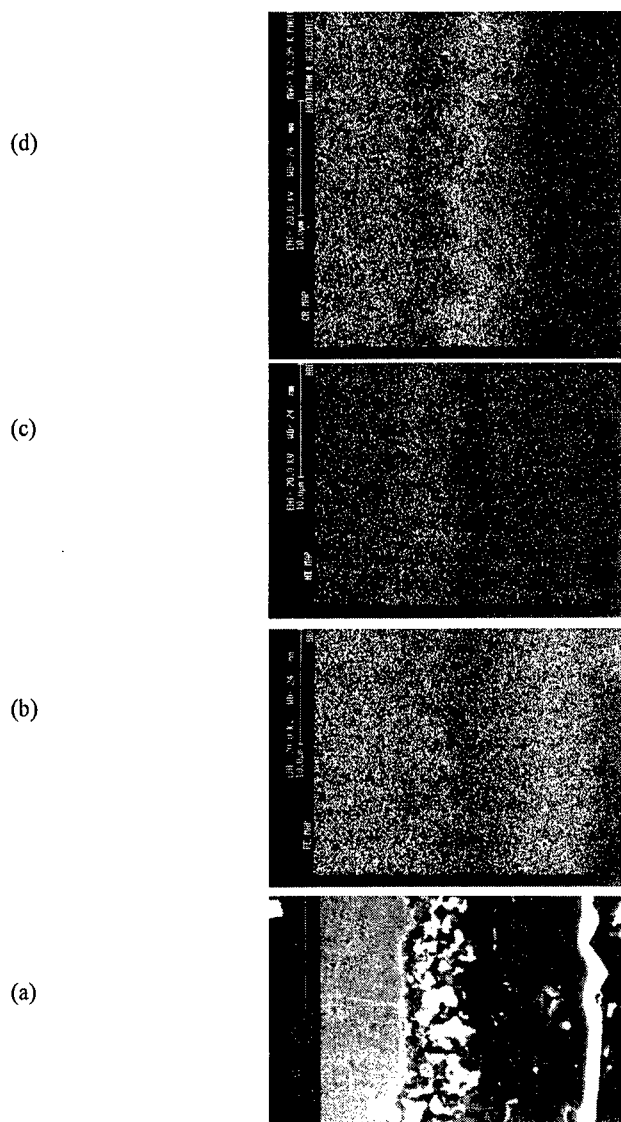
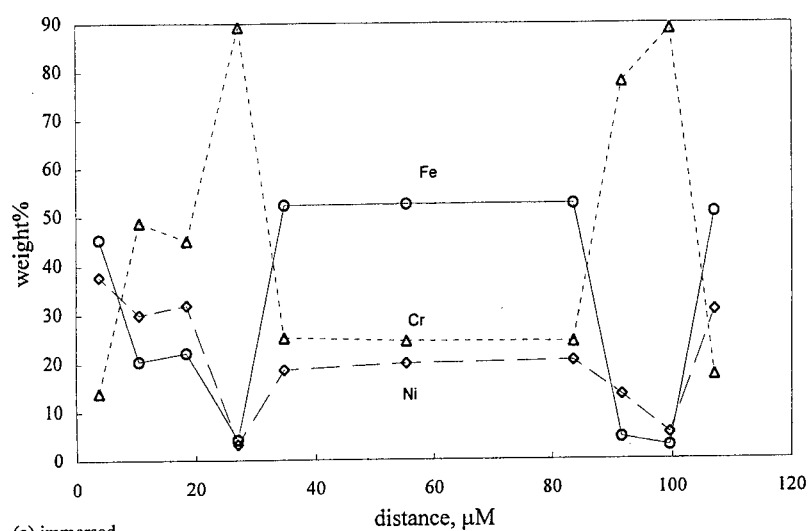
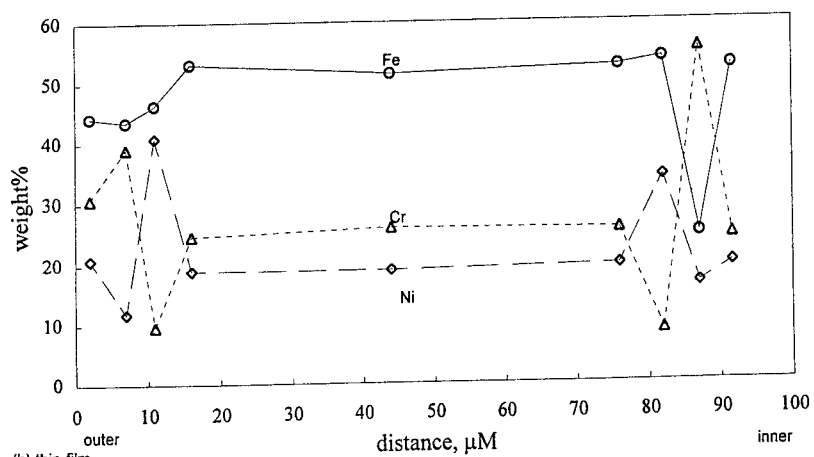


Figure 9. Map analysis on the (a) cross-section of thin-film covered Type 310 for (b) Fe, (c) Ni and (d) Cr



(a) immersed



(b) thin-film

Figure 10. Concentration profiles at the cross-section of (a) immersed and (b) thin-film covered Type 310 stainless steel

**THERMOCHEMISTRY, PHYSICO-CHEMICAL
PROPERTIES AND MODELING OF THE LIQUID
MX-LnX₃ MIXTURES (M = alkali, Ln = rare-earth, X = halide)**

M. Gaune-Escard

IUSTI, UMR 139 CNRS
Université de Provence, Centre de St Jérôme
13397 Marseille Cedex 20, FRANCE

ABSTRACT

Complementary techniques have been used to characterize the LnX₃ lanthanide chlorides (Ln = La, Ce, Pr, Nd, Gd, Dy, Er, Tm), their mixtures and compounds with the MX alkali chlorides (M = Li, Na, K, Rb, Cs).

Enthalpies of mixing were determined by direct high temperature calorimetry.

Enthalpies of formation or of phase transition were reported.

Heat capacities were determined by Differential Scanning Calorimetry.

Electrical conductivity and molar volume measurements were also performed.

The short range structure of molten ErCl₃ was studied by X-ray diffraction ; possible anionic pairs are discussed in terms of interatomic distances and bond angles.

A thermodynamic modelling of the experimental enthalpies of mixing was proposed.

The mixing enthalpy of the molten NaCl-DyCl₃ system, measured by direct calorimetry, was examined by molecular dynamics (MD) simulation and the stabilization of the Dy³⁺ ion in this system was interpreted in terms of complexes.

INTRODUCTION

During the last few years, we have investigated the thermodynamic and physicochemical properties of a number of compounds and systems formed by the lanthanide halides with alkali halides, namely :

LnCl₃ lanthanide chlorides, where Ln = La, Ce, Pr, Nd, Gd, Dy, Er, Tm (1),

MCl-LnCl₃ liquid mixtures, where M = Li, Na, K, Rb, Cs and Ln = Pr, Nd, Dy (2, 3, 4, 5),

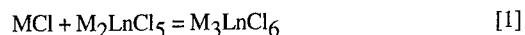
Table 1 : Summary of properties, melts and compounds investigated.

ΔH_{mix}	$\Delta H_{\text{tr}} / \Delta H_{\text{fus}}$	Cp	κ	structure
	LaCl ₃	LaCl ₃	LaCl ₃	
	K ₂ LaCl ₅			
	M ₃ LaCl ₆ M = K, Rb, Cs		M ₃ LaCl ₆ M = K, Rb, Cs	
			Cs ₃ LaCl ₆	
	CeCl ₃	CeCl ₃	CeCl ₃	
	M ₃ CeCl ₆ M = K, Rb, Cs		M ₃ CeCl ₆ M = K, Rb, Cs	
	PrCl ₃	PrCl ₃	PrCl ₃	
PrCl ₃ -MCl M = Na, K, Rb, Cs	M ₃ PrCl ₆ M = K, Rb, Cs		M ₃ PrCl ₆ M = K, Rb, Cs	
PrCl ₃ -CaCl ₂				
	NdCl ₃	NdCl ₃	NdCl ₃	
NdCl ₃ -MCl M = Na, K, Rb, Cs	M ₃ NdCl ₆ M = K, Rb, Cs		M ₃ NdCl ₆ M = K, Rb, Cs	
NdCl ₃ -CaCl ₂				
	GdCl ₃	GdCl ₃		
	DyCl ₃	DyCl ₃		
	ErCl ₃		ErCl ₃	ErCl ₃
		ErCl ₃ -NaCl	ErCl ₃ -NaCl	
		ErCl ₃ -KCl	ErCl ₃ -KCl	
	TmCl ₃			
DyCl ₃ -NaCl				DyCl ₃ -NaCl
DyCl ₃ -KCl				
DyCl ₃ -PrCl ₃				
LaBr ₃ -MCl M = Li, Na, K, Rb, Cs				
NdBr ₃ -MCl M = Li, Na, K, Rb, Cs	M ₃ NdBr ₆ M = K, Rb, Cs			

liquid $\text{CaCl}_2\text{-PrCl}_3$, $\text{CaCl}_2\text{-NdCl}_3$ (6) and $\text{DyCl}_3\text{-PrCl}_3$ (4) mixtures,
 M_3LnCl_6 compounds, where $\text{M} = \text{K, Rb, Cs}$ and $\text{Ln} = \text{La, Ce, Pr, Nd}$ (6).

Table 1 summarizes the systems and compounds investigated and indicates the techniques employed.

The congruently melting M_3LnCl_6 compounds exist in all the MCl-LnCl_3 systems (where $\text{Ln} = \text{La, Ce, Pr, Nd}$ and $\text{M} = \text{K, Rb, Cs}$) with the only exception of the KCl-LnCl_3 system (7, 8, 9, 10). It was found from e.m.f. measurements that potassium and rubidium compounds are stable only at higher temperatures and they are metastable at ambient temperature (11, 12). These compounds are formed according to the reaction :



Caesium compounds are stable at ambient temperature and undergo phase transition during heating.

Enthalpy of mixing

Enthalpies of mixing were determined by direct high temperature calorimetry. Several families of MX-LnX_3 mixtures have been investigated.

As usual in common anion systems, for a given family (e.g. the MCl-LnCl_3 systems with $\text{M} = \text{Li, Na, K, Rb, Cs}$) the absolute magnitude of enthalpy of mixing ΔH increases with the alkali ion size). This had been observed for almost all the simple (symmetrical) or more complex (asymmetrical).

A general feature of these MX-LnX_3 mixtures is the location of the minimum enthalpy at about $x(\text{LnX}_3) = 0.4$.

Figure 1 reports as an example the composition dependence of ΔH in the MCl-NdCl_3 mixtures.

Formation / phase transition enthalpy

The enthalpies of formation or of phase transition have been reported, for all the M_3LnCl_6 compounds (where $\text{Ln} = \text{La, Ce, Pr, Nd}$ and $\text{M} = \text{K, Rb, Cs}$), in a previous paper (6). Some new calorimetric results on the M_3NdBr_6 compounds are presented in the following and a comparison is established with the chloride analogues.

K_3NdX_6 compounds ($\text{X} = \text{Cl, Br}$)

K_3NdCl_6 forms at 724 K according to reaction [1] from KCl and K_2NdCl_5 with the corresponding enthalpy 46.3 kJ mol^{-1} . The temperatures of formation and melting were determined and are in a good agreement with literature data (10) (that work also reports

e.m.f. and X-ray measurements). It has been reported that K_3NdBr_6 undergoes solid-solid phase transition at 683 K and melts at 933 K (13). However, the large value (42.4 kJ mol^{-1}) of the effect at 684 K (683 K according to reference (13)) suggests that it is not arising from a phase transition but from the formation of K_3NdBr_6 from KBr and K_2NdBr_5 as observed for the K_3NdCl_6 analogue. Moreover, the melting temperature of K_3NdBr_6 determined during our experiments is 15 K lower than the temperature given in reference (13). Of course, this conclusion about the formation of K_3NdBr_6 at 684 K should be confirmed by X-ray or e.m.f. measurements. Molar enthalpies and entropies of formation and of melting are given in table 2 for K_3NdCl_6 and K_3NdBr_6 .

Table 2. Molar enthalpies and entropies of formation (including transition) and melting of K_3NdCl_6 and K_3NdBr_6

	T_f (K)	$\Delta_f H_m$ (kJ mol^{-1})	$\Delta_f S_m$ ($\text{J mol}^{-1} \text{K}^{-1}$)	T_{fus} (K)	$\Delta_{fus} H_m$ (kJ mol^{-1})	$\Delta_{fus} S_m$ ($\text{J mol}^{-1} \text{K}^{-1}$)	ref
K_3NdCl_6	724 719	46.3	63.1	973 972	48.0	49.3	(10)
K_3NdBr_6	684 683 *	44.0	64.3	918 933	41.4	45.1	(14)

*indicated in ref (13) as the temperature of a solid-solid phase transition

There was only one single effect observed on the heating curves of K_3NdCl_6 and K_3NdBr_6 before melting. This effect was ascribed to the formation reaction of compounds according to reaction [1]. However for K_3NdBr_6 , this effect was splitted into two independent peaks on cooling. Several runs were performed at different heating and cooling rates and are presented in figure 2. From the analysis of results, it is possible to conclude that the temperature and enthalpy of K_3NdBr_6 formation are not dependent on heating rate (with exception of the highest rate - 30 K.min^{-1}) and are equal to 684 K and 44.0 kJ mol^{-1} , respectively. Upon cooling the first effect was observed at 657 K (at higher cooling rates this temperature was shifted to a slightly lower value). The enthalpy of this effect was equal to 7.0 kJ mol^{-1} . The temperature of the second effect gradually decreased at increasing cooling rates. Its enthalpy seems to decrease also but this decrease may be the result of incorrect peak area determination (cooling rates 5.0 and 10.0

K.min⁻¹). At the cooling rate 30.0 K.min⁻¹ this effect was not observed and a metastable phase of K₃NdBr₆ was obtained. During heating of the metastable phase a well shaped exothermic effect was observed on the DSC thermograms in the temperature range of 500 - 520 K. The enthalpy change related to this effect was equal to - 24 kJ mol⁻¹. Very similar thermal properties were reported by Seifert for Rb₃NdCl₆ (14). The observed exothermic effects are very likely due to the of metastable decomposition of K₃NdBr₆ (or Rb₃NdCl₆ (14)). Table 2 summarizes the entropies determined from the measured enthalpies.

Rb₃NdX₆ compounds (X = Cl, Br)

We did not observe any effect of compound formation on the DTA curves of Rb₃NdCl₆ and Rb₃NdBr₆. The single effects on heating curves are rather phase transitions than reactions of formation. This conclusion comes from the comparison of the enthalpies related to these effects with the corresponding enthalpies for the caesium and potassium analogous compounds. However, according to Seifert (10), Rb₃NdCl₆ is unstable at room temperature and forms from RbCl and Rb₂NdCl₅ at 547 K then undergoes phase transition at 667 K. On cooling the metastable phase of the compound is obtained and its decomposition may take place only under specific conditions, e.g. with catalytic action of water (12). Taking into account Seifert's remarks, we may assume that during our experiments only one modification of Rb₃NdCl₆ was involved - stable at higher temperatures, metastable at lower temperatures. We cannot explain the origin of the small effect observed on the heating curves of Rb₃NdCl₆ at 382 K.

It is known from literature (15) that the M₃LaBr₆ compounds in the RbBr-LaBr₃ and CsBr-LaBr₃ systems crystallize in a cubic elapsolite structure above the phase transition temperature (701 K for Rb₃LaBr₆ and 712 K for Cs₃LaBr₆) and are monoclinic below this temperature. Metastable Rb₃LaBr₆ may be obtained only by quenching. These similarities between lanthanum and neodymium compounds suggest that it would be interesting to determine structure of Rb₃NdBr₆ and carry out the e.m.f. measurements described by Seifert.

Cs₃NdX₆ compounds (X = Cl, Br)

Cs₃NdCl₆ and Cs₃NdBr₆ are stable at room temperature and undergo solid-solid phase transitions at 678 and 731 K, respectively, with the corresponding enthalpies 7.4 kJ mol⁻¹ and 8.8 kJ mol⁻¹. No supercooling effects were observed for these compounds. Cs₃NdCl₆ is cubic elapsolite above the temperature of phase transition and monoclinic

below this temperature (10). Enthalpies and entropies of phase transition in the solid state and melting were determined for Cs_3NdCl_6 and Cs_3NdBr_6 .

Heat capacity

Pure lanthanide halides

Very few data exist on pure lanthanide halides. Also when data are available, they are often contradictory : for instance two very different values are reported for the heat capacity of liquid LaCl_3 ($349.8 \text{ J}\cdot\text{mol}^{-1}\text{K}^{-1}$ (16) and $158 \text{ J}\cdot\text{mol}^{-1}\text{K}^{-1}$ (17), respectively).

Table 3. Coefficients in the heat capacity equation $C_{p,m} (\text{J}\cdot\text{mol}^{-1}\text{K}^{-1}) = a + bT$, for the LnCl_3 compounds. SE - Standard error of estimation.(s)-solid, (l)-liquid.

Compound	Temperature range/K	a	b	SE
LaCl_3 (s)	300-1100	82.51	$3.816 \cdot 10^{-2}$	2.01
CeCl_3 (s)	300-1040	89.05	$1.790 \cdot 10^{-2}$	1.10
PrCl_3 (s)	300-1000	91.32	$3.459 \cdot 10^{-2}$	1.11
PrCl_3 (l)	1068-1090	155.28	-	1.24
NdCl_3 (s)	300-980	102.27	$2.170 \cdot 10^{-2}$	1.71
NdCl_3 (l)	1035-1090	149.53	-	2.39
GdCl_3 (s)	300-700	95.29	$1.584 \cdot 10^{-2}$	1.51
GdCl_3 (l)	880-970	139.89	-	1.14
DyCl_3 (s)	300-610;635-860	98.65	$1.102 \cdot 10^{-2}$	3.6
DyCl_3 (l)	935-960	159.43	-	1.35

We investigated CeCl_3 , PrCl_3 , NdCl_3 , GdCl_3 and DyCl_3 by Differential Scanning Calorimetry. Figure 3 shows as an example the C_p values measured for CeCl_3 . We also reported the estimated values of literature. Pankratz's (17) estimates, based on Walden and Smith's (18) drop calorimetry measurements, appears to exhibit an unusual temperature dependence. Surprisingly, the same estimate was obtained by Knacke *et al.* (19) even if in an earlier compilation Barin and Knacke (20) had given a more reliable dependence. Our experimental results agree within $\pm 4\%$ with the later. Heat capacities were obtained both for the solid and liquid state, except for LaCl_3 and CeCl_3 since their melting temperature was beyond the experimental range.

The experimental heat capacity data were fitted to analytical equations $C_p = a + bT$ both in the solid and the liquid state. The coefficients and the temperature ranges are given in Table 3.

Definite compounds

The heat capacities of the M_3LnCl_6 compounds, where $\text{M} = \text{K}, \text{Rb}, \text{Cs}$ and $\text{Ln} = \text{La}, \text{Ce}, \text{Pr}, \text{Nd}$ have been determined by differential scanning calorimetry (DSC) in the temperature range 300 - 1100 K. Most of these compounds are characterized by a limited stability range and phase transitions in the solid state. $C_{p,m}$ exhibits a specific behavior since it decreases with temperature from the phase transition temperature up to 150-200 K above this transition. This was observed for the: Rb_3CeCl_6 , Rb_3PrCl_6 , Rb_3NdCl_6 and Cs_3LnCl_6 compounds. The phenomenon was not observed for K_2LaCl_5 , K_3LnCl_6 and Rb_3LaCl_6 . We report as an example the heat capacity of the Cs_3LnCl_6 compounds (Figure 4).

Electrical conductivity

Pure lanthanide halides

Several works have been reported so far on the structure of rare earth chlorides (LnCl_3) by X-ray diffraction (21, 22), neutron diffraction (23) and Raman spectroscopy (21, 24, 25, 26), revealing that there existed in melt the octahedral complex anion LnCl_3^{3-} and a loose disordered network of corner- or edge-sharing octahedral units. Moreover, the measurements of conductivities are originally, of much use in studying dynamics of molten salts, reflecting the average dynamical structure. The molar conductivities of several rare earth chlorides were reported (27, 28, 29, 30) and the results suggested that the existence of dimeric or more polymeric complex anions may be presumed in these melts. The structures of molten ErCl_3 , $\text{ErCl}_3 \cdot 3\text{NaCl}$ and $\text{ErCl}_3 \cdot 3\text{KCl}$

were investigated (22, 31) and the existence of octahedral complex ions, ErCl_6^{3-} , was confirmed. Also expected is some clustering of distorted octahedral with edge-sharing. The molar volumes and the conductivities of molten ErCl_3 and of the ErCl_3 -NaCl and ErCl_3 -KCl systems have been measured, and the molar conductivities estimated (32). We have also determined the conductivities of the LnCl_3 and M_3LnCl_6 compounds ($\text{Ln} = \text{La, Ce, Pr, Nd}$; $\text{M} = \text{K, Rb, Cs}$) (33). The experimental electrical conductivities of the pure melts were fitted to the equation

$$\kappa = a + bT + cT^2 \quad [2]$$

with T being the absolute temperature.

The parameters a , b and c in this empirical conductivity equation are shown in Table 4.

Table 4. Coefficients of the electrical conductivity equation. S.E. standard error

Compound	Temperature K	a 10^{-2} S m^{-1}	b $\text{S m}^{-1} \text{ K}^{-1}$	c $10^{-4} \text{ S m}^{-1} \text{ K}^{-2}$	S.E. S m^{-1}
LaCl_3	1144-1234	-7.170	1.189	-3.77	0.322
CeCl_3	1090-1254	-3.551	0.584	-1.68	0.168
PrCl_3	1070-1170	-8.392	1.431	-5.38	0.113
NdCl_3	1017-1135	-5.191	0.869	-2.57	0.408
ErCl_3	1069-1178	-1.801	2.505	-0.448	0.006

The molar conductivity of a molten salt is given by :

$$\Lambda = \kappa V_m \quad [3]$$

where Λ is the molar conductivity, κ the specific conductivity and V_m the molar volume of the salt. The V_m data were taken from literature (34, 35) or measured (ErCl_3).

Since the $\ln \Lambda$ vs $1/T$ plots were straight lines, the molar conductivities were smoothed by Arrhenius-type equations

$$\Lambda = \Lambda_0 \exp(-E_A/RT) \quad [4]$$

where R is the gas constant in $\text{J.mol}^{-1}.\text{K}^{-1}$, Λ_0 the characteristic constant of the melt, and E_A the activation energy for electrical conduction. The values of Λ_0 and E_A are presented in Table 5.

Table 5. Molar electrical conductivity ($\Lambda/\text{Sm}^2\text{mol}^{-1}$) of LnCl_3

Compound	$\Lambda_0/\text{Sm}^2\text{mol}^{-1}$	$E_A/\text{kJ.mol}^{-1}$
LaCl_3	1.168	29.62
CeCl_3	0.103	25.36
PrCl_3	0.143	28.32
NdCl_3	0.204	28.05
ErCl_3	656.5	37.78

A few investigations of molten LaCl_3 specific conductivity have been reported (36, 37, 38, 39, 40, 41). Our results were compared with literature data. They are in good agreement with Jaffe and van Artsdalen's results (37) i.e a maximum deviation less than 0.7% in the whole experimental range. Smirnov and Khokhlov's (41) and Voigt and Biltz's (39) conductivity values are consistently lower than ours (about 17% and 25% at 1250 K, respectively).

The specific conductivity of CeCl_3 was measured by Bronstein, Dworkin and Bredig (42) and by Mellors and Senderoff (35), results which are larger than ours by 7-9% and 23-25%, respectively. As the uncertainty in Mellors and Senderoff's specific conductance values was estimated at about 15% (43), the agreement with our results is quite good.

Three specific conductivity investigations have been reported for molten PrCl_3 (39, 44, 27). The present results are significantly smaller than those obtained by Dworkin, Bronstein and Bredig (44) and Iwade, Igarashi and Mochinaga (27) (e.g. 22% and 18% at 1090 K) but they are in good agreement with Voigt and Biltz's data (39) (Fig.5). The maximum departure between them does not exceed 2.5% in the experimental temperature range.

The specific conductivity results for molten NdCl_3 are compared with literature data (39, 40, 28) in Fig.6. They are significantly higher (e.g. the departure from Föhrthmann, Vogel and Schneider's results (40) is about 25%).

The lanthanide chlorides used in this work for electrical conductivity measurements have been previously used in calorimetric investigations (1). The enthalpies of fusion and

melting temperatures values were in excellent agreement with literature data. The values $\Delta_{\text{fus}}H_m$ and T_{fus} are the following : LaCl_3 - 55.7 kJ mol⁻¹ and 1127 K, CeCl_3 - 55.5 kJ mol⁻¹ and 1086K, PrCl_3 - 52.1 kJ mol⁻¹ and 1061K, NdCl_3 - 48.1 kJ mol⁻¹ and 1032K while literature reported : 54.3 kJ mol⁻¹ and 1128K (45), 53.5 kJ mol⁻¹ and 1090K (46), 50.6 kJ mol⁻¹ and 1059 K (47) ; 50.2 kJ mol⁻¹ and 1032 K (47) respectively. This agreement confirms the purity of the compounds used in the present investigations.

Mixtures

There are only few data reported in literature for the electrical conductivity of the M_3LnCl_6 compounds. K_3NdCl_6 (40, 28), K_3PrCl_6 (40, 27), Rb_3LaCl_6 and Cs_3LaCl_6 compounds (only at 1195 K) (40).were investigated. The electrical conductivity of the M_3CeCl_6 , Rb_3PrCl_6 , Cs_3PrCl_6 , Rb_3NdCl_6 and Cs_3NdCl_6 compounds was measured for the first time in the present work.

The comparison of our results with literature data for K_3PrCl_6 and K_3NdCl_6 is shown in Fig. 7 and 8. They are about 20% lower than Iwadata, Igarashi and Mochinaga's (27) for K_3PrCl_6 and about 35% higher than Mochinaga and Iwadata's values (28) for K_3NdCl_6 . Our results for Rb_3LaCl_6 and Cs_3LaCl_6 at the reference temperature 1195 K are 90.1 Sm⁻¹ and 75.0 Sm⁻¹ compared with 130.7 Sm⁻¹ and 101.19 Sm⁻¹ (Forthmann, Vogel and Schneider (40)), respectively.

The results obtained showed that the activation energy for electrical conductivity does not depend significantly on alkali metal cation. The electrical conductivity decreases with increasing ionic radius of alkali metal cation. It depends also on lanthanide complex anion which is formed in the melts.

In the case of the K_3LnCl_6 compounds, the electrical conductivity of K_3NdCl_6 is significantly higher than that of the K_3PrCl_6 and K_3CeCl_6 compounds. It can be explained by polymer formation.

It was shown that Ln_6^{3-} complexes are formed in the KCl-LnCl_3 melts (27, 28). The formation of dimers $\text{Ln}_2\text{Cl}_{11}^{5-}$ also takes place (28). As product of dimerization free Cl^- ions with higher ionic mobility are produced. The possibility of dimerization or polymerization is higher for K_3NdCl_6 and its electrical conductivity larger.

For the Rb_3LnCl_6 compounds, the electrical conductivity of Rb_3NdCl_6 is also significantly higher than that of Rb_3LaCl_6 , Rb_3PrCl_6 and Rb_3CeCl_6 . Probably the dimerization can also take place but the degree of dimerization is lower than for the K_3NdCl_6 compound.

In the case of Cs_3LnCl_6 compounds the dimerization is not possible and the values of electrical conductivity of all compounds are very close altogether because of the similarity of lanthanide cations.

Molar volume

Pure lanthanide halides

ErCl_3 forms a monoclinic crystal (48). In order to study the volume change on melting, the molar volume, V , in the crystalline state was calculated by the equation

$$V = abc \sin b (N_A/Z) \quad [5]$$

where a , b , c , and b are the lattice constants. N_A and Z are Avogadro's number and the number of stoichiometric units contained in the unit cell, respectively.

The molar volume of molten ErCl_3 was measured and expressed as a linear function of temperature as $V_m = 59.63 + 1.562 \times 10^{-2} T$, with V_m and T in $\text{cm}^3 \text{mol}^{-1}$ and K , respectively. The molar volumes of several lanthanide trichlorides are given in Table 6.

Table 6. Molar volume changes on melting.

Compound	T_{fus}/K	$V_s/\text{cm}^3 \text{mol}^{-1}$	$V_m/\text{cm}^3 \text{mol}^{-1}$	$100 (V_m - V_s) V_s^{-1} / \%$
LaCl_3	1150	63.90	76.30	19.1
PrCl_3	1059	61.40	74.30	21.0
NdCl_3	1029	60.47	73.65	21.8
SmCl_3	935	59.23	73.73	24.5
GdCl_3	875	58.03	73.34	26.4
DyCl_3	928	74.38	74.62	0.3
HoCl_3	993	73.02	74.00	1.3
ErCl_3	1046	72.11	75.65	4.9
YCl_3	987	74.83	75.17	0.5

As can be seen from Table 6, the changes on melting of the molar volume of UCl_3 -type lanthanide trichlorides are very large, those lanthanide trichlorides of AlCl_3 -type being small. Therefore, the nearest neighbour ordering in molten ErCl_3 appears to be similar to that in the solid state.

Mixtures

The molar volumes of the ErCl_3 -NaCl and ErCl_3 -KCl mixtures were measured on the whole composition range between 752 K and 1178 K. In each system, a small deviation from additivity was observed. From these volume data, we calculated the corresponding excess molar volumes which were plotted against composition. Figure 9 shows the plots obtained at 1000 K and evidences the weak deviation from ideality (less than $2 \text{ cm}^3 \text{ mol}^{-1}$ compared with volumes around $75 \text{ cm}^3 \text{ mol}^{-1}$). This deviation is negative in the alkali-rich region while it became slightly positive in the rare-earth-rich region.

Structure

Pioneering high temperature Raman spectroscopic studies have been carried out in the 1970's on rare earth chloride systems in the liquid and solid state (49, 24, 25). Structural analyses have been made by X-ray diffraction and Raman spectroscopy on the pure lanthanide trichlorides. (21, 50) with UCl_3 -type crystal structure (hexagonal). Those results indicated that the nearest neighbour chloride coordination number of a lanthanide ion changed from 9 in the crystal to 6 in the melt, allowing for octahedral geometry around the lanthanide ions. Little is known about melts of lanthanide trichlorides with AlCl_3 -type crystal structure (monoclinic), except for YCl_3 (23). The melting behavior of ErCl_3 might be similar to that of YCl_3 , having the same crystal structure. Recently structural correlations in molten trivalent metal chlorides have been estimated as functions of the metal ion size for LaCl_3 and AlCl_3 -type lanthanide trichlorides, using a charged soft-sphere model and the hypernetted chain approximation (51). Furthermore, Erbölükbas et al. (52) have analyzed the available data on bond lengths and Raman frequencies by treating an isolated octahedral complex ion within a model which adopts charged soft-sphere interionic potentials, supplemented by taking ionic polarization into account.

The short range structure of molten ErCl_3 was studied by X-ray diffraction (22) ; possible anionic pairs are discussed in terms of interatomic distances and bond angles. The center of the first peak in $G(r)$ appeared in the range 2.60 Å to 2.65 Å. Considering the sum of individual ionic radii given by Shannon (53) with Er^{3+} and Cl^- being 0.89 Å and 1.81 Å, respectively, the first peak was assigned to the nearest neighbour correlation,

$\text{Er}^{3+}\text{-Cl}^-$; the other correlations hardly contributed to this peak. The coordination number of Cl^- ions around one Er^{3+} ion was estimated at 5.8 ± 0.2 by integration of the area under the peak of $D(r)$. The second peak was found at 3.6-4.3 Å, being assignable to the $\text{Cl}^- \text{-Cl}^-$ and the $\text{Er}^{3+} \text{-Er}^{3+}$ correlations. For example, the $\text{Er}^{3+} \text{-Er}^{3+}$ distance in the solid ErCl_3 was estimated at 3.91 Å from crystallographical data (48). A structure model was taken into account, and the reduced intensity function $Q_i(Q)$, of the model was reversely computed.

From these results, the nearest neighbour distance was estimated at 2.63 Å and the coordination number of Cl^- around Er^{3+} was 5.8. Like-ion pair distances of $\text{Cl}^- \text{-Cl}^-$ and $\text{Er}^{3+} \text{-Er}^{3+}$ were calculated to be 3.75 Å and 4.05 Å, respectively. The ratio of r_-/r_+ was 1.43, being close to the 1.41 value for octahedral geometry.

The interatomic structure, especially in the $\text{Er}^{3+} \text{-Er}^{3+}$ correlation, was considered in terms of molar volume and the short range structural parameters were obtained. If the Er^{3+} ions were distributed isotropically in the ErCl_3 melt, the average $\text{Er}^{3+} \text{-Er}^{3+}$ pair-distance would be 5.01 Å. The corresponding distance obtained from the X-ray diffraction analyses was 4.05 Å. This indicates that, as to the $\text{Er}^{3+} \text{-Er}^{3+}$ pair, there is some specific configuration in the melt.

In order to discuss the medium range structure of the melt, the following models were taken into account : (i) edge-sharing octahedra, (ii) corner-sharing octahedra. when undistorted octahedral anions form an edge-sharing configuration, the $\text{Er}^{3+} \text{-Er}^{3+}$ pair distance would be about 3.73 Å at most. This value is, however, smaller than that obtained by X-ray diffraction or molar volume analyses. The rigid octahedra edge-sharing model is thus not suitable for the medium range structure of molten ErCl_3 but a model assuming flexible octahedra with variable $\text{Er}^{3+} \text{-Cl}^-$ and $\text{Cl}^- \text{-Cl}^-$ bond lengths could be valid. This supports the suggestion by Sabounji et al. (23) that molten ErCl_3 may have a structure similar to YCl_3 . Next, a linear arrangement of octahedral ions was considered on the basis of corner-sharing. In this model, the $\text{Er}^{3+} \text{-Er}^{3+}$ pair-distance became 5.28 Å, too a large value. If the arrangement is not linear, i.e. $\angle \text{Er}^{3+} \text{-Cl}^- \text{-Er}^{3+} \approx 100^\circ$, and two octahedra were twisted with each other, this structure might exist. But corner-sharing is less probable than edge-sharing because of the steric hindrance between Cl^- ions, although corner-sharing has been expected from numerical calculations on Raman frequencies (52).

Molecular dynamics simulations

As quoted previously, the enthalpy of mixing $\Delta_{\text{mix}} H_m$ of the NaCl-DyCl_3 system was measured at 1100 K by direct calorimetry in the whole composition range. The

enthalpy-of-mixing values are negative with a minimum value at $x(\text{DyCl}_3) \approx 0.4$.

Isothermal molecular dynamics (MD) simulations of the molten DyCl_3 and NaCl-DyCl_3 systems were carried out to calculate the mixing enthalpy, and then the structure in these systems was investigated (5).

The thermodynamic properties and the phase diagrams of lanthanide halides in molten alkali chloride solvents show that the lanthanide ions are much stabilized, (i.e. that their activities become much smaller) than in the pure melts. The structure of the molten lanthanide halides or of halides containing a trivalent cation is not accurately known so far since most structural investigations were performed on monovalent and divalent molten salts (54, 55, 56, 57).

Although structure of the molten lanthanide halides and their mixtures have been scarcely revealed, Mochinaga and Igarashi (50) suggested more complicated complexes than MX_6^{3-} , (M : lanthanide ion and X : halide ion) which were determined by X-ray diffraction.

The mixing enthalpy of the molten NaCl-DyCl_3 system was measured by direct calorimetry and the stabilization of the Dy^{3+} ion in this system was interpreted in terms of complexes by molecular dynamics (MD) simulation.

In order to carry out MD simulations, the following pair potential (U_{ij}) between ions i and j was employed.

$$U_{ij}(r) = z_i z_j e^2 / 4 \pi \epsilon_0 r + b A_{ij} \exp[(r_i^\circ + r_j^\circ - r) / \rho] \quad [6]$$

where z , e , ϵ_0 , r , b , r° and ρ are the separation distance between ions i and j , the valence number, the elementary charge of electron, the dielectric constant of vacuum, the pre-exponential term, the Pauling factor, an ionic radius and a softness parameter, respectively. Since the values of r° and r of Dy^{3+} ion are not available, they were adjusted to reproduce experimental structure factors (58) of the molten DyCl_3 and the molten NaCl-DyCl_3 systems. In order to compare the experimental and computational structure factors, MD simulations of two systems were carried out, i. e., one is for the pure molten DyCl_3 at 973K and the other one for the equimolar NaCl-DyCl_3 system at 743 K. The basic cells contained 108 Dy and 324 Cl ions for the pure DyCl_3 , and 80 Dy, 80 Na and 320 Cl ions for the NaCl-DyCl_3 (50/50 mol%) mixture. The softness parameter ρ for NaCl is given by Fumi and Tosi (59) and ρ in the mixture was evaluated according to Larsen and Forland (60). The simulated systems were well annealed (more than 10^4 time steps : $\Delta t = 0.5$ fs) by the Verlet method, then the isothermal MD simulation proposed by Nose (61) was adopted. The structure factors were estimated in the basic

cells by the Debye equation.

$$Q_i(Q) = \sum \sum f_i f_j \sin(Q r_{ij}) / r_{ij} \quad [7]$$

where Q and f_i are the wave number and the atomic structure factor of a component i , respectively.

Then, we made MD simulations at 1100K to obtain the enthalpy of mixing in this system. The potential energy ϕ was estimated and the Coulomb energy was evaluated by the Ewald method. The internal energy U was calculated by

$$U = \phi + K.E. \quad [8]$$

where K.E. is the kinetic energy. Although one can obtain enthalpy by

$$H = U + pV \quad [9]$$

where p and V are pressure and molar volume, respectively, it is usually difficult to estimate p , because p is the small difference between two large quantities (coulombic and repulsive). In condensed phases pV is so small that it can be neglected : in this work pV is less than 0.1 kJ/mol. Thus in this work the internal energy is employed as enthalpy.

The interaction parameter λ , is deduced from the enthalpy of mixing $\Delta_{\text{mix}}H_m$ by :

$$\Delta_{\text{mix}}H_m = \lambda x(\text{DyCl}_3) \cdot [1 - x(\text{DyCl}_3)] \quad [10]$$

where $x(\text{DyCl}_3)$ is the mole fraction of DyCl_3 , and was obtained by the least square fitting of calorimetric data.

$$\lambda = -48.74 x(\text{DyCl}_3)^3 + 20.90 x(\text{DyCl}_3)^2 + 62.92 x(\text{DyCl}_3) - 56.44 \text{ kJ/mol} \quad [11]$$

The adjusted parameters ($r_{\text{Dy}}^p = 0.113 \text{ nm}$ and $r = 0.025 \text{ nm}$) give reasonable agreement between experimental and computational structure factors.

The mixing enthalpy in the simulated system was calculated from the following equation :

$$\Delta_{\text{mix}}H_m = H_m(x_{\text{NaCl}}, x(\text{DyCl}_3)) - x_{\text{NaCl}} \cdot H_m(\text{NaCl}) - x(\text{DyCl}_3) \cdot H_m(\text{DyCl}_3) \quad [12]$$

where $H_m(\text{NaCl})$ and $H_m(\text{DyCl}_3)$ are the enthalpies of the pure components.

DISCUSSION

Enthalpy of mixing

The representation of enthalpy-of-mixing data vs composition is often done by least squares fitted polynomials: for the present mixtures, a large number of parameters is involved and they have no physical meaning. Another route is modeling which, if based on structural and energetic hypothesis, will allow a good representation of experimental data and a reliable basis for further estimation of unknown melts.

As shown for different types of molten salt systems (62), thermodynamic modeling should take into account structural properties. Previous investigations indicated that the MX-LnX_3 melts contain complexes as detailed in the following. We therefore used the Hoch-Arpshofen model (63) which is based on the existence of complexes within the liquid. Though this approach revealed successful for several kinds of high temperature liquids such as alloys (64), oxides (65) and some simpler molten salt mixtures (66), it failed representing the composition dependence of enthalpy for the lanthanide melts.

A different modeling should be developed in order to take into account the specific structure information obtained on these melts. Such an approach is in progress (67). In the meantime, we have examined the behavior of dilute solutions. The limiting partial enthalpies $\overline{\Delta H}_{\text{LnX}_3(\text{MX})}^\infty$ and $\overline{\Delta H}_{\text{MX}(\text{LnX}_3)}^\infty$ were obtained from the integral enthalpy of mixing data. Since no modeling of the composition dependence was checked satisfactorily, as explained above, we optimized the values deduced from both a least-square polynomial fitting and from the "Surrounded Ion Model" (SIM) originally developed for ionic melts. Though the later would not be fully relevant for the present complex-containing melts, it can be considered as a reasonable estimate for the dilute solutions of MX_3 in the ionic MX.

The "Surrounded Ion Model" (SIM) (68,69,70) was extended to the lanthanide systems. Enthalpy of mixing is given by :

$$\Delta H = (3-2x)x^*(1-x^*)\{[\overline{\Delta H}_{\text{MX}(\text{LnX}_3)}^\infty - (1/3)\overline{\Delta H}_{\text{LnX}_3(\text{MX})}^\infty]x^* + (1/3)\overline{\Delta H}_{\text{LnX}_3(\text{MX})}^\infty\} \quad [13]$$

$$\begin{aligned} \text{with } x^* &= x^*(\text{LnX}_3) \\ &= [3x(\text{LnX}_3)] / [1 + 2x(\text{LnX}_3)] \end{aligned} \quad [14]$$

while the "equivalent" interaction parameter λ^* :

$$\lambda^* = \Delta H / (3-2x)x^*(1-x^*) \quad [15]$$

depends linearly on the limiting partial molar enthalpies $\overline{\Delta H}_{MX(LnX_3)}^\infty$ and $\overline{\Delta H}_{LnX_3(MX)}^\infty$

Correlations have been made in molten salts systems between the magnitude of the excess enthalpy and various parameters. For the most simple AX-BX melts (common anion, symmetrical cations) a simple dependence on the so-called distance parameter δ_{AB} is observed within the same family (nitrates, chlorides, ...).

$$\delta_{AB} = (1/d_{AX}) - (1/d_{BX}) \quad \text{with } d_{AX} = r_{A+} + r_{X-} \text{ and } d_{BX} = r_{B+} + r_{X-}$$

For mixtures involving ions with different valences, AX-BX₂ for instance, the interaction parameter was found correlated to the difference between the ionic potentials :

$$\Delta IP = \left| z_A / r_A^+ \right| - \left| z_B / r_B^{2+} \right| \quad [16]$$

In this case also, this correlation applies within a same melt family.

For the lanthanide chloride and bromide melts, we calculated the limiting partial molar enthalpy $\Delta H_{LnX_3(MX)}^\infty$ (i.e. the equivalent interaction parameter at $x^* = 0$)

$$\Delta IP = \left| z_M / r_M^+ \right| - \left| z_{Ln} / r_{Ln}^{3+} \right| \quad [17]$$

The dependence of $\Delta H_{LnX_3(MX)}^\infty$ against ΔIP was examined. No simple correlation could be observed for the 21 systems quoted in table 1. We have however noticed that the limiting partial enthalpy of $LnCl_3$ in MX is a linear function of the ionic radius ratio $r(M^+)/r(Ln^{3+})$: this dependence is illustrated in Figure 10.

Enthalpy of phase transition

All the investigated compounds undergo a phase transition in the solid state. The difference between the melting temperatures and the temperatures of phase transitions increases with the atomic number of alkali metal and decreases for the heavier halide.

Caesium and rubidium compounds are stable from ambient temperature up to melting. K_3NdCl_6 and K_3NdBr_6 form at higher temperatures.

Experiments with K_3NdBr_6 reveal that it is possible to separate the

formation/decomposition and phase transition effects during cooling. The decomposition temperature of K_3NdBr_6 decreases at increasing cooling rates. At $30\text{ K}\cdot\text{min}^{-1}$ it is possible to preserve the metastable form of K_3NdBr_6 even at ambient temperature and then to observe the exothermic decomposition effect during subsequent heating of the compound.

Heat capacity

We have measured the heat capacities of solid and liquid $LaCl_3$, $CeCl_3$, $PrCl_3$, $NdCl_3$, $GdCl_3$ and $DyCl_3$.

The only original data found in literature for solid lanthanide chloride were given by Dworkin and Bredig (46, 47), Sommers and Westrum's (71, 72), Walden (18) and Reuter and Seifert (73). In the high temperature solid range only the C_p values at the melting temperature were reported by (46, 47); for $LaCl_3$, however, data exist on the temperature range 200 K - 770 K. In the liquid range, the C_p range from $140\text{ J mol}^{-1}\text{K}^{-1}$ to $160\text{ J mol}^{-1}\text{K}^{-1}$; Dworkin and Bredig (46, 47) had obtained values of the same magnitude while the values reported by Savin *et al.* (16) for $LaCl_3$, $PrCl_3$ and $DyCl_3$ differ by 10% to 100% from ours or from the estimated values (17, 20, 19).

Due to a discontinuity in the vicinity of a phase transition, it is not possible to describe the heat capacity temperature dependence with conventional polynomials when the transition temperature is approached. The experimental C_p values were fitted by equations making this description possible (74). From these heat capacities, we calculated the formation enthalpies of some compounds in the liquid state. The enthalpies of formation are 6-7 times larger than the enthalpies of phase transition. All the K_3LnCl_6 compounds exist in a very limited temperature range (200K). The corresponding temperatures of formation increase in the sequence $Nd < Pr < Ce$ while the melting temperatures decrease. All the Cs_3LnCl_6 (stable from room temperature up to fusion) undergo phase transition. Furthermore, the temperature for this phase transition is almost the same for all the compounds. The melting temperatures are not very different and increase smoothly in the sequence La to Nd. Finally, the Rb_3LnCl_6 have all the features exhibited individually by the previous compounds: they form at rather high temperatures and undergo phase transition.

Electrical conductivity

Taking into account the magnitude of Λ 's and the structure deduced from the other

rare earth trichloride melts, complex ions ErCl_6^{3-} and its dimeric species ErCl_{11}^{5-} and $\text{Er}_2\text{Cl}_{10}^{4-}$ might exist in molten ErCl_3 and its mixture melts as well as other rare earth chloride melts. As shown in the first three rows of Table 1, LaCl_3 , PrCl_3 and NdCl_3 in the solid state possess the UCl_3 -type structure (48). On the other hand, YCl_3 and ErCl_3 crystals have the AlCl_3 -type structure (48). These five rare earth chloride melts are not so different from one another in terms of molar volume but the Λ 's of the former group, are apparently larger than those of the latter group, reflecting the order of cationic radius. It was reported that the dimers with corner-sharing of octahedral units exist in molten LaCl_3 , PrCl_3 and NdCl_3 (21) and these with edge-sharing in the molten YCl_3 (23) and ErCl_3 (22). It might be through that the melts with corner-sharing of octahedral units have larger Λ 's than the melts with edge-sharing.

Structure

Although there are some discrepancies between experimental and simulated enthalpies of the NaCl-DyCl_3 melt, MD simulation reproduces quite well the interaction around $x(\text{DyCl}_3) = 0.35$.

i) Another peak at $x(\text{DyCl}_3) = 0.50$ was also found by simulation, while in the experimental enthalpy, one peak at $x(\text{DyCl}_3) = 0.30$ and one shoulder around $x(\text{DyCl}_3) = 0.80$ have been observed. The peaks imply a preferential interaction between ions. In this MD simulation, ionic sizes and charges alone are taken into account. An orientational interaction of orbital electrons cannot be included. Then the simulated peaks correspond to a geometrical preferential arrangement.

ii) The magnitude of the mixing enthalpy in the simulated system is about 4 times larger than that in the experimental system. The pair potential given by Eq. [1] does not include dispersion terms, which may affect the repulsion parameter ρ . While interaction distance between Cl-Cl does not significantly depend on composition, the interaction distance between Dy and Cl increases with an increase of $x(\text{DyCl})_3$, and that between Dy and Dy drastically increases at $x(\text{DyCl})_3 = 0.4$. An increase in separation distance between ions with opposite sign will bring increase of the internal energy and vice versa. At all compositions in the simulated systems the coordination number of Cl^- ions around one Dy^{3+} ion is 6. $\text{Dy}_2\text{Cl}_{11}^{5-}$ and $\text{Dy}_3\text{Cl}_{16}^{7-}$ were observed as well as DyCl_6^{3-} . Although most of these polymers share apex Cl^- ions, edge-sharing polymers were found around $x(\text{DyCl}_3) \approx 0.4$.

CONCLUSION

New investigations are in progress in order to elucidate the rather complex features of the rare-earth halides. Some new spectroscopic results will be reported at the present conference by the group in Patras (Greece) and in Liège (Belgique) and we will perform neutron diffraction experiments at ILL (Grenoble, France) immediately after the present International Symposium on Molten Salts.

ACKNOWLEDGEMENTS

This work is a part of a cooperation between Chiba University (Chiba, Japan), Technical University (Wroclaw, Poland), Tokyo Institute of Technology (Tokyo, Japan) and IUSTI (Marseille, France). It was contributed by A. Bogacz (TU), K. Fukushima (CU), T. Ikumi (CU), Y. Iwade (CU), J. Mochinaga (CU), L. Rycerz (TU), W. Szczepaniak (TU), R. Tagaki (TIT).

REFERENCES

1. M.Gaune-Escard, L.Rycerz, W.Szczepaniak, A.Bogacz, Journal of Alloys and Compounds, 204 , 193, (1994).
2. M.Gaune-Escard, A.Bogacz, L.Rycerz, W.Szczepaniak, Thermochemica Acta, in press
3. M. Gaune-Escard, A.Bogacz, L.Rycerz, W.Szczepaniak, Thermochemica Acta, 236, 67, (1994).
4. M.Gaune-Escard, L.Rycerz, A.Bogacz, Journal of Alloys and Compounds, 204 , 185, (1994).
5. R.Takagi, L.Rycerz, M.Gaune-Escard, Denki Kagaku, 62, 240, (1994).
6. M.Gaune-Escard, L.Rycerz, W.Szczepaniak, A.Bogacz, Journal of Alloys and Compounds, 204, 189, (1994).
7. H.J.Seifert, H.Fink, G.Thiel, J.Less-Common Met., 110 , 139, (1985).
8. H.J.Seifert, J.Sandrock, G.Thiel, J.Thermal Anal., 31, 1309, (1986).
9. H.J.Seifert, J.Sandrock, J.Uebach, Z.Anorg.Allg.Chem., 555, 143, (1987).
10. H.J.Seifert, H.Fink, J.Uebach, J.Thermal Anal., 33 , 625, (1988).
11. H.J.Seifert, H.Fink, B.Baumgartner, Journal of Solid State Chemistry, 107, 19, (1993)
12. H.J.Seifert, J.Thermal Anal., 35, 1879, (1989).
13. R.Blachnik, A.Jaeger-Kasper, Z.Anorg.Allg.Chem., 461, 74, (1980).
14. H.J. Seifert, Private Communication.
15. H.J. Seifert, Y. Yuan, J. Less Common Met., 170, 135, (1991).
16. V. D. Savin, N. P. Mikhailova, V. A. Morozova, Zh. Fiz. Khim., 53, 1410, (1979)
17. Z. B. Pankratz, *Thermodynamic properties of halides*, US Bureau of Mines, Bull. 674, (1984).
18. G. E. Walden, D. F. Smith, US Bureau of Mines, RI 5859, (1962).
19. O. Knacke, O. Kubaschewski, K. Hesselman, *Thermochemical properties of inorganic substances* , I, 2nd edition, Springer-Verlag, Berlin-Heidelberg, (1991).
20. I. Barin, O. Knacke, *Thermochemical properties of inorganic substances* , Springer-Verlag, Berlin-Heidelberg-New York, (1973 and 1977).
21. J. Mochinaga, Y. Iwate and K. Fukushima, Mater. Sci. Forum, 73-75, 147, (1991).
22. Y. Iwate, T. Iida, K. Fukushima, J. Mochinaga, M. Gaune-Escard., Z. Naturforsch, 49 a, 811-814, (1994).
23. M. L. Saboungi, D.L. Price, C. Scamehorn and M.P. Tosi, Europhys. Lett., 15 283, (1991).
24. G.N. Papatheodorou, Inorg. Nucl. Chem. Lett., 11, 483, (1975).
25. G.N. Papatheodorou, J. Chem. Phys., 66 , 2893, (1977) .

26. A. Matsuoka, K. Fukushima, K. Igarashi, Y. Iwadate and J. Mochinaga, *Nippon Kagaku Kaishi*, 471, (1993).
27. Y. Iwadate, K. Igarashi, J. Mochinaga and T. Adachi, *J. Electrochem. Soc.*, 133, 1162, (1986).
28. J. Mochinaga, Y. Iwadate and K. Igarashi, *J. Electrochem. Soc.*, 138, 3588, (1991).
29. K. Fukushima, Y. Iwadate, Y. Andou, T. Kawashima, and J. Mochinaga, *Z. Naturforsch.*, 46a, 1055, (1991).
30. J. Mochinaga, K. Fukushima, Y. Iwadate, H. Kuroda, and Kawashima, *J. Alloy. Comp.*, 193, 33, (1993).
31. Y. Iwadate, T. Iida, K. Fukushima, J. Mochinaga, M. Gaune-Escard, J.P. Bros and G. Hatem, *Proceedings of the 60th annual meeting of the Electrochemical Society of Japan*, Tokyo, p.116, (1993).
32. K. Fukushima, T. Ikumi, J. Mochinaga, R. Takagi, M. Gaune-Escard, Y. Iwadate, *J. Alloy. Comp.*, 229, 274, (1995).
33. P. Gaune, M. Gaune-Escard, L. Rycerz, A. Bogacz, *J. Alloys Compounds*, 235, 143-149, (1996).
34. K. Igarashi, J. Mochinaga, *Z. Naturforsch.*, 42a, 777, (1987).
35. G.W. Mellors, S. Senderoff, *J. Phys. Chem.*, 64, 294, (1960).
36. W. Biltz, W. Klemm, *Z. anorg. Chem.*, 152, 225, 267, (1926).
37. J.S. Jaffe, E.R. van Artsdalen, *Chemistry Division Semiannual Progress Report*, Oak Ridge National Laboratory, ORNL-2159, 77, (1956).
38. A.S. Dworkin, H.R. Bronstein, M.A. Bredig, *Discussion Faraday Soc.*, 32, 188, (1961).
39. A. Voigt, W. Biltz, *Z. Anorg. Chem.*, 133, 277, (1924).
40. R. Förthmann, G. Vogel, A. Schneider, *Z. anorg. allg. Chem.*, 367, 19, (1969).
41. M.W. Smirnov, V.A. Khokhlov, *Zh. Prikl. Khim.*, 2, 302, (1970).
42. H.R. Bronstein, A.S. Dworkin, M.A. Bredig, *J. Phys. Chem.*, 66, 44, (1962).
43. G.I. Janz, F.W. Dampier, G.R. Lakshminarayanan, P.K. Lorenz, R.P.T. Tomkins, *Molten Salts: Volume 1, Electrical Conductance, Density and Viscosity Data*, NSRDS-NBS 15, 8, (1968).
44. A.S. Dworkin, H.R. Bronstein, M.A. Bredig, *J. Phys. Chem.*, 66, 1201, (1962).
45. R. Thoma, *"The Rare Earth Halides" in "Progress in the Science and Technology of the Rare Earths"*, ed. by Leroy Eyring, Pergamon Press, (1960).
46. A.S. Dworkin, M.A. Bredig, *High Temp. Sci.*, 3, 81, (1971).
47. A.S. Dworkin, M.A. Bredig, *J. Phys. Chem.*, 67, 697, (1963).
48. R.W. Wyckoff, *Crystal structures*, vol.2, Interscience, New York, p. 57 and 78, (1964).

49. V.A. Maroni, E.J. Hathaway, G.N. Papatheodorou, J. Phys. Chem., 78, 1134, (1974).
50. J. Mochinaga, K. Igarashi, Rare Earths, n° 15, 13, (1989)
51. H. Tatlipinar, Z. Akdeniz, G. Pastore, M.P. Tosi, J. Phys. Condens. Matter, 4, 8933, (1992).
52. A. Erbölükbas, Z. Akdeniz, M.P. Tosi, Il Nuovo Cimento, 14, 87, (1992).
53. R.D. Shannon, Acta Cryst. A32, 751, (1976).
54. J. E. Enderby, D. M. North P. A. Egelstaff, Phil. Mag. 14, 961, (1966).
55. J. E. Enderby and S. Biggins in "Advances in Molten Salt Chemistry", vol. 5, ed. G. Mamantov, p. 1, Elsevier (1983).
56. N. D. Wood, R. A. Howe, R. J. Newport, J. Faber, J. Phys. C : Solid State Physics 21, 669, (1988)
57. N. D. Wood, R. A. Howe, J. Phys. C : Solid State Physics 21, 3177, (1988)
58. J. Mochinaga, Y. Miyagi, K. Igarashi, T. Fukushima, and Y. Iwade, Nippon Kagaku, Kaishi, 459, (1993).
59. F.G. Fumi, M.P. Tosi, J. Phys. Chem. Solids, 25, 31, (1964).
60. B. Larsen, T. Forland, Mol. Phys., 26, 1521, (1973).
61. S. Nose, Mol. Phys., 52, 255, (1984).
62. M. Gaune-Escard, G. Hatem, High Temperature Science, 26, 275, (1990).
63. M. Hoch, I. Arpshofen, Z. Metallkde, 75, 23 (1984).
64. M. Hoch, Proc. ASM Meeting, Orlando, (1966).
65. M. Hoch, CALPHAD, 11, (1987).
66. G. Hatem, M. Gaune-Escard, M. Hoch, J. Non-Crystalline Solids, 161, 91-97 (1993).
67. G. Hatem, M. Gaune-Escard, to be published.
68. M. Gaune-Escard, J.C. Mathieu, P. Desré, Y. Doucet, J. Chim. Phys. 9, 1390, (1972).
69. M. Gaune-Escard, J.C. Mathieu, P. Desré, Y. Doucet, J. Chim. Phys. 9, 1397, (1972).
70. M. Gaune-Escard, J.C. Mathieu, P. Desré, Y. Doucet, J. Chim. Phys. 11-12, 1666, (1972).
71. A. Sommers, E.F. Westrum, J. Chem. Thermodynamics, 8, 1115, (1976).
72. A. Sommers, E.F. Westrum, J. Chem. Thermodynamics, 9, 1, (1977).
73. G. Reuter, H.J. Seifert, Thermochimica Acta, 237, 219, (1994).
74. M. Gaune-Escard, L. Rycerz, W. Szczepaniak, to be published

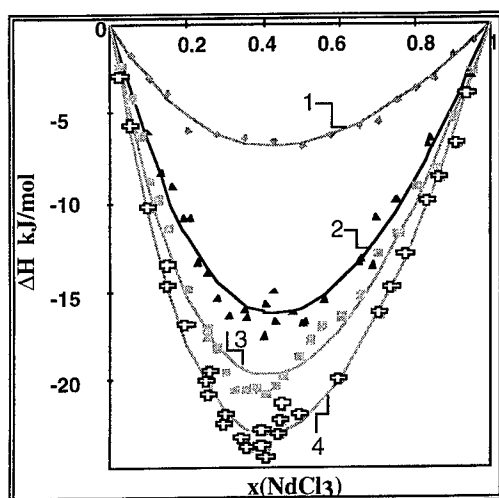


Figure 1 : Composition dependence of enthalpy of mixing ΔH in the $MCl-NdCl_3$ systems, from Ref.(3)
1-NaCl, 2-KCl, 3-RbCl, 4- CsCl

Figure 2. DSC cooling curves of K_3NdBr_6 at different cooling rates: 1 - 30.0 $K.min^{-1}$, 2 - 10.0 $K.min^{-1}$, 3 - 5.0 $K.min^{-1}$, 4 - 2.0 $K.min^{-1}$, 5 - 1.0 $K.min^{-1}$, 6 - 0.1 $K.min^{-1}$. Heat flow in arbitrary units (heat flow values in $mW * 30\{\text{cooling rate} = 30\}$; with exception of curve 6 where heat flow values are in $mW * 50$).

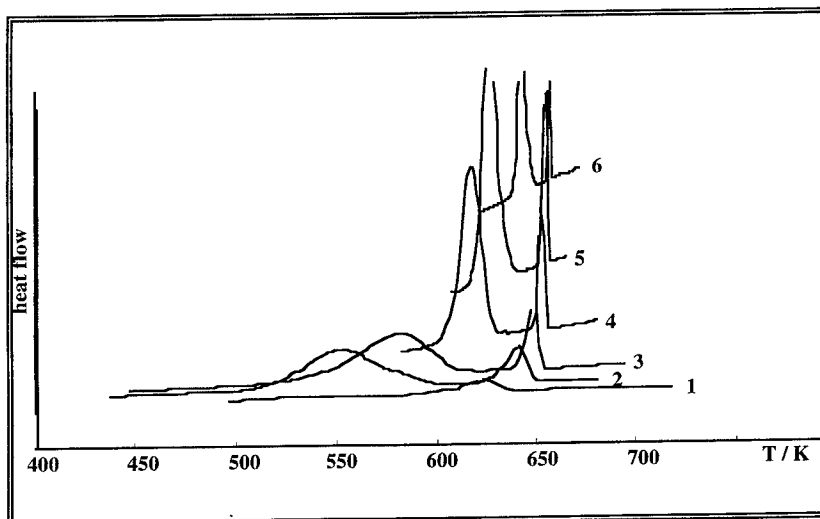


Figure 3. Heat capacity of CeCl_3 . O this work, 1 - linear fitting of experimental data, 2 - Pankratz estimation, 3- Barin and Knacke estimation, 4 - Knacke, Kubaschewski and Hesselman estimation

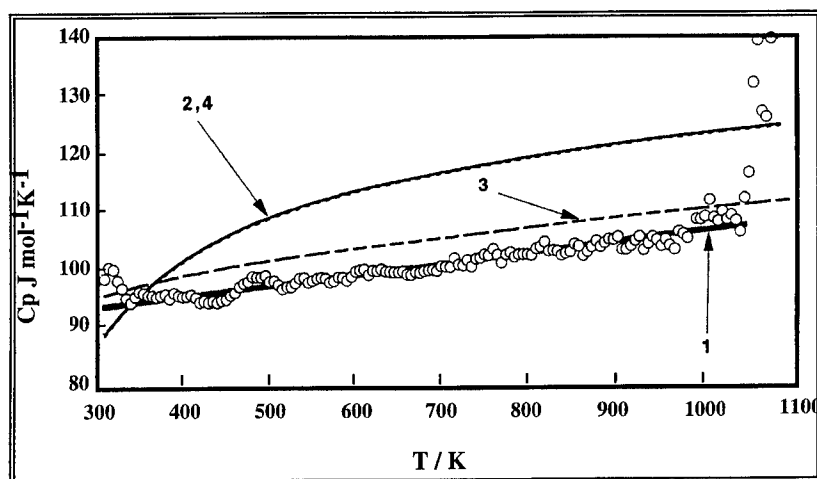
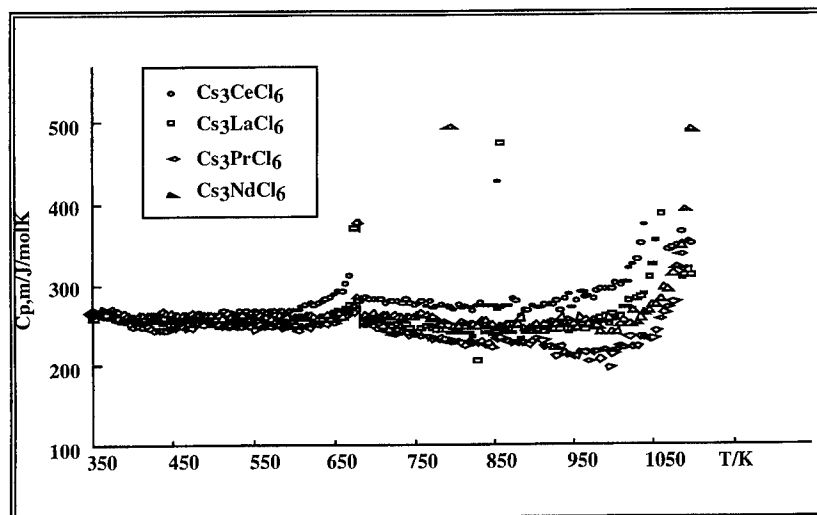


Figure 4. Heat capacity of the Cs_3LnCl_6 compounds



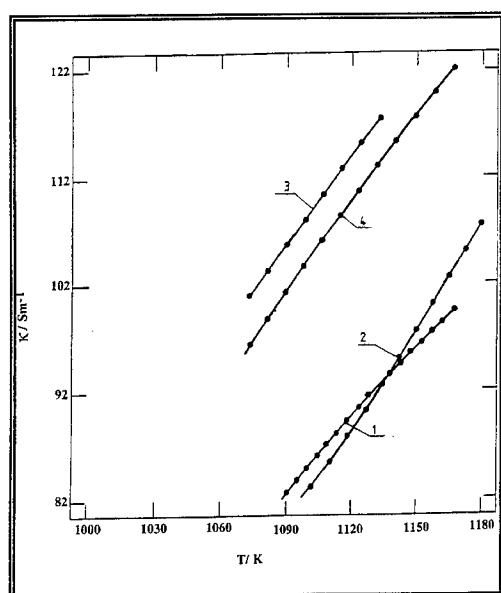


Figure 5. Temperature dependence of PrCl_3 specific conductivity: 1 - Gaune, Ref (33), 2 - Voigt and Biltz, Ref (39), 3 - Dworkin, Bronstein, and Bredig, Ref (44), 4 - Iwadate, Igarashi and Mochinaga, Ref (27).

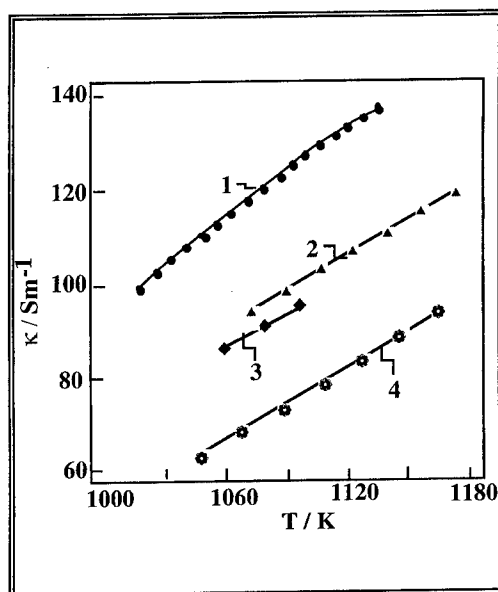


Figure 6. Temperature dependence of NdCl_3 specific conductivity: 1 - Gaune, Ref (33), 2 - Förthmann, Vogel and Schneider, Ref (40), 3 - Mochinaga and Iwadate, Ref (28), 4 - Voigt and Biltz, Ref (39)

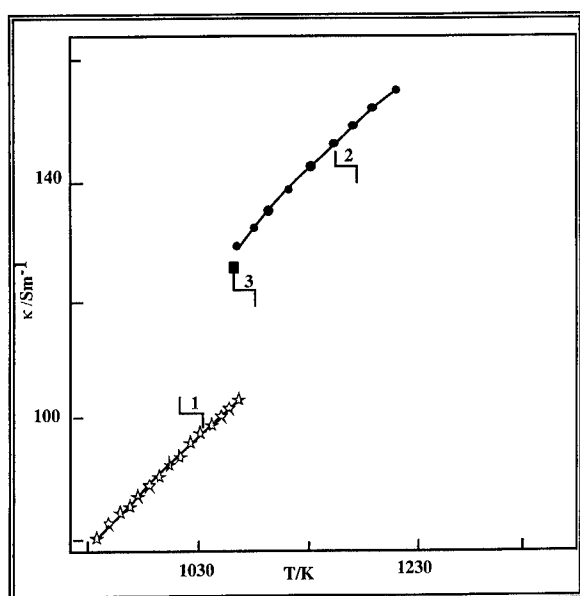
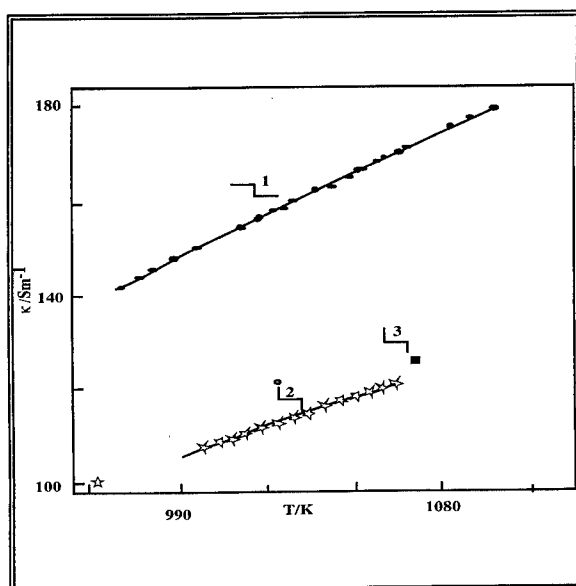


Figure 7 .
Temperature
dependence of the
specific conductivity
of K_3PrCl_6 on
temperature : 1 -
Gaune, Ref (33), 2 -
Iwadate, Igarashi,
Mochinaga , Ref
(27), 3 - Förthmann
Vogel and Schneider,
Ref (40)

Figure 8. Temperature
dependence of the
specific conductivity
of K_3NdCl_6

1 - Gaune, Ref (33),
2 - Mochinaga and
Iwadate, Ref (28) , 3
- Förthmann, Vogel
and Schneider , Ref
(40)



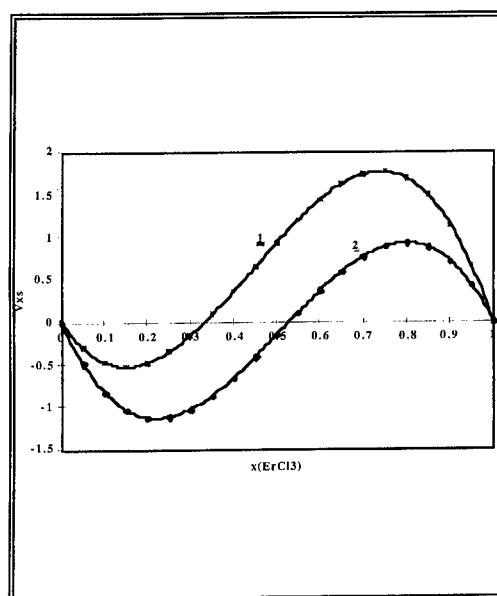


Figure 9. Excess molar volume of the NaCl- ErCl_3 (1) and KCl- ErCl_3 (2) systems, from Ref (32)

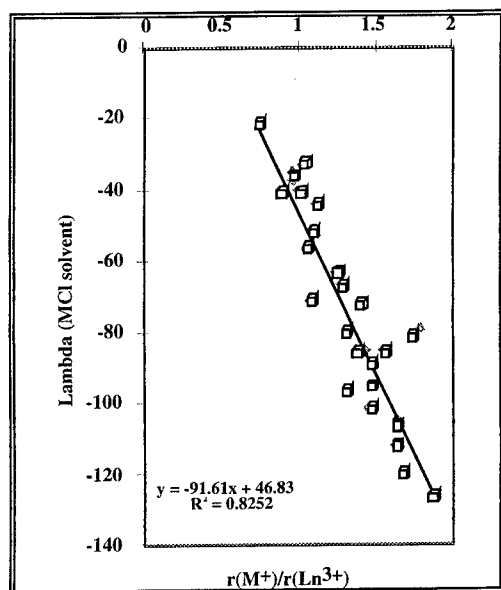
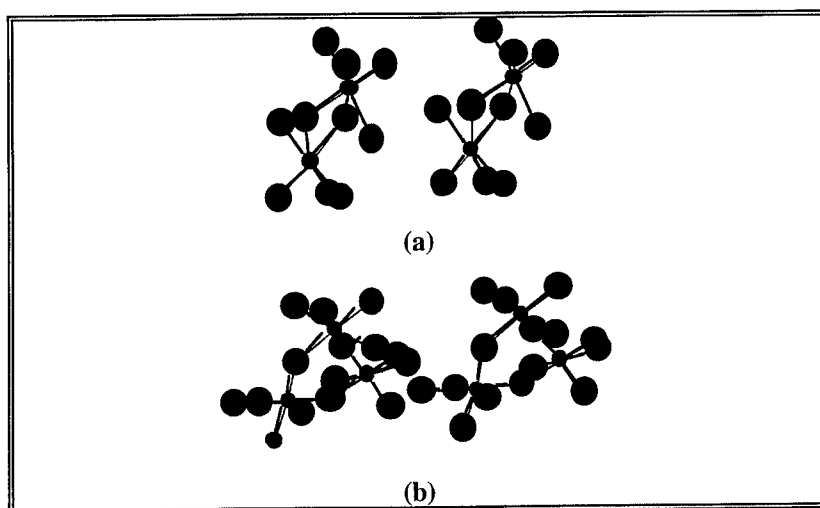


Figure 10. Limiting partial enthalpies of LnCl_3 in the MCl alkali chlorides plotted vs the ionic radius ratio

Figure 11. Stereoscopic view of complex ions (a) $\text{Dy}_2\text{Cl}_{10}^{4-}$ (b) $\text{Dy}_3\text{Cl}_{15}^{6-}$
from Ref (5)



Electron Mobilities in Solutions of Alkali Metals in Molten Alkali Halides

G.M. Haarberg and J.J. Egan *

Department of Electrochemistry
Norwegian University of Science and Technology
N-7034 Trondheim, Norway

*Brookhaven National Laboratory
Department of Applied Science
Upton, NY 11973

Abstract

The mobility of electrons in molten sodium and potassium halides was studied by potential step measurements using a Wagner polarization cell setup. The diffusion coefficient of electrons did not vary significantly with temperature and alkali metal activities lower than 0.2. The diffusion coefficient was found to be higher in the bromide and iodide systems than in the chlorides, the actual numbers varying in the range $0.01 - 0.02 \text{ cm}^2 \text{ s}^{-1}$.

Introduction

This work is a continuation of measurements of electronic conductivities and electron mobilities in molten alkali halides. Previous papers on NaBr and NaI /1/, NaCl /2/, and cryolite alumina melts /3/, have explained the implementation of the Wagner polarization method to molten salts. Results are presented here for sodium and potassium halides; namely, NaCl, NaBr,

NaI, KCl, KBr, and KI. Some of the older results are included in the present paper. An earlier paper on LiCl-KCl (eut.) /4/ reports erroneous results on electronic conductivity and should be disregarded. The apparatus contained quartz which reacts with Li during the measurement. The electron-hole measurements reported in ref. 4 should be valid.

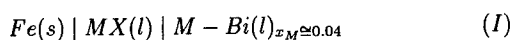
Bredig and coworkers /5/ carried out a comprehensive examination of physical properties of binary mixtures of molten salts and metals. The electrical conductivity was found to increase upon introduction of metal to the molten salt, especially in the potassium systems. The excess conductivity is electronic. At elevated temperatures the systems undergo a continuous transition of the electronic structure from nonmetallic to metallic states as the content of alkali metal increases. Interaction between alkali metals and molten alkali halides gives rise to formation of defects such as F-centers and mobile electrons. The properties of dilute solutions of alkali metals in molten alkali halides can be explained by using a thermodynamic defect model proposed by Egan and Freyland /6/. Results from conductivity measurements /1,2/ and optical absorption spectroscopy /7/ are in accordance with predictions from the model. Activities of sodium and potassium in the molten alkali halides have been determined by Smirnov et al. /8/ and Barnard et al. /9/.

Techniques for the Measurement of Electronic Conduction and Electron Mobilities

Electronic Conductivity

The Wagner polarization technique is usually used to study electrical conduction in solids exhibiting both ionic and electronic transport. The method has been thoroughly treated in the literature especially by Wagner in his original paper/10/ and in a more readily accessible review by Kroger /11/. A brief description of its implementation to molten salts is presented here for the convenience of the reader.

This is a dc method using cells of the following type



where the M-Bi (1) alloy serves as a reference electrode with known activity

of sodium or potassium and the iron serves as an inert electron conductor often referred to as a blocking electrode. MX is any of the six sodium and potassium salts studied. One applies potentials across the cell which are lower than those necessary to decompose the potassium salt, the iron electrode being negative. In this way ionic currents are suppressed and only electronic current flows. There is no gradient of electrical potential within the bulk of the potassium salt otherwise ions would move. Under steady state conditions which take up to 30 minutes after each potential change the current density is given by

$$J_e = \frac{\kappa_e}{F} \left(\frac{\partial \eta_e}{\partial x} \right) \quad (1)$$

where κ_e is the electronic conductivity in the melt, F is the Faraday and η_e is the electrochemical potential of electrons (see Wagner /10/ or Kroger /11/). The ionic current density is given by

$$J_{ion} = -\frac{\kappa_{ion}}{F} \left(\frac{\partial \mu_M}{\partial x} - \frac{\partial \eta_e}{\partial x} \right) \quad (2)$$

where μ_M is the chemical potential of M in the melt. Since $J_{ion} = 0$

$$\frac{\partial \mu_M}{\partial x} = \frac{\partial \eta_e}{\partial x} \quad (3)$$

Since the cell is designed (see experimental section) so that the electrolyte compartment under study has a constant cross section, integration of eqn. (1) using eqn. (3) gives

$$lJ_e = \frac{1}{F} \int_{\mu_M^{ref}}^{\mu_M^e} \kappa_e d\mu_M \quad (4)$$

where l is the length. The chemical potential of M at the iron electrode is related to the voltage impressed across the cell, E , by

$$\mu_M^{Fe} - \mu_M^{ref} = -FE \quad (5)$$

Differentiation of (4) and (5) with respect to μ_M^{Fe} and substitution gives

$$\kappa_e = l \frac{d|J_e|}{dE} = G \frac{d|I|}{dE} \quad (6)$$

where G is the cell constant and I is the steady state current of cell (I). In order to obtain the electronic conductivity in the melt, steady state current-potential curves were obtained and then differentiated to yield κ_e from eqn. 6. The differentiation was performed by fitting the data points to the following exponential equation using a least square method /12/

$$I = A_1 \left[\exp \left(\frac{EF}{2RT} \right) - 1 \right] + A_2 \left[\exp \left(\frac{3EF}{2RT} \right) - 1 \right] \quad (7)$$

where A_1 and A_2 are constants given by the least squares fit and E is the absolute potential. The electronic conductivity is then given by

$$\kappa_e = G \left[\frac{A_1 F}{2RT} \exp \left(\frac{EF}{2RT} \right) + \frac{3A_2 F}{2RT} \exp \left(\frac{3EF}{2RT} \right) \right] \quad (8)$$

Further, the conductivity was obtained as a function of sodium or potassium activity using

$$a_K = \exp \left[\frac{(E - E^0)F}{RT} \right] \quad (9)$$

where E^0 is the potential of the M-Bi electrode vs. pure sodium or potassium taken from the literature on the sodium /13,14,15,16/ and potassium system /16,17/.

Electron mobilities

The diffusion coefficient and mobility of electrons in the melt may also be measured by observing the cell's approach to steady state. When a potential is imposed on the iron electrode, a chemical potential of sodium is produced in the melt at this point and with it a given concentration of electrons. These electrons then diffuse toward the reference electrode according to Fick's second law. The concentration of electrons as a function of time and distance from the iron electrode is given by the following equation (see for example Crank /18/)

$$c = c_1 + (c_0 - c_1) \frac{x}{l} + \frac{2}{\pi} \sum_{n=1}^{\infty} \frac{c_0 \cos n\pi - c_1}{n} \sin \frac{n\pi x}{l} \exp \left(-\frac{Dn^2\pi^2 t}{l^2} \right) + \frac{4c_0}{\pi} \sum_{m=0}^{\infty} \frac{1}{2m+1} \sin \frac{(2m+1)\pi x}{l} \exp \left(-\frac{D(2m+1)^2\pi^2 t}{l^2} \right) \quad (10)$$

where c_1 is the electron concentration at the iron electrode, c_0 is the concentration at the reference electrode, x is the distance from the iron electrode, D is the diffusion coefficient of electrons, l the distance between the iron electrode and the reference electrode, and t is the time in seconds. The flow of electrons, j , is then given by

$$j = -D \left(\frac{\partial c}{\partial x} \right)_{x=0} = \frac{D(c_1 - c_0)}{l} - \frac{2Dc_0}{l} \sum_{n=1}^{\infty} (-1)^n \exp \left(-\frac{Dn^2\pi^2 t}{l^2} \right) + \frac{2Dc_1}{l} \sum_{n=1}^{\infty} \exp \left(-\frac{Dn^2\pi^2 t}{l^2} \right) - \frac{4Dc_0}{l} \sum_{m=0}^{\infty} \left(-\frac{D(2m+1)^2\pi^2 t}{l^2} \right) \quad (11)$$

The quantity of electrons flowing in the cell is given by

$$Q_t = \int_0^t j \, dt = \frac{D(c_1 - c_0)}{l} t - \frac{2l}{\pi^2} \sum_{n=1}^{\infty} \frac{c_0 \cos n\pi - c_1}{n^2} \left[1 - \exp \left(-\frac{Dn^2\pi^2 t}{l^2} \right) \right] - \frac{4c_0 l}{\pi^2} \sum_{m=0}^{\infty} \frac{1}{(2m+1)^2} \left[1 - \exp \left(-\frac{D(2m+1)^2\pi^2 t}{l^2} \right) \right] \quad (12)$$

At longer times with $t \rightarrow \infty$ equation (10) reduces to

$$Q_t = \frac{D(c_1 - c_0)}{l} t + \frac{l}{3} (c_1 - c_0) \quad (13)$$

The total number of coulombs passed through the cell as a function of time is given by

$$Q = \frac{D(c_1 - c_0)FA}{l} t + \frac{l}{3} (c_1 - c_0)FA \quad (14)$$

where F is the Faraday constant and A is the area of the melt compartment. Thus if one imposes a voltage across the cell at $t = 0$ and measures the coulombs until steady state, one obtains the diffusion coefficient of electrons as follows. The slope of a plot of Q vs. t is given by

$$\text{Slope} = \frac{D(c_1 - c_0)FA}{l} \cong \frac{Dc_1FA}{l} \quad (15)$$

when the concentration of electrons at the reference electrode is much smaller than that generated at the iron electrode. The intercept of the plot is given by

$$\text{Intercept} = \frac{l}{3} (c_1 - c_0)FA \cong \frac{l}{3} c_1FA \quad (16)$$

$$D = \frac{\text{Slope}}{\text{Intercept}} \frac{l^2}{3} \quad (17)$$

Since $I = dQ/dt$

$$D = \frac{I l^2}{(Q - It)3} \quad (18)$$

Therefore measurements of Q were taken for a time t until steady state was reached and eqn. (16) used to obtain values of D . The mobility of electrons was then calculated from the Nernst-Einstein equation

$$u_e = (DF)/(RT) \quad (19)$$

Experimental Details

The experimental apparatus is shown in Fig. 1. A large tantalum crucible, which resides inside of a vacuum tight Vycor container (not shown), contains the molten salt in contact with a molten M-Bi alloy. The molten salts were obtained from single crystals of optical grade. The Fe electrode is placed inside a sapphire capillary (4.2 cm long, 3 mm inside diameter). A vacuum tight seal is formed between iron and sapphire. This seal prevents the evaporation of alkali metal, which is essential for obtaining good results. A constant potential is imposed across the cell making the Ta cup positive and the Fe electrode negative. The current through the cell is measured as a function of time, and the steady state value is recorded. A series of such corresponding data is measured to obtain a current versus potential curve. The electronic conductivity can be calculated as a function of potential. The cell constant is determined by the geometry of the sapphire capillary. ac resistance measurements are also made periodically between the Ta cup and the Fe electrode as a control.

A transient technique is applied to the same cell in order to measure the diffusion coefficient of electrons. The current response to a potential applied across the electrodes is measured until steady state is attained. The total number of coulombs passed is recorded along with the time and the diffusion coefficient calculated from eqn. (18).

A reference electrode consisting of a M-Bi alloy placed inside an alumina tube is also shown. The amount of Bi is accurately known. This reference

electrode is used to check the composition of the M-Bi alloy in the tantalum cup which can vary over a period of several days due to evaporation of potassium. All sodium or potassium is coulometrically removed from the reference electrode and then added again until the potential between the reference alloy and the larger M-Bi alloy is zero. The composition of the M-Bi alloy in the tantalum cup is then known, and the metal activity is calculated from thermodynamic data for M-Bi alloys [13-17].

Results and Discussion

Results of the I versus E curves taken on cell (I) at various temperatures were fitted according to eqn. 7 and used to determine electronic conductivities as a function of the alkali metal activity using eqns. 8 and 9. The electronic conductivity was found to increase with increasing alkali metal activity and increasing temperature for all the six systems [1,2,18]. Bredig and coworkers [5] have made a few measurements of total conductivity in the salt rich regions studied here. Their results with ionic conduction subtracted showed good agreement with our results.

Transient measurements on the approach to steady state yield diffusion coefficients and mobilities of electrons and are shown in Tables 1-6. The mobilities of electrons in these systems remain constant with increasing M activity and electron concentration up to an alkali metal activity of about 0.1. For the KI system several transient measurements were deliberately made at K activities greater than 0.1 ($E \approx 0.78$) as shown in Table 6. The results show that the diffusion coefficient is starting to vary with K activity. Since the diffusion equations used in our transient method require a constant diffusion coefficient, the method is not valid at higher K activities. Thus the values obtained at K activities too high to be valid are shown in parentheses. Table 7 shows typical values for the concentration of electrons at relatively high K activities. The sodium systems show similar behavior. The electron mobility does not vary significantly with temperature, while the electronic conductivity increases with increasing temperature due to increasing electron concentration. The electron mobility was found to be higher in the bromide and iodide systems than the chlorides.

The work reported here and in the previous papers shows that molten alkali halides under reducing conditions are mixed conductors and contain

a considerable concentration of electrons that have mobilities of the order of $0.1 \text{ cm}^2\text{volt}^{-1}\text{sec}^{-1}$. This has a noticeable effect on the efficiency of the production of metals, as was shown in the case of cryolite. It must also be taken into consideration in the design of molten salt batteries because self-discharge currents are affected. Other measurements that could be affected include double-layer capacitance and electrode kinetics.

Acknowledgements

This work was supported by the Division of Chemical Sciences, U.S. Department of Energy under Contract No. DE-AC02-76CH00016. G. M. Haarberg was supported by the Norwegian Research Council.

References

1. G. M. Haarberg, K. S. Osen, J. J. Egan, H. Heyer, W. Freyland, *Ber. Bunsenges. Phys. Chem.* **92**, 139 (1988).
2. G. M. Haarberg, K. S. Osen, R. J. Heus and J. J. Egan, *J. Electrochem. Soc.* **137**, 2777 (1990).
3. G. M. Haarberg, K. S. Osen, J. Thonstad, R. J. Heus and J. J. Egan, *Metall. Trans. B* **24B**, 729 (1993).
4. R. J. Heus and J. J. Egan, *J. Phys. Chem.* **77**, 1989 (1973).
5. M.A. Bredig, "Mixtures of Metals with Molten Salts" in *Molten Salt Chemistry*, M. Blander, Editor, Interscience, New York, 1964.
6. J.J. Egan, W. Freyland, *Ber. Bunsenges. Phys. Chem.* **89**, 381 (1985).
7. D. Nattland, Th. Rauch, W. Freyland, *J. Chem. Phys.* **98**, 4429 (1993).
8. M. V. Smirnov, V. V. Chebykin, L. A. Tsiovkina, *Electrochem. Acta* **26**, 1275 (1981).
9. J. Bernard, J. Blessing, J. Schummer, and W. Freyland, *Ber. Bunsenges. Phys. Chem.* **97**, 177 (1993).
10. C. Wagner, *Proc. CITCE* **7**, 361 (1957).
11. F. A. Kroger, *The Chemistry of Imperfect Crystals*, Vol. 3, p. 149 North Holland Pub., American Elsevier, 1974.
12. D. W. Marquardt, *J. Soc. Ind. Appl. Math.* **2**, 431 (1963).
13. E.A. Miorova, A.G. Morachevskii, *J. Appl. Chem. USSR* **48**, 1303 (1975).
14. T-S. Yih, J.C. Thompson, *J. Phys. F:Met. Phys.* **12**, 1625, (1982).
15. M.-L. Saboungi, T.P. Corbin, *ibid* **14**, 13 (1984).
16. J. J. Egan, *High Temp. Science* **19**, 111 (1985).
17. A. Petric A. D. Pelton, M-L. Saboungi, *J. Phys. F: Met. Phys.* **18**, 1473 (1988).
18. J. Crank, *The Mathematics of Diffusion*, 2nd. ed., Oxford University Press, Ely House, London (1975).
19. G.M. Haarberg, J.J. Egan, "Electronic Conduction and Electron Mobilities in Molten KCl-K, KBr-K, and KI-K Solutions", To be published.

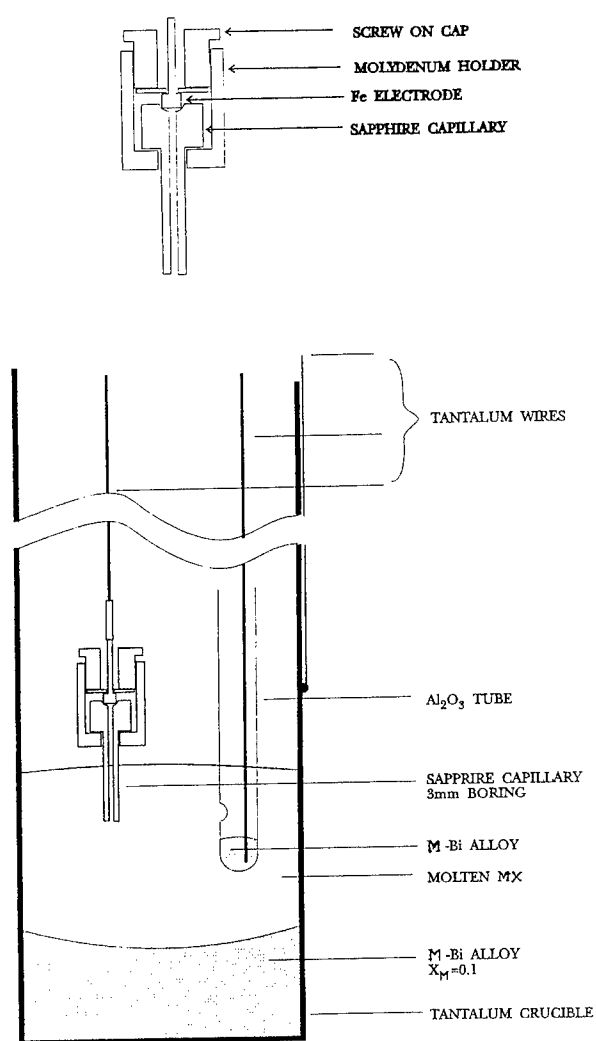


Fig. 1: Experimental arrangement used for cell (I).

Table 1: Results of Transient Measurements on NaCl.

$T = 850^{\circ}C \quad E^0 = 0.867 \quad V_m = 38.20$			
E[volts]	D[$cm^2 sec^{-1}$]	$I_{steady}[\mu amps]$	$u_e[cm^2 volt^{-1} sec^{-1}]$
0.650	0.0094	284	.097
0.675	0.0093	349	.096
0.700	0.0095	454	.098
0.675	0.0095	590	.098
0.675	0.0101	787	.104
$T = 900^{\circ}C \quad E^0 = 0.874 \quad V_m = 38.91$			
E[volts]	D[$cm^2 sec^{-1}$]	$I_{steady}[\mu amps]$	$u_e[cm^2 volt^{-1} sec^{-1}]$
0.675	0.0120	596	.119
0.700	0.0123	670	.122
0.725	0.0123	814	.122
0.750	0.0125	1011	.124

Table 2: Results of Transient Measurements on NaBr

$T = 850^{\circ}C \quad E^0 = 0.774 \quad V_m = 45.58$			
E[volts]	D[$cm^2 sec^{-1}$]	$I_{steady}[\mu amps]$	$u_e[cm^2 volt^{-1} sec^{-1}]$
0.450	0.023	483	.242
0.500	0.021	690	.218
0.550	0.020	1042	.208
0.600	0.020	1625	.210
$T = 900^{\circ}C \quad E^0 = 0.777 \quad V_m = 46.41$			
E[volts]	D[$cm^2 sec^{-1}$]	$I_{steady}[\mu amps]$	$u_e[cm^2 volt^{-1} sec^{-1}]$
0.450	0.028	789	.277
0.500	0.026	1093	.258
0.550	0.023	1551	.231
0.600	0.024	2327	.242

Table 3: Results of Transient Measurements on NaI.

$T = 725^{\circ}C$ $E^0 = 0.897$ $V_m = 54.50$			
E[volts]	D[$cm^2 sec^{-1}$]	I_{steady} [μ amps]	$u_e[cm^2 volt^{-1} sec^{-1}]$
0.676	0.015	490	.174
0.717	0.013	930	.151
0.733	0.013	733	.151
0.758	0.013	1040	.151
0.843	(0.017)	2495	(.198)
$T = 750^{\circ}C$ $E^0 = 0.901$ $V_m = 55.44$			
E[volts]	D[$cm^2 sec^{-1}$]	I_{steady} [μ amps]	$u_e[cm^2 volt^{-1} sec^{-1}]$
0.704	0.016	752	.182
0.725	0.012	863	.136
0.739	0.013	1056	.147
0.814	0.016	2155	.182
$T = 775^{\circ}C$ $E^0 = 0.906$ $V_m = 56.10$			
E[volts]	D[$cm^2 sec^{-1}$]	I_{steady} [μ amps]	$u_e[cm^2 volt^{-1} sec^{-1}]$
0.678	0.015	742	.166
0.749	0.014	1315	.155
0.780	0.014	1700	.155
0.820	0.015	2479	.166
0.850	(0.017)	3270	(0.188)
$T = 800^{\circ}C$ $E^0 = 0.910$ $V_m = 56.90$			
E[volts]	D[$cm^2 sec^{-1}$]	I_{steady} [μ amps]	$u_e[cm^2 volt^{-1} sec^{-1}]$
0.730	0.015	1208	.162
0.819	0.016	2630	.173
$T = 850^{\circ}C$ $E^0 = 0.919$ $V_m = 58.52$			
E[volts]	D[$cm^2 sec^{-1}$]	I_{steady} [μ amps]	$u_e[cm^2 volt^{-1} sec^{-1}]$
0.762	0.015	1815	.155
0.822	0.016	3025	.165
$T = 900^{\circ}C$ $E^0 = 0.928$ $V_m = 59.12$			
E[volts]	D[$cm^2 sec^{-1}$]	I_{steady} [μ amps]	$u_e[cm^2 volt^{-1} sec^{-1}]$
0.766	0.016	2155	.158

Table 6: Results of Transient Measurements on KI.

$T = 725^{\circ}C \quad E^0 = 0.983 \quad V_m = 69.01$			
E[volts]	D[cm ² sec ⁻¹]	I _{steady} [μamps]	u _e [cm ² volt ⁻¹ sec ⁻¹]
0.700	0.016	352	.186
0.800	0.015	904	.175
0.850	(0.023)	1570	(.268)
$T = 750^{\circ}C \quad E^0 = 0.984 \quad V_m = 69.70$			
E[volts]	D[cm ² sec ⁻¹]	I _{steady} [μamps]	u _e [cm ² volt ⁻¹ sec ⁻¹]
0.750	0.016	780	.182
0.800	(0.019)	1271	(.216)
$T = 800^{\circ}C \quad E^0 = 0.986 \quad V_m = 71.12$			
E[volts]	D[cm ² sec ⁻¹]	I _{steady} [μamps]	u _e [cm ² volt ⁻¹ sec ⁻¹]
0.727	0.017	980	.184
0.765	(0.020)	1415	(.216)
0.785	(0.024)	1790	(.260)
$T = 830^{\circ}C \quad E^0 = 0.986 \quad V_m = 72.01$			
E[volts]	D[cm ² sec ⁻¹]	I _{steady} [μamps]	u _e [cm ² volt ⁻¹ sec ⁻¹]
0.712	0.016	1175	.168
0.733	0.017	1418	.179
0.759	(0.019)	1740	(.200)
0.789	(0.026)	2310	(.274)
$T = 850^{\circ}C \quad E^0 = 0.987 \quad V_m = 72.61$			
E[volts]	D[cm ² sec ⁻¹]	I _{steady} [μamps]	u _e [cm ² volt ⁻¹ sec ⁻¹]
0.684	0.015	1050	.155
0.708	0.016	1275	.165
0.735	0.018	1595	.186
0.755	(0.021)	1935	(.217)
$T = 885^{\circ}C \quad E^0 = 0.988 \quad V_m = 73.61$			
E[volts]	D[cm ² sec ⁻¹]	I _{steady} [μamps]	u _e [cm ² volt ⁻¹ sec ⁻¹]
0.685	0.016	1295	.162
0.716	0.018	1695	.182
0.735	(0.020)	1985	(.202)

Table 5: Results of Transient Measurements on KBr.

$T = 780^{\circ}C \quad E^0 = 0.985 \quad V_m = 56.96$			
E[volts]	D[$cm^2 sec^{-1}$]	$I_{steady}[\mu amps]$	$u_e[cm^2 volt^{-1} sec^{-1}]$
0.700	0.016	617	.176
0.780	0.016	1207	.176
0.800	0.017	1391	.187
$T = 800^{\circ}C \quad E^0 = 0.986 \quad V_m = 57.41$			
E[volts]	D[$cm^2 sec^{-1}$]	$I_{steady}[\mu amps]$	$u_e[cm^2 volt^{-1} sec^{-1}]$
0.730	0.016	962	.173
0.750	0.018	1130	.194
0.770	0.016	1291	.173
$T = 850^{\circ}C \quad E^0 = 0.987 \quad V_m = 58.58$			
E[volts]	D[$cm^2 sec^{-1}$]	$I_{steady}[\mu amps]$	$u_e[cm^2 volt^{-1} sec^{-1}]$
0.608	0.0170	543	.176
0.750	0.0170	1444	.176
0.770	0.0170	1712	.176

Table 6: Results of Transient Measurements on KI.

$T = 725^{\circ}C \quad E^0 = 0.983 \quad V_m = 69.01$			
E[volts]	D[$cm^2 sec^{-1}$]	$I_{steady}[\mu amps]$	$u_e[cm^2 volt^{-1} sec^{-1}]$
0.700	0.016	352	.186
0.800	0.015	904	.175
0.850	(0.023)	1570	(.268)
$T = 750^{\circ}C \quad E^0 = 0.984 \quad V_m = 69.70$			
E[volts]	D[$cm^2 sec^{-1}$]	$I_{steady}[\mu amps]$	$u_e[cm^2 volt^{-1} sec^{-1}]$
0.750	0.016	780	.182
0.800	(0.019)	1271	(.216)
$T = 800^{\circ}C \quad E^0 = 0.986 \quad V_m = 71.12$			
E[volts]	D[$cm^2 sec^{-1}$]	$I_{steady}[\mu amps]$	$u_e[cm^2 volt^{-1} sec^{-1}]$
0.727	0.017	980	.184
0.765	(0.020)	1415	(.216)
0.785	(0.024)	1790	(.260)
$T = 830^{\circ}C \quad E^0 = 0.986 \quad V_m = 72.01$			
E[volts]	D[$cm^2 sec^{-1}$]	$I_{steady}[\mu amps]$	$u_e[cm^2 volt^{-1} sec^{-1}]$
0.712	0.016	1175	.168
0.733	0.017	1418	.179
0.759	(0.019)	1740	(.200)
0.789	(0.026)	2310	(.274)
$T = 850^{\circ}C \quad E^0 = 0.987 \quad V_m = 72.61$			
E[volts]	D[$cm^2 sec^{-1}$]	$I_{steady}[\mu amps]$	$u_e[cm^2 volt^{-1} sec^{-1}]$
0.684	0.015	1050	.155
0.708	0.016	1275	.165
0.735	0.018	1595	.186
0.755	(0.021)	1935	(.217)
$T = 885^{\circ}C \quad E^0 = 0.988 \quad V_m = 73.61$			

Table 7: Number of Electrons at Different Activities in KI

$T = 725^{\circ}C \quad E^0 = 0.983 \quad V_m = 69.01$				
E[volts]	a_K	$\kappa_e[ohm^{-1}cm^{-1}]$	$n_e[no./cm^3]$	$u_e[cm^2volt^{-1}sec^{-1}]$
0.700	0.037	.175	5.88×10^{18}	.186
0.800	0.119	.566	2.02×10^{19}	.175
$T = 750^{\circ}C \quad E^0 = 0.984 \quad V_m = 69.70$				
E[volts]	a_K	$\kappa_e[ohm^{-1}cm^{-1}]$	$n_e[no./cm^3]$	$u_e[cm^2volt^{-1}sec^{-1}]$
0.750	0.070	.395	1.36×10^{19}	.182
$T = 800^{\circ}C \quad E^0 = 0.986 \quad V_m = 71.12$				
E[volts]	a_K	$\kappa_e[ohm^{-1}cm^{-1}]$	$n_e[no./cm^3]$	$u_e[cm^2volt^{-1}sec^{-1}]$
0.727	0.061	.527	1.79×10^{19}	.184
$T = 830^{\circ}C \quad E^0 = 0.986 \quad V_m = 72.01$				
E[volts]	a_K	$\kappa_e[ohm^{-1}cm^{-1}]$	$n_e[no./cm^3]$	$u_e[cm^2volt^{-1}sec^{-1}]$
0.712	0.056	.550	2.05×10^{19}	.168
0.733	0.070	.681	2.38×10^{19}	.179
$T = 850^{\circ}C \quad E^0 = 0.987 \quad V_m = 72.61$				
E[volts]	a_K	$\kappa_e[ohm^{-1}cm^{-1}]$	$n_e[no./cm^3]$	$u_e[cm^2volt^{-1}sec^{-1}]$
0.684	0.044	.487	1.95×10^{19}	.155
0.708	0.056	.612	2.32×10^{19}	.165
$T = 885^{\circ}C \quad E^0 = 0.988 \quad V_m = 73.61$				
E[volts]	a_K	$\kappa_e[ohm^{-1}cm^{-1}]$	$n_e[no./cm^3]$	$u_e[cm^2volt^{-1}sec^{-1}]$
0.685	0.047	.625	2.41×10^{19}	.162
0.716	0.064	.845	2.90×10^{19}	.182

APPLICATION OF THERMODYNAMIC DATABASES TO CALCULATION OF SURFACE TENSION OF MOLTEN SALT MIXTURES

Toshihiro Tanaka and Shigeta Hara

Department of Materials Science and Processing, Faculty of Engineering,
Osaka University, 2-1 Yamadaoka, Suita, Osaka 565, Japan.

The authors discussed the application of thermodynamic solution databases, which have been constructed so far to calculate thermodynamic properties and phase diagrams, to the evaluation of surface tension of molten salt mixtures.

INTRODUCTION

Various thermodynamic databases have been constructed to be mainly applied to the calculation of phase diagrams of alloys, salts and oxides (1). The accumulation and assessment of thermodynamic data and phase equilibrium information to establish those databases is sometimes called CALPHAD (Computer **C**alculation of **P**hase **D**iagrams) approach(2), which has been recognized to be useful in various aspects of materials science and engineering (1,2). If it would be possible to use the thermodynamic databases to evaluate physical properties of liquid solutions as well as phase equilibria, we could enlarge not only the utility of those thermodynamic databases but also the understanding of the physical properties of the liquid solutions. The authors have applied the thermodynamic databases to the evaluation of the surface tension of liquid alloys and molten ionic mixtures(3,4). In the previous work(4), we investigated mainly the difference between the equations for the surface tension of liquid alloys and those of ionic solutions. In the present work, we focus molten salt mixtures, and discuss the application of the thermodynamic database, which has been constructed to the calculation of phase diagrams of salt mixtures, to evaluate the surface tension of the molten salt mixtures considering the thermodynamic characteristics of those mixtures.

BUTLER'S EQUATION FOR SURFACE TENSION OF A-B BINARY LIQUID

We use here the Butler's equation(5) for surface tension σ of A-B binary liquid solution as we have applied it for liquid alloys in the previous work(3,4). Butler derived the following equation [1] assuming an equilibrium between a bulk phase and a surface phase. The surface phase is regarded as a hypothetical independent phase and consists of the outermost monolayer of the surface as shown in Fig.1.

$$\begin{aligned}\sigma &= \sigma_A + \frac{RT}{A_A} \ln \frac{(1-N_B^S)}{(1-N_B^B)} + \frac{1}{A_A} \bar{G}_A^{E,S}(T, N_B^S) - \frac{1}{A_A} \bar{G}_A^{E,B}(T, N_B^B) \\ &= \sigma_B + \frac{RT}{A_B} \ln \frac{N_B^S}{N_B^B} + \frac{1}{A_B} \bar{G}_B^{E,S}(T, N_B^S) - \frac{1}{A_B} \bar{G}_B^{E,B}(T, N_B^B)\end{aligned}\quad [1]$$

where R is the gas constant, T temperature, σ_X surface tension of pure liquid X , A_X molar surface area in a monolayer of pure liquid X ($X=A$ or B). A_X can be obtained from the following equation.

$$A_X = LN_0^{1/3} V_X^{2/3} \quad [2]$$

N_0 Avogadro number, V_X molar volume of pure liquid X . L in Eq.[2] is set to be unity for molten salts(2). N_X^S and N_X^B in Eq.[1] are mole fractions of a component X in the surface phase and the bulk phase, respectively; $\bar{G}_X^{E,S}(T, N_B^S)$ partial excess Gibbs energy of X in the surface phase as a function of T and N_B^S ; $\bar{G}_X^{E,B}(T, N_B^B)$ partial excess Gibbs energy of X in the bulk phase as a function of T and N_B^B ($X=A$ or B).

PARTIAL EXCESS GIBBS ENERGY IN SURFACE PHASE

Since $\bar{G}_X^{E,B}(T, N_B^B)$ in the bulk phase in Eq.[1] can be obtained directly from thermodynamic databases, we only need the additional information on $\bar{G}_X^{E,S}(T, N_B^S)$ in the surface phase. Speiser et al.(6,7), Hoar & Melford(8), Monma & Sudo(9) and Kasama(10) proposed their own models for $\bar{G}_X^{E,S}(T, N_B^S)$, which can be summarized as follows(3),(4):

$$\bar{G}_X^{E,S}(T, N_B^S) = \beta \cdot \bar{G}_X^{E,B}(T, N_B^S) \quad [3]$$

The above four groups(6-10) proposed their own values of β , but we have determined β as follows(3,4):

1) The surface tension σ_X of pure molten salt X at its melting point is assumed to be determined by the following relation.

$$\begin{aligned}A_X \cdot \sigma_X &= LN_0^{1/3} V_X^{2/3} \cdot \sigma_X \\ &= (-U_X^B) - (-U_X^S) \\ &= (-U_X^B) - \beta^* \cdot (-U_X^B) \\ &= \Delta H_{Eva,X} - \beta^* \cdot \Delta H_{Eva,X} = (1 - \beta^*) \cdot \Delta H_{Eva,X}\end{aligned}\quad [4]$$

where U_X^B and U_X^S are binding energies in the bulk phase and the surface phase respectively, and $\beta^* = U_X^S / U_X^B$. In the above equation, surface entropy terms are

neglected, and $(-U_X^B)$ is assumed to be approximately equal to evaporation energy $\Delta H_{\text{Eva},X}$ at the melting point.

2) We assume the following relation;

$$\begin{aligned} \beta^* (=U_X^S/U_X^B) &: \text{for pure molten salts} \\ = \beta \{=\bar{G}_X^{E,S}(T,N_B^S)/\bar{G}_X^{E,B}(T,N_B^S)\} &: \text{for molten salt mixtures} \end{aligned} \quad [5]$$

3) The relation between σ_X and $\Delta H_{\text{Eva}}/(LN_0^{1/3}V_X^{2/3})$ for pure molten salts is shown in Fig.2. The values of σ_X were taken from the NIST database (12). We obtained V_X from the selected density of pure component salts in the NIST database(12) with the molar weights of cations and anions. From the linear relation between σ_X and $\Delta H_{\text{Eva}}/(LN_0^{1/3}V_X^{2/3})$ in Fig.2 and the above assumption 2), we have determined β in Eq.[3] to be 0.94 for molten salt mixtures. In our previous work(3,4), we have determined the value of β for liquid alloys to be 0.83.

PROCEDURE OF CALCULATION OF SURFACE TENSION OF SOLUTIONS

The surface tension σ of molten salt mixtures can be calculated as follows:

<1> Setting T and N_B^B of a solution. <2> Determining the values for σ_X, V_X and excess Gibbs energies in the bulk phase at the above T and N_B^B , and substituting them in Eq.[1]. <3> One pair between the two equations on the right-hand side of Eq.[1] becomes the equation with unknown N_B^S . This equation is solved for N_B^S , and the value of N_B^S is substituted again into e.g. the first equation of the right-hand side of Eq.[1] to calculate the surface tension σ on the left-hand side of Eq.[1].

APPLICATION OF THERMODYNAMIC DATABASES TO EVALUATION OF SURFACE TENSION OF MOLTEN SALT MIXTURES

Nissen & Van Domelen(13) reported the thermodynamic calculation of the surface tension of some molten salt mixtures using Guggenheim's equation with thermodynamic interaction parameters. They used only the regular solution model for thermodynamic solutions, and the interaction parameters were evaluated from mixing enthalpy data. In the present work, we have used Pelton's thermodynamic database(14,15), which has been assessed to provide calculation of thermodynamic properties and phase diagrams of salt mixtures according to the CALPHAD approach, to calculate the surface tension of some molten salt mixtures. Common ion systems considering of the following ions have been treated here:

Cations : $\text{Li}^+, \text{Na}^+, \text{K}^+, \text{Rb}^+, \text{Cs}^+$; Anions : $\text{F}^-, \text{Cl}^-, \text{Br}^-, \text{I}^-, \text{NO}_3^-, \text{SO}_4^{2-}$
Surface tension data of pure component salts, σ_X in Eq.[1], were taken from the NIST database(12). We obtained V_X in Eq.[2] from the selected density of pure component salts in the NIST database(12) with the molar weights of cations and anions. Figure 3

shows the calculated results for surface tension σ of a few molten salt mixtures, which have large negative excess Gibbs energies, using $\beta = 0.94, 0.83$ and $3/4$. The hatched zones in Fig.3 show the uncertainties of the experimental values (13) for the surface tension of molten salt mixtures. The uncertainties have been determined from the scatter of the experimental values of σ_X for pure substances in the NIST database (12). As shown in this figure, the values $3/4$ and 0.83 for β , which are adequate for liquid alloys(3,4), are unsuitable for the calculation of the surface tension of some molten salt mixtures. In addition, the uncertainties of the experimental values are recognized to be about $\pm 5 \text{ mNm}^{-1}$ from Fig.3. Figure 4 shows the comparison of the calculated results obtained from Eqs.[1], [2] and [3] for the surface tension of various molten salt mixtures, of which excess Gibbs energies are not so large, with the experimental values stored in NIST database(12). As can be seen from this figure, the calculated results agree well with the experimental data in those systems. However, in some systems, of which excess Gibbs energies are large as shown in Fig.5, the composition dependencies of the surface tension have large downward curvatures from the linearity, as pointed out by Goodisman(16) and others, and the calculated results of those systems show the discrepancies with the experimental values although the discrepancies are almost within the uncertainties of the experimental values as described above. Thus, we might need to revise the equation for the excess Gibbs energy in the surface phase in Eq.[3] for molten salt mixtures. In ionic solutions, the interaction between different ions extends over the most outer monolayer of the surface because of their Coulomb's force, which is one of the long-distance forces. A possible way to derive an alternative equation for Eq.[3] is to consider a "relaxation layer" between the surface phase and the bulk phase as shown in Fig.6. The relaxation layer is considered to be within the bulk phase region, but to be influenced by the surface phase. An equation can be proposed as follows :

$$\bar{G}_X^{E,S}(T, N_B^S) = \beta \cdot \bar{G}_X^{E,B}(T, N_B^S) + S \cdot \bar{G}_X^{E,B}(T, N_B^B) \quad [6]$$

In the above equation, the first term in the right-hand side shows the contribution of the interaction among ions in the outermost monolayer, and the second term shows the contribution of the relaxation layer, i.e., the effect of the interaction among ions in the surface phase to the bulk phase region, which is a function of temperature T and the mole fraction of B in the bulk phase, N_B^B . The value of S shows the fraction of the effect of the relaxation layer to $\bar{G}_X^{E,S}(T, N_B^S)$. The chain curves in Fig.5 show the calculated results from the combination of Eqs.[1], [2] and [6] when we set the value of S to be 0.2. The calculated results with Eq[6] agree with the experimental values better than those with Eq.[3]. There are, however, still some binary systems, in which the satisfied results are not obtained from the above calculation as shown in Fig.7. The experimental values show the large downward-curvatures of the composition dependence of the surface tension. Consequently, in order to extend the above

application of the thermodynamic databases to the evaluation of the surface tension of molten salt mixtures, we need still detail investigations on the following subjects :

- 1) More precise experimental data should be accumulated on the surface tension of molten salt mixtures.
- 2) We should consider the characteristics of the atomic structures near the surface of molten salt mixtures in more detail to derive adequate thermodynamic models for the surface tension of those mixtures.
- 3) The thermodynamic data should be reevaluated based on more information about the thermodynamic data, phase equilibria etc.

CONCLUDING REMARKS

The surface tensions of some molten salt mixtures have been calculated using the thermodynamic data, which have been taken from the database assessed according to the CALPHAD approach. Furthermore, some relationships between the excess Gibbs energy in the bulk phase and that in the surface phase of molten salt mixtures have been discussed. Although we still have some problems to revise the excess Gibbs energy of the surface phase of those mixtures, the present approach will enable us to develop a multi-functional thermodynamic databank system, which will be of wide applicability in the evaluation of physico-chemical properties of molten salt mixtures with the simultaneous calculation of the phase equilibria in those mixtures.

REFERENCES

1. C.W. Bale and G. Eriksson, *Can. Metall. Quar.*, **29**, 105 (1990).
2. T. Nishizawa, *Mat. Trans. JIM.*, **33**, 713 (1992).
3. T. Tanaka and T. Iida, *Steel Research*, **65**, 21 (1994).
4. T. Tanaka, K. Hack, T. Iida and S. Hara, *Z. Metallkd.*, **87**, No.5 (1996).
5. J.A.V. Butler, *Proc. Roy. Soc. A.* **135**, 348 (1935).
6. R. Speiser, D.R. Poirier and K. Yeum, *Scripta Metall.*, **21**, 687 (1987).
7. K.S. Yeum, R. Speiser and D.R. Poirier, *Metall. Trans., B*, **20B**, 693 (1989).
8. T.P. Hoar and D.A. Melford, *Trans. Faraday Soc.*, **53**, 315 (1957).
9. A. Kasama, *Dr. Eng. Thesis*, p.113, Osaka University (1978).
10. K. Monma and H. Sudo, *J. Jpn. Inst. Metals*, **24**, 117 (1960).
11. O. Kubaschewski and C.B. Alcock, *Metallurgical Thermochemistry*, 5th ed., p.326, Pergamon Press, Oxford (1979).
12. NIST molten salt database, National Institute of Standards and Technology (1987).
13. D.A. Nissen and B.H. Van Doremelen, *J. Phys. Chem.*, **79**, 2003 (1975).
14. A.D. Pelton, *CALPHAD*, **12**, 127 (1988).
15. J.M. Sangster and A.D. Pelton, in *Phase Diagrams for Ceramists*, Vol.VII, L.P. Cook, Editor, Amer. Ceram. Soc., Westerville, (1983).
16. J. Goodisman, *J. Colloid and Interface Sci.*, **73**, 115 (1980).

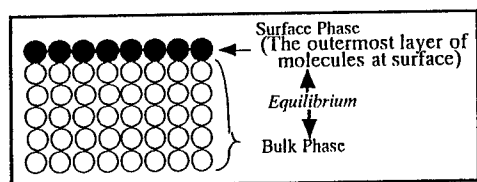


Figure 1
Schematic diagram of
the equilibrium between
the surface phase
and the bulk phase.

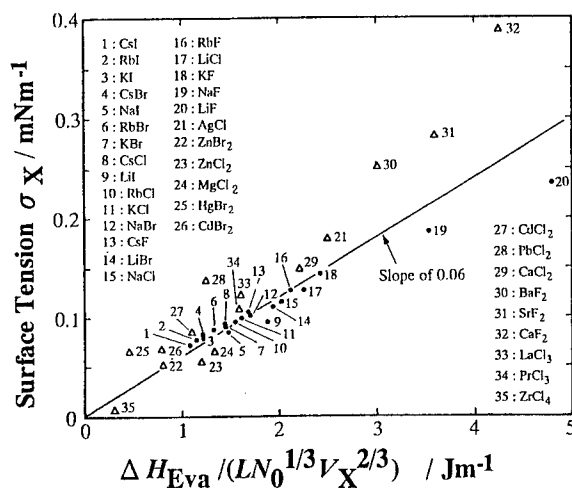


Figure 2
Correlation of σ_X and
 $\Delta H_{Eva} / (LN_0^{1/3} V_X^{2/3})$
for various pure molten
salts.

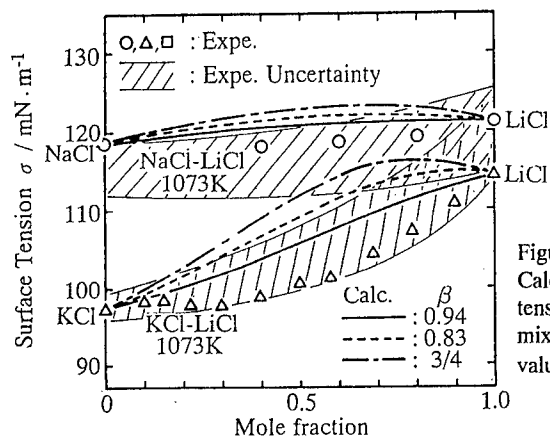


Figure 3
Calculated results for surface
tension of some molten salt
mixtures obtained from various
values of β .

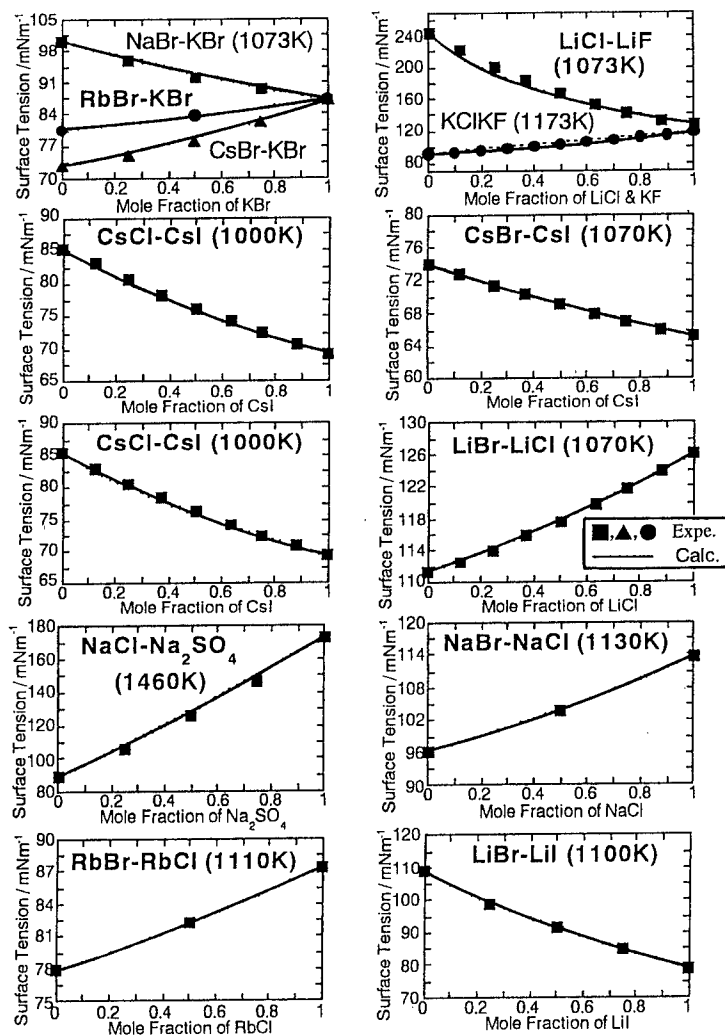


Figure 4 Calculated results for surface tension of molten salt mixtures, of which excess Gibbs energies are not so large, with experimental values.

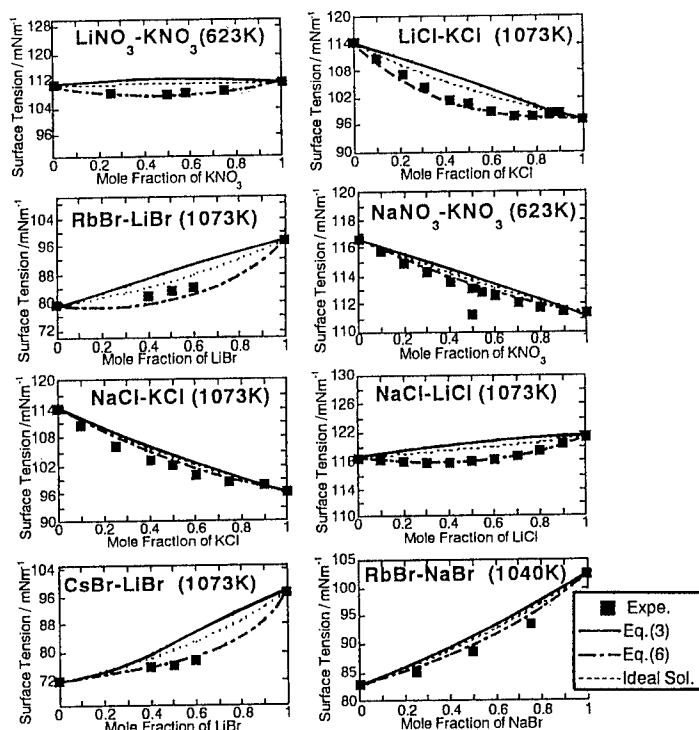


Figure 5 Calculated results for surface tension of molten salt mixtures with large excess Gibbs energies with experimental values.

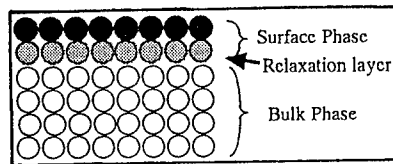


Figure 6 Schematic diagram of the relaxation layer between the surface phase and the bulk phase.

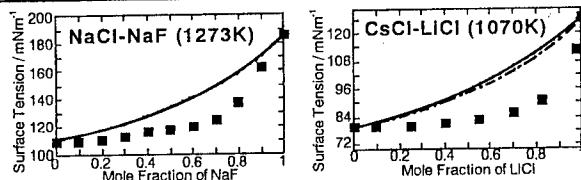


Figure 7 Calculated results for surface tension of molten salt mixtures with experimental values showing large downward curvatures.

Copper Deposition from Cu(I) Ions in CuCl-BPC Molten Salts -Microstructural Analysis of the Melts

N. Koura, N. Tanabe, and S. Seiki

Faculty of Science and Technology, Tokyo University of Science,
2641 Yamazaki, Noda, Chiba 278, Japan

S. Takahashi*, M.-L. Saboungi, L.A. Curtiss, and K. Suzuya**

Argonne National Laboratory, Argonne, Illinois 60439-4814, U. S. A.

*On leave from Nisshin Steel Co. Ltd., 7-1 Koyashinmachi, Ichikawa, Chiba 272, Japan

**Present address: Japan Atomic Energy Research Institute, Kamigori, 678-12, Japan.

ABSTRACT

The characteristics of a CuCl-BPC room-temperature molten salt electrolyte and the morphology of the Cu deposits are strongly dependent on CuCl content. It has been assumed that these changes are affected by the ionic species in the melt. Molar fractions of the ionic species were calculated by the simulation method, and their structures computed by *ab initio* molecular orbital method. The structure deduced from neutron diffraction measurements are consistent with the calculated results.

1. INTRODUCTION

Copper is usually electrodeposited from Cu(II) ions in aqueous media. There are some advantages in using CuCl-BPC molten salt as an electrolyte. Since this does not include oxygen or H₂O, it is possible to obtain oxygen-free high-purity copper in a single process involving a one-electron reaction. It was found that the morphology of the copper deposit depends significantly on electrolyte composition; this has been attributed to changes in the abundance of various ionic species in the melt with the composition(1, 2). In this work, we try to analyze the structure of the melt and study the relation between compositional changes on the one hand and electrochemical performance and structure on the other.

2. EXPERIMENTAL METHODS

2.1 Physical and electrochemical properties

Viscosity and conductivity were measured using a vibroviscometer and conductivity meter, respectively. For the electrode potential measurements, the working electrode was a 99.99 % Cu wire and the reference electrode was a 99.99 % Cu wire immersed in 66.7 mol% CuCl-33.3 mol% BPC melt. The molten salt electrolytes were prepared by mixing predried CuCl and BPC. All experiments were performed under a dry nitrogen atmosphere.

2.2 *Ab initio* molecular orbital calculations

Ab initio molecular orbital calculations were carried out to determine the

equilibrium structure and harmonic vibrational frequencies. The polarized split valence 6-311G* basis set as defined in the Gaussian 94 program (3). The *ab initio* calculations were carried out at the Hartree-Fock (HF) level using the Gaussian 94 program to determine the structures of the ionic species. To minimize the CPU time, the calculation was first carried out using minimal STO-3G basis set. After optimizing the most stable structure at this level, the HF/6-311G* calculation was carried out.

2.3 Neutron diffraction measurements

Measurements were made on the Glass Liquid and Amorphous Diffractometer (GLAD) instrument at Intense Pulsed Neutron Source (IPNS) of Argonne National Laboratory. Three melt compositions with 44.0, 66.7, and 71.0 mol% CuCl were selected. Measurements were made on each sample and on an empty container of the same dimensions. For purposes of instrument calibration and data normalization, measurements were also carried out on a 0.64 cm diameter vanadium standard and with the spectrometer empty. All measurements were done at 298 K.

The samples were prepared by mixing CuCl with fully deuterated BPC in a glove box, where the H₂O and O₂ levels were maintained at less than 2 ppm. The melts were contained in a fused silica tube of 1 mm thickness and 3 mm inner diameter which was sealed under vacuum.

2.4 Calculation of structure factors $S(Q)$ from the *ab initio* results

The structure factor, $S(Q)$ of each ionic species was calculated as a function of wavevector, Q by substituting the interatomic distances obtained in the *ab initio* calculations in the Debye equation [1]. The average $S(Q)$ for each composition was then obtained from a sum of the $S(Q)$'s of the ionic isolated species involved in the specific melt.

$$S(Q) = 1 + \frac{1}{n \langle b \rangle^2} \sum_{i \neq j}^n \sum_{j=1}^n b_i b_j \frac{\sin(Q r_{ij})}{Q r_{ij}} \quad [1]$$

b_i, b_j : Scattering amplitudes
 n : Number of atoms in the unit
 r_{ij} : Interatomic distances

3. RESULTS AND DISCUSSION

3.1 Measurements of the melt properties

The viscosity and conductivity as a function of CuCl content are shown in Fig. 1. The viscosity shows a minimum of ~ 8 cP at ~ 50.0 mol% CuCl. The conductivity exhibits a maximum of ~ 35 mS·cm⁻¹ at ~ 50 mol%. As stated before, it has been considered that the characteristics of these melts are strongly affected by the ionic species present. The electrode potentials of Cu in the melts are shown in Fig. 2. The Cu potential changes with the molar fraction of CuCl, especially around 50.0 mol%. This suggests that the ionic species in the melt changes with the CuCl content. Molar fractions of each ionic species calculated by the simulation method (4-6) are shown in Fig. 3.

3.2 *Ab initio* molecular orbital calculations

From Fig. 3 it is assumed that the major anionic species in the equimolar melt is CuCl_2^- , those in the 66.7 mol% melt are CuCl_2^- and Cu_3Cl_4^- , and that in the 71.0 mol% melt is Cu_3Cl_4^- . The major cationic species is the BP^+ cation (1). The structures of the ionic species were determined from *ab initio* calculations.

1-butylpyridinium cation (BP^+). At the HF/6-311G* level, the fully optimized cation has a structure with C_1 symmetry, shown in Fig. 4.

CuCl_2^- . This anion has a $D_{\infty h}$ structure at the HF/6-311G* level with a bond length of 2.238 Å, shown in Fig. 5(a).

Cu_3Cl_4^- . At the HF/6-311G* level, the Cu_3Cl_4^- anion has a C_{2v} structure with a bent Cu-Cl-Cu angle ($=132.3^\circ$) shown in Fig. 5(b). These calculations were done for the closed shell anion, i.e., the low spin state.

The structures of ionic species in the melt are different. For example, the Cu - Cl bond lengths of CuCl_2^- are 2.238 Å, and of Cu_3Cl_4^- are 2.211, 2.261, 2.293 Å.

3.3 Neutron diffraction

The measured structure factors $S(Q)$ for the three melts are shown in Fig. 6. Differences can be seen in the peak features around 3 and 6 Å⁻¹, confirming that the abundance of ionic species change with CuCl content.

The corresponding pair distribution functions $g(r)$ are shown in Fig. 7. From the *ab initio* results, the peak around 2.2 Å is considered to be the Cu-Cl pair. With increasing CuCl content, the position of this peak shifts to larger r . As shown in Fig. 5, the Cu-Cl distance is 2.238 Å for CuCl_2^- and from 2.211 to 2.293 Å for Cu_3Cl_4^- as computed from the *ab initio* calculations. Thus, the major ionic species in the melt appears to change from CuCl_2^- to Cu_3Cl_4^- with increasing CuCl content. In addition, this peak is broader in the 66.7 mol% CuCl melt than the others suggesting that two ionic species are present. These conclusions are supported by the simulation and *ab initio* results.

Using the major ionic species obtained from the simulation results (Fig. 3), we calculated average $S(Q)$'s for isolated ions for the three melts. The results shown in Fig. 8 exhibit good agreement with the experimental $S(Q)$ at higher Q . However, the agreement for Q below 3 Å⁻¹ is poor, possibly due to the fact that the interactions between the cation and anion are not properly accounted for. We are now calculating these interactions and will also calculate the harmonic vibrational frequencies and compare the results with those derived from Raman spectroscopy.

4. CONCLUSION

The physical properties of the melts, i.e., viscosity, conductivity, electrode potential, and morphology of the deposited Cu change with CuCl content. These changes are ascribed to changes in the abundance of different ionic species, i.e., CuCl_2^- and Cu_3Cl_4^- . The molar fractions of these species were calculated by the simulation method, and the structures by the *ab initio* molecular orbital method. Results from neutron diffraction measurements on three melts with different CuCl contents were

presented. The experimental $S(Q)$ and $g(r)$ were found to be in good agreement compared with the results derived from the simulation and *ab initio* calculations, especially at high Q when the interionic interactions can be neglected.

ACKNOWLEDGMENTS

We thank the Computer Center of the Molecular Science Institute (Japan) for time on the supercomputer. MLS and LAC are supported by the US-Department of Energy, BES-MS under contract #W31-100-109-ENG-38.

REFERENCES

1. N. Koura, M. Iwai, K. Ueda and A. Suzuki, *J. Surf. Fin. Jpn.*, **44**, 439(1993).
2. N. Koura, A. Suzuki and S. Ito, *Proceedings of the International Symposium on Molten Salt Chemistry and Technology-1993*, p70-80, Honolulu(1993).
3. M.J. Frisch, et al, "GAUSSIAN 94," Gaussian Inc., Pittsburgh, PA 1995.
4. L.G. Boxall, H.L. Jons and R.A. Osteryoung, *J. Electrochem. Soc.*, **120**, 223(1973).
5. S.A. Bolkan and J.T. Yoke, *J. Chem. Eng. Data*, **31**, 194(1986).
6. S.A. Bolkan and J.T. Yoke, *J. Electrochem. Soc.*, **134**, 1698(1987).

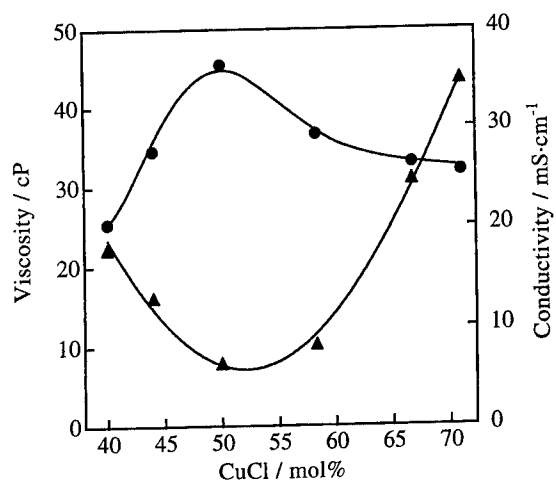


Fig. 1 Effect of CuCl content in a CuCl-BPC melt on viscosity and conductivity at 90 °C.

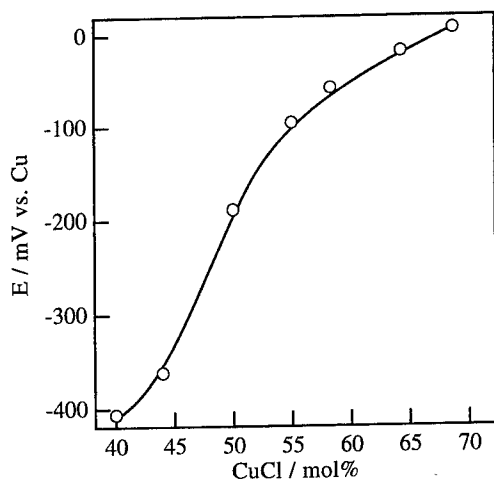


Fig. 2 Effect of CuCl content in a CuCl-BPC melt on electrode potential at 90 °C.

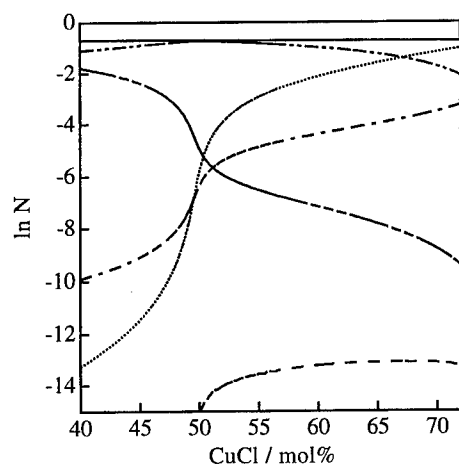


Fig. 3 Molar fraction (N) change of ionic species in a CuCl-BPC melt with the CuCl content at 90 °C.

--- : CuCl_2^- , - - : Cu_2Cl_3^- , : Cu_3Cl_4^-
 — : CuCl , - - - : Cl^- , — : BP^+

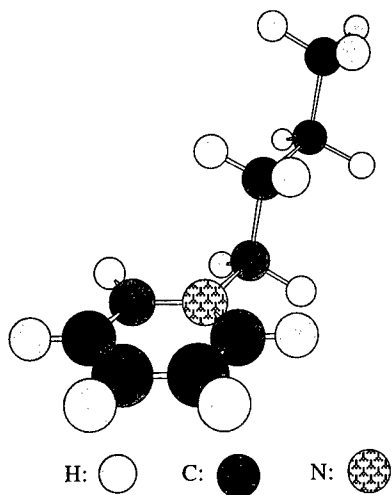


Fig. 4 HF/6-311G* optimized structure for BP^+ .

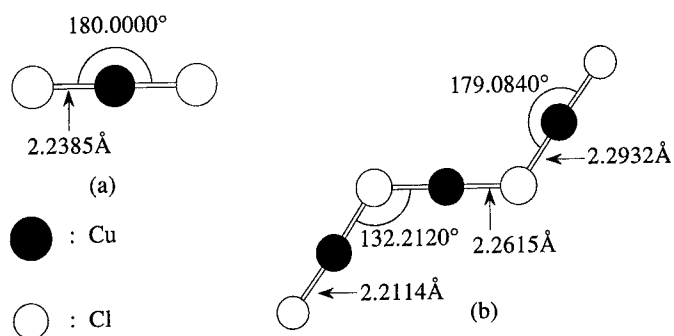


Fig. 5 HF/6-311G* optimized structures for anionic species.
(a) CuCl_2^- , (b) Cu_3Cl_4^-

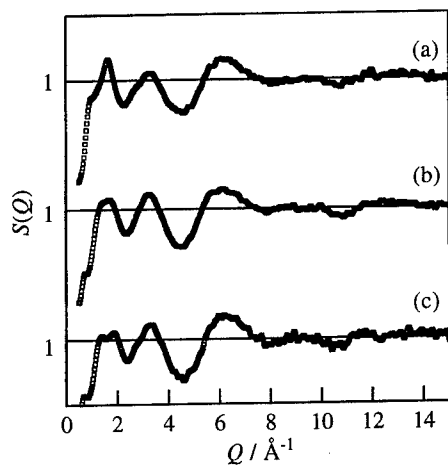


Fig. 6 Structure factors $S(Q)$ for CuCl melts.
(a) 50.0 mol%CuCl-50.0 mol%BPC melt
(b) 66.7 mol%CuCl-33.3 mol%BPC melt
(c) 71.0 mol%CuCl-29.0 mol%BPC melt

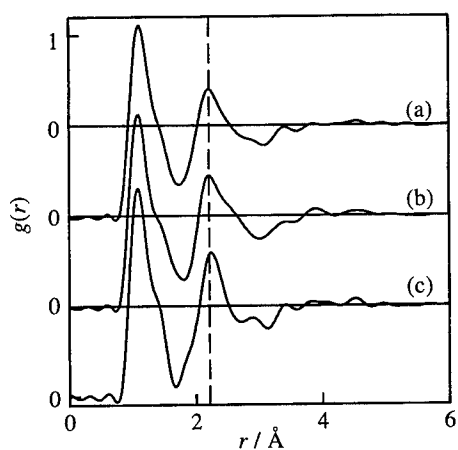


Fig. 7 Pair distribution functions $g(r)$ for CuCl melts.

- (a) 50.0 mol% CuCl-50.0 mol% BPC melt
- (b) 66.7 mol% CuCl-33.3 mol% BPC melt
- (c) 71.0 mol% CuCl-29.0 mol% BPC melt

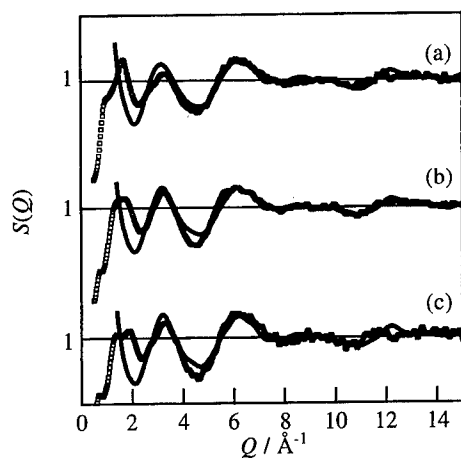


Fig. 8 Structure factors $S(Q)$ for CuCl melts.

- (a) 50.0 mol% CuCl-50.0 mol% BPC melt
- (b) 66.7 mol% CuCl-33.3 mol% BPC melt
- (c) 71.0 mol% CuCl-29.0 mol% BPC melt

□: experimental, —: Calculated

IONIC DISSOCIATION MODEL FOR (Li, K)X BINARY MELTS (X=F, Cl, Br OR I)

Pascal HEBANT, Gérard S. PICARD

Laboratoire d'Electrochimie et de Chimie Analytique
(Unité de recherche associée au C.N.R.S. n° 216).
Ecole Nationale Supérieure de Chimie de Paris,
11 rue P & M Curie, 75231 Paris Cedex 05, France

ABSTRACT

Quantum mechanics combined with thermostatical computations allowed us to establish the binary lithium potassium halide melt dissociations. These latter can be well described taking into account the formation both of simple and complex ions :



Except for the lithium iodide - potassium iodide molten mixtures - whose dissociations are satisfactory described assuming the formation of simple ions only (reaction i). The existence of the ionic complexes LiX_2^- and K_2X^+ well explains qualitatively the electrical conductivity of melts whatever the melt composition and temperature.

INTRODUCTION

Alkali halides binary melts undergo a dissociation both into simple cations and anions and complex ionic species. The nature and concentration of these last species are of primary importance because they are responsible for the major part of the physicochemical behaviours of melts. In particular, a realistic dissociation model is crucial for the understanding of the acidobasic and solvation powers of melts. The great percentage of free ions (1) made possible the investigations of melt properties by considering only simple ion-ion interactions such as in Molecular Dynamics studies performed e.g. by Lantelme et al (2) and Okada et al (3-5) which gave satisfactory results and tendencies.

Applying quantum mechanics to the study of molten salt structure is very useful to determine the existing complexes and their relative stability, and hence to derive complex dissociation models. In a previous paper (6), the influence of the counter-cation M on the melt dissociation was studied for the particular case of (Li,M)Cl binary melts. The complex ions LiCl_2^- and M_2Cl^+ were evidenced and their stabilities and proportions were computed as a function of melt composition and temperature, explaining the corresponding variations of electrical conductivity.

In this work, the effect of the anion on melt dissociation and electrical conductivity has been more deeply investigated in the case of (Li, K)X melts ($\text{X}=\text{F}, \text{Cl}, \text{Br}$ or I). The following procedure was used. Firstly, Molecular Modelling techniques were employed to reach the structures of complex ionic species the more likely to occur in the dissociation of melts. Secondly, the temperature dependence of complex dissociation of melts was studied using thermostatical computations. Finally, the Fukui functions (7, 8) were applied for investigating the reaction mechanism of melt dissociation.

COMPUTATIONAL PROCEDURE

Quantum mechanics. Calculations were performed with DMol 2.36 (9, 10) from Biosym Technologies Inc., on a Silicon Graphics Iris Indigo R4400 workstation. This software is based on the Density Functional Theory -DFT- (11-13). The DNP basis, similar to the 6-31G** Gaussian basis set (14) which is very efficient and able to deal with anions of low charge (6), was used. All calculations include the Becke-Lee-Yang-Parr gradient correction (15, 16) at the Unrestricted Hartree-Fock (UHF) level. Vibrational frequencies calculations were performed for all species because (i) they allow us to determine if the studied system corresponds to a stable complex by checking if some of frequencies are negative (ii) they are needed for a further thermostatical calculation routine.

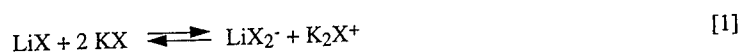
Thermodynamic data. For species whose thermodynamic data are not at our disposal in usual thermodynamics tables, we used thermostatical computations using our DFT results (6, 17, 18) in order to reach them as previously described in reference (6). Available thermodynamic data, were taken in references (19, 20).

RESULTS AND DISCUSSION

Dissociation model

Conformational and energetic data for lithium and potassium halide species were obtained. Table I summarizes the stable and unstable isolated species (vacuum) at 0 K. It must be pointed out that K_2I^+ is not stable contrary to its homologues with other halides. This is an important result, because if M_2Cl^+ is involved in the melt dissociation scheme of (Li, M)Cl melts (6), K_2I^+ cannot intervene in the dissociation of LiI-KI melts. In every case, conformational analysis i.e. geometrical optimization of greater ionic assemblies such as MX_4^{3-} (M=Li or K) demonstrated that the stable systems are indeed $MX_3^{2-} + X^-$ (expulsion of one chlorine). With an analogous procedure, we found that $M_iM'_{3-i}X_3$ (M, M' = Li or K ; $i=0, \dots, 3$) systems are combinations of smaller ones.

Using the total energies obtained with DMol, we are able to compute chemical reaction energies, ΔU_0 , that can occurs between species. Results collected in Table II show that the following reaction involving complex ionic species :



has the lowest energy among all the melt dissociation reaction schemes considered. This equilibrium is similar to the one we found in reference (6) for the (Li, M)Cl series (M=Li, Na, K or Rb). In the case of LiI-KI mixtures, because of the non existence of K_2I^+ the reaction to be considered is :



with a much lower extent. Giving the high positive value for ΔU_0 of reaction [2], the dissociation of iodide binary melts is practically well described by considering only the simple ions Li^+ , K^+ and I^- .

On the contrary, for the other binary melts reaction [1] has to be considered. The effect of temperature has hence to be taken into account. As ΔU_0 is quite small for reaction [1], the entropic part, $T\Delta S_T$ of the reaction free enthalpy, ΔG_0 , has to be considered. ΔS_T has been estimated with statistical techniques. Results are shown in table III. Knowing

ΔG_T allows us to compute the percentage of lithium complexed following the scheme of reaction [1] as a function of both temperature and melt composition solving the equation :

$$4\xi^3 + \left(e^{\frac{\Delta G_T}{RT}} - 4 \right) \xi^2 + (4x_{KX} - 3x_{KX}^2) \xi + x_{KX}^2 (x_{KX} - 1) = 0 \quad [3]$$

where ξ is the degree of advancement of reaction [1]. The percentage of complexed lithium is then given by :

$$\% \text{complexed Li} = \frac{\xi}{1 - x_{KX}} \times 100 \quad [4]$$

Results are given in Fig 1. One can see that lithium complexation decreases from fluorine to bromine and becomes very small in the case of LiBr-KBr. In a similar way, the temperature influence is getting more important from fluorine to bromine, for a given melt composition.

Consistency of our model.

The experimental electrical conductance values for (Li, K)F, (Li, K)Cl and (Li, K)I mixtures at various compositions and temperatures (after (21)) can be correlated to our model of melt dissociation. We know that when $\Delta\kappa$ ($\Delta\kappa = [(\kappa - \kappa^{\text{ideal}})/\kappa] \times 100$, with κ standing for the electrical conductance), is very negative, ionic complexes are present in melts (22). In fact, for (Li, K)F and (Li, K)Cl melts, we can see in Fig. 2 that $\Delta\kappa$ is highly negative (presence of LiX_2^- and K_2X^+), but not for (Li, K)I melts (presence of Li^+ , K^+ and I^- only). This is in agreement with the results we found, as reaction [1] cannot occurs in LiI-KI mixtures.

Going further, we have plotted in Fig.3 the calculated total percentage of complexes :

$$\text{Total \% complexes} = 2\xi \times 100 \quad [5]$$

as a function of melt composition and temperature. We notice that an increase of the mole fraction of KX, x_{KX} , increases the number of ionic complexes, this is in good agreement with the corresponding experimental decrease of $\Delta\kappa$. Moreover, we observe in Fig.3 that

the maximum for the calculated number of complexes occurs when the experimental value of $\Delta\kappa$ is minimum. After that, the number of ionic complexes becomes smaller when x_{KX} still increases and simultaneously $\Delta\kappa$ raises. This observed correlation between experimental $\Delta\kappa$ and calculated percentage of ionic complexes remains true whatever the temperature.

Reaction mechanism.

DFT calculation results such as electronic density maps and Fukui functions (7), allows more insight in the reactivity of the species involved in reaction [1]. Electronic density maps (see Fig. 4) show that LiX is more covalent than KX and thus KX will be able to give X^- anion more easily than LiX. When the size of X increases, the difference between LiI and KI is less pronounced than for LiF and KF.

We have also computed the Fukui functions f^+ and f^- for nucleophilic and electrophilic attacks. In fact the maxima of these Fukui functions enable us to determine the privileged sites of attack (23). The following relations (7, 8) were used for calculating these two functions :

$$f^+(\bar{r}) \approx |\Psi_{LUMO}|^2 \quad f^-(\bar{r}) \approx |\Psi_{HOMO}|^2 \quad [4]$$

In every case, the maximum of f^+ is located on Li or K and the maximum of f^- on X as expected because a nucleophilic attack cannot occur on the X atom as well as an electrophilic attack on Li or K. Results (see Table IV) show that in LiX-KX melts, the nucleophilic attack occurs on the lithium of LiX and the electrophilic attack on the halide of KX. These results suggest the following two step mechanism :



CONCLUSION

Use of quantum mechanics combined with thermostistical computations enable us to clarify the reaction mechanisms of binary alkali halide melt dissociations. Except for the lithium iodide - potassium iodide molten mixtures - whose dissociations are satisfactory

described assuming the formation of simple ions only - we have to consider complex ionic species to account for the dissociation reactions of the other alkali halide mixtures. These complex species are essentially LiX_2^- and K_2X^+ . The existence of these ionic complexes well explains qualitatively the electrical conductivity of melts whatever the melt composition and temperature. NMR studies are currently in progress for experimentally evidencing these ionic complexes at the microscopic scale [26].

ACKNOWLEDGEMENTS

The authors wish to thank la Compagnie Générale des Matières Nucléaires (COGEMA) for the financial support of this work. One author (P.H.) thanks l'Association Nationale de la Recherche Technique (A.N.R.T) and COGEMA for providing a C.I.F.R.E (Conventions Industrielles de Formation par la Recherche) doctoral grant.

REFERENCES

1. P. Hébant, G. Picard, L. Mouron and J. J. Legendre, *J. Am. Inst. Phys.*, to be published (1996).
2. F. Lantelme and P. Turq, *J. Phys. Chem.*, **77**, 3177 (1981).
3. I. Okada, R. Takagi and K. Kawamura, *Z. Naturforsch.*, **35a**, 493 (1980).
4. I. Okada, *Z. Naturforsch.*, **39a**, 880 (1984).
5. I. Okada, *Z. Naturforsch.*, **42a**, 21 (1987).
6. P. Hébant and G. S. Picard, *J. Mol. Struct. (Theochem)*, **358**, 39 (1995).
7. J. L. Gázquez, in *Chemical Hardness*, Coll. Structure and Bonding **80**, K.D. Sen Ed., Springer-Verlag, Berlin (1993).
8. P. K. Chatteraj and R. G. Parr, in *Chemical Hardness*, Coll. Structure and Bonding **80**, K.D. Sen Ed., Springer-Verlag, Berlin (1993).
9. B. Delley, *J. Chem. Phys.*, **92**, 508 (1990).
10. B. Delley, in *Density functional methods in chemistry*, J.K. Labanowski and J.W. Andzelm Eds., Springer Verlag, New York (1991).
11. R. G. Parr, *Ann. Rev. Phys. Chem.*, **34**, 631 (1983).
12. J. Callaway and N. H. March, *Solid State Phys.*, **38**, 135 (1984).
13. R. O. Jones and O. Gunnarsson, *Rev. Mod. Phys.*, **61**, 689 (1989).
14. DMol 2.3.5 User Guide, Biosym Technologies, San Diego (1993).

15. A. D. Becke, J. Chem. Phys. , **88**, 2547 (1988).
16. C. Lee, W. Yang and R. G. Parr, Phys. Rev. B , **37**, 785 (1988).
17. P. Héban and G. S. Picard, J. Mol. Struct. (Theochem) , to be published (1996).
18. F. Bouyer, G. Picard and J. J. Legendre., J. Chem. Information & Comp. Sci. , In press (1996).
19. JANAF Thermochemical Tables, M. W. Chase Jr, C. A. Davies, J. R. Downey Jr, D. J. Frurip, R. A. McDonald and A. N. Syverud Eds. , Coll. J. Phys. Chem. Ref. Data, **14** Supplement 1 , American Chemical Society - American Institute of Physics, New York (1985).
20. I. Barin, Thermochemical data of pure substances, VCH, Weinheim (1989).
21. Properties of Molten Salts Database 2.0, G.J. Janz Ed, National Institute of Standards and Technology (1992).
22. Y. K. Delimarskii and B. F. Markov, Electrochemistry of fused salts, The Sigma Press, Washington (1961).
23. R. G. Parr and W. Yang, J. Am. Chem. Soc. , **106**, 4049 (1984).
24. Phase diagrams for ceramist, E. M. Levin, C. R. Robbins and H. F. McMurdie Eds., The American Ceramic Society Inc., Columbus (1964-1989).
25. E. Elchardus and P. Laffitte, Bull. Soc. Chim. , **51**, 1572 (1932).
26. P. Héban, C. Bessada and G. Picard, to be published

TABLES AND FIGURES

Species		X=F	X=Cl	X=Br	X=I
LiX	KX	Y Y	Y Y	Y Y	Y Y
LiX ₂ ⁻	KX ₂ ⁻	Y Y	Y Y	Y Y	Y Y
LiX ₃ ²⁻	KX ₃ ²⁻	Y Y	Y Y	Y Y	Y Y
LiX ₄ ³⁻	KX ₄ ³⁻	N N	N N	N N	N N
Li ₂ X ⁺	K ₂ X ⁺	Y Y	Y Y	N Y	N N
Li ₂ X ₂	K ₂ X ₂	Y Y	Y Y	Y Y	Y N
LiKX ₂		Y	Y	Y	Y
LiKX ⁺		Y	Y	N	N
Li ₃ X ₃		N	N	N	N
Li ₂ KX ₃		N	N	N	N
LiK ₂ X ₃		N	N	N	N
K ₃ X ₃		N	N	N	N

Table I : Stability under DFT conditions of molecular or ionic systems constituted with salt components. Y means stable and N not stable

Réaction	ΔU_0 (kJ.mol ⁻¹)			
	X=F	X=Cl	X=Br	X=I
$\text{Li}^+ + \text{X}^- \leftrightarrow \text{LiX}$	-827.34	-663.14	-642.19	-594.93
$\text{LiX} + \text{X}^- \leftrightarrow \text{LiX}_2^-$	-328.75	-245.45	-234.08	-451.72
$\text{LiX} + \text{Li}^+ \leftrightarrow \text{Li}_2\text{X}^+$	-280.39	-206.98		
$\text{LiX}_2^- + \text{X}^- \leftrightarrow \text{LiX}_3^{2-}$	259.64	224.30	213.27	199.05
$2\text{LiX} \leftrightarrow \text{Li}_2\text{X}_2$	-245.54	-197.49	-185.53	-170.22
$\text{Li}^+ + \text{LiX}_2^- \leftrightarrow \text{Li}_2\text{X}_2$	-744.12	-615.18	-593.64	-556.52
$\text{Li}_2\text{X}^+ + \text{X}^- \leftrightarrow \text{Li}_2\text{X}_2$	-792.49	-653.65		
$3 \text{LiX} \leftrightarrow \text{LiX}_2^- + \text{Li}_2\text{X}^+$	218.20	210.72		
$2 \text{LiX} \leftrightarrow \text{LiX}_2^- + \text{Li}^+$	498.59	417.69	408.11	398.59
$2 \text{LiX} \leftrightarrow \text{X}^- + \text{Li}_2\text{X}^+$	546.95	456.16		
$\text{K}^+ + \text{X}^- \leftrightarrow \text{KX}$	-623.20	-502.24	-486.28	-451.72
$\text{KX} + \text{X}^- \leftrightarrow \text{KX}_2^-$	-210.62	-180.92	-174.80	-162.55
$\text{KX} + \text{K}^+ \leftrightarrow \text{K}_2\text{X}^+$	-221.10	-177.95	-167.05	
$\text{KX}_2^- + \text{X}^- \leftrightarrow \text{KX}_3^{2-}$	171.48	149.10	143.22	143.22
$2\text{KX} \leftrightarrow \text{K}_2\text{X}_2$	-194.44	-166.66	-159.38	
$\text{K}^+ + \text{KX}_2^- \leftrightarrow \text{K}_2\text{X}_2$	-607.02	-487.98	-470.86	
$\text{K}_2\text{X}^+ + \text{X}^- \leftrightarrow \text{K}_2\text{X}_2$	-596.54	-490.94	-478.62	
$3 \text{KX} \leftrightarrow \text{KX}_2^- + \text{K}_2\text{X}^+$	191.48	143.37	144.43	
$2 \text{KX} \leftrightarrow \text{KX}_2^- + \text{K}^+$	412.58	321.32	311.48	289.17
$2 \text{KX} \leftrightarrow \text{X}^- + \text{K}_2\text{X}^+$	402.10	324.28	319.24	
$\text{LiX} + 2\text{KX} \leftrightarrow \text{LiX}_2^- + \text{K}_2\text{X}^+$	73.35	78.84	85.16	
$\text{LiX} + 2 \text{KX} \leftrightarrow \text{KX}_2^- + \text{LiKX}^+$	250.24	198.55		
$2\text{LiX} + \text{KX} \leftrightarrow \text{KX}_2^- + \text{Li}_2\text{X}^+$	336.34	275.25		
$2\text{LiX} + \text{KX} \leftrightarrow \text{LiX}_2^- + \text{LiKX}^+$	132.10	134.02		
$\text{LiX} + \text{KX} \leftrightarrow \text{LiX}_2^- + \text{K}^+$	294.44	256.79	252.21	243.09
$\text{LiX} + \text{KX} \leftrightarrow \text{KX}_2^- + \text{Li}^+$	616.73	482.22	467.38	432.38
$\text{LiX}_2^- + \text{K}^+ \leftrightarrow \text{LiKX}_2$	-533.19	-449.69	-434.90	-410.11
$\text{KX}_2^- + \text{Li}^+ \leftrightarrow \text{LiKX}_2$	-855.47	-675.13	-650.07	-599.41

Table II : Total energy differences, ΔU_0 , for reactions that can occur with the computed species. A gray pattern indicates that the reaction is not possible due to the unstability of one or more species involved

species	a	b	c	Temperature	Reference
LiF	45	0.09	$-1.66 \cdot 10^{-5}$	700-1400	(20)
KF	75	0.05	$-8.79 \cdot 10^{-6}$	700-1400	(20)
LiCl	36	0.16	$-4.8 \cdot 10^{-5}$	500-1400	(19)
KCl	53	0.17	$-4.8 \cdot 10^{-5}$	600-1200	(19)
LiBr	77	0.11	$-2.18 \cdot 10^{-5}$	500-1200	(20)
KBr	100	0.13	$-2.27 \cdot 10^{-5}$	500-1200	(20)
(LiF ₂ ⁻ , K ₂ F ⁺)	458	0.22	$-5.56 \cdot 10^{-5}$	700-1400	This work
(LiCl ₂ ⁻ , K ₂ Cl ⁺)	458	0.26	$-7.3 \cdot 10^{-5}$	600-1200	(6)
(LiBr ₂ ⁻ , K ₂ Br ⁺)	451	0.23	$-5.7 \cdot 10^{-5}$	500-1200	This work

Table III : Estimated entropic data in $\text{J} \cdot \text{mol}^{-1} \cdot \text{K}^{-1}$. $S_T = a + bT + cT^2$.

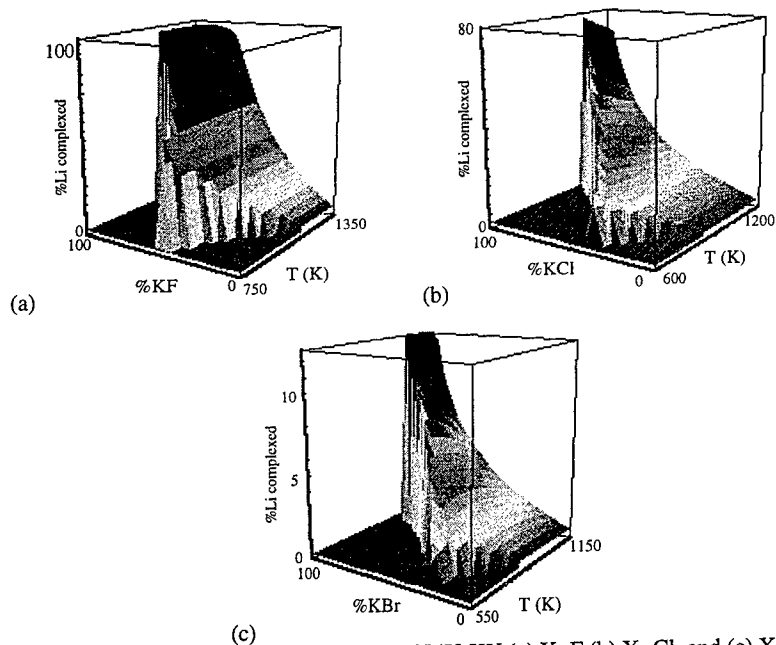


Figure 1 : 3D graph of the complexation of LiX-KX (a) X=F (b) X=Cl, and (c) X=Br as a function of temperature and melt composition. Temperature range follow phase diagrams (24, 25)

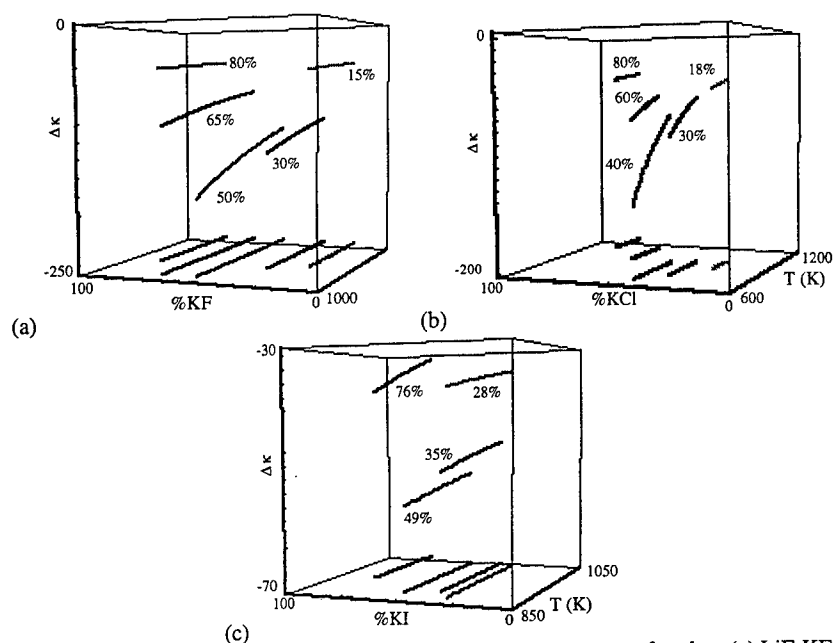


Figure 2 : Relative gap from ideality for the electrical conductance of molten (a) LiF-KF, (b) LiCl-KCl and (c) LiI-KI. (after (21))

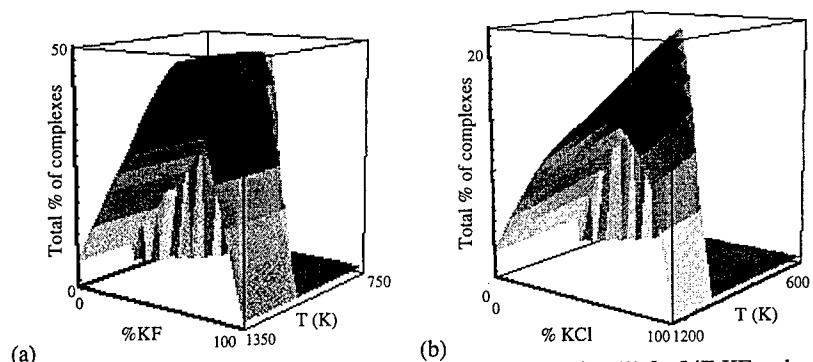


Figure 3 : Total percentage of complexes according to reaction (1) for LiF-KF and LiCl-KCl

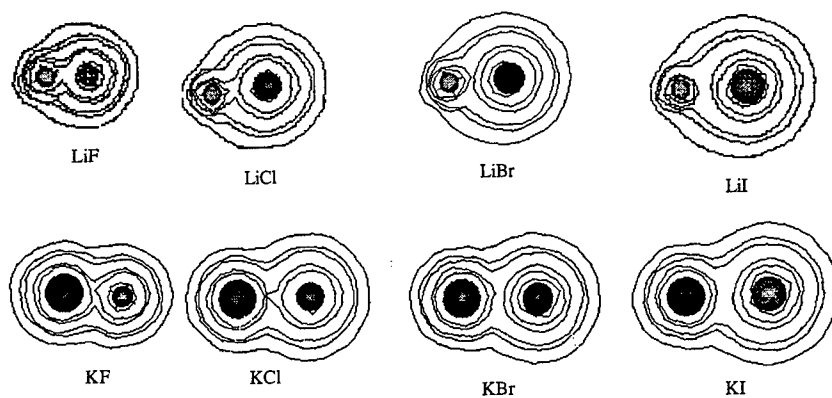


Figure 4 : electronic density maps for LiX and KX families. Contour values from border to centre are 0.007, 0.035, 0.07, 0.35, 0.7 and 3.5 electron. \AA^{-3} . The drawing scale is the same for all molecules

Molecule	$f(\vec{r})$	$f^+(\vec{r})$
LiF	$5.35 \cdot 10^{-1}$	$7.79 \cdot 10^{-2}$
KF	$6.51 \cdot 10^{-1}$	$1.93 \cdot 10^{-2}$
KCl	$8.11 \cdot 10^{-2}$	$3.77 \cdot 10^{-2}$
LiCl	$6.8 \cdot 10^{-2}$	$9.14 \cdot 10^{-2}$
LiBr	$7.70 \cdot 10^{-2}$	$2.94 \cdot 10^{-2}$
KBr	$8.32 \cdot 10^{-2}$	$1.24 \cdot 10^{-2}$

Table IV : Fukui functions maxima in Ha.Bohr⁻³

ANOMALOUS BEHAVIOR OF AG(I) AND TL(I) IONS IN MOBILITIES OF MOLTEN NITRATES

Isao Okada and Pao-hwa Chou
Department of Electronic Chemistry,
Tokyo Institute of Technology
Nagatsuta 4259, Midori-ku, Yokohama 226, Japan

The data on internal cation mobilities, u , in the molten binary nitrate systems (M, Ag)NO₃ and (M, Tl)NO₃ (M=alkali metal ion) determined by Klemm's countercurrent electromigration method are reexamined. In binary alkali nitrates u is well expressed by an empirical equation $u = \{A/(V_m - V_0)\} \exp(-E/RT)$, where V_m is the molar volume; A , V_0 and E are constants nearly independent of coexisting cations. If Ag⁺ is contained, the u_M of coexisting cations M negatively deviates from such an equation, and, on the contrary, if Tl⁺ is contained, the u_M positively deviates. Thus, Ag⁺ and Tl⁺ having relatively high polarizabilities have the opposite effects on u_M , that is tranquilization effect and agitation effect, respectively. The reason has been interpreted in terms of the high polarizabilities and the difference in the sizes of Ag⁺ and Tl⁺.

INTRODUCTION

Since molten alkali nitrates have relatively low melting points, these are suitable media for experiments for a better understanding of the mechanism of ionic conductance in molten salts. As for the mechanism of ionic mobility, binary systems with a common anion supply us with more information than pure salts do, because mobilities of two cations can be compared under the same conditions.

We have so far measured the internal mobilities, u , in molten binary alkali nitrates by countercurrent electromigration, and found that u_{M1} of cations M1 such as Li, Na and K are well expressed by an empirical equation (1):

$$u_{M1} = \{A/(V_m - V_0)\} \exp(-E/RT) \quad , \quad [1]$$

where V_m is the molar volume of the mixture, and A , V_0 and E are constants characteristic of M1 and nearly independent of coexisting cations.

More than 30 years ago Blander(2) proposed to compare the differences in the properties of Ag⁺ and Tl⁺ ions from those of Na⁺ and Rb⁺ for separating the physical properties in molten salts related to the relatively high polarizabilities. However, the role of polarizabilities for transport phenomena such as mobilities and diffusion coefficients has not explicitly been clarified yet. Thus, in the present work we have systematically reexamined the feature of cation internal mobilities in molten binary nitrate mixtures when Ag⁺ or Tl⁺ having high polarizabilities is contained as one of the binary cations.

EXPERIMENTAL

In molten binary nitrates (M1, M2)NO₃ [M1=alkali metal ion, M2=Ag or Tl] countercurrent electromigration presented by Klemm (3) was performed to obtain the relative differences in internal mobilities of M1 and M2

$$\varepsilon = (u_{M1} - u_{M2}) / (x_{M1}u_{M1} + x_{M2}u_{M2}), \quad [2]$$

where x_i is the mole fraction of i. The experimental details were previously described (4).

From the ε values and the data available on densities and electric conductivities, the internal mobilities were calculated by

$$u_{M1} = (\kappa V_m / F)(1 + x_{M2} \varepsilon), \quad [3]$$

$$u_{M2} = (\kappa V_m / F)(1 - x_{M1} \varepsilon), \quad [4]$$

where κ is the electric conductivity, V_m the molar volume, and F the Faraday constant.

RESULTS

Detailed results on the internal mobilities in the binary systems (Ag, M)NO₃ and (Tl, M)NO₃ (M=alkali metal ion) measured by Klemm's countercurrent electromigration method have been given elsewhere (see Table 1).

Table 1. References where the internal mobilities in (M1, M2)NO₃ are given.

M1 \ M2	Li	Na	K	Rb	Cs
Ag	(5)	(4)	(5)	(6)	(6)
Tl	(7)	(8)	(9)	(7)	(9)

Internal mobilities in the molten system (Ag, Tl)NO₃ have also been measured (10).

The isotherms of internal cation mobilities in (Ag, M)NO₃ and (Tl, M)NO₃ are shown in Figs. 1 and 2, respectively.

DISCUSSION

In Table 2 some fundamental properties of alkali metal, Ag(I) and Tl(I) ions and their nitrate melts are given.

In Table 3 a comparison of u_{M1} and u_{M2} in (M1, M2)NO₃ is given, which is seen from Figs. 1 and 2.

Table 2. Some fundamental properties of alkali metal, Ag(I) and Tl(I) ions and their nitrate melts.

	LiNO ₃	NaNO ₃	KNO ₃	RbNO ₃	CsNO ₃	AgNO ₃	TlNO ₃
Cation							
ionic radius * (11) (pm)	59(IV)	102(VI)	138(VI)	152(VI)	167(VI)	115(VI)	150(VI)
ionic mass (g mol ⁻¹)	6.941	22.98	39.09	85.46	132.9	107.8	204.3
polarizability (2) (10 ⁻³⁰ m ³)	0.030	0.182	0.844	1.42	2.45	1.72	3.50
polarizability/ionic radius ³	0.146	0.172	0.321	0.404	0.526	1.13	1.04
Nitrate							
melting point (°C)	261	308	333	316	414	212	206
molar volume at 350 °C (10 ⁻⁶ m ³ mol ⁻¹)	39.64	44.95	54.24	59.34	67.48**	44.49	57.28

* The roman numerals in the parentheses indicate coordination numbers for which the ionic radii are given here.

** The value under the melting point is the extrapolated value with respect to temperature.

Table 3. A comparison of u_{M1} and u_{M2} in (M1, M2)NO₃.

M1 \ M2	Li	Na	K	Rb	Cs
Ag			$u_{Ag} > u_{M1}$		
Tl	Chemla effect	Chemla effect	$u_{Tl} > u_K$	$u_{Tl} > u_{Rb}$	$u_{Tl} > u_{Cs}$

Table 4. An effect on u_{M1} caused by M2 in (M1, M2)NO₃ melts.

M1 \ M2	Li	Na	K	Rb	Cs
Ag	no effect	tranquilization effect			
Tl	agitation effect				

(M1, Ag)NO₃ mixtures

Internal mobility of Ag⁺, u_{Ag} . In (M1, Ag)NO₃, u_{Ag} is greater than u_{M1} under all the experimental conditions.

We have previously found that internal mobilities are strongly related with separating motion of neighboring cation and anion called the self-exchange velocity (SEV) (12), which can be calculated by molecular dynamics simulation (MD). For molten AgNO₃ MD has not been performed yet. However, the SEV may be

considered in terms of the potential profiles. The separating motion of a cation of interest (Ag; C in Fig. 3) from the referenced anion (NO_3 ; A in Fig. 3) may be classified in three stages as shown in Fig. 3:

- (1) another anion (NO_3 ; B) reaches the cation,
- (2) the cation(C) moves away from the referenced anion(A) toward the anion (B), as the potential barrier becomes low enough compared with the kinetic energy, and
- (3) the cation(C) moves away together with the other anion (B) from the referenced anion(A).

As the potentials for AgNO_3 are not available, Ag-Cl potentials (13) are used here, which may be sufficient for the present qualitative discussion. The potential profiles are considered for ions arranged, for simplicity, in one dimension. In Fig. 4 the potential felt by Ag^+ collinearly located between two Cl^- is shown. This is obtained by superposition of the two pair potentials. The shape of the potential depends also on the distance between the two anions. The potential without the dispersion term is also shown here, which resembles that for Na^+ to some extent. When the dispersion term, which is caused by the polarizability, is included, the flat region of the potential well becomes wider, and therefore the SEV of Ag^+ will become large. The flat region for Ag^+ on varying the distance between the two anions may be wider than that for other cations such as Li^+ , Na^+ and K^+ . This may be the reason why the internal mobility of Ag^+ is greater than that of any other cations.

The internal mobilities of Ag^+ in $(\text{Ag}, \text{M2})\text{NO}_3$ as a function of molar volume are shown in Fig. 5. Figure 5 reveals that u_{Ag} is well expressed by such an equation as Eq. (1) with the parameters: $A=7.01 \times 10^{-11} \text{ m}^2 \text{ V}^{-1} \text{ s}^{-1} \text{ mol}^{-1}$, $V_0 = (49.05 - 0.048(T/K)) \times 10^{-6} \text{ m}^3 \text{ mol}^{-1}$ and $E=19.86 \text{ kJ mol}^{-1}$. Thus, u_{Ag} is not affected by the kind of M1 except for Li^+ and Tl^+ . The former is due to the free space effect, and the latter is attributed to the agitation effect, which will be discussed later.

Internal mobility of M1, u_{M1} As seen from Table 2, the molar volume of AgNO_3 is slightly smaller than that of NaNO_3 , whereas the ionic radius of Ag^+ is considerably greater than that of Na^+ . This suggests that the distances of $\text{Ag}^+-\text{NO}_3^-$ and Ag^+-Ag^+ become smaller owing to the high polarizability.

In Figs. 6, 7 and 8, u_{Li} , u_{Na} and u_{K} as a function of the molar volume are shown, respectively. The u_{Na} and u_{K} in the mixtures with AgNO_3 slightly but appreciably deviate negatively. The u_{Rb} and u_{Cs} also show a similar tendency. These are ascribed to the tranquilization effect caused by Ag^+ . If a cation (C_i) shown by a dotted circle in Fig. 3 strongly interacts with anion B, the motion of anion B will be retarded, which will tranquilize the SEV of cation C from anion A. This tranquilization effect is caused by the strong interaction of $\text{Ag}^+-\text{NO}_3^-$ due to the high polarizability of Ag^+ . On the other hand, as shown in the inset of Fig. 6, u_{Li} in the mixture system $(\text{Li}, \text{Ag})\text{NO}_3$ lies on the empirical equation at higher molar volume, that is at high concentration of Ag^+ , but deviates negatively at low molar volume.

The reason that Ag^+ does not play the role of a tranquilizer for u_{Li} in $(\text{Li}, \text{Ag})\text{NO}_3$ is explained as follows: the potential profile felt by anion B from cation C and cation C_i is shown in Fig. 9 for the case B as Cl^- , C as Li^+ and C_i as Ag^+ . Here, the potential of Cl^- is adopted for anion B instead of NO_3^- ; for Li^+-Cl^- pair potential, the one presented by Tosi and Fumi (14) is used. Since the interaction of Li^+ -anion is stronger than that of Ag^+ -anion, Ag^+ does not play a role of a

tranquilizer for u_{Li} .

Incidentally, the negative deviation at high concentration of Li^+ may be attributed to the free space effect caused by the restricted rotational motion of NO_3^- due to the small free space. The fact that, while u_{Li} in pure $LiCl$ is considerably greater than u_{Na} in pure $NaCl$, u_{Li} in pure $LiNO_3$ is nearly equal to u_{Na} in pure $NaNO_3$ will support this assumption; u_{Li} and u_{Na} in pure $LiNO_3$ and $NaNO_3$ are $5.414 \times 10^{-8} m^2 V^{-1} s^{-1}$ and $5.427 \times 10^{-8} m^2 V^{-1} s^{-1}$, respectively, at 623 K, and u_{Li} and u_{Na} in pure $LiCl$ and $NaCl$ are $20.53 \times 10^{-8} m^2 V^{-1} s^{-1}$ and $14.15 \times 10^{-8} m^2 V^{-1} s^{-1}$, respectively, at 1083 K.

(M1, Tl⁺)NO₃ Mixtures

Internal mobility of Tl⁺, u_{Tl} In $(Li, Tl)NO_3$ and $(Na, Tl)NO_3$ the Chemla effect (1) occurs, that is the isotherms of the mobilities of the two cations have a crossing point.

It is interesting to note that in $(K, Tl)NO_3$ u_{Tl} is greater than u_K , whereas the ionic radius of Tl^+ is greater than K^+ . This may be accounted for on the assumption that due to the high polarizability of Tl^+ the accessible distance of Tl^+-Tl^+ is shorter than that of K^+-K^+ , even if the distance between nuclei is slightly greater for the former than for the latter. This feature is schematically shown in Fig. 10. The $Tl^+-NO_3^-$ distance is also considered to become shorter owing to the high polarizability than that in a hypothetical case of its lower polarizability. The NO_3^- neighboring to Tl^+ more favorably moves away than that neighboring to K^+ does. Thus, internal mobility of Tl^+ is greater than that of K^+ . In Fig. 11 the radial distribution functions (15) for molten KNO_3 and $TlNO_3$ obtained by X-ray diffraction are shown. Although the peak around 460 pm assignable to Tl^+-Tl^+ correlation seems to be slightly more distant than that assignable to the sum of K^+-K^+ and O^--O^+ interactions, the former is tailed toward shorter distance than the latter. Further, the assumption that the motion of NO_3^- is vigorous in the systems containing Tl^+ may be also supported by the finding that the external transport number of NO_3^- in pure $TlNO_3$ is relatively large (0.69 at 220 °C (16)).

Since the ionic radii of Rb^+ and Cs^+ are greater than that of K^+ , u_{Tl} is naturally expected to be greater than u_{Rb} or u_{Cs} .

In Fig. 12 u_{Tl} as a function of molar volume is shown, as compared with u_{Rb} . The u_{Tl} cannot be expressed by such an equation as Eq. (1). The u_{Tl} most positively deviates from u_{Rb} at pure $TlNO_3$. This means that u_{Tl} is a function not only of the molar volume but also of the concentration of Tl^+ . Figure 10 suggests that NO_3^- neighboring to Tl^+ favorably moves away toward another NO_3^- .

Internal mobility of M1, u_{M1} As partly shown in Figs. 6, 7 and 8, the internal mobilities of all alkali metal ions and Ag^+ deviate positively in the presence of Tl^+ . In general, upward deviations may be explained in terms of the agitation effect (1). This means that Tl^+ has an agitation effect on the internal mobilities of these cations. The reason why Tl^+ having a large mass and a relatively large ionic radius has an agitation effect is explained as follows. As explained above by using Fig. 10, the motion of NO_3^- becomes more vigorous, and therefore u_{M1} also becomes large.

Comparison of the behavior of Ag^+ and Tl^+

It is noteworthy that, while Ag^+ and Tl^+ have high polarizabilities, these ions have the opposite effects on the internal mobilities of coexisting cations. As

mentioned above, Ag^+ has a tranquilization effect except for the case of (Li, Ag) NO_3 , whereas Tl^+ has an agitation effect.

The ionic radius of Ag^+ is smaller than that of Tl^+ , and therefore the coulombic interaction of Ag^+ with NO_3^- is considerably stronger than that of Tl^+ with NO_3^- . Thus, the motion of NO_3^- is restricted, which causes the tranquilization effect on the mobilities of coexisting cations. Whether the restriction involves the rotational motion of NO_3^- or not could be examined by comparing the behavior with that in chloride systems.

CONCLUSION

Although Ag^+ and Tl^+ have large polarizabilities, these ions have the opposite effects on the internal mobilities of coexisting alkali ions; that is, the tranquilization effect caused by Ag^+ and the agitation effect by Tl^+ . The tranquilization effect may be caused by the strong attraction of $\text{Ag}^+-\text{NO}_3^-$ and the agitation effect by the small repulsion of $\text{Tl}^+-\text{NO}_3^-$ and approach of $\text{Tl}^+-\text{NO}_3^-$ and hence the more active motion of NO_3^- .

The high polarizabilities of Ag^+ and Tl^+ make the internal mobilities of these ions themselves larger than expected for a hypothetical case of lower polarizabilities. However, the mechanism for enhancing u_{Ag} and u_{Tl} seems to be different in these two cases owing to the difference in the ionic sizes. The high polarizabilities have quite different effects on the internal mobilities of coexisting cations. This difference is also caused by the ionic radii of these ions.

The present explanation needs to be substantiated by molecular dynamics simulation.

ACKNOWLEDGMENT

The present work was financially supported by the Ministry of Education, Science and Culture for Scientific Research, Japan (No. 07236103 and No. 03453046).

REFERENCES

1. M.Chemla and I.Okada, *Electrochim. Acta*, **35**, 1761(1990).
2. M.Blander, in *Molten Salt Chemistry*, M.Blander, p. 127, Interscience Pub., New York(1964).
3. A. Klemm, H. Hintenberger and P.Hoernes, *Z. Naturforsch.*, **2a**, 245 (1947).
4. K.Ichioka, I.Okada and A. Klemm, *Z.Naturforsch.*, **44a**, 747(1989).
5. I.Okada and K.Ichioka, *Z.Naturforsch.*, **47a**, 781(1992).
6. P.Chou, H.Matsuura, I.Okada and C.Yang, *Z. Naturforsch.*, **48a**, 1207(1993).
7. K.Kawamura, I. Okada and O. Odawara, *Z. Naturforsch.*, **30a**, 69 (1975).
8. S.Baluja, J. Habasaki and I.Okada, *Z. Naturforsch.*, **42a**, 377 (1987).
9. P.Chou and I.Okada, *Z. Naturforsch.*, in press.
10. P.Chou and I.Okada, *Z. Naturforsch.*, **51a**, 197 (1996).
11. R.D.Shannon, *Acta Cryst.*, **A32**, 751(1976).
12. I. Okada, R. Takagi and K. Kawamura, *Z. Naturforsch.*, **35a**, 493(1980).
13. C.Margheritis and C. Sinistri, *Z. Naturforsch.*, **43a**, 751(1988).
14. M.P.Tosi and F.G.Fumi, *J.Phys.Chem.Solids*, **25**, 45(1964).
15. H.Ohno, K.Igarashi, N. Umesaki and K. Furukawa, *X-Ray Diffraction Analysis of Ionic Liquids*, Trans. Tech. Pub., 1994.
16. I.G.Murgulescu and D. Topor, *Z.Physik.Chem.(Leipzig)*, **221**, 39(1962).

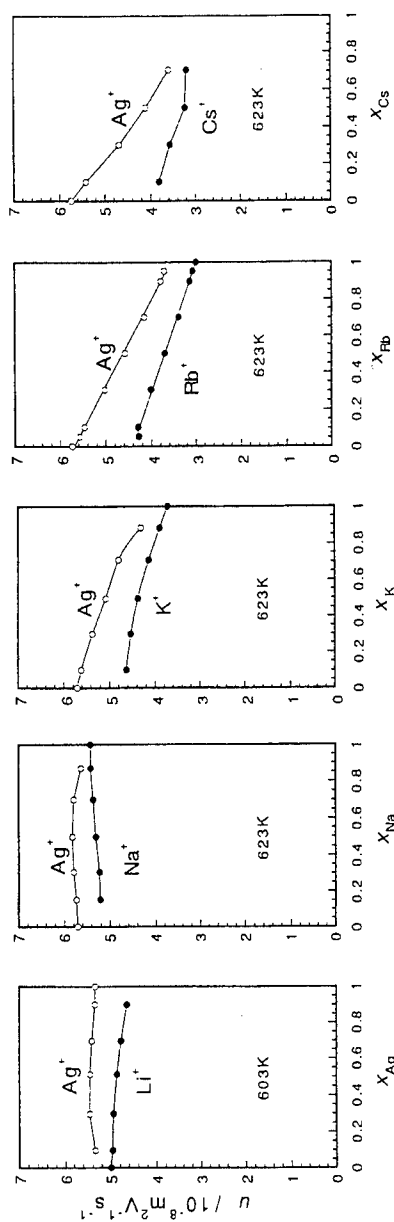


Fig. 1. Internal cation mobilities in the molten binary systems (M1, Ag)NO₃. The mole fraction of the nitrate having larger molar volume is taken as the abscissa. It is assumed here that the molar volume of NaNO₃ is greater than that of AgNO₃.

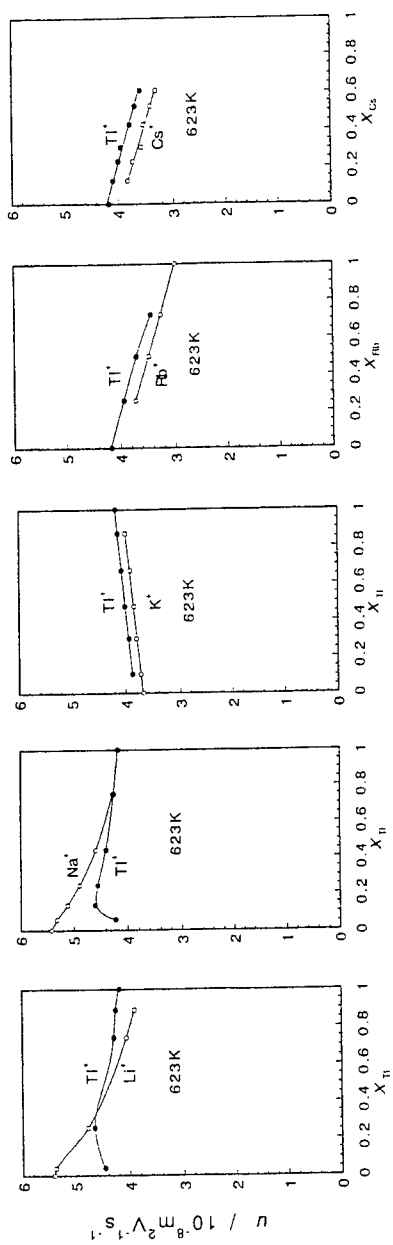


Fig. 2. Internal cation mobilities in the molten binary systems (M1, Tl)NO₃ at 623 K.

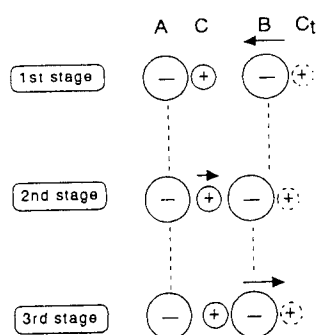


Fig. 3. Three stages for leaving of cation C from the referenced anion A. B is the anion of the same kind with A; C_t is a tranquilizer ion.

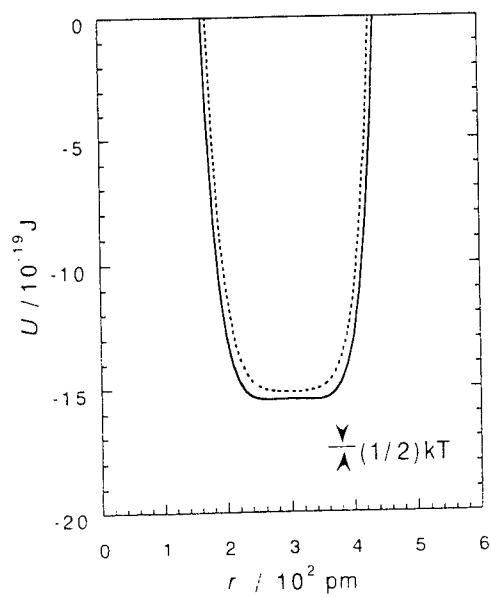


Fig. 4. The potential felt by Ag^+ collinearly located between two Cl^- ions separated by 600 pm. The dotted line is for a hypothetical case without the dispersion term. The magnitude of the kinetic energy $(1/2)kT$ at $T=1000 \text{ K}$ is shown for comparison.

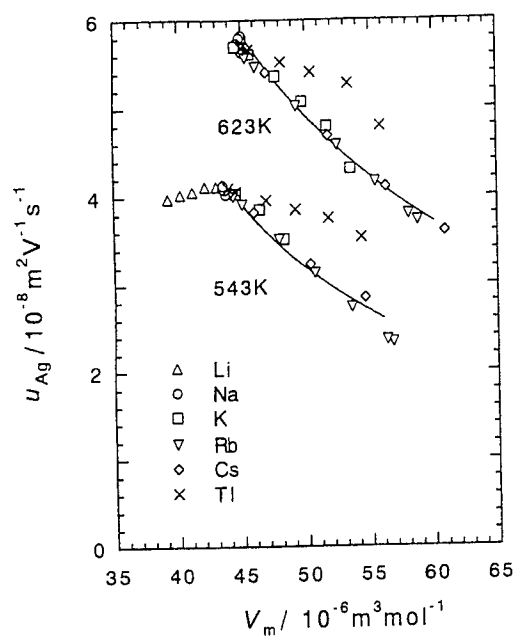


Fig. 5. Internal mobilities of Ag^+ in $(\text{Ag}, \text{M2})\text{NO}_3$ at 623 K as a function of the molar volume.

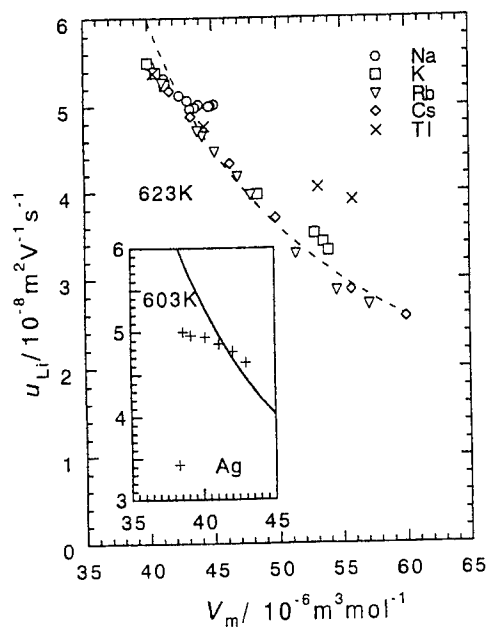


Fig. 6. Internal mobilities of Li^+ in $(\text{Li}, \text{M2})\text{NO}_3$ at 623 K as a function of the molar volume. In the inset, u_{Li} 's in $(\text{Li}, \text{Ag})\text{NO}_3$ at 603 K are shown, as the data at 623 K are not available. The dashed and solid lines are drawn according to Eq.(1) with the parameters: $A=2.84 \times 10^{-11} \text{ m}^5 \text{ V}^{-1} \text{ s}^{-1} \text{ mol}^{-1}$, $V_0=24.7 \times 10^{-6} \text{ m}^3 \text{ mol}^{-1}$ and $E=17.80 \text{ kJ mol}^{-1}(1)$.

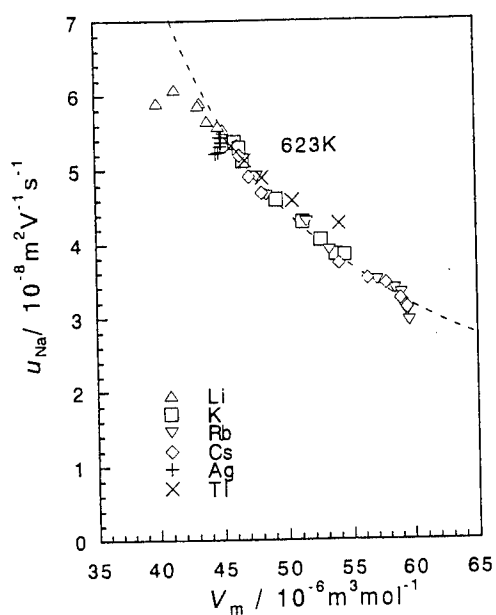


Fig. 7. Internal mobilities of Na^+ in $(\text{Na}, \text{M2})\text{NO}_3$ at 623 K as a function of the molar volume. The dashed line is drawn according to Eq.(1) with the parameters: $A=6.60 \times 10^{-11} \text{ m}^5 \text{ V}^{-1} \text{ s}^{-1} \text{ mol}^{-1}$, $V_0=(43.21-0.028(T/\text{K})) \times 10^{-6} \text{ m}^3 \text{ mol}^{-1}$ and $E=21.31 \text{ kJ mol}^{-1}(1)$.

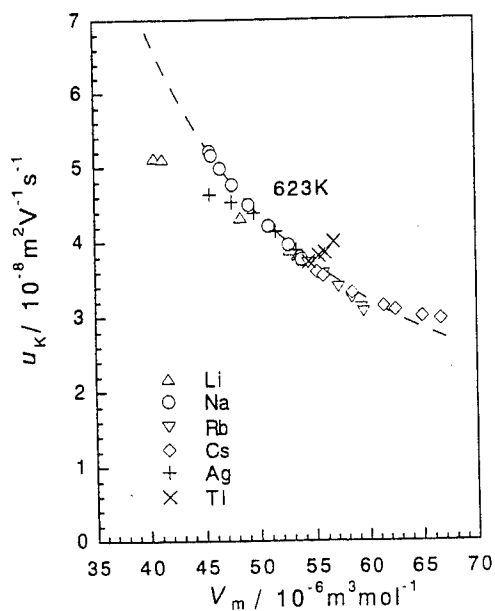


Fig. 8. Internal mobilities of K^+ in $(\text{K}, \text{M2})\text{NO}_3$ at 623 K as a function of the molar volume. The dashed line is drawn according to Eq.(1) with the parameters: $A=3.95 \times 10^{-11} \text{ m}^5 \text{ V}^{-1} \text{ s}^{-1} \text{ mol}^{-1}$, $V_0=22.1 \times 10^{-6} \text{ m}^3 \text{ mol}^{-1}$ and $E=18.00 \text{ kJ mol}^{-1}(1)$.

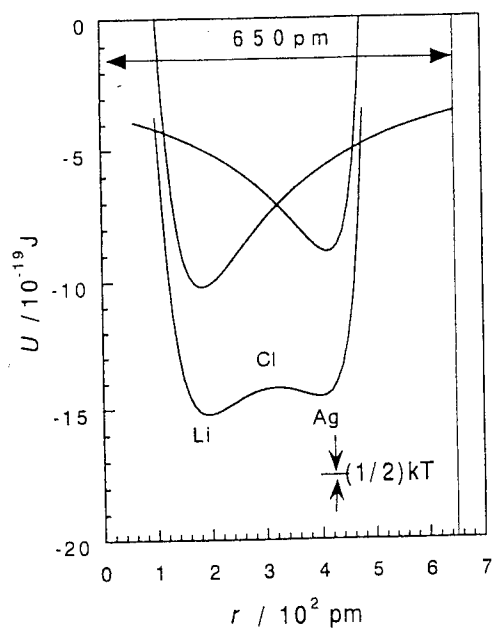
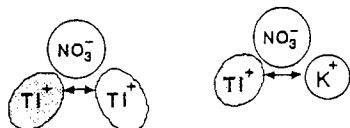


Fig. 9. Potential profile felt by Cl^- collinearly located between two different cations Li^+ and Ag^+ .

Separating motion of NO_3^- from K^+



Separating motion of NO_3^- from Tl^+



The shortest accessible distance between two cations:



Fig. 10. Schematic representation of separating motion of NO_3^- from the referenced Tl^+ or K^+ ion.

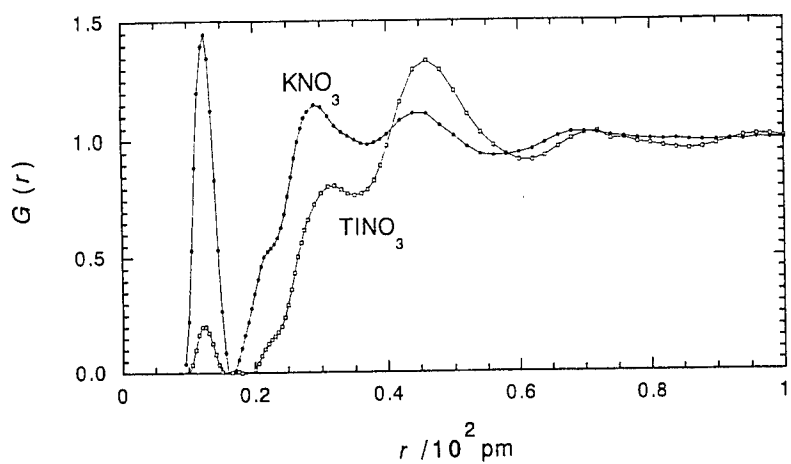


Fig. 11. X-ray weighted radial distribution functions of KNO_3 at 653 K and TiNO_3 at 503 K (15).

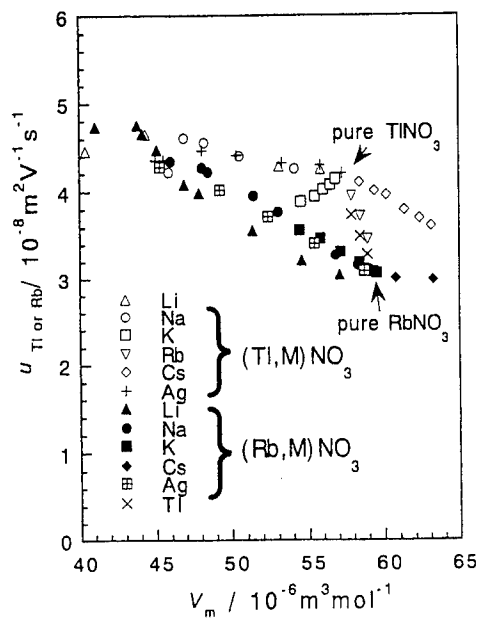


Fig. 12. Internal mobilities of Ti^+ in $(\text{M}, \text{Ti})\text{NO}_3$ as a function of the molar volume as compared with those of Rb^+ .

New Development of Fiberoptic Raman Spectroscopic Probes for High Temperature Molten Salts

S. Dai,[†]

[†]Chemical Technology Division
Oak Ridge National Laboratory
Oak Ridge, TN 37831

H.M. Xiao,[‡] Y.H. Lee,[‡] J.P. Young,[‡]
[‡]Chemical and Analytical Sciences Division
Oak Ridge National Laboratory
Oak Ridge, TN 37831

Abstract

Two strategies have been proposed to measure Raman spectroscopy of corrosive melts via fiberoptic instrumentation. The protective sheath approach requires a certain window for the all-silica fiberoptic probe we developed previously. Addition of the window will give rise to large silica background signals in Stokes Raman spectra recorded via this kind of probe. However, minimum silica signals are found in Anti-Stokes Raman spectra measured with the windowed probe. The second strategy involves the use of Dilor fiberoptic super head. The application of this system in obtaining molten carbonates has been demonstrated.

INTRODUCTION

Measurements of Laser Raman spectroscopy using optical fibers have recently become an active area of study.¹⁻⁵ The technique requires minimum alignment of samples with respect to an input laser beam or collection optics, and the sample may be located some distance from the spectrometer in a hostile environment. Most fiberoptic probes employed for such spectroscopic measurements have been constructed by sealing the collecting fibers and one input fiber into a metal or glass protective tube with a special kind of epoxy cement. These materials in a probe impose difficulties in the collection of spectra in some hostile chemical environments due to chemical reactions of the epoxy resin with surrounding environment. Recently we have reported the fabrication of an all silica fiberoptic probe that is useful for measuring Raman spectra of molten salt systems such as molten chlorides and nitrates at high temperature.⁶⁻⁷ Nevertheless, this probe can not be used to measure Raman spectroscopy of corrosive melts such as carbonate and fluoride melts, because of the reaction of silica with these melt systems. Two strategies have been implemented to extend applications of fiberoptic instrumentation in the measurement of Raman spectroscopy of these systems. The first strategy involves the development of a protective windowed-sheath for our all silica fiberoptic probes, while the second one utilizes Dilor fiberoptic super head as an alternative new approach. For

fluoride melts, the best window material is the diamond. However, one of drawbacks of windowed fiberoptic Raman probe is large silica background Raman signals which are generated from the excitation optic fiber itself and reflected to the collection fibers at the interface between probe and window.^{3,5} Therefore, the major requirement of the remote Raman spectroscopy is the reduction of the unwanted silica background signals to a level below that of sample Raman signals. Myrick and Angel have reported the use of optical interference filters to filter out the background fiber signals.³ In that study, a bandpass filter was used at the tip of the excitation optical fiber to reject any fluorescence or unwanted background signals from the excitation fiber which, at the same time, allows transmission of the large portion of the laser beam. Similar techniques have also been employed by Sharma and his coworkers in their recent remote fiberoptic studies.⁵ Usually, these optical filters can not survive high temperature conditions. Here we want to discuss a simple and yet efficient method to minimize the fiber background signals for high temperature remote Raman spectroscopy. The performance of the method was characterized by the measurement of Raman spectra of a molten MgCl_2 - CaCl_2 - KCl - NaCl (15-15-35-35 mole%) melt by a simulated windowed probe. In addition, we want to report some recent fiberoptic instrumentation to permit Raman spectral studies of corrosive melts such as carbonate melts via a fiberoptic super head system.

EXPERIMENTAL

Reagents: Anhydrous magnesium chloride was synthesized by the decomposition of the corresponding carnallite salt^{7,8}, followed by distillation using a double bulb quartz vessel.⁹ No IR bands of hydroxide or magnesium oxide species were found in the magnesium chloride thus synthesized.¹⁰ The procedure for the purification of the other starting materials (NaCl and KCl) has been described previously.¹¹ Lithium carbonate and sodium carbonate are from Aldrich Chemical Company.

Raman Spectroscopy: Raman spectra were recorded with a Ramanor HG.2S spectrophotometer equipped with concave-aberration-corrected holographic gratings. This instrument, manufactured by Jobin Yvon (Instruments SA), employs a double monochromator. Excitation of the spectra was by means of the 514.5 nm-line from an argon-ion laser (Coherent). Spectral data were stored in a 4096 channel Nicolet model 1170 signal averager which permitted the averaging of spectra over repeated scans.

The fabrication of the all-silica probe has been described in detail elsewhere.^{6,7} Briefly, the probe was constructed by the fusion of two 400 μm all-silica fibers into a quartz tube under vacuum. Vacuum was applied to make a seal and minimize bubbling of the quartz during the fusion process. This fusion method is very similar to those used in the fabrication of microelectrodes.¹² Once fused, the probe tip was carefully cut and polished with successively finer grades of emery paper to a smooth finish.

RESULTS AND DISCUSSIONS

Removal of Silica Background from Window Reflection of the Sheathed Fiberoptic Probe via Recording Anti-Stokes: Although the fiber Raman emissivity, generated in our fiberoptic probe, is weak, the measured fiber signal is strong because of the length of the

excitation optical fiber. Consider that Raman exciting laser is focused into the end of the fiber and follow the derivation by Walrafen and Stone¹³. Then, the intensity of the generated Raman scattered light dI_R in the fiber in length dx is given by :

$$dI_R = G_R I dx - \alpha I_R dx \quad (1)$$

where

$$G_R = g_R \pi \theta_c^2 \quad (2).$$

In the above eq 1 and eq 2, g_R is the Raman scattering differential cross section, $\pi \theta_c^2$ is the solid angle of light guided in the forward direction in the core, I and I_R are the exciting and Raman intensities, and α is the loss coefficient for light traveling in the fiber. It is a good assumption that the loss coefficient in the fiber is the same at the wave length of the Raman or exciting laser and the amount of the light converted to Raman radiation is small, then

$$dI = -\alpha I dx \quad (3)$$

and

$$I = I_0 e^{-\alpha x} \quad (4)$$

where I_0 is the intensity of the exciting light at $x=0$. Substituting eq 4 into eq 1 gives rise to

$$dI_R = G_R I_0 e^{-\alpha x} dx - \alpha I_R dx. \quad (5)$$

The solution of eq 5 is

$$I_R = G_R I_0 x e^{-\alpha x} \quad (6).$$

Combining eq 4 and eq 6 yields

$$\frac{I_R}{I} = G_R x \quad (7).$$

From the above equation, it is clear that the amount of Raman background signals from an optical fiber increases indefinitely with fiber length. These background signals originating from the excitation optical fiber can be reflected into the collection optical fibers through the window interface of the sheathed fiberoptic probe. Therefore, the background signals from the excitation optical fiber can be dominant in the remote fiberoptic Raman spectroscopy using sheathed probe. Since fused silica fibers are used in all fiberoptic

remote Raman spectroscopy, the fiber background signals are fused silica Raman signals.

The large background Raman signals from the exciting fiber can interfere with the measurement of sample Raman signals that occur in the same energy region. The method we propose to minimize these unwanted silica signals is through utilizing anti-Stokes Raman spectra for high temperature systems. The essence of the technique is to make use of the fact that most of the excitation fiber is at the ambient temperature. Based on basic Raman spectroscopy theory,¹⁴ the ratio of the intensity of the anti-Stokes line to Stokes line is given by

$$\frac{I_a}{I_s} \propto \exp \left(- \frac{h\nu}{kT} \right)$$

At ambient temperature extremely small anti-Stokes silica signals are expected to be generated in the excitation fiber. This known attribute of Raman scattering can be utilized to benefit studies in high temperature systems where the desired analyte exhibits a temperature-enhanced anti-Stokes signal while the bulk of the silica fiber remains at room temperature resulting in a weak anti-Stokes signal. An extra bonus of recording anti-Stokes instead of Stokes Raman spectra is the removal of fluorescence interference since fluorescence occurs to the red of the excitation laser frequency.

Fig. 1 gives a comparison of Stokes and anti-Stokes Raman spectra for MgCl_4^{2-} in a four component melt consisting of MgCl_2 - CaCl_2 - KCl - NaCl (15-15-35-35 mole%) at 800°C, which are recorded by a diamond-windowed all-silica probe. The Raman band around 250 cm^{-1} in both recorded spectra is assigned^{15,16} to a totally symmetric stretch mode(A_1) of MgCl_4^{2-} . The broad shoulder around 500 cm^{-1} is due to the silica signals from the exciting optical fiber. As seen from Fig. 1a, there are large silica Raman signals in the Stokes Raman spectrum, whereas little such signals appears in the corresponding anti-Stokes Spectrum. This demonstrates the advantage of obtaining Raman spectra of high temperature systems via recording anti-Stokes Raman over that through recording Stokes Raman through windowed fiberoptic probes.

Raman Measurement with Dilor Instrumentation: Fig. 2 gives the setup for measurement of molten salt Raman spectra via Dilor super head. The Dilor super head system uses separate fibers, but the optical coupling to the sample medium is performed through an optical sensor head, which consists of two spectral filters, a lens relay and a beamsplitter arrangement. A first narrow-band interference filter isolates the monochromatic laser excitation at the exit of the excitation fiber and removes the intense Raman bands due to the silica fiber materials. A second notch filter is placed in the light path between the sample and the return fiber, to reject the retroscattered radiation at the laser wavelength. The exit excitation laser forms a parallel beam, which can be focused on the sample through any objective lens. In our high-temperature applications, we used a silica tube (length = 20 cm) with one end attached to a silica objective lens ($f = 1$ cm) to focus the laser onto the sample. This tube attachment provides the enough distance to isolate the super head from the heated furnace area. Fig. 3 shows the Raman spectrum of a

$\text{Li}_2\text{CO}_3/\text{Na}_2\text{CO}_3$ (53/47) melt at 550°C , measured by the setup shown in Fig. 2. The Raman band is located at 1055 cm^{-1} , which is very close to those reported in the literature.¹⁷

Conclusions: Two strategies have been proposed to measure Raman spectroscopy of corrosive melts via fiberoptic instrumentation. The protective sheath approach requires a certain window for the all-silica fiberoptic probe we developed previously. Addition of the window will give rise to large silica background signals in Stokes Raman spectra recorded via this kind of probe. However, minimum silica signals are found in Anti-Stokes Raman spectra measured with the windowed probe. The second strategy involves the use of a dilor fiberoptic super head. The application of this system in obtaining molten carbonates has been demonstrated.

Acknowledgments

This research is sponsored by U.S. Department of Energy under contract with Lockheed Martin Energy Research Corporation (LMER) and a Cooperative Research and Development Agreement (CRADA) NO. 95-0361, between AlumaX Aluminum Corp.; Kaiser Aluminum Corp.; Reynolds Metals Co. and LMER.

References

1. S.D. Schwab and R.L. McCreery, *Anal. Chem.*; **1984**, *56*, 2199.
2. C.D. Allred and R.L. McCreery, *Appl. Spectrosc.*; **1990**, *44*, 1229.
3. M.L. Myrick and S.M. Angel, *Appl. Spectrosc.*; **1990**, *44*, 565.
4. B. Yang and M.D. Morris, *Appl. Spectrosc.*; **1991**, *45*, 512.
5. C.L. Schoen, T.F. Cooney, S.K. Sharma and D.M. Carey, *Applied Optics*; **1992**, *31*, 7707.
6. S. Dai, J.P. Young, G.M. Begun, J.E. Coffield and G. Mamantov, *Microchimica Acta*, **1992**, *108*, 261.
7. S. Dai, J.P. Young, G.M. Begun, J.E. Coffield and G. Mamantov, *Proceedings of the International Symposium on Molten Salts*, p66-71, Spring Meeting of the Electrochemical Society, St. Louis, MO, May 1992.
8. W.K. Behl and H.C. Gaur, *J. Sci. Industr. Res.*, **1961**, *20B*, 231.
9. G.P. Smith and C.R. Boston, *J. Chem. Phys.*; **1965**, *46*, 4051.
10. S. Dai, J.P. Young and G. Mamantov, *Appl. Spectrosc.*; In press.
11. R. Marassi, J.Q. Chambers, G. Mamantov, *J. Electroanal. Chem. Interfacial Electrochem.*; **1976**, *69*, 345.
12. C. Lee, C.J. Miller and A.J. Bard, *Anal. Chem.*; **1991**, *63*, 78.
13. G.E. Walrafen and J. Stone, *Appl. Spectrosc.*; **1972**, *26*, 585.
14. D.P. Strommen and K. Nakamoto, *Laboratory Raman Spectroscopy*, John Wiley & Sons: New York, 1984.
15. V.A. Maroni, *J. Chem. Phys.*, **1971**, *55*, 4789.
16. H. Brooker, *J. Chem. Phys.*; **1975**, *63*, 3054.
17. S. Okazaki, M. Matsumoto, and I. Okada, *Mol. Phys.*, **1993**, *79*, 611.

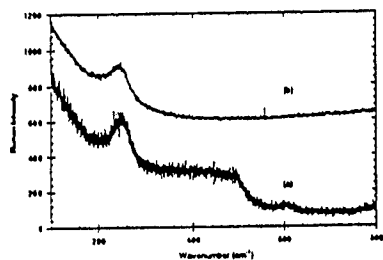


Figure 1 Comparison of Stokes (a) and anti-Stokes (b) Raman spectra recorded by a diamond-windowed fiberoptic probe.

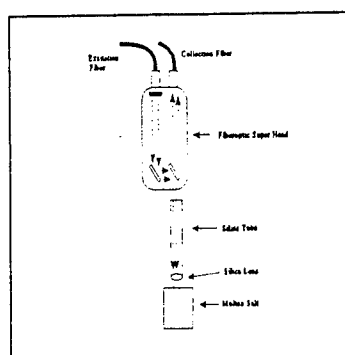


Figure 2 Setup of super head for measurement of Raman spectra of corrosive melts.

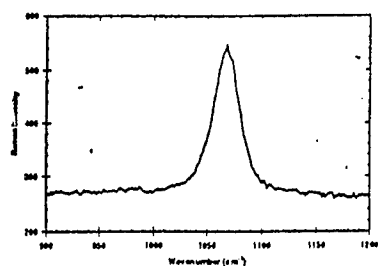


Figure 3 Raman spectrum of a $\text{Li}_2\text{CO}_3/\text{Na}_2\text{CO}_3$ (53/47) melt measured at 550°C by Dilor super head.

RAMAN SPECTROSCOPIC AND ELECTROCHEMICAL STUDIES OF TUNGSTEN IN ALKALI CHLORIDE MELTS

G. Carountzos, C. Hasiotis and C. Kontoyannis

Institute of Chemical Engineering and High Temperature Chemical Processes (ICE/HT-FORTH) and Department of Pharmacy, University of Patras, P. O. Box 1414, GR 265 00 Patras, GREECE

The chemistry of tungsten chlorides in LiCl-KCl eutectic composition has been investigated by spectroscopic and electrochemical techniques at 450°C. It has been found that W(VI) is reduced to W(V) directly by the free Cl⁻ ion in the melt and the octahedral complex ion [WCl₆]⁻ is formed. Addition of metals (Al, Zn, Pb, W) causes further reduction of W(V). Depending on the metal added [WCl₆]²⁻ or W metal are obtained. A single reduction wave appears for the electroreduction of W(V) and W(IV) which corresponds to the electrochemical generation of W(II). This electrode-reaction process is diffusion controlled and irreversible.

INTRODUCTION

The chemistry and electrochemistry of tungsten is counted among the most complex of the transition metals due to the variety of the oxidation states the metal exhibits ranging from +6 to +2. It is not surprising that very few are known about the chemistry of tungsten in halide melts comparing with other refractory metals such as Ta and Nb. Even though tungsten is very important from a technological point of view, relatively few studies of its chemistry in molten salt systems have been reported [1-9].

The binary AlCl₃-NaCl_{sat} is the only molten salt system in which the dissolution of tungsten chloro-compounds has been studied by means of Raman spectroscopy. It has been suggested that the dissolution of WCl₆ in this melt results in the formation of [WCl₆]⁻, as a product of the chemical reduction of WCl₆ by the excess of the free chloride ion in the melt [3]. Other spectroscopic methods such as Infrared and UV-visible absorption have been also employed in order to identify the tungsten species that are formed mainly in AlCl₃-NaCl melt [1-4].

The information available from previous electrochemical studies is contradictory. Zuckerbrod reported that in LiCl-KCl eutectic W(V) can be reversibly reduced to W(IV) which can be further reduced irreversibly to W(II), while the final process is the formation of tungsten metal [5]. In contrast, Balko found that in the same melt W(V) and W(IV) are reduced to W(III), whilst W(III) is finally reduced to W(0) [6]. Recently, Sequeira claimed that W(V) and W(IV) are irreversibly reduced to W(III) which is not further reduced [7,8]. In parallel, Katagiri has obtained coherent metallic

tungsten deposits from the ZnCl_2 -NaCl melt through the reduction of WCl_6 [9] while Mamantov et al. [4] have comprehensively examined the electrochemistry of W(V) in AlCl_3 -NaCl_{sat} melt proposing a possible reaction sequence.

In the light of these studies it is obvious that additional research is needed to understand the chemistry of tungsten in molten salts. The purpose of this work was the spectroscopic identification of tungsten species formed in the LiCl-KCl eutectic and the elucidation of their electroreduction mechanism.

EXPERIMENTAL

Chemicals. LiCl and KCl were analytical grade chemicals (Merck). Before the preparation of the eutectic mixture (59.5 + 40.5 mole percent) they were dried for at least 24 hours at 150°C under vacuum and purified by melt recrystallization. WCl_6 (Alfa) was sublimed under vacuum in a sealed pyrex tube by using a temperature gradient. KWCl_6 was synthesized by an equimolar mixture of WCl_6 -KCl according to the method proposed by Zaitseva [10] and K_2WCl_6 was prepared by heating KWCl_6 at ~350°C under vacuum as reported by Dickinson et al. [11]. Because of the significant air- and moisture-sensitivity of tungsten compounds all handling of materials was done in a nitrogen-filled dry box (moisture level <1ppm).

Raman System. Raman spectra were excited with the 488 or 514.5 nm line of an argon laser and the 647.1 nm line of a krypton laser (Spectra-Physics). A cylindrical lens with a 127 mm focal length was used to focus the laser line on the liquid sample. The Raman cell was aligned in an optical furnace and the scattered light was collected at an angle of 90° and analyzed with a 0.85-m double monochromator (Model 1403, Spex Industries) equipped with an RCA model C-31034 photomultiplier tube (PMT). The detection system included PAR photon counting and rate meter electronics (EG&G/Ortec). Typical spectra width and time constant were 3 cm^{-1} and 0.3 s respectively. The system was also interfaced to a PC and the spectra recorded were digitized and stored on disc. The spectra were obtained at 400-500°C.

Electrochemical Measurements. For the electrochemical experiments a glassy carbon cell was used. The cell was placed in a home-made temperature controlled furnace capable of sustaining an inert atmosphere. Furthermore, it was equipped with a home-constructed boron nitride cover which was penetrated by three alumina tubes fused on it, through which Pt electrodes could be introduced. Another assembly consisted of a fused silica tube and a bronze flat flange joined together at the upper open end with epoxy was also used. A teflon cover through which the electrodes and the gas tubes were introduced was tightly connected to the flange. A Kanthal wire-wound furnace enabled the temperature to be controlled to $\pm 2^\circ\text{C}$ at the area where the cell containing the melt was placed. A Pt wire and a Pt sheet served as the working and the counter-electrode respectively. A platinum wire immersed directly in the bulk melt was used as a quasi-reference electrode. The electronic setup consisted of a PAR

model 173 potentiostat connected with a home-made function generator. The potentiostat was also interfaced to a PC via an A-D/D-A card.

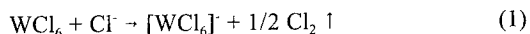
RESULTS AND DISCUSSION

A. Raman Spectroscopic Investigation of the Tungsten Species Formed in the LiCl-KCl Eutectic Composition

1. WCl₆ and K₂WCl₆. The dissolution of 1.5 mol % tungsten hexachloride in the eutectic LiCl/KCl was quite fast. A two-phase separation was observed. It has been reported that the solubility of WCl₆ decreases significantly in Lewis basic melts [1]. Dark yellow vapors typical of the hexachloride's were present above the melt. The spectra recorded (647.1 nm laser-line) for both the dark orange transparent upper phase (Fig. 1d) and the black heavier phase were characterized by the presence of a strongly polarized band at 385 and a depolarized one at 168 cm⁻¹. No other bands were observed. The similarity of the spectra's appearance with those obtained from the crystalline, liquid and gas WCl₆ (Fig. 1a-c), strongly supported that the species formed should be of the same symmetry (O_h). The shift in frequency denoted the lowering of the oxidation state of W in accordance with what has been previously reported for other refractory metals [12]. The spectrum of the vapor phase showed that apart from WCl₆, gas chlorine was also present giving a characteristic band contour at ~550 cm⁻¹. The evolution of Cl₂ confirmed that a redox process occurred in the melt. The octahedral complex ion [WCl₆]⁻ of W(V) was suggested to be the most probable species existed in both phases of the liquid system LiCl/KCl(eut)-WCl₆. The heavier phase was mainly consisted of K₂WCl₆.

In order to verify the previous assumption, the dissolution of K₂WCl₆ in the same eutectic was also studied. Dark green potassium hexachlorotungstate is known to be a direct source of W(V) in the form of [WCl₆]⁻ [3, 13]. Two phases exhibiting the same colours as previously mentioned were observed. Neither the existence of vapor phase nor the evolution of Cl₂ were noticed in this case. The spectra obtained were identical to those of the system LiCl/KCl(eut)-WCl₆.

The spectrum shown in Fig. 1d was attributed to the presence of the complex ion [WCl₆]⁻ in the melt. This species was formed by the direct reduction of W(VI) by the excess of the free chloride ion (Cl⁻) in the melt according to :



The two bands observed at 385 cm⁻¹ (polarized) and 168 cm⁻¹ (depolarized) were assigned to the ν₁ (A_g) and ν₅ (T_{2g}) modes of the [WCl₆]⁻ octahedra. The expected for an octahedron ν₂ (E_g) mode which is in general rather weak, was not observed in the spectra obtained.

2. K_2WCl_6 . The dark red dipotassium hexachlorotungstate was expected to be a direct source of W(IV) in the form of the ion $[WCl_6]^{2-}$. Its dissolution in the eutectic resulted in the formation of a transparent light olive-green upper phase. The color was typical of the existence of the former ion [14]. The bands corresponding to the ν_1 (345 cm^{-1}) and ν_2 (158 cm^{-1}) vibrational modes of the octahedral $[WCl_6]^{2-}$ can be observed in the spectrum which was excited by the 647.1 nm laser-line and shown in Fig. 1e. The lowering of tungsten's oxidation number from V to IV caused a new red shift of the band frequencies. The ν_2 mode was not observed. The black heavier phase was considered to be dominated by the same species as the upper one since the spectra obtained from both phases were alike.

3. Addition of Metals as Reductants. Metals have been used as reducing agents in the system $LiCl/KCl(\text{eut})-WCl_6$. Their reducing potentials in the eutectic $LiCl-KCl$ are presented in the Table 1. All the spectra were excited by the 514.5 nm laser line due to the green colour these molten systems exhibited.

a. The Case of Al and Zn. The addition of aluminum and zinc in excess led to a rather rapid (approx. 3 hours) color-change of the initially orange-colored upper phase to olive-green. The temperature was maintained at 500°C . Although the color was reminiscent of what had been previously observed for the system $LiCl/KCl(\text{eut})-K_2WCl_6$, the characteristic frequencies of $[WCl_6]^{2-}$ were not detected while the remaining $[WCl_6]^-$ could be still observed (Al-case, Fig. 2a).

Presumably, the reduction of W(V) led mainly to tungsten metal, while the traces of the intermediate product $[WCl_6]^{2-}$ were dominated by the complex ions $[AlCl_4]^-$ and $[ZnCl_4]^{2-}$ formed in each case [15]. In less than five hours (total time elapsed) the upper phase turned into colorless indicating the completion of the reduction and sustaining the assumption that no tungsten species were present in the melt any longer (Fig. 2b and c). The gray-black precipitate observed as the heavier phase cannot be attributed to a subvalent tungsten chloride species such as $[W_2Cl_9]^{3-}$ or $[W_6Cl_{14}]^{4-}$ mainly because of the total indissolubility that the solidified heavier phase proved to have in several solvents.

b. The Case of Pb. The change occurred when lead was introduced to the system was almost doubly time-consuming than in the previous case. Only an one-stage reduction process was found to occur since no other tungsten species except $[WCl_6]^{2-}$ were identified to be present in the melt at 500°C . In the spectrum shown in Fig. 2d the polarised band at 345 cm^{-1} was accompanied by two other bands both polarised which were attributed to the complex ion species with the general formula $[PbCl_n]^{2-n}$. The weaker band at $\sim 250\text{ cm}^{-1}$ was attributed to the ion $[PbCl_3]^-$ [15], while the more intense band at 230 cm^{-1} was proposed [present work] to be assigned to the ν_1 vibration of a species where n should be greater than three.

c. The Case of W. Addition of excess of tungsten resulted in the relatively slow (approx. 15 hours) reduction of W(V) at 500°C . The reduction stages observed for the system $LiCl/KCl(\text{eut})-WCl_6-W$ can be seen in Fig. 3. The complex ion $[WCl_6]^-$ (Fig.

3a) was gradually reduced to $[\text{WCl}_6]^{2-}$ (Fig. 3b) according to :

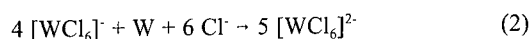


Fig. 3b clearly shows an intermediate stage (10 hours) of the reduction of W(V) to W(IV) where the bands of both the ions $[\text{WCl}_6]^-$ and $[\text{WCl}_6]^{2-}$ co-existed in the melt. Eventually, the octahedral complex ion $[\text{WCl}_6]^{2-}$ was found to be the major species of the liquid system (Fig. 3c).

The sharp strong band at 223 cm^{-1} of the spectrum illustrated in Fig. 3c was attributed to traces of the linear oxo-bridged complex ion $[\text{W}_2\text{OCl}_{10}]^{4-}$ whose intensity was Resonance Raman enhanced [16], while the weak band at 444 cm^{-1} was assigned to the first harmonic $2\nu_1$. The near resonance 514.5 nm laser-line which was used for the excitation of the spectrum fell into the electronic envelope of the unusually strong absorption maximum of the oxyanion $[\text{W}_2\text{OCl}_{10}]^{4-}$ at $\sim 19100 \text{ cm}^{-1}$ [21] giving rise to Resonance Raman effect. In any case, the presence of this species in the melt should be considered as negligible since its concentration might be a few orders of magnitude less than the concentration of the major species. The faster reduction process occurred in the systems containing Al, Zn and Pb was probably the reason of not observing the oxyanion impurity in their spectra.

Table 1 Metals used as reductants in the system $\text{LiCl/KCl(eut)-WCl}_6$ and their corresponding standard electromotive force series in the LiCl-KCl eutectic [20].

Redox Couple	Al(III)/Al(0)	Zn(II)/Zn(0)	Pb(II)/Pb(0)	W(II)/W(0)	Pt(II)/Pt(0)
$E^\circ_{\text{M/V vs. Pt(II)/Pt(0)}}$	- 1.762	- 1.566	- 1.101	- 0.585	0.000

B. Voltammetric Characteristics of Tungsten Compounds at Pt Electrode in LiCl-KCl Eutectic Composition

1. WCl_6 and KWCl_6 . Preliminary voltammetric measurements at platinum (Pt) cathodes revealed that the cyclic voltammograms of solutions prepared by the dissolution of WCl_6 in LiCl-KCl were essentially the same as those obtained from solutions of KWCl_6 . The similarity of these voltammograms supported the contention that addition of WCl_6 to the LiCl-KCl melt produced the $[\text{WCl}_6]^-$ ion.

In order to verify electrochemically the chemical reduction of WCl_6 in the melt, the cyclic voltammogram was initially scanned in the positive direction from the rest potential. Given that the melt contains $[\text{WCl}_6]$, one would expect anodic current to be appeared. As shown in Fig. 4A (inset a) anodic current due to the one-electron oxidation of $[\text{WCl}_6]$ was not detected, up to the potential where anodic dissolution of Pt occurs. The peaks I_a and I_c were attributed to the Pt^{2+}/Pt redox couple [17,18]. This behavior indicated that the electrooxidation of $[\text{WCl}_6]$ might commence at more positive potentials and could be presumably studied at other electrodes usually used (i.e glassy carbon).

When the voltammograms were scanned in the negative direction from the rest potential, a broad cathodic peak appeared (Fig. 4A). Even though this peak could not be well characterized numerically, it seemed to be controlled by diffusion. A small non-reproducible anodic peak of variable shape and position also appeared at around 0.2 V. At the present state of our investigation the reduction process which corresponded to the cathodic wave could not be determined. In fact, the broad shape of the reduction peak might be attributed to the presence of oxychlorides formed by the oxide contamination of the melt. However, the fact that the reduction process occurred at the potential range where the reduction wave of W(IV) appeared (see below), permitted the speculation that the final product of these electrochemical processes was the same.

2. K_2WCl_6 . Cyclic voltammograms obtained at Pt from solutions prepared by the dissolution of K_2WCl_6 in LiCl-KCl eutectic melt at 450°C are shown in the Fig. 4B. A single cathodic peak appeared at around -250 mV. No further reduction processes were observed upon sweeping up to the cathodic limit. The peak potential of the cathodic wave shifted cathodically with increasing scan-rate. These shifts implied that an irreversible electron-transfer reaction occurred, as also suggested by the absence of reoxidation waves.

It is noteworthy that although anodic peak was not observed, the current exhibited diffusion character. Actually, the peak current scaled linearly with $v^{1/2}$ (inset b of Fig. 4B) verifying the diffusion controlled behavior of the reduction process. The above observations implied that either the product obtained from the electrode reaction was chemically converted into another derivative that did not present redox properties, or the product was insoluble. The latter was the most probable since the current function $i_p/v^{1/2}$ did not decrease with increasing sweep rate (inset c of Fig. 4B) which indicated that an EC mechanism did not occur. This conclusion was confirmed by the impossibility of identifying electrochemically the product obtained from exhaustive electrolysis of the solution.

Bulk controlled potential electrolysis was also used in an attempt to determine the overall number of electrons involved in the electrode reaction. Values around 2 for the number of electrons transferred per molecule were found corresponding to the two-electron reduction of W(IV) to W(II) .

Sequeira has recently reported [8] that the electroreduction product of K_2WCl_6 was insoluble and claimed that W(IV) underwent an one-electron reduction to W(III). Zuckerbrod and Johnston had observed that W(III) was rapidly dissolved in the melt, though [5,19]. Zuckerbrod also found that W(IV) was reduced to W(II) which was further converted to tungsten metal by disproportionation. In the present investigation the formation of W(0) during the bulk electrolysis experiments was not observed.

CONCLUSIONS

Raman spectra of the liquid systems $LiCl/KCl(eut)-WCl_6$ and $LiCl/KCl(eut)-WCl_6-M$ ($M = W, Pb, Zn, Al$) have been recorded and evidence for the complex ions formed have been found, while cyclic voltammetry has been also employed to elucidate the electroreduction mechanism of the same species.

The data obtained by both techniques have shown that:

1. The octahedral WCl_6 was reduced by decomposition upon dissolution in the $LiCl-KCl$ eutectic and the octahedral five valence state $[WCl_6]^-$ species formed while gas Cl_2 evolved. That was also confirmed indirectly by CV since the voltammograms for solutions of WCl_6 were essentially the same as those obtained for solutions of $KWCl_6$.
2. The presence of W metal caused the further reduction of $[WCl_6]^-$ and the octahedral $[WCl_6]^{2-}$ could be observed. Excess of metal did not lead to lower valence state species such as $[W_2Cl_9]^{3-}$ and $[W_6Cl_{14}]^{2-}$. Minor oxide impurities were identified as the linear oxo-bridged complex ion $[W_2OCl_{10}]^{4-}$.
3. Addition of Al and Zn caused the rapid reduction of W(V) to W(0) and the formation of the complex ions $[AlCl_4]^-$ and $[ZnCl_4]^{2-}$ respectively. The presence of Pb metal resulted in the reduction of W(V) to W(IV) and the simultaneous formation of the ions with general formula $[PbCl_n]^{2-n}$.
4. The complex ion $[WCl_6]^{2-}$ underwent an irreversible two-electron electroreduction to the insoluble W(II). The reduction current was controlled by diffusion.

REFERENCES

1. K. Tanemoto, G. Mamantov and G. M. Begun, *Inorg. Chim. Acta*, **76**, L79 (1983).
2. Jean-Paul Schoebrechts, Paul A. Flowers, Glen W. Hance and Gleb Mamantov, *J. Electrochem. Soc.*, **135**, 3057 (1988).
3. I.-Wen Sun, Anna G. Edwards and Gleb Mamantov, *J. Electrochem. Soc.*, **140**, 2733 (1993).
4. Gleb Mamantov, Guang-sen Chen, Haiming Xiao, Yihui Yang and Ellen Hondrogiannis, *J. Electrochem. Soc.*, **142**, 1758 (1995).
5. D. Zuckerbrod, *Ph.D Thesis*, Rensselaer Polytechnic Institute, 1982.
6. E. N. Balko, *Ph.D Thesis*, Rensselaer Polytechnic Institute, 1971.

7. C. A. C. Sequeira, *Mater. Sci. Forum*, **73-75**, 569 (1991).
8. C. A. C. Sequeira, *J. Electrochem. Soc.*, **140**, 2526 (1993).
9. A. Katagiri, *Mater. Sci. Forum*, **73-75**, 415 (1991).
10. N. D. Zaitseva, *Russ. J. Inorg. Chem.*, **8**, 1239 (1963)
11. R. N. Dickinson, Susan E. Feil, F. N. Collier, W. W. Horner and S. Y. Tyree, *Inorg. Chem.*, **3**, 1600 (1964).
12. G. A. Voyiatzis, E. A. Pavlatou, G. N. Papatheodorou and M. Bachtler, W. Freyland, "*Proc. of the 4th Int. Symp. on molten salt chemistry and technology*", **93-99**, 252 (1993)
13. T. L. Brown, W. G. McDugle, Jr. and L. G. Kent, *J. Am. Chem. Soc.*, **92**, 3645 (1970)
14. C. D. Kennedy and R. D. Peacock, *J. Chem. Soc. A*, 3392 (1963)
15. K. Nakamoto, "*Infrared and Raman Spectra of Inorganic and Coordination Compounds*", 4th edition, John Wiley & Sons, NY, 1986.
16. J. San Filippo, Jr., R. L. Grayson and H. J. Sniadoch, *Inorg. Chem.*, **15**, 269 (1976)
17. J. de Lepinary et M. J. Barbier, *J. Electroanal. Chem.*, **45**, 419 (1973).
18. A. de Haan et H. Vander Poorten, *Electrochim. Acta*, **19**, 519 (1974).
19. R. O. Johnston, *Ph. D Thesis*, University of Illinois, 1974.
20. J. A. Plambeck, "*Encyclopedia of Electrochemistry of the Elements*", vol. X, editor Allen J. Bard, Marcel Dekker, Inc., NY, 1976
21. E. Konig, *Inorg. Chem.*, **8**, 1278 (1969)

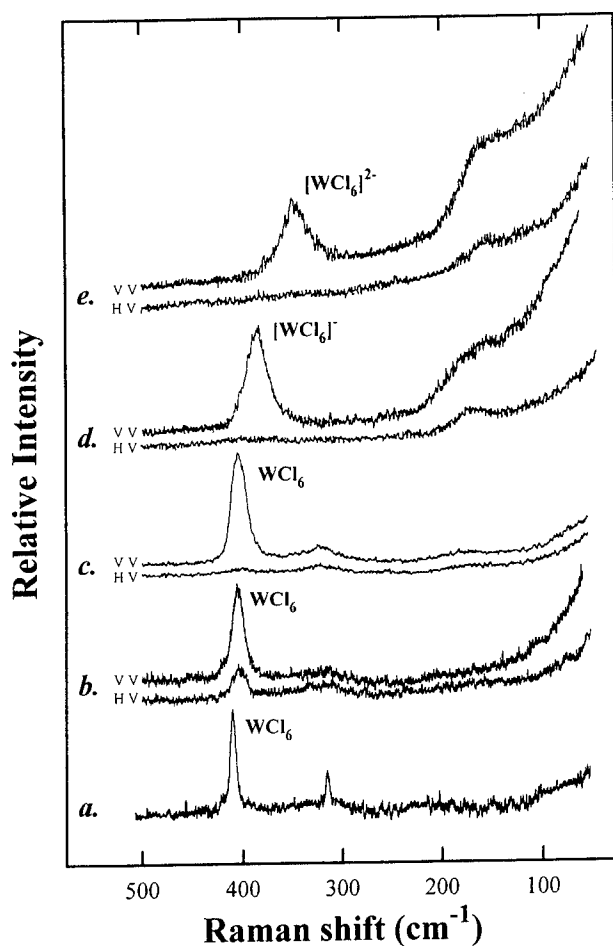


Figure 1. Raman spectra of the :

- a. crystalline WCl_6 (ν_1 : 410 cm^{-1} , ν_2 : 317 cm^{-1} , ν_3 : vw)
- b. liquid WCl_6 at 300°C (ν_1 : 405 cm^{-1} , ν_2 : 314 cm^{-1} , ν_3 : vw)
- c. gas WCl_6 at 300°C (ν_1 : 404 cm^{-1} , ν_2 : 324 cm^{-1} , ν_3 : 180 cm^{-1})
- d. system $\text{LiCl/KCl(eut)-WCl}_6$ at 450°C (~1.5 mol % WCl_6)
(ν_1 : 385 cm^{-1} , ν_2 : vw, ν_3 : 168 cm^{-1})
- e. system $\text{LiCl/KCl(eut)-K}_2\text{WCl}_6$ at 500°C (~1.1 mol % K_2WCl_6)
(ν_1 : 345 cm^{-1} , ν_2 : vw, ν_3 : 158 cm^{-1})

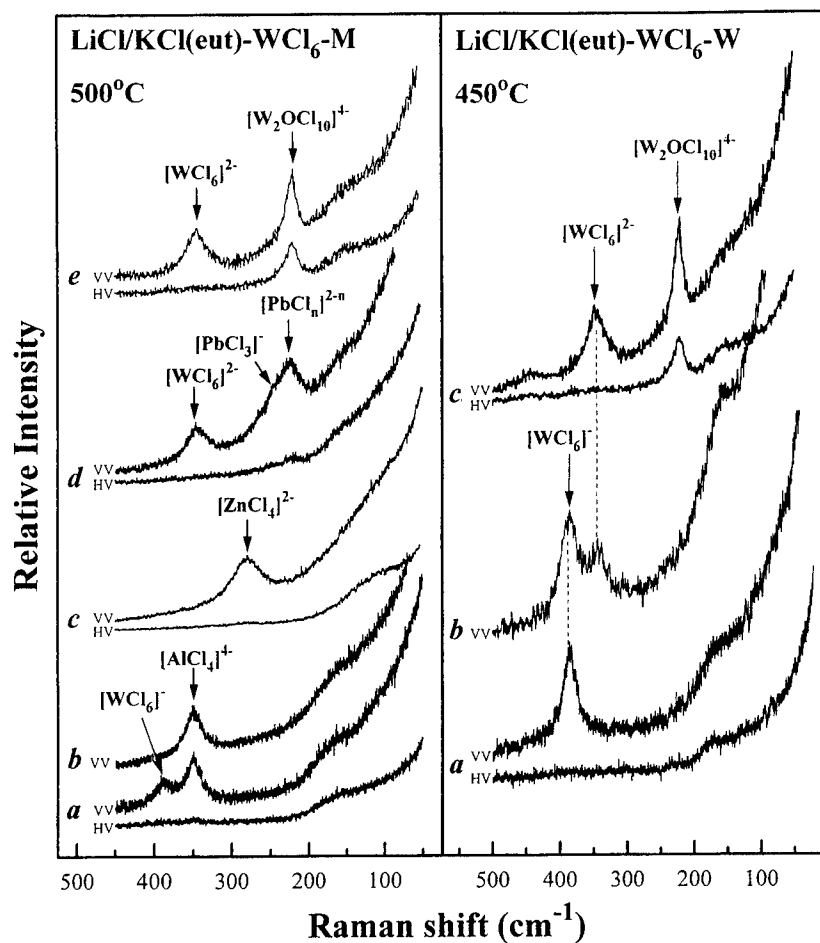


Figure 2. Influence of the addition of metals as reducing agents on the system LiCl/KCl(eut)-WCl₆ (at 500°C) :

- a. M = Al (3 h - partial reduction)
- b. M = Al (5 h - full reduction)
- c. M = Zn (6 h - full reduction)
- d. M = Pb (10 h - steady state)
- e. M = W (15 h - steady state)

Figure 3. Reductions stages occurred in the system LiCl/KCl(eut)-WCl₆-W :

- a. [WCl₆]⁻ (formed instantly)
- b. [WCl₆]⁻ and [WCl₆]²⁻ (10 h)
- c. [WCl₆]²⁻ and [W₂OCl₁₀]⁴⁺ (15 h)

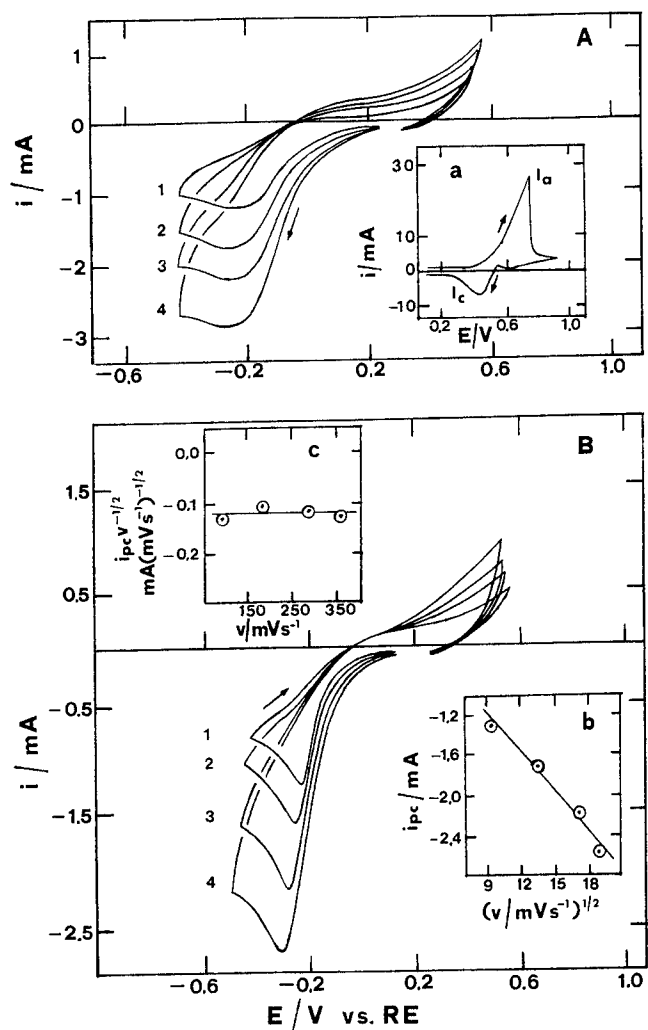


Figure 4. (A) Cyclic voltammograms of KWCl_6 (0.3 mol%) at Pt in LiCl-KCl eutectic. Scan rates v (mVs $^{-1}$): (1) 90; (2) 180; (3) 287; (4) 359. (B) Cyclic voltammograms of K_2WCl_6 (0.3 mol%) at Pt in LiCl-KCl eutectic. Scan rates v (mVs $^{-1}$): (1) 75; (2) 170; (3) 265; (4) 470. Insets: (b) plot of i_p vs. $v^{1/2}$; (c) plot of $i_p v^{-1/2}$ vs. v .

LOCAL STRUCTURE OF K_2O - SiO_2 GLASSES AND MELTS

Norimasa Umesaki^{*,†}, Katsumi Handa^{**}, Norikazu Ohtori^{***} and
Nagao Kamijo^{*}

* Osaka National Research Institute (ONRI), AIST
1-8-31, Midoriga-oka, Ikeda, Osaka563, Japan

** Department of Physics, Ritsumeikan University
1916, Noji-cho, Kusatsu, Siga525-77, Japan

*** Graduate School of Science and Technology, Niigata University
Igarashi 2-no cho, Niigata950-21, Japan

ABSTRACT

Raman scattering measurements have been performed on K_2O - $4SiO_2$ glasses at room temperature and in the corresponding melts to study the structural relationship between the glasses and the melts. The fractions of SiO_3^{2-} chain, $Si_2O_5^{2-}$ sheet and SiO_2^0 three-dimensional network units in the glasses and melts were determined from the Raman results. It is found that above the glass transition temperature T_g the neutral SiO_2^0 species are gradually destroyed and the highly charged $Si_2O_5^{2-}$ created as the temperature is increased.

Using the laboratory XAFS facility, we have performed to determine the local structure in potassium silicate glasses (K_2O - $4SiO_2$, K_2O - $3SiO_2$, K_2O - $2SiO_2$ and $0.2(Al_2O_3) \cdot 0.8(K_2O \cdot 4SiO_2)$) respectively in order to elucidate the environment of modifying potassium ion which is extremely sensitive to the morphology of the network structure of glass system. The coordination numbers of oxygen around K^+ ion in K_2O - $2SiO_2$ and K_2O - $3SiO_2$ glasses are found to be 4~5 which is small compared with those of K_2O - $4SiO_2$ glass and crystalline nepheline ~9. The result indicates that the introduction of K_2O leads to the disruption of SiO_4 network structure and the formation of SiO_3^{2-} chain like structure or nonbridging oxygen ions as increasing quantity of K_2O . The local structure around silicon ions in some potassium silicate glasses are also compared with those of crystalline SiO_2 such as quartz and cristobalite.

INTRODUCTION

In metallurgical and welding process, silicate mixtures applied to slag or flux are always used in molten states. Therefore, it has been become important to understand the melt structures which control various physical properties such as density, viscosity, diffusion, electrical conductance, etc. of molten silicates. Silicates made up tetrahedral SiO_4 units easily form glasses by solidification from the melts with high melting points. For this reasons, as a zero-order approximation, these melt structures have been indirectly estimated from the corresponding glass structures to avoid the various experimental difficulties under high temperature conditions. Most data shown below on the structure in silicate melts have been obtained through measurements on quenched samples at room temperature, and only very limited direct information on the structure of

[†] Corresponding author: Tel: +81-(0)727-9536, Telefax: +81-(0)727-9631, E-mail: Umesaki@onri.go.jp, Present address: Department of Optical Materials, Osaka National Research Institute (ONRI), AIST, 1-8-31, Midoriga-oka, Ikeda, Osaka563, Japan.

melts at high temperature is available (1). It is still controverted that the glass structures are quite similar to the corresponding melt structures. Therefore, in order to relate from the structural information of silicate glasses to the structural features of corresponding melts, it is necessary to accumulate the direct experimental proof of structural similarity between the melts and their glasses.

It is generally accepted that the introduction of network modifier such as alkali oxide M_2O to SiO_2 glass and melt break the Si-O-Si bridging bond SiO_4 linking units with 0, 1, 2, 3 and 4 NBO/Si's (NBO/Si: Non-Bridging Oxygen per Si). According to the modified random network (MRN) model (2), the addition of one network modifier unit M_2O causes one bridging oxygen (BO) ion between two connected tetrahedral SiO_4 to be replaced by two non-bridging (NBO) ions. The number of NBO/Si in silicate melts and glasses increases with increasing modifying oxide content (3,4), and also with increasing temperature (5). Unfortunately, the detailed modifying cations such as alkali and alkaline-earth ions is still unknown.

Raman spectroscopy is a powerful method for the identification of distinct SiO_4 units of silicate crystals and glasses. The stretching vibration of Si-O bonds in silicate crystals and glasses can be easily observed in the frequency region from 800 to $1200cm^{-1}$ by Raman spectroscopy. Many earlier investigations on silicate glasses were reported (6-12). The 800- $1200cm^{-1}$ frequency region of the measured Raman spectra can be generally be assigned to the Si-O stretching motions of five SiO_4 units with 0-4 NBO/Si; SiO_4^0 three-dimensional network (NBO/Si=0), $Si_2O_5^{2-}$ sheet (NBO/Si=1), SiO_3^{3-} chain (NBO/Si=2), $Si_2O_7^{6-}$ dimer (NBO/Si=3) and SiO_4^{4-} monomer (NBO/Si=4). Tsunawaki et al. (9,10) determined the fractions of bridging oxygen "-O-" or "O⁰" (i.e., coordination to two silicon ions), non-bridging oxygen "O" (i.e., coordinated to one silicon ion) and free or fully-active oxygen "O²⁻" (i.e., nor coordinated to silicon ion) in glasses $PbO-SiO_2$, $CaO-SiO_2$ and $CaO-CaF_2-SiO_2$ from the relative intensity stretching Raman bands. Recently, Umesaki et al. (13) indicated that the Raman relative intensities of the four SiO_4 units with 1, 2, 3 and 4 NBO/Si in the rapidly quenched Li_2O-SiO_2 glasses are equivalent to the abundance of the corresponding SiO_4 units from their Raman analysis of these glasses.

Although X-ray (14-16) and neutron (14, 16) diffraction studies of alkali silicate glasses have verified the tetrahedral coordination of oxygen around silicon, these methods have been unsuccessful in deducing anything definite about the local structural environments of modifying cations in these glasses. This is due to the need to disentangle several pair correlation functions from the total diffraction intensity.

X-ray absorption fine structure (XAFS) spectroscopy has been used extensively as an aid to understanding the local coordination characteristics, and the pair correlation functions for specific element can be obtained. However, XAFS experiments in the soft X-ray domain 700-3000eV such as Si (K-edge: 1839eV) and K (3607eV) appear less developed than those in the hard X-ray or VUV regions: the reasons for this may lie in some intrinsic experimental difficulties in sample preparation and weak theoretical background, etc. (14).

In this paper, the structural features of Si and K coordination environments for K_2O-SiO_2 glasses and melts are discussed mainly based on the experiments by High temperature Raman spectroscopy and on Si and K K-edges by a laboratory XAFS facility.

EXPERIMENTAL

Sample Preparation

Samples studied here including glasses and crystals were as follows: SiO_2 , $K_2O-4SiO_2$, $K_2O-3SiO_2$, $K_2O-2SiO_2$ and $0.2(Al_2O_3) \cdot 0.8(K_2O-4SiO_2)$ glasses, SiO_2 quartz and cristobalite, $KNa_3(AlSiO_4)_4$ nepheline, K_2CO_3 and silicon crystals. All K_2O-SiO_2 glasses

were prepared from analytical reagent grade powders SiO_2 , K_2CO_3 and Al_2O_3 . About 5–10g batches were mixed and then melted at the temperature about 100K above their melting points in a Pt crucible inside electrical furnace. After melting, the melts were cooled to room temperature to obtain the glass samples.

High temperature Raman measurement

Unpolarized Raman spectra were measured on a JASCO model R-800 double-grating spectrometer at scanning angle of 90° . The excitation source was 5145\AA^{-1} (19435.6cm^{-1}) or 4880\AA^{-1} (19435.6cm^{-1}) line NEC GLG-3300 model argon laser at a power level from 300 to 800mW.

A furnace for high temperature Raman spectroscopy was fabricated as shown in Fig. 1. The heating elements consists of the Pt main heater and nichrome sub-heater in order to maintain high temperature easily. As shown in Fig. 1, the melted sample could be placed on the Pt ring wire by its surface tension. The furnace can be easily generate the maximum temperature of 1773K, but high temperature Raman spectroscopic measurement in this study was limited to 1473K due to the disturbance of thermal radiation from the furnace and sample. The sample temperature was controlled within a maximum error of $\pm 5^\circ\text{C}$ throughout the Raman measurement. The uncertainty in the sample temperature caused by the local heating by laser beam can be ignored. With the exception of the glass spectra, the sample have been held at temperature for times exceeding the relaxation times so that structural, though metastable, equilibrium was attained for the high-temperature runs. Each Raman spectrum obtained was deconvoluted into several Gaussian peaks (14).

Soft X-ray XAFS Measurement

We performed the transmission experiments at the K (3607eV) and Si (1839eV) K -edges of the above-mentioned sample films by the use of the laboratory XAFS facility which consists of rotating anode X-ray generator having thin Be window ($25\mu\text{m}$), curved-crystal monochromator and Si(Li) solid state detector (SSD). In the present study, the copper rotating-anode as X-ray source was operated at 10–12.5kV and 40–75mA. Johansson-type LiF(200) ($2d=4.026\text{\AA}$) and PET(002) (Pentaerythritol $\text{C}(\text{CH}_2\text{OH})_4$, $2d=8.742\text{\AA}$) monochromators, which are commercially available from the Quartz and Silice Co., France, were used for potassium K - and silicon K -edge XAFS measurement respectively. Energy resolution of the PET monochromator was estimated to be 2.5eV at the Si K -edge based on a tungsten $M\alpha$ (α_1 : 1775.5eV, α_2 : 1773.2eV) curve measurement due to the volatilization of tungsten from filament. In silica, the white line is reported to be 2.6eV wide (15). Therefore, we may obtain good resolution features in K K - and Si K -edge XAFS regions by the use of our laboratory XAFS facility. Due to the soft nature of K K - and Si K -X-rays used, we used a conventional vacuum system, the vacuum being maintained inside X-ray path by means of a thin Be window ($25\mu\text{m}$) at the front of the rotating anode X-ray generator during XAFS measurement.

The K K - and Si K -edge absorption spectra of the samples have been collected up to about 400eV, the absorption near edge structure (XANES) studies.

The obtained EXAFS data were analyzed using standard procedure (16). The threshold energy, E_0 , was taken as photon energy at the first inflection point of the edge. After the subtraction of the Victoreen-type baseline of the pre-edge region, the EXAFS spectrum $k^3\chi(k)$ make the radial structure function in R space

$$\Phi(R_j) = \frac{1}{\sqrt{\pi}} \int_{k_{\min}}^{k_{\max}} W(k) k^3 \chi(k) \exp[-i2kR] dk, \quad [1]$$

where the Hanning window function, $W(k)$, reduces the effect of the restricting the Fourier transform to the finite range of k ($k_{\min} = 2.5 \text{ \AA}^{-1} \leq k \leq k_{\max} = 11.0 \text{ \AA}^{-1}$). In order to obtain the local structure around potassium and silicon atoms, non-linear least-square fitting, given by

$$\chi(k) = -\frac{A(k)}{k} \sum_j \frac{N_j}{R_j^2} |f_j(\pi)| \exp(-2\sigma_j^2 k^2) \exp\left(-\frac{2R_j}{\lambda}\right) \sin(2kR_j + 2\delta + \psi_j), \quad [2]$$

were carried out in the filtered k -space, utilizing the theoretical phase and amplitude functions of McKale et al. (17). Here R_j is the interatomic distance between the absorber and the j th neighboring atom, N_j is the coordination number and σ_j is the mean square relative displacement resulting from thermal vibration and static disorder.

Results and Discussion

Network structure of $K_2O \cdot 4SiO_2$ glass and melts from high temperature Raman measurement

Raman spectrum of $K_2O \cdot 4SiO_2$ glass at room temperature shows in Fig. 2. The bands appearing in the Raman spectrum can be grouped conveniently into two frequency regions, $500\text{--}800\text{ cm}^{-1}$ and $800\text{--}1200\text{ cm}^{-1}$. As summarized in Table 1 (6-14), the $800\text{--}1200\text{ cm}^{-1}$ frequency region of the measured Raman spectrum is attributed to the Si-O stretching modes of three SiO_4 units with 0-2 NBO/Si; that is, SiO_4^0 three-dimensional network (NBO/Si=0), $Si_2O_5^{2-}$ sheet (NBO/Si=1) and SiO_3^{2-} chain (NBO/Si=2).

Fig. 2 shows the Raman spectra from the $K_2O \cdot 4SiO_2$ glasses to the corresponding melts. As temperature increases there is a systematically intensity decrease in the peak shoulder around 1150 cm^{-1} . It can be also seen in this figure that the weak band in the $940\text{--}970\text{ cm}^{-1}$ range is increasing above the glass transition temperature T_g ($T_g/T_m \approx 2/3$ (18); $T_g \approx 789\text{ K}$). There are no literature data available for comparisons for the range from room temperature through the glass transition up to the melting temperature.

The bulk NBO/Si can be easily calculated from the expression (13, 14, 19-20)

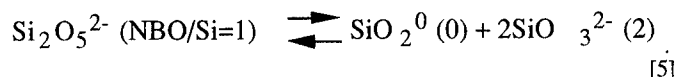
$$\sum_{i=1}^3 X_i n_i = \text{NBO} / \text{Si}, \quad [3]$$

where X_i is the mole fraction of SiO_4 units, with n_i non-bridging oxygen per silicon. The fraction X_i is related to the corresponding relative Raman intensity, A_i , by

$$X_i = \alpha_i A_i \quad [4]$$

where α_i is the normalized Raman cross-section of SiO_4 units, and A_i in equation [3] corresponds to the ratio of the area of Gaussian peak i to the total area, that is, the relative intensity. The α_i factors were determined 1.02, 1.02, 1.15 and 0.90 for $Si_2O_5^{2-}$ sheet, SiO_3^{2-} chain, $Si_2O_7^{6-}$ dimer and SiO_4^{4-} monomer in the Li_2O - SiO_2 glasses (13). This result demonstrates that the scattering efficiencies of the four SiO_4 units with 1, 2, 3 and 4 NBO/Si are almost equivalent in alkali-silicate glasses.

Fig. 3 shows the temperature dependence of the proportions of SiO_4 units with 0-2 NBO/Si and the fractions of bridging oxygen (O^b) and non-bridging oxygen (O^n) in the $\text{K}_2\text{O}\cdot 4\text{SiO}_2$ from the glasses to the corresponding melts. As shown in this figure, the obtained Raman result indicates that the proportion behavior of SiO_4 units in the $\text{K}_2\text{O}\cdot 4\text{SiO}_2$ from glasses to the corresponding melts demonstrates no clear change for range from room temperature through the T_g up to the T_m , and the proportion gradually changes from above the T_g . It may be attributed to the depolymerization between SiO_4 units by rupturing Si-O-Si bonds in network with increasing temperature that the concentration of $\text{Si}_2\text{O}_5^{2-}$ sheet gradually increases, whereas the concentration of SiO_2^0 three-dimensional network decreases. The peak positions of the SiO_3^{2-} chain, $\text{Si}_2\text{O}_5^{2-}$ sheet and SiO_2^0 three-dimensional network species are only weakly temperature dependent as Fig. 4. This temperature effect may be as follows. Shiraishi (22) explained breakage of Si-O bridging bond with an increase of temperature from viscosity behavior of silicate melts. The $\text{K}_2\text{O}\cdot 4\text{SiO}_2$ glass and melt consist of major $\text{Si}_2\text{O}_5^{2-}$ sheet and SiO_2^0 three-dimensional network, and small amounts of SiO_3^{2-} chain units. The variation of SiO_4 units from the $\text{K}_2\text{O}\cdot 4\text{SiO}_2$ glass to the corresponding melt suggests that these SiO_4 species should arise from the following reaction:



By using the proportion of the SiO_4 units present in the $\text{K}_2\text{O}\cdot 4\text{SiO}_2$ glass and melt, the average coordination numbers can be calculated for the nearest-neighbor atomic pairs Si-Si, O-Si and O-O; i.e. $N_{\text{Si/Si}}$, $N_{\text{O/Si}}$ and $N_{\text{O/O}}$ were determined. These coordination numbers can be estimated using the following method.

(Method) Table 2 shows the average coordination numbers of the nearest-neighbor correlations Si-Si, O-Si and O-O for the SiO_4 units with 0-4 NBO/Si, i.e. $n_{\text{Si/Si}}$, $n_{\text{O/Si}}$ and $n_{\text{O/O}}$. The relationship between the bulk- and SiO_4 -unit's coordination numbers can be given as follows

$$\left. \begin{aligned} N_{\text{Si/Si}} &= 3 f_{(\text{NBO/Si}=1)} + 2 f_{(2)} \\ N_{\text{O/Si}} &= 1.75 f_{(1)} + 1.50 f_{(2)} \\ N_{\text{O/O}} &= 5.25 f_{(1)} + 4.50 f_{(2)} \end{aligned} \right\} \quad [6]$$

where $f_{(i)}$ ($i=1-2$) is the proportion of the SiO_4 units with the NBO/Si= i as indicated in Table 2. The results calculated from this method indicate in Table 3 and Fig. 5. The estimated values $N_{\text{Si/Si}}$, $N_{\text{O/Si}}$ and $N_{\text{O/O}}$ drop reasonably with the increase in the M_2O content due to a depolymerization reaction between SiO_4 units. As shown in Fig. 5, this tendency of the coordination obtained from the Raman results confirms that the prediction from simple consideration on basis of composition dependence of alkali silicate melt structure. The values of the coordination numbers for molten $\text{Na}_2\text{O}\cdot\text{SiO}_2$ obtained from X-ray diffraction measurement by Waseda et al. (24) are included in Fig. 6 for comparison. Waseda and his coworkers systematically carried out X-ray structural analysis of alkali alkaline earth silicate melts (24). As shown in Fig. 6, Waseda's results unfortunately indicate that the addition of Na_2O up to 60mol% has no effect on $N_{\text{Si/Si}}$ and $N_{\text{O/O}}$ in the molten $\text{Na}_2\text{O}\cdot\text{SiO}_2$ system (24), which is not agreement with our Raman results. When

M_2O (where M is an alkali metal) is added to an SiO_2 melt, it is widely accepted that physical properties such as viscosity drastically change (22), owing to the rupture of three-dimensional network structure. In the MRN model (2), the addition of one network modifier unit, M_2O , cause on bridging oxygen (BO) between two connected SiO_4 tetrahedra to be replaced by two non-bridging oxygen (NBO) atoms. The negative charge on the singly charged NBO's is balanced by the positively charged M^+ ions. Therefore, the authors consider that there is room for the X-ray results reported by Waseda et al. (24) to be remeasured.

Local structure of K_2O-SiO_2 glasses from soft XAFS measurement

Fig. 6 shows XANES spectra on K K -edge of the K_2O-SiO_2 system and $0.2(Al_2O_3)-0.8(K_2O-4SiO_2)$ glasses with those of the reference sample, nepheline and K_2CO_3 crystals. K-XANES obtained in this study are of good enough quality for comparisons to be useful in detecting structural differences in K^+ environments. Unfortunately, most of these spectra are probably due to multiple scattering about K^+ ions and not well understood. Therefore, XANES spectra can only be used as fingerprints for various known potassium coordination in the crystalline samples and can be compared with those of the glasses. As shown in Fig. 6, the obtained XANES spectra of these glasses are similar with each other.

EXAFS spectra of these potassium silicate glasses and crystalline compounds are of poor quality which is because of small back scattering amplitude and large disorder factor of oxygen. Normalized K EXAFS $k\chi(k)$ of $K_2O-4SiO_2$ glass is shown in Fig. 7. EXAFS oscillation out to a maximum k of only 7.5\AA^{-1} can be used in the data analysis, while the usable EXAFS spectra start as 2.5\AA^{-1} . For such a narrow range in k -space, only two clearly defined oscillations, and at times noisy third oscillation, can be included in our analysis. Analysis of such a narrow k -space range results in uncertainties in amplitude information retrieved from the EXAFS. This uncertainty influences the believability of coordination number and Debye-Waller factor values generated from non-linear least-squares fitting of $k^3\chi(k)$ data. The structure parameters, coordination number N (atoms), bond distance R (\AA) and Debye-Waller factor σ^2 (\AA^2), of the nearest neighbor pair K-O in K_2O-SiO_2 glasses as obtained from the least-squares fitting procedure are summarized in Table 4. Here, the N values obtained are normalized with that of reference sample, nepheline. As shown in Table 1, we have obtained double shell model (two kinds of nearest neighbor distance between potassium and oxygen ions) in $K_2O-4SiO_2$ glass, while in other two K_2O-SiO_2 glasses we have obtained single shell model, the bond distances of them being $3.0-3.07\text{\AA}$. The obtained K-O distances are not inconsistent with the sum of K^+ and O^{2-} ionic radii and with the bond distance value reported from the X-ray diffraction (27, 28). The results lead us to the disruption of network structure of SiO_4 tetrahedra and the formation of chain-like structure or nonbridging oxygen ions of SiO_4 tetrahedra as follows.

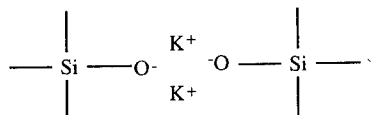


Fig. 8 shows the XANES spectra on Si K -edge of three kinds of silicate glasses with those of reference samples. The calculations of Si K -XANES for various silicon clusters have been reported (31, 32). The XANES spectra of crystalline nepheline and these three

silicate glasses in Fig. 8 exhibit quite similar feature with that of small SiO_4 cluster given by Fouil et. al.(31,32).

The whole range of XAFS spectra on Si K -edge are given in Fig. 9. The structure parameters, coordination number N (atoms), bond distance R (\AA) and Debye-Waller factor s^2 (\AA^2), of the nearest neighbor pairs Si-O in $\text{K}_2\text{O-SiO}_2$ glasses as obtained from the least-squares fitting procedure are listed in Table 5. Here average coordination numbers around Si atoms are fixed to the value of 4 in common during the curve fitting procedures because SiO_4 tetrahedra is the structural unit in the glass samples. The obtained bond distances are quite reasonable as compared with crystallographic data.

CONCLUSION

Raman spectra of $\text{K}_2\text{O-4SiO}_2$ glass and melt at different temperatures were measured by using high temperature Raman spectroscopy. Raman spectra observed in the frequency region from 800 to 1200cm^{-1} consist of four Raman bands near $960\sim980\text{cm}^{-1}$, $1020\sim1060\text{cm}^{-1}$, $1090\sim1110\text{cm}^{-1}$ and $1140\sim1160\text{cm}^{-1}$. These bands are attributed to the Si-O stretching vibrations for SiO_3^{2-} chain, $\text{Si}_2\text{O}_5^{2-}$ sheet and SiO_2^0 three-dimensional network units with two, one and zero non-bridging oxygen per silicon atom, respectively, and can be approximated by Gaussian curves. As a result, above the glass transition temperature T_g the SiO_2^0 species are gradually destroyed and the highly charged $\text{Si}_2\text{O}_5^{2-}$ sheet created with increasing temperature. The Raman results suggest that the reaction (5) is shifted to the left with increasing temperature. It is believed that the depolymerization of SiO_4 units with increasing temperature corresponds to the observed viscosity behavior of silicate melts. However, there is only slight difference between the Raman spectra of $\text{K}_2\text{O-4SiO}_2$ glass and melt, so that the glass structure is roughly similar to the corresponding melt as a zeroth-order approximation. The coordination numbers of the nearest neighbor correlations Si-Si, O-Si and O-O pairs in $\text{K}_2\text{O-4SiO}_2$ glass and melt are estimated from the fractions of the three SiO_4 species, and found to be in good agreement with the values in $\text{K}_2\text{O-4SiO}_2$ crystal.

Using the laboratory XAFS facility, we have performed to determine the local structure in potassium silicate glasses ($\text{K}_2\text{O-4SiO}_2$, $\text{K}_2\text{O-3SiO}_2$, $\text{K}_2\text{O-2SiO}_2$ and $0.2(\text{Al}_2\text{O}_3)\cdot0.8(\text{K}_2\text{O-4SiO}_2)$) respectively in order to elucidate the environment of modifying potassium ion which is extremely sensitive to the morphology of the network structure of glass system. The coordination numbers of oxygen around K^+ ion in $\text{K}_2\text{O-2SiO}_2$ and $\text{K}_2\text{O-3SiO}_2$ glasses are found to be 4~5 which is small compared with those of $\text{K}_2\text{O-4SiO}_2$ glass and crystalline nepheline ~9. The result indicates that the introduction of K_2O leads to the disruption of SiO_4 network structure and the formation of SiO_3^{2-} chain like structure or nonbridging oxygen ions as increasing quantity of K_2O . The local structure around silicon ions in some potassium silicate glasses are also compared with those of crystalline SiO_2 such as quartz and cristobalite.

REFERENCES

1. H. Ohno, N. Igarashi, N. Umesaki and K. Furukawa, "X-ray Diffraction Analysis of Ionic Liquids", Molten Salt Forum Vol. 3 (Trans Tech Publications, Switzerland, 1994), p. 1-230.
2. B. E. Warren and J. Biscoe, J. Am. Ceram., **21** (1938) 259.
3. R. Dupree, D. Holland, P. W. McMillan and R. F. Pettifer, J. Non-Cryst. Solids, **68** (1984) 399.
4. C. M. Schramm, B. H. W. S. de Jong and V. E. Parziale, J. Am. Chem. Soc., **106** (1984) 4396.

- 5 N. Iwamoto, N. Umesaki and K. Dohi, Trans. Japan Inst. Metals, **47** (1983) 382.
- 6 S. A. Brawer and W. B. White, J. Chem. Phys., **63** (1975) 2421.
- 7 B. O. Mysen, D. Virgo and C. M. Scare, Am. Mineral., **65** (1975) 2.
- 8 D. Virgo, B. O. Mysen and T. Kushiro, Science, **208** (1980) 1371.
- 9 N. Iwamoto, Y. Tsunawaki and S. Miyago, Trans. Inst. Metals, **43** (1979) 1138.
- 10 Y. Tsunawaki, N. Iwamoto, T. Hatori and A. Mitsuishi, J. Non-Cryst. Solids, **44** (1981) 369.
- 11 T. Furukawa, K. E. Fox and W. B. White, J. Chem. Phys., **75** (1980) 3226.
- 12 P. McMillan, Am. Mineral., **69** (1984) 622.
- 13 N. Umesaki, M. Takahashi, M. Tatsumisago and T. Minami, J. Mat. Sci., **28** (1993) 3473.
- 14 B. O. Mysen, L. W. Finger, D. Virgo and F. A. Seifert, Am. Mineral. **67** (1982) 686.
- 15 C. Senemaund, M. T. Costa Lima, J. A. Roger and A. Cachand, Chem. Phys. Lett. **26** (1974) 431.
- 16 H. Maeda, J. Phys. Soc. Japan **56** (1987) 2777.
- 17 G. A. Mckale, B. W. Veal, A. P. Paulikas, S. K. Chan and G. S. Knapp, J. Am. Chem. Soc. **110** (1988) 3763.
- 18 H. Scholze, "Glass-Nature, Structure and Properties", translated by M. J. Lakin, (Springer-Verlag, New York, 1990), p.73.
- 19 B. O. Mysen, D. Virgo and F. A. Seifert, Am. Mineral. **70** (1985) 88.
- 20 E. I. Kamitos, J. A. Kapoutsis, H. Jain and C. H. Hsein, J. Non-Cryst. Solids **171** (1994) 31.
- 21 B. M. Smets and T. P. Lommen, Phys. Chem. Glasses **22** (1981) 158; J. Non-Cryst. Solids **46** (1981) 21.
- 22 Y. Shiraishi and L. Granasy, Bulletin on the Research Institute of Mineral Dressing and Metallurgy Tohoku University **42** (1986) 42.
- 23 T. F. Soules, J. Chem. Phys. **71** (1979) 4570.
- 24 Y. Waseda, Progress in Materials Science **26** (1981) 85.
- 25 V. H. Schweinsberg and F. Libau, Acta Cryst. **B30** (1974) 2206.
- 26 N. Umesaki, M. Takahashi, M. Tatsumisago and T. Minami, J. Non-Cryst. Solids in press.
- 27 Waseda and H. Suito, Trans. Iron Steel Inst. Japan **62** (1976) 19.
- 28 I. Yasui, H. Hasegawa and M. Imaoka, Phys. Chem. Glasses **24** (1983) 65.
- 29 A. C. Hanoi, B. Vessal and J. M. Parker, J. Non-Cryst. Solids, **150** (1992) 97.
- 30 H. Schweinsberg and F. Liebau, Acta Cryst. **B30** (1974) 2206.
- 31 D. L. Foulis and A. M. Flank, *X-ray Absorption Fine Structure*, ed. S. Samar Hasnain, Ellis Horwood, New York, 1991, p.41-.
- 32 D. L. Foulis, R. F. Pettifer, C. R. Natori and M. Benfatto, Phys. Rev. **A41** (1990) 6922.

Table 1 Raman frequencies of the Si-O stretching modes due to SiO_4 units with 0~4
NBO/Si in alkali and alkaline earth silicate glasses (6-14).

SiO_4 unit	Bonding state of bound oxygen	NBO/Si number	Frequency (cm^{-1})
SiO_2^0 three-dimensional network	$\begin{array}{c} \\ \text{O} \\ \\ \text{---O---Si---O---} \\ \\ \text{O} \\ \end{array}$	0	1060~1065 1190~1200
$\text{Si}_2\text{O}_5^{2-}$ sheet	$\begin{array}{c} \cdot\text{O} \\ \\ \text{---O---Si---O---} \\ \\ \text{O} \\ \end{array}$	1	1030~1100
SiO_3^{2-} chain	$\begin{array}{c} \cdot\text{O} \\ \\ \text{---O---Si---O---} \\ \\ \cdot\text{O} \end{array}$	2	950~970
$\text{Si}_2\text{O}_7^{6-}$ dimer	$\begin{array}{c} \cdot\text{O} \\ \\ \cdot\text{O---Si---O---} \\ \\ \cdot\text{O} \end{array}$	3	900~930
SiO_4^{4-} monomer	$\begin{array}{c} \cdot\text{O} \\ \\ \cdot\text{O---Si---O}\cdot \\ \\ \cdot\text{O} \end{array}$	4	850~890

Table 2 Coordination numbers of nearest neighbor correlation Si-Si, O-Si and O-O for SiO_4 units with 0~2 NBO/Si.

SiO_4 unit	Bonding state of bound oxygen	NBO/Si number	Coordination number		
			$n_{\text{Si/Si}}$	$n_{\text{O/Si}}$	$n_{\text{O/O}}$
SiO_2^0 three-dimensional network	<pre> O —O—Si—O— O </pre>	0	4.00	2.00	6.00
$\text{Si}_2\text{O}_5^{2-}$ sheet	<pre> ·O —O—Si—O— O </pre>	1	3.00	1.75	5.25
SiO_3^{2-} chain	<pre> ·O —O—Si—O— ·O </pre>	2	2.00	1.50	4.50

Table 3 Coordination numbers of the nearest neighbor Si-Si, O-Si and O-O pairs in $M_2O \cdot 4SiO_2$ (M=Na, K and Rb) glass, melt and crystal.

Sample	Temperature (K)	Coordination			Method	Ref.
		NSi/Si	NO/Si	NO/O		
Na ₂ O 4SiO ₂	r. temp. (G)	4.2	—	6.1	MD	Soules (23)
	1723 (M)	3.9	—	5.5	X.D.	Waseda (24)
K ₂ O 4SiO ₂	r. temp. (G)	3.60	1.91	5.73	R.S.	This work
	743 (G)	3.44	1.86	5.58		
	793 (G)	3.41	1.85	5.56		
	993 (G)	3.30	1.83	5.48		
	1143 (M)	3.43	1.87	5.60		
K ₂ O 4SiO ₂	1273 (M)	3.41	1.87	5.61	X.D.	Scweinsberg (25) Waseda (24)
	r. temp. (C)	3.5	1.88	5.63		
	1383 (M)	3.9	—	3.8		
Rb ₂ O 4SiO ₂	r. temp. (G)	3.38	1.85	5.54	R.S.	Umesaki (26)
	603 (G)	3.40	1.85	5.55		
	783 (G)	3.37	1.84	5.53		
	1023 (G)	3.30	1.82	5.47		
	1143 (G)	3.35	1.84	5.51		
	1303 (M)	3.23	1.81	5.42		

C: Crystal; G: Glass; M: Melt

R.S.: Raman Spectroscopy; X.D.: X-ray Diffraction; MD: Molecular Dynamics

Table 4 The structural parameters obtained by curve-fitting analysis. The obtained coordination number N (atoms), bond distance R (Å) and Debye-Waller factor σ^2 (Å²) of the nearest neighbor K-O in K₂O-SiO₂ glasses are listed.

Sample	K-O		
	N (atoms)	R (Å)	σ^2 (Å ²)
(EXAFS)			
K ₂ O 4SiO ₂ glass	5) 4) ⁹	2.72 3.00	0.013 0.014
K ₂ O 3SiO ₂ glass	4~5	3.00	0.014
K ₂ O 2SiO ₂ glass	4~5	3.10	0.020
(ND)			
0.261K ₂ O 0.739SiO ₂ glass (29)	3.85	2.67 ^{b)}	0.0113 ^{b)}
(ND)			
0.172Li ₂ O 0.147K ₂ O 0.73SiO ₂ glass (29)	3.40	2.67 ^{b)}	0.012 ^{b)}
K ₂ O 0.2SiO ₂ glass (27)	7.6 ^{a)}	2.65 ^{b)}	0.014 ^{b)}
(XRD)	6.9 ^{a)}	2.65 ^{b)}	0.016 ^{b)}
(ND)			
(XRD)			
K ₂ O-SiO ₂ glass (28)	7	2.750~3.342	
(XRD)			
K ₄ Si ₈ O ₁₈ crystal (30)	6	2.677~3.171	
(EXAFS)			
Nepheline KNa ₃ (AlSiO ₄) ₄	6	2.687~3.152	
(XRD)			
Nepheline KNa ₃ (AlSiO ₄) ₄	9	3.02	

XRD: X-ray Diffraction; ND: Neutron Diffraction

a) These values are estimated from the assumption that the coordination number of O-O pair is the constant value of 5.6 in pure SiO₂.

b) These values represent the sum of the nearest neighbor O-O and K-O pairs due to the combined O-O and K-O peaks in the obtained radial distribution function r.d.f.).

Table 5 The structural parameters obtained by curve fitting analysis. The obtained coordination number N (atoms), distance R (Å) and Debye-Waller factor σ^2 (Å²) of the nearest neighbor Si-O in K₂O-SiO₂ glasses are listed.

Sample	Si-O		
	N (atoms)	R (Å)	σ^2 (Å ²)
(EXAFS) K ₂ O-4SiO ₂ glass	4	1.63	0.001
0.2(Al ₂ O ₃)-0.8(K ₂ O- 4SiO ₂) glass	4	1.65	0.006
SiO ₂ glass	4	1.64	0.005
SiO ₂ quartz	4	1.64	0.002
SiO ₂ cristobalite	4	1.64	0.002

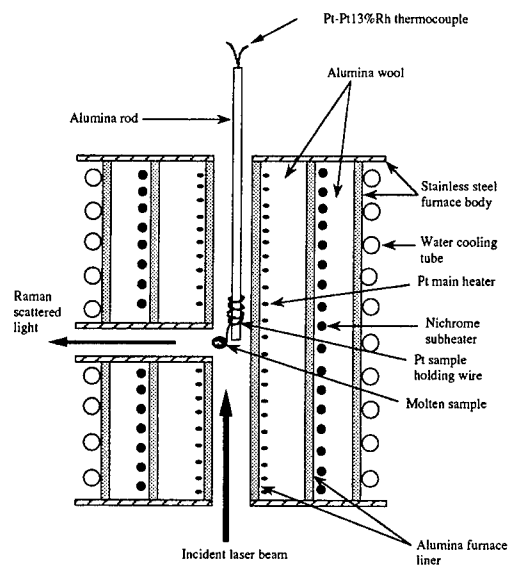


Fig. 1 Schematic diagram of a furnace for high temperature Raman spectroscopy.

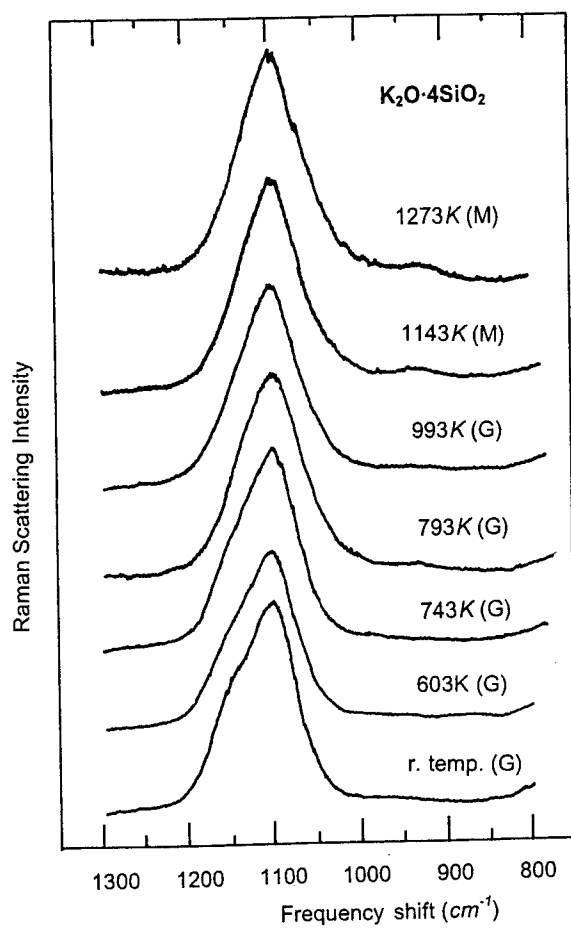


Fig. 2 Raman spectra of $K_2O \cdot 4SiO_2$ glass and melt at different temperatures.

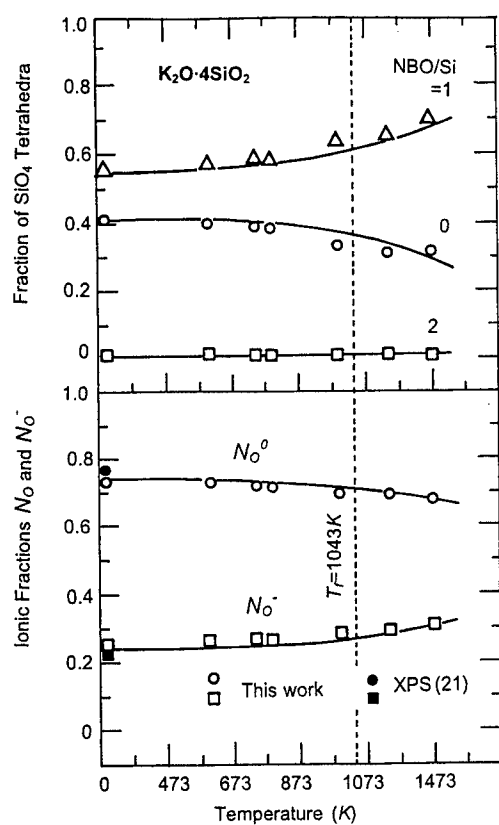


Fig. 3 Temperature dependence of the fractions of (a) SiO_4 units with 0, 1 and 2 NBO/Si, and (b) O^0 and O^- in $\text{K}_2\text{O} \cdot 4\text{SiO}_2$ glass and melt. Included in this figure for comparison are the data for $\text{M}_2\text{O} \cdot 4\text{SiO}_2$ ($\text{M}=\text{Na}$ and K) glasses obtained by XPS measurement (21).

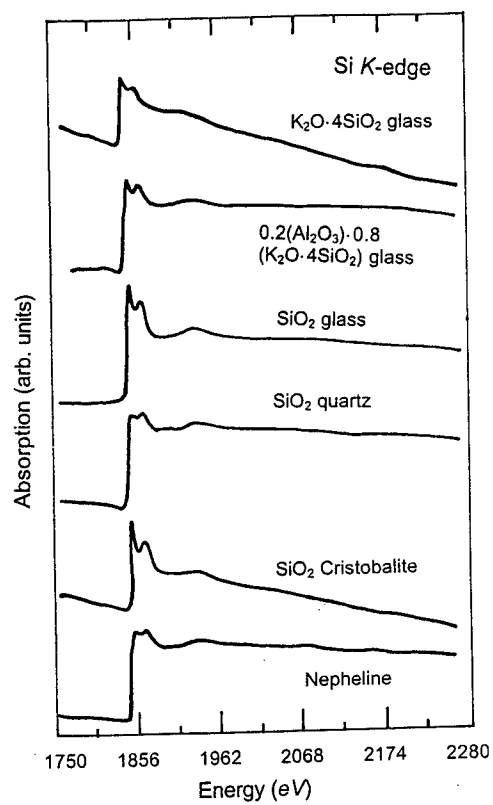


Fig. 9 EXAFS spectra of Si K-edge in K₂O-SiO₂ glasses and reference samples.

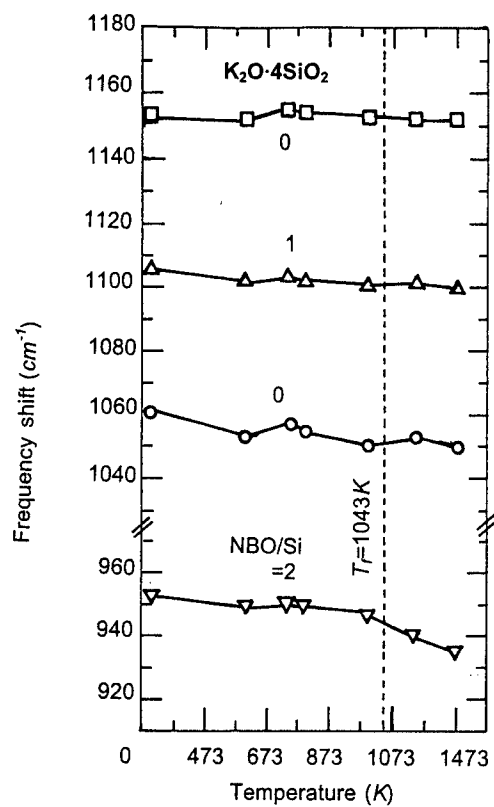


Fig. 4 Temperature dependence of the four Gaussian band positions of $K_2O \cdot 4SiO_2$ glass and melt.

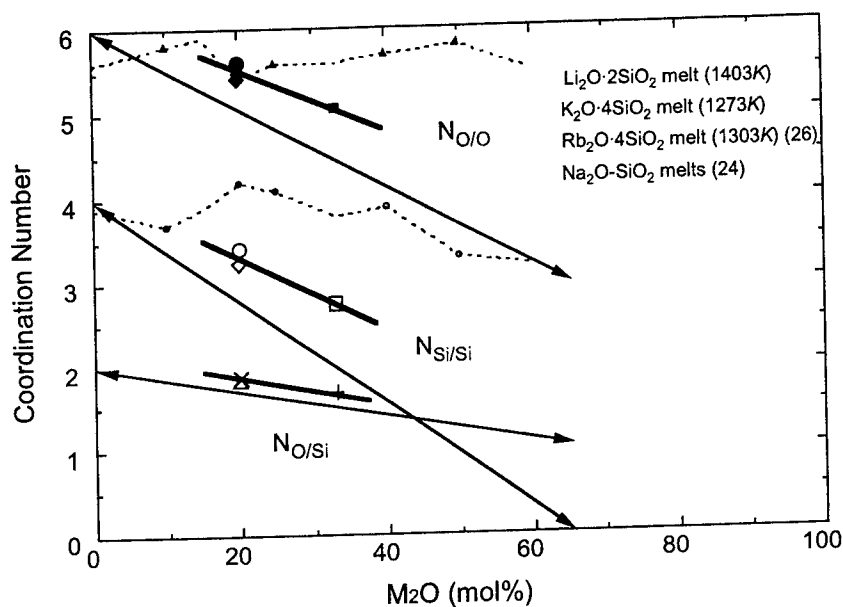


Fig. 5 Composition dependence of the coordination numbers (dotted line) of the nearest neighbor correlations Si-Si, O-Si and O-O in molten $M_2O \cdot 4SiO_2$ ($M=Na$ and K) and $Li_2O \cdot 2SiO_2$ at 1403K (5) obtained from the Raman spectra. The solid lines represent the coordination number estimated from the composition dependence on silicate units. Included in this figure for comparison are the data for molten system $Na_2O \cdot SiO_2$ obtained by X-ray diffraction (26).

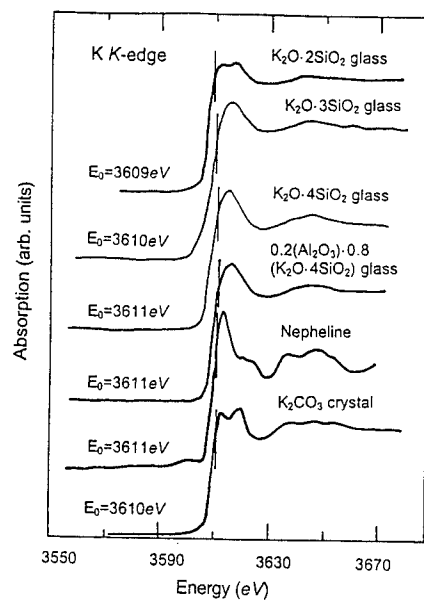


Fig. 6 XANES spectra of K *K*-edge in K_2O-SiO_2 glasses and reference crystals. Here, E_0 indicates the primary inflection point in the edge.

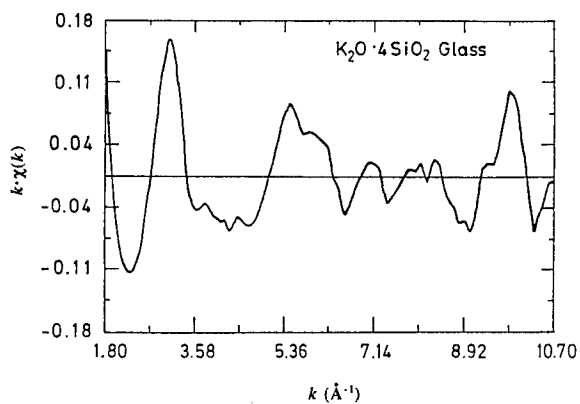


Fig. 7 k -weighted EXAFS oscillation of $K_2O \cdot 4SiO_2$ glass.

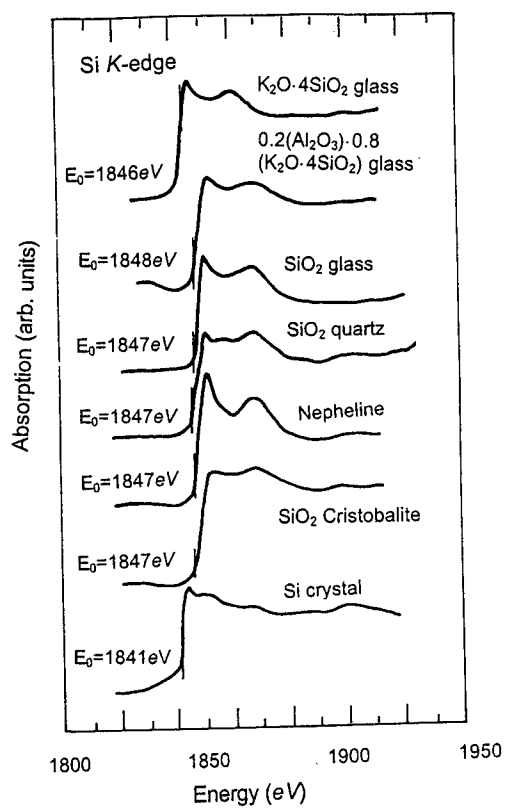


Fig. 8 XANES spectra of Si K-edge in $\text{K}_2\text{O}\text{-SiO}_2$ glasses and reference crystals. Here, E_0 indicates the primary inflection point in the edge.

AUTHOR INDEX

- | | |
|----------------------------------|-------------------------------|
| Akai, Y. 230 | Gilbert, B. 11 |
| Arsenin, K. I 312 | Goto, T. 62 |
| Asai, T. 417 | Haarberg, G. M. 157, 290, 468 |
| Bi, G. 53 | Handa, K. 541 |
| Bjerrum, N. J. 1 | Hara, S. 484 |
| Blander, M. 3 | Hasiotis, C. 530 |
| Boghosian, S. 74 | Hayashi, S. 334 |
| Böhme, O. 396 | Hayes, G. R. 152 |
| Børresen, B. 11, 157 | Hebant, P. 500 |
| Brenscheidt, Th. 396 | Henriksen, G. L. 342 |
| Carlin, R. T. 104, 284, 362, 372 | Hoshino, Y. 222 |
| Carmo, A. J. S. 125 | Hussey, C. L. 36 |
| Carountzos, G. 530 | Ichino, R. 320 |
| Chandler, W. D. 92 | Inoue, T. 334 |
| Chauvin, Y. 70 | Ishikawa, T. 236 |
| Cheek, G. T. 116 | Ito, Y. 62 |
| Chamelot, P. 269 | Iwabuchi, K. 179 |
| Chou, P. 511 | Jansen, A. N. 342 |
| Chrissanthopoulos, A. 74 | Jentoftsen, T. E. 290 |
| Cina, T. S. 53 | Johnson, K. E. 92 |
| Curtiss, L. A. 492 | Kamijo, N. 541 |
| Dai, S. 152, 524 | Kamiya, N. 406 |
| Deki, S. 28 | Kanematsu, H. 334 |
| Del Cul, G. D. 152 | Kanjinami, A. 28 |
| De Long, H. C. 276, 284 | Kaptay, G. 303, 312 |
| Deviatkin, S. V. 303, 312 | Katagiri, A. 244 |
| Dracopoulos, V. 11 | Kaun, T. D. 342 |
| Dubsky, J. 53 | Kawagoe, T. 144 |
| Egan, J. J. 468 | Kawaguchi, N. 179, 189 |
| Elias, A. M. 125 | Kawakami, M. 171 |
| Elias, M. E. 125 | Kazmierczak, J. 157 |
| Endo, M. 179, 204, 222 | Kijima, Y. 213 |
| Eriksen, K. M. 74 | King, D. 80 |
| Fahlman, B. D. 92 | Kisza, A. 157 |
| Fehrmann, R. 74 | Kojima, T. 406, 417 |
| Fujita, R. 230 | Konda, S. 236 |
| Fukamachi, T. 213 | Kondo, J. 28 |
| Fuller, J. 362, 372 | Kontoyannis, C. G. 530 |
| Gaune-Escard, M. 439 | Koura, N. 492 |

- Kunieda, Y. 334
 Kuznetsov, S. A. 303
 Lafage, B. 269
 Lee, Y. H. 524
 Leis, K. S. 135
 Lugovoi, V. P. 303
 Mantz, R. A. 104
 Masters, S. G. 74
 Matsunaga, M. 355
 Minamoto, K. 355
 Mitani, Y. 171
 Mitchell, J. A. 36
 Miyazaki, Y. 417
 Mohamedi, M. 189
 Morimitsu, M. 355
 Motohira, N. 406
 Nakahara, H. 28
 Newman, D. S. 53, 135
 Nielsen, K. 74
 Oehlers, C. 74
 Ohtori, N. 541
 Okada, I. 511
 Okano, Y. 244
 Oki, T. 334
 Okido, M. 320
 Olivier, H. 70
 Osada, T. 144
 Osteryoung, R. A. 80, 104
 Ota, K. 204, 222, 406
 Papatheodorou, G. N. 11
 Peterson, J. R. 152
 Peterson, R. D. 254
 Photiadis, G. 11
 Picard, G. S. 500
 Pitner, W. R. 36
 Riechel, T. L. 381
 Rosinski, J. 135
 Ryan, D. M. 381
 Saboungi, M.-L. 492
 Saito, S. 179
 Sakata, T. 204, 213, 222, 236
 Sato, Y. 179, 189
 Seiki, S. 492
 Selman, J. R. 388, 422
 Snavely, D. L. 53
 Stafford, G. R. 36
 Støre, T. 290
 Sugimoto, A. 171
 Suzuki, T. 204, 213, 222
 Suzuya, K. 492
 Tada, M. 62
 Takahashi, J. 213
 Takahashi, S. 492
 Takasawa, Y. 204
 Takenaka, T. 171
 Tamiya, Y. 417
 Tamura, R. 320
 Tanabe, N. 492
 Tanaka, T. 484
 Tanimoto, K. 417
 Tasaka, A. 144
 Taxil, P. 269
 Teramae, N. 204
 Toda, K. 406
 Toth, L. M. 152
 Toyabe, K. 213
 Tsuchiya, H. 204, 213, 222
 Tunold, R. 157, 290
 Trulove, P. C. 104, 276
 Ueda, M. 236
 Umesaki, N. 541
 Vissers, D. R. 342
 Wang, X. 254
 Wendt, H. 396
 Xiao, H. M. 524
 Yamagami, S. 204, 222
 Yamamura, T. 179, 189
 Yanagida, M. 417
 Yazici, M. S. 388, 422
 Young, J. P. 524
 Zamborini, F. 53
 Zhu, H. 179

SUBJECT INDEX

- Acetonitrile/LiAlCl₄ 116
Acid-Base Chemistry 80, 92, 104, 116, 125, 152
Actinide Halides 230
Acyl Halides 116
Adiabatic Compressibility 28
AlF₃-NaF 236
AlF₃-B₂O₃ 312
Alkylaluminiums 70
Aluminum Alloys 36, 179, 276, 284, 303, 334, 342, 362
Aluminum Chloride 36, 53, 70, 80, 92, 104, 116, 135, 152, 179, 276, 284, 355, 362, 372, 381
Aluminum Electrorefining 236, 254, 334
Ambient Temperature/Room Temperature 28, 36, 53, 70, 80, 92, 104, 116, 125, 135, 152, 276, 284, 362, 372, 381, 492
Anthracene 80

BaCl₂-NaCl 236
BaF₂-LiF-UF₄ 204, 222
Batteries 320, 342, 355, 362, 372, 381
Benzoyl Chloride 116
Beta"-Alumina 355
BF₄⁻ 70, 303, 362
BF₃-HF-MF 92
Biomass 3
Borides 303
Brønsted Acidity 80, 92
Buffered Chloroaluminate Melt 80, 104, 362, 372, 381

CaCO₃ 3
Carbonate Electrolytes for Fuel Cells 388, 396, 406, 417, 422, 524
CaSO₄ 3
Carboxylate 28
Catalysis 70, 74
Chlorine 213
Chloroaluminate 36, 53, 70, 80, 92, 104, 116, 135, 179, 276, 284, 355, 362, 372, 381
Chromium 276, 388
Coatings 62, 303
Conductivity 254, 439, 492, 500
Cobalt 36, 284
Combustion 3

Copper 492
Corrosion 3, 222, 244, 388, 406, 417
CuCl 492
Cryolite 254

Differential Scanning Calorimetry 135
Dimerization 70
Dissolution 334

Electrochemical Quartz Crystal Microbalance (EQCM) 276, 284
Electrodeposition 36, 62, 157, 171, 179, 189, 204, 230, 236, 269, 276, 284, 290,
303, 320, 362, 372, 492, 530
Electron Mobility 468
Electrolysis 144
Enthalpies 439

FeS₂ 342
Fiber Optics 524
Flemion 53
Fluoride Addition 171
Friedel-Crafts 53
Fuel Cells 388, 396, 406, 417, 422
Fuel Cell Additives 396, 417

Glass Transition 125
Glasses 541
Glassy Carbon 244, 303
Graphite 222
Gutmann Acceptor 104

Hexamethylbenzene 80
High Power Battery 342
Homogeneous Catalysis 70, 74
Hydrates 28
Hydrogen Bonding 28, 92, 125
Hydrogen Chloride 80, 92, 125
Hydrogen Fluoride 92, 144
Hydroformylation 70
Hydrogen Absorption 320
Hydrogenation 70
Hydrophobic 28

Imidazolium 36, 70, 80, 104, 116, 276, 284, 362

Impedance Spectroscopy 355
Infrared Spectroscopy 53, 125
Ionic Dissociation 500
Ionic Mobility 396, 511
Iron 388

KBr 468
KCl 254, 468
KCl-LiCl 62, 230, 290, 320, 530
KCl-NaCl 171, 334
 K_2CO_3 3
KI 468
Kinetics 135
 K_2O-SiO_2 541
 K_2SO_4 3
 $K_2S_2O_7-V_2O_5$ 72

LaNi₅ 320
Lanthanide Halides 11, 230, 439
Latent acidity 80, 104
Lead 290
Lewis Acidity 104, 116, 152
LiAl alloys 342, 362
LiAlCl₄ 116
LiCl-LiBr-KBr 342
LiF-NaF 269
Li/FeS₂ Battery 342
Li₃N 62
Lithium 362, 372
Lithium Halide Additive 342
LiX-KX Ionic Dissociation 500

Magnesium 157
Melting Point Transition 125
 $MgCl_2-CaCl_2KCl-NaCl$ 524
 $MgCl_2-NaCl$ 157, 189
Molten Carbonate Fuel Cells (MCFC) 388, 396, 406, 417, 422
Molybdenum 222

NaAlCl₄ 179, 355
NaBr 468
NaCl 254, 468
NaCl-KCl-KBF₄-K₂ZrF₆ 303

NaI 468
 NaNO₃-KNO₃
 Nb₃Cl₈ 179, 189
 Near-IR Spectroscopy 152
 Neutron Diffraction 492
 NH₄F-HF 144
 Nickel 244, 320, 388
 Niobium 179, 189, 269
 Nitrates 511
 Nitride 62
 Nitrogen 62
 Nitrogen Fluorides 144
 NMR 92, 104
 NO_x 74
 Nucleation 157, 290

 Olefin 70
 Optical Microscopy 372
 Oxidation 74

 PbCl₂ 290
 PF₆⁻ 70
 Phase diagram 236
 Picolinium 125
 Platinum 244, 254
 Polymer 53
 Protective Coatings 62, 303
 Pyridinium 53, 125, 135, 492

 Raman Spectroscopy 11, 524, 530
 Rare Earth Halides 11, 230, 439

 SbCl₅-HCl 92
 SbF₆⁻ 70
 Separation Factor 230
 Separator 53, 355, 417, 422
 Silicate Glasses 531
 Silicon 334
 Silver Ion 511
 SO₂ 74
 SOCl₂ 152, 362, 372
 Sodium 362, 372
 Solid Electrolyte Interphase (SEI) 362, 372

Square Wave Voltammetry 269
Stainless Steel 388, 417, 422
Surface Tension 484

Tantalum 269, 406
Thallium Ion 511
Theoretical Structure Calculations 92, 439, 492, 500, 511
Thermodynamic Calculations 3, 303, 312, 439, 484
Thin Films 62, 320,
Thionyl Chloride 152
TiN 62
Titanium 171
Transuranium Elements 230
Triflate 70
Tungsten 222, 244, 530
Two-Phase Catalysis 70

Ultrasonic Velocity 28
Underpotential Deposition (UPD) 36, 276, 284
Uranium 152, 204, 213, 222
Uranium Fluorides 204
Uranium Chlorides 152, 213
UV-vis Spectroscopy 80, 152, 381

Vanadium Oxide Cathodes 381
Viscosity 492
 V_2O_5 74, 381

Water 28, 352

XAFS 531
XANES 531
XPS 144

Zinc 244
Zirconium Diboride 303
 $ZnCl_2$ -NaCl 244

